A magnetic study of the west Iberia and conjugate rifted continental margins: constraints on rift-to-/drift processes

Russell, Simon Mark

A Magnetic Study of the West Iberia and Conjugate Rifted Continental Margins: Constraints on Rift-to-Drift Processes

Simon Mark Russell

A thesis submitted for the degree of Doctor of Philosophy

University of Durham

Department of Geological Sciences

1999

To Mum

Acknowledgements

This thesis would not have been possible without the help and encouragement of many people from both inside and outside the academic community. Firstly, I wish to thank my two supervisors, Bob Whitmarsh and Roger Searle, without whom this project would not have been possible. I am indebted to Bob for his exceedingly prompt and thorough reviews. I thank Roger for providing the opportunity for me to participate in an additional research cruise to the Mid-Atlantic Ridge. My participation in national and international conferences and meetings would not have been possible without the additional funds made available by them both.

I also wish to thank Peter Miles at SOC for providing a large part of the dataset used in this thesis, and also for providing additional help, especially during my initial stay in Southampton. Thanks also to Jean-Claude Sibuet, Eliane Le Drezen and the SAR technicians for working hard to provide the SAR data under extremely difficult conditions, and to the crew and scientists who participated during RRS Discovery Cruise 215.

I have enjoyed fruitful discussion with Tim Minshull, Simon Dean, Simon Pickup, Simon Allerton, Javier Escartin and Lawrence Hopkinson, amongst others, regarding subjects related to this thesis and further afield. Lastly, I thank my friends and piers in Durham and Southampton for helping me along during the last three and a half years, in particular Chris Gosden for providing lodgings during my extended stay in Southampton.

This Ph.D. was funded by the Natural Environment Research Council with additional funding provided by Southampton Oceanography Centre under the CASE scheme.

Abstract

The analysis and modelling of magnetic anomalies at the conjugate rifted continental margins of the southern Iberia Abyssal Plain (IAP) and Newfoundland Basin have revealed that the sources of magnetic anomalies are distinctly different across both each margin and between the two margins.

Analyses of synthetic anomalies and gridded sea surface magnetic anomaly charts west of Iberia and east of Newfoundland were accomplished by the methods of Euler deconvolution, forward and inverse modelling of the power spectrum, reduction-to-the-pole, and forward and inverse indirect methods. In addition, three near-bottom magnetometer profiles were analysed by the same methods in addition to the application of componental magnetometry. The results have revealed that oceanic crust, transitional basement and thinned continental crust are defined by magnetic sources with different characteristics.

Over oceanic crust, magnetic sources are present as lava-flow-like bodies whose depths coincide with the top of acoustic basement seen on MCS profiles. Top-basement source depths are consistent with those determined in two other regions of oceanic crust. In the southern IAP, oceanic crust, ~4 km thick with magnetizations up to ±1.5 A/m, generated by organized seafloor spreading was first accreted ~126 Ma at the position of a N-S oriented segmented basement peridotite ridge. To the west, seafloor spreading anomalies can be modelled at spreading rates of 10 mm/yr or more. Immediately to the east, in a zone ~10-20 km in width, I identify seafloor spreading anomalies which can only be modelled assuming variable spreading rates.

In the OCT, sources of magnetic anomalies are present at the top of basement and up to ~6 km beneath. I interpret the uppermost source as serpentinized peridotite, and the lowermost source as intruded gabbroic bodies which were impeded, whilst rising upwards, by the lower density serpentinized peridotites. Intrusion was accompanied by tectonism and a gradual change in conditions from rifting to seafloor spreading as the North Atlantic rift propagated northwards in Early Cretaceous times.

Within thinned continental crust, sources are poorly lineated, and distributed in depth. Scaling relationships of susceptibility are consistent with the sources of magnetic anomalies within continental crust. OCT-type intrusions may be present in the mantle beneath continental crust.

At the conjugate Newfoundland margin, seafloor spreading anomalies can be modelled at rates of 8 and 10 mm/yr suggesting an onset age consistent with that of the IAP. In the OCT there, I propose that magnetic anomalies are sourced in near top-basement serpentinized peridotites. An absence of magmatic material and the differences in basement character (with the IAP) suggest that conjugate margin evolution may have been asymmetric.

Contents

List of Figures

List of Tables

Chapter One

Introduction

Rifted continental margins mark the juxtaposition of continental and oceanic lithosphere within a plate interior. They are the product of a) successful lithospheric rupture within an intracontinental rift zone followed by b) continental separation accomplished by the process of seafloor spreading (Hess, 1962). The primary aim of this thesis is to better understand how these processes have contributed to the formation of the West Iberia rifted continental margin and its conjugate margin adjacent to the Grand Banks of Newfoundland. The means of achieving this aim comes from the detailed analysis and interpretation of the local magnetic field in and around these two regions by the application of traditional and new magnetic techniques.

In this short chapter, sections 1.1 and 1.2 introduce the general features and processes responsible for the formation of rifted continental margins and oceanic crust in general. Section 1.3 introduces some aspects concerning the geomagnetic field, section 1.4 concerns itself with aspects of magnetic field measurement and analysis, whilst in section 1.5 I present a very brief review of the sources of near-surface magnetic anomalies.

1.1 Lithospheric rupture and the formation of rifted continental margins

Continental rifting is a geological process dominated by tectonism. Magmatism contributes to a greater or lesser degree depending on various characteristics of the lithosphere and underlying asthenosphere at the position and time of rifting. Typically, modern rift zones are areas marked by abundant normal faulting, shallow earthquake activity, varying degrees of volcanism, and usually high topographic relief, such as the East African rift system and the Baikal rift of central former USSR. A simple definition of a continental rift, modified from that of Burke (1977), is given by Olsen and Morgan (1995) and is defined as "an elongate tectonic depression associated with which the entire lithosphere has been modified in extension". This does not necessarily imply that deformation is uniformly vertically distributed, as in the model of Wernicke (1985) for example, but it does rule out small extensional features in which only the upper part of the lithosphere is in extension. The definition also implicitly includes the transient thermal and permanent structural

and compositional alterations made to the lithosphere during the extensional process. Based on this definition, continental rifts can be further classified into modern rifts and palaeorifts. Modern rifts have active extension-related tectonic and/or magmatic activity, and/or have a transient thermal phenomena, such as high heat flow, thermal uplift or low mantle seismic velocities (Ramberg and Morgan, 1984). Examples include the East African rift system, the European Cenozoic rift system, the Baikal rift system and the Rio Grande rift. Palaeorifts are tectonically and magmatically inactive with no transient thermal phenomena (Neumann and Ramberg, 1978; Ramberg and Morgan, 1984). Examples include the Oslo rift, the West and Central African rift system, the USA Mid-continent rift system and conjugate rifted continental margin pairs whose ages exceed the 60 Ma time constant for thermal relaxation of the lithosphere.

The initiation of the rifting process, and the origin of the tensional stresses, have been the subject of much debate for over two decades. The uncertainty as to whether rifts are either active or passive features, in general, or in specific cases, has been addressed by many authors (e.g. Sengor and Burke, 1978; Illies, 1981; Spohn and Schubert, 1982; Buck, 1986). So-called active rifting is driven by the convection of hot asthenospheric mantle which upwells onto the base of the continental lithosphere causing plate thinning and plateau uplift. A mantle plume is an example of the cause of such rifting. Passive rifting is driven by far field tensional forces that cause lithospheric plate extension and necking whereby asthenospheric mantle flows upward to accommodate the potential void. Such tensional forces may be created within, or behind, collision zones (Lesne et al., 1998), for example. Theoretically, it should be possible to distinguish between models on the basis of relative timing of volcanism, uplift and extension but field observations suggest these models are too simplistic. It seems that the mechanisms of active and passive rifting are likely to be extremes in a continuous spectrum of processes. Regardless of the mechanism for rifting, asthenospheric upwelling is a fundamental process in the formation of a continental rift (Basaltic Volcanism Study Project, 1981). Moreover, the fact that either mechanism (of passive and active rifting) is only responsible for the *initiation* of rifting suggests that once underway subsequent development of the rift is complicated by the interaction of other processes.

The degree of magmatism in the rifting process is of prime importance here. If continental rifting continues until lithospheric rupture occurs and oceanic accretionary crust is formed, then the resultant rifted margin can broadly be classed as either volcanic or non-volcanic (Fig. 1.1). Rifted margins associated with high degrees of magmatism are called volcanic continental margins, whereas rifted margins associated with very low degrees or no magmatism are called non-volcanic

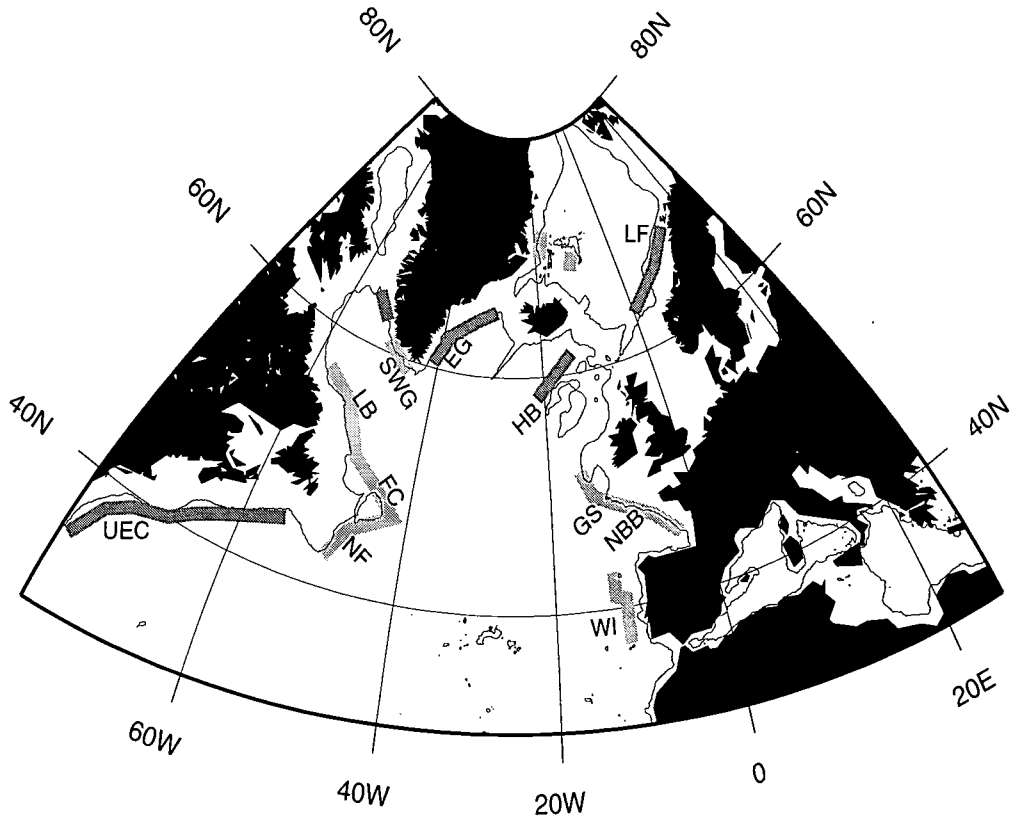

Figure 1.1 Distribution of volcanic (dark grey) and non-volcanic (light grey) continental margins in the North Atlantic. UEC=US East Coast margin, WI=West Iberia margin, NF=Newfoundland margin, GS=Goban Spur, NBB=Northern Bay of Biscay margin, FC=Flemish Cap, HB=Hatton Bank, SWG=Southwest Greenland margin, LB=Labrador margin, EG=East Greenland margin, LF=Lofoten margin.

margins. Typical features of volcanic margins are seaward dipping lava flow sequences at or in the uppermost continental and oceanic crust, and magmatic material underplated at the base of the crust and/or intruded into the lower crust. Non-volcanic margins are generally characterized by tilted and rotated continental fault blocks with little sign of intrusive or extrusive igneous activity. Such fault blocks may exist at volcanic margins, although they are masked by thick lava flow and intrusive bodies making them almost impossible to image on seismic reflection profiles. Hatton Bank and Goban Spur margins are used as examples of volcanic and non-volcanic end members, respectively (Fig. 1.2).

With this simple bipolar classification scheme came explanations and models of formation of the two types of margins. Bott (1995) suggested that if rifting resulted in lithospheric rupture and the formation of an ocean basin, the process of active rifting would give rise to the formation of volcanic type margins, whereas the process of passive rifting would give rise to the formation of

non-volcanic margins. Furthermore, the emplacement of large volumes of melt derived products is commonly attributed to steady state mantle plume activity (e.g., White, 1989; White and McKenzie, 1989; Duncan and Richards, 1991; Larson, 1991). Examples of such margins are the Hatton Bank, Southeast Greenland, and Lofoten margins, all of which were formed by the interaction of the Iceland plume with the base of the lithosphere. Although mantle plume activity might often explain the presence of large amounts of igneous material at volcanic margins, it is not a necessary condition. Along the US East Coast margin, a 20-25 km thick igneous crustal section, 60 km wide and 2000 km long, is thought to be present. However, there is an absence of any independent evidence to suggest a mantle plume was responsible for its formation (Holbrook and Keleman, 1993; Talwani et al., 1995). A relatively long-lived mantle plume would leave a track of anomalously thick oceanic crust in the form of an aseismic ridge as the plate moved over the plume, as exemplified by the association of the Rio Grande Rise and Walvis Ridge with the Tristan da Cunha hotspot. This phenomenon is not seen along any part of the US East Coast margin. Possible explanations for the large volume of magmatic products include lateral plume-derived melt migration, 'hot blobs' (Holbrook and Keleman, 1993), secondary convection (Mutter et al., 1988; Zehnder et al., 1990; Vogt, 1991; Hopper et al., 1992), and broad upper mantle generated thermal anomalies (Gurnis, 1988; Anderson et al., 1992). Although two archetypal end members exist, many margins show features common to both margin types. This suggests that there exists a continuum of processes responsible for the formation of rifted continental margins in general. However, it is believed that the West Iberia margin sits very firmly at the non-volcanic end of the spectrum because of the lack of evidence of melt derived products (e.g. Whitmarsh et al., 1990; Pinheiro et al., 1992; Sibuet, 1992; Whitmarsh et al., 1993; Whitmarsh and Miles, 1995; Pickup et al., 1996; Whitmarsh and Sawyer, 1996).

The degree of volcanism is highly dependent upon the duration of rifting, the amount of extension (β), the initial lithospheric (mechanical boundary layer) thickness, and hence the depth of onset of melting, and the potential temperature of the underlying asthenospheric mantle (Foucher et al., 1982; Furlong and Fountain, 1986; McKenzie and Bickle, 1988; Pedersen and Ro, 1992; Bown and White, 1995). The model of Bown and White (1995) has been used to calculate actual thicknesses of melt produced under certain assumptions; continental lithosphere, 125 km thick overlying an asthenosphere with potential temperature of 1400 °C, is allowed to thin by pure shear extension (McKenzie, 1978) so that the asthenosphere-lithosphere boundary moves vertically upwards through time. As a volume of asthenospheric material ascends, it decompresses and its

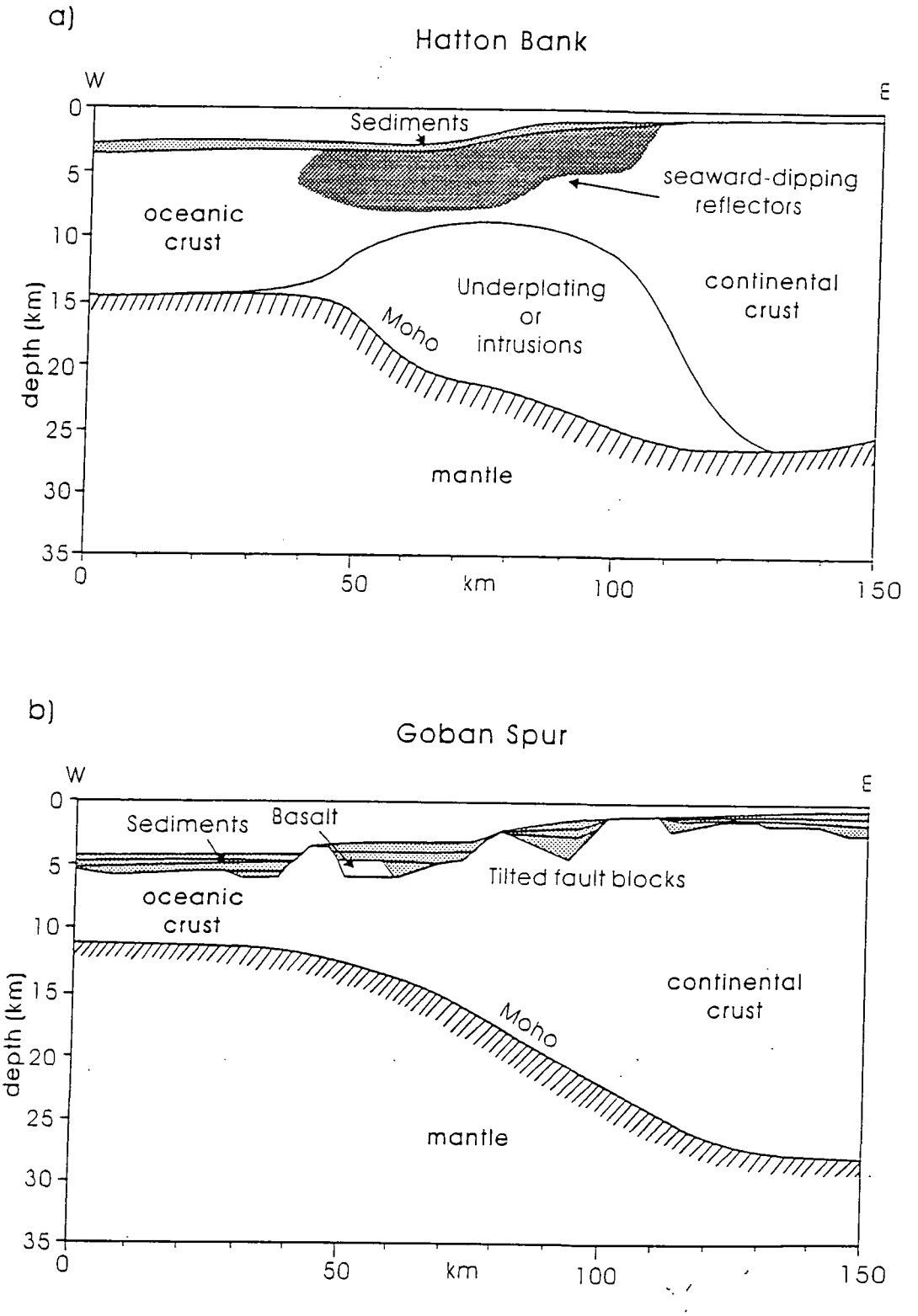

Figure 1.2 Cross sections showing the typical structure through (a) the Hatton Bank continental margin (from White et al., 1987b; Morgan et al., 1989), an example of a volcanic margin and (b) the Goban Spur continental margin (from Horsefield et al., 1994, after White, 1992), an example of a non-volcanic margin.

associated pertubated geotherm may intersect the solidus of the mantle material, which is generally assumed to be anhydrous lherzolite (McKenzie and Bickle, 1988). This method of melt generation is known as adiabatic decompression melting. The rate of extension plays a particularly important role because of time dependent conductive cooling effects. At low extension rates the effect of conductive cooling is significant as heat is lost vertically and horizontally thus reducing the amount of melt generated (Fig. 1.3). It is important to note here that an asthenospheric potential temperature of 1400°C represents a situation in which the mantle is hotter than normal (1280°C), for example due to a mantle plume.

Based on the degree of magmatism at continental rift zones, Barberi et al. (1982) classified rifts into low volcanicity rifts (LVRs) and high volcanicity rifts (HVRs). This classification system has yet to be linked to those associated with active and passive rifting, or the formation of volcanic and non-volcanic margins. LVRs are typified by low crustal extension rates, small volumes of eruptives, discontinuous volcanism and predominantly alkalic magmas, with transitional types becoming more abundant as the volume of eruptives increases. In contrast, HVRs are characterized by higher crustal extension rates, more voluminous magmatic activity and predominantly mildly alkalic basalts. Moreover, there is an apparent decrease in the alkalinity of erupted magmas with time and spatially towards the rift axis (Baker, 1987). This may be explained in terms of increasing degrees of partial melting in the ascending asthenospheric mantle (Baker et al., 1972) which is related to increasing rates of crustal extension and mantle upwelling (Bown and White, 1995). Wilson (1989) has suggested that the first rift related melt products are derived from the subcontinental lithosphere[1] and MORB-source asthenospheric mantle only becomes extensively involved in the most actively extending rifts at later stages of the rifting process. In other words, this model implies a temporal progression from early lithosphere-dominated magma sources to later asthenosphere-dominated sources, in a passive type rifting scenario. Lavecchia and Stoppa (1996) confirm, from field observations, that a model of this kind may exist. White and McKenzie (1989) have suggested, from seismic velocity measurements and independent evidence (Clarke, 1970), that the large volume of underplated igneous material at volcanic margins has higher than normal MgO concentrations. The associated theoretically calculated seismic velocity perturbations are in agreement with those observed. The increase in MgO concentrations would result in a density increase. For this reason much of the volume of magma is underplated beneath the continental crust

[1] Here subcontinental lithosphere means thermal boundary layer (TBL). The geochemist's definition of lithosphere, unlike the seismologist's, does not include the TBL. The seismologist's definition is used throughout this thesis unless clearly stated otherwise.

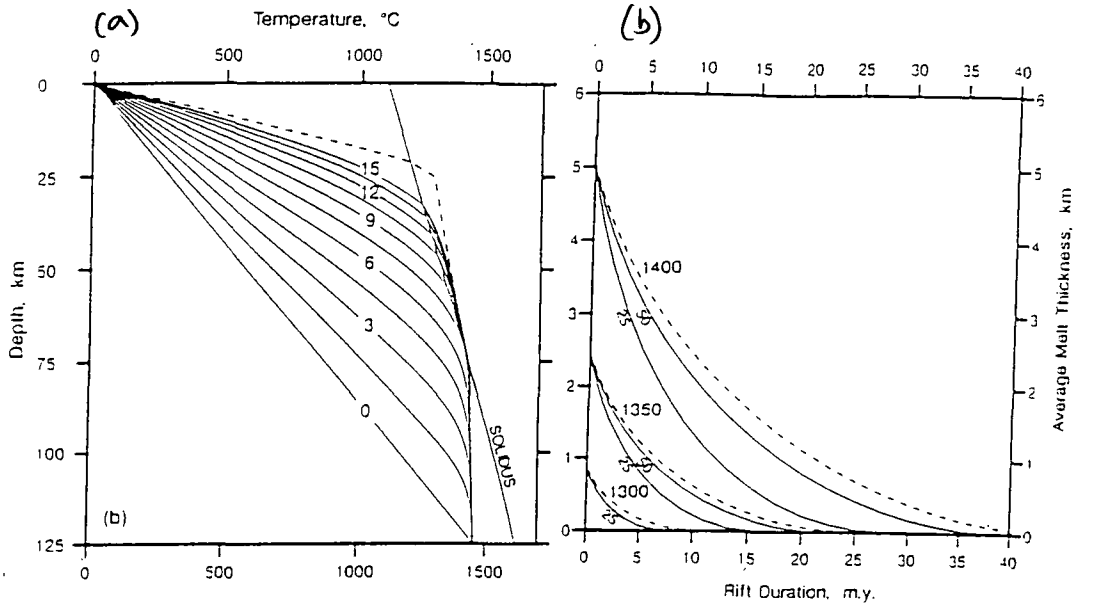

Figure 1.3 (a) Temperature distribution with depth, at 1.5 Ma increments, during a rifting phase of 15 Ma in which continental lithosphere initially 125 km thick and in thermal equilibrium with the asthenosphere at 1400°C is extended by a beta value of 5. Heat loss by conduction is assumed. Solidus of dry lherzolite from McKenzie and Bickle (1988). (b) Average melt thickness at the end of rifting versus rift duration, for asthenospheric potential temperatures of 1400°C, 1350°C and 1300°C, and initial rift half-widths of 25 km and 50 km (labelled solid lines) with heat conduction, and without heat conduction (dashed line). Stretching factor (β) varies linearly from the centre of the rift (β=5) to the rift edges (β=1). Average melt thickness per unit length along the rift is equal to the total volume of melt divided by rift width. From Bown and White (1995).

due to a lack of relative buoyancy. Cox (1980) has suggested that such picritic (high MgO) magma ponds, at depths of 25-40 km in the crust, may be potential feeders to the flood basalts.

The crustal section within a rift zone may be weakened by the thermal effects of a rapidly rising asthenosphere and/or the intrusion of magmatic bodies and the passage of melt. Although rheology is of major significance to the deformational behaviour of the lithosphere and the understanding of the rifting process (Bassi, 1995), its exact role in further tectonic extension is not fully understood, principally because of its non-linear dependence on temperature. Numerical modeling is not yet capable of simulating fully the effects of magma within the lithosphere during rifting (Harry and Sawyer, 1992; Tett and Sawyer, 1996) although Bassi et al. (1993) include the

effects of the changing geotherm. Nevertheless, qualitatively it is fair to reason that such igneous bodies weaken the crust. This process is likely to contribute greatly to the rupture of continental lithosphere and the onset of steady state seafloor spreading. This occurs when the amount of crustal extension approaches infinity and the asthenosphere has become shallow enough to accrete new oceanic crust. The tectonic models of continental rifting will be discussed in Chapter 7.

1.2 The Formation of Oceanic Crust

Oceanic lithosphere is generated as a consequence of the partial melting of upper mantle asthenospheric lherzolites by adiabatic decompression in a narrow zone of upwelling. Partial melting results in the formation of basaltic magma which leaks rapidly upwards by buoyancy driven porous flow into a narrow zone at the rift axis. McKenzie and Bickle (1988) have shown that anhydrous lherzolite begins to melt at ~50 km depth, and that partial mantle melting does not exceed 24%. If the magma reaches the surface, volcanism occurs, often in the form of pillow lavas, but much of the magma cools at depth, as dyke-like, sill-like, layered or massive intrusions, to form an oceanic crustal section. Petrologically, the igneous crustal section is described as being MORB (Mid-Ocean Ridge Basalt) in origin, essentially olivine tholeiite, and represents an incredibly uniform magma type in terms of their major element geochemistry.

Present day mid-ocean ridge systems can be classified based on the rate of separation of the two tectonic plates. Seafloor spreading at rates[2] of less than 10 mm/yr is classed as ultra-slow, between 10 and 35 mm/yr classed as slow, between 35 and 50 mm/yr as intermediate and greater than 50 mm/yr as fast. Slow spreading ridges characteristically have a distinct 2-4 km deep median valley depression up to 30 km wide, often fault bounded, with discontinuous spreading centres in the form of volcanic edifices along the axis (e.g. Brown and Karson, 1988). The axis is offset along its length by transform faults and non-transform offsets to form segments which have an along-axis depth profile that deepens towards the segment ends. Earthquake activity is almost continuous spatially (Solomon et al., 1988) and source mechanisms suggest faults can extend to 10 (15) km depth into the upper mantle for spreading rates of 10 (2) mm/yr . The Mid-Atlantic Ridge is the archetypal slow spreading ridge. The overall geometry and morphology of slow spreading ridges resembles some continental rifts, therefore highlighting the partially analogous oceanic and continental rift systems to be discussed. Ultra-slow spreading ridges have similar features but these

[2] Throughout this thesis seafloor spreading rates refer to half-rates.

features are often accentuated (e.g. Gakkel Ridge, Coakley and Cochran, 1998). Fast spreading ridges, in contrast, have much longer and more continuous segments, with an axial volcanic high rather than a fault bounded median valley. Earthquake activity is low (Solomon et al., 1988) and volcanic activity is abundant and spatially and temporally (on geological timescales) near continuous. The role of magmatism is much greater at fast spreading ridges whereas the role of mechanical deformation is much greater at slow spreading ridges (Mutter and Karson, 1993). In fact there is a continuum between ultra-slow and fast end members, in that properties and processes vary continuously between.

In contrast to the diversity of axial morphology, White et al. (1992) have shown from seismic refraction experiments and inversion of rare earth element concentrations that crustal thickness is relatively constant for spreading rates above 10 mm/yr, but decreases significantly at lower spreading rates. A mean crustal thickness of 7.1 ± 0.8 km was determined from seismic refraction experiments, whereas rare earth element inversions suggest 8.3 ± 1.5 km. Melt retained by the source, perhaps of 1%, or systematic errors in the assumed mantle rare earth element concentrations would account for the mis-fit of thicknesses determined from each method (McKenzie and O'Nions, 1991). Thin crust accreted at ultra-slow spreading rates is probably a result of conductive heat loss from the mantle that causes a reduction in the amount of melt generated by decompression melting (Reid and Jackson, 1981). Likewise, thin oceanic crust adjacent to non-volcanic continental margins is probably caused by the same process of conductive heat loss, in this case as the mantle cools under slowly stretching continental crust (White, 1992). This is the same mechanism by which Bown and White (1995) suggested the amount of melt was suppressed under continental rift zones (section 1.1).

The models discussed above do not take fully into account the contribution of tectonic processes. Melt generation and heat loss calculations of Bown and White (1995) assume pure shear extension of the whole lithosphere in response to extensional forces (McKenzie, 1978). However, it has been shown that continental extension may be non-uniform with depth (Bassi et al., 1993) as might be the case with oceanic extension. If rotation of crustal blocks occurs after accretion of oceanic crust then a reduction in crustal thickness can be apparent (Srivastava and Keen, 1995). At the extinct Labrador Sea spreading centre, Louden et al. (1996) suggest a discontinuous process whereby the space generated by plate separation is not matched by the drop in the instantaneous rate of melt supply caused by the gradual decrease in spreading before its cessation and relocation to the NE Atlantic (see section 2.2). An accretionary phase in which

normal thickness oceanic crust is generated is followed by a tectonic phase which causes block rotation, and thinning. Rubin and Pollard (1988) and Rubin (1992) have shown from seismic and geodetic monitoring on Iceland and in the Afar rift that dyke intrusion triggers surface faulting, and not vice versa. Moreover, Chadwick and Emblely (1998) have shown that this association occurs at submarine accretionary axes.

The closely linked magmatic and tectonic processes that occur at the present day mid-ocean ridge systems once occurred immediately adjacent to all rifted continental margins in their respective ocean basins. The degree to which the processes observed at present operated in the past is of particular interest to the subject of this thesis. In particular, the processes occurring at ultra-slow spreading ridges have significance for two reasons: (1) the ocean-continent transition zone in the southern Iberia Abyssal Plain (IAP) west of Iberia has been hypothesized to be the product of ultraslow seafloor spreading (Sawyer, 1994; Whitmarsh and Sawyer, 1996); (2) the process of formation of initial oceanic crust adjacent to non-volcanic margins has been likened to that of the formation of ultra-slow spreading oceanic crust (White et al., 1992).

1.3 The Earth's magnetic field

The study of the Earth's magnetic field is of prime importance to solid Earth, particularly marine, geophysical research. Not only does the study of the field itself provide information concerning the processes occurring in the Earth's deep interior, but it can also be used as a tool to study geological processes that once occurred much nearer to the Earth's surface. The nature of the field is discussed briefly here.

In geophysics, magnetic induction (or magnetic flux density) is loosely called magnetic field (strictly speaking the magnetic field gives rise to the magnetic induction). Throughout this thesis magnetic field is used in place of magnetic induction. The S.I. unit of magnetic field is the Tesla (T), the practical unit being the nanoTesla (nT). The magnetic moment, of a small current loop of area δA and current I, is defined to have magnitude $I\delta A$ and a direction perpendicular to the loop, with a sense defined by the right hand corkscrew rule. The units of magnetic moment are Am^2. Magnetization is defined as the magnetic moment per unit volume and has units of A/m. It is the vector sum of the induced and permanent magnetizations thus,

$$\mathbf{J} = \mathbf{J}_p + \frac{k\mathbf{B}}{\mu_0 \mu} \tag{1.1}$$

where, $\mathbf{J}$ is the total, or effective magnetization, $\mathbf{J}_p$ is the permanent, or remanent magnetization, k is the susceptibility, $\mathbf{B}$ is the Earth's magnetic field vector, μ_0 is the permeability of free space, and μ is the relative permeability. The permeability of free space is $4\pi \times 10^{-7}$ H/m, and the relative permeability is assumed, in geophysics, to be unity for common rocks and minerals. The second term on the right hand side of equation (1.1) is the induced magnetization term. Magnetic susceptibility is a dimensionless measure of the degree to which a rock or mineral can be magnetized by an external field. Rock magnetization is discussed in section 1.5.

Measurement of the field is dealt with in section 1.4. Magnetic field, like magnetic moment and magnetization, is a vector quantity which varies in magnitude and direction spatially over the surface of the Earth and with depth, and also with time. At any point it can therefore be described by three orthogonal components, or a magnitude, inclination and declination.

Four major components contribute to the Earth's magnetic field: (1) the dipole field, originating within the outer core at depths greater than 3000 km; (2) the non-dipole field, also originating in the outer core, contributing 5-10% of the overall field; (3) near surface (less than ~40 km depth) anomalous magnetic bodies; (4) and short period, such as diurnal, variations which are of external origin but induce an internal magnetic field in the Earth's outer layer. Often considered as a separate component, secular variations of the dipole and non-dipole field also contribute to the magnetic field. The dipole and non-dipole fields, and their secular variations, collectively called the main geomagnetic field, produce long wavelength signals which can be predicted based on theoretical models. The secular variation of the field is the continual fluctuation of the Earth's magnetic field, in magnitude and direction, with periodicities of decades to millennia. This reference field, known as the International Geomagnetic Reference Field is updated and published every five years corresponding to the newly defined model for successive five year epochs. The IGRF is a series of mathematical models representing the main magnetic field, whereby each model comprises a set of Gaussian spherical harmonic coefficients in a series expansion of the geomagnetic potential. By measuring the components of the field over the surface of the Earth, these coefficients can be calculated for the past and extrapolated five years into the future. Previous models of the IGRF are updated once actual observations have been made, and this field is called the Definitive Geomagnetic Reference Field (DGRF). For example, the IGRF

now consists of a new set of IGRF models at five year epochs from 1900 to 1940, the existing DGRF models at five year epochs from 1945 to 1985, a new DGRF 1990 model that replaces the IGRF 1990, and a new IGRF 1995 model that includes secular variation terms from 1995 to the year 2000 (IAGA, 1996). Errors of the order of 250 nT, calculated from the uncertainties in the IGRF coefficients, are typical.

The Earth's magnetic field is non-constant in magnitude and direction over time scales as short as hours and as long as millions of years. Disregarding diurnal and secular variations, it frequently changes its polarity over durations commonly thousands of years. Cox and Dalrymple (1967) suggested the reversal process takes place over 5000 years whilst Ninkovich et al. (1966) suggested a duration of about 1000 years; either way the duration is instantaneous in geological terms. The field can remain in a mono-polarity state for as short as 20,000 years or as long as 60 My (Irving and parry, 1963; Mankinen and Dalrymple, 1979). Periods of time where the field is predominantly one polarity, lasting of the order of 1 My, are called magnetic polarity epochs or chrons, whereas shorter intervals, of the order of 0.1 My, are called events or subchrons. The reversal timescale is dealt with in more detail in section 2.1.

1.4 Marine Magnetic Methods

The objectives of this short sub-section are to highlight the main magnetic acquisition, processing and interpretational methods and techniques used or mentioned in this thesis.

For many centuries the use of the geomagnetic field as a tool for iron-ore prospecting has proven successful because of the relative ease with which measurements can be made and simple interpretations applied. This systematic utilization of one of the Earth's physical properties lead to the development of the method within the field of marine geophysics. Its main triumph has been in the identification of marine magnetic anomalies and the development of the Vine-Matthews hypothesis (Vine and Matthews, 1963). Together with the then recent discovery concerning the reversals of the Earth's field (Irving and Parry, 1963) the discovery of 'seafloor stripes' proved to be the most supportive piece of evidence for the proposed theory of seafloor spreading (Hess, 1962).

In an ideal situation, the local magnetic field, or the magnetic anomaly representing perturbations in the magnetic structure at crustal and uppermost mantle levels, is simply the observed field minus the geomagnetic reference field (IGRF; IAGA, 1996). However, in practice

the computation of absolute magnetic anomalies is more complex.

Total field proton precession magnetometers are commonly used in airborne and shipborne measurements due to their operational simplicity, reliability of the sensors, ability to measure the absolute field with a high degree of accuracy, and the non-requirement of an oriented sensor. They record absolute total magnetic field intensity, providing the circuit parameters in the magnetometer electronics are stable and known, with measurement accuracies of 0.1 to 0.5 nT and have sensitivities of typically 0.1 nT (e.g. Belyaev and Filin, 1995). They do not suffer from instrument drift. In contrast, fluxgate magnetometers are able to measure individual directional components of the geomagnetic field by measuring the field component directed along the magnetic axis of the sensor. Calibration of the magnetometer is required to define and remove 'zero-offsets' (apparent magnetic field measurement when the sensor is located in zero field), and also to calculate misalignments between the sensor's magnetic axis and its geometric axis. In practice, three fluxgate magnetometers are arranged orthogonally, for example north, east and vertically down. This type of geometry allows additional magnetic field information to be recorded. Not only can total field intensity, and therefore total anomaly field, be calculated from the three orthogonal components, but the three orthogonal anomaly field components can also be calculated providing the directional IGRF values are known.

The practical aspects of retrieving the local anomaly field from marine magnetic observations are further complicated by a non-stationary observation platform and magnetic effects of the platform. Moreover, the magnetic effects of the platform can be divided into a contribution from its permanent magnetization, and one from its induced magnetization, the latter also being a function of platform attitude. A typical survey involves towing a proton precession magnetometer usually 100-150 m astern of a ship. Even at such distances, the magnetic field of the ship is non-zero . Bullard and Mason (1961) developed a formula for the disturbance of the magnetic field as a function of ship heading and distance astern due to the proximity of the ship to the magnetometer. In a similar fashion, Isezaki (1986) developed a system for removing the magnetic effects of the ship which are a function of the ship's yaw, pitch and roll, from shipborne three-component magnetometer readings. The same principles can be applied to any orthogonal three component data providing accurate attitude data are logged simultaneously (see Appendix I).

Marine magnetic observations can also be made much nearer to the source by attaching magnetometers to deep-towed instruments and towing along track near to the seabed (e.g., Klitgord et al., 1975; Miller et al., 1985; Tivey and Johnson, 1987; Searle et al., 1998; Fig. 1.7). If the

assumption that the basic magnetic body is dipolar is correct, then the amplitude of a given magnetic anomaly depends on the square of the depth. For example, if magnetic basement were to lie 3 km below the seabed which is 5 km below the sea surface, then observations at the seabed would be approximately 7 times larger in amplitude than those at the sea surface. Similarly, if basement were only 1 km below the seabed in the same water depth then the seabed observations would be 36 times larger in amplitude than those at the sea surface. The close proximity of near bottom observations to the source makes some anomalies that are perhaps undetectable at the sea surface detectable at near bottom depths (Fig. 1.8). In addition, shorter wavelength features can be resolved although random spatial noise may be introduced (McKenzie and Sclater, 1971). Part of the work in this thesis concerns itself with the processing and interpretation of near bottom triaxial fluxgate magnetometer observations in the Iberia Abyssal Plain. In appendix I an account of a three-component magnetometer correction procedure is given. This method is then extended to the near bottom observations in the southern Iberia Abyssal Plain.

In broad terms, there are three main quantitative approaches, besides qualitative approaches, to the interpretation of potential field anomalies. Techniques used on the magnetic field can also be used on the gravity field since both satisfy Laplace's equation. Firstly, parametric methods are used to fit simple geometric shapes and place limits on bodies. As suggested by the name the method determines the parameters of a given magnetic body. Most methods assume that the anomaly is generated by a simple shape, for example a sphere or a dyke. The shape of the anomaly gives an approximate depth to the top or centre of the body (e.g. Peters 1949). In a similar way, Smith (1959) formulated rules for the maximum depth to a body. However, all parametric methods rely on assumptions that are often highly unlikely, such as specific length to width ratios, shapes, magnetizations or densities. In addition, the method is only applicable to individual anomalies. Overlapping (interfering) anomalies cause most parametric methods to fail. In general, the method is only used in very simple scenarios to make a very approximate interpretation, for example, in gravity, over an isolated near spherical salt dome, or in magnetics to study an isolated dyke.

The second group of interpretational methods is classed as indirect methods and in general involve either the solution of the forward or inverse problem based on a number of assumptions. The forward problem, executed in either the space domain (e.g. Coggan, 1976; Kunaratnam, 1981) or the wavenumber domain (e.g. Schouten and McAmy, 1972; Parker, 1973), is the conventional way in which theoretical fields are calculated and then compared with observed fields to assess the

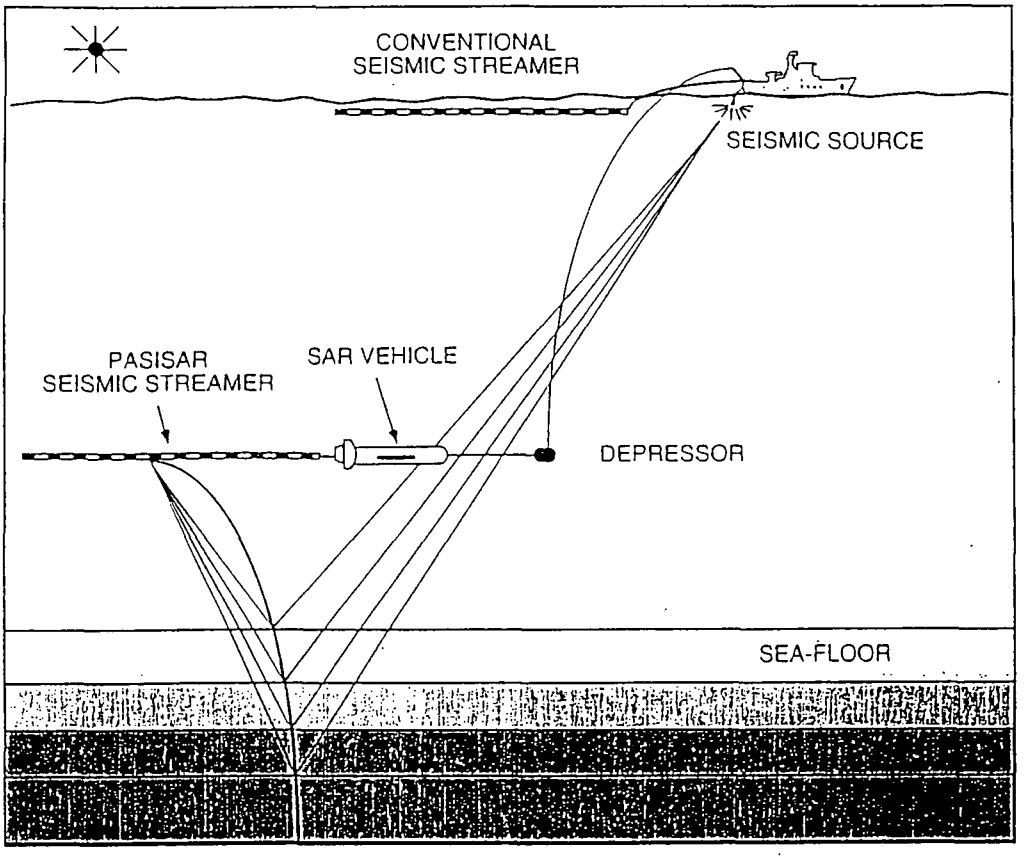

Figure 1.4 Geometry of a near-bottom geophysical experiment as exemplified by IFREMER's System Acoustique Remorque (SAR). Three orthogonal fluxgate magnetometers are mounted externally on the vehicle to minimize the effects of electrical noise generated by the SAR's circuitry. The vehicle is towed at near constant altitude above the seabed either by altering the length of tow cable out or by changing the ship speed. Noise derived from the motion of the ship is damped by the use of an umbilical between the depressor weight and the ship. The SAR is also capable of towing a seismic streamer (from Minshull, 1995).

degree of match. The method is not restricted to isolated, geometrically simple magnetic bodies, but can operate on any number of bodies of arbitrary shape. It is therefore far superior to the parametric approach. Although this method suffers from inherent non-uniqueness it is by far the most common means of interpreting magnetic anomalies because of its relative ease of application. In contrast, the solution of the inverse problem is not such a simple procedure and is therefore used to a lesser extent. Its application in magnetics has almost exclusively involved the solution of a magnetization distribution for a given set of assumptions.

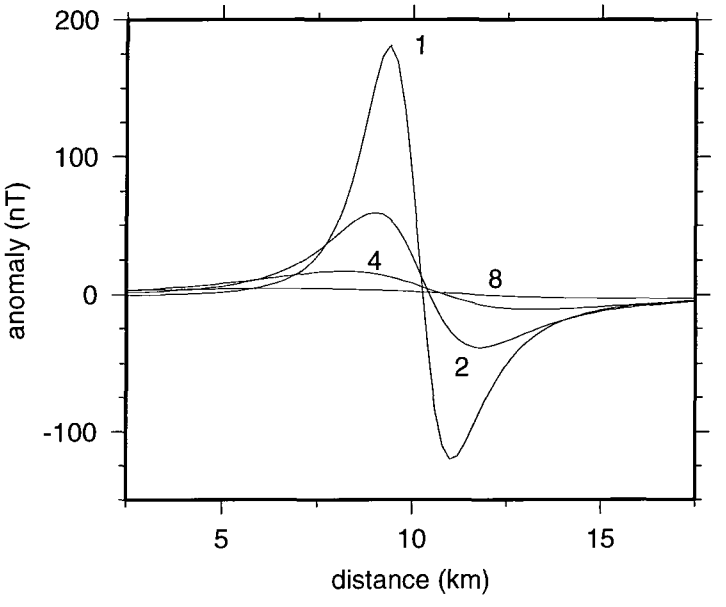

Figure 1.5 Theoretical effect of depth to source (1, 2, 4 and 8 km below observation level) on magnetic anomaly amplitude. Two-dimensional magnetic anomaly calculated along a N-S profile over a 0.5 km square magnetic body with an effective magnetization of 4 A/m. A source at 8 km depth is barely detected at the surface. In contrast, the same source at 1 km depth produces an anomaly with peak-to-trough amplitude in excess of 300 nT.

For example, Parker and Huestis (1974) have developed a procedure for calculating a magnetization magnitude distribution in the wavenumber domain, providing assumptions are made about the magnetization direction and the layer thickness, which must be constant. Alternatively, a method for calculating layer thickness was proposed by Louvel et al. (1997) whereby assumptions about the magnetization must be made. In general, the indirect method is based on assumptions. Chapter 3 is dedicated to testing the validity of the indirect method and the significance of the assumptions with reference to magnetic anomalies west of Iberia.

The third group of interpretational methods are called direct methods. Unlike indirect methods, they make no or very few assumptions, especially concerning the geological and geophysical properties sought after. For this reason they provide a very objective starting point of analysis, although, as will be shown, the interpretation of results must be approached with caution (see Chapter 4). However, direct methods generally allow 'ball park' estimates concerning the unknown geophysical quantities to be made. Specific operations include spectral analysis, Euler

deconvolution, upward and downward continuation and reduction-to-the-pole. Also included are the methods used in componental magnetometry. The results of the direct method are tested by application of forward modelling.

In general, the procedures used in magnetic interpretation are similar to those used in gravimetric interpretation. However, there are important contrasts which are outlined below. Density is a scalar quantity and therefore gravity anomalies are relatively more easily related to their causative bodies. In contrast, the vector quantity of magnetization means anomalies do not necessarily lie directly over their causative bodies. In addition, the Earth's field direction varies spatially and temporally and therefore introduces further complications. As a result, the indirect method is much harder to apply to magnetic anomalies than to gravity anomalies.

Much of the work in this thesis involves quantitative interpretation of magnetic anomalies. However, interpretation is made difficult since there is no unique solution to the magnetic problem. Rock magnetization properties and spatial distribution cannot be determined from magnetic anomalies alone. The use of complementary methods further reduces ambiguity but it must also be noted that the resolution and target of each method differs.

1.5 Rock magnetization

The objectives of studying magnetic anomalies is to infer differences in characteristics of a source from its surroundings. These characteristics fall into two categories; spatial and magnetic. Spatial characteristics include position, shape, depth and thickness of the magnetic body, whilst magnetic characteristics are defined by the magnetization magnitude and direction of the component minerals making up the rock. Without magnetic characteristics a geological unit (e.g. a dyke or lithological layer) is not a magnetic source body, regardless of its spatial character or other physical properties (e.g. seismic velocity).

All minerals and native elements are magnetic to some extent. However, only minerals that are ferrimagnetic are of importance in geophysics; those that are diamagnetic, paramagnetic or antiferromagnetic have susceptibilities approximately less than 10^{-3} and are therefore below the practical measurable level (at 40°N, magnetization [A/m] is approximately 35 times the susceptibility; see equation 1.1). In contrast, the strongest magnetism, ferromagnetism, does not occur in common minerals; only native metals acquire a ferromagnetism and are therefore of little interest outside mineral prospecting. Most magnetic minerals possess ferrimagnetism and have

susceptibilities up to ~15. The main magnetic minerals are the titanomagnetites (including magnetite *sensu strictu*), pyrrotite and the ilmenite-haematite series. For most common rocks, rock magnetism depends almost exclusively on the amount of titanomagnetite (*sensu latu*) present.

Magnetic minerals can posses an induced and/or a permanent (remanent or NRM) component of magnetization. The magnitude of a mineral's induced magnetization is governed by its susceptibility and the magnitude and direction of the external field, which for the purposes here is the Earth's magnetic field (see second term on right of equation 1.1). A mineral's induced magnetization is therefore always parallel the Earth's field. In contrast, a remanent magnetization can be in any direction; the orientation of the Earth's field at the time of NRM acquisition determines the direction of magnetization. Of importance here are minerals possessing thermoremanent magnetization (TRM), chemical remanent magnetization (CRM) and viscous remanent magnetization (VRM), all of which are types of natural remanent magnetization (NRM). TRM is acquired when a mineral cools through its Curie temperature in the presence of an external field. The Curie temperature of magnetite is 575°C, much lower than the temperature at which minerals crystallize within cooling magma (~1100-800°C). Igneous rocks are the main carrier of TRM. CRM is acquired by the chemical growth of magnetic mineral phases in the presence of an external field, subsequent to their initial formation. Thus, CRM can be acquired at any temperature. VRM is a type of NRM that is acquired slowly if a magnetic mineral is exposed to an external field. The effective magnetization of a given rock unit is not only dependant on the amount and type of magnetic minerals present, but also on the grain size of the magnetic minerals; in general, for a given mineral, its magnetization increases with decreasing grain size.

In the context of marine magnetics, and in particular a magnetic study of an OCT, there are essentially three scenarios in which magnetic anomalies are produced. Firstly, continental crustal basement rocks are generally acidic metamorphic and meta-igneous rocks of varying grade. Magnetite is present as the main magnetic mineral throughout the crustal section above the Curie isotherm (Frost and Shive, 1986) or the Moho (Wasilewiski et al., 1979), whichever is shallower, although it generally possess no NRM and has low susceptibilities; the average induced magnetization of the most magnetic samples is rarely greater than 1 A/m (Shive and Fountain, 1988) and susceptibilities commonly of 10^{-3} are encountered (Shive and Fountain, 1988; equivalent to 0.35 A/m at 40°N). Secondly, although unaltered mantle peridotites are generally non-magnetic (Wasilewiski et al., 1979), the process of serpentinization of ultramafics produces a considerable amount of magnetite which can acquire a significant CRM, as well as carrying an induced

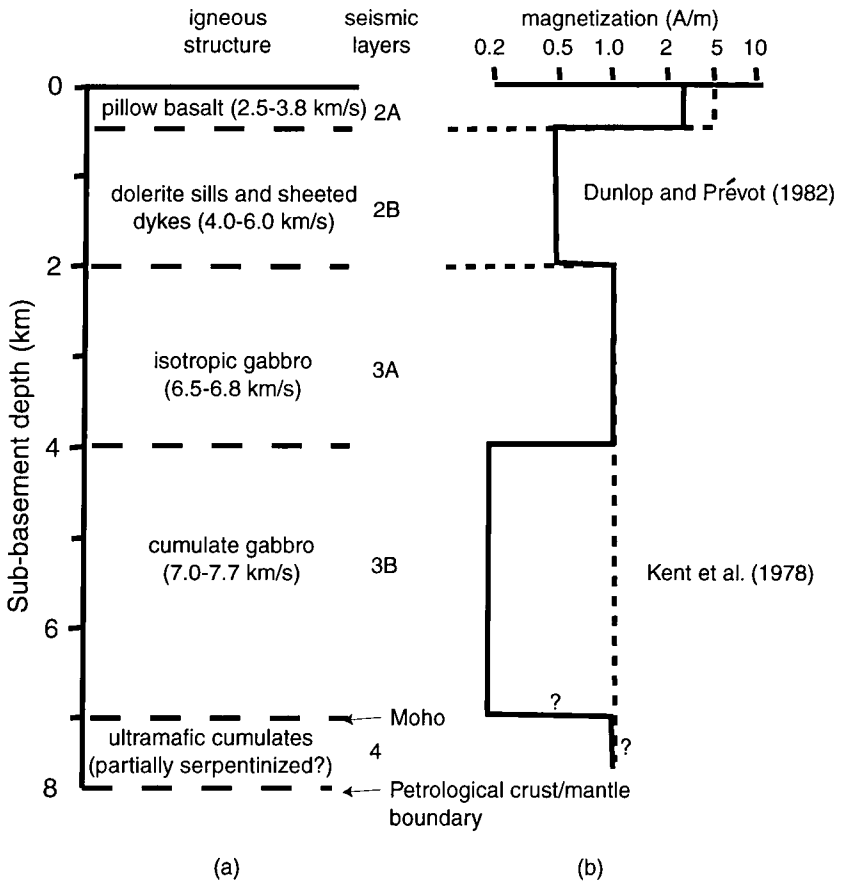

Figure 1.6 (a) [illegible] and igneous structure of a typical layered oceanic crust. (b) Corresponding vertical magnetization models of Kent et al. (1978; dashed line) and Dunlop and Prevot (1982; solid line).

component of magnetization. Thirdly, mafic rocks, which make up the oceanic crustal section and many intrusive bodies, do carry a significant NRM (>> induced component). Studies of oceanic rock magnetic properties have led to many models of a layered magnetic crustal section, all of which follow a general theme; here the models of Kent et al. (1978) and Dunlop and Prévot (1982) are used as two examples of the magnetic structure within oceanic crust (Fig. 1.6).

1.6 General aims and outline of thesis

The primary aim of this thesis is to provide further constraints of the processes that occurred during the formation of the West Iberia continental margin, and in particular the formation of the ocean-continent transition zone in the southern Iberia Abyssal Plain (IAP). The means by which I tackle this problem is via the analyses of the local magnetic field over and

adjacent to the continental margin in the southern IAP. Gridded sea surface two-dimensional magnetic intensity anomalies and three near-bottom magnetometer profiles, two of which recorded three orthogonal components of the magnetic field, are used for the analyses. In addition, depth to acoustic basement on over 1500 line km of multichannel seismic profiles was interpreted and gridded to provide necessary constraints on magnetic models. Further constraints were provided by the results of ODP Legs 149 and 173.

Subsidiary aims of this research are to successfully use standard and traditional magnetic methods, which have previously been applied only sparingly at the West Iberia margin, and to develop and quantify the use of alternative methods for magnetic analysis, which also have not previously been used at the West Iberia margin, and rarely in marine magnetic problems. The methods of forward and inverse modelling, traditionally used in marine magnetic problems, are coupled with the methods of Euler deconvolution, spectral analyses and componental magnetometry. The successful application of alternative methods shows that, potentially, the methods can be used in other geographical locations where good quality magnetic data are available, such as the in the Tagus Abyssal Plain, which this thesis aims to encourage. In particular, some of these methods have been applied to the local magnetic field at the conjugate Newfoundland margin in order to provide further constraints on the rift-to-drift processes that resulted in the separation of Iberia and Newfoundland during the opening of the North Atlantic.

In this chapter I have introduced the geological, geophysical and geochemical problems that face Earth scientists in the fields of continental rifting, seafloor spreading and the formation of continental margins. In the next chapter I introduce the specific geological and geophysical problems faced at the West Iberia margin, with emphasis of the role of magnetics, and also the magnetic data that will be analysed in the following chapters. In Chapters 3 and 4 I introduce the theoretical, methodological and interpretational aspects and problems which arise from the indirect and direct magnetic methods, respectively. In these chapters, the methods are tested on theoretical data to provide a means of determining whether the methods will prove successful when applied to the observations.

In Chapter 5 I analyze the gridded sea surface magnetic anomaly chart west of Iberia in order to determine whether significant differences in magnetic anomaly sources exist across the margin. Interpretational analyses of the results of reduction-to-the-pole, spectral analysis and Euler deconvolution provide constraints of the depths and trends of magnetic anomalies; it will be shown that the sources of magnetic anomalies within continental crust, oceanic crust and the OCT have

different characteristics. In Chapter 6, the different characteristics are interpreted, geologically, by further analyses of the surface magnetic field by inverse methods and analyses of three high resolution near-bottom magnetometer profiles. Multichannel seismic data and the results of ODP drilling are used to constrain magnetic models. The location and timing of the onset of seafloor spreading, and the geological nature of the sources of magnetic anomalies within the OCT are addressed. Models for the origin of the magnetic anomalies are discussed with reference to the results of other geological and geophysical studies.

In Chapter 7 I introduce the conjugate Newfoundland rifted margin and analyse gridded magnetic anomalies in the same manner as was implemented in Chapters 5 and 6. A comparison of the nature of magnetic sources at the two conjugate margins provides further constraint on models of margin development. Finally, geological and geophysical results from the Red Sea rift, slow and ultraslow seafloor spreading centres, and the non-volcanic southwest Greenland-Labrador continental margins are discussed.

Chapter Two

Formation of the West Iberia continental margin during North Atlantic Opening

In this Chapter I introduce the reader to the general background behind the previously proposed models of formation of the West Iberia continental margin within the context of the North Atlantic rift system. I attempt to place strong emphasis on the use of magnetics to further constrain models of margin development, although, until now, its use has been limited to date. I also introduce the magnetic data that are used to provide further constraints on the models of formation of the ocean-continent transition zone in the southern Iberia Abyssal Plain.

2.1 A note on time scales

The absolute timing of geological events is of importance to the study of rifting and the initiation of seafloor spreading during the development of a continental margin. For the purpose of this study correlation of geomagnetic field polarity reversals, and therefore seafloor spreading magnetic anomalies, with absolute ages requires a reliable time scale developed from magnetochronostratigraphic studies. In this thesis I use the timescale of Gradstein et al. (1995) for the Mesozoic and that of Harland et al. (1990) for the Cenozoic.

Because magnetic anomalies, periods of constant magnetic polarity, and even regions of the seafloor where rocks are normally or reversely magnetized, are often used to identify the age of a geological event or rock type, I adopt a system of nomenclature, which is used throughout this thesis, as follows. For clarity, periods of constant magnetic polarity (magnetic anomaly chrons) are noted with a preceding 'C', whereas seafloor spreading magnetic anomalies, corresponding to such periods, are labelled by a preceding 'a'. Chrons of normal polarity, and dominantly positive magnetic anomalies are also labelled with a succeeding '(N)', and chrons of reversed polarity and dominantly negative magnetic anomalies are labelled with a succeeding '(R)'. Seafloor spreading 'blocks', i.e. regions of oceanic crust whose magnetization direction is opposite to that of the adjacent oceanic crust, are labelled with a succeeding '(N)' or '(R)' only, to indicate whether the material is positively or negatively magnetized. For example, consider the period 124.72-126.73 Ma. This chron is referred to as CM3(R). During seafloor spreading the oceanic crustal block created during CM3(R) is

labelled M3(R) and the dominantly negative magnetic anomaly caused by the magnetized block is labelled aM3(R). Figure 2.1 shows the relevant section (Lower Cretaceous and Upper Jurassic) of the magnetochronostratigraphic column that is used in this thesis, with labelled chrons consistent with the system described above.

2.2 The North Atlantic propagating rift system

In Late Triassic-Early Jurassic times rifting took place between what are now the land masses of Africa and Central and North America. It is believed that during the rifting period a thermal anomaly within the mantle existed which gave rise to the large volume of underplated magmatic material observed along the East Coast US margin (Holbrook and Keleman, 1993; White and McKenzie, 1989). Seaward-dipping reflectors, interpreted as subaerial lava flows, and a 20-25 km thick igneous section at the base of the continental crust, are interpreted to extend for ~1000 km along the length of the margin and to make up as much as 3.2 million cubic kilometers (Holbrook and Keleman, 1983; Klitgord et al., 1988). Such volumes of melt cannot be explained by the decompression melting of asthenospheric mantle at potential temperatures of ~1300°C. Although classed as a volcanic margin (Fig. 1.1) it is believed that non-plume processes are responsible for the thick crust observed (section 1.1; Holbrook and Keleman, 1983).

After the final stage of rifting, seafloor spreading adjacent to the East Coast US margin commenced ~180 Ma (Emery and Uchupi, 1984), approximately 20-25 Ma after the onset of rifting. The eventual rupture of continental lithosphere gave way to the formation of accretionary crust as the North Atlantic Rift System propagated northwards. As a result, the continental region to the north of what is now the Newfoundland Fracture Zone and the Azores-Gibraltar Fracture Zone underwent a phase of rifting in the late Oxfordian/early Kimmeridgian (~155 Ma; Srivastava et al., 1990b). A later phase of rifting, which began some 10 Ma after the first phase, led to the eventual breakup of Europe and North America and the formation of the West Iberia and Newfoundland margins (Fig. 1.1). Seafloor spreading then commenced progressively northwards offshore Iberia; adjacent to the Tagus Abyssal Plain at 133-134 Ma (CM11(R) time; Pinheiro et al., 1992; Whitmarsh and Miles, 1995), adjacent to the Iberia Abyssal Plain at ~127-132 Ma (approximately CM3(R) time; Whitmarsh et al., 1990; Whitmarsh and Miles, 1995; Whitmarsh et al., 1996a), and adjacent to Galicia Bank at 118 Ma (during the Cretaceous Magnetic Quiet Zone, C34(N); Boillot et al., 1988a). In contrast to the East Coast US margin, it is believed that little or no melt was produced during

rifting between Iberia and Newfoundland, thus forming the so-called non-volcanic margins.

As the focus of continental rifting propagated further northward in the region north of Iberia and south of what is now the Charlie Gibbs Fracture Zone, a triple junction developed which created extension between the plates of Europe, North America and Iberia (Sibuet and Srivastava, 1994). Eventually seafloor spreading began in the Bay of Biscay by eastward rift propagation which caused Iberia to rotate (Srivastava et al., 1990a) resulting in the formation of the northern and southern Bay of Biscay margins (Fig. 1.1). During this time (~85-121 Ma, C34(N)) continental extension continued northwards on the northwestern arm of the triple junction under rifting conditions which led to the formation of the northern Flemish Cap, Goban Spur and Porcupine non-volcanic continental margins in the Albian (99-112 Ma; Fig. 1.1; Roberts et al., 1981). At ~80 Ma seafloor spreading in the Bay of Biscay ceased (Verhoef et al., 1986; Srivastava et al., 1990a and b; Sibuet and Collette, 1991) rendering the triple junction inactive.

The ongoing northward propagation of the rift, which at present is represented by the Mid-Atlantic Ridge, resulted in the formation of the Rockall Trough. However, shortly after the formation of the Rockall Trough the focus of rifting shifted into the region which is now occupied by the Labrador Sea (Chalmers et al., 1995). The exact timing at which this occurred is still a subject of contention because magnetic anomaly identification earlier than CM27 is ambiguous. Roest and Srivastava (1989) and Srivastava and Roest (1995) have identified magnetic anomalies as old as anomaly a33O(N), which corresponds to an age of ~83.5 Ma for the initiation of seafloor spreading. However, there are some difficulties in identifying anomalies a27(N) to a33O(N), as noted by Keen et al. (1994), Chian and Louden (1994), Chalmers and Laursen (1995) and Chian et al. (1995), for example. Regardless of the exact timing, rifting and subsequent seafloor spreading in the Labrador Sea resulted in the formation of the southwest Greenland and Labrador non-volcanic margins (Fig. 1.1). Although considered non-volcanic in the south, there may be some evidence to suggest that syn-rift volcanism did occur further north; seaward dipping reflectors at the southwest Greenland margin, interpreted to be lava flows (Chalmers et al., 1995) and volcanics in Baffin Bay and the Davies Strait (Hyndman, 1973, 1975) suggest that volcanism did accompany rifting. However, White and McKenzie (1989) suggest that the effects of the (later) Iceland Plume head may be responsible for these features. Nevertheless, many parallels can be drawn between the West Iberia margin and the southwest Greenland and Labrador margins and a discussion is left until Chapter 7.

At approximately anomaly 24 time (Early Eocene, 54.7-57.2 Ma) seafloor spreading commenced in the northeast Atlantic creating the volcanic margins of Hatton Bank and East

Greenland (Fig. 1.1; White and McKenzie, 1989). At the same time the production of oceanic crust in the Labrador Sea diminished culminating in cessation in the Early Oligocene (~34 Ma). The active northeast Atlantic spreading centre then propagated northeastwards into the Norwegian Sea resulting in the formation of the Lofoten margin (Fig. 1.1). The Hatton Bank, East Greenland and Lofoten margins are all volcanic margins where large volumes of magmatic material, created by the thermal anomaly of the Iceland Plume, have been extruded and underplated. In the Late Oligocene-Early Miocene (10-27 Ma) the spreading axis shifted to the northwest when the Jan Mayen Ridge, a continental fragment, broke away from east Greenland (Talwani and Eldholm, 1977; Hinz and Schluter, 1978; Vogt et al., 1980; Myhre et al., 1984). The rifting then continued northwards into the Greenland Sea and Arctic Ocean where at present the Knipovitch Ridge and Gakkel Ridge are the active spreading centres. At the very eastern end of the Gakkel Ridge, where spreading rates are < 4 mm/yr, a broad zone of continental rifting is present on the Laptev Shelf which when traced south into Siberia approaches the pole of opening and loses its identity as an extensional rift system (Grachev, 1982).

The identification of seafloor spreading marine magnetic anomalies has provided vital insight into the timing of onset of seafloor spreading, and allowed the development of the propagating rift model. Furthermore, the position of the North Atlantic seafloor spreading anomalies, when correctly identified, have been used to create plate reconstructions at given times in the geological past (e.g. Bullard et al., 1965; Masson and Miles, 1984; Klitgord and Schouten, 1986; Srivastava and Tapscott, 1986; Srivastava et al., 1988a and b; Srivastava et al., 1990a and b; Srivastava and Verhoef, 1992; Sibuet and Srivastava, 1994). Past plate locations can therefore be predicted. Of importance here is the reconstruction made at the time of the oldest identifiable seafloor spreading magnetic anomaly adjacent to the West Iberia continental margin. One such reconstruction was made by Srivastava and Verhoef (1992) at chron CM0(R) time (~121 Ma; Fig. 2.2; although CM0(R) has been shown to be younger than the oldest identifiable seafloor spreading anomaly adjacent to the southern IAP; Fig. 2.3; Whitmarsh et al., 1990; Whitmarsh and Miles, 1995; Whitmarsh et al., 1996a). Even with estimates of continental stretching in sedimentary basins accounted for there are regions of mismatch between West Iberia and Newfoundland. Although Galicia Bank and the southern Flemish Cap are joined, a ~130 km gap is present between the margin in the southern Iberia Abyssal Plain and its conjugate offshore Newfoundland. Although some of the gap can be accounted for by the accretion of oceanic crust after and during CM3(R), there still exists a gap in excess of 100 km. It is this region that is called the ocean-continent transition zone (OCT) and its proposed origins to date are discussed below.

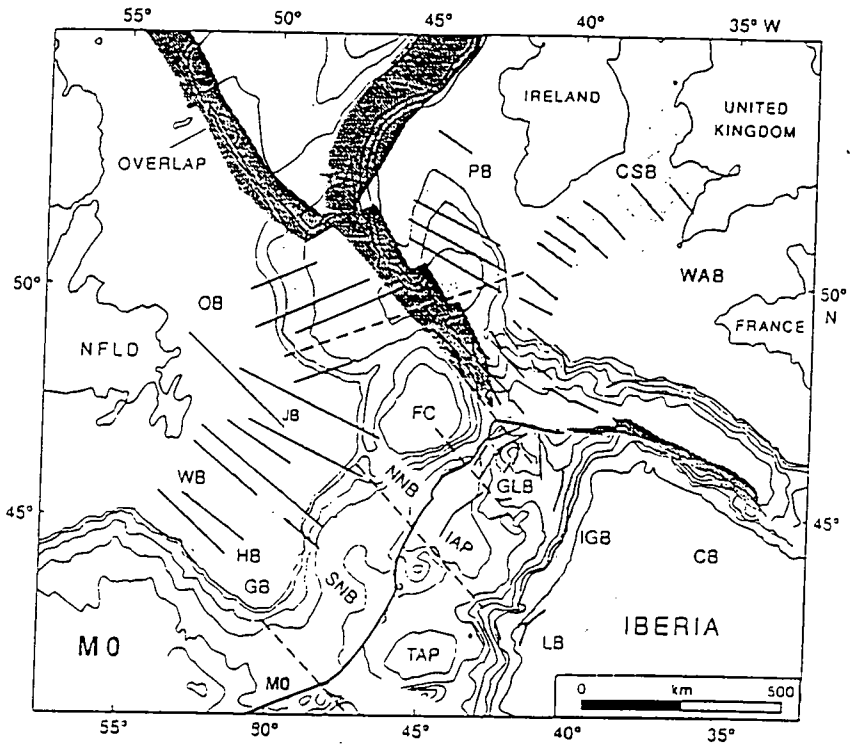

Figure 2.2 Reconstruction of the North Central Atlantic at chron CM0(R) time (~121 Ma) showing a simplified bathymetry on each plate, outlines of the sedimentary basins (shaded) and their tectonic features (continuous lines) (from Srivastava and Verhoef, 1992). Plate motion directions and regions of overlap are shown by dashed lines and dark stippled regions, respectively. JB=Jean d'Arc Basin; WB=Whale Basin; HB=Horseshoe Basin; OB=Orphan Basin; FC=Flemish Cap; CSB=Celtic Sea Basin; WAB=Western Approaches Basin; PB=Porcupine Basin; GLB=Galicia Bank; IGB=Inner Galicia Basin; LB=Lusitanian Basin; CB=Cantabrian Basin; NNB=North Newfoundland Basin; SNB= South Newfoundland Basin; IAP=Iberia Abyssal Plain; TAP=Tagus Abyssal Plain

2.3 The West Iberia continental margin

The continental margin offshore West Iberia extends approximately 800 km north to south from Cape Finisterre to Cape Saint Vincent (Fig. 2.4). A consistently narrow continental shelf and a steep slope along most of its length describe a N-S trending and relatively straight margin with a number of physiographic features that divide it into three segments. In the north between 41°N and 43°30'N, Galicia Bank, a marginal plateau, in places less than 1 km below sea level, is separated from the mainland of Iberia by the Galicia Interior Basin. Galicia Bank lies ~250 km offshore Iberia, a similar distance that the Flemish Cap, a structurally similar feature at the conjugate Newfoundland margin (Fig. 1.1), lies from the Grand Banks of Newfoundland. On the western flank of Galicia Bank, bathymetry increases into the northern

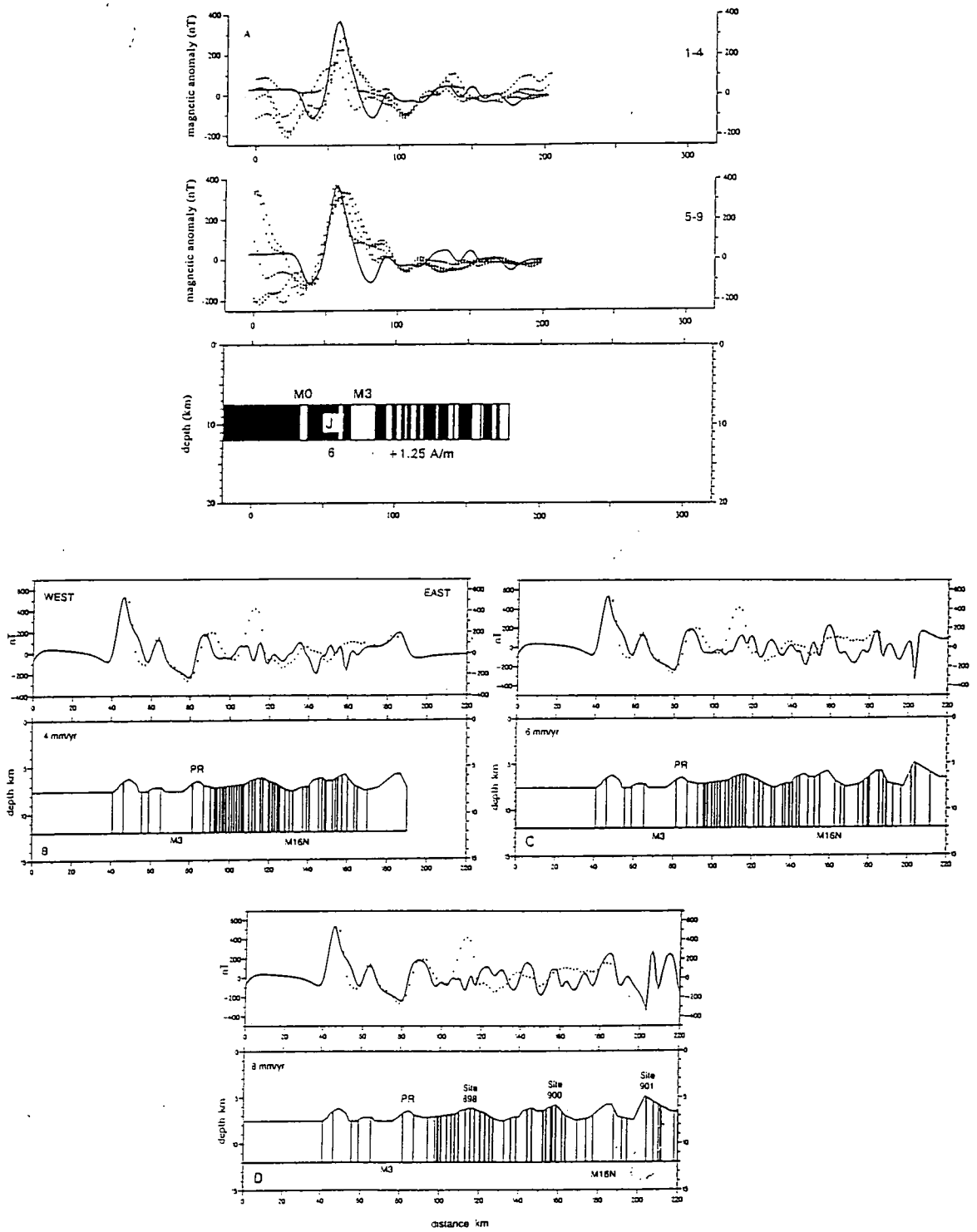

Fig. 2.3 Magnetic (forward) models of Whitmarsh and Miles (1995) and Whitmarsh et al. (1996a) derived from sea surface and near-bottom magnetic measurements, respectively, across the southern Iberia Abyssal Plain. (a) Ten 010° trending sea surface magnetic anomaly profiles (crosses in top and middle panels) and calculated anomaly (solid line) assuming a spreading rate of 9 mm/yr (model in lower panel). (b), (c) and (d) Near-bottom magnetic anomaly (crosses) along profile TOBI91 and calculated anomalies (solid lines) assuming a seafloor spreading model at rates of 10 mm/yr west of peridotite ridge (PR) and (b) 4 mm/yr, (c) 6 mm/yr, and (d) 8 mm/ry east of PR.

part of the Iberia Abyssal Plain where water depths of more than 5 km are encountered. Within the region between Galicia Bank and the northern part of the Iberia Abyssal Plain lies the ocean-continent transition zone whose western flank is thought to be bounded by two, of four, northernmost segments, R1 and R2, of a basement peridotite ridge which in places subcrops at the seafloor (Fig. 2.4; Boillot et al., 1988a and b, 1995; Beslier et al., 1993).

Along the southern edge of, and structurally continuous with, Galicia Bank are the Vigo and Vasco da Gama seamounts. Immediately to the south of the seamounts lies the southern part of the Iberia Abyssal Plain which is bounded to the east by Porto seamount and the continental slope and to the south by Estremadura Spur and Tore seamount. Beneath the southern Iberia Abyssal Plain, between 12°W and 13°W, lies the southward continuation of the basement peridotite ridge, here represented as segments R3 and R4 (Beslier et al., 1993; Pickup et al., 1996). In contrast to the margin off Galicia Bank, the width of the OCT is up to ~7 times greater; compared to a maximum distance of ~25 km off Galicia Bank (Whitmarsh et al., 1996) OCT widths in the southern IAP have been estimated to be >40 km (Chian et al., in press) and ~130-160 km (Pickup et al., 1996; Dean et al., submitted) at 40°40'N and 40°20'N, respectively (Fig. 2.4). The nature of this OCT is presented later and is the subject of this thesis.

South of the Iberia Abyssal Plain lies the Tagus Abyssal Plain, a sub-circular basin which is bounded to the north by Estremadura Spur and Tore seamount, to the east by the continental slope and to the south by Gorringe Bank. Beneath the Tagus Abyssal Plain lies the third and most southerly segment of the West Iberia margin. Although relatively poorly investigated, an OCT is believed to be present between oceanic crust and continental crust, which may be up to ~130 km wide (Fig. 2.4; Pinheiro et al., 1992).

In the following three subsections I present the nature of the OCT in the three segments of the West Iberia margin, which exhibit both similar and different characteristics. The OCT is strictly defined as the region between the most seaward, unambiguous continental crust and the most landward unambiguous oceanic crust.

2.3.1 The OCT off Galicia Bank

The Galicia Bank section of the West Iberia margin has been intensively studied by seismic reflection, seismic refraction and heat flow profiles (de Charpal et al., 1978; Hoffman and Reston, 1992; Sibuet et al., 1987, 1995; Louden et al., 1989; Mauffret and Montadert, 1987, 1988; Montadert et al., 1979; Reston et al., 1995, 1996; Whitmarsh et al., 1996b),

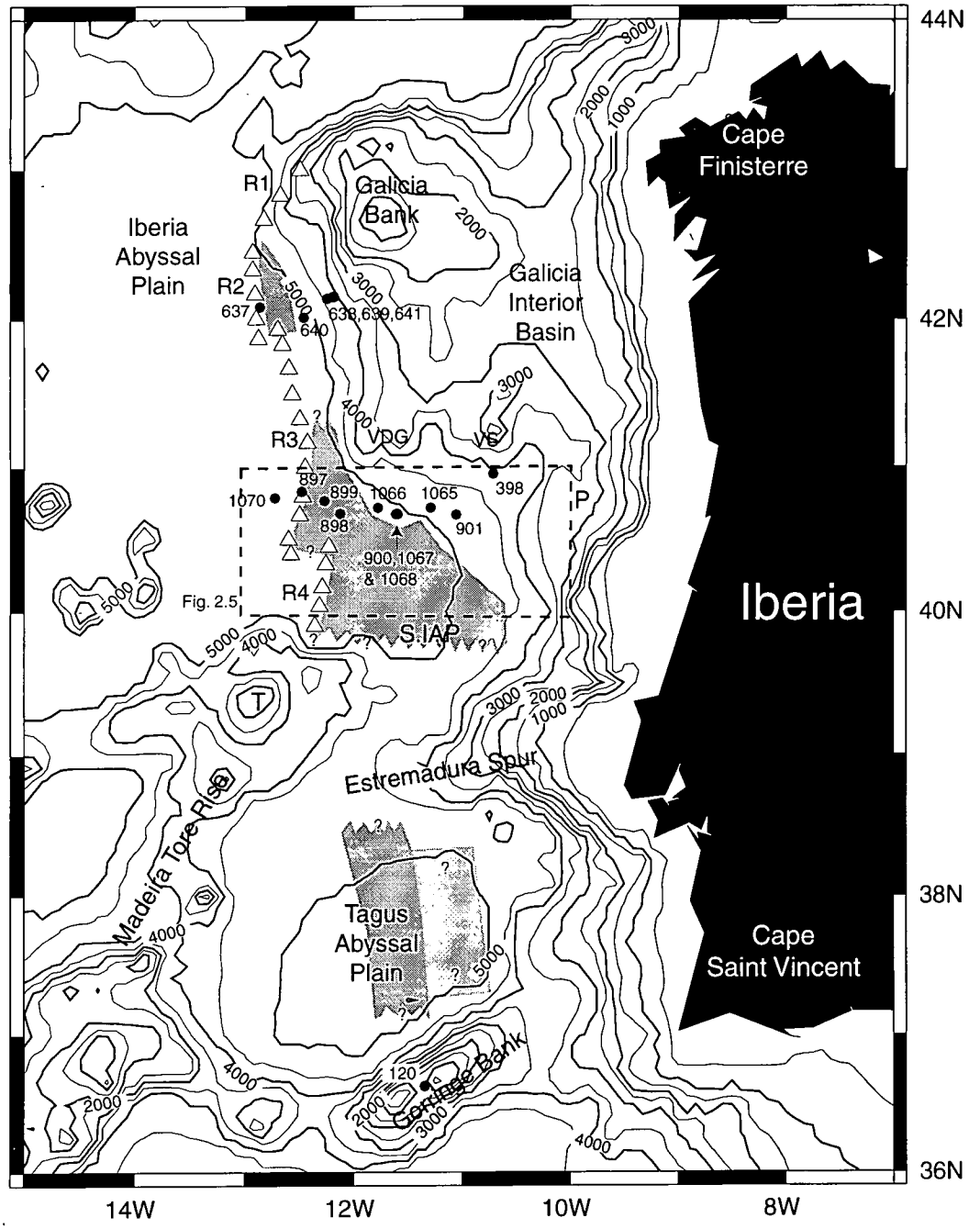

Figure 2.4 Bathymetric chart (500 m contours) west of Iberia showing the three segments of the continental margin. White triangles denote the four segments (R1-R4) of the peridotite ridge (Beslier et al., 1993; Pickup et al., 1996) and the dark shaded areas show the extent of the OCTs (light shaded area is a possible extension of the OCT in the Tagus Abyssal Plain). Black dots mark the positions of drill sites from DSDP Legs 13 (site 120) and 47B (site 398) and ODP Legs 103 (sites 637-641), 149 (sites 897-901) and 173 (sites 1065, 1067-1070). S.IAP=southern Iberia Abyssal Plain; VDG=Vasco da Gama seamount; VS=Vigo seamount; P=Porto seamount; T=Tore seamount. Dashed box marks position of Figure 2.5.

by dredging (Boillot et al., 1979; Dupeuple et al., 1976, 1987; Groupe Galice, 1979; Mauffret and Montadert, 1987), by submersible dives (Boillot et al., 1988b, 1995; Mamet et al., 1991) and by drilling (Boillot et al., 1988a). Mantle rocks were sampled at the Galicia margin thus first demonstrating that the formation of oceanic crust immediately after continental breakup is complicated by the interaction of mantle and the formation of an ocean-continent transition zone.

The basement structure across the margin is interpreted as follows. Continental crust, thinned to about 2-3 km lies east of a basement serpentinized peridotite ridge (segment R2; Fig. 2.4). In a region ~20 km wide immediately east of the peridotite ridge the thinned continental crust is underlain by a layer 3-4 km thick with seismic velocity 7.0-7.6 km/s. This has been interpreted to be either a layer of underplated material (Horsefield, 1992) or serpentinized upper mantle peridotite (Whitmarsh et al., 1996b), the latter of which is consistent with dredge hauls and drilling on the peridotite ridge itself (Boillot et al., 1979; Dupeuple et al., 1976, 1987; Groupe Galice, 1979; Mauffret and Montadert, 1987; Boillot, Winterer et al., 1988). The peridotite ridge is ~10 km wide and has seismic velocities as low as 3.5 km/s (Goldberg and Zinszner, 1988; Whitmarsh et al., 1996b). To the west of the peridotite ridge lies a thin (3 km) oceanic crustal section which is underlain by a ~3-4 km thick layer of high velocity, interpreted to be serpentinized peridotite (Whitmarsh et al., 1996b). At a distance of ~20 km west of R2 oceanic crust ~7 km thick is interpreted, from seismic velocities, to exist (Whitmarsh et al., 1996b). Although Sibuet et al. (1995) modelled deep-tow and surface magnetic profiles and showed that oceanic crust, typified by high (5 A/m) magnetization amplitudes, abuts the western side of the peridotite ridge, the use of magnetics is limited because the timing of rifting and accretion of oceanic crust coincided with the Cretaceous Normal Polarity Chron. As a result, normal and reversed magnetic blocks are not present. Instead the only significant contrast (excluding effects of topography) is caused by the juxtaposition of highly normally magnetized oceanic crust with relatively weakly magnetized continental crust. However, beneath a "breakup unconformity" observed in Leg 103 cores (Fig. 2.4; Boillot, Winterer, Meyer et al., 1987) a reversed polarity interval at Site 631 identified as CM0(R) (Ogg, 1988) indicates that breakup occurred ~120 Ma, near to the onset of the Cretaceous Magnetic Quiet Period.

In addition to basement samples of serpentinized peridotite made along the length of ridge segments R1 and R2, igneous intrusive rocks, associated with the peridotites (Charpentier et al., 1998), have also been sampled. Intrusive gabbros (Boillot et al., 1980, 1988b, 1995; Boillot, Winterer, et al., 1988) which are believed to be derived from the sub-continental mantle have been dated at 122.1±0.3 Ma (Scharer et al., 1995). Similarly mylonitized dioritic

rocks, also samples from the peridotite ridge, have been dated at 122±0.6 Ma (Féraud et al., 1988). Both gabbros and diorites have been interpreted to be representative of syn-rift intrusives. In contrast, a thin undeformed basaltic layer, which covers the oceanward side of the northernmost section of the peridotite ridge, has been dated at 100±5 Ma. Therefore, the sampled basaltic rocks are assumed to be the products of early post-rift oceanic accretion. Such an origin agrees formidably with the magnetic modelling of Sibuet et al. (1995).

2.3.2 The OCT in the southern Iberia Abyssal Plain

The segment of margin in the southern IAP has been intensively studied by seismic refraction (Whitmarsh et al., 1990; Whitmarsh et al., 1993; Discovery 215 Working Group, 1998; Chian et al., in press; Dean et al., submitted), seismic reflection (Beslier et al., 1993; Whitmarsh et al., 1993; Krawczyk et al., 1996; Pickup et al., 1996; Wilson et al., 1996), magnetics (Whitmarsh et al., 1990; Whitmarsh et al., 1993; Whitmarsh and Miles, 1995; Whitmarsh et al., 1996a; Discovery 215 Working Group, 1998), heat flow (Louden et al., 1997), gravity (Whitmarsh et al., 1993) and drilling (Sawyer, Whitmarsh, Klaus et al., 1994; Whitmarsh, Beslier, Wallace et al., 1998) and in general the results indicate that the OCT varies in width from ~40 km in the north to 130-160 km in the south, thus considerably greater than the OCT width adjacent to Galicia Bank (Fig. 2.4). Figure 2.5 shows the location of multichannel seismic profiles (MCS) and seismic refraction profiles in the southern Iberia Abyssal Plain.

The nature of the OCT has been determined from cores and downhole measurements beneath 10 ODP Sites (Fig. 2.6). However, the origin of the OCT basement from geophysical studies is still at present undecided. There are essentially three schools of thought regarding the nature of the OCT. Firstly, Whitmarsh and Sawyer (1996) suggest that the OCT could actually be the product of ultra-slow seafloor spreading (in which case it is strictly incorrect to call the region an OCT); they derive an ultra-slow spreading rate of no greater than 6.3 mm/yr, and more likely 5 mm/yr, from (1) modelled seafloor spreading block M3(R) (Fig. 2.3) immediately west of the peridotite ridge, dated at ~127 Ma, (2) a Tithonian (~146 Ma) date for the deepest sediments drilled at Site 901 (Sawyer et al., 1994), (3) the distance of approximately 130 km between the two locations, providing the basement is oceanic in origin. They argue that because none of the rocks cored during Leg 149 are continental in origin, and more specifically that the Site 900 gabbro has MORB characteristics (Seifert et al., 1996), together with the fact that

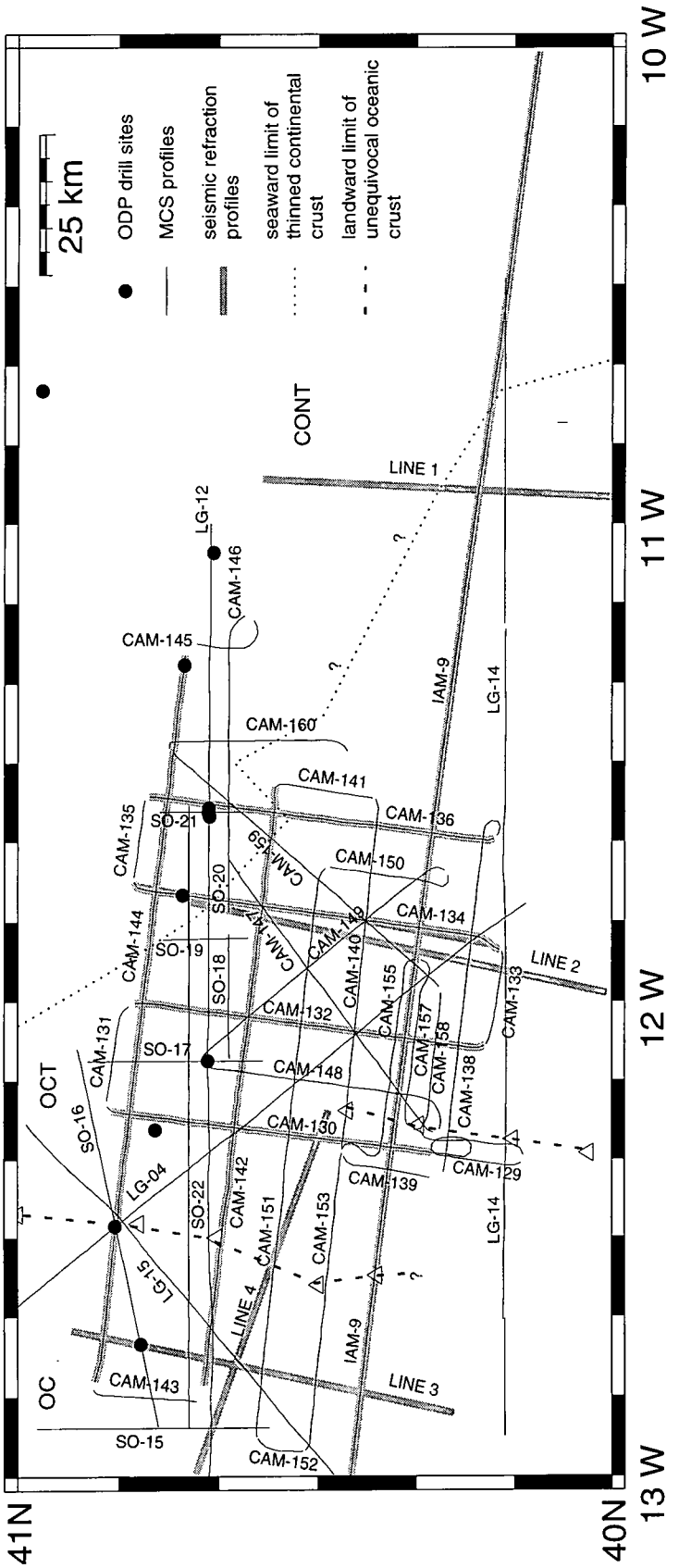

Figure 2.5 MCS and seismic refraction profiles in the vicinity of the ocean-continent transition zone in the southern Iberia Abyssal Plain. MCS profiles acquired on cruises Discovery 215 (CAM profiles; Minshull et al., 1995), Sonne 75 (SO profiles; Roeser et al., 1992), Lusigal 90 (LG; Boillot et al., 1990) and by the IAM projects (Torne et al., 1993; Banda et al., 1995). Seismic refraction lines 1-4 of Whitmarsh et al. (1990), and those coincident with CAM lines and IAM-9 of Chian et al. (1998) and Dean et al. (1998), respectively. The region between the most seaward thinned continental crust (CONT) and the most landward unequivocal oceanic crust (OC) is defined as the ocean-continent transition zone (OCT).

peridotites are commonly exposed at slow and ultraslow accretionary axes (Cannat, 1993) due to a reduction in melt supply (Bown and White, 1995), the rocks within the OCT in the southern Iberia Abyssal Plain are a product of ultra-slow seafloor spreading. Because some of the arguments are involved and many analogues are drawn a full discussion is left until Chapter 7. However, it is important to note that their model is consistent with the drilling results and all published geophysical data with the exception of magnetic anomaly data, which cannot at present be explained by seafloor spreading models (Whitmarsh and Miles, 1995; Whitmarsh et al., 1996a).

A second hypothesis for the nature of the OCT is that the zone consists of serpentinized mantle peridotite with little or no melt products (Pickup et al., 1996; Discovery 215 Working Group, 1998; Chian et al., in press; Dean et al., submitted). Anomalously high velocities (4.5-7.0 km/s) and high velocity gradients within the uppermost 2-4 km of basement, underlain by a high velocity (~7.6 km/s) and low velocity gradient layer up to ~4 km thick have been interpreted to be serpentinized mantle peridotite in which the upper layer represents peridotite serpentinized up to 100% (Discovery 215 Working Group, 1988; Chian et al., in press; Dean et al., submitted). The uppermost highly serpentinized layer may be equivalent to the ~3 km 'unreflective' layer of Pickup et al. (1996), which has been interpreted to be the result of vigorous seawater circulation within unroofed mantle causing a loss of internal character and therefore a decrease in seismic reflectivity. ODP Leg 149 and 173 encountered serpentinized peridotites at Sites 897, 899, 1068 and 1070 within the OCT (Fig. 2.6).

The analysis and modelling of the sea surface magnetic field has revealed that east of peridotite ridge segment R3 the uppermost basement is in general very weakly magnetized (moduli < 0.5 A/m) relative to the oceanic crust west of R3, with the exception of 3 or 4 local magnetic highs (moduli >1.0 A/m; Discovery 215 Working Group, 1998). Moreover, the depths of the magnetic sources computed from the Euler deconvolution of the magnetic field along profile IAM-9, coincident with the MCS profile of Pickup et al. (1996) and the seismic velocity model of Dean et al. (submitted), are predicted to be, in some instances, up to ~3 km below the basement surface as well as at the basement surface (Discovery 215 Working Group, 1998). They suggest that the sources of magnetic anomalies within the OCT could result from hetrogeneities within peridotite mantle or intrusive mafic bodies at (~3 km) depth.

A third hypothesis for the nature of the OCT is that it is a zone of thinned and magmatically disrupted continental crust (Whitmarsh and Miles, 1995). Their evidence stems from magnetic observations alone; linear anomalies within the OCT cannot be explained by seafloor spreading and therefore they suggest that within the framework of a northward propagating rift model the anomalies can be explained by the syn-rift intrusion, and possibly

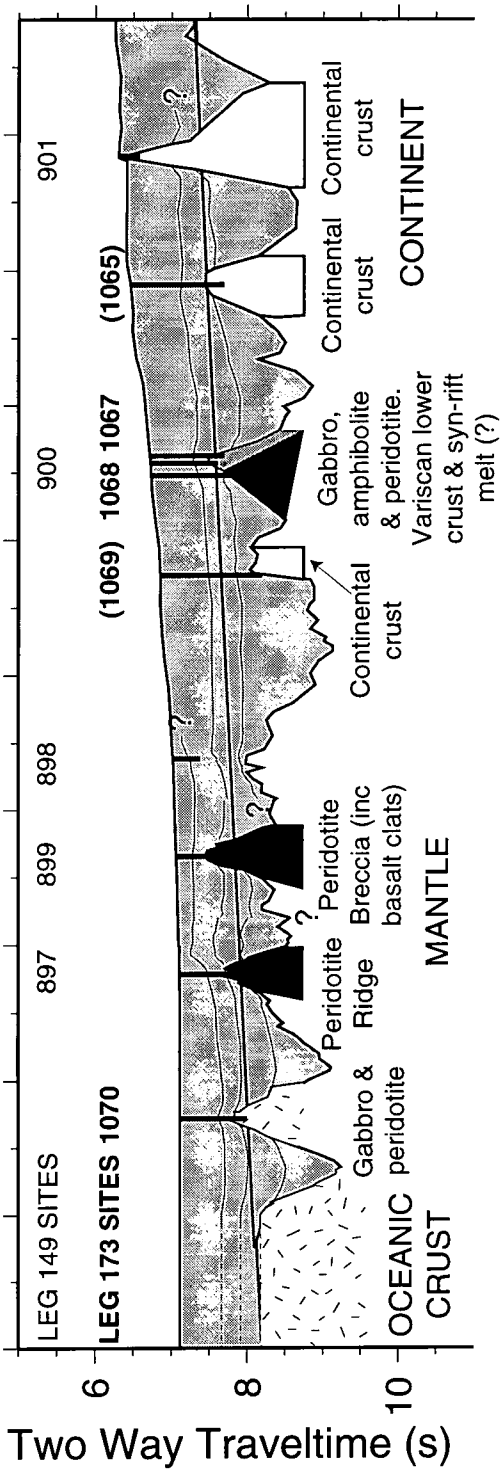

Figure 2.6 Composite sediment and basement profile through ODP sites 1070, 897, 899, 898, 1068, 900, 1067 and 901, and near to ODP Sites 1069 and 1065, derived from multichannel seismic reflction profiles (see Fig. 2.5). Folding in sediments (light grey) is shown by thin lines. Acoustic basement is interpreted to be oceanic crust (dashed), upper mantle (black), syn-rift melt (mid-grey) and continental crust (white) from core lithologies (after ODP Leg 173 Shipboard Scientific Party, 1998).

extrusion, of magmatic material into thinned continental crust. At the end of rifting, the unroofing/emplacement of mantle at the peridotite ridge at the seafloor results in serpentinization of peridotite by seawater, which also penetrates the sub-continental mantle beneath the thinned and intruded continental crust. Although this model satisfies the velocity models of Whitmarsh et al. (1990), recent seismic refraction experiments reveal a high velocity (~7.6 km/s) ~4 km thick lower layer and an upper 2-4 km thick lower velocity (4.5-7.0 km/s) layer with steep gradient (Chian et al., in press; Dean et al., submitted), both of which have been interpreted as non-continental layers. In addition, MCS data (e.g. Pickup et al., 1996) show no signs of tilted continental fault blocks within the OCT.

2.3.3 The OCT in the Tagus Abyssal Plain

In contrast to the OCTs off Galicia Bank and in the southern Iberia Abyssal Plain there is a relative sparsity of data in the Tagus Abyssal Plain. The OCT has been defined to be the region east of ~11°45'W (Fig. 2.4), the most landward position at which magnetic anomalies can be modelled by seafloor spreading (Pinheiro et al., 1992). Immediately east of this location, basement depths increase from ~8 km to ~10 km in a region ~100-130 km wide. In this region magnetic anomalies cannot be explained by seafloor spreading models but instead by a series of blocks whose magnetization magnitudes (0.6-1.1 A/m) are nearer to those required to model seafloor spreading (1 A/m) than typical magnetization magnitudes of continental rocks (<0.1 A/m; see Chapter 3). Within this region, a 2 km thick layer with velocities of 4.4-6.3 km/s is underlain by a 6-8 km thick layer with a velocity of 7.6 km/s. They therefore interpret the zone as an OCT in which intrusive, and possibly extrusive, material is present above a layer of high seismic velocity (7.6-7.8 km/s) interpreted to be serpentinized peridotite.

Bounding the Tagus Abyssal Plain to the south is Gorringe Bank, a 180 km long ENE-WSW ridge which stands, in places, more than 4 km above the abyssal plain (Fig. 2.4). Gorringe Bank is the surface expression of the Africa-Eurasia plate boundary and is believed to be a portion of Mesozoic lithosphere uplifted in the Cenozoic due to local transpressional forces along the plate boundary. From studies on dredged and cored rocks, Cyagor II Group et al. (1984), Féraud et al. (1986) and Prichard and Cann, (1982) have suggested that Gorringe Bank may represent a cross section of oceanic lithosphere similar to that produced immediately after the onset of seafloor spreading, whilst Girardeau et al. (in press) and Whitmarsh et al. (1993) have suggested that it represents a cross section of the OCT itself. Recovered rock

samples consist of serpentinized peridotites with crosscutting dolerite dykes (Cyagor Group, 1978; Auzende et al., 1978, 1979; Cyagor II Group, 1984; Prichard and Cann, 1982). Moreover, plagioclase and clinopyroxenes recovered within the peridotites suggest that they have been impregnated by basaltic magmas (Serri et al., 1988). In addition, recovered mylonitized gabbros are suggested to be associated with the Early Cretaceous rifting episode.

2.3.4 Margin-parallel similarities and differences in basement character

In broad terms, all three segments of the West Iberia margin possess the following common margin-normal characteristics, (1) in the west, a thin (2-4 km) oceanic crust over which the magnetic field can be modelled using a seafloor spreading model magnetization magnitudes typical of oceanic crust ($\geq$ ~1 A/m); (2) a central zone in which a 2-4 km thick upper low velocity, high velocity gradient layer is underlain by a layer of high velocity and low velocity gradient interpreted to be serpentinized peridotite; (3) in the east, tilted fault blocks of thinned and extended continental crust.

The central zone, although having a lower layer of high velocity which is common to all three segments of the margin, shows differences in (a) its upper layer velocity structure, (b) magnetic anomaly character (see next section), and (c) width. West of Galicia Bank the upper layer is, on the whole, interpreted to be thinned continental crust based on its seismic velocity structure (Whitmarsh et al., 1996b), presence of tilted fault blocks, and low amplitude magnetic anomalies (Sibuet et al., 1995). Only a region ~10 km wide (the peridotite ridge itself) is interpreted to be serpentinized upper mantle peridotite. In contrast, in the southern IAP the uppermost layer in the OCT is unequivocally non-continental and non-oceanic based on its velocity structure and linear magnetic anomalies. Similarly in the TAP, an equivalent zone up to 130 km wide is present. The OCT's of the southern IAP and TAP are, at present, thought to consist largely of serpentinized peridotite at the top of basement. Only small amounts of melt products have been recovered from all three segments of the margin.

2.4 Further constraints on the nature and origin of the OCT in the southern Iberia Abyssal Plain.

Given the review of the interpretation of data collected from the West Iberia continental margin, it is clear that the geological characteristics of the basement across the

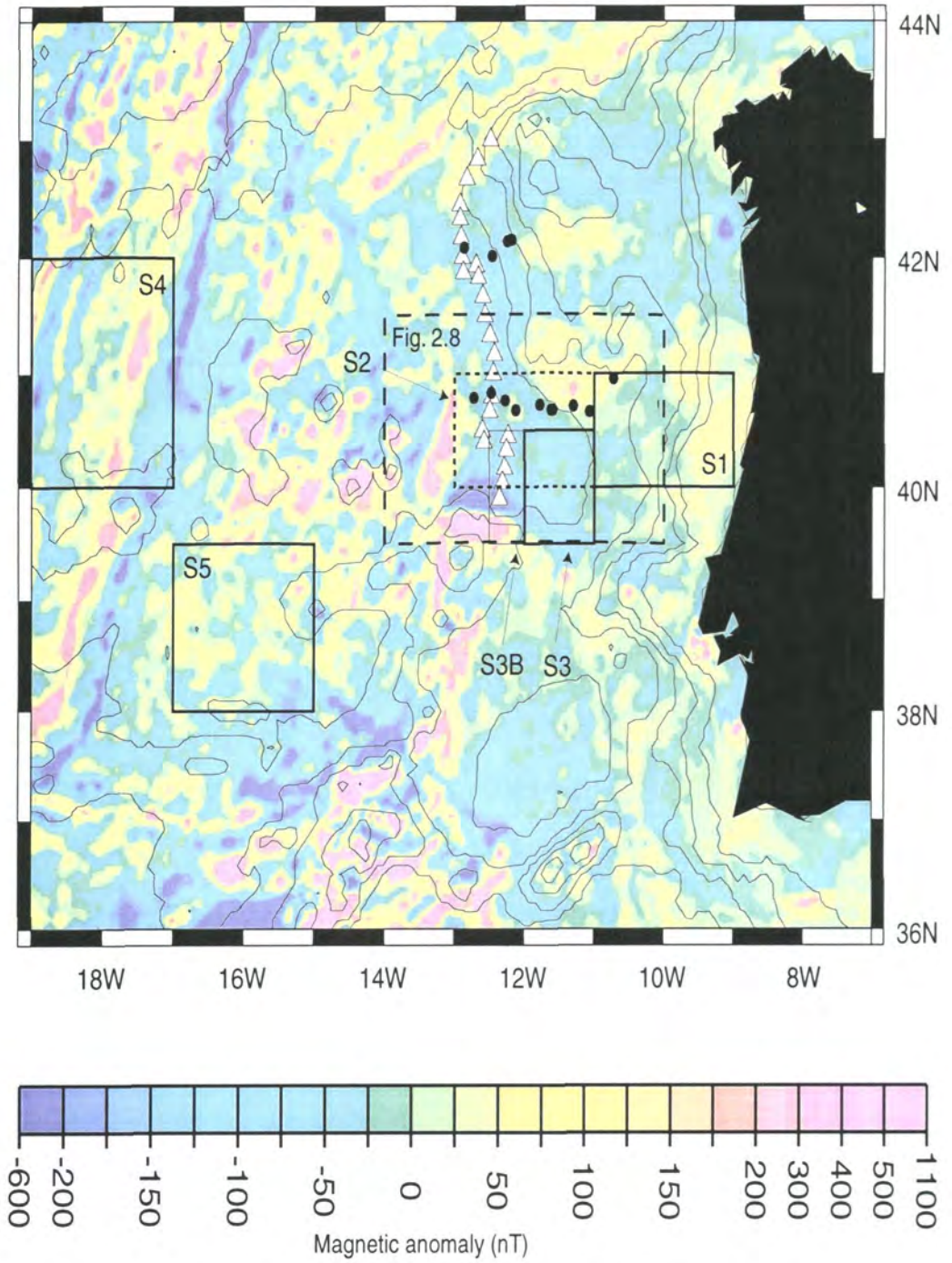

Figure 2.7 Magnetic anomalies west of Iberia (Miles et al., 1996) overlayed by bathymetry contoured at 1000 m intervals. Large dashed box outlines magnetic anomalies used by Whitmarsh and Miles (1995) in their analyses (Fig. 2.8), whilst small dashed box (region S2) outlines the region of dense seismic data coverage; this region is the focus of a detailed magnetic study presented in this thesis. Regions S1, S2, S3, S3B, S4 and S5 are used for analyses in Chapter 5. Note non-linear colour palette. Triangles=peridotite ridge; black dots=ODP and DSDP drill sites (see Fig. 2.4).

margin, and in particular within the OCT, are relatively poorly constrained by the analysis of the magnetic field. Therefore this thesis aims to provide further constraints from the application of traditional and new analyses of the magnetic field in the southern IAP.

The largest dataset used in this thesis is the compiled west of Iberia magnetic anomaly chart of Miles et al. (1996; Fig. 2.7). A subset of this region in the southern IAP between 11°W and 13°W, which has exceedingly good track control (Fig. 2.8), was used for the bulk of the study because of the large amount of independent data available there (Fig. 2.5). Additional magnetic anomaly data, in the form of two pre-existing (Whitmarsh et al., 1996a), and one new, near-bottom magnetometer profiles are utilized in this thesis. The two pre-existing profiles, TOBI91 and SAR93, acquired by three component fluxgate magnetometer sensors mounted on Towed Ocean Bottom Instrument (TOBI) and System Acoustique Remorqué (SAR) were towed by Charles Darwin and Le Suroit, respectively, proved to be highly successful in further constraining the origin of basement within and adjacent to the OCT near ODP Leg 149 Sites 897, 898, 899, 900 and 901 and the subsequent ODP Leg 173 Sites 1067, 1068, 1069 and 1070. This prompted further investigation by near-bottom magnetic profiling.

In the summer of 1995, SAR was towed near-bottom during Discovery 215 along the track of pre-existing MCS profile IAM-9 at ~40°20'N (Minshull, 1995). The initial plan was to collect magnetometer data along two long profiles, both of which crossed thinned continental crust, the OCT, the peridotite ridges and the oceanic crust beneath and adjacent to the J anomaly. Unfortunately, due to a series of technical problems with the SAR, the conducting cable and the depressor weight, in addition to logistical problems associated with SAR recovery, downtime was sufficiently long to only warrant the acquisition of one 200 km profile. This profile, SAR95, however, was acquired east of peridotite ridge R4, across the transition zone and continental slope onto the shelf. A second but much shorter reversed profile was run ~1 km to the north across the shelf and down the continental slope. A strict schedule meant that profiling was terminated prior to sampling transition zone basement on this second profile. Therefore, in total only three useful near-bottom magnetometer profiles exist, two of which (TOBI91 and SAR95) recorded the three spatially orthogonal components of the magnetic field, whereas only total magnetic intensity was recorded on SAR93. Profiles SAR93 and SAR95 were calibrated to remove the effects of motion of the vehicle and its magnetic field by an empirical method (see Appendix I).

Additional data used to complement my magnetic analyses are MCS profiles, totalling over 1500 line kilometers, recorded during cruise Discovery 215 (Minshull, 1995), as well as records of MCS profiles from cruises Sonne-75 (Roeser et al., 1992) , Lusigal-90 (Boillot et al., 1990) and IAM-project (Torne et al., 1993; Banda et al., 1995).

In Chapter 7 I analyse sea surface magnetic intensity data from the conjugate continental margin offshore Newfoundland using a subset of the recently compiled GAMMAA5 dataset (Macnab, pers. comm.).

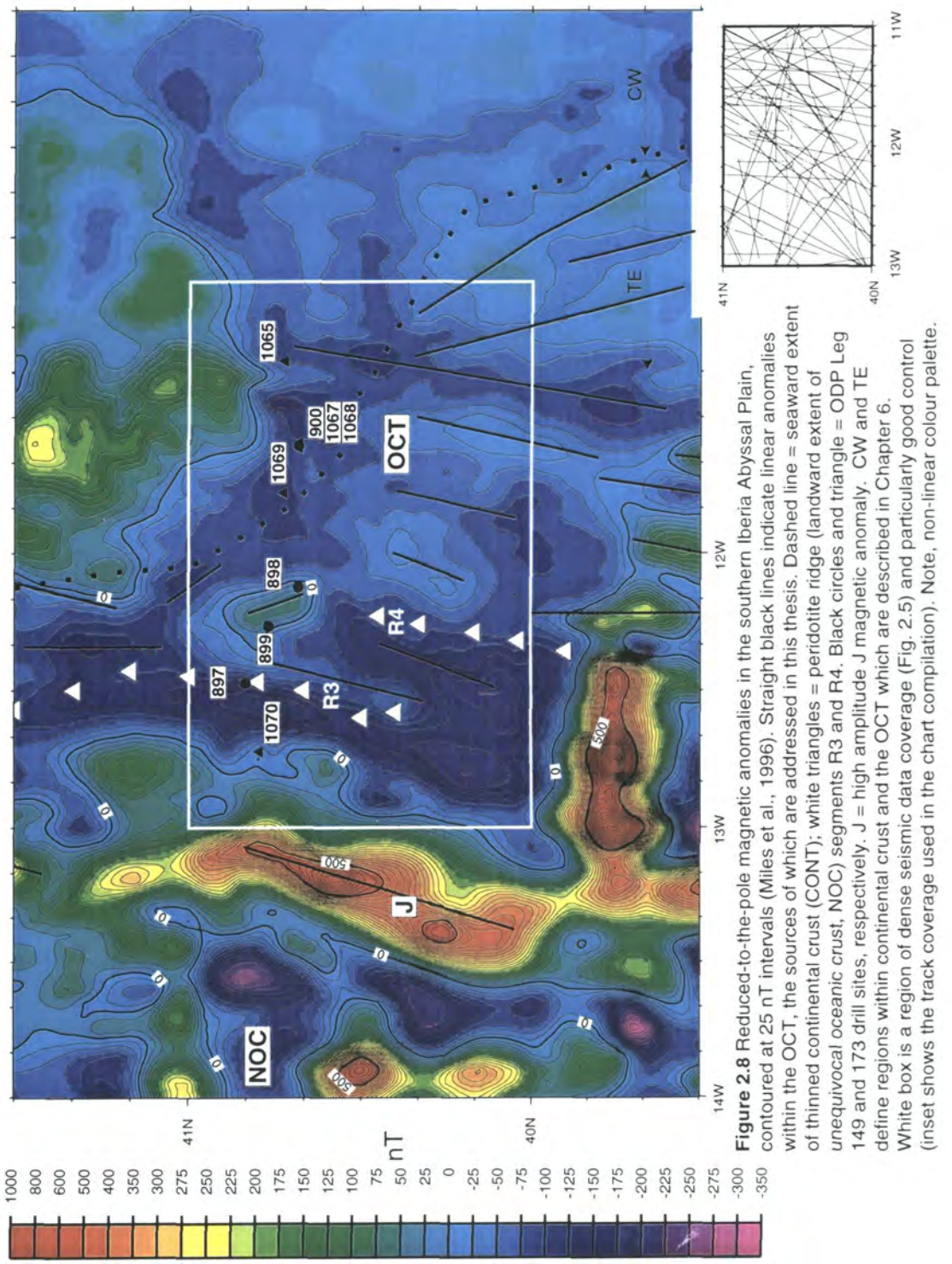

Figure 2.8 Reduced-to-the-pole magnetic anomalies in the southern Iberia Abyssal Plain, contoured at 25 nT intervals (Miles et al., 1996). Straight black lines indicate linear anomalies within the OCT, the sources of which are addressed in this thesis. Dashed line = seaward extent of thinned continental crust (CONT); white triangles = peridotite ridge (landward extent of *unequivocal oceanic crust*, NOC) segments R3 and R4. Black circles and triangle = ODP Leg 149 and 173 drill sites, respectively. J = high amplitude J magnetic anomaly. CW and TE define regions within continental crust and the OCT which are described in Chapter 6. White box is a region of dense seismic data coverage (Fig. 2.5) and particularly good control (inset shows the track coverage used in the chart compilation). Note, non-linear colour palette.

Chapter Three

Indirect magnetic interpretation methods: Methodology and application to theoretical models and anomalies

In this Chapter I give an account of the theory and methodology of the forward and inverse problems. In addition, the results of theoretical tests are used to monitor the signal response to systematic changes in model parameters. Theoretical anomalies based on simple models for the development of the West Iberia margin are generated and their significance discussed. The tests help to provide information on limits of the methods. The results in this Chapter (and Chapter 4) provide the rationale for the analyses on observed data in Chapters 5, 6 and 7.

3.1 Formulation of the forward problem

The traditional way of analyzing potential field data by 'trial and error' matching an observed magnetic anomaly to one generated by a model provides a means of finding a representation of the real subsurface. The theoretical model is one solution to the forward problem providing the calculated field matches the observed field within the bounds of a set of specified conditions.

The theoretical field can be calculated in one of two ways; in the space domain by, for example, Talwani's method (Talwani and Heirtzler, 1964), or in the wavenumber domain by, for example, the method of Parker (1972). Space domain methods are generally based on breaking up a given magnetic body into a set of simpler geometric objects whose associated magnetic fields are calculated individually and summed.

The approach to the solution of the forward problem in the wavenumber domain was successfully applied by Parker (1972), primarily to reduce the number of calculations required to solve the problem. In contrast to the space domain solution, which assumes that each body has a discrete and uniform magnetization, the wavenumber domain solution permits continuous along

axis magnetization magnitude variations, $M(x)$, in a layer whose top is described by $h(x)$ and base is described by $g(x)$. The magnetic layer is assumed to have a constant magnetization vector direction, $\hat{\mathbf{M}}_0$, also described by a dip, I_r, and azimuth, D_r, from true north. Likewise the Earth's field can be described by a constant vector direction, $\hat{\mathbf{B}}_0$, or its associated inclination, I_i, and declination, D_i. The directions of true north and vertically down are given by the unit vectors, $\hat{\mathbf{x}}$, and $\hat{\mathbf{z}}$ respectively. An anomaly $A(x)$ along a profile of bearing β from true north can be described in the wavenumber domain, assuming it is relatively small compared with the observed field (Parker, 1972), by,

$$\Im[A(x)] = \tfrac{1}{2}\mu_0 e^{-|k|z_0} V(k) \cdot \sum_{n=1}^{\infty} \frac{|k|^{n-1}}{n!} \Im\left[M(x) \cdot \left\{(h(x)-z_0)^n - (g(x)-z_0)^n\right\}\right] \tag{3.1}$$

where, $\Im[f(x)]$ is the Fourier transform of function f, μ_0 is the permeability of free space, k denotes wavenumber, z_0 is an arbitrary reference level and,

$$V(k) = \hat{\mathbf{B}}_0 \cdot \left(\hat{\mathbf{z}} + i\hat{\mathbf{x}}\frac{k}{|k|}\right)\hat{\mathbf{M}}_0 \cdot \left(\hat{\mathbf{z}} + i\hat{\mathbf{x}}\frac{k}{|k|}\right) \tag{3.2}$$

which is a complex function and is equivalent to,

$$V(k) = \left(\sin I_i - i\frac{k}{|k|}\cos I_i \cos(\beta - D_i)\right) \cdot \left(\sin I_r - i\frac{k}{|k|}\cos I_r \cos(\beta - D_r)\right) \tag{3.3}$$

In practice, the solution is greatly simplified if the magnetic source layer is of constant thickness, h_0. In addition, the infinite sum is terminated after p summations, when the perturbation from the 'topography terms' (terms for n>0) is less than a given proportion of the previously calculated anomaly. Equation (3.1) can then be rewritten as (Parker, 1972),

$$\Im[A(x)] = \tfrac{1}{2}\mu_0 e^{-|k|z_0}\left(1 - e^{-|k|h_0}\right)V(k) \cdot \sum_{n=0}^{\infty} \frac{|k|^n}{n!} \Im\left[M(x) \cdot (h(x)-z_0)^n\right] \tag{3.4}$$

Each method of forward calculation has its relative merits. Regardless of the fact that the wavenumber domain approach is computationally very fast (because it makes use of the fast Fourier transform), the main advantage is that it allows magnetization variations to be continuous. If the same model were to be constructed in the space domain, very many bodies would be required to simulate a continuous change.

Although the wavenumber domain approach will not allow discrete magnetization steps, such features can be approximated with high wavenumbers. The highest wavenumber faithfully represented is determined by the Nyquist wavenumber, k_N. The associated Nyquist wavelength, λ_N is given by $2\Delta x$, where Δx is the sample spacing.

Unfortunately, a geophysical trade-off exists. In order to apply the forward problem in the wavenumber domain, assumptions must first be made (see Table 3.1). The most limiting assumption is one of a constant magnetization direction; if the subsurface consists of rocks possessing an entirely remanent, or entirely induced, magnetization then the assumption is valid. However, a scenario in which a subsurface consisting of rocks possessing both types of magnetization, and the direction of the Earth's field magnetic field vector is significantly different from the direction of the remanent vector, the assumption is invalid.

The assumption of the level of z_0 is critical to the convergence of the sum in equation (3.4). Although not shown here, optimum convergence is acquired when z_0 is situated between the highest and lowest topographic points on $h(x)$ (Parker, 1972).

If the crust is assumed to be the sole contributor to the magnetic anomaly then the assumption of constant layer thickness may also be reasonable. White et al. (1992) have shown that oceanic crustal thickness is remarkably constant. However, in regions where the oceanic (or continental) crustal layer is non-constant, or the exact source of the magnetic field is uncertain, this poses a serious drawback. In particular, the depth to the top of the magnetic source layer is often assumed to be the top of acoustic (crystalline) basement. For oceanic crust created at ridges spreading at greater than 10 mm/yr, this is almost always a fair assumption. For continental crust, exhumed upper mantle, or oceanic crust created at rates less than 10 mm/yr, it may not be a fair assumption due to the large uncertainty in determining the nature of the source. Indeed, this is one of the aims of the use of the magnetic method in this thesis.

Variables	Assumptions
anomaly, $A(x)$	Earth's field vector, $\mathbf{B_0}$
topography, $h(x)$	Magnetization direction, $\mathbf{M_0}$
Magnetization magnitude, $M(x)$	Reference level, z_0
	Layer thickness, h_0

Table 3.1 Variables and assumptions used in the wavenumber domain forward problem.

Although both the space domain and wavenumber domain forward methods compute the anomaly, $A(x)$, at a constant level, the methods can be extended to calculating $A(x,z)$, i.e. the anomaly on an uneven observation track. In both methods, the observation plane is usually assumed to be at a greater height than the highest topographic point everywhere. However, observations on an uneven observation track that fall below the highest topographic level may cause significant error in the calculation of the anomaly by the wavenumber domain method (Hussenoeder, 1995). The general procedure is to assume an equivalent geometry in which the altitude of the observation level above the top of the source is maintained (Pilkington and Urquhart, 1990). For deep-tow magnetic observations west of Iberia, the acquisition altitudes are great enough for the error involved in the transformation of geometries to be negligible. I therefore use an approximate equivalence without a correction term. In contrast, space domain methods do not suffer from variations in observational plane altitude differences.

In addition to solutions of $A(x)$ and $A(x,z)$, the solution to the forward problem in two dimensions over a level plane, $A(x,y)$, can be calculated. The anomaly over a three-dimensional body is calculated in the space domain by a similar method. However, the description of bodies in terms of the spatial location of vertices and their graphical representation is not easily accomplished. For these reasons, three-dimensional forward modelling using space domain methods is not considered in this thesis. However, the extension of the wavenumber domain equation (3.4) to two dimensions is readily accomplished by the substitution of the scalar wavenumber by a directional wavevector, and assigning $M = M(x,y)$ and $h = h(x,y)$, and performing the two-dimensional fast Fourier transform.

3.2 Criteria for determining goodness of fit

Regardless of the method of obtaining a solution to the forward problem, it is important to

match the theoretical anomaly to the observed anomaly within specified bounds. Models whose solutions fall outside the limits of these bounds are not potential candidates for interpretation. All solutions falling within these bounds are mathematical solutions, but their respective models are not necessarily realistic representations of the subsurface. However, in the absence of further information, all models associated with a mathematical solution are considered. The interpretation is further based on a translation of the model parameters into geological terms. If the geological terms are highly unreasonable then the model is dismissed. Nevertheless, many models may satisfy the observed field.

The degree of match between the observed and forward calculated profiles can be tested by a number of techniques:

(1) The residual between the observed and forward calculated anomalies. This method of comparison is the simplest and approximates to slightly quantitative visual fitting. It is effective because, as function of x, it permits comparison of forward and calculated anomalies over different parts of a model.

(2) The root mean square (RMS) of the residual between the two given anomalies. If the RMS for a given profile falls below a defined threshold then the calculated profile matches the observed within the bounds of the RMS test. The RMS test is insensitive to the absolute values of $F_{obs}(x)$ and $F_{calc}(x)$ and therefore should be used with caution.

(3) Normalized RMS allows a means of comparing the RMS residuals of different observed-calculated anomaly pairs, and therefore provides a means of comparing the effectiveness of models in different circumstances. This is particularly beneficial for comparing an RMS residual between a calculated-observed anomaly pair at the sea surface and one made in near bottom observations. The method used here is to normalize the residual against the maximum peak-to-trough amplitude of the anomaly. Because proportional differences are calculated, rather than absolute differences, the normalized RMS test is not biased by large errors that are associated with large absolute values in $F_{obs}(x)$, for example.

(4) The correlation coefficient (CC) between the observed and calculated anomalies. If $CC = 0$ then the two time- (or space-) series are uncorrelated. If $CC = 1$ then perfect correlation is achieved. If $CC = -1$ then the profiles are perfectly anti-correlated.

The solution of the forward problem need not necessarily be used to match an observed profile. Alternatively, they can be used to monitor the effect of changing model parameters on magnetic anomaly response.

3.3 Experimental application of the forward problem

The following five subsections are aimed at evaluating the effects of some common phenomena associated with the modelling of magnetic anomalies. These are, (1) finite along strike length of bodies, (2) magnetization magnitude and direction, (3) vertical changes in magnetic structure, (4) seafloor spreading rates, and (5) source layer topography. In all cases, unless otherwise stated, anomalies are computed along profiles trending 100° over theoretical models whose remanent magnetization vector direction is typical of crust adjacent to the West Iberia rifted margin in Cretaceous times (declination = -43°, inclination = 58°; Galdeano et al., 1989), and whose magnetization magnitude is ±1 A/m. Profiles of this orientation are approximately normal to seafloor spreading anomalies and anomalies in the ocean-continent transition zone west of Iberia.

The situation described above allows the most probable theoretical anomalies to be generated if basement offshore West Iberia is assumed to possess a predominantly remanent magnetization. The indirect methods, because of their implicit assumptions, especially concerning magnetization direction, lend themselves to a study of this nature. For this reason, the problem is formulated in such a way as to test a particular hypothesis, by the use of assumptions concerning the *general* nature of the basement (i.e. oceanic or continental). In contrast, Chapter 4 is concerned with direct methods which, in general, do not rely on assumptions concerning the magnetization vector of the source, and therefore can be used in a more objective manner.

3.3.1 Test of two-dimensionality

The success with which a model can generate a magnetic anomaly which is similar to an observed anomaly is dependent on the means of generating the anomaly. In the geological sciences many models are assumed to be two-dimensional, i.e. continue to infinity in a direction perpendicular to the line of the profile, but this may not necessarily always be a good representation of the real subsurface. However, many geological situations have a degree of two dimensionality in that features have a finite strike length perpendicular to the profile, and are therefore described as two and a half-dimensional. A 2.5 D feature, or body, can be described by a half-strike length. When the half-strike length approaches the along-axis length the feature is then truly three dimensional. Track to track correlation of anomalies provides a means of testing two

dimensionality. Indeed, surveys are often designed to cross over the centres of bodies, perpendicular to the strike, in order to minimize body end effects and effects of oblique crossings.

To test the effects of finite strike length, anomalies calculated over magnetic bodies with cross sectional geometries of 20 km wide by 6 km thick with varying strike length were compared. The method used to calculate the anomalies was a modification of Talwani's approach in which end correction terms are included (Shuey and Pasquale, 1973). Observations were made at altitudes of 7 km and 2 km above the source in order to simulate observations made at the sea surface and at near-bottom altitudes (deep-tow experiments) west of Iberia, respectively. The half-strike length of the body was varied from 100 km to 5 km and the calculated fields compared with the field generated by a truly two dimensional model (Fig. 3.1). A comparison of the RMS residuals between the 2-D anomaly and the 2.5-D anomalies acts as a check on the goodness of fit. In particular, the RMS residual normalized against the peak-to-trough amplitude acts as a means of comparing the effects of a 2.5-D structure at 7 km and 2 km above the top of the source (Fig. 3.2). It can be seen that models whose half-strikes are greater than 100 km are essentially two dimensional features; their RMS residuals are less than 1 nT, whether observed 2 km or 7 km above the top of the source. This represents a less than 1 % error when compared with the maximum peak-to-trough amplitude. Half strike lengths greater than ~ 20 km generate a less than 5 % error in observation. It can be seen that the shape of the anomaly does not differ significantly until half-strike lengths are as small as 5-10 km (Fig. 3.1). The magnetic effect of the ends of bodies is proportionally greater at a distance of 7 km above the source compared to 2 km above the source, although the difference is insignificant.

3.3.2 Effect of susceptibility on total field observations

As discussed in Chapter 2, a magnetic body can have a remanent magnetization and/or a susceptibility that gives rise to magnetic anomalies. The aim of this subsection is to determine the effect and its significance, if any, that these two types of magnetization have on the resultant magnetic field.

West of Iberia, the remanent vector direction of magnetic sources formed during Cretaceous times is given by an inclination of 58° and a declination -43° (Galdeano et al, 1989). Of course, the vector polarity will be dependent on the polarity of the Earth's field at the time of acquisition of the magnetization. In contrast, an induced magnetization vector is always parallel to the Earth's present day magnetic field, and therefore possesses positive polarity. The present day

field is given by an inclination of 55° and a declination of -6°. Most magnetic bodies possess both types of magnetization, although most common rock types are dominated by one type.

Consider a 25 km wide, 7 km thick magnetic body, whose top is at a depth of 7 km. If the body is magnetized with a resultant magnetization vector whose contributions from remanent and induced components are reasonable, then it is possible to calculate potentially reasonable magnetic fields for a range of bodies. Table 3.2 shows the components of magnetization in a number of given models, whilst Figure 3.3 shows the magnetic field response of the models. If the addition of an induced magnetization is coupled with the loss of the same amount of remanent magnetization, then the effective magnetization magnitude is approximately constant due to the not too dissimilar inclinations and declinations of the two vectors. The resultant magnetic fields sit within an envelope

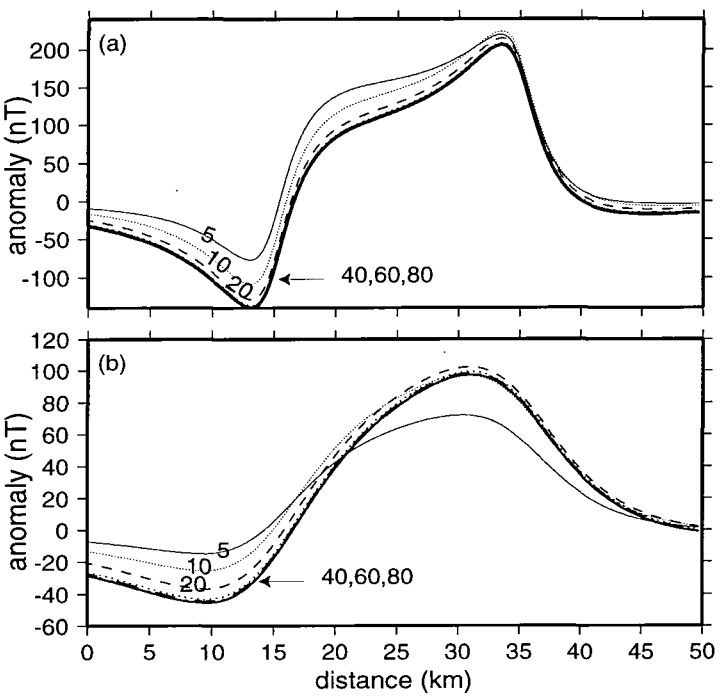

Figure 3.1 The effect of body half-strike length of on calculated magnetic anomaly. Anomaly computed along a track trending 100° over a source body 20 km wide (15-35 km distance) extending from 7 km to 13 km depth. Source body magnetization +1 A/m, D=-43°, I=+58°. Anomaly calculated (a) 2 km above top of source and (b) 7 km above the source to simulate seasurface and near-bottom magnetic observations. Half-strike lengths of 80 km (thick dashed), 60 km (heavy dotted), 40 km (medium dotted), 20 km (medium dashed), 10 km (light dotted) and 5 km (fine solid; also labelled).

whose residual is no greater than 20 nT everywhere. In contrast, if the induced magnetization is added to a remanent magnetization, the outcome is highly dependent on the polarity of the remanent magnetization. Models 5 and 6 (Table 3.2) demonstrate the effect of a susceptibility on normally and reversely magnetized crust, respectively (Fig. 3.3).

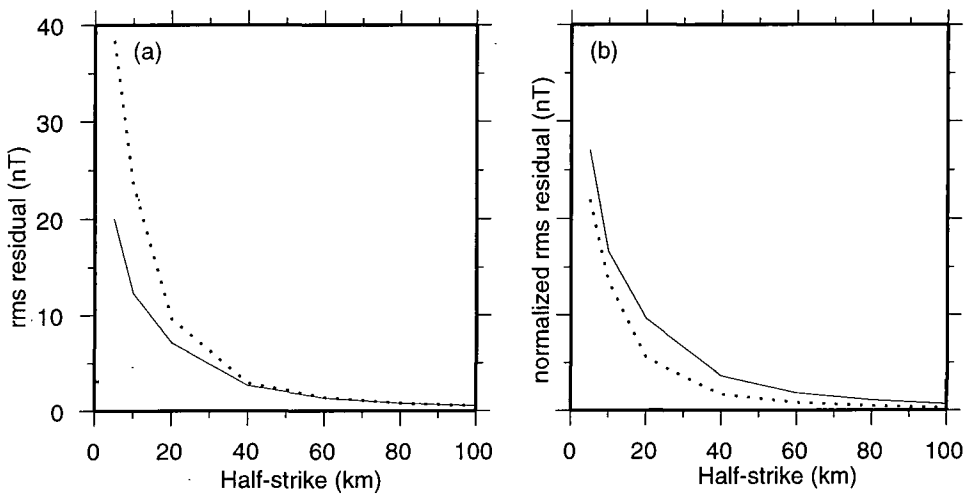

Figure 3.2 The effect of ignoring finite source body length on magnetic anomaly amplitude computed 2 km (dotted line) and 7 km (solid line) above the source (see Fig. 3.1 caption). (a) Rms residual between anomaly computed from 2.5-D body and a 2-D body. (b) As (a) but normalized against the maximum range from the 2-D model. A 2-D body makes a good approximation to a 2.5-D body with misfits < 5% of the maximum signal range when half-strike lengths are > 20 km.

model #	$\lvert\mathbf{J}_R\rvert$ (A/m)	k	$\lvert\mathbf{J}_I\rvert$ (A/m)	$\lvert\mathbf{J}\rvert$ (A/m)
1	0.665	0.001	0.035	0.698
2	0.525	0.005	0.175	0.692
3	0.35	0.01	0.35	0.689
4	0.0	0.02	0.7	0.7
5	0.7	0.02	0.7	1.379
6	-0.7	0.02	0.7	0.243

Table 3.2 Magnetic properties of models 1-6 whose magnetic fields are shown in Figure 3.3. $\lvert\mathbf{J}_R\rvert$, $\lvert\mathbf{J}_I\rvert$ and $\lvert\mathbf{J}\rvert$ are remanent, induced and resultant effective magnetization magnitudes, respectively, whilst k is susceptibility. The induced magnetization is calculated from the susceptibility assuming an ambient magnetic field of 44400 nT.

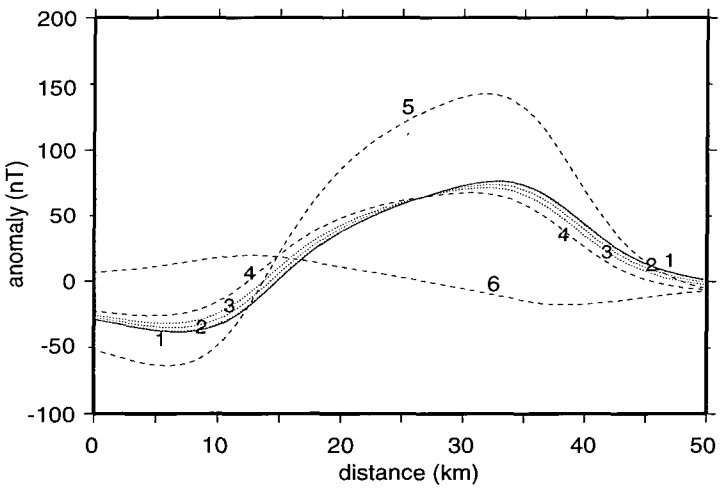

Figure 3.3 The effect of varying the strength of remanent and induced magnetization on synthetic magnetic anomaly amplitude. Magnetic source body as in Fig. 3.1 except at 12.5-37.5 km distance, at 7-14 km depth and magnetization vectors defined by models 1-6 (labelled) in Table 3.1. Models whose magnetization comprises entirely positive remanent magnetization (0.7 A/m; solid line) and entirely induced magnetization (model 4) generate magnetic anomalies which define an envelope with maximum range < 20 nT. Models 1-4 fall within the envelope. Addition of induced magnetization to remanent magnetization in the model generates anomalies 5 and 6.

3.3.3 Effect of vertical oceanic crustal structure on total field observations

Direct observation and sampling of oceanic crustal rocks, via boreholes or dredge hauls, provide the only means with which to determine their exact magnetic properties. Nevertheless, the small-scale description of a hand specimen or core is not necessarily representative of a whole region, making it very difficult to infer the gross magnetic properties of the oceanic crust. Therefore, the vertical and horizontal changes in magnetic properties are of paramount importance if a realistic first order crustal magnetization model is to be used as a partial constraint in magnetic modelling. The link between the igneous model of oceanic crust with that of the layer model determined seismically is of prime importance to the understanding of oceanic crust. Together with models of the distribution of magnetic minerals within specific rock types (Fig. 1.6), a magnetically layered crust can be approximated by a simple vertically sided block model of uniform magnetization by the forward problem.

In Chapter 1 I presented two magnetization models of the oceanic crust (Kent et al., 1978; Dunlop and Prévot, 1982). Here their quantitative magnetic anomaly expressions are computed in order to show the degree to which they match a uniform (magnetization) vertically sided block model. A vertically sided block model with uniform magnetization distribution is preferred because it represents the crust in its most simple form, thus making the process of forward modelling much easier logistically. In addition, the assumption of a constant thickness single magnetized layer made in the forward and inverse wavenumber domain methods is more easily put into context.

	magnetization (A/m)							
model #	2A (0.5)	2B (1.5)	3A (2.0)	3B (3.0)	4(a) (1.0)	approx. uniform model* (A/m)	RMS (nT)	Description
Fig. 3.4a & b								
1	**2.5**	**0.5**	**1.0**	**0.2**	**0.0**	0.7	3.04	Dunlop and Prévot (1982) with no serpentinized layer 4
2	**5.0**	**0.0**	**1.0**	**1.0**	**0.0**	1.1	2.38	Kent et al. (1978) with no serpentinized layer 4
3	**2.5**	**0.0**	**1.0**	**1.0**	**0.0**	0.9	1.08	Model 2 with a reduced layer 2A magnetization
Fig. 3.4a								
4	**5.0**	**0.0**	**0.0**	**0.0**	**0.0**	0.9	27.58	Crust approximated by layer 2A only
5	**2.5**	**2.5**	**0.0**	**0.0**	**0.0**	0.5	16.98	Equivalent of 2 km thick layer 2A
6	**2.5**	**0.0**	**0.0**	**0.0**	**0.0**	0.1	51.16	
7	**2.5**	**0.0**	**0.0**	**0.0**	**0.0**	0.1	4.10	Magnetization vector parallel with present Earth's field
Fig. 3.4b								
4	**2.5**	**0.5**	**1.0**	**0.2**	**2.5**	1.0	1.50	Dunlop and Prévot (1982) 1 km serpentinized layer 4
5	**2.5**	**0.5**	**1.0**	**0.2**	**1.0**	0.9	2.32	
6	**2.5**	**0.5**	**1.0**	**0.2**	**0.5**	0.8	4.65	
7	**2.5**	**0.0**	**1.0**	**1.0**	**2.5**	1.1	3.32	Kent et al. (1978; reduced 2A magnetization) with 1 km serpentinized layer 4
8	**2.5**	**0.0**	**1.0**	**1.0**	**1.0**	1.0	1.65	
9	**2.5**	**0.0**	**1.0**	**1.0**	**0.5**	0.9	2.21	

Table 3.3 Magnetization (A/m) of individual layers (bold) in a multi-layered model comprising oceanic layers 2A, 2B, 3A, 3B, and a 1 km upper mantle source layer. Thicknesses (km) of individual layers are shown. Approximate equivalent uniformly magnetized (A/m) uni-layer block models (underlined) and RMS differences between these and the multi-layer models are shown. * = uniform layer is 7 km thick.

The amplitude of the two-dimensional magnetic anomaly over an oceanic crustal block 25 km wide and 7 km thick with its upper surface at 7 km depth is highly dependent upon the magnitude of magnetization (Fig. 3.4). The peak-to-trough amplitude of the anomaly increases approximately by 150 nT per A/m increase in magnetization of the block model. On comparing uniform (single layer) block models with previously hypothesized (multiple layer) crustal magnetization models, the model of Dunlop and Prévot (1982) can be very closely approximated by the uniform model of 0.7 A/m (solid line in Fig. 3.4). The RMS residual between the two theoretical profiles is 3.04 nT, and their correlation is 99 %. The model of Kent et al. (1978) very closely approximates to a uniform model of 1.1 A/m (dashed line in Fig. 3.4) with a RMS residual of 2.38 nT and a correlation of 99 %. A model similar to the one of Kent et al. (1978), but instead with a reduced magnetization of layer 2A[1] from 5.0 A/m to 2.5 A/m, can be approximated by a uniform block model of magnetization 0.9 A/m. A reduction in magnetization of layer 2A is compatible with a decay of TRM through time (Raymond and LaBrecque, 1987).

An RMS residual of 1.08 nT and a correlation coefficient of 99 % means that the two models produce almost identical magnetic fields and therefore represent a pair of non-unique solutions in an infinite family. Table 3.3 and Figure 3.4a show the results of various other models. All models correlate 99% except model 7 in Figure 3.4a. It can be seen that crustal magnetization models in which seismic layer 2A is the sole contributor (Talwani et al., 1971) cannot be approximated by the uniform 7 km thick block model to the same extent as models in which the whole crust contributes, but not necessarily evenly, to the magnetization distribution (models 4-7 in Table 3.3 and Figure 3.4a). RMS residuals or correlation coefficients fall below the limits that define a good fit. For models possessing entirely remanent magnetization (models 1-6), the mis-match between the uniform block model and one described by a magnetic layer 2A is described statistically by the RMS residual and correlation coefficient. In real terms there exists a phase shift and amplitude error between the two theoretical anomalies. Amplitudes are reasonably well matched but the phases of the two anomaly profiles are mis-matched, especially near the edges of the body. This phenomenon is intrinsically linked with the concept of anomalous skewness (Schouten and McCamy, 1972; Cande, 1976, 1978; Cande and Kristofferson, 1977; Roest et al., 1992a; Dyment et al., 1994; and others). The conventional two-dimensional oceanic crustal magnetization model is one in which layer 2A, a rectangular prism of constant magnetization

[1] Although there is not a 1:1 correspondence between seismic layer 2A and the extrusive layer (Leinen, Rea et al., 1986) the two are considered the same here.

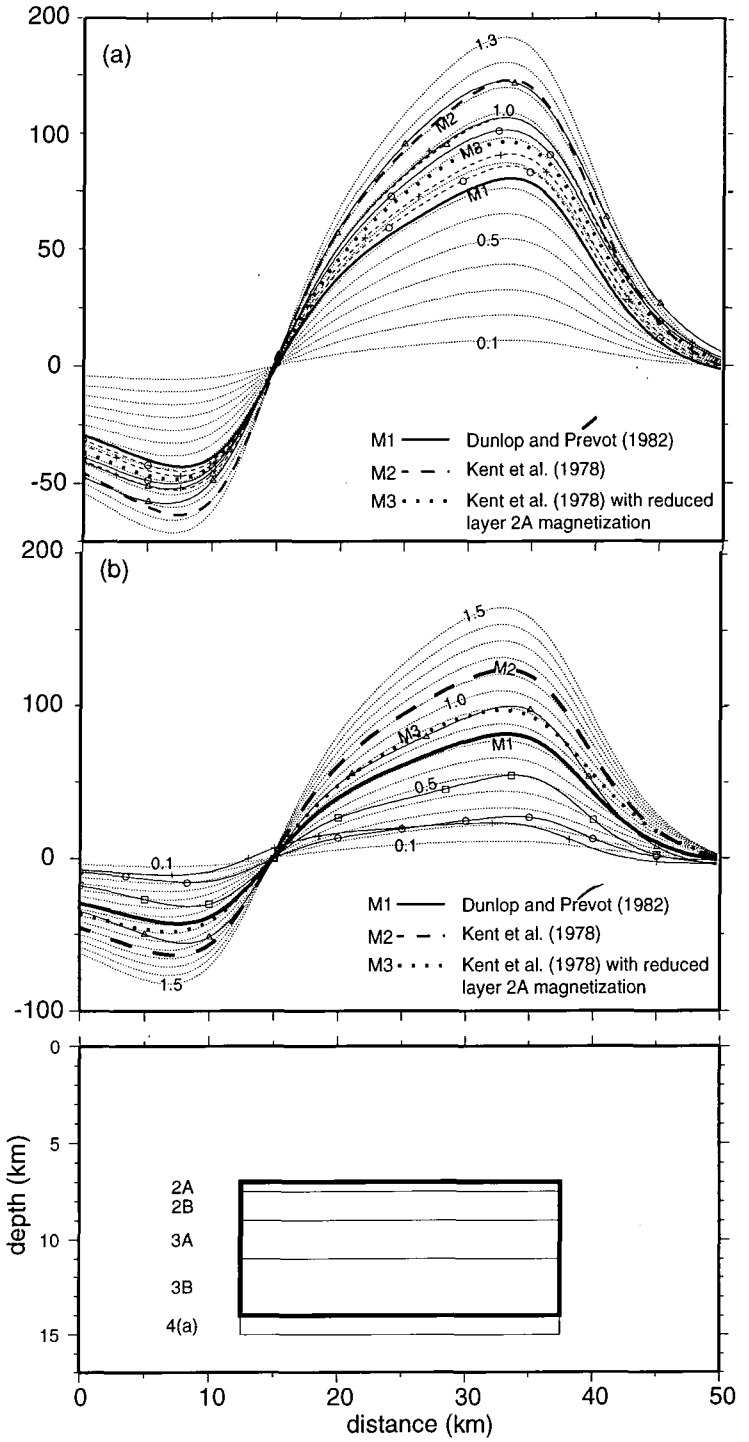

Figure 3.4 Comparison of magnetic anomalies produced by layered oceanic crustal magnetization models and uniform magnetization block models. Lower panel shows geometry of layered models (layers defined by thin lines) and block model (heavy box). (a) and (b) Synthetic magnetic anomalies produced by uniform block models (thin dotted lines; magnetization magnitude incremented by 0.1 A/m and labelled A/m) and layered models 1, 2 and 3 (labelled M1, M2 amd M3; see Table 3.3). (a) Models with an additional serpentinized upper mantle layer 4(a) are described in Table 3.3 and their anomalies given by thin dashed lines augmented with triangles (model 4), crosses (model 5), and circles (model 6) when variants of model 1, and given by thin solid lines augmented by triangles (model 7), crosses (model 8) and circles (model 9) when variants of model 2. (b) As (a) except thin solid lines augmented by triangles (model 4), squares (model 5), circles (model 6) and crosses (model 7) represent anomalies produced by models defined in Table 3.3. See text for discussion.

direction and magnitude, is the only contributor to the magnetic field. The phase of the anomaly primarily depends on the inclination of the magnetization vector of the extrusive layer and the geomagnetic field vector, but additional phase shifts may be due to contribution from lower crustal rocks which are disregarded in the conventional model (e.g. Pariso and Johnson, 1993a & b; Dyment and Arkani-Hamed, 1995). The model sought here is one in which the whole crust contributes to the magnetic field.

If seismic layer 2A has been significantly altered since its formation, then a secondary chemical remanent magnetization (CRM) may develop, within the first 20 Ma of crustal evolution, parallel to the ambient field at the time of formation (Raymond and LaBrecque, 1987). Because the acquisition of a CRM is usually at the expense of the primary TRM, the resultant magnetization vector can take a range of magnetization directions and magnitudes. The age of the basalt is significant in that layer 2A TRM decays exponentially with a time constant of the order of 5 Ma through alteration, and the exponential growth of secondary CRM has the same time constant. Therefore, oceanic rocks 20 Ma old have, by this process, only ~2% of their original TRM remaining, whilst oceanic rocks over 100 Ma will have significantly less (10^{-11} if exponential decay continues), and consist of almost all secondary CRM. The following discussion therefore considers rocks with NRM consisting entirely of CRM.

The rotation of Iberia took place in late Cretaceous times (Srivastava et al., 1990a), therefore the ambient field declination at any given time of normal polarity between late Cretaceous and will be bounded by -43° (prior to rotation; Galdeano et al., 1989) and 0°. Geographic north acts as the minimum bound because of the assumption that declination of the Earth's field vector averages to zero through time (geocentric dipole field hypothesis). The magnetic inclinations of 58° in late Cretaceous times (Galdeano et al., 1989) and 56° at present can be assumed to be reasonably constant due to the lack of a north-south component of motion along the almost continuous north-south trend of the Mid-Atlantic Ridge. Thus, the phase difference between unaltered normally magnetized basaltic layer and the equivalent altered layer, which has acquired its magnetization within a normal polarity chron subsequent to the start of rotation of Iberia, will be small (Fig. 3.5). Likewise if primary reversely magnetized basaltic layer 2A acquires a secondary CRM within a reversed polarity chron, the phase difference between the two anomalies will be small.

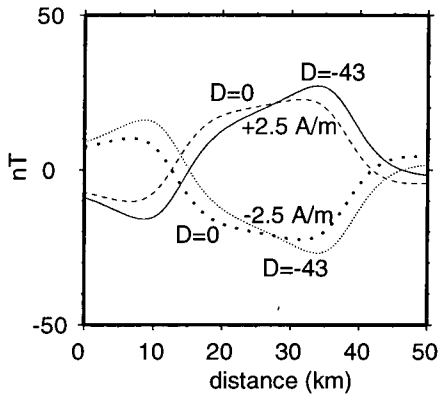

Figure 3.5 Effect of change in declination of remanent magnetization on synthetic magnetic anomaly. Magnetic source is equivalent to a ±2.5 A/m (I=57°) magnetized layer 2A (see Fig. 3.4) at a distance of 12.5-37.5 A/m. Declinations of remanent vectors are labelled.

In all cases, the amplitude difference will depend on the effective magnetization of the secondary CRM. Although the acquisition of a secondary CRM makes only small differences to anomalies, the assumption (that a significant CRM is acquired) has been criticized based on two lines of evidence: (1) rock magnetism studies (Beske-Diehl, 1989); (2) the reversed polarity of blocks M0(R) and M1(R), which immediately precede the Cretaceous Magnetic Quiet Zone (CMQZ; they should be inverted). Because M0(R) and M1(R) are not inverted, I assume that no significant secondary CRM is present in models of the oceanic crust, in general, although the decay of TRM is still likely to occur through time.

In addition to lower crustal sources, it has been proposed that upper mantle sources, in the form of serpentinized peridotites, can contribute greatly to the magnetic field (e.g. Dunlop and Prévot, 1982; Harrison, 1987; Dyment and Arkani-Hamed, 1995). The effect of adding a 1 km thick layer to the base of layer 3B in models (1) and (3) above is to increase the amplitude of the theoretical field anomaly so that it matches with the anomaly of a uniform block model of slightly higher magnetization (Table 3.3 and Fig. 3.4b).

The reduction of a magnetically layered crust to a vertically sided block model of uniform magnetization is also successful in situations where more than one body exists (Fig. 3.6). This therefore allows a means of constructing simple models of a realistic oceanic crust in which the theoretical anomaly can be compared with those observed at the sea surface.

The theoretical magnetic field over a given model is extremely sensitive to the depth to the upper surface of the model. As was shown in Figure 1.5, the amplitude of the anomaly due to a point source is approximately proportional to the square of the depth. In the broadest sense, any arbitrarily shaped body is composed of many point sources. Therefore the contribution to the magnetic field of layer 3B, for example, in a layered oceanic crustal model, is greatly increased if it is nearer to the level of observation. Such differences in distance from a model source to an

observation level become important if near bottom magnetic field observations are made. At present day accretionary axes, the top of the magnetic layer is at, or within a few meters of, the seabed. However, in the southern Iberia Abyssal Plain the magnetic source layer is commonly ~2 km below the seabed, if the top of the magnetic layer is assumed to be coincident with the top of acoustic basement.

The effect of computing the magnetic field on an observation level 2 km above the top of an oceanic crustal model, compared with 7 km, is to increase the anomaly amplitude approximately three-fold (Fig. 3.7, cf. Fig. 3.6). Theoretically, for an isolated point dipole source, the increase in

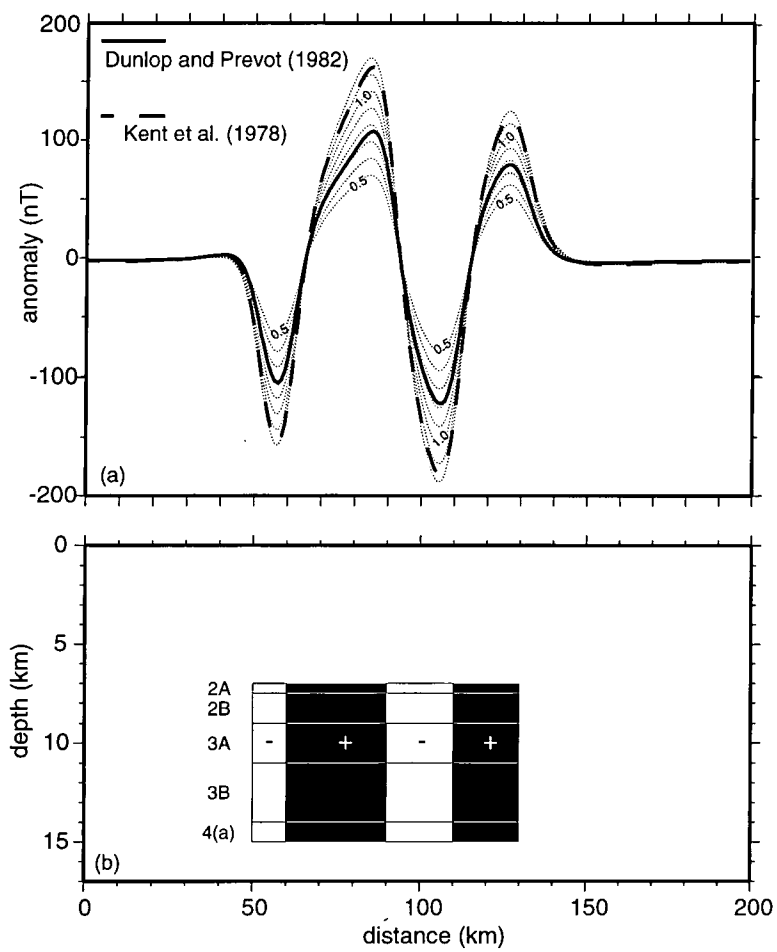

Figure 3.6 (a) Comparison of magnetic anomalies produced by layered oceanic crustal magnetization models and uniform magnetization block models for normal and reversed blocks. Synthetic magnetic anomalies produced by uniform block models (thin dotted lines; magnetization magnitude incremented by 0.1 A/m and labelled) and layered models of Dunlop and Prevot (1982) and Kent et al. (1978). (b) Geometry of magnetic models; black=positive magnetization, white=negetive magnetization. Blocks with magnetization magnitudes 0.7-1.1 A/m make good approximations to a realistic layered magnetized crust when observations are made 7 km above the source layer.

anomaly amplitude should be approximately twelve-fold (for the 7 km case). Realistically the subsurface is represented by non-point dipole source bodies whose magnetizations are distributed throughout a finite volume, rather than focused at a point, and therefore the theoretical twelve-fold increase is never achieved. Nevertheless, the magnetization models of Dunlop and Prévot (1982) and Kent et al. (1978) can be approximated by uniformly vertically sided block models by the method of comparing the magnetic fields generated by both models in the same manner as above (Fig. 3.7). The model of Dunlop and Prévot (1982) is best represented by a model of uniform magnetization of 0.7 A/m, whereas the model of Kent et al. (1978) is best represented by a model of uniform magnetization of 1.1 A/m. The RMS residuals are ~ 25 nT in both cases (fig. 3.8). Exactly the same result was found when the theoretical field was computed 7 km above the top of layer 2A, representative of observations at the sea surface (Fig. 3.6). However the RMS residual between the two anomalies in this case (computed for uniform model and layered model) was found to be less than ~ 3 nT in both cases. The difference in the RMS residuals at the two observation planes once normalized against the maximum peak-to-trough amplitude suggests that a uniform block model is a slightly better representation of the crust when observations are made 7 km above the source rather than 2 km above the source. The normalized RMS results are shown in Table 3.4. It can be seen that the RMS errors are never greater than 4.0 % of the maximum range and therefore the difference in absolute RMS values is not significant.

The overall effect is that geologically reasonable layered crustal magnetization structures can be described by vertically sided prisms, with flat upper and lower surfaces and uniform magnetization distributions. The bulk magnetization usually falls in the range 0.7 A/m to 1.2 A/m. This result greatly simplifies the procedure of modelling more complex observed anomalies.

Observation level (km)	Dunlop and Prévot (1982) model and uniform 0.7 A/m	Kent et al. (1978) model and uniform 1.1 A/m
2	**4.0**	**2.8**
7	**1.3**	**0.1**

Table 3.4 RMS errors between layered and best fit block models for given observation altitudes, given as a percentage of the maximum peak-to-trough amplitude (bold).

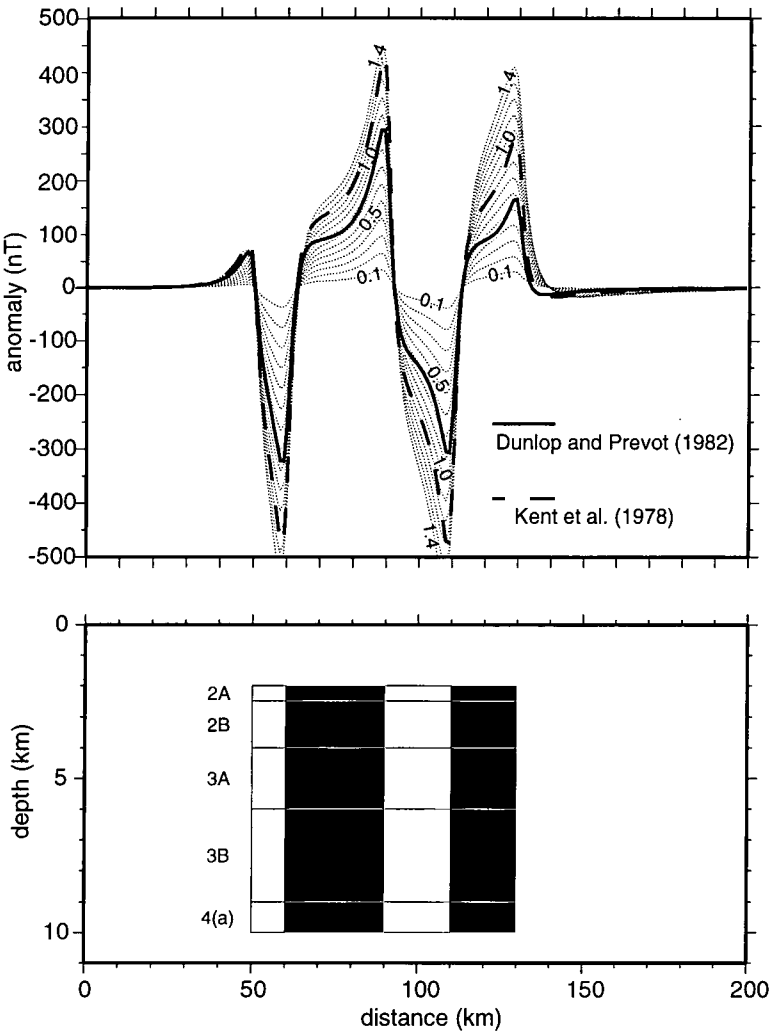

Figure 3.7 As Fig. 3.6 except magnetic anomalies are computed 2 km above the top of the models in order to simulate near-bottom observations. The models of Dunlop and Prevot (1982) and Kent et al. (1978) can be approximated by uniform magnetization block models (0.6-1.3 A/m).

3.3.4 The effect of spreading rate on total field observations

Many characteristics of the morphology and structure of oceanic crust are dependent upon spreading rate, none more so than the distribution of magnetization. Together with the reversal timescale, the main effect of the spreading rate on the magnetic structure of oceanic crust is to determine the horizontal spacing of adjacent normal and reversely magnetized blocks and the degree to which anomalies caused by short-lived polarity intervals can be resolved. In addition, the spreading rate can also have an effect on the vertical magnetic structure, but this is not considered in this section.

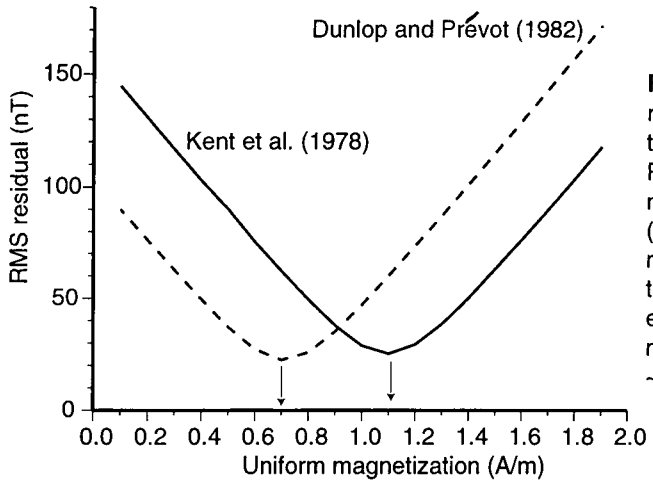

Figure 3.8 Theoretical errors made in the reduction of a layered magnetization model to a uniform magnetization block model. Rms residua between (1) the layered magnetization model of Dunlop and Prévot (1982) and a block model of uniform magnetization magnitude 0.7 A/m and (b) the layered magnetization model of Kent et al. (1978) and a block model of uniform magnetization magnitude 1.1 A/m, are ~20 nT.

Any prismatic magnetic body whose magnetization vector is inclined to the vertical will produce a magnetic anomaly consisting of a peak associated with one its sides, and a trough associated with the opposite side. The polarity of the vector determines the direction in which the anomaly is skewed. A profile trending 100° across 2-D seafloor spreading blocks with a reasonable remanent magnetization vector (Galdeano et al., 1989) produces a magnetic anomaly whose peak is over the eastern side of the block with a trough over its western side. It is the identification of these linear anomalies, and their correlation with the reversal timescale, which acts as the main line of evidence for the assumption that oceanic crust, rather than continental crust or mantle, is present. However, the isolation of these anomalies is determined by the spacing of the sources. If the sources are too close to each other then the individual anomalies interfere and the resultant anomaly cannot be easily related to the bodies.

Assuming the reversal timescale of Gradstein et al. (1995; Fig. 2.1) and that the formation of oceanic crust can be approximated by vertically sided blocks, two-dimensional magnetic anomalies have been computed over oceanic crust along a track trending 100°. The magnitude of magnetization of each reversal unit is assumed to be ±0.8 A/m (approximating the model of Dunlop and Prévot. 1982), and distributed evenly within a 7 km thick layer. Anomalies over accretionary oceanic crust generated between chron CM0 time (~120.38 Ma) and chron CM29 time (~156.85 Ma), at spreading rates from 2 mm/yr to 16 mm/yr, in 2 mm/yr increments, were calculated on observation levels 7 km (Fig. 3.9) and 2 km (Fig. 3.10) above the uppermost layer of the model in order to approximately simulate theoretical anomalies at the sea surface and in near-bottom observations.

Typically peak to trough amplitudes of 200 nT and wavelengths of 10 km or more are

observed on an observation plane 7 km above the source, although the spreading rate is a controlling factor. For all the spreading rates used, anomalies east of aM3(R) or aM4(N) (equivalent to those older than CM3(R) and CM4(N)) are not discernible in terms of a distinctive peak or trough being clearly independent of the overall response. Anomaly aM3(R) is a distinctive negative feature at spreading rates as low as 4 mm/yr, whilst the effects of M2(N) and M1(N) give rise to a broad positive feature. For spreading rates equal to or greater than 10 mm/yr distinct positive anomalies aM2(N) and aM1(N) are separated by a distinct negative anomaly aM1(R) whilst at spreading rates less than 10 mm/yr the effects of the two positively magnetized blocks merge to form a single positive anomaly. The large duration of chrons CM1(N) and CM3(R) means that the anomalies are distinct even at very low spreading rates when anomaly blocks are very narrow. In contrast, chrons older than CM4(N) are mostly short and therefore the resultant block widths are narrow even at spreading rates as large as 16 mm/yr. The associated anomalies therefore interfere and the result is a subdued anomaly profile with few distinct peaks or troughs. However, there are two exceptions; (1) the trough-peak pair associated with the effects of M11(R) and M11A(N) and M12.1(N) together which can be seen at spreading rates as low as 8 mm/yr (P in Fig. 3.9), and (2) the peak-trough pair associated with the effects of M16(N) and M17(R) which can be seen at spreading rates as low as 4 mm/yr (Q in Fig. 3.9). However, in general anomalies east of aM4(N) are subdued with peak to trough amplitudes < 100 nT.

For spreading rates of 4 mm/yr or more, the overall effect of the relatively large chron duration of ~1 Ma in the early part of the M-series (CM0(R) to CM4(N)), compared to the short duration (< 0.5 Ma) of older chrons (CM5(R) and older) is to give the appearance of an edge effect, which defines two zones of anomaly character. To the west of aM3(R) and aM4(N) anomalies are relatively easily correlated to their causative bodies, especially at spreading rates of 10 mm/yr or more. East of aM4(N) the interference of anomalies arising from narrower blocks means that individual blocks do not have distinctive associated anomalies. This relatively simple observation may have a significant effect on the interpretation of anomalies observed at the sea surface west of Iberia and offshore Newfoundland.

The effect of spreading rate on the calculated total field magnetic anomalies is much more significant on observation planes that are nearer to the source. Near-bottom observations, simulated by an observation level 2 km above the tops of the magnetic sources, reveal a much finer detailed magnetic anomaly pattern in the aforementioned zone east of anomaly aM4(N) (Fig. 3.10). Chrons older than CM4(N) produce distinct associated anomalies for models in which the

spreading rate is as low as 6 mm/yr, with the exception of short chrons (< ~0.3 Ma in duration) between CM6(R) and CM14(R). Not unless the spreading rate is 16 mm/yr or more do these reversals produce any noticeable anomaly.

At a spreading rate of 10 mm/yr anomalies in the range aM4(N) to aM11(R) have peak to trough amplitudes of ~ 100 to 200 nT. In contrast, anomalies aM0(R) to aM4(N) have peak to trough amplitudes in the range 350 to 600 nT. Wavelengths are varied depending on the block width. Again there is an apparent segregation at the position of anomaly aM4(N) based on the character of anomalies.

In general, calculated anomalies over models of the oceanic crust with spreading rates of 6 mm/yr to 12 mm/yr show a distinct partition of types at the position of anomaly aM4(N). This segregation is a result of the decrease in average duration of chrons older than CM4(N) (and younger than CM14(R)) compared with those younger than CM4(N). Typical chron durations of 0.5 Ma or less east of aM4(N) means that crustal blocks of constant polarity are 5 km or less in width for a spreading rate of 10 mm/yr. Individual anomalies east of aM4(N), calculated 2 km above the source, are discernible with amplitudes of ~100 nT compared to 350-600 nT west of aM4(N). In contrast, anomalies east of aM4(N) calculated 7 km above the source have peak to trough amplitudes no greater than 50 nT compared with ~200 nT west of aM4(N), and high wavenumbers are attenuated because of the greater distance of the observation level from the source. The segregation is more noticeable the nearer the observation level is to the source. Anomaly amplitudes and wavelengths steadily increase as the blocks become larger with an increase in spreading rate. Anomalies both east and west of aM4(N) are similar in character for models whose spreading rate is greater than 16 mm/yr or less than 6 mm/yr.

Figure 3.9 (next page) The effect of spreading rate on the synthetic M-series magnetic anomalies (age CM0(R) and older; see Fig. 2.1) computed 7 km above the top of the source layer to simulate observations made at sea surface altitudes in the southern Iberia Abyssal Plain. Pairs of panels show model (lower panel; black= +0.8 A/m, white=-0.8 A/m) and synthetic anomalies (upper panel) computed for spreading rates of 16-2 mm/yr in 2 mm/yr increments. Anomalies aM1(R) and aM4(N) are labelled whilst (unlabelled) upward pointing arrow marks anomaly aM3(R). Solid bars labelled P and Q mark the positions of a trough-peak pair and a peak-trough pair, respectively; P = anomaly associated with M11(R), M11A(N) and M12.1(N); Q = anomaly associated with M16(N) and M17(R). Other than P and Q anomalies east of aM4(N) are subdued with peak-trough amplitudes < 100 nT, for all spreading rates.

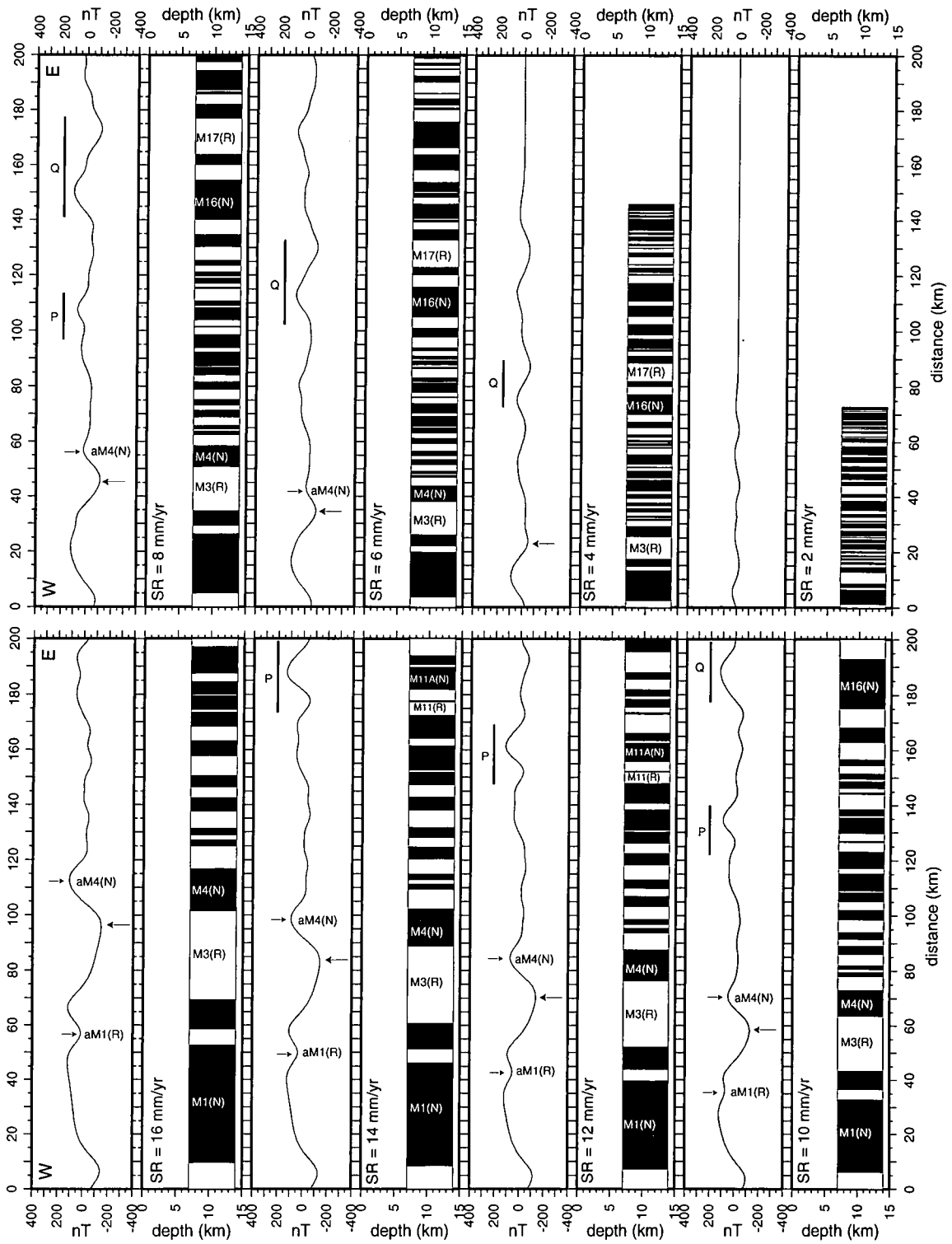
E
W
Q
P
aM4(N)
aM1(R)
M17(R)
M16(N)
M4(N)
M3(R)
M11A(N)
M11(R)
M1(N)
SR = 8 mm/yr
SR = 6 mm/yr
SR = 4 mm/yr
SR = 2 mm/yr
SR = 16 mm/yr
SR = 14 mm/yr
SR = 12 mm/yr
SR = 10 mm/yr
nT
depth (km)
distance (km)

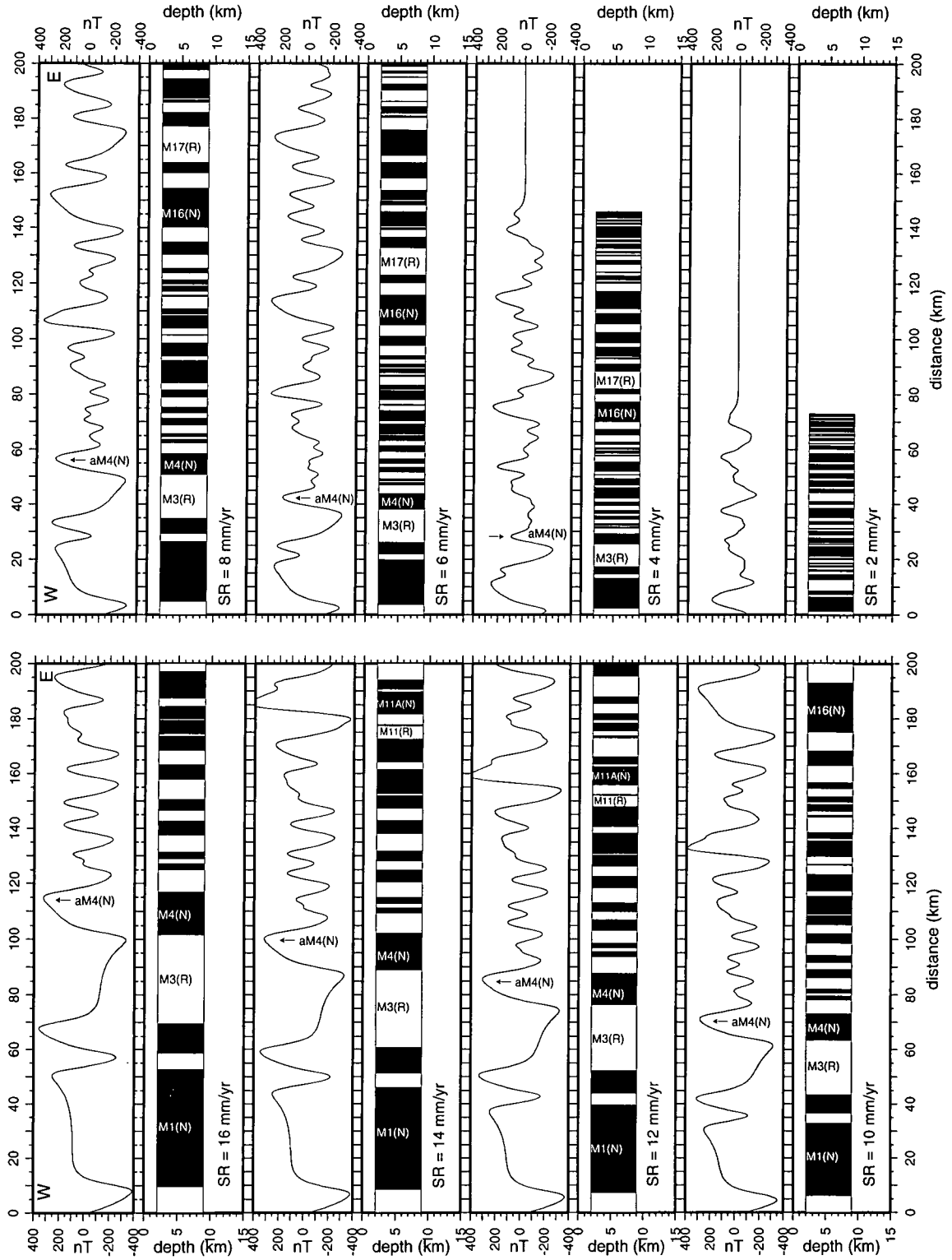
W
E
nT
depth (km)
distance (km)
aM4(N)
M17(R)
M16(N)
M4(N)
M3(R)
M11A(N)
M11(R)
M1(N)
SR = 8 mm/yr
SR = 6 mm/yr
SR = 4 mm/yr
SR = 2 mm/yr
SR = 16 mm/yr
SR = 14 mm/yr
SR = 12 mm/yr
SR = 10 mm/yr

Figure 3.10 (Previous page) As Fig. 3.9 except synthetic anomalies computed 2 km above top of source layer to simulate observations made near-bottom in the southern Iberia Abyssal Plain. In contrast to the anomalies generated 7 km above the source layer (Fig. 3.9), here distinct anomalies east of aM4(N) can be associated with individual block.

3.3.5 The contribution of topography to total field observations

One of the first and most important pieces of information concerning the interpretation of real magnetic anomalies is to quantify the contribution of the topography of the top and bottom of the source layer to the total magnetic field. The topography of the bottom of the source layer, however, is less significant due to its greater distance from the observation level. Moreover, the topography of the base of the source layer is generally an unknown.

The contribution is defined as the magnetic field produced by a magnetized layer of constant magnetization direction and magnitude, whose base is at constant depth, and whose upper surface has a topography. It has significance for two reasons: (1) the top of the magnetized layer is often equivalent to the top of acoustic basement and therefore can be derived from MSC profiles; (2) if the observed anomaly is totally described within given specified bounds by the basement relief then local geology is homogeneous above a length scale defined by the resolution of the method. This means that the magnetic field cannot contribute to a geological investigation in any way other than estimating a relative magetization contrast between basement and sediments, for example. If the contribution is significant then topographic effects must be included in forward models. The degree of significance, in a quantitative sense, between real observations of the field and basement topography is tested in Chapter 5.

In order to exclude the effects of change in parameters other than topographic variations, solutions to the forward problem have been found for a range of parameters (Fig. 3.11). Three 'external' parameters; magnitude of magnetization, direction of magnetization and depth to base of magnetic layer are tested. For an assumed induced magnetization vector the effective magnetizations were calculated assuming an external field of 44400 nT, based on the IGRF 1995.0 epoch for a latitude of 40°N. Remanent vector magnitudes are within the realistic bounds for block models as calculated in the previous section. Anomalies were computed assuming a profile trend of 100°, roughly at right angles to linear anomalies in and adjacent to the OCT offshore Iberia, and the magnetic layer is assumed to be two dimensional. The topographic variation is synthetic and

allowed to vary between 5.5 km and 8.5 km depth from the observation plane.

The first step is to quantify the changes in the topographic anomaly due to changes in other parameters, then to quantify the topographic anomaly itself. The effects of the magnetization vector direction are insignificant. The maximum perturbation to the topographic anomaly due to the difference in direction between induced and remanent magnetization vectors occurs when the relief is the most extreme (Fig. 3.11a) and is 17 nT. This assumes both vectors have a constant magnitude of 1.5 A/m and the basement relief is 3 km over a horizontal distance of 5 km. For lower magnetizations and/or smaller relief variations the error is approximately 5 nT and therefore considered insignificant.

The topographic anomaly is almost completely insensitive to the basal depth of the layer. Only when a magnetization of 1.5 A/m is assumed does the effect of changing the depth to the base from 10 km to 16 km create a variation of 5 nT in the theoretical anomaly. For lower layer magnetizations, the variation is often less than 2 nT and therefore insignificant (Fig. 3.11b).

The factor to which the topographic anomaly is by far the most sensitive is magnetization. For a topographic step of 3 km over 5 km laterally and a magnetization of 1.5 A/m, the resultant topographic anomaly has a peak-to-trough amplitude of ~150 nT. A magnetization of 0.5 A/m with the same topographic variation produces a topographic anomaly with peak-to-trough amplitude ~100 nT. Figure 3.11c shows the effect of magnetization on the amplitude of the topographic anomaly. For a uniform layer magnetization of 0.7 A/m, and realistic topographic variations (Fig. 3.14d), peak-to-trough topographic anomalies in a profile 7 km above the source are likely to be in the range of 50-75 nT. Therefore variations in topography of a constant magnetization layer may be significant in contributing to observed anomalies. In particular, near-bottom observations as close as 2 km above the source will be highly susceptible to the topographic effects (ca. 150-200 nT) of the source.

Anomalies west of Iberia have a similar amplitude to those generated here by basement topography alone (Fig. 2.8). In Chapter 5 the significance of the basement relief is tested by comparison with forward calculated profiles. The coherency between observed anomalies and theoretical anomalies acts as a statistical means of testing the significance of the contribution of basement relief.

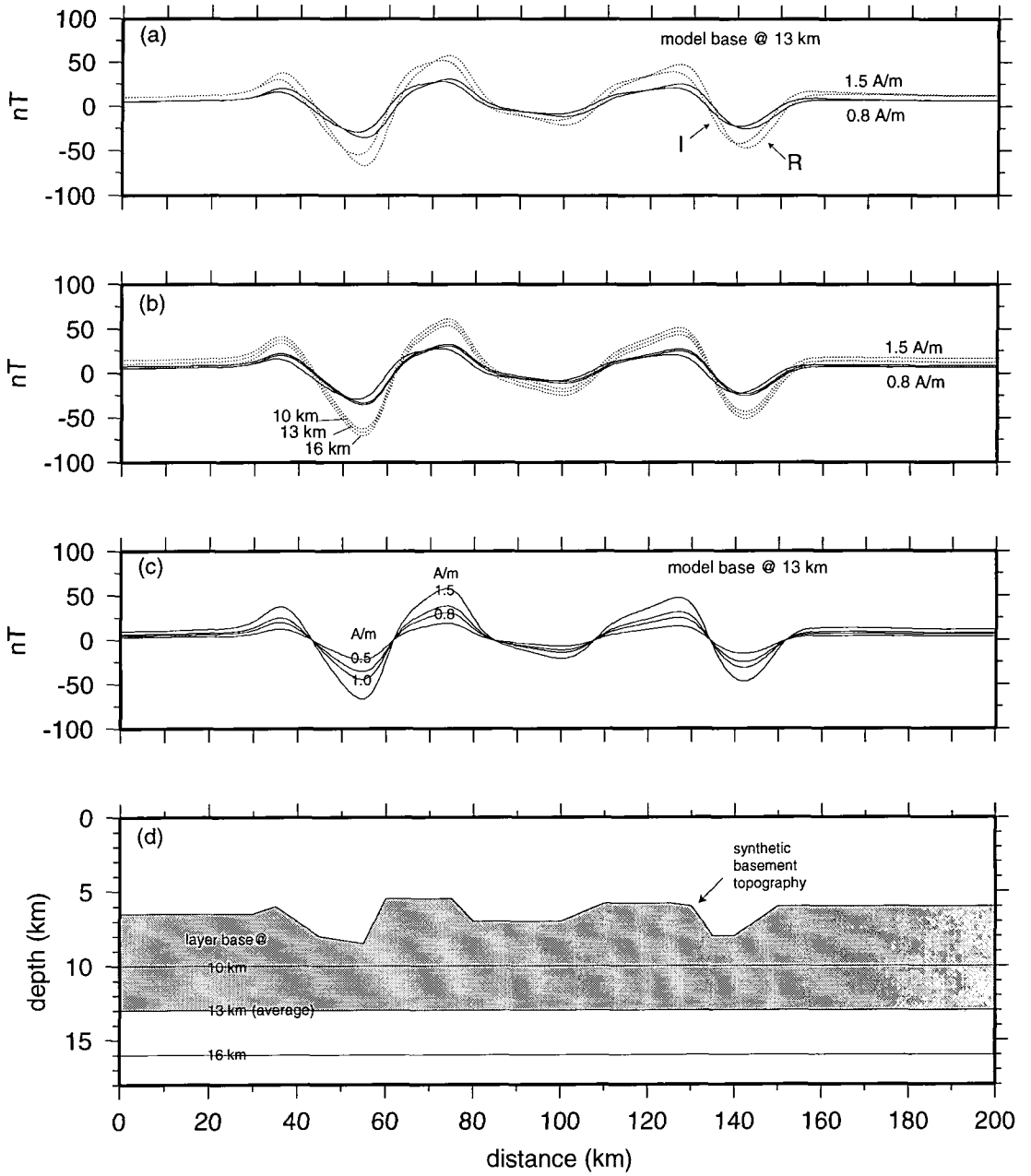

Figure 3.11 Effect of a realistic basement topography on synthetic magnetic anomaly. (a) Magnetic anomalies computed from a layer with topography as upper surface (see d) and its base at 13 km depth with remanent magnetization vector (labelled R) and induced magnetization vector (labelled I) and magnetization magnitudes of 0.8 A/m (solid lines) and 1.5 A/m (dotted lines). (b) Magnetic anomalies computed from layer whose base is at 10, 13 and 16 km (labelled) assuming remanent magnetization vector direction with magnitudes of 0.8 A/m (solid lines) and 1.5 A/m (dotted lines). (c) Magnetic anomalies computed from layer whose base is at 13 km with remanent magnetization vector with magnitudes of 0.5, 0.8, 1.0 and 1.5 A/m (labelled). (d) Models used in (a)-(c). Realistic model parameters predict ~100 nT anomaly due to source layer topography.

3.4 Formulation of the inverse problem

The forward problem provides a means of obtaining a model of the subsurface by comparing an observed anomaly with an anomaly calculated from a proposed model. In contrast, the inverse problem, or an inversion procedure, provides an 'objective' means of determining a model directly from the observed anomaly without comparison of a forward calculated anomaly. Nevertheless, in practice the final model is usually checked by forward calculation of the anomaly and comparison with the observations in a similar fashion to the solution of the forward problem.

As discussed in section 3.1 the number of models whose magnetic anomalies match the observed anomaly within specified statistical bounds provides a means of estimating the uniqueness of the solution. In addition, the number of models whose parameters, for example spatial extent and magnetization magnitude, fall within 'sensible' geological bounds can further reduce the number of acceptable solutions and therefore the non-uniqueness. If these parameter bounds are relatively narrow then the determination of the physical properties can provide useful geological information. The solution of the inverse problem necessarily falls within these bounds. In particular, the non-uniqueness bounds, whether statistical or geological, are critically dependent upon the assumptions of the inverse procedure.

In the formulation of the problem, one of the first considerations is to determine the number of unknown parameters and their relationship to the observed anomaly. The standard procedure is to make reasonable assumptions concerning all but one of the unknown parameters and solve for variations in the one remaining unknown. The means of obtaining the solution is highly dependent on whether the unknown parameter is linearly related to the anomaly or not. Linear inverse procedures are relatively easily accomplished, unlike non-linear methods. It is also very common to obtain a solution that is reliant on an initial estimate of the unknown, which is then iteratively refined. In this case, it is crucial that the initial estimate is geologically plausible since the final solution is normally a perturbation of an initial 'guestimate'.

It is advantageous to repeat any inversion process more than once in order to produce a set of solutions in which each member corresponds to a given set of reasonable assumptions. In this way a whole suite of solutions that span a geologically reasonable set of model assumptions is produced, although a narrower subset exists within the possible bounds in which the assumptions are more probable, based on complementary evidence. The inverse problem is formulated such that the assumptions are set to test a particular geological hypothesis in which variations in the

unknown parameter are assumed to be greater than the variations in the assumptions. Here I present two means by which the process of inversion of magnetic anomaly observations can potentially provide quantitative information regarding the subsurface geology offshore Iberia.

3.4.1 Magnetization variation solutions

The variation in magnetization of subsurface rocks is highly dependent on the rock type and/or the geological, geochemical and geophysical processes affecting the rock during or after its formation. It is therefore worthwhile seeking a magnetization solution that can potentially provide constraints on the subsurface geology. However, a magnetization solution can only be obtained if some limitation relating to the spatial extent of the magnetic source is made, in the form of an assumption. The easiest situation, in a mathematical sense, is for the source to be described by an upper surface $h(x)$ and a constant thickness h_0. The upper surface is assumed to be the top of acoustic basement and the thickness consistent with estimates of crustal thickness from wide-angle seismic experiments. The latter assumption is dependent on the whole crust contributing to the magnetic field. Oceanic crust that develops a layered magmatic structure can be approximated by a block model of bulk magnetization (see section 3.3.3), likewise for continental crust (Frost and Shive, 1986). In addition to the assumptions concerning the dimensions of the magnetic body, the direction of the Earth's field vector and the magnetization vector are required.

The two dimensional inverse solution of a magnetic anomaly, observed on a horizontal track, is a magnetization function of distance along track, $M(x)$, and obtained by the rearrangement of equation (3.4) such that (Parker and Huestis, 1974),

$$\Im[M(x)] = \frac{\Im[A(x)]e^{|k|z_0}}{\frac{1}{2}\mu_0\left[1-e^{-|k|h_0}\right]V(k)} - \sum_{n=1}^{\infty}\frac{|k|^n}{n!}\Im\left[M(x)\cdot(h(x)-z_0)^n\right] \qquad (3.5)$$

where $\Im[f(x)]$ is the Fourier transform of the function $f(x)$, and $V(x)$, z_0 and h_0 are defined in section 3.1. In practical terms, a solution to $M(x)$ is obtained by iterative refinement of a given initial estimate of the magnetization. Moreover, the practical implementation must be highly dependent on the convergence of the infinite sum in equation (3.5). Parker and Huestis (1974) have shown that the infinite sum converges most rapidly if the arbitrary reference level, z_0, lies midway between the

highest and lowest points of the topography, $h(x)$. In contrast, the iterative inverse procedure converges most rapidly if the reference level lies just above the highest topographic point. The practical means of achieving convergence of both the infinite sum and the iteration is by applying an appropriate adjustment of levels at each stage. The summation is carried out assuming a temporary origin in the optimum position for convergence of the sum, after which it is effectively upward continued to the optimum level for convergence of the iteration, the difference in levels being given by $\tilde{h}$. The two reference levels, for optimum convergence of summation and iteration, respectively, are therefore given by,

$$z_s(x) = \max(h(x)) - \tilde{h} \tag{3.6}$$

and

$$z_i(x) = |\max(h(x))| \tag{3.7}$$

where,

$$\tilde{h} = \tfrac{1}{2}|\max(h(x)) - \min(h(x))| \tag{3.8}$$

The practical inversion procedure is thus given by,

$$\Im\left[M_{j+1}(x)\right] = \Im\left[M_0(x)\right] - F_H(k)\left\{e^{-|k|\tilde{h}} \sum_{n=1}^{p} \frac{|k|^n}{n!} \Im\left[M_j(x)\cdot(h(x)-z_s)^n\right] - \Im\left[M_j(x)\right]\right\} \tag{3.9}$$

where,

$$\Im\left[M_0(x)\right] = \frac{F_H(k)\cdot F_L(k)\cdot \Im[A(x)]e^{|k|z_i}}{\frac{1}{2}\mu_0\left[1-e^{-|k|h_0}\right]V(k)} \tag{3.10}$$

and $F_H(k)$ and $F_L(k)$ are high-cut and low-cut wavenumber domain filters respectively. The application of a high-cut filter is necessary in order to reduce the short wavelength (high wavenumber) amplification generated by (1) the term in the infinite sum (equation (3.9)), and (2) spurious high wavenumbers in the anomaly, $A(x)$ (equation (3.10)). The application of the low-cut filter is necessary in order to reduce the long wavelength (low wavenumber) instability generated by the bracketed denominator term in equation (3.10). In reality, removal of the mean and

wavenumbers corresponding to $k = 0$ is sufficient.

The solution in equation (3.9) is initiated by allowing the first term, $M_1(x)$, to be equal to zero and then proceeding with the computation of a second estimate of the magnetization distribution, $M_2(x)$, which is only dependent on the term $M_0(x)$. It is worth mentioning that $M_2(x)$ is effectively the magnetization distribution in a uniform layer possessing flat upper and lower surfaces. Schouten and McCamy (1972) describe the process of retrieving a magnetization solution in a uniform layer as simply the product of the anomaly with an earth filter and a phase filter in the wavenumber domain. Here, the phase filter is given by $V(x)$ and the earth filter by the other terms in equation (3.10), excluding the high-cut and low-cut filters $F_H(k)$ and $F_L(k)$. Calculation of terms $M_3(x)$ and higher introduces perturbations in the magnetization distribution caused by the presence of the topography which are not included in the method of Schouten and McCamy (1972). The final magnetization solution, $M_{end}(x)$ is given by $M_{j+1}(x)$ and can be defined by one of the methods; (1) when the difference between $M_{j+1}(x)$ and $M_j(x)$ is less than a given tolerance; (2) when the RMS residual between the forward calculated anomaly at the $(j+1)^{th}$ step and the forward calculated anomaly at the j^{th} step is less than a given amount; (3) when $j = q$. If neither the first nor the second condition is satisfied whilst $j < q$, then the third condition will be applied, simply to reduce the running time of inversions. In all the models in this thesis $q = 21$.

The magnetization, $M(x)$, does not have a unique solution because of the potential presence of a magnetic annihilator (Parker and Huestis, 1974). For a layer of finite extent no exact annihilator exists, but a distribution, $\Lambda(x)$ which produces minimal magnetic field can be found by defining $M_1(x) = 1$ in equation (3.9). The resultant magnetization solution which satisfies equation (3.9) is thus $M(x) + \alpha\Lambda(x)$, where α is any scalar. The fact that the mean value of $\Lambda(x)$ is unity implies that there is a bias in the magnetization distribution. In reality this may exist if the profile crosses over crust of predominantly one polarity, such as over continental crust whose induced magnetization is dominant. For profiles over oceanic crust, a mean level of zero is expected if equal amounts of normally and reversely magnetized crust are crossed.

3.4.2 Retrieval of a magnetization solution from synthetic total field magnetic anomalies.

To illustrate the capabilities and limitations of the inversion procedure, synthetic magnetic anomalies have been generated by the space domain forward method, and then inverted by the method described above. Calculated theoretical anomalies of potentially realistic models of the

subsurface can aid the interpretation of observed anomalies by the inverse method. In addition, numerical examples contribute to the development of such methods, although this is not a priority of this thesis.

The most trivial solution is one in which the method aims to retrieve the magnetization of a block model of constant magnetization and with horizontal upper and lower surfaces, providing the magnetic field observations are made on a horizontal level. Alternatively, a perfectly draped survey is an equivalent geometry. Practically this will never be achieved at rifted continental margins due to the large thickness of sediments, and only in rare cases nearer to oceanic accretionary axes. This most trivial solution is akin to the solution given by Schouten and McCamy (1972) or the solution given here in which $M_{end}(x) = M_2(x)$. The degree to which the method can retrieve the 'correct' solution here represents the best possible situation. Inclusion of higher order terms due to a topography necessarily creates a more complex model whose anomaly is more difficult to invert with the same degree of success.

The inverse method was tested through the use of synthetic forward calculated anomalies shown in Figures 3.9 and 3.10. The corner wavelength of the high-cut wavenumber domain filter is particularly critical; solutions in which the corner wavelength is similar to, or greater than, the depth to basement, match reasonably well with the true magnetization, although the range in degree of mis-match with the actual magnetization distribution is variable (Figures 3.12a,b and 3.13a,b). An optimum filter exists where there is enough high wavenumber content to describe narrow magnetization changes without introduction of too much high wavenumber energy. For a magnetic field calculated 7 km above the source and filter cut-off wavelengths of ~5 km, the reversal sequence for a model whose spreading rate is 10 mm/yr is reasonably well retrieved (Fig. 3.12b). Ideally, reversal boundary locations between magnetic anomaly blocks are defined on the basis of local zero crossings (e.g. Channell et al., 1995), but in reality narrow anomaly blocks are implied by smaller amplitude deflections of the solution that do not cross the zero line (e.g. Fig. 3.12b, 90 km).

Magnetization solutions based on the inversion of the field at a distance of 2 km above the source are able to retrieve the theoretical model with much better precision. The reason for this is that higher wavenumber components, that represent sharper magnetization transitions, are more stable due to the closer proximity of the observation plane to the source. Even at spreading rates as low as 6 mm/yr the method can retrieve the reversal sequence in terms of position of boundaries and amplitudes of blocks (Fig. 3.13). However, the presence of higher wavenumbers in the solution

necessarily makes the solution very 'ringy' due to Gibb's phenomenon. In addition to reversal boundaries, the amplitude of magnetization variations is retrieved to greater relative precision.

The examples above, although tested on models of oceanic crust, are used to demonstrate that the inverse method can successfully retrieve a magnetization solution if sensible assumptions are made. The method has greater potential success for use on near-bottom observations due to the ability to pass a greater amount of high wavenumber energy with lesser degrees of spurious amplification. In both cases the method demonstrates that a reasonably accurate model can be obtained from a quantitative analysis of the anomalies rather than qualitative identification of anomalies which provide relatively little information.

3.4.3 Layer thickness variations

Unlike the inverse procedure for calculation of a magnetization solution, the equivalent procedure used for the calculation of layer thickness variations has not been developed and applied to the same extent. There are two main reasons for this: (1) the main emphasis of marine magnetic surveys has been to recognize seafloor spreading anomalies in oceanic crust, over either on-axis crust or normal thickness off-axis crust; (2) the inverse problem is non-linear and therefore much more difficult to apply. However, Louvel (1995) and Louvel et al. (1997) formulated the problem to help resolve and constrain the structure of the Goban Spur continental margin.

The equation of Parker (1972; equation 3.1) forms the basis for the formulation of the problem. Instead of the assumption of a constant source layer thickness, here the aim is to describe the thickness, $t(x)$, based on the assumption that the source layer possess a constant magnetization magnitude and direction. Equation (3.1) can therefore be rearranged and manipulated so that the layer thickness becomes the subject of the equation,

Figure 3.12 (next page) Degree with which inversion of synthetic magnetic field can retrieve true magnetization structure as a function of spreading rate (SR) and high-cut filter corner wavelength (F). Upper panels show synthetic anomalies (computed 7 km above source; solid lines) from Fig. 3.9 (spreading rates of 6 mm/yr and 10 mm/yr) and recomputed anomaly derived from inverse model (dotted lines). Lower panels show true normal-reversed magnetization (dotted lines) and computed (inverted) magnetization (solid lines) (a) SR=6 mm/yr, F=7 km; (b) SR=10 mm/yr, F=7 km; (c) SR=10 mm/yr, F=2 km. See text for discussion.

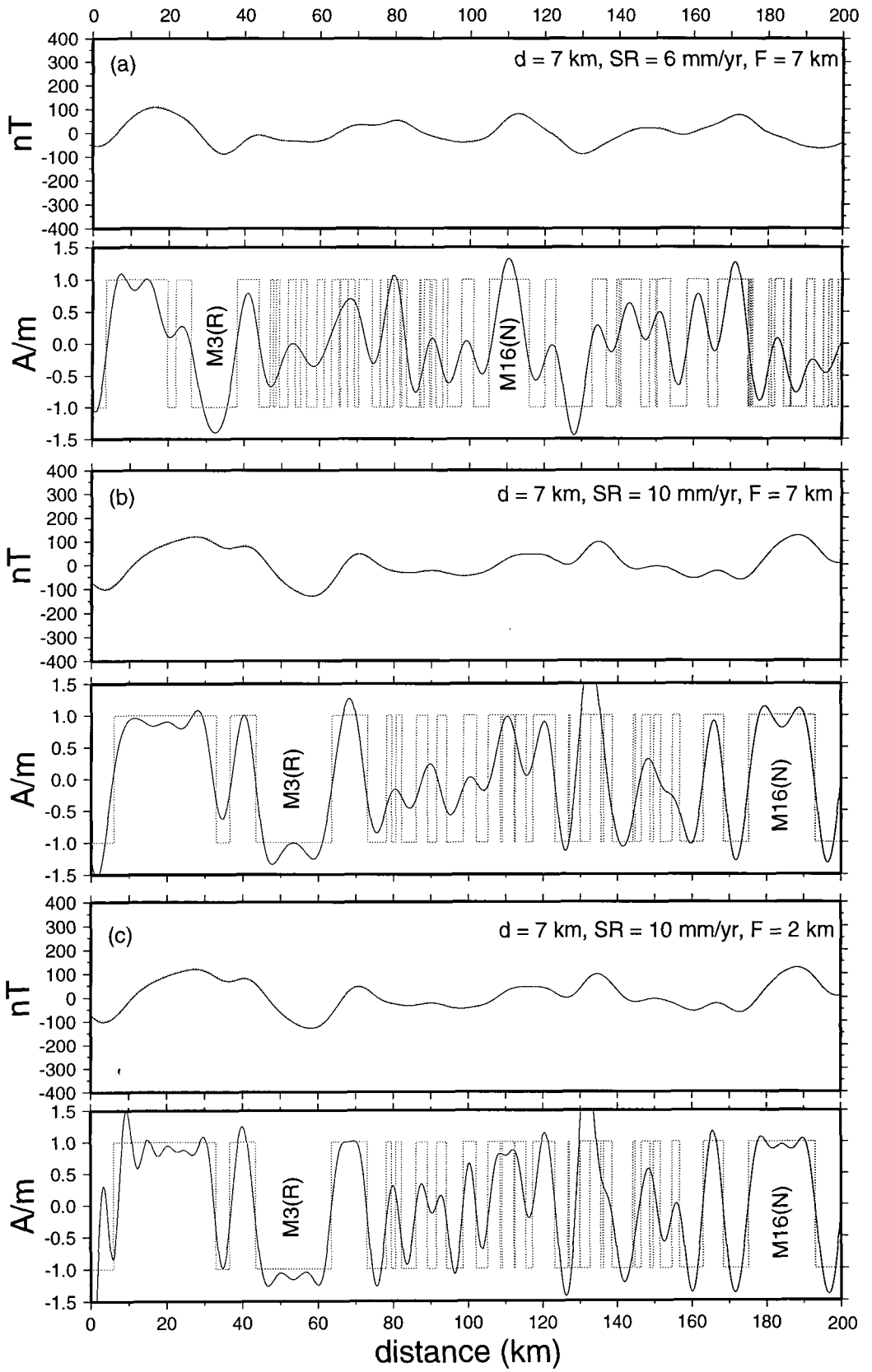
(a)
d = 7 km, SR = 6 mm/yr, F = 7 km
nT
A/m
M3(R)
M16(N)
(b)
d = 7 km, SR = 10 mm/yr, F = 7 km
nT
A/m
M3(R)
M16(N)
(c)
d = 7 km, SR = 10 mm/yr, F = 2 km
nT
A/m
M3(R)
M16(N)
distance (km)

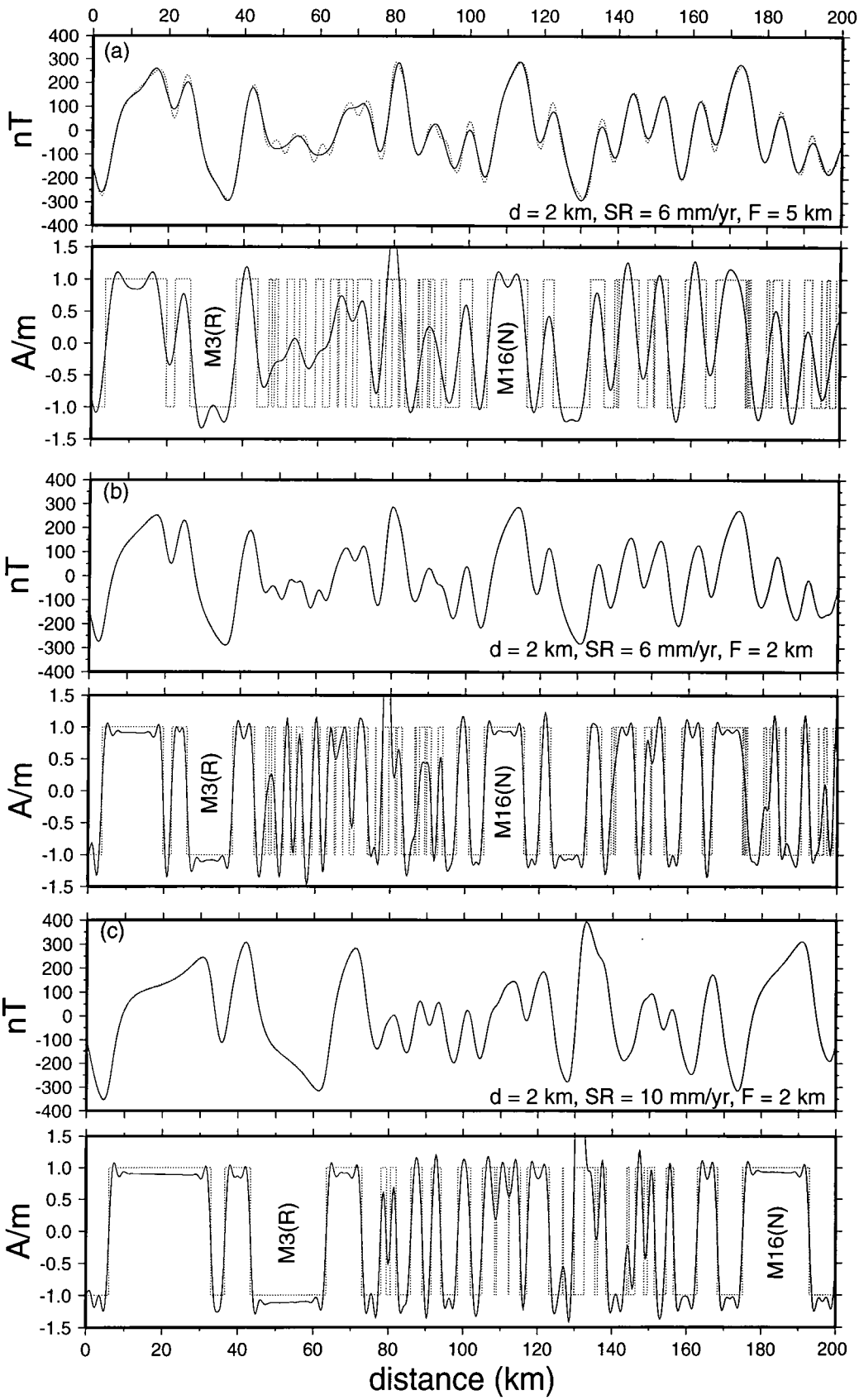
(a)
nT
d = 2 km, SR = 6 mm/yr, F = 5 km
A/m
M3(R)
M16(N)
(b)
nT
d = 2 km, SR = 6 mm/yr, F = 2 km
A/m
M3(R)
M16(N)
(c)
nT
d = 2 km, SR = 10 mm/yr, F = 2 km
A/m
M3(R)
M16(N)
distance (km)

Figure 3.13 (previous page) As Fig. 3.12 except anomalies computed 2 km above top of source layer (Fig. 3.10) and (a) SR = 6 mm/yr, F = 5 km; (b) SR = 6 mm/yr, F = 2 km; (c) SR = 10 mm/yr, F = 2 km. See text for discussion.

$$\Im[t(x)] = \frac{\Im[A(x)]e^{|k|z_0}}{\frac{1}{2}\mu_0 V(k) M_0} - \frac{1}{|k|}\sum_{n=2}^{\infty}\frac{|k|^n}{n!}\Im\left[(h(x)-z_0)^n - (h(x)-t(x)-z_0)^n\right] \tag{3.11}$$

where $\Im[f(x)]$ represents the Fourier transform of the function $f(x)$, $t(x)$ is the magnetic source layer thickness, $h(x)$ is the source topography, $A(x)$ is the observed anomaly, M_0 is a constant magnetization, z_0 is an arbitrary reference level and $V(k)$ defines the direction of the magnetization and Earth's field vectors as in equations (3.2) and (3.3). The function $g(x)$, the basal source layer surface, is related to the upper surface by $g(x) = h(x) - t(x)$. This form of the equation differs slightly from that of Louvel et al. (1997) in that here I adopt a positive z-axis upwards, and I make no assumption regarding the reduction to the pole of the field. The practical implementation of the iterative Fourier procedure is thus given by,

$$\Im\left[t_{j+1}(x)\right] = \Im\left[t_0(x)\right] - F_H(k)\left\{\frac{1}{|k|}\sum_{n=2}^{p}\frac{|k|^n}{n!}\Im\left[(h(x)-z_0)^n - (h(x)-t_j(x)-z_0)^n\right] - \Im\left[t_j(x)\right]\right\} \tag{3.12}$$

where,

$$\Im[t_0(x)] = \frac{F_H(k)F_L(k)\Im[A(x)]e^{|k|z_0}}{\frac{1}{2}\mu_0 V(k) M_0} \tag{3.13}$$

and $F_H(k)$ and $F_L(k)$ are high-cut and a low-cut filters respectively. As with the inversion for magnetization, an analogous iterative procedure is adopted, namely the j^{th} estimate of $t(x)$ is used to compute a $(j+1)^{th}$ estimate. However, some important differences between the methods exist. The convergence of the infinite sum in equation (3.12) is dependent on both the depth to the top of the source, $h(x)$ and the depth to the base of the source, $g(x)$, and therefore the sum can be explicitly represented by two separate summations whose optimum levels for convergence are at different

positions. As pointed out by Parker (1972), the summation in the forward solution in equation (3.1) is uniformly convergent and achieved most readily if the reference level is midway between the highest and lowest points of $h(x)$, if the source layer is of constant thickness. However, if the depth to the base is also a variable, then the convergence of the summation is most readily achieved if the reference level is midway between the highest and lowest points of both $h(x)$ and $g(x)$ simultaneously. This can be clearly seen by considering the Fredholm integral equation (see Parker and Huestis, 1974) which suggests that the rate of convergence is improved by minimizing $\left|(h(x)-z_0)\right|$ and $\left|(h(x)-t_j(x)-z_0)\right|$. The optimum level cannot be achieved in both cases for a singular valued reference level, z_0, and therefore I have adopted two procedures to test the convergence of the sum: (1) since $g(x)$ is in part governed by the outcome of $t_j(x)$, the optimum stable reference level will be a function of j, due to the outcome of the iteration, and has therefore been chosen arbitrarily to be midway between the highest and lowest points of the upper surface, $h(x)$. This means that z_0 is described by z_s in equation (3.6); (2) not dissimilar to the adjustment of reference levels between those for optimum convergence of the summation process and iterative processes (equation 3.9), an adjustment of levels is applied to the component parts of the summation in equation (3.12). Because of the additive properties of Fourier transforms and summations, the new iterative procedure is thus given by,

$$\Im\left[t_{j+1}(x)\right]=\Im\left[t_0(x)\right]-F_H(k)\left\{e^{-|k|\tilde{h}_1}\frac{1}{|k|}\sum_{n=2}^{p}\frac{|k|^n}{n!}\Im\left[(h(x)-z_{s1})^n\right]\right.$$
$$\left.-e^{-|k|\tilde{h}_2}\frac{1}{|k|}\sum_{n=2}^{p}\frac{|k|^n}{n!}\Im\left[(h(x)-t_j(x)-z_{s2})^n\right]-\Im\left[t_j(x)\right]\right\} \tag{3.14}$$

where the reference levels for the convergence of the iteration, convergence of the first summation and convergence of the second summation are given respectively by,

$$z_i = z_0 = \left|\max(h(x))\right|, \tag{3.15}$$

$$z_{s1} = \max(h(x)) - \tilde{h}_1, \tag{3.16}$$

$$z_{s2} = \max(h(x)-t_j(x)) - \tilde{h}_2 \tag{3.17}$$

and the adjustment factors are given by $e^{-|k|\tilde{h}_1}$ and $e^{-|k|\tilde{h}_2}$,where,

$$\tilde{h}_1 = \tfrac{1}{2}\left|\max(h(x)) - \min(h(x))\right| \tag{3.18}$$

$$\tilde{h}_2 = \tfrac{1}{2}\left|\max(h(x) - t_j(x)) - \min(h(x) - t_j(x))\right| \tag{3.19}$$

As a result of these complications, and the lack of previous detailed studies (Louvel, 1995; Louvel et al., 1996), it is very difficult to establish any analytical means of ensuring convergence of both the iteration and the summation.

The convergence of the iteration procedure is of paramount importance to the solution of the inverse problem. As discussed by Oldenburg (1974), there is no control over the convergence of the iterative procedure and it is further complicated by the nonlinear nature of $t_j(x)$ on the right of equation (3.14). Louvel et al. (1997) chose a method for obtaining apparent convergence in which the RMS residual between successive estimates of $t(x)$ is less than a given quantity, which is large enough to avoid the generation of fictitious high frequencies. However, my further analysis (see next section) of this method has shown that the inversion procedure ceases at the beginning of the inversion process because of the unreasonably high RMS error threshold between successive estimates of $t(x)$. The effect is that convergence is not tested and therefore cessation of the procedure can occur, even with a strongly diverging solution, providing successive thickness estimates fall within the specified limit. It is in fact the high wavenumber oscillations that characterize most diverging solutions and the straight-forward application of the inversion without sensible filtering operations can rarely be applied successfully. Only in the case of a topography with a small enough relief will high wavenumbers make a sufficiently small contribution. However, even if this is achieved by filtering of the top basement depth and magnetic anomaly data profiles, the solution is still likely to contain fictitious amplified high wavenumbers created by the 'downward continuation' term in the numerator of the first term in equation (3.13), and the summation terms in equation (3.19). Attempts at employing this inversion procedure are presented in section 6.1.2.

3.5 Chapter summary

This chapter has dealt with the theoretical, methodological and experimental aspects of magnetic anomaly analysis by the indirect method of interpretation. The following conclusions can be drawn from this chapter,

(1) The forward and inverse problems can be formulated in such a manner as to test a given geological hypothesis. This is achieved practically by the application of realistic model assumptions.

(2) The uniqueness of a solution is highly dependent on *a priori* information, theoretical assumptions, 'goodness of fit' criteria, and the translation of the physical model into a geological context.

(3) Although realistic subsurface bodies have finite along-strike length, 2-D models are good approximations to 2.5-D bodies, with errors less than 5% when model half-strike lengths are 20 km or greater. The effect of finite strike length can be up to 50% less for near-bottom observations compared with sea surface observations.

(4) Vertically sided block models with uniform magnetization in the range 0.7 A/m to 1.2 A/m are good representations of a realistically layered oceanic crust. The error introduced by the approximation is less than 5% when anomalies are calculated at a distance of 2 km from the source representative of near-bottom observations, and considerably less than this for anomalies calculated at distances representative of sea surface observations.

(5) Seafloor spreading anomalies, associated with chrons in the range CM4 to CM29, cannot be seen at the sea surface as isolated anomalies at spreading rates less than at least 16 mm/yr. In contrast, observations made at a distance of 2 km above the source layer are able to isolate major individual anomalies at spreading rates of 8 mm/yr or more.

(6) Realistic topographic variation in the upper surface of a source layer, whose magnetization is realistic, can produce sea surface anomalies with significant peak-to-trough amplitudes. This emphasizes the need to include magnetic source layer topographic variations in models, especially when working with profiles collected at near-bottom altitudes.

(7) Seafloor spreading reversal sequence magnetization solutions for spreading rates of 10 and 6 mm/yr can be retrieved by the inverse method, from sea surface and near-bottom observations respectively, providing realistic model and theoretical assumptions are made.

(8) The inverse method of retrieving magnetic layer thickness variations is difficult to apply because of theoretical problems associated with the convergence of a non-linear problem. Further development and analytical considerations to improve and successfully implement the method are beyond the scope of this thesis.

In particular, the work in this chapter has contributed to the aims of this thesis in that the methods adopted for analysis have provided information, and can provide further information, regarding the nature of the potential/hypothesized basement offshore West Iberia and Newfoundland.

Chapter Four

Direct and gradient magnetic interpretation methods: Methodology and application to theoretical anomalies

In an analogous manner to that of Chapter 3, the purpose of this chapter is to introduce the theory and methodology of the indirect magnetic interpretation methods, and to apply the methods to forward calculated anomalies in order to monitor their limits and resolving powers. The segregation between indirect and direct methods, although in some cases somewhat artificial, is based upon the degree and type of assumption made. Here, I classify direct methods as those which facilitate less restrictive assumptions concerning the physical, *sensu stricto* nature of the source, i.e., no *specific* assumption concerned with source geometry and/or magnetization vector is necessary. The definition excludes assumptions concerned with the *sensu latu* nature of the source, such as the dipolar nature of the source magnetization vector or its distribution being fractal in nature. Although the distinction between types of assumption is rather subjective, the methods presented in this thesis are classified based essentially on the type of estimate made concerning the nature of the source. In addition, many of the direct interpretation methods involve the use of the gradients of the magnetic field.

4.1 Depth estimation of magnetic source bodies

Of all the unknowns concerned with a subsurface magnetic structure, knowledge of the depth to magnetic source bodies can strongly constrain the origin of such bodies, and perhaps even constrain geological models concerned with the formation and development of the local subsurface. In particular, estimates of magnetic source depths from observed magnetic field measurements in the southern Iberia Abyssal Plain may provide information that can distinguish between previously hypothesized models of development of the West Iberia continental margin (section 2.3.2). The rationale comes from the fact that the expected depths of the magnetic sources, and in particular the range and precision of estimates, from each of the three geological models, are likely to be mutually exclusive (see Chapter 2). Moreover, the

analysis of anomalies in this way may provide information which supports a new or revised geological hypothesis for the development of the rifted margin in the southern IAP. A discussion of this nature is dealt with in Chapters 6 and 7.

Two methods of determining source depth from magnetic anomaly charts and profiles are used. Firstly, the analysis and interpretation of power spectra, a wavenumber domain approach, and secondly, the method of Euler deconvolution, essentially a space domain approach with some minor wavenumber domain considerations. The latter can also provide information concerning the along axis or spatial extent of magnetic sources, and it is therefore potentially a very powerful tool for not only determining source depth but also source position. In the following sections I give an account of the theoretical and methodological aspects of the two methods. In addition, the potential success of each method is analyzed by its application to theoretical anomalies, forward calculated from realistic models by the method described in section 3.1.

4.1.1 Formulation of the 'traditional' power spectral method

Spectral analysis of potential field data has been used successfully and extensively over the last three decades to estimate the depths of typical magnetic sources, such as the top of basement (e.g., Bhattacharyya, 1966; Naidu, 1968; Spector and Grant, 1970; Hahn et al., 1976; Connard et al., 1983; Garcia-Abdeslem and Ness, 1994). The aim of this study is to determine the depths of magnetic sources on sub-crustal and sub-lithospheric scales along profiles and in regions where coincident seismic reflection profiles exist. Good quality seismic sections enable the application of further constraints on the depth to top basement.

The method is based on the expression for the radially averaged power spectrum of the total field magnetic anomaly produced by a uniformly magnetized rectangular prism (Bhattacharyya, 1966) buried at a depth h, of thickness t, length a, width b, and magnetization vector **M**. The power density spectrum is defined as the Fourier transform of the autocorrelation function of an anomaly, $\phi(x)$. This simply translates as the square of the amplitude spectrum in the wavenumber domain, $\left|\Im[A(x)]\right|^2 = \Im[A(x)]\Im[A(x)]^*$, whilst 'radially averaged' means that powers for equal lengths of the wavevector are averaged radially, as a function of θ, thus applying no bias to any particular wavevector direction. This simplification means that a 2-D spectrum is transformed to a 1-D spectrum by the elimination of the θ dependence, and the shape of the power spectrum then becomes independent of the

direction of the local geomagnetic field and the direction of magnetization, **M**. The orthogonal wavevectors k_x and k_y are therefore represented by the wavenumber, $k = \sqrt{k_x^2 + k_y^2}$.

The power spectral expression of the total field magnetic anomaly produced by a uniformly magnetized rectangular prism, first given by Bhattacharyya (1966), was successfully extended by Spector and Grant (1970) to model in excess of one prism, thus rendering the method practical. In their method, a magnetic layer is modelled, in a forward sense, by assuming that it consists of an ensemble of vertical prisms characterized by a joint probability distribution of the parameters h, t, a, b, **M**, and the local geomagnetic inclination, I, and declination, D. Based upon the assumption that the parameters of any one block obey the probabilities common to the entire set, and that the probability distribution of each parameter is uniform, the method of Spector and Grant (1970) predicts that the shape of the power spectrum of the anomaly is dependent on ensemble depth, thickness and horizontal extent, such that,

$$\langle P_{\text{mod}}(k)\rangle = C_0 \langle H(k)\rangle^2 \langle T(k)\rangle^2 \langle S(k)\rangle^2 \tag{4.1}$$

where, C_0 is a constant equal to $(\mu_0 \mathbf{M}_0/2\pi)^2$, $\langle\cdot\rangle$ means mathematical expectation, and $H(k)$, $T(k)$ and $S(k)$ are probability distribution functions for the depth, thickness and horizontal extent parameters, respectively. The depth parameter is invariably the dominating factor in the power spectrum, and that the thickness factor plays an interesting, but lesser role in shaping the power spectrum (see below). The effect of horizontal extent is to slightly perturb the effect of the depth parameter, but its effects are not considered here. The explicit forms of $H(k)$ and $T(k)$ are e^{-hk} and $(1-e^{-tk})$, respectively, and in addition, if the ensemble parameter probability distributions are assumed to be uniform and rectangular, their expectations can be approximated by the very same functions for relatively small wavenumbers. The power spectrum, in explicit form, is thus given by,

$$P_{\text{mod}}(k) = C_1 \exp(-2hk)\left(1-\exp(-tk)\right)^2 \tag{4.2}$$

and its logarithm by,

$$\ln\left[P_{\text{mod}}(k)\right] = K_1 - 2hk + 2\ln\left[1-e^{-tk}\right] \tag{4.3}$$

where K_1 is a constant. It can be seen that the shape of the natural logarithm of the power spectrum is dominated by the average depth of the ensemble, h, such that the slope of a plot of $\ln[P_{mod}(k)]$ against k is given by $-2h$. Figure 4.1 is used as an example.

The shape of the power spectrum is modified slightly by a finite thickness, t, only at low wavenumbers when $k < 1/t$. The effect of the third term on the right hand side of equation (4.3) is to introduce a peak in the log spectrum at a wavenumber, $k_t = 2\pi/\lambda_t$. It has been shown by Blakely (1995) that,

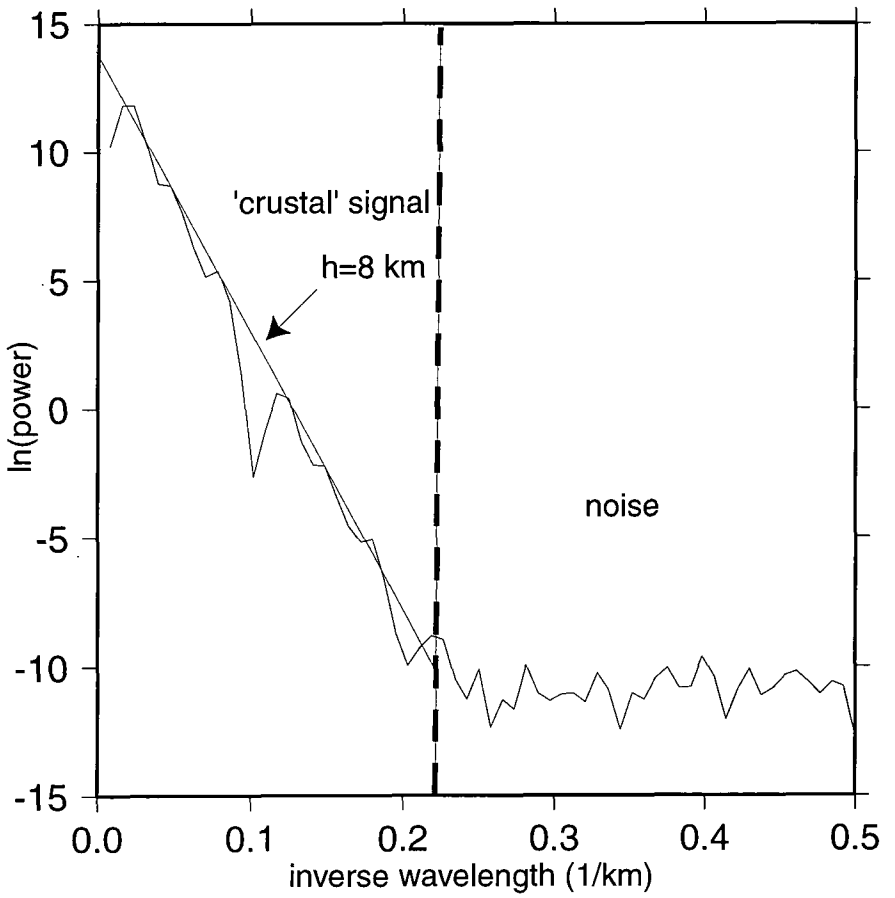

Figure 4.1 Natural logarithm of the power spectrum of the magnetic anomaly generated by a block model whose characteristics are: upper surface at a depth of 7 km, thickness 7 km, magnetization 0.7 A/m (see figure 3.6). The power spectrum is described by two bands: at wavelengths > ~5 km a crustal (geological) signal, whose slope corresponds to a depth of ~8 km, dominates the spectrum; at wavelengths < ~5 km a white noise dominates the spectrum.

$$k_t = \frac{\ln z_2 - \ln z_1}{z_2 - z_1} \tag{4.4}$$

where $z_1 = h$ is the depth to the top of the source and $z_2 = h + t$ is the depth to the base of the source. Figure 4.2 shows how a theoretical $1/\lambda_t$ varies with sensible changes in z_1 and z_2. Blakely (1995) also notes that the solution of this problem is one of the most difficult tasks in potential theory; z_2 cannot be determined independently of z_1. With this in mind, I have attempted to obtain a solution to the layer thickness problem by trial and error solution of equation (4.3) by calculating values of $k_t = 2\pi/\lambda_t$ based on sensible estimates of thickness.

Consider the power spectrum of Figure. (4.1). Blakely's (1995) method predicts that $k_t = 0.1$ (for the model described in Fig. 4.1) and therefore $1/\lambda_t = k_t/2\pi = 0.016$. This is in fact a reasonable estimate since the first 'peak' of the power spectrum in Figure 4.1 occurs in the range $0.015 < 1/\lambda < 0.023$.

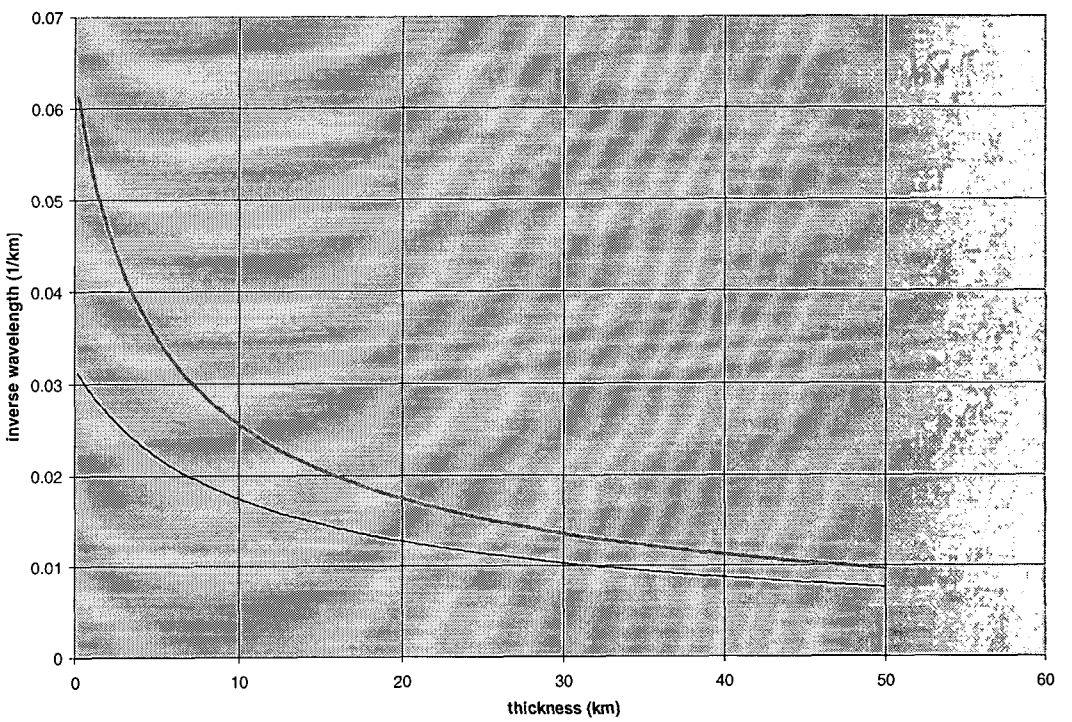

Figure 4.2. Theoretical inverse wavelength variations with change in layer thickness for a body whose depth to the top, h=5 km (thick line) and h=10 km (thin line). Thicknesses of 20 km or more may be assumed to be infinite. Realistic changes in thickness in the range $10 > t > 2$ have corresponding changes in inverse wavelength of only 0.03.

Although a theoretical maximum exists at k_t, it is often the case that a peak cannot be distinguished in real data (see spectra modelled in Chapter 5). This may occur due to any one or more of the following reasons: (1) the peak occurs over a very narrow wavenumber range and is therefore aliased due to windowing effects in the ensemble averaging process during the computation of the power spectrum (Wessel and Smith, 1991); (2) the base of the layer is at a depth whereby its contribution to the magnetic field, and therefore power spectrum, is negligible; (3) for cases of multiple ensembles (see later) the peak is indistinguishable from the depth effects of a deeper ensemble (at smaller wavenumbers); (4) the effects of the lateral width of the ensemble interfere with effects from thickness. It will be shown in chapters 5 and 6 that the success of determining ensemble thickness from real and synthetic power spectra is very variable. The best approach is to make a sensible estimate of t, and compute k_t via equation (4.4). If there exists a significant peak at the corresponding inverse wavenumber, the estimate of t may be valid, i.e., a trial and error procedure must be adopted.

Of particular importance to this study is the extension of the method described above to one in which multiple ensembles can be analyzed. This was first developed by Spector and Grant (1970) based on the concept of ensemble averaging, in which they state that the power spectrum over two or more ensembles is simply given by the summation of the individual power spectra due to each ensemble. Thus, although with no theoretical grounding[1], the log power spectrum of a double ensemble, for example, consists of two parts defined by two distinct slopes corresponding to two ensembles of sources at depths h_1 and h_2,

$$\ln\left[P_{\text{mod}}(k)\right] = \begin{cases} K_1 - 2h_1 k & ,k > k_b \\ K_2 - 2h_2 k + 2\ln\left[1 - e^{-t_2 k}\right], & k < k_b \end{cases} \tag{4.6}$$

where $h_1 > h_2$, $K_1 > K_2$ and t_2 is the thickness of the shallower source. In this case the maximum associated with the thickness of the shallower layer will occur at $(k_t - k_b)$. For example, consider a 3-D subsurface source distribution consisting of two sets of randomly distributed cuboid bodies; the depth to the top of one set is 5 km and the other 10 km. All bodies have thicknesses of 2 km, magnetization magnitudes of 0.7 A/m, and vector directions typical of some sources west of Iberia (Galdeano et al., 1989; Fig. 4.3a). The power spectrum of the resultant field in the > 5 km band contains both depth and thickness information for the

[1] For the three power spectra given by $P_A = P_B + P_C$, $\ln P_A = \ln\left[P_B + P_C\right] \neq \ln P_B + \ln P_C$.

two sets of sources. Practical interpretation is best achieved by hand; automated best-fit algorithms do not have the ability to interpret typical signal characteristics.

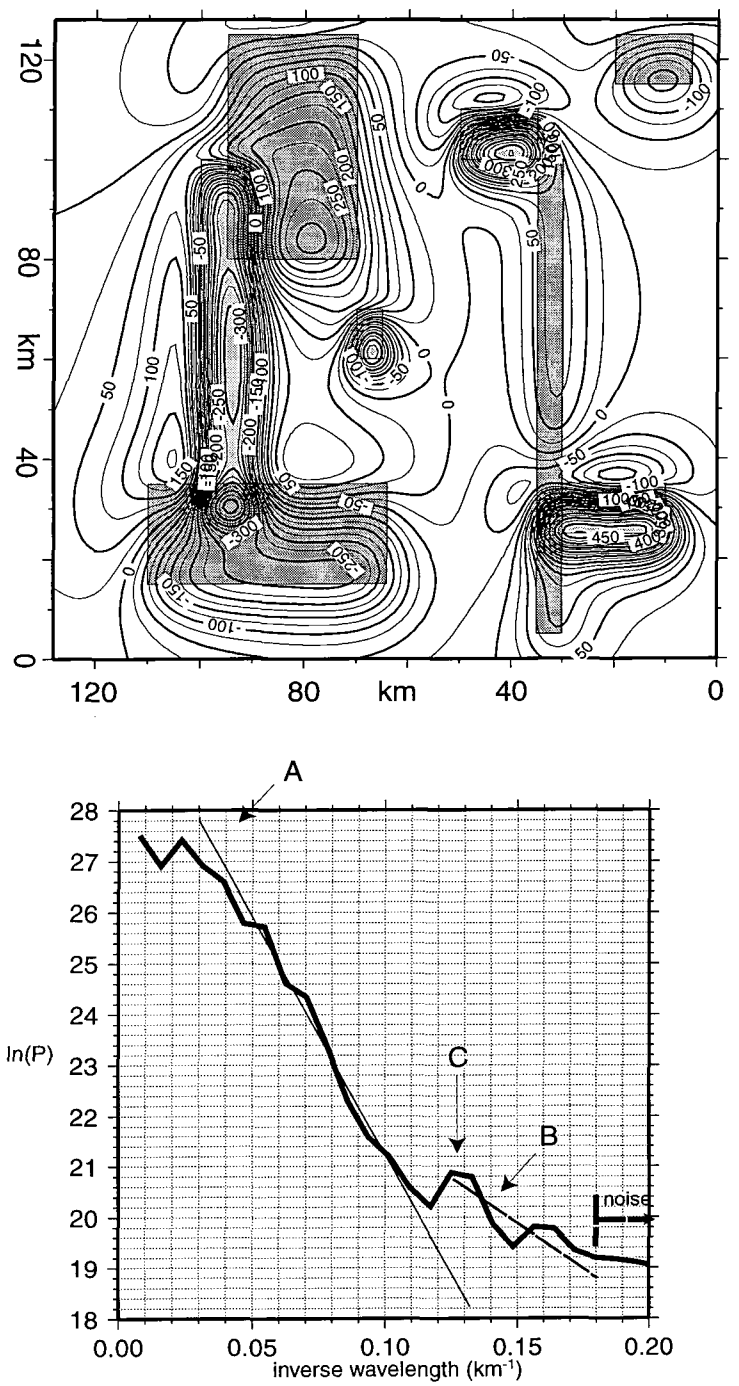

Figure 4.3 (a) Forward calculated two dimensional total magnetic field (contours at 25 nT) computed over a synthetic subsurface in a 128x128 km grid. Sources belong to two sets; those whose upper surfaces are at depths of 5 (light grey) and 10 km (dark grey); all bodies are 2 km thick.(b) Logarithm of the power spectrum of the field generated in (a). A and B represent the slope of the log spectrum generated by the upper and lower sources with estimated depths of 3 km and 7.5 km, respectively. C represents the best positional estimates of the thickness markers for upper source.

The presence of peak C (Fig. 4.3b) at relatively high wavenumbers in the 'crustal' band may be indicative of a two source system. Therefore the spectrum can be divided into two sections either side of $1/\lambda_b = 0.115$. A depth of 3 km is determined from the slope of the spectrum in the band greater than 0.115 km^{-1}. The presence of a peak necessarily creates an underestimate in h_2. Providing the peak, C, in Figure 4.3b is associated with k_t, a trial and error procedure for determining layer thickness suggests $(k_t - k_b) = (1/\lambda_t) - (1/\lambda_b)$ values of 0.04, 0.03 and 0.04 km^{-1} for layer thicknesses of 2, 5 and 10 km, respectively. An estimated value of 0.03 therefore suggests a layer thickness of 5 km. However, as indicated in Figure 4.2, the layer thickness is extremely sensitive to very small changes in inverse wavelength, and therefore the method cannot be used to determine the layer thickness of the shallower source. The depth to the deeper set of sources is estimated at 7.5 km, suggesting $1/\lambda_t$ values of 0.016, 0.015, 0.014 and 0.012 km^{-1} for layer thicknesses of 1, 2, 5 and 10 km, respectively. The errors involved in choosing the correct inverse wavelength value are greater than the variation caused by thickness variations of considerable geological significance. The method can therefore only be used to estimate orders of magnitude, such as determining the order of magnitude of the depth to the Curie point isotherm.

4.1.2 Probability distributions of magnetic source layer parameters

The interpretation of the power spectrum of a total field magnetic anomaly is dependent upon the correct description of the magnetic layer in terms of the probability distribution functions of its parameters. In the last section it was shown that the slope of the power spectrum is proportional to the depth to the source, and that the source layer thickness is retrievable, at least theoretically if not always practically. However, the retrieval of the correct depth and thickness is based strongly on the probability distributions of the functions $H(k)$ and $T(k)$ from equation (4.1), and consequently, the explicit forms of $\langle H(k) \rangle$ and $\langle T(k) \rangle$ may be significantly modified by a realistic change in distribution.

The method of Spector and Grant (1970) (section 4.1.1) is based upon a uniform rectangular probability distribution of the ensemble parameters, that is, the depth is described by $h \pm \Delta h$, and the thickness by $t \pm \Delta t$, where $\Delta h << h$ and $\Delta t << t$. Because of the indeterminable nature of the problem, there is no reason to doubt that a distribution of this sort exists, but by the same token, the distribution may take another form. One such statistical variant of the method has been proposed by Garcia-Abdeslem and Ness (1994), in which they

assume the model parameters are described by a Gaussian distribution. The depth is therefore described by a mean, h, and a variance, σ_h^2, and the thickness described by a mean, t, and a variance σ_t^2. The expectations of the parameter functions are thus given by (Garcia-Abdeslem and Ness, 1994),

$$\langle H(k)\rangle = \exp\left(-hk + \tfrac{1}{2}k^2\sigma_h^2\right) \tag{4.7}$$

and,

$$\langle T(k)\rangle = 1 - \exp\left(-tk + \tfrac{1}{2}k^2\sigma_t^2\right) \tag{4.8}$$

It can be seen that once evaluated, the logarithm of the power spectrum is much more complex than the uniform distribution case. In order to reduce the complexity of the problem, the effects of layer thickness are assumed negligible and the logarithm of the power spectrum is thus given by,

$$\ln\left[P_{\text{mod}}(k)\right] = K_1 - 2hk + k^2\sigma_h^2 \tag{4.10}$$

In real terms, the assumption of a negligible layer thickness term is valid based on the four points mentioned in section 4.1.1. Moreover, the depth to the source can provide potentially more information with respect to the geological nature of the subsurface, and is generally more accurate than a thickness estimate.

A comparison, in terms of practical application to real data, of the modified power spectral method presented here with that of Spector and Grant (1970), suggests that both methods have their relative advantages and disadvantages. The Spector and Grant (1970) method is advantageous in that it can easily retrieve multiple depth estimates of a multi-layer model, which potentially do occur in nature, and in some cases a layer thickness can be retrieved. However, the choice of wavenumber at which the rate of decay of the power spectrum changes, i.e., at k_b , is rather subjective, and likewise the slopes of the straight line segments are determined in a forward sense. In the same way, the location of the maximum associated with k_t is hard to resolve.

In contrast, the method in which a Gaussian parameter distribution is assumed is less easily applied, in a forward sense, due to the non-linear relationship between $\ln\left[P_{\text{mod}}(k)\right]$ and k. However, the method provides additional constraint in that an estimate of σ_h^2 (the variance

of h), and therefore a measure of the spread of the forward calculated depth estimates, can be made. If a magnetic source layer possesses a topography, σ_h can provide a measure of the maximum range in the topographic variation. In particular, the 'Gaussian method' is more conveniently applied in an inverse sense whereby objective but independent estimates of h and σ_h can be made.

4.1.3 Scaling nature of crustal magnetization and power spectra

By implication, the method described in section 4.1.1 is necessarily identical to downward continuation (e.g. Parker, 1972; Schouten and McCamy, 1972) of the field until the power spectrum is flat, i.e., all wavenumbers contribute equal amounts to the power of the signal; the distance of continuation is thus equal to the depth to the top of the source, and is often called the 'white depth' (Hahn et al., 1976). Implicit in this technique is the assumption that magnetic sources at different depths are statistically uncorrelated, i.e., there exists no scaling or fractal relationship between length scales (in this case represented by wavenumbers). The commonly considered case of a 'white noise' is an example of this phenomenon.

In recent years it has been suggested that a statistical correlation, or self-similarity (Mandlebrot, 1967), exists between the different wavenumber components of the magnetic field (Gregotski et al., 1991; Pilkington and Todoeschuck, 1993; 1995). This correlation can therefore be described by a spectral exponent, γ, of the wavenumber, k. If the magnetic source parameters also exhibit fractal behaviour (Pilkington and Todoeschuck, 1993; Maus and Dimri, 1994; 1996), and have Gaussian probability distribution functions, then the models of Maus and Dimri (1996) and Garcia-Abdeslem and Ness (1994) can be combined in a manner similar to that of Zhou and Thybo (1998),

$$P_{\mathrm{mod}}(k) = C_3 k^{-\gamma} \exp\left(-2hk + k^2\sigma_h^2\right) \tag{4.10}$$

The natural logarithm of equation (4.10) is thus,

$$\ln\left[P_{\mathrm{mod}}(k)\right] = \ln C_3 - \gamma \ln k - 2hk + k^2\sigma_h^2 \tag{4.11}$$

which is solved by the method of least-squares inversion and is dealt with, theoretically, in Appendix II.

In addition to the sought solutions of h, and a measure of its spread, σ_h^2, the solution of the scaling exponent, γ, may also [indirectly] provide additional geological information. Although the exponent, γ, is a measure of the scaling behaviour of the field, it has been shown to be related to the scaling exponent of the source distribution, β (notation after Turcotte, 1992), such that (Maus and Dimri, 1994),

$$\beta_{3D} = \beta_{2D} + 1 = \beta_{1D} + 2 = \gamma_{1D} + 2 = \gamma_{2D} + 1 \tag{4.12}$$

where subscripts denote the dimensionality of the source (β's) or the field (γ's).

An estimated value of γ can also provide a measure of the two dimensionality of the source. It has been shown directly in a number of cases that $\gamma_{2D} = 3$ (Gregotski et al., 1991; Pilkington and Todoeschuck, 1993, 1995) and $\gamma_{1D} = 2$ (Pilkington and Todoeschuck, 1993). Providing the theory of Maus and Dimri (1994) is correct, this necessarily implies $\beta_{3D} = 4$. Therefore, estimated γ_{1D} values from the power spectra of magnetic profiles, and γ_{2D} values from the power spectra of magnetic charts can provide some indication of any anisotropic magnetization distribution. However, more recently it has been suggested that crustal magnetization does not follow a constant scaling law with a constant scaling exponent (Leonardi and Kumpel, 1996; Zhou and Thybo, 1998).

4.2 Euler deconvolution

The spectral methods of section 4.1 can be used to make estimates of the depths to magnetic sources in a statistical sense. In a different manner, the method of Euler deconvolution, which combines depth estimation with source body location, belongs essentially to the class of gradient methods.

A potential field can be described as the convolution of a source distribution with a function which is dependent upon the assumptions of potential theory. If this function can be determined, then the determination of the source distribution is implicitly a convolution of the observed field with the inverse operator, i.e., a deconvolution. The determination of the mathematical expression of the operator relies upon a potential field satisfying Euler's equation. Theoretical considerations are dealt with in the next section.

Methods of both three-dimensional and two-dimensional Euler deconvolution are applied to magnetic anomaly charts and profiles, respectively, to determine source depth and

position simultaneously. The following sub-section deals essentially with the 3-D method, which is then reduced to the 2-D case.

4.2.1 Theoretical and methodological considerations

Thompson (1982) and Reid et al. (1990) have shown that a homogeneous three-dimensional magnetic field satisfies Euler's equation such that,

$$(x-x_0)\frac{\partial T}{\partial x}+(y-y_0)\frac{\partial T}{\partial y}+(z-z_0)\frac{\partial T}{\partial z}=\begin{cases}N(B-T), & N>0 \quad (4.13a)\\ A, & N=0 \quad (4.13b)\end{cases}$$

where the position of the magnetic source is described by (x_0, y_0, z_0), and the total field, T, whose background is B, is measured at a position described by (x, y, z). A represents a function dependent on dip and strike of a source body. N, the negative of the degree of homogeneity (η) of the field, and also of Euler's equation, is given by $0 \leq N \leq 3$, and is referred to as a structural index (SI; Thompson, 1982). The SI is a measure of the rate of change of the field, with respect to distance, and is therefore dependent on the geometry of the source. A source in this context is a description of a particular feature, usually a subset of a larger magnetic body, that gives rise to a specific anomaly with a specific fall-off rate (rate of change of field with respect to distance). Simple examples include the edges or corners of bodies. The meaning and interpretation of SI will be considered later.

The practical application of 3-D and 2-D Euler deconvolution to magnetic anomalies is achieved through the method of least-squares inversion. As briefly outlined by Reid et al. (1990), the 3-D method of determining the position of magnetic sources in a region is applied to gridded anomaly data as follows,

1) The partial spatial derivatives, $\frac{\partial T}{\partial x}$, $\frac{\partial T}{\partial y}$ and $\frac{\partial T}{\partial z}$, i.e., the directional gradients of the magnetic anomaly, are calculated in the wavenumber domain (see Appendix III) at each grid location by use of the Fast Fourier Transform. Each grid cell therefore has a total field measurement and three estimates of the spatial derivatives.

2) A subset of the gridded anomaly and its three spatial derivatives is extracted, in the form of

a window of size n by n grid cells.

3) A value of N is chosen, either arbitrarily or to best describe a geologically likely source type. Together with the n^2 sets of points from step 2, either equation (4.13a) or (4.13b) is solved to determine the source position (x_0, y_0, z_0) depending on the value of N chosen. In addition to source position, B and A in equations (4.13a) or (4.13b), respectively, are also unknown variables and are therefore included in the solutions of the respective equation. The solution of the n^2 equations is obtained in a least-squares sense, providing $n^2 > 4$, whereby the error energy between the known observations and the computed model is minimized (see Appendix III).

4) Repeat steps 2 and 3 for all possible window positions in a given grid.

5) If the nature of the source is unknown, repeat steps 2 to 4 for a range of structural indices.

4.2.2 A 2-D approach

The reduction of the 3-D problem to one of two dimensions relies on the second term on the left of equation (4.13) being identically zero. If the assumption of two-dimensionality is made, i.e. the body extends infinitely in both positive and negative y-directions, then $\partial T/\partial y = 0$. An alternative assumption is one in which the profile is assumed to pass directly over the centre of a body, of finite extent, striking in the y-direction. Such transverse symmetry necessarily implies that $y - y_0 = 0$. Either assumption necessarily results in the 2-D Euler equation,

$$(x - x_0)\frac{\partial T}{\partial x} + (z - z_0)\frac{\partial T}{\partial z} = \begin{cases} N(B - T), & N > 0 \quad (4.14a) \\ A, & N = 0 \quad (4.14b) \end{cases}$$

As seen in section 3.3.1, if body half-strike lengths are greater than 20 km rms errors no greater than 5 % are generated.

4.2.3 Significance of structural index

A measure of the rate of change with distance of a potential field is the negative of the degree of homogeneity of Euler's equation, referred to as the structural index of a given model (Thompson, 1982). In fact, the rate of fall-off of the field is directly related to the geometry of a simple magnetic model, rather than to the magnetization distribution of the model (Smellie, 1956; Slack et al., 1967). The SI therefore provides a means of determining the geometry of the source, which can be used to make geological and geophysical inferences concerning the source of the magnetic anomaly, independent of magnetization direction or magnitude.

The rate of fall-off of an anomaly, and therefore the SI of the causative body, can be shown to be related to simple theoretical geometries (Smellie, 1956; Hood, 1965; Slack et al., 1967; Thompson, 1982; Reid et al., 1990). Although for most theoretical models N is described as an integer value or zero, Thompson (1982), and more recently Reid et al. (1990), point out that non-integer values may be common if the source is described by a geometry mid-way between two simple geometric shapes. Table 4.1 shows the relationship between N and some common geometries and geological situations.

If an incorrect SI is assigned to a model, solutions become scattered and biased; an overestimate in SI produces an overestimate in source depth, and an underestimate in SI produces an underestimate in source depth (Figure 4.4 and Reid et al., 1990). Moreover, the assignment of an incorrect SI creates quasi-concentric 'fanning' patterns, centred approximately on the correct spatial location, which are generally $\cup$-shaped when the SI is over-estimated, or $\cap$-shaped when the SI is underestimated. There is some potential in using such patterns, albeit limited and qualitative.

Although the method described above provides an inverse means of determining source position, it still requires an assumption concerning the structural index. Practically, the inverse solution is repeated a number of times for a range of SI values, in just the same way as the indirect inverse magnetization solution is obtained for a range of layer thickness values (see section 3.4.1). The inverse indirect wavenumber domain approach to solve for layer thickness variations, let alone in addition to magnetization solutions, is by no means an easy task, as was shown in section 3.4.3. Equally difficult is the solution of equation 4.13 or 4.14 for N in addition to source position and A or B.

N	magnetic model	geometrical model	example geological model
0.0	extended body	semi-infinite vertical or sloping contact	large offset fault, side of large oceanic reversal block, edge of pluton
↕			
0.5	extended body	non-infinite step	small offset fault, basement topography
↕			
1.0	line of poles	Line or edge	thin dyke, sill edge, lava flow edge
↕			
2.0	point pole	semi-infinite vertical cylinder	intrusive igneous pipe (volcanic conduits)
↕			
3.0	point dipole	sphere	intrusive boss or stock
↕			
2.0	line of dipoles	infinite horizontal cylinder	basement step(?)

Table 4.1 Relationship between structural index (N) and magnetic, geometrical and geological models. ↕ symbol implies that there is a continuum of index values. High indices can describe more than one type of magnetic model hence two entries for N=2.0

4.2.4 Synthetic Euler responses

To test the efficiency of the method, a suite of realistic magnetic models was created and their total field anomalies computed at 1 km intervals. Two-dimensional examples are used for easy illustration. The gradients of the field are calculated by the FFT method of Appendix III. Models of a sill, dyke, infinite vertical contact[2] and finite vertical contact, each with a remanent vector characteristic of sources west of Iberia (Galdeano, 1989), are shown in Figure 4.4a-d. In addition, two synthetic subsurfaces consisting of two or more bodies are generated (Fig. 4.4e,f).

[2] Infinite here means that the depth to the lower point of the contact >> the depth to the upper layer

Deconvolution of the calculated anomaly profiles was performed using a window length of 10 km for each model. A solution whose depth uncertainty is less than 20 % of its calculated depth was passed as an acceptable solution.

It can be seen that the apex of the vertical contact is best described by a structural index of 0.0. Indices of 0.5 and 1.0 clearly overestimate the depth and show typical $\cup$-shaped fanning patterns (Fig. 4.4a); these quasi-concentric features are centred approximately on the apex of the contact, i.e. the true depth. In contrast, a step model is best described by an index of 0.5 (Fig. 4.4b). An SI of 0.0 generated solutions that were underestimated in depth, as exemplified by their $\cap$-shaped patterns.

Thin bodies, such as dykes, sills or lava flows, are best described by indices of 1.0 (Fig. 4.4c,d). Again, underestimates in depth are generated by indices of 0.0 and 0.5 as seen by the $\cap$-shaped patterns.

Because a subsurface source that extends over a large area, commonly 100's of km^2, is more likely to contain multiple source bodies rather than a single solitary source, the Euler response was tested for multiple bodies. In a sense, the sill of Figure 4.4d consists of two sources: its two ends. Because the ends are at sufficient distance apart for their respective anomalies not to combine in any way, the method resolves well. However, the proximity of source bodies can have the effect of underestimating solution depths (Fig. 4.4e). Extreme proximity not only causes the defocusing of depth estimates, but also causes the lateral position of solutions to be erroneous (Fig. 4.4f).

4.2.5 Solution errors

Any given solution has an associated error. For most other geophysical methods used in this thesis, and elsewhere, it is usually acceptable to display all solutions with their associated errors. However, because of the large number of solutions obtained by the Euler deconvolution method, and the nature of the solutions, some must be immediately dismissed based on the failure to satisfy certain predescribed criteria.

If an anomaly grid consists of p by q grid cells, then the Euler deconvolution, using a window m by m grid cells, of an anomaly over a given region will produce N_{theo} theoretical solutions given by,

$$N_{theo(3D)} = (p - m + 1) \times (q - m + 1) \tag{4.15}$$

and the equivalent number of solutions in the 2-D case for a profile consisting of p discrete along profile samples, and a window m samples in length,

$$N_{theo(2D)} = (p - m + 1) \tag{4.16}$$

Thus, for example, if a window of size 10 by 10 is used to deconvolve the field over a region of interest 100 km by 100 km with magnetic observations gridded at 1 km intervals, then 8281 solutions are produced. If the region is instead, 200 km by 200 km, the same operator and grid interval produces 36481 solutions. An approximate equivalent 2-D case is much less severe; a profile 200 km long with a discrete sampling interval of 1 km and a window of length 10 km produces only 191 solutions. Not surprisingly, the number of solutions is at least one order of magnitude smaller for 2-D, rather than 3-D, deconvolution. It is therefore necessary to reduce the number of solutions, especially for the 3-D case, in a systematic way:

(1) a solution whose depth uncertainty, or standard deviation, is less than a given percentage, p_{cut}, of its calculated depth is accepted. If the set S contains all the solutions to equation (AIII.5), then the elements of the set of acceptable solutions, $S_a \subseteq S$, are limited by the inequality,

$$\sigma_z \leq p_{cut} z_0 \tag{4.17}$$

where σ_z is the standard deviation of z_0. Typically, $1 < p_{cut} < 5\,\%$ and $10 < p_{cut} < 20\,\%$ are used to optimize the number of 3-D and 2-D solutions, respectively. However, it can readily be seen from equation 4.17 that a deep solution may be accepted in the set S_a whilst a relatively shallower solution with an equal depth uncertainty may not. This result is not surprising since deeper solutions are by nature less certain. In addition, solutions to Euler's equation become more directly related to the depth of the source as $N \rightarrow 0$ and therefore solutions are still open to a degree of subjective interpretation.

(2) a solution whose absolute depth estimate is not within acceptable geological bounds is rejected. If a coincident seismic reflection profile exists, then the depth converted two-way travel time to top basement acts as a minimum depth bound on solutions, providing it is assumed to be the top of the magnetic layer. Otherwise, a probable minimum bound is used,

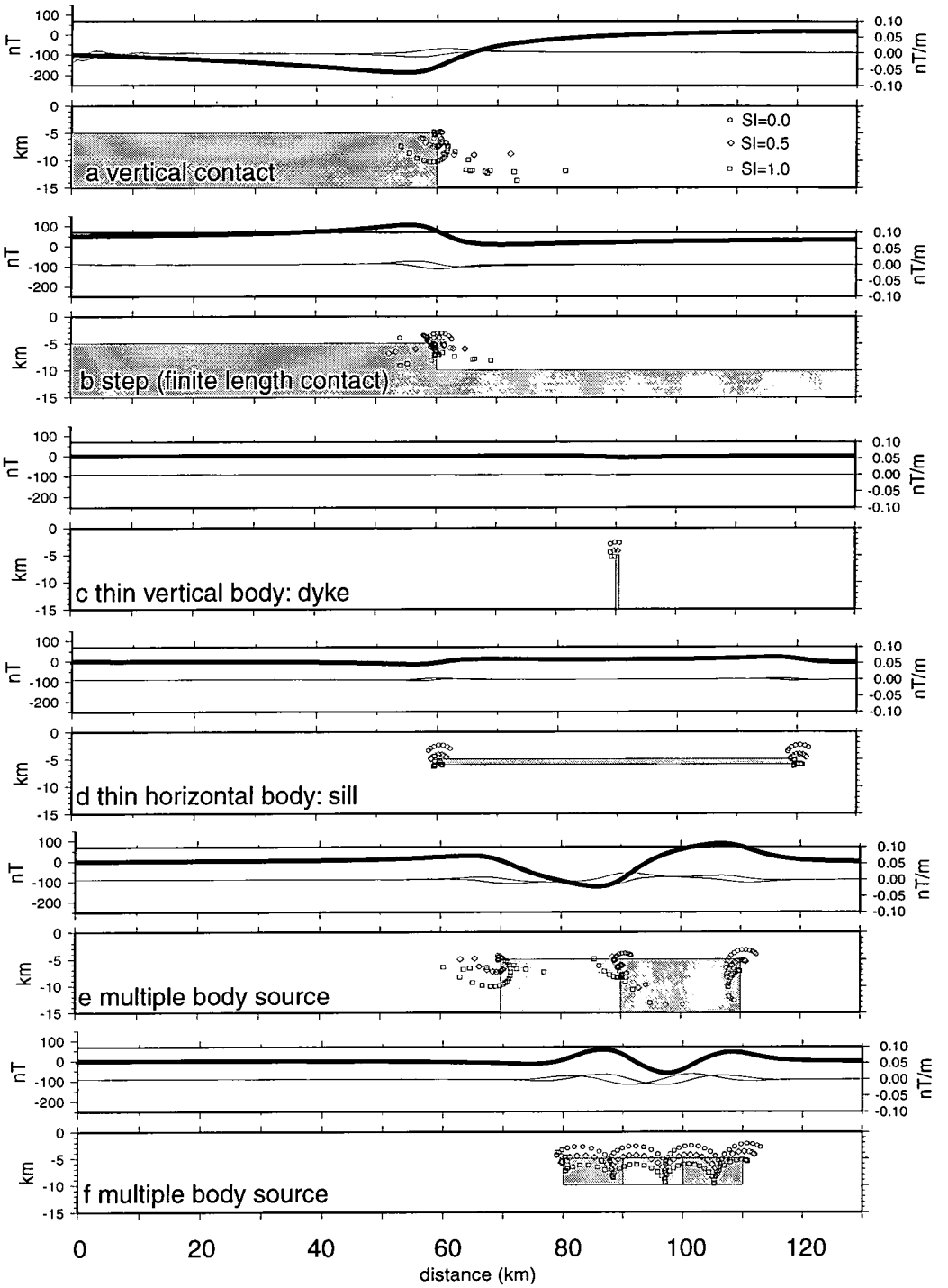

Figure 4.4 Six pairs of panels showing the total field (thick line; upper panels) and vertical and horizontal gradients (thin lines; upper panels) of six theoretical 2-D models (shaded; lower panels). Models are magnetized +0.7 A/m (darker shading) and -0.7 A/m (lighter shading). Euler deconvolution solutions whose depth uncertainties are less than 20 % of their calculated depths are shown for structural indices of 0.0 (circles), 0.5 (diamonds) and 1.0 (squares). See text for discussion.

e.g. the seabed. In a similar manner, the depth to the Curie isotherm provides a maximum bound to depth solutions.

The estimated location of the source in the horizontal plane, (x_0, y_0), or along profile, (x_0), also has an associated error. The allocated solution position is defined to be at the centre of the window over which the estimate was made. The rationale comes from the fact that the root mean square difference between each grid cell location and the true location is a minimum if the grid interval is constant in both x and y directions and the operating window is square. Therefore, the maximum positional error in both x and y directions is implicitly $< m\sqrt{2}/2$ providing the source of the anomaly within the window actually lies within the range of the window. The equivalent 2-D error is no greater than $m/2$.

4.2.6 Window size, non-linearity and interference

Not only does the window size govern the number of solutions obtained in a given area or along a given profile, but more importantly, it strongly influences the nature of the solution, in terms of whether a good representation of the actual source is made. The reason for this is that Euler's equation (equations 4.13 and 4.14), which is solved over a given window of the data, is only valid for a single source. If two or more sources are within close proximity, Euler's equation becomes non-linear and any solutions to the linear Euler equation become distorted. Thus, to minimize solution distortion, it is necessary to design a window whose size is as small as feasibly possible. Theoretically, this is governed by the number of unknowns; the solution of the 2-D problem limits the maximum window length to $3\Delta x$, Δx being the data sampling interval, whilst the 3-D problem limits the maximum window to a square $4\Delta x$ by $4\Delta x$. In contrast, a too small window of the data may not fully describe an anomaly and a depth solution, z_0, will necessarily have a greater standard deviation.

As mentioned previously, a real geological feature can be approximated by a geometrical model, which in turn can be represented by a magnetic model, i.e. a single source. Thus if two or more geological features are within close proximity to each other, the anomaly will be the resultant of the magnetic effect of each source, i.e. the individual anomalies merge as the distance between features decreases. In the context of alternate normally and reversely magnetized seafloor spreading blocks, this was demonstrated in section 3.3.4, but nevertheless the inverse indirect method was able to retrieve a magnetization model not entirely dissimilar to

the real model. Therefore, although it may seem difficult to visually relate the anomaly to its causative bodies, the anomaly, and in particular, the directional gradients of the anomaly, do potentially contain sufficient information for reasonable success of the Euler method. However, the concept of non-linearity will still introduce some error.

The distortion effects of non-linearity can theoretically be reduced by decreasing the size of the respective window. Figure 4.5 shows the deconvolution of a forward calculated field over a simple three-block model using windows of 20, 10, 5 and 3 times the data spacing, which in this case is 0.67 km. In general, a larger window passes a greater number of solutions. This may seem contradictory based on equation (4.16) but the important result to note is that solutions derived from larger windows have relatively smaller uncertainties than those derived from smaller windows.

A reduction in window size, although having the effect of reducing the number of solutions, yields better positional estimates of subsurface sources, in terms of depth and lateral position. Figure 4.5 shows that solutions obtained by windows of 13.3 km and 6.7 km, that is using 20 and 10 equations to solve for 4 unknowns, grossly underestimate the true depths. Typical $\cap$-shaped patterns have their apices displaced from the true locations. Alternatively, if the true depth to the source was known and a SI sought instead, the outcome of the experiment using a 20 km window, for example, would suggest the source be best represented by SI=1.0. In contrast, a large window has the advantage that it can determine all the subsurface sources (4 corners), albeit with large vertical and horizontal error (Fig. 4.5e).

Window sizes of 2 km and 3.3 km are able to satisfactorily locate the true depths and positions suggesting the best SI=0.5 which is expected for bodies midway between vertical contacts and sill-like in nature.

Inherent in all the techniques mentioned so far is the assumption that the absolute magnitude of any anomaly in a given solution windows is greater than the noise level in that window. As noted by Farrelly (1997), the process of computing derivatives by FFT can create short wavelength noise, which may be comparable in amplitude to some anomalies. It is therefore necessary to high-cut filter the directional derivative data to remove such noise (see Appendix III).

4.2.7 Statistical interpretation

In light of the discussion concerning the non-linearity of Euler's equation and the interference patterns resulting from neighbouring sources, together with the inability to invert

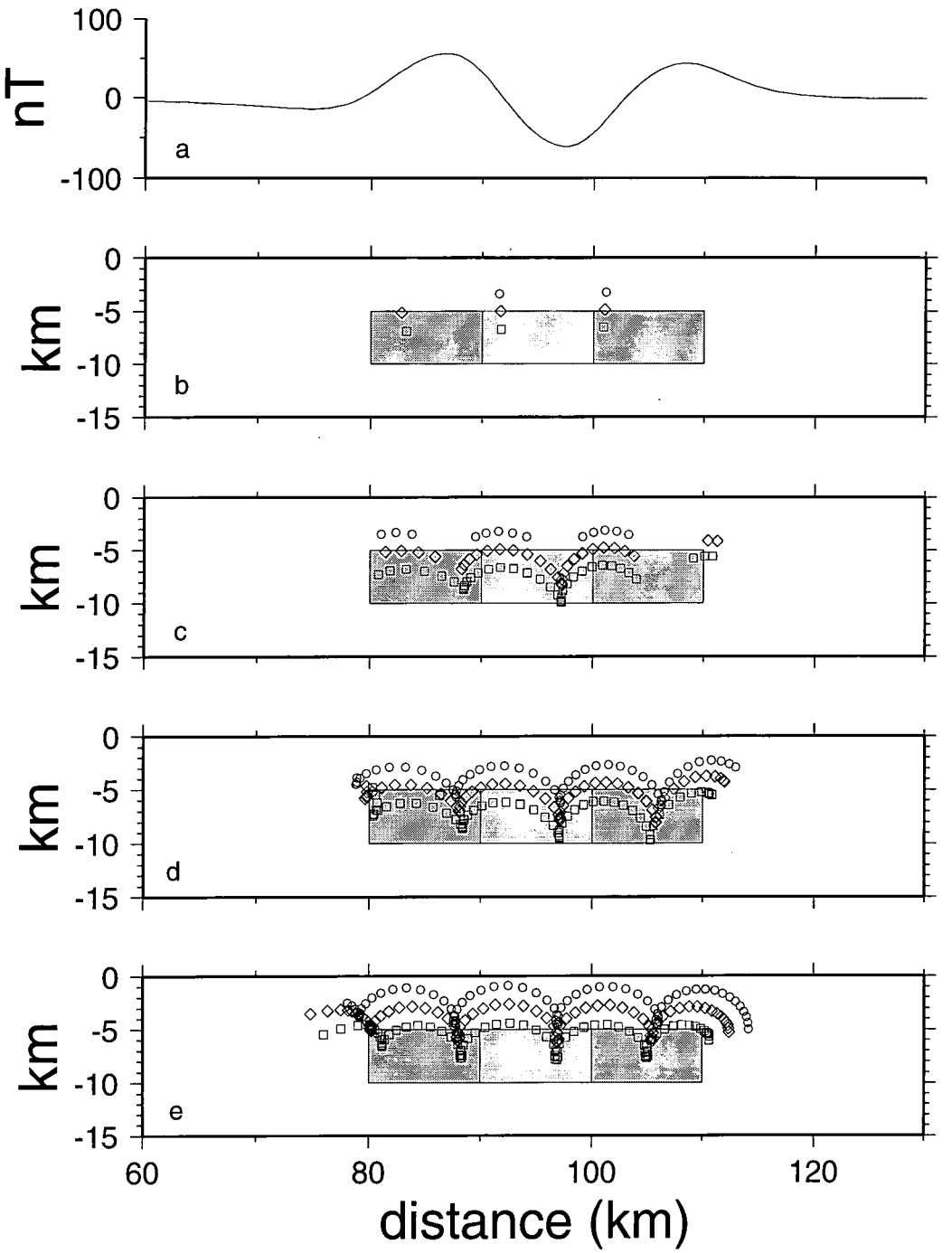

Figure 4.5 Euler deconvolution of the field (panel a) generated by model of figure 4.4 (f) with window lengths of 2, 3.3, 6.7 and 13.3 km (b-e, respectively). Structural indices of 0.0 (circles), 0.5 (diamonds) and 1.0 (squares). See text for discussion.

for a structural index or correctly define the SI for an unknown source geometry, I proceed with the interpretation of solutions in a statistical sense. The philosophy and assumption of the approach is that, on average, depth estimates correctly define the true solution depth within the bounds of its uncertainty, and that the number of over-estimated and under-estimated source depths contribute equally to the total number of solutions. Using Figure 4.5d as an example, it

can be seen that estimates made assuming an SI of 0.5 are distributed approximately evenly about the true depth. In addition, it is considered that the degree of lateral offset of solutions is negligible and that the linearity of anomalies is faithfully represented.

Consider a given magnetic profile or chart. For a fixed SI, all acceptable solutions can be regarded as part of a distribution set (S_a) whose characteristics describe the magnetic subsurface as a whole. The distribution is now considered univariate; a function of source body depth alone. Its central tendency, spread and shape can be described by its mean, median, mode, standard deviation, maximum range, skewness and kurtosis; all of which almost fully describe the distribution histogram[3]. Together they can provide geological information, in a statistical sense, concerning the depth of the likely magnetic sources. For example, if the data are normally distributed, the mean provides a measure of the most common source depth, whereas highly skewed solutions are better analyzed through the median. If subsurface sources are present at more than one depth, distributions will be leptokurtic (relatively large tails; high positive kurtosis values), whereas a highly platykurtic (relatively small tails; high negative kurtosis values) distribution with a narrow range may suggest good focusing of solutions on a single source depth.

In addition, if the same statistics are calculated for structural indices in the range $0 \leq N \leq 3$ then it is possible to monitor the effect of SI and provide an, albeit subjective, means of determining the SI that best represents the source. In particular, any significant 'jump' in a statistic may provide a qualitative means of selecting an appropriate SI since the statistics should vary smoothly with change in SI.

To illustrate the method two examples are used. Firstly, the statistics from the example of Figure 4.5 show that 100% of all acceptable solutions lie at a depth of 5 ± 0.25 km if a window width of 2 km is used to deconvolve the field whose causative body is assumed to have a structural index of 0.5 (Fig 4.6). Nevertheless, other SI=0.5 depth distributions for window widths of 3.4 km, 6.7 km and 13.4 km still suggest that the most likely solution be at ~5 km depth, although the spread of the data increases with increase in window size. Moreover, all four distributions are essentially platykurtic suggesting all the sources are at a single depth, or at least in a depth range given by solution errors and their collective variance.

Making a statistical interpretation is all very well assuming that the correct structural index is allocated to the sources in a particular unknown subsurface. However, an incorrect assumption in SI may lead to either an overestimate or underestimate in the depth solution. As Figure 4.6 shows, the above criteria for determining the most likely depth are also satisfied for

[3] In addition, the description of a histogram requires a measure of two of its percentiles.

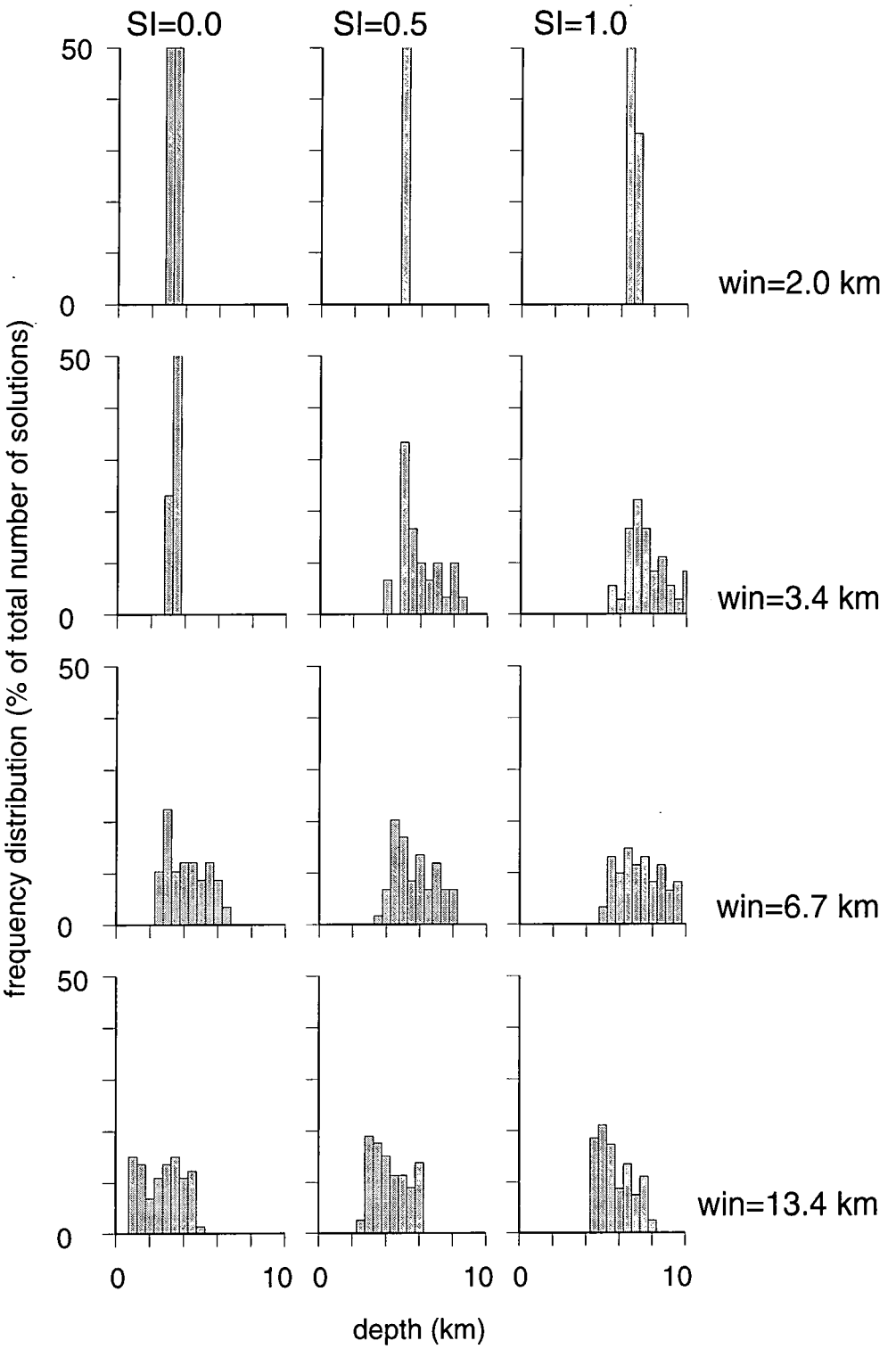

Figure 4.6 A matrix of histograms representing the distribution of solutions generated by the deconvolution of the field of Figure 4.5; rows show solution histograms for a given window size (win); columns show solution histograms for a given structural index (SI). Data are binned in 0.5 km intervals and shown as the percentage of the total number of solutions for the given deconvolution (fixed win and SI).

structural indices of 0.0 and 1.0 but in these cases, corresponding depths of 3.5 km and 6.5 km, respectively, are likely to be obtained (Fig. 4.6) as the most likely depths of magnetic sources.

In my second example, a more rigorous statistical approach is adopted. The field of Figure 4.3a, whose causative bodies are two sets of sources at 5 km and 10 km depth, is deconvolved for structural indices of 0.0 to 3.0, using an operating window of 4 km by 4 km. Solutions whose uncertainties are less than 5 % are accepted and used in the analysis. Figure 4.7a shows how solutions obtained for SI=0.5 delineate the source bodies reasonably well, even those that overlap or are within close proximity.

However, even this simple example shows that interpretation of solution depths is hindered by other shallower solutions, often the result of depth underestimation. Interpretation of solutions extracted along profiles or 'corridors' is usually inadequate since diagnostic interference patterns may be intersected and only partially imaged (Fig. 4.7b). Moreover, corridor width can have a disproportionate effect on the interpretation.

A statistical approach is preferred to analyze large data sets. Semi-quantitative statistical estimates, in the manner adopted for the first example, can be made from observation of solution histograms. Figure 4.8 shows the distribution of solutions from the deconvolution of the field of Figure 4.3 for structural indices of 0.0, 0.5 and 1.0; the most probable depths are 4 km, 5 km and 7 km respectively. However, unlike the distributions of Figure 4.6, here there exists a significant positive skewness with a relatively large tail extending to depths approximately twice the modal depth. Although merely qualitative, this result is significant in that it can indicate either (a) the tail is a result of a multi-source subsurface, or (b) solutions are biased towards underestimation rather than overestimation, implying the correct index has not been used. The choice is dependent on the outcome of a full statistical analysis.

The statistics of each field deconvolution are shown as functions of SI in Figure 4.9. Although structural indices as high as 3.0 are uncommon in nature they are shown here for completeness. Important to note initially are the high positive kurtosis values for all SI, i.e., a significant proportion of the data lies in the tails. The mean and median therefore contain only limited depth information being the result of 'averaging'. The second feature to note is the approximately constant positive skewness over all SI. This implicitly suggests a multi-source subsurface; skewness due to the incorrect assignment of SI, thus causing underestimation or overestimation bias, would vanish, or change sign, at the most desirable SI to describe the source. Therefore, it is highly probable that two or more sources are present in the subsurface. Moreover, if a realistic SI is chosen, i.e., $0.0 \leq N \leq 1.5$, it is probable, to the 95 % confidence limit, that the sources lie within the range 4.5 km to 17 km. Although with no theoretical

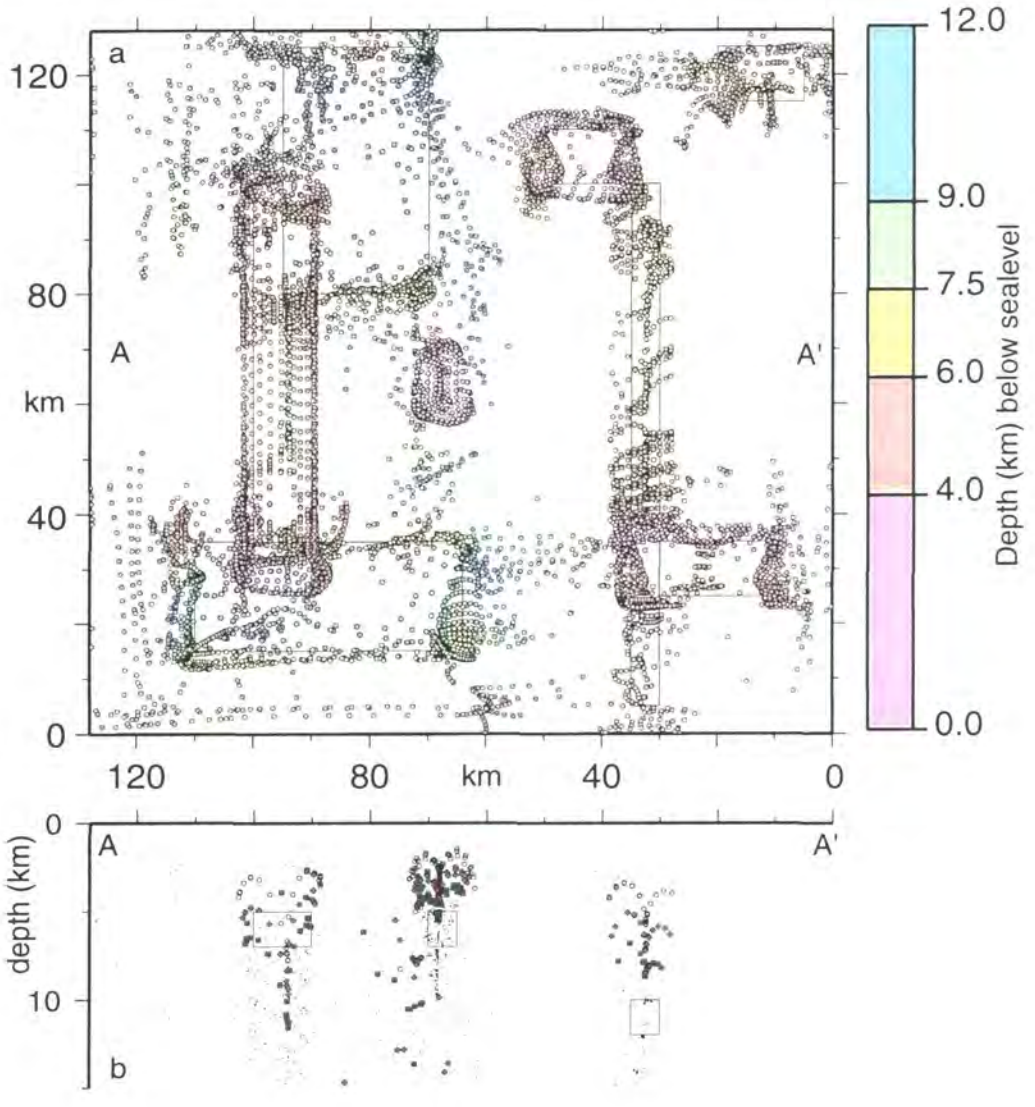

Figure 4.7 (a) Euler deconvolution solutions of the field in Figure 4.3a using a structural index of 0.5 and a window size of 4 km by 4 km. Solutions are colour coded depending on their depth (scale bar shows intervals) and superimposed upon the actual sources (solid light and dark grey; see figure 4.3 caption). (b) Depth section taken across A-A' of part (a); Euler solutions in a corridor 2.5 km either side of A-A' and whose depth uncertainties < 20 % of calculated depth are plotted for structural indices of 0.0 (open circles), 0.5 (red diamonds=all solutions in part (a)), 1.0 (green squares) and 1.5-3.0 (dots).

grounding, the most significant statistical discontinuities occur at a SI value of 1.0, suggesting that, on average, the sources are best represented by sill- or dyke-like features.

4.3 Componental magnetometry

The entirety of Chapter 3 and the sections of the present chapter thus far have leant themselves to the analysis of the magnitude of the total magnetic field anomaly, i.e. a scalar

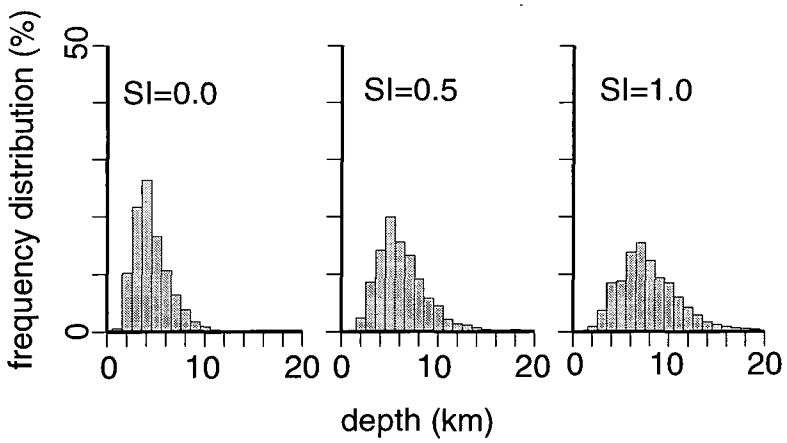

Figure 4.8 Solution distribution histograms for the deconvolved field of Figure 4.3a for a window size of 4 km by 4 km and structural indices 0.0, 0.5 and 1.0. Data are binned in 1.0 km intervals and shown as the percentage of the total number of solutions.

single component field. I have shown that the application of different techniques for analysis of the total field can potentially provide useful insight into the source(s) of a magnetic anomaly field. However, the character of a unicomponent field necessarily provides less interpretative information than an equivalent multicomponent counterpart. In the broadest sense, a multicomponent field is defined as any two or more functions, each of one or more independent variables. For example, the magnetic field is a vector field and can therefore be measured in three spatially orthogonal directions; the components F_N, F_E and F_V, in the Earth's fixed coordinate system, or F_X, F_Y and F_Z, in a fixed platform coordinate system, for example. Usually, the three components are measured using a fluxgate magnetometer mounted on an aeroplane, ship or deep-towed underwater instrument. Therefore, each component is measured as a function of profile orientation, p. The three component data used in this thesis were obtained using fluxgate magnetometers mounted on deep-towed underwater vehicles (TOBI and SAR; see Chapter 2) towed along almost straight line profiles. Therefore, the components available are F_X, F_Y, F_Z and T. The relative wealth of information provided by componental magnetometry can potentially provide a more constrained model of the subsurface.

4.3.1 Magnetic boundary character

Not entirely dissimilar to the absolute analytic signal method (e.g., Roest et al., 1992b)

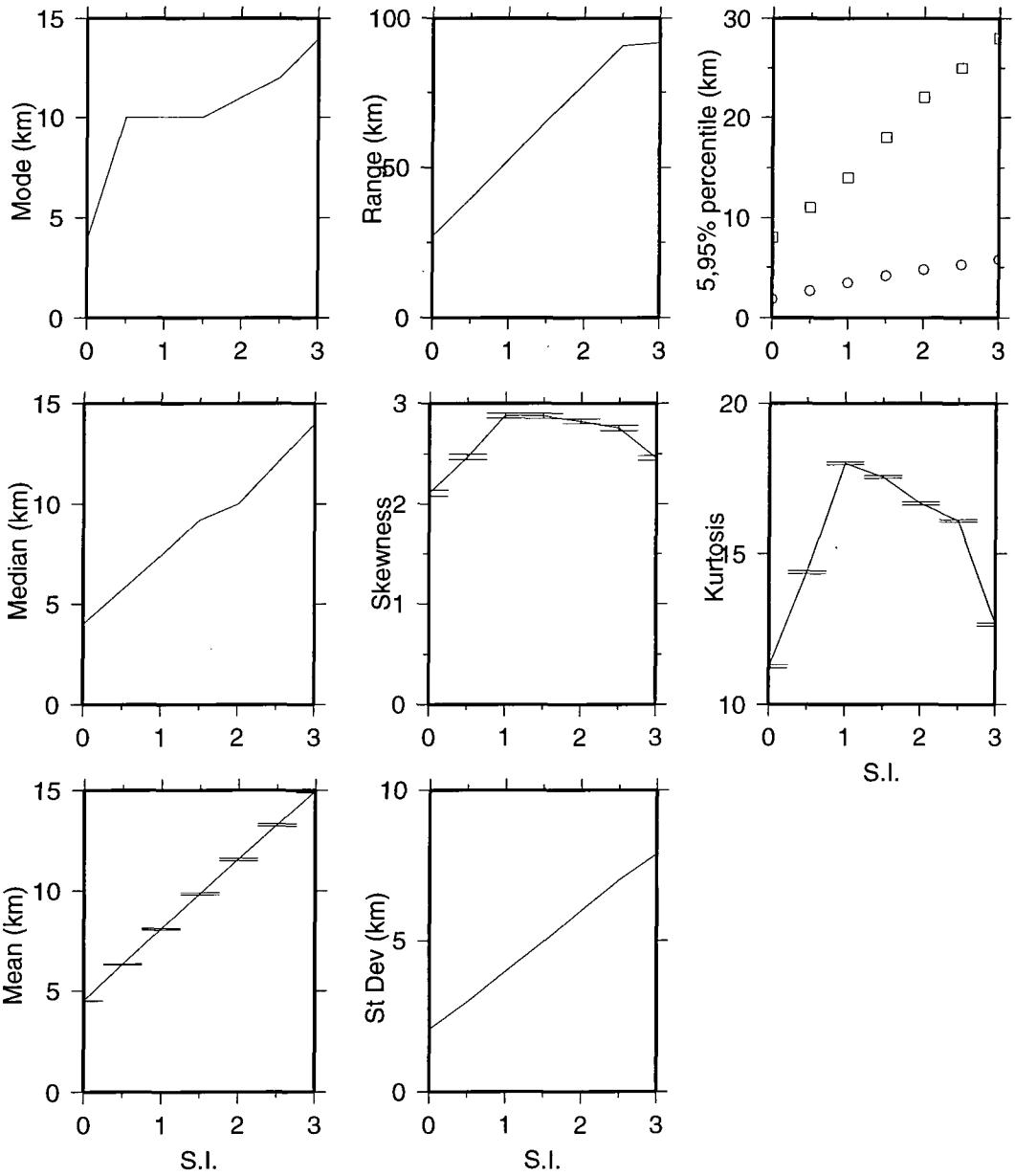

Figure 4.9 Statistics of the deconvolution of the field in figure 4.3a shown as a function of structural index. Error bars shown on mean, skewness and kurtosis. See text for discussion.

used for the location of boundaries of magnetic bodies, Seama et al. (1993) proposed a method of boundary strike estimation, in addition to boundary position estimation, via the use of vector anomalies. Korenaga (1995) further developed some of the ideas of Seama et al. (1993) and Isezaki (1986) to make predictions concerning the dimensionality of the source and relative magnetization contrasts. The following subsections briefly outline some of the theory and method of Seama et al. (1993) and Korenaga (1995), in addition to some of my own findings and adaptations.

4.3.1.1 Boundary location

For a corrected magnetic vector profile (for corrections see Appendix I) crossing a given vertical magnetic boundary between two domains, a quantity known as the intensity of spatial differential vectors (ISDV) can be calculated,

$$\mathrm{ISDV} = \left|\frac{\partial \mathbf{T}}{\partial p}\right| = \sqrt{\left(\frac{\partial F_N}{\partial p}\right)^2 + \left(\frac{\partial F_E}{\partial p}\right)^2 + \left(\frac{\partial F_Z}{\partial p}\right)^2} \tag{4.18}$$

where F_N, F_E and F_Z are north, east and vertically downward orthogonal components of the local magnetic field measured along a track whose direction is given by p. The line of the profile, P, is assumed to be at an angle, q, to the strike of the boundary (y-axis). Maxima in ISDV occur directly over the boundaries, although for two or more boundaries with equal magnetization contrast(s) a positional error dependent on the depth to the source and the proximity of the boundaries may be present (see Korenaga, 1995). Moreover, ISDV maxima associated with two adjacent boundaries merge when the separation $\leq$ ~1.36 times the mean depth to the source.

As a hypothetical example, if the magnetic sources within the southern Iberia Abyssal Plain are 7 km thick and on average their upper surfaces are 2 km below the observation track, the location of magnetic boundaries will only be possible if the individual magnetic blocks are > 7.5 km in width (see Fig. 3.10). If oceanic crust spreading at 10 mm/yr is assumed, the reasoning of Korenaga (1995) predicts that most of the reversal sequence anomalies within the range aM3(R) to aM15(N) will not be correctly located. Figure 4.10 shows the positional error as a function of mean depth and block width. This phenomenon is similar to the effect of spreading rate on total field anomalies as discussed in section 3.3.4. and the loss of resolution of the absolute analytic signal for closely spaced magnetic boundaries (Atchuta Rao et al., 1981).

In addition to the positional error of ISDV maxima, noise may introduce false maxima. It is therefore necessary to selectively dismiss maxima which occur below a given threshold. The remaining maxima are assumed to occur over any of the following magnetic boundaries (Seama et al., 1993): (1) reversal sequence blocks; (2) at edges of other intrusive bodies; (3) significant basement relief; (4) magnetization variations within the basement.

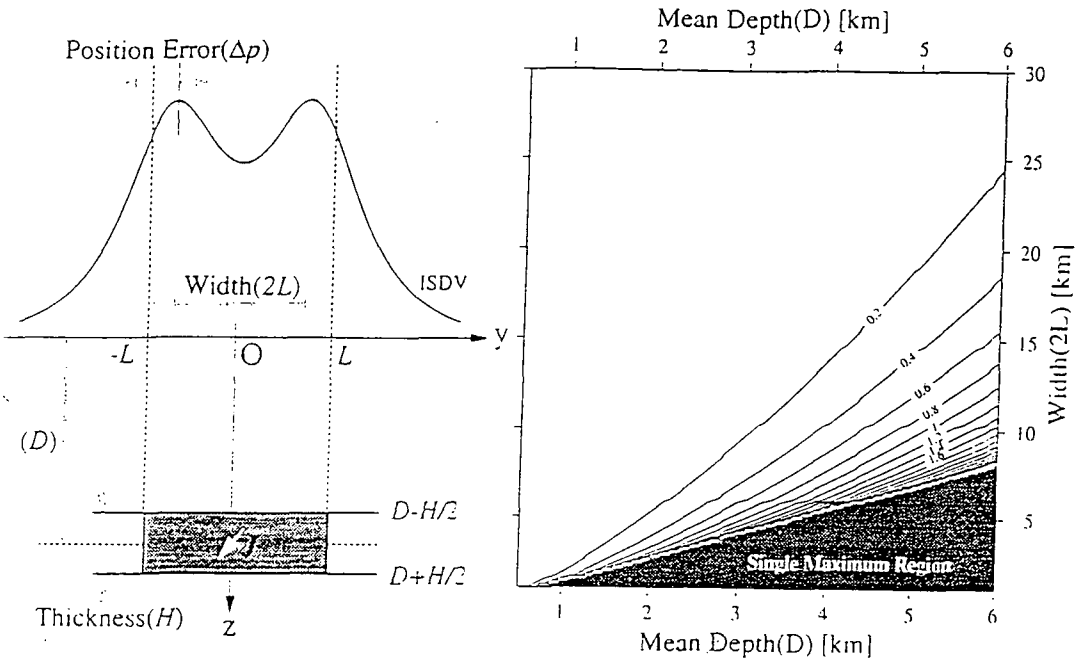

Figure 4.10 (a) Simplified model with two magnetic boundaries separated by a distance 2*L*. Layer thickness is *H*, and mean depth to layer is *D*. magnetization of the layer is J. Position error (Δp) is defined as difference between actual boundary and ISDV position. (b) Results of model calculations; position error is shown as contours (0.2 km interval). ISDV profile has only single peak in shaded region. Figure and caption from Korenaga (1995).

4.3.1.2 Boundary strike

Consider two juxtaposed magnetic bodies of equal depth and thickness. If the two bodies possess magnetization vectors, $\mathbf{m}_1$ and $\mathbf{m}_2$, and $\mathbf{m}_1 \neq \mathbf{m}_2$, then a magnetization contrast will be present at the boundary between the two bodies. If the bodies are infinite in length [or above a critical half-length; see section 3.3.1] in the direction parallel to the strike of their common boundary, the component of the magnetic field in the direction parallel to the strike will be zero for all x, regardless of the angle between $\mathbf{m}_1$ and/or $\mathbf{m}_2$, and the boundary strike. Thus, for a truly two-dimensional conjugate source pair, three component orthogonal observations made along a profile at any given orientation, once corrected, are capable of determining the strike of the magnetic boundary. I achieve practical implementation by the following procedure, which differs from the procedures outlined by Seama et al. (1993) and Korenaga (1995). If a vector, $\hat{\mathbf{b}}$, is defined, in terms of north and east components, as a

horizontal unit vector parallel to the boundary, i.e. $\hat{\mathbf{b}} = \mathbf{b}/|\mathbf{b}| = b_N\mathbf{n} + b_E\mathbf{e}$, then its scalar product with the magnetic field vector, **T**, or with the derivative of **T** with respect to the along profile direction, is zero at or near the magnetic boundary,

$$\mathbf{T}\cdot\hat{\mathbf{b}} = F_N b_N + F_E b_E + C = 0 \tag{4.19a}$$

$$\left(\frac{\partial \mathbf{T}}{\partial p}\right)\cdot\hat{\mathbf{b}} = \frac{\partial F_N}{\partial p} b_N + \frac{\partial F_E}{\partial p} b_E = 0 \tag{4.19b}$$

where C represents any measurement bias or error in IGRF, and is assumed constant over the ISDV peak. Because of measurement errors in **T**, or errors in the IGRF, it is favourable to use equation (4.19b). Providing **T** is observed at more than two locations across the ISDV peak, data in a window of length w can be used to estimate $(b_N\ b_E)$ in a least-squares sense. The procedure is valid because the ISDV peak is not a spike and therefore the effects of the boundary are observable over a finite distance on both sides of the boundary. The value of w is thus chosen accordingly. The actual boundary strike is given by the best-fit model of $(b_N\ b_E)$,

$$\text{strike} = \arctan\left(\frac{\hat{b}_E}{\hat{b}_N}\right) \tag{4.20}$$

Seama et al. (1993) implied that boundary dip information can be extracted by a similar procedure, whereby the boundary strike unit vector is given by $\hat{\mathbf{b}} = b_N\mathbf{n} + b_E\mathbf{e} + b_Z\mathbf{z}$, and an inverse solution is found for $(b_N\ b_E\ b_Z)$ in a similar fashion. However, for a vector to contain dip information of a planar surface it must be representing the normal to the surface; in which case the vector **T**, or its derivative $\partial\mathbf{T}/\partial p$ is no longer perpendicular to $\hat{\mathbf{b}}$. Alternatively, if $\hat{\mathbf{b}}$ were to represent a resultant of the strike and dip unit vectors in the boundary plane it also would be no longer perpendicular to **T**. In fact, it would no longer be parallel to the strike. In both cases equations 4.19a and 4.19b would be no longer valid.

4.4 Chapter summary

This Chapter has dealt with the theoretical, methodological and experimental aspects

of magnetic anomaly analysis by the direct and gradient methods of interpretation. The following conclusions can be drawn from this Chapter,

1) The direct and gradient methods are particularly useful in testing some of the assumptions on which other magnetic methods rely.

2) Source body depth information can be retrieved from the analysis of total field data by power spectral methods and Euler deconvolution. Source thickness estimates are practically impossible to derive by analyses of power spectra.

3) Inversion of magnetic anomaly power spectra, by three different methods, can provide information concerning the depth and scaling nature of magnetic sources.

4) Euler deconvolution is most successful when a statistical interpretational approach is adopted. Analyses of solution distributions, rather than individual solutions, can provide more realistic estimates of the most probable depths of magnetic sources.

5) Componental magnetometry is capable of retrieving the absolute position of magnetic boundaries although for bodies with widths < ~10 km positional errors are comparable with the absolute body location estimates. Strikes of magnetic boundaries, but not dips, can be derived from the three orthogonal components of the magnetic field.

The remainder of this thesis is concerned with the application of the methods described in Chapter 3 and the present Chapter to the observed magnetic anomalies offshore West Iberia and Newfoundland, and to the geological and geophysical interpretation of the results.

Chapter Five

Depth and trend characteristics of magnetic sources beneath the southern Iberia Abyssal Plain

The bulk of this chapter is concerned with the presentation of the results of an interpretative analysis of magnetic anomalies offshore West Iberia, in particular beneath the southern Iberia Abyssal Plain, with respect to the depths and trends of causative bodies.

5.1 Analysis of digital magnetic anomaly charts

Observed total field[1] magnetic anomaly charts can contain a wealth of information of different types. However, the integrity of the chart is dependant to some extent on the accuracy of compilation, reduction and pre-processing of magnetic measurements made along ship tracks and during aeromagnetic surveys. One such high quality digital magnetic anomaly chart exists offshore west Iberia from 36°N to 46°N and from 6°W to 19°W (Miles et al., 1994; Fig. 2.7); a subset of this dataset, which has substantially better control than the whole dataset, from 39.5°N to 42°N and from 9°W to 14°W is shown in Figure 5.1b. This subset forms a major dataset of this thesis, and in particular a further subset from 40°N to 41°N and from 11°W to 13°W. The analysis of anomalies is not exclusive to this latter region but there, strong constraints from the interpretation of seismic reflection profiles, seismic refraction profiles and basement samples aid the interpretation of the magnetic measurements (see section 2.3.2 and also section 5.2).

5.1.1 Preparation of charts

Reduction-to-the-pole (RTP) of the magnetic anomaly chart of Figure 2.7 was carried out in 1993 (Miles et al., 1996) and subsequently a subset (39.5°N to 42°N, 9°W to 14°W) was described by Whitmarsh and Miles (1995). The interpretation of Whitmarsh and Miles (1995) is dependant upon the assumptions of the RTP. It is therefore necessary to test these assumptions before further interpretation is made.

[1]Observed field strictly means no processing has been applied, for example reduction-to-the-pole (excluding corrections and pre-processing)

The RTP procedure is essentially a linear wavenumber domain filtering operation (Schouten and McCamy, 1972); the RTP field is the result of the multiplication of the Fourier transform of the observed anomaly ($\Im[A(x,y)]$) with a wavenumber domain phase filter. The phase filter is a complex filter that is dependant upon the inclination (I) and declination (D) of both the present geomagnetic field and the assumed magnetization vector of the causative body. It can therefore be described by an angular parameter since it is independent of the depth, shape and magnetization intensity of the causative body. The effect of RTP is to change the phase of anomalies at all wavenumbers such that the resultant field is equivalent to the field generated by the same source, except possessing a vertical magnetization vector, and observed at the magnetic north pole, where the geomagnetic vector is also vertical. A RTP anomaly is therefore placed directly above its causative body. However, correct relocation of anomalies is dependant upon the assumption of the correct source magnetization vector direction (the geomagnetic field vector is easily determined; IAGA, 1996).

The chart of Miles et al. (1996) was reduced-to-the-pole employing the assumption that all causative bodies possess a common remanent magnetization vector described (appropriate to the late Cretaceous) by $I = 46°$, $D = 0°$ (Van der Voo, 1990), and that the geomagnetic field vector (for epoch 1993.0) is described by $I = 57°$, $D = -9°$ (IAGA, 1996). In this geocentric dipole model, an average vector for North Atlantic oceanic crustal rocks adjacent to the West Iberia continental margin was used since the application of a spatially variable reduction-to-the-pole filter (differential RTP; Arkani-Hamed, 1988) proved to be problematic (P. Miles, pers. comm.). However, this vector is representative of rocks certainly Maastrictian and younger in age (71 Ma; C31 time; Van der Voo, 1969; Van den Berg and Zijderveld, 1982) and possibly CM0 and younger (121 Ma, Aptian-Barremian boundary); prior to C31 Iberia experienced an anticlockwise rotation of ~35° (Srivastava et al., 1990a) when it behaved as an independent plate during the opening of the Bay of Biscay (see section 2.2). Moreover, Galdeano et al. (1989) have shown that 30° of this rotation took place in the interval CM11 to CM0 (Hauterivian-Aptian), whilst, more recently, Juárez et al. (1998) constrain 17° of ~~counter~~/clockwise rotation between 125 and 95 Ma (CM3 to mid-CMQZ). Therefore, oceanic crustal rocks, or indeed any rock type likely to acquire a primary natural remanent magnetization (NRM), that accreted/formed in this interval will necessarily possess a remanent magnetization vector different to that suggested by Van der Voo (1990) and used by Miles et al. (1996). With this in mind I embarked upon a revised procedure of reduction-to-the-pole of the observed magnetic anomalies west of Iberia.

Based on the two extreme vector directions (particularly in declination) of Galdeano et al. (1989) and Van der Voo (1990), reduction-to-the-pole of the observed anomalies was

implemented based on eight different magnetization vector directions and a single geomagnetic vector direction (I=57°, D=-9°; IAGA, 1996). Of the eight vector directions, four are given inclinations of 46° (after Van der Voo, 1990) and four given inclinations of 58° (after Galdeano et al., 1989). Although not shown here, a difference in inclination of 12° produces no significant difference in the resultant anomaly for any constant declination. I chose to utilize an inclination of 46°; an inclination of 58° implies no net N-S plate motion since acquisition of magnetization, whereas an approximate 5° northward change in latitude over ~130 Ma is more likely (due to the east of north trend of the Mid-Atlantic Ridge). An inclination of 46° was combined with discrete declinations of 0°, -15°, -30° and -43° to fully describe each vector; ~15° represents the minimum step in declination for which any noticeable changes occur. Figure 5.1 shows the resultant RTP anomaly charts, together with the parent chart of observed anomalies.

5.1.2 Description of reduced-to-the-pole magnetic anomalies

The success of RTP, i.e. identification of the correct vector direction, can be gauged by some preconceived notions of anomaly sources. For example, 'sharpening' of linear oceanic seafloor spreading anomalies should occur when the correct magnetization declination is used; some interference of anomaly peaks and troughs is removed when they are relocated directly over the centre of normal and reverse polarity bodies, respectively. Moreover, non-linear observed anomalies that become lineated after RTP can be assigned to lineated causal bodies. Because the processes of rifting and seafloor spreading produce, on the whole, two-dimensional features (e.g. tilted fault blocks and intrusions with across margin/axis changes >> along margin/axis changes), here I assume that the sources of the magnetic anomalies are more linear than circular. However, an oceanic origin can only be inferred from quantitative modelling of the magnetic field (see Chapter 6) and other independent evidence.

West of 13°W (50 km; Fig. 5.1c,d,e) at 40° to 41°N (50-160 km; defined as zone 1) the presence of oceanic crust is strongly implied; the observed anomaly chart (Fig. 5.1b) is dominated by the high amplitude linear J anomaly. Although not an isochron and apparently unrelated to the reversal timescale, J has been modelled throughout the North Atlantic and has been shown to be present near to, and within, oceanic crust accreted during chron CM0-CM2 time (Pitman and Talwani, 1972; Rabinowitz et al., 1978; Tucholke and Ludwig, 1982). The 'sharpening' of J, and anomalies immediately adjacent to it, is best achieved using a source magnetization vector declination of 0° (Fig. 5.1c). The two linear troughs immediately east of, and parallel to J also become apparent after such an RTP (Fig. 5.1c). At increased [westerly] declinations these

anomalies, and J, loose their linear character and become less coherent as linear anomalies. A qualitative interpretation therefore indicates the presence of a strongly lineated source with a geocentric (D=0°) magnetization vector. Zone 1 here is synonymous with the western zone of Whitmarsh and Miles (1995).

In the region east of zone 1 (100-210 km) linear anomalies become apparent regardless of the magnetization vector declination used (defined as zone 2; Fig. 5.1c,d,e,f). Although not ubiquitous, 010° trending anomalies are the dominant trend within this region. Magnetization declinations of 0° and -15° produce more linear anomalies which are, in general, laterally more persistent (up to lengths of 125 km). Only the positive magnetic anomaly between ODP Leg 149 Sites 897 and 899 (110,130 km), and a negative anomaly immediately adjacent to and northeast of it, are significant anomalies trending ~350° for any given declination. Although a dominant trend is highlighted many anomalies are sub-circular in shape, especially for when reduced-to-the-pole with magnetization declinations <0°.

Progression eastwards is accompanied by a change of anomaly trends to approximately 350°. Zone 3 (east of ~200 km), similar to the eastern zone of Whitmarsh and Miles (1995), is characterized by relatively continuous linear N-S to NNW-SSE trending anomalies that are best imaged with a magnetization declination of -15° (Fig. 5.1d), although many of the same trends are apparent at other declinations.

New reduction-to-the-pole processing of the observed anomaly chart has shown that the region between ~75-200 km (E-W), which includes most of the OCT, may be underlain by rocks whose magnetization vector declination lies in the range 0° to -30°. Reduction-to-the-pole of magnetic anomalies in zone 1 (west of ~75 km) and zone 3 (east of ~200 km) suggest that the sources possess magnetization vector declinations of 0° and 0° or –15°, respectively. These declination directions agree with those expected for oceanic crust (younger than CM0(R)) and continental crust (with an induced magnetization), respectively.

The results of this RTP study alone cannot determine the most likely magnetization declination of rocks within the OCT. Therefore, constraining the timing (pre- or post-rotation of Iberia) of the acquisition of rock NRM is made difficult. For example, assuming the palaeomagnetic studies (see above) are correct, a successful RTP assuming a declination of -43° would suggest that NRM acquisition occurred prior to the rotation, whereas a declination of ~0° would suggest NRM acquisition occurred post-rotation. However, there are other considerations and therefore a discussion concerning the rotation of Iberia is left until section 7.1.2, after the results of a magnetic study at the conjugate Newfoundland margin are presented. Nevertheless, the study here suggests that NRM declinations of OCT rocks take values 0° to –43°.

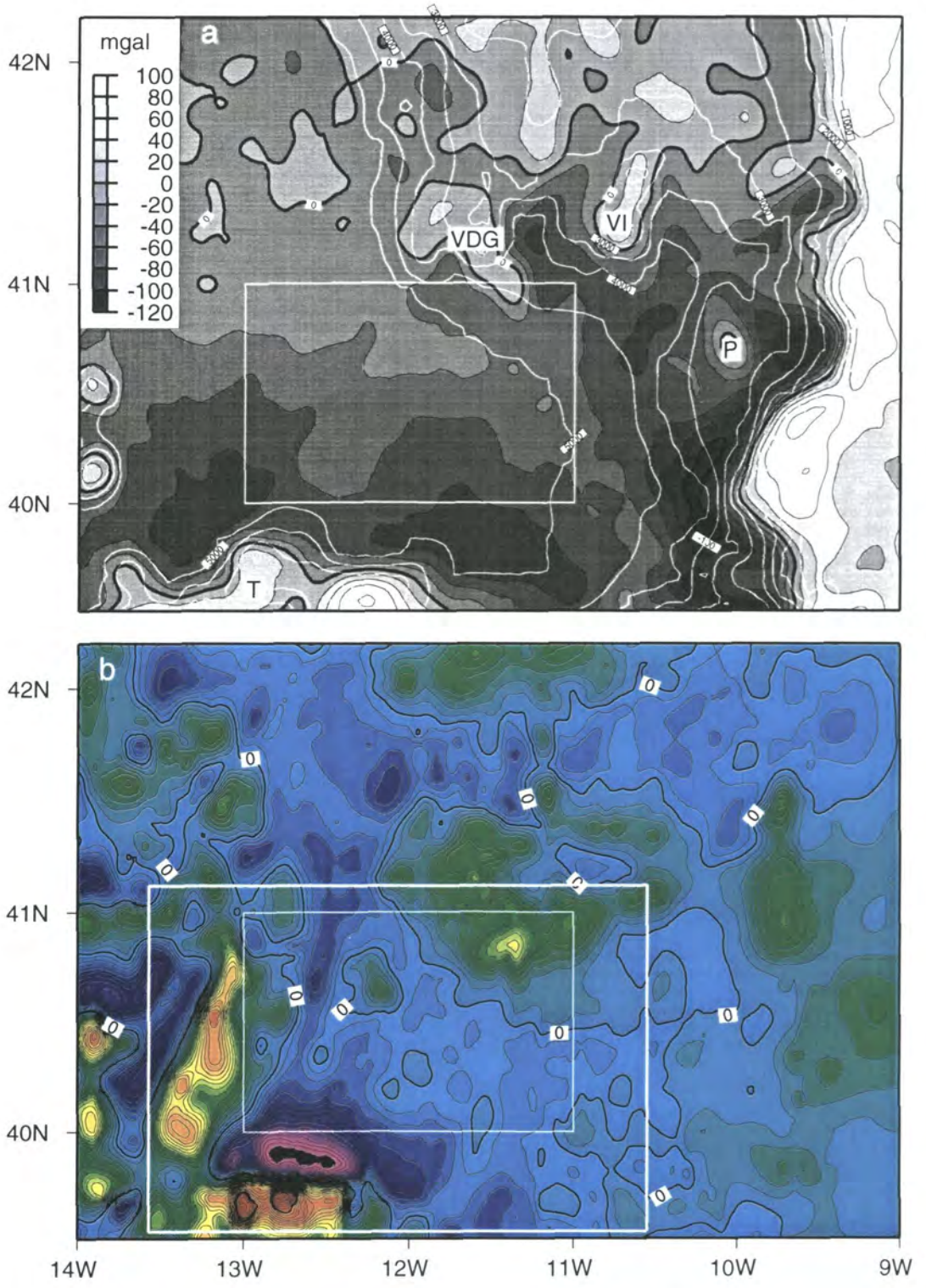

Figure 5.1 (a) Bathymetry (white contours; interval 500 m) on free air gravity anomaly (grey shade) derived from satellite altimetry (Sandwell and Smith, 1997) across the West Iberia continental margin. P=Porto seamount, T=Tore seamount, VDG=vasco da Gama seamount, VI=Vigo seamount. Small white box (region S2; Fig. 2.7) marks approximate location of the OCT in the southern Iberia Abyssal Plain. (b) Observed magnetic anomalies (contours 25 nT). (Cont. over).

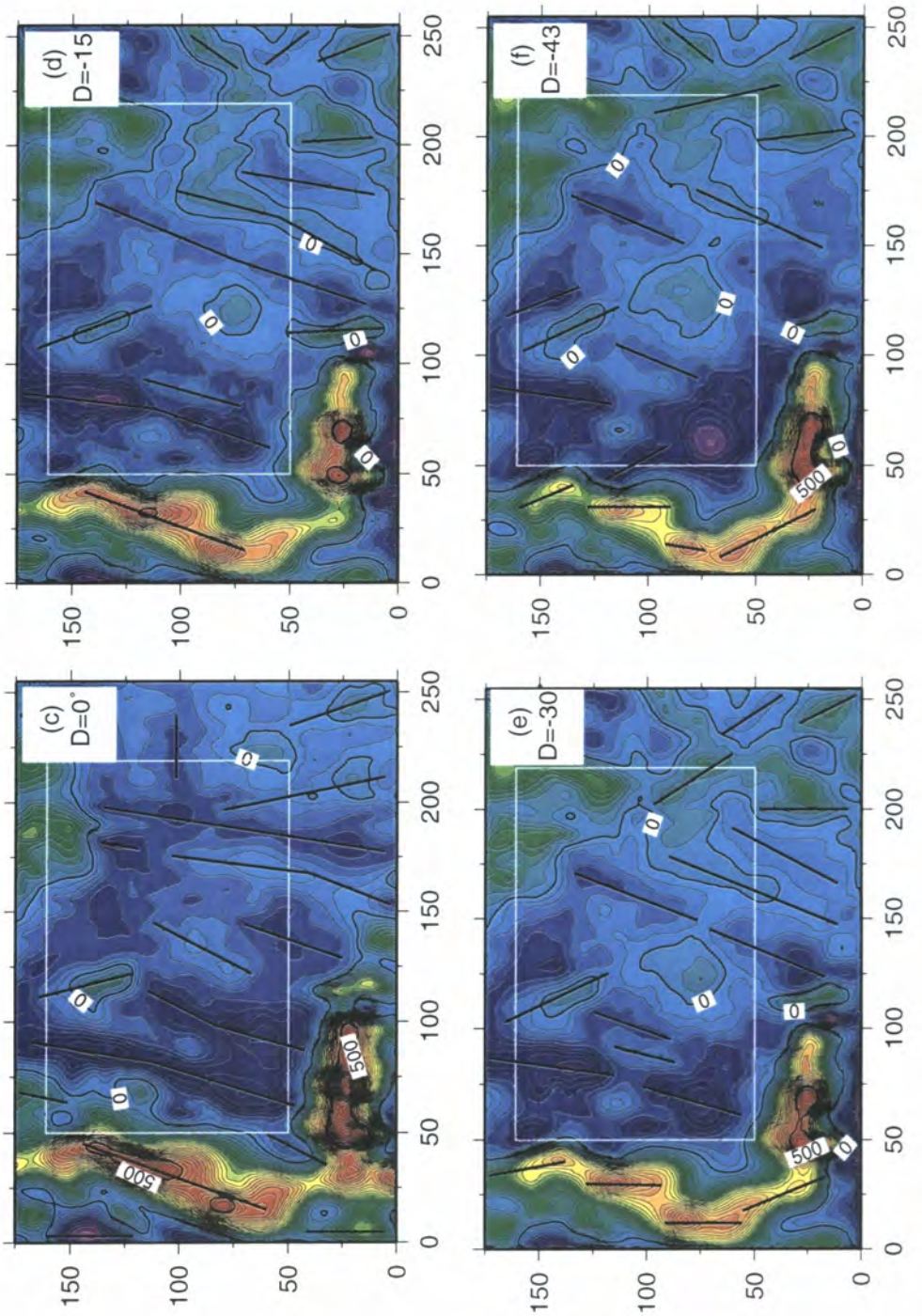

(c) Magnetic anomalies in large white box in (b) reduced-to-the-pole with parameters I_M=46°, D_M=0°, I_G=57° and D_G=-9° (I=inclination, D=declination, subscript M=rock magnetization, subscript G=geomagnetic field). Latitude and longitude converted to kilometers. (d) As (c) except I_M=46°, D_M=-15°. (e) As (c) except I_M=46°, D_M=-30°. (f) As (c) except I_M=46°, D_M=-43°. Black and white lines=trends of anomalies. See text for discussion.

5.2 Depth to acoustic basement chart

In almost all marine geological settings the uppermost surface of acoustic basement represents a minimum depth at which any significant magnetic source exists; sediments and the water column above are non-magnetic, whereas crystalline metamorphic, igneous and meta-igneous rocks beneath have the potential of possessing a significant remanent and/or induced magnetization. More specifically, along an E-W transect in the southern Iberia Abyssal Plain ODP Legs 149 and 173 have proven that post- and pre-rift sediments are non-magnetic (Sawyer et al., 1994; Whitmarsh et al., 1998). Therefore, the depth to the top of acoustic basement provides a strong constraint on the minimum magnetic source depth during interpretation of magnetic anomaly measurements and their respective models.

5.2.1 Chart preparation

Multichannel seismic (MCS) reflection profiles totalling approximately 2200 line kilometers acquired on four cruises (Sonne-75 , Lusigal-90 , IAM-project and Discovery 215) were used to pick the two-way travel time (twtt) to the top of acoustic basement. Table 5.1 shows a data listing of all the lines used whilst Figure 2.5 shows track coverage. The basement surface was picked at constant intervals of 10 shot points from time sections as a boundary between continuous, sub-horizontal events above shorter, mainly dipping discontinuous and incoherent events. Practical achievement was made difficult due to: (1) Uncollapsed diffraction patterns on filtered stacks that obscure and distort the character of the event between sediment and basement (Fig. 5.3); (2) On both migrated sections and filtered stacks the character of the top basement event is markedly different over basement topographic highs compared with basement lows (basins; Fig. 5.4). Nevertheless, the first trough with characteristics of the top basement event was picked with an accuracy of ~0.1 s twtt, and in some cases considerably better. In addition the seafloor reflector was picked at the same shot point positions.

The reconciliation of line cross-over differences was achieved via an iterative procedure. Travel times (twtt) on intersecting lines were compared at the exact cross-over location; those with a twtt difference of 0.1 s or more were flagged as problematic. Reconciliation was achieved by an iterative refinement of the two twtt picks until their difference was within the 0.1 s limit. However, in some instances repicking of the top basement reflector at, and within the vicinity of, the cross-over necessarily continued to greater distances; in a few extreme cases corrected cross-overs further along line became uncorrected. Perpetual reconciliation was avoided by attributing

Cruise and line numbers (inclusive)	Processing
Discovery-215 (Minshull, 1995)	FS
CAM 128, 129, 131-133, 138-141,142 (E half),143, 148-158	
CAM 130, 134, 136, 142 (W half), 144, 147, 159,160	M
Sonne-75 (Roeser et al., 1992)	M
SO 15-22	
Lusigal-90 (Boillot et al., 1990)	M
LG 04, 12, 14, 15	
IAM project (Torne et al., 1993; Banda et al., 1995)	
IAM 9	M (part DM)

Table 5.1. List of multichannel seismic cruises (bold) and lines used to interpret top basement reflector in the southern IAP. FS=filtered stacks; M=time migrated; DM=depth migrated

errors to 'out of the plane' effects. The residual error is dealt with in a later step.

Time to depth conversion of top basement picks was implemented using a single best-fit velocity function for the whole region derived from multichannel stacking velocities (Pickup, 1997) and travel-time modelling of sonobuoys (Whitmarsh and Miles, 1990),

$$d = \begin{cases} -0.15 + 1.02062t + 9.7203 \times 10^{-5} t^2, & t \leq 1688 \\ 2000.01 + 1.93212(t - 1688) + 3.10102 \times 10^{-4} (t - 1688)^2, & t > 1688 \end{cases} \quad (5.1)$$

where d is depth below the seabed in meters and t is twtt below the seabed event in msec. Total depth below sea surface was calculated by addition of the depth of the water column assuming a seawater velocity of 1.5 km/s.

A continuous depth-to-top-basement surface was achieved by contouring. The main objective in obtaining a depth-to-top-basement chart was to provide further constraint in magnetic modelling, particularly inverse indirect modelling. Therefore, these practical requirements necessitated a continuous digital depth grid; a hand contoured chart would have severe limitations because of its analogue nature. Thus, data were first binned in 0.5 km by 0.5 km cells over the whole region and a single value assigned to each cell by mean averaging all picks, the purpose being to remove the residual cross-over errors and to avoid spatial aliassing in the contouring procedure. These data were merged with redigitized analogue swath bathymetric data over Vasco da Gama seamount (J-C. Sibuet, pers. comm.) where sub-cropping basement is present. The merged data were contoured by means of an adjustable tension continuous curvature surface

gridding algorithm in the GMT package (Wessel and Smith, 1991). A tension factor of 0.35, typically used for steep topographies, was used in order to suppress undesired spurious oscillations and false maxima and minima. The final depth to top basement chart is shown in Figure 5.2 and by Discovery 215 Working Group (1998).

5.2.2 Description of chart

Basement character can be characterized into four distinct zones (Fig. 5.2);

(A) West of ~12°30'W basement is characterized by linear elongated 010° trending topographic highs and lows at average depths of 6 km and 7.5 km, respectively. In extreme cases relief as great as 2.5 km occurs over distances as short as ~15 km, although topographic wavelengths and variations are typically 20-25 km and 1.5 km, respectively. Along the strike of the topographic highs and lows themselves, there are variations in depth which give the appearance of isolated sub-circular peaks and basins although these variations are approximately half of those between features. The easternmost limit of the zone is characterized by a 010° trending broad ridge whose western flank gradient is at least twice that of its eastern flank gradient, thus giving the appearance of a basement 'plateau' (in zone B). The ridge defining the eastern limit of zone A has greater continuity than ridges to the west of it with relatively little along strike variation, and curves to the east at its southern tip. This ridge, continuous from at least 40°24'N to ~41°N, has previously been imaged and described as peridotite ridge segment R3 (Beslier et al., 1993).

(B) A plateau-like region, at ~7 km depth, extends east from R3 a distance of 25km in the south at ~40°20'N and 40 km further north at 40°50'N. The easternmost limit is characterized by steep gradients in basement topography which rapidly falls to depths of 8-8.5 km over distances of 10 km. Unlike its western limit the boundary with zone C is an extremely non-linear feature; in particular, two positive topographic 'fingers', trending NNW-SSE to N-S, protrude into zone C up to 25 km from the main body of zone B. In addition, two sub-circular peaks, beneath ODP Leg 149 Sites 898 and 899, protrude 2 km from the 'plateau' and reach depths of less than 5 km below sea level.

(C) Zone C is characterized by relatively subdued relief and little topographic variation. Depths average 8.5 km below sea level and in some cases exceed 9 km. Basement rises above 7.5 km in places but features are small compared to those in zones A and B.

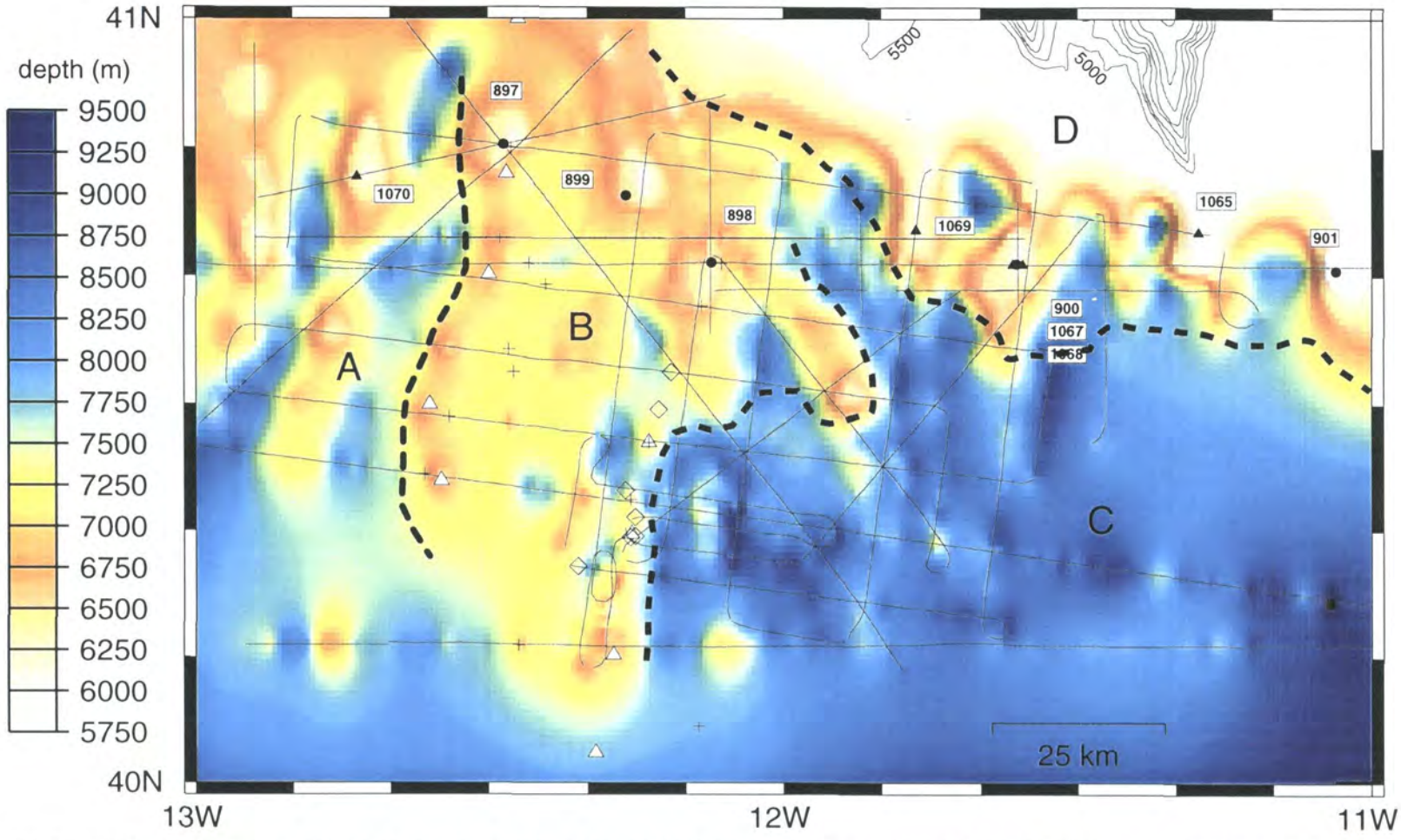

Figure 5.2 Depth to acoustic basement (m) in the southern Iberia Abyssal Plain derived from multichannel seismic reflection profiles (thin lines) and swath bathymetry over Vasco da Gama seamount (J.-C. Sibuet, pers. comm.; 500 m contours). Four zones based on the character of basement labelled A-D and their approximate boundaries are defined by the thick dashed lines. Oceanic crust (A) occurs west of peridotite ridge segments R3 and R4 (white triangles). The OCT is split into two zones (B and C) whilst continental crust is defined by zone D. Solid black circles and solid black triangles show position of ODP legs 149 and 173 drill sites, respectively. Crosses and open diamonds mark the positions of the inflection points of westward facing monoclines in the overlying post-rift sediments due to strong and weak folding, respectively (see text). Locations not plotting on MCS lines were derivedfrom single channel seismic lines. The quasi-linear trends of strong and weak fold inflection points fall within the limits of zone B.

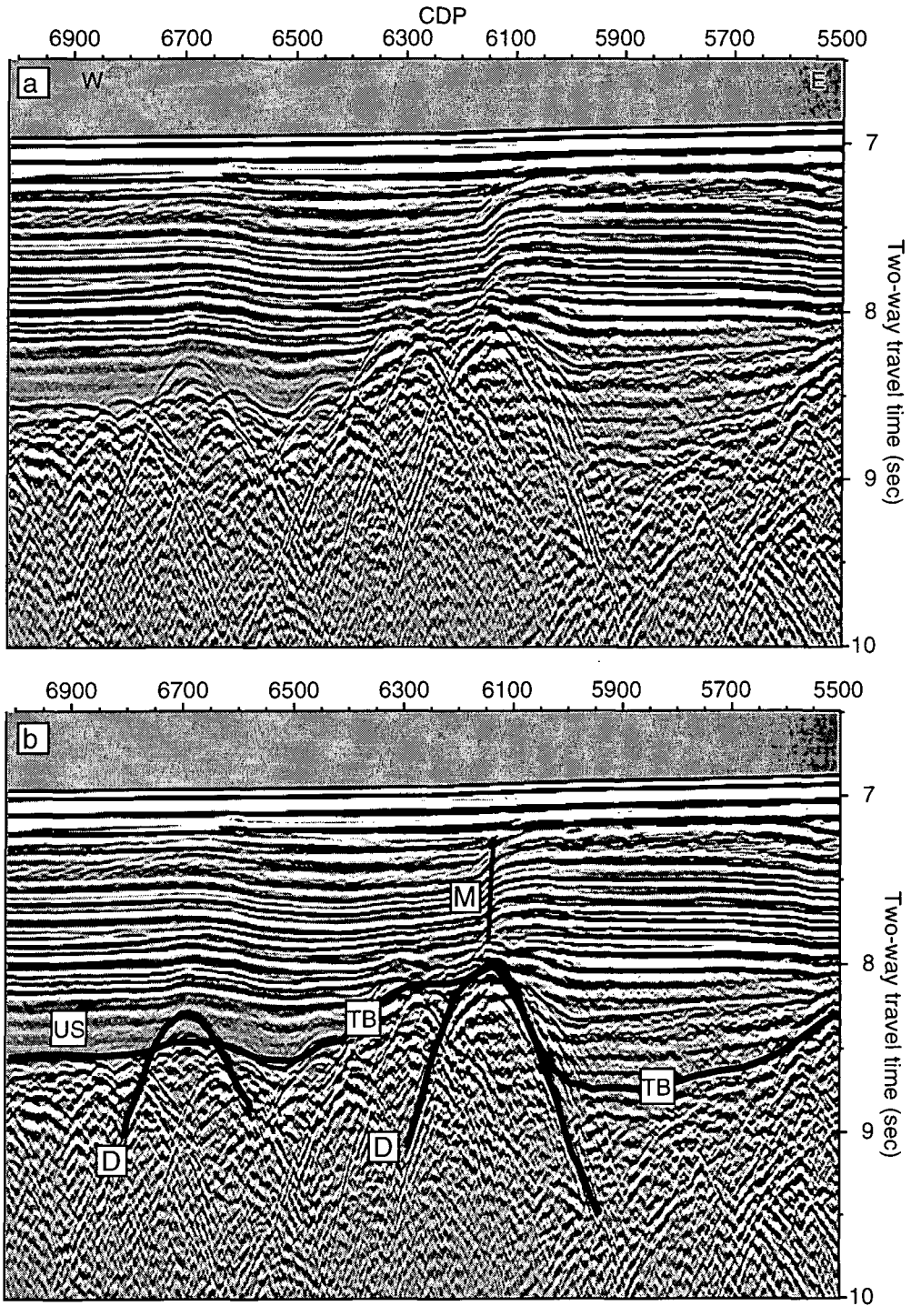

Figure 5.3 Multichannel seismic reflection profile CAM-142 between CDP 5500 and 7000. (a) uninterpreted section, (b) interpreted section. Top basemet event picked and interpreted and shown as heavy line (TB), which is commonly obscured by diffractions (D) making precise interpretation of travel time picks difficult. M indicates axis of monocline in post-rift sediments directly above the basement high over which ODP Leg 149 drill site 898 lies 8 km along strike to the north. The basement high is possibly the northern continuation of peridotite ridge segment R4. US denotes the lowermost package of sediments (directly above top basement) which have little internal character and approximately the same velocity as the uppermost basement (Dean et al., submitted; see Chapter 6) introducing further difficulty in defining TB, especially in basement lows.

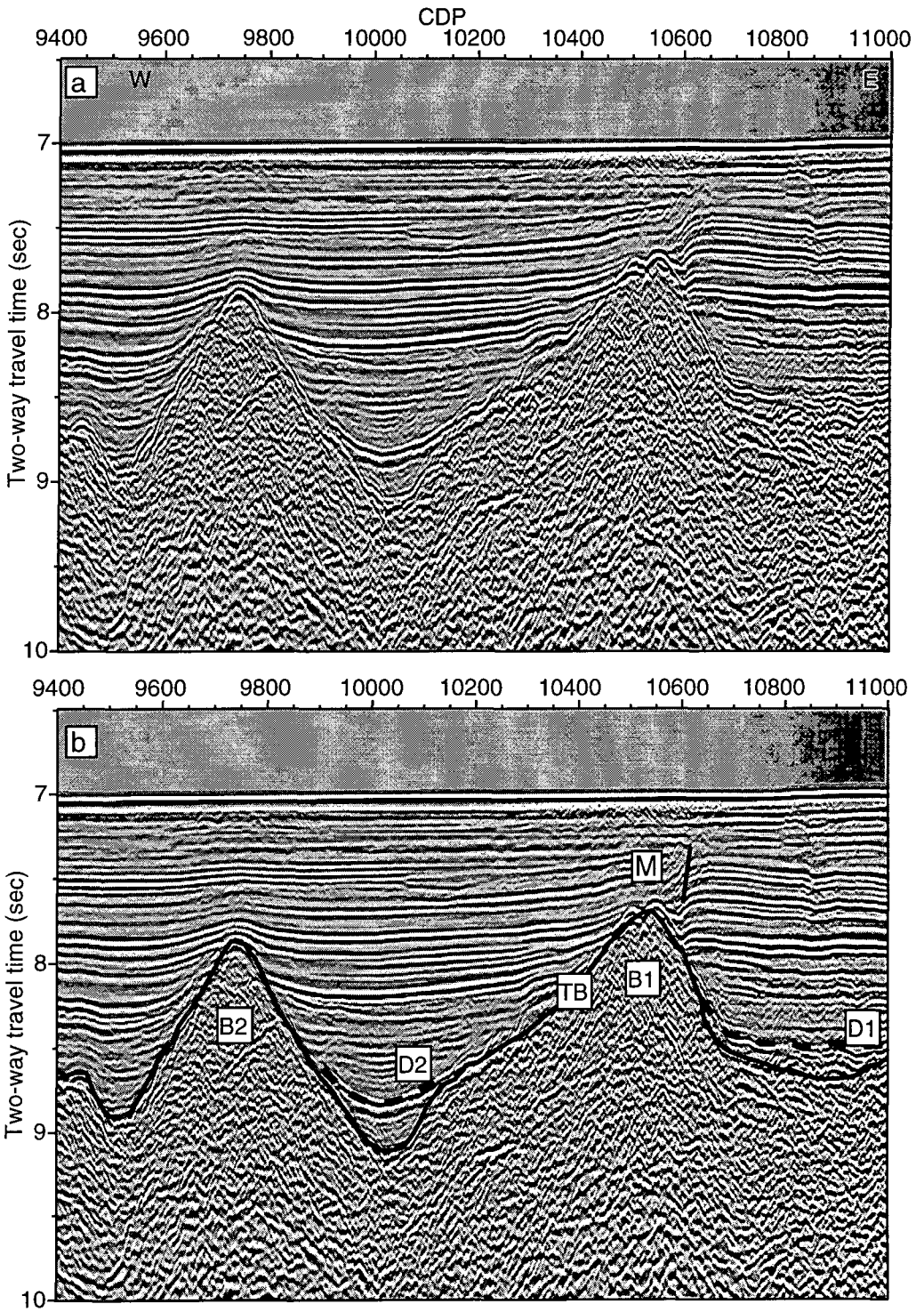

Figure 5.4 Multichannel seismic reflection profile CAM-144 between CDP 9400 and 11000. (a) uninterpreted section, (b) interpreted section. Top basemet event picked and interpreted and shown as heavy line (TB). TB is easily identified over highs B1 and B2 although some diffractions are still present at the apex of B1 even after migration. In contrast, TB is difficult to define in some basement lows; dashed line D1 shows the ambiguity in picking TB at CDP >1250. *Dashed line D2 marks* the equivalent event in the basement low between CDP 9900 and 10125 which indicates clearly that D2 is not the top basement event.M indicates axis of monocline in post-rift sediments directly above the basement high B1 over which ODP Leg 149 Site 897 lies. B1 is equivalent to peridotite ridge segment R3. B2 is ~9 km up strike from ODP Leg 173 Site 1070 and assumed to be oceanic crust.

(D) North of zone C and north-east of zone B sub-parallel N-S trending elongate basement highs, commonly at depths of 6 km or less, form fingers that protrude into zone C. Less than 15 km northward three similar linear features, which are almost perfectly aligned with three basement ridges determined from MCS, have been imaged by a swath bathymetric survey over Vasco da Gama seamount (J-C Sibuet, pers. comm.). Although at present no control exists in the region between, these two sets of features may be the same phenomenon thus implying the elongate basement highs may be up to 50 km in length.

Not only can the morphological character of basement be used to estimate, in part, its nature, but in addition, the mechanical properties of basement rocks are governed by their dominant lithology. With reference to the mid-Miocene compressional phase, which was contemporaneous with the Betic orogeny, zones associated with basement weakness are inferred to be present beneath the most deformed post-rift sediments offshore West Iberia (Masson et al., 1994). In a far less detailed manner to that employed by Masson et al. (1994), asymmetric westward facing monoclines were mapped to show the pattern and location of post-rift sediment folds (Fig. 5.2). Inflection points on monoclines were mapped and the intensity of folding classified as weak or strong based arbitrarily on the relative wavelengths and amplitudes of the folds.

It can be seen that all significant sediment folding is confined to zone B. Moreover, fold inflection points appear to be grouped into two distinct linear zones; more intense folding present on the western side of zone B and less intense folding present on the eastern side of zone B. In addition, the general trend parallels the trend of major basement features including peridotite ridge segments R3 and R4 (Beslier et al., 1993; Pickup et al., 1996), although folding rarely coincides exactly with minima in basement depth.

Although the full significance of the sediment folding is beyond the scope of this thesis, its limitation to zone B further suggests that the nature of the basement (or at least its response to compression) within the OCT is clearly defined by two distinct zones (B and C).

5.2.3 Contribution of basement relief to magnetic anomalies

In section 3.3.5 I quantified the potential contribution, to the magnetic field, of realistic topographic variations of a hypothetical magnetic layer. There, I concluded that such variations in relief can potentially produce sea surface magnetic anomalies with amplitudes similar to those observed in the OCT west of Iberia (see Fig. 5.1). To complement the hypothetical analysis, the actual contribution of the basement relief west of Iberia is now analysed in two ways. Firstly, if

the top basement surface is indeed an interface between non-magnetic sediments and a magnetic basement, 3-D Euler deconvolution solutions for a structural index of 0.5 (step model; see section 4.2) should theoretically plot at, or near to (depending on the horizontal error), significant gradients in basement topography. For basement depths of 5 km or more I consider only the steepest of gradients as significant. Nevertheless, a second method of comparing forward calculated anomalies with observed anomalies in both the space domain and wavenumber domain can provide a more quantitative analysis. The space domain approach was adopted, in part, by Whitmarsh et al. (1996a) in the southern IAP and their results provided some of the rationale for further enquiry in the form of this thesis.

(1) 3-D Euler solutions whose depths exceed that of top basement and whose uncertainties do not exceed 1 % of their calculated depths are shown in Figure 5.5. Of the potential 16320 solutions, 7550 had acceptable uncertainties (46 % pass rate) of which only 1649 (22 %) underlay top basement. Such statistics suggest many solutions are underestimated, but nevertheless, those that fall near to top basement follow the trend of some steep regions of basement. A rough estimate (by eye) indicates that ~25 % of solutions falling within 1 km of the top of basement are related to significant basement topographic variation.

(2) 29 evenly spaced parallel profiles whose position and orientation (100°; Fig. 5.6) were chosen to cross the dominant trend of linear basement features and observed magnetic anomalies approximately at right angles were chosen for the analysis. Demeaned 2-D anomaly profiles extracted from the observed magnetic anomaly chart of Figure 5.1b are compared with demeaned forward calculated anomalies. Each forward calculated anomaly is generated from a 2-D model whose upper surface is extracted from the basement chart (Fig. 5.2), coincident with the extracted magnetic observations, and whose lower surface is at a constant depth of 14 km. Three models were generated for each profile whereby constant magnetization vector directions were used corresponding to a remanent vector direction given by Van der Voo (1990), a remanent vector direction given by Galdeano et al. (1989) and an induced magnetization direction. A constant magnetization magnitude of +1 A/m was used for each model. A statistical comparison between each observed-calculated profile pair is made in two ways.

(a) In the space domain, the linear correlation coefficient and residual between each observed and forward calculated anomaly profile was calculated. Figure 5.7(a) shows that little correlation along the 29 test lines exists regardless of the choice of magnetization vector direction. A significant correlation is given by values >0.5 or values <-0.5, the latter indicating that a

negative, rather than positive, magnetization provides a better model. Of the 29 profiles, only 3 marginally exceed the threshold of significant positive correlation.

Residua, although sensitive to absolute magnetization values, are able to provide along line (~E-W) and across line (~N-S) information regarding the degree of match of observations with calculated anomalies. Across line variations in rms residua follow a quasi-sinusoidal pattern; highs (50-60 nT) in the region between lines 18-25, and lows (15-30 nT) in the region between lines 3-15 (Fig. 5.7a). This general result suggests that observations south of line 15 are better explained by basement topographic variations than those to the north.

Along line variations in residua are gauged through the analysis of residua as functions of distance along profile. Residua between the observed anomaly and each model generated anomaly along each track were normalized against the minimum rms residual of 15 nT and plotted to show variations in match (Figure 5.7b,c,d). As a result, the degree of match can be segregated along the approximate boundaries of zones A-D described in section 5.2.2. The degree of match, expressed as an areal proportion of each zone, is represented as a function of $rms_{\min}^{(50)}$ and $rms_{\min}^{(100)}$ i.e. greater than 100% and 50% of the minimum rms residual, respectively (Table 5.2).

Zone	$> rms_{\min}^{(100)}$ (% area)	$> rms_{\min}^{(50)}$ (% area)
A	50	90
B	25	75
C	0	15
D	20	60

Table 5.2 Proportion, by area, of each of the four zones A-D in which the normalized residua between observed anomalies and forward calculated anomalies (from a model describing top basement topographic variations only) exceeds 100% and 50% of the minimum rms residual of 15 nT.

The results suggest that sources other than simply basement topographic variation contribute to observed magnetic anomalies, more so in zones A, B and D than in zone C. However, caution is of the essence; basement in zone C is on average ~2 km deeper than basement in zones A, B and D, and possesses a more subdued relief which may account for the apparent match between observed magnetic anomalies and anomalies generated by relief.

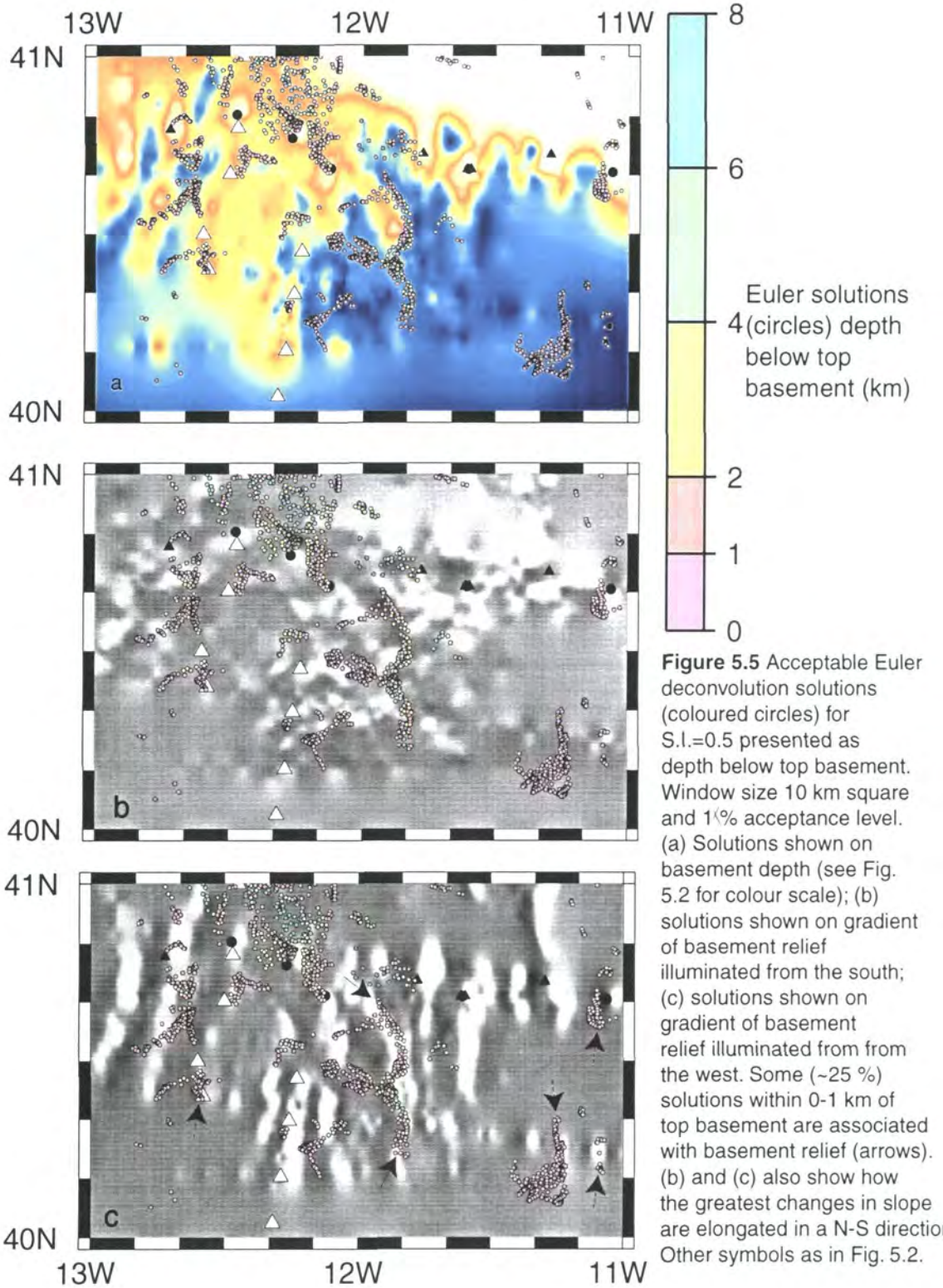

Figure 5.5 Acceptable Euler deconvolution solutions (coloured circles) for S.I.=0.5 presented as depth below top basement. Window size 10 km square and 1% acceptance level. (a) Solutions shown on basement depth (see Fig. 5.2 for colour scale); (b) solutions shown on gradient of basement relief illuminated from the south; (c) solutions shown on gradient of basement relief illuminated from from the west. Some (~25 %) solutions within 0-1 km of top basement are associated with basement relief (arrows). (b) and (c) also show how the greatest changes in slope are elongated in a N-S direction. Other symbols as in Fig. 5.2.

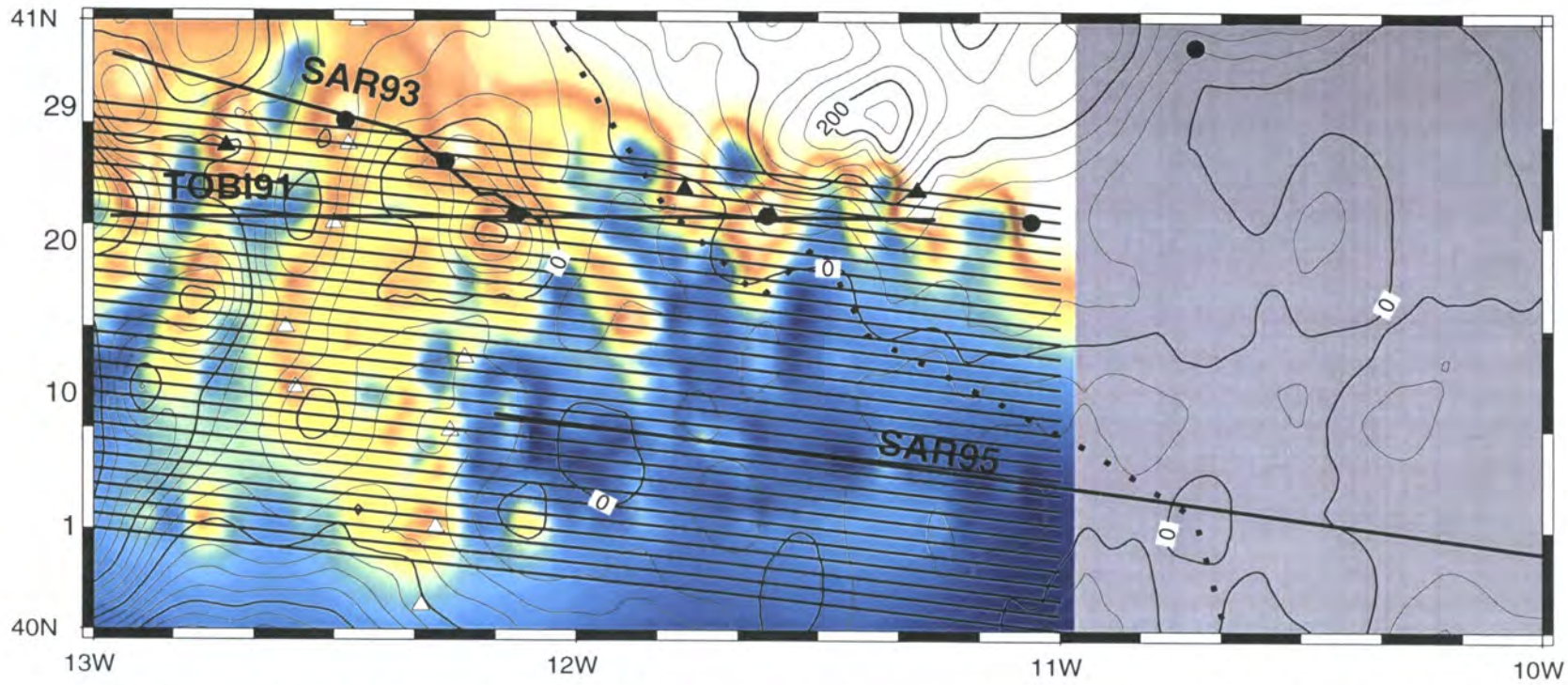

Figure 5.6 Seasurface observed magnetic field (25 nT contours) on shaded basement relief (colour palette shown in Fig. 5.2) in southern Iberia Abyssal Plain. Masked grey region marks region with no basement depth control. Solid circles, solid triangles and open triangles are ODP Leg 149 and 173 drill sites, and peridotite ridge segments, respectively. Thin black lines (1-29) trending 100° run approximately at right angles to the dominant trend in significant basement features and observed magnetic anomalies. Magnetic field observations and coincident basement relief profiles extracted from their respective charts are analysed to test the contribution of basement relief to the magnetic field (see text). Thick black lines are deep-tow magnetometer profiles SAR95, TOBI91 and SAR93. Dotted line marks the probable westerly and southerly extent of continental crust based on the most ladward tilted continental fault blocks. Numbers of test lines 1-29 shown on left of chart.

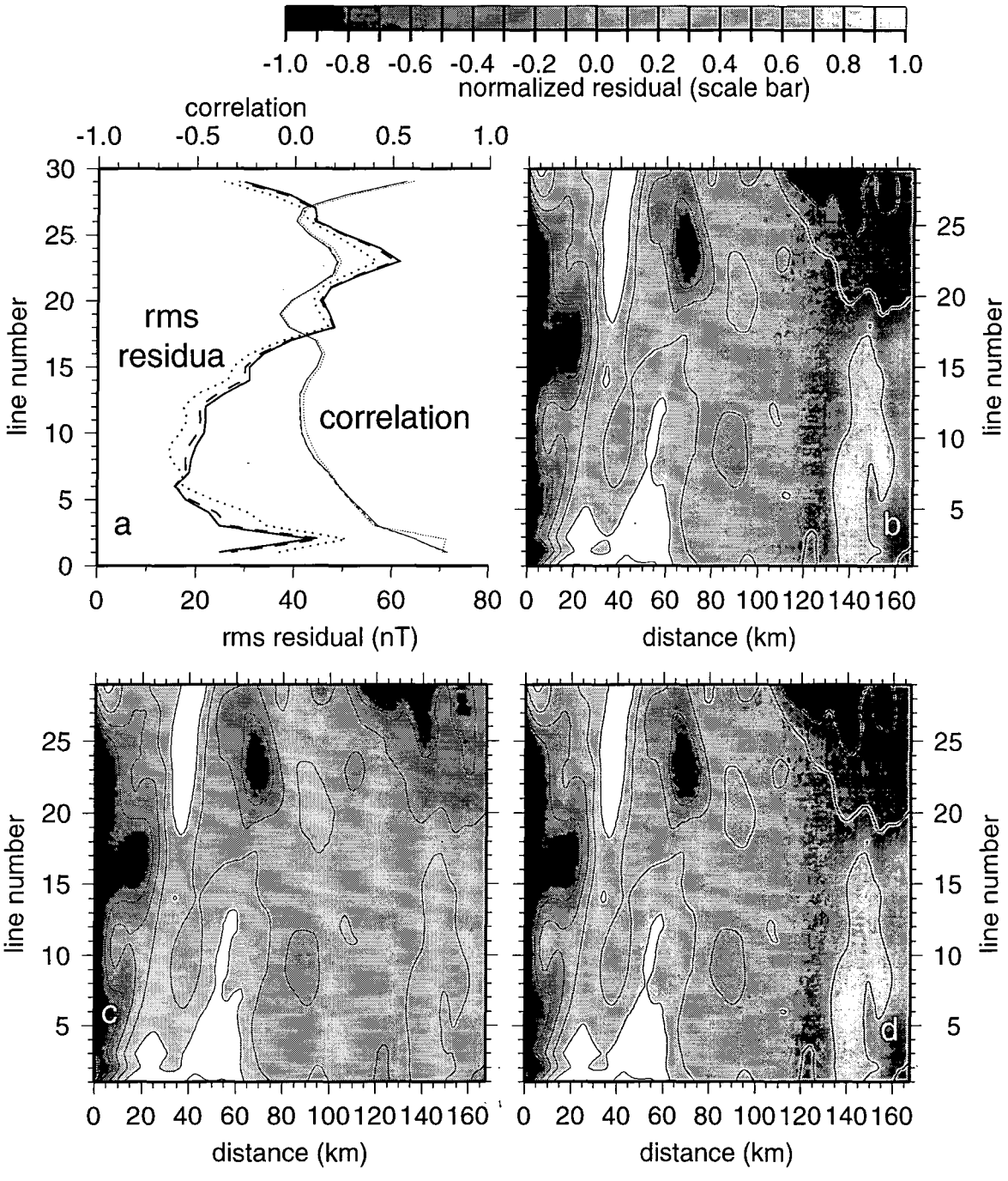

Figure 5.7 (a) Correlation coefficients (thin lines) and rms residua (thick lines) between the observed magnetic field and a forward calculated magnetic field along each of the lines 1-29 of figure 5.6. Each forward calculated field was computed from a model whose upper surface was extracted from the depth to basement chart (Fig. 5.2) along the coincident line. Each model was described by a lower surface at 14 km depth and a magnetization vector defined by Van der Voo (1990; I=46, D=0; solid line), Galdeano et al. (1989; I=58°, D=-43°; dashed line) and an induced magnetization vector (I=57, D=-9).
(b), (c) and (d) Residua (as function of along profile distance) normalized to the minimum rms residual (15 nT) and contoured (interval 0.5) over the region of lines 1-29. Magnetization vector makes little difference to the results; Van der Voo (1990; (b)), Galdeano et al. (1989; (c)) and an induced magnetization vector (d).

(b) To test the correlation of the magnetic anomalies with basement features as a function of wavenumber, and therefore wavelength, the squared coherency (γ^2_{ot}) spectrum between the observed anomaly and the anomaly generated by a model assuming the Van der Voo (1990) magnetization direction for each of the 29 lines was computed. Squared coherency spectra for each profile were contoured and are shown in figure 5.8. For inverse wavelengths in the band <0.2 km^{-1} there is no significant correlation (i.e. $\gamma^2_{ot} < 0.5$) at any wavenumber along any profile, with the exception of a significant correlation (i.e. $\gamma^2_{ot} > 0.5$) at a wavelength of ~15 km along line 12. In general, squared coherency values are less than 0.2, although between lines 11-14 there is a somewhat marked increase in correlation (>0.4) in the band equivalent to wavelengths 12.5 km to 25 km.

Observed magnetic anomalies west of Iberia must therefore be attributed to variations in magnetic basement character other than simply topographic variations of the top of acoustic basement. Nevertheless, the combined effects of basement relief variation with thickness and/or magnetization variations for example, may produce a significantly different anomaly to one created by a simple flat top model with the same lateral thickness and/or magnetization variation (e.g., Parker and Huestis, 1974). Therefore, not only do the results here provide the impetus for further investigation, but also the inclusion of basement relief in source depth or source shape dependant models may be important.

Advantageous to the techniques described above, with the exception of analyses of residua, is the independence of model magnetization intensity. Euler deconvolution utilizes anomaly gradients whilst correlation and coherency tests normalize anomaly amplitudes. Thus, although the methods are only sensitive to changes in the phase of anomalies (whose causal process is a change in model magnetization direction) even realistic variations in magnetization vector direction only reveal a slight link between anomalies observed west of Iberia and the mapped basement surface.

5.3 Depths and trends of magnetic sources

Here I apply spectral and Euler methods to the observed sea surface magnetic field in order to make depth-to-source estimates across the margin. Because the depth to basement (minimum source depth) is typically 5-9 km it is necessary to analyse anomalies on long profiles or over large areas to faithfully represent the broadest wavenumber bandwidth possible. The

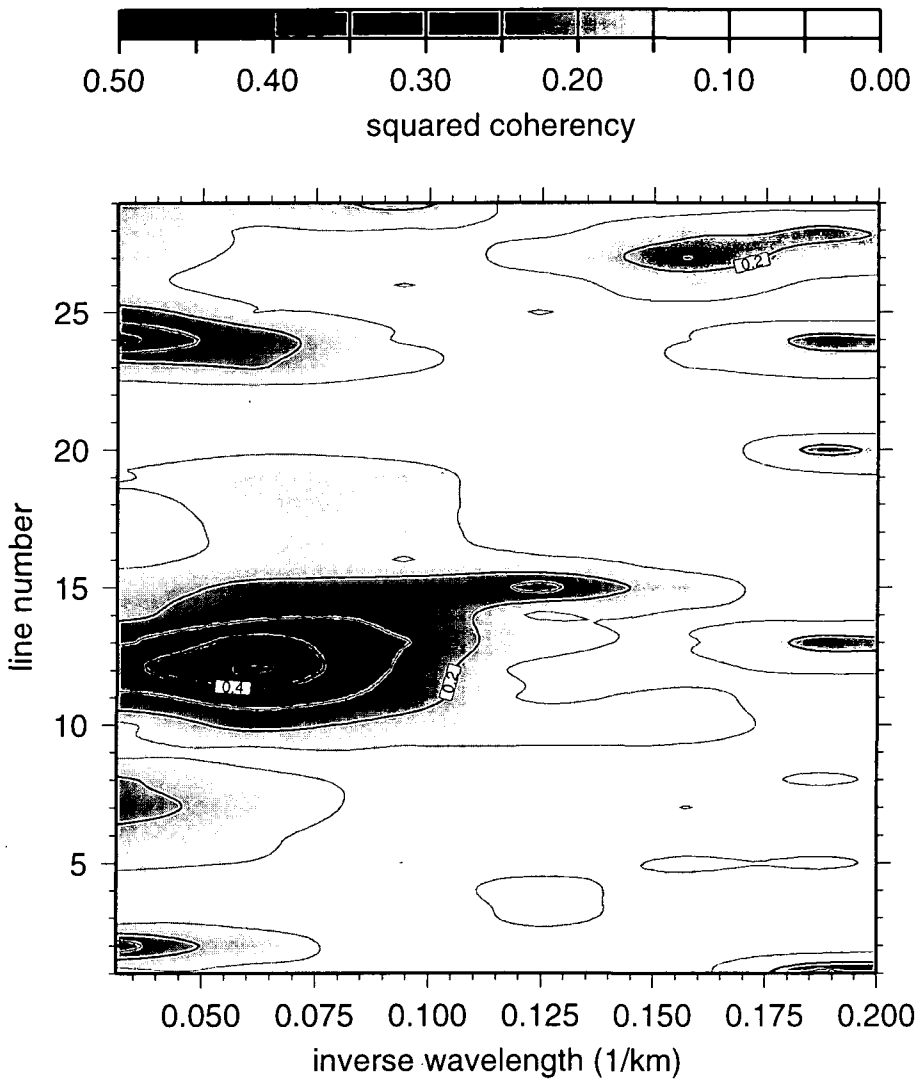

Figure 5.8 Squared coherency between observed and calculated magnetic anomalies along each of the profiles 1-29 of figure 5.6 contoured (0.1 intervals) in line number-inverse wavelength space. Forward calculated anomalies from a model whose magnetization vector is defined by Van der Voo (1990; I=46°, D=0°) and geometry as in figure 5.7. On the whole no significant correlation exists (values<0.5; greys) between observed magnetic field and basement topographic variations at any wavelength on any line, with the exception of 15 km wavelength on line 12 (values>0.5; red).

analysis is therefore divided into three regions based on previous investigation and interpretation of the new charts (section 5.1; Fig. 5.1): (1) east of the most seaward, tilted continental fault block (continental crust); (2) east of peridotite ridges R3 and R4 and west of region (1) (OCT); (3) west of peridotite ridges R3 and R4 (oceanic crust).

5.3.1 Continental crust

Continental crust is almost certainly present in the region 40°N to 41°N, 9°W to 11°W (see Figs. 2.4, 2.5 and 2.7; region S1). A westernmost bound of ~11°W is constrained by the N-S refraction Line 1 of Whitmarsh et al. (1990) and the most seaward tilted continental fault block observed on MCS profiles (Fig. 2.5); the correlation of tilted fault blocks with continental crust is based on P-wave velocity models (R.B. Whitmarsh, pers. comm.) and results of ODP Legs 149 and 173 (Sites 901, 1065, 1069; discussed later). Although the basement chart (Fig. 5.2) does not cover this region, the northern end of profile IAM-8 and profiles IAM-9, LG-12 and LG-14 at their eastern ends do, in part, traverse this region. From these profiles it can be seen that basement is very near to the seabed (within 1 km). Gridded bathymetric data (GEBCO digital atlas) therefore provides a rough constraint on source layer depth. Basement in this region varies dramatically due to the presence of the continental slope; from as deep as ~9 km in the west to ~1 km in the east.

5.3.1.1 Spectral character

The radially averaged power spectrum was estimated and modelled using the three inverse methods presented in sections 4.1.1, 4.1.2 and 4.1.3 (Fig. 5.9). In addition, fitting straight line segments to the observed power spectrum, suggests that three sets of sources exist within this region at depths of 8.4, 3.0 and 0.5 km (Fig. 5.9a). The first apparent change in slope, at an inverse wavelength of ~0.1 km^{-1}, is reasonably striking. In contrast, the second change in slope, at an inverse wavelength of ~0.4 km^{-1}, is less obvious. Moreover, an average depth to source of 0.5 km is impossible; average basement depths, and even seabed depths, are at least 4.8 km deeper. In addition, a change in the character of the spectrum occurs at ~0.4 km^{-1} (Fig. 5.9a); spectral estimates at inverse wavelengths >~ 0.4 km^{-1} exhibit greater scatter than those at inverse wavelengths <~ 0.4 km^{-1}. Comparison with the theoretical spectrum of Figure 4.1 may suggest that the 'crustal' wavenumber band is limited to inverse wavelengths <~0.4 km^{-1}. At higher inverse wavelengths noise begins to dominate the spectrum. The 'crustal', band is broader than those suggested for theoretical examples in Chapter 4, but the result is not surprising since source depths are probably shallower in this region.

Inverse methods, described below, also support the idea that 'crustal' energy occurs at inverse wavelengths <~0.4 km^{-1}. The power spectrum was modelled in an inverse sense by the method of section 4.1.2, first by using the full bandwidth of data (model C1), second by assuming

the 'crustal' signal occurs at inverse wavelengths < 0.4 km^{-1} (model C2), and third by assuming the 'crustal' signal occurs at inverse wavelengths < 0.15 km^{-1} (model C3). Table 5.3 shows the optimum solution parameter triplets ($\ln C_3, h, \gamma$), whilst Figure 5.9b,c,d shows the recomputed spectra for each model. In all three models source depth falls within the likely range of basement depth (~1-9 km).

The success of the method is heavily governed by the bandwidth of the signal. Choosing a narrow band at low wavenumbers in this case (i.e. 0-0.15 km^{-1}; model C3) results in a depth variance, σ_h^2, comparable to the computed depth. It is therefore considered a poor estimate of depth. More favourable is a depth estimate of ~6 km, based on the inversion of data within the 0-0.4 km^{-1} band (model C2), due to its relatively low variance and uncertainty, and the change in character of the spectrum, mentioned above. Model C1 probably models high wavenumber noise in addition to signal; an inverse wavenumber of 0.6 km^{-1} represents a wavelength of 1.7 km, a likely wavelength of noise generated by regridding of magnetic observations.

It has been suggested that a more realistic statistical description of the crustal susceptibility distribution is one in which a long-range dependence exists (Maus and Dimri, 1996 and others; see section 4.1.3). Therefore, the same power spectrum was modelled in an inverse sense via the method of section 4.1.3, for the three bandwidths described by models C1, C2 and C3. Two approaches were taken; one in which the depth is described exactly (models C4, C5 and C6) and one in which the depth is described by a Gaussian probability distribution (models C7, C8 and C9). Table 5.4 shows the optimum parameter triplets ($\ln C_3, h, \gamma$) and quadruplets ($\ln C_3, h, \gamma, \sigma_h^2$) with uncertainties in depth and scaling exponent, for each approach, respectively. Figure 5.9 shows the equivalent forward calculated spectra.

band width (km^{-1})	$\ln C_3$	h (km)	σ_{hinv} (km)	σ_h^2 (km^2)
0-0.6 (C1)	17.39	4.41	0.17	1.43
0-0.39 (C2)	18.55	5.97	0.31	2.60
0-0.1 (C3)	20.26	9.67	1.36	8.26

Table 5.3. Optimum parameter triplets describing the best-fit power spectra from the inversion of the radially averaged power spectrum in three band widths (models C1, C2 and C3) over continental crust. $\ln C_3$=constant; h =mean depth of source; σ_{hinv} =uncertainty in depth estimate; σ_h^2 =variance in source depth.

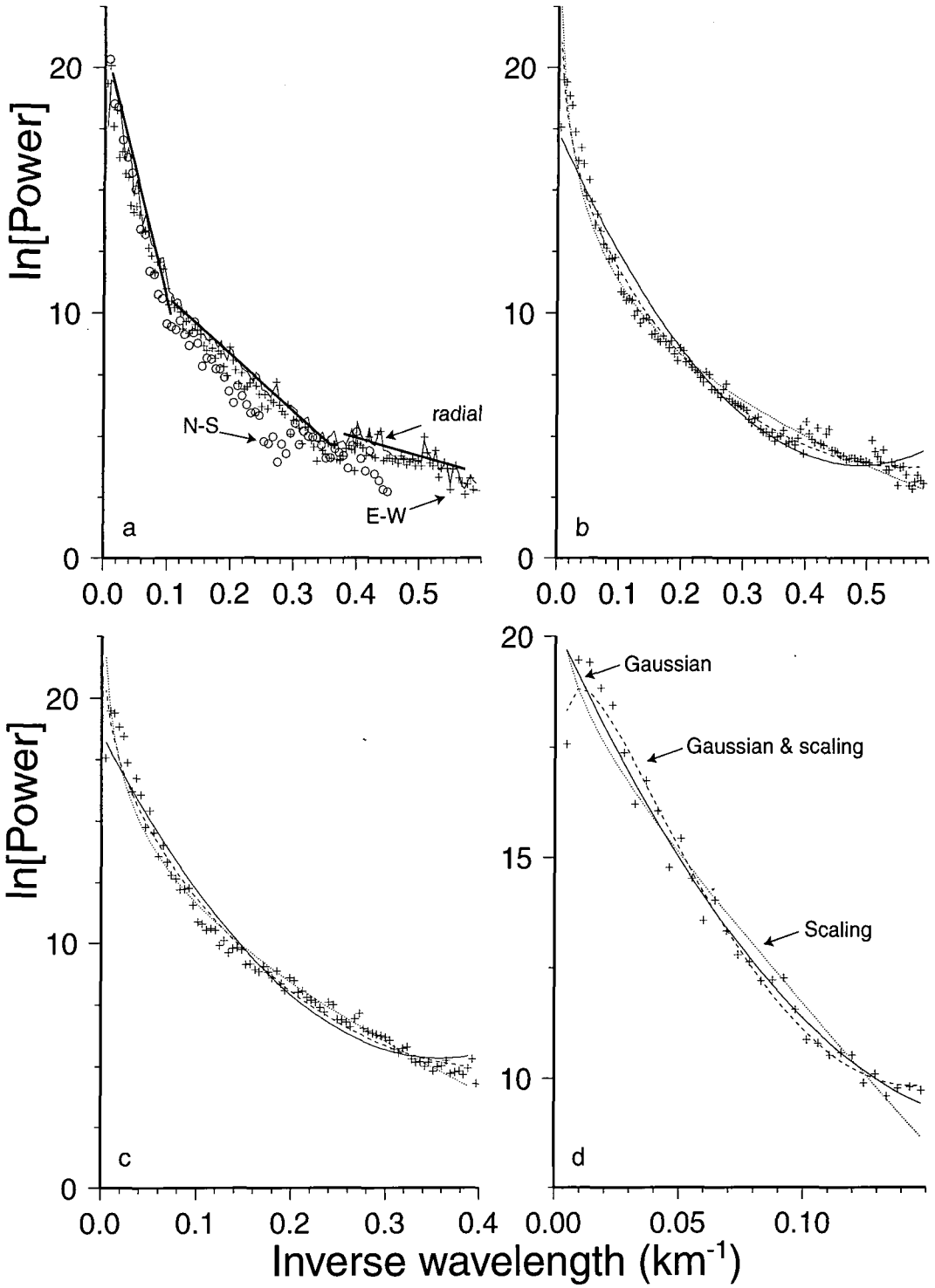

Figure 5.9 (a) Radially averaged (thin line), N-S (circles) and E-W (crosses) power spectra computed from the observed magnetic anomaly in region S1 (40°-41°N, 9°-11°W) over continental crust. Thick lines fitted to segments of the radially averaged power spectrum have slopes proportional to twice the depth of magnetic sources (Spector and Grant; 1970); these depths are 8.4 km, 3.0 km and 0.5 km. (b), (c) and (d) show recalculated spectra from the inversion of the radially averaged power spectrum (crosses) in inverse wavenumber bands of (b) 0-0.6 km^{-1}, (c) 0-0.4 km^{-1}, and (d) and 0-0.15 km^{-1} by the Gaussian method (solid line), scaling method (dotted line) and combined Gaussian and scaling method (dashed line). Optimum parameter triplets and quadruplets are shown in Tables 5.3 and 5.4.

Consider now the trade off between depth estimates and scaling exponents. Two schools of thought exist; one in which the power spectrum contains limited depth information and is dominated by scaling properties (e.g. Maus and Dimri, 1996), and another in which the power spectrum contains source depth information and is not dominated by scaling properties. The latter should predict $\gamma = 0$ and give a measure of the depth to magnetic sources, whereas the former will give a measure of the way in which susceptibility changes over varying length scales, via γ, but provide no, or little, measure of source depth. However, it is conceivable that a continuum exists between these two end members. γ values of 3, 2, 1 and 0 imply scaling properties in 3, 2, 1 and 0 Cartesian dimension(s), respectively, and therefore as the scaling exponent decreases it would seem appropriate that progressively more depth information is contained in the spectrum. Since depth estimates generated from fractal crustal magnetization distributions are always underestimated (e.g. Maus and Dimri, 1996), the measure of depth acts as a minimum bound regardless of the scaling relationship. The smaller the scaling exponent, the better the minimum bound.

As models C4-C9 show, again the optimum inversion parameters are highly dependant on the spectral bandwidth chosen. This may at first seem to be a severe drawback in all the methods, but in fact can provide some useful information. Consider models C4-C6 (Table 5.4). It may be a fair assumption to discount model C4 because it is unlikely that signal is present at such high wavenumbers (equivalent to inverse wavelengths in the band 0.4-0.6 km^{-1}), i.e. noise is being modelled. Models C5 and C6 are therefore considered the result of the inversion of signal. In the bandwidth equivalent to inverse wavelengths < 0.39 km^{-1} (model C5) a scaling exponent of 2.87±0.27 (near 3) suggests that very little depth information resides in the power spectrum. Thus, susceptibility variations on scales of 2.5 km or more are self-similar in three Cartesian dimensions. In contrast, model C6, based on inversion of the spectrum in the band equivalent to inverse wavelengths of 1.5 km^{-1} or less, favours a scaling exponent of 0.83±0.53. Therefore, self similarity of susceptibility on scales of 6.7 km or more is more likely uni-dimensional, and a depth of 4.52 km may provide a good minimum bound. These results necessarily imply that self-similar susceptibility variations are focussed at wavelengths in the band 2.5 to 6.7 km.

The two equivalent models employing a Gaussian depth probability distribution together with a scaling relationship (models C8 and C9) can be assessed in a similar way. However, inversion of the spectrum in the band 0-0.15 km^{-1} results in a negative scaling exponent and an unreasonably large depth estimate with a large variance, and is therefore considered a poor model. A depth derived from model C8, however, compares favourably with that of model C6 (3.54 km with a variance of 1.45 km compared with 4.52 km).

The interpretation of the results from all methods is somewhat subjective; because of the indeterminable nature of the problem the depth chosen is entirely dependant upon other constraints and the interpreters experience and standpoint. If source depth is well constrained, for example seen in outcrop, the third inverse method can provide a measure on γ and the likely probability distribution of the depth parameter (see models C7 and C8; Table 5.4). It is clear that further constraints are required and whichever approach is taken (and I leave the reader to decide) caution is of the essence.

band width (km^{-1})	$\ln C_3$	h (km)	σ_{hinv} (km)	σ_h^2	γ	$\sigma_{\gamma inv}$
0-0.6 (C4)	9.95	0.32	0.09	N/A	3.62	0.21
0-0.39 (C5)	11.54	0.98	0.18	N/A	2.87	0.27
0-0.15 (C6)	16.99	4.52	0.84	N/A	0.83	0.53
0-0.6 (C7)	13.02	2.09	0.39	0.67	2.30	0.35
0-0.39 (C8)	15.02	3.54	0.78	1.45	1.55	0.47
0-0.15 (C9)	26.67	17.12		17.54	4.00	1.04

Table 5.4. Optimum parameter triplets and quadruplets describing the best-fit power spectra from the inversion of the radially averaged power spectrum in three band widths over continental crust. Parameter definitions as Table 5.3 plus γ =scaling exponent; $\sigma_{\gamma inv}$ =uncertainty in γ estimate.

Directional power spectra were also computed (Fig. 5.9a) to investigate the possibility of a dominant trend in anomalies. Within the 'crustal' band, energy from anomalies in N-S and E-W directions is of the same order of magnitude (base *e*) implying that either (a) the sources are lineated but there is no preferred lineation of anomalies in the (*x*-*y*) plane, or (b) the sources are not lineated in the (*x*-*y*) plane but instead are more likely to be approximated by point, or vertically aligned, sources.

5.3.1.2 Euler analysis

3-D Euler deconvolution of the observed magnetic field, using a 5 km square operating window, yielded solutions for structural indices in the range 0.0-3.0 at discrete 0.5 steps. Practical implementation was complicated due to the physical nature of the dataset. The subset of the chart of Miles et al. (1996; Fig 5.1) is gridded at an interval of 0.01° of latitude and longitude which equates to grid intervals, in an equivalent Cartesian system, of 1.11 km and 0.85 km, in

north-south (x) and east-west (y; at 40.5°N) directions, respectively. Because of this Cartesian grid anisotropy, and the requirement of a square window in the 3-D Euler method, the surface was recomputed at 1 km intervals in both x and y directions. Spatial aliasing of short wavelengths in the x-direction was avoided by 'block averaging' whereas false oscillations in the y-direction were suppressed by computation of the harmonic surface using a continuous curvature surface gridding algorithm in full tension (Wessel and Smith, 1991).

The region described above, once translated to a Cartesian coordinate system, covers a grid 169 km by 111 km. Efficient computation of total field gradients by FFT requires a radix-2 number of points. Instead of bordering (padding) the data with mirror-images of itself, or part thereof, the desired regions of real observed field, surrounding the designated study region, were used; 44.5 km both east and west, and 72.5 km both north and south. These data were then smoothed, by application of a space-domain cosine ramp, from the edges of the study region to the edges of the 256 km by 256 km grid in order to nullify the generation of fictitious wavenumbers during FFT. Exactly the same preparation is applied to all 3-D Euler deconvolution problems pertaining to real data (rather than synthetic) in this thesis.

An Euler solution falling within the defined study region was considered acceptable if its depth uncertainty did not exceed 1% of its depth, calculated by least-squares inversion. A statistical analysis was applied to the acceptable solutions (Fig. 5.10) and the interpretation is given in the list below. The second theoretical example of section 4.2.7 acts as a particularly useful comparison and is therefore cross-referenced.

(1) Only one acceptable solution exists for an assumed structural index of 0.0, at a depth of 2.9 km, due to large depth uncertainties. Contrary to the norm, shallower solutions here which are generally associated with low structural indices (SI), have relatively low depth uncertainties than their higher SI counterparts. This anomalous result immediately suggests that sources may be better imaged with higher structural indices.

(2) Kurtosis values are near zero (cf. Fig. 4.9) for all indices except for a large positive anomaly at SI=1.0. Together with a range of no more than ~38 km (for all indices), and no more than 25 km (for realistic indices ≤ 1.5), this result strongly suggests good focussing of solutions on a single depth if $SI \neq 1.0$. The measures of average (mean, median and mode), therefore, potentially contain depth information.

(3) Mean, median and modal depths are greater than 5 km and do not exceed 20 km for all SI. Therefore, under any assumption of source geometry (excluding indices of 0.0 and 1.0 from points (1) and (2) above), the analysis provides a highly probable depth window for the generation of magnetic anomalies within continental crust. This has implication for the results of

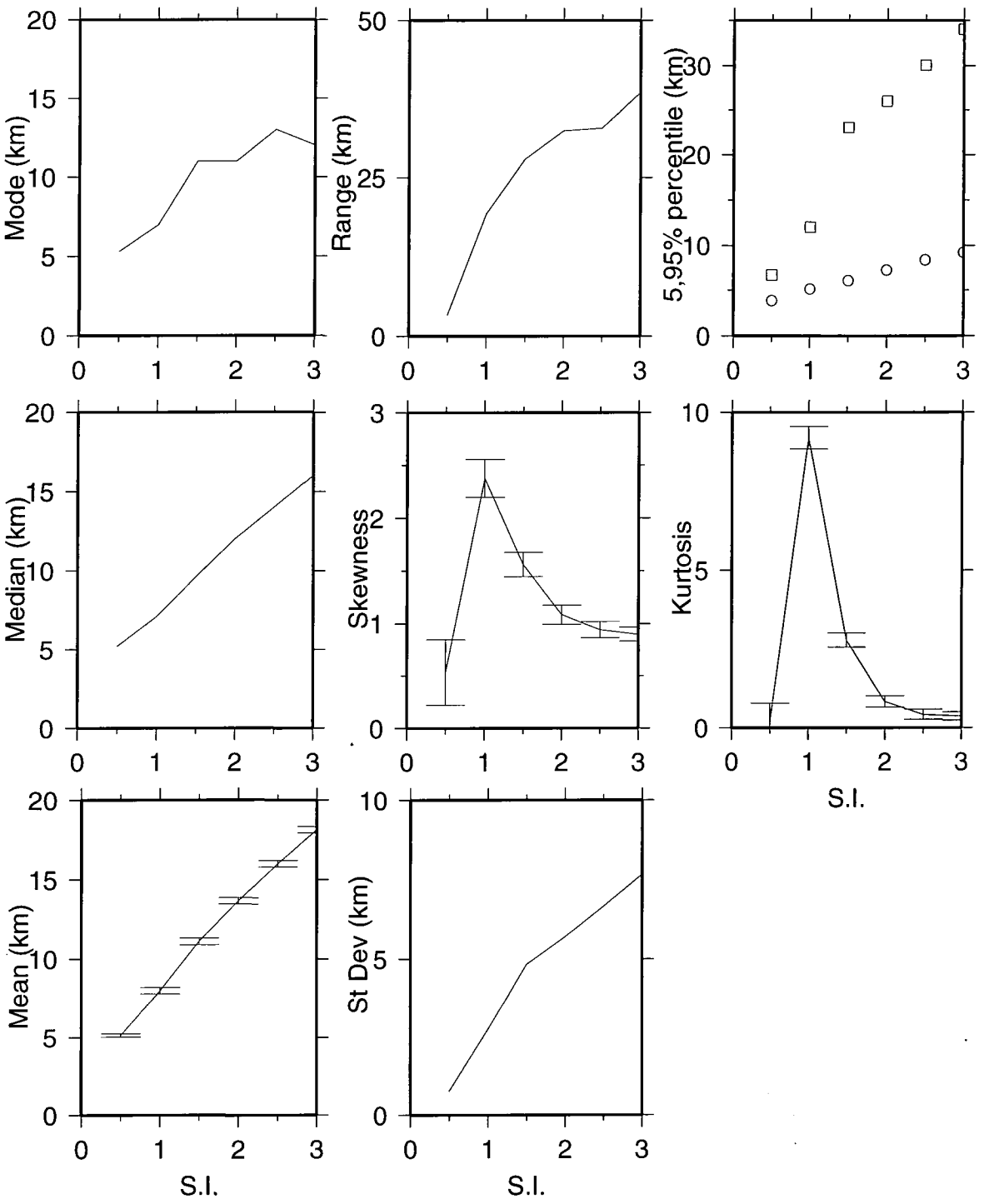

Figure 5.10 Results of a statistical analysis of source solutions derived from the 3-D Euler deconvolution of the observed magnetic field in the region 40°-41°N, 9°-11°W over continental crust. Statistics are computed from all acceptable solutions (depth uncertainty < 1% of calculated depth) derived from the deconvolution using structural indices (S.I.) of 0.5-3.0 at discrete 0.5 steps. Only one solution for S.I.=0.0 was found (depth=2.9 km). Error bars shown on mean, skewness and kurtosis plots. See text for discussion.

spectral analyses of section 5.3.1.1.

(4) A relatively high positive skewness and an extremely high positive kurtosis at SI=1.0, flanked by decreasing values at higher and lower indices, implies that two significant populations of solutions exist. Observation of the histograms, and a measure of the standard deviations, suggest source depths of 7±2.5 km and 12±2.5 km for a structural index of 1.0 (Fig. 5.11).

(5) Significant discontinuities in skewness and kurtosis, and standard deviation, mode and range

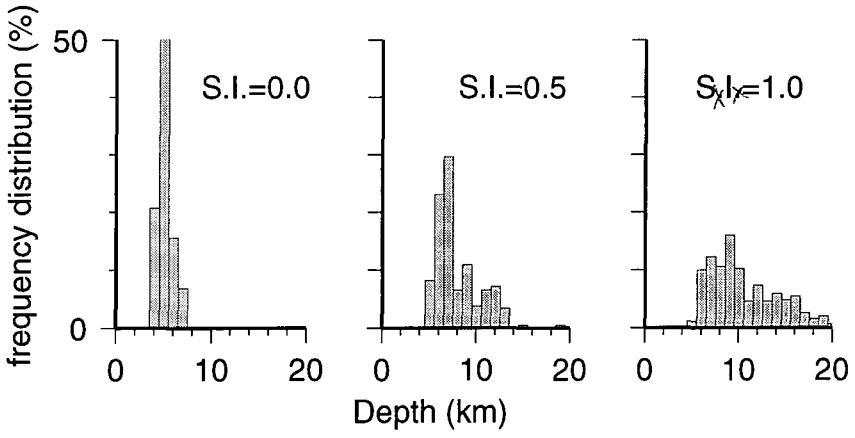

Figure 5.11 Euler deconvolution solution distributions for structural indices (S.I.) of 0.0, 0.5 and 1.0 over the region of continental crust (see Fig. 5.10).

may suggest the most desirable structural index is given by 1.0 or 1.5, respectively.

In summary, the analysis of the magnetic field, by spectral and Euler methods (the method is indicated in the square parentheses) in the region 40°N to 41°N, 9°W to 11°W, has contributed to the understanding of the nature of magnetic sources within (or beneath) thinned continental crust such that they;

(1) are either (a) lineated with no preferred orientation or (b) not lineated but instead are point, or vertically aligned, sources [analysis of power spectra];

(2) are either (a) distributed 5-38 km in depth for any type of source geometry, or (b) more likely, from (b) in (1) above, represented on the whole, by vertically aligned structures, possibly dykes, at depths of ~7.5 km on average, with ~±2.5 km of spread [Euler deconvolution];

(3) have magnetization distributions (described by field scaling exponents, γ of ~2) which may suggest that variations occur in only two dimensions, consistent with (1) and (2) above [analysis of power spectra].

If all possible scenarios are considered, magnetic sources may be interpreted to be (a) a uniformly magnetized continental crust, and (b) dyke-like intrusions within or at the base of thinned continental crust.

5.3.2 The ocean-continent transition zone (OCT) and its bounds

The region defined as OCT is analysed here in the same manner as was continental crust in section 5.3.1. The eastern and western bounds of the OCT, based on previous work, and its definition, were presented in Chapter 2. Although the inductivist's view of making no preconceived notions should be applied to this study, practical implementation requires bounds upon the region inferred to be OCT. Smaller scale features and anomalous zones within the OCT are considered in Chapter 6.

Regions S2 and S3 (Fig. 2.7), described by 40°N to 41°N, 11°W to 13°W and 39.5°N to 40.5°N, 11°W to 12°W, are used for Euler and spectral analyses, respectively. Region S2 is equivalent to the area of the basement chart (Fig. 5.2) and so is the preferred region for analysis; magnetic source depths are constrained. However, because region S2 contains slivers of continental and oceanic basement, as well as basement of unknown character (which is the target of the analyses), region S3, which can be assumed to be exclusively within the OCT, is used for spectral analyses; Euler deconvolution solutions within the OCT section of region S2 can be isolated whereas power spectral analyses cannot.

5.3.2.1 Spectral character

Power spectra in E-W, N-S and radial directions were estimated in region S3 (Fig. 2.7) and modelled in exactly the same manner as in section 5.3.1.1. Fitting straight line segments to the radially averaged power spectrum resulted in source depth estimates of 6.2 km and 2.0 km (Fig. 5.12a). The results of inversion of the spectrum are shown in Table 5.5.

As with models C1-C9, a similar problem associated with defining the correct assumptions in, and therefore utilizing, the correct inverse method, is present here. Based on the arguments of section 5.3.1.1, the interpretation of results of Table 5.5 as a whole suggest either: (a) the average source depth is ~5.5 km with a variance no greater than ~2.5 km^2 and a depth error of ~±1 km (models T1, T2, T3, T7 and T8), or (b) no depth information is contained in the power spectrum but instead a scaling exponent of ~2 or zero describes the self-similarity in the

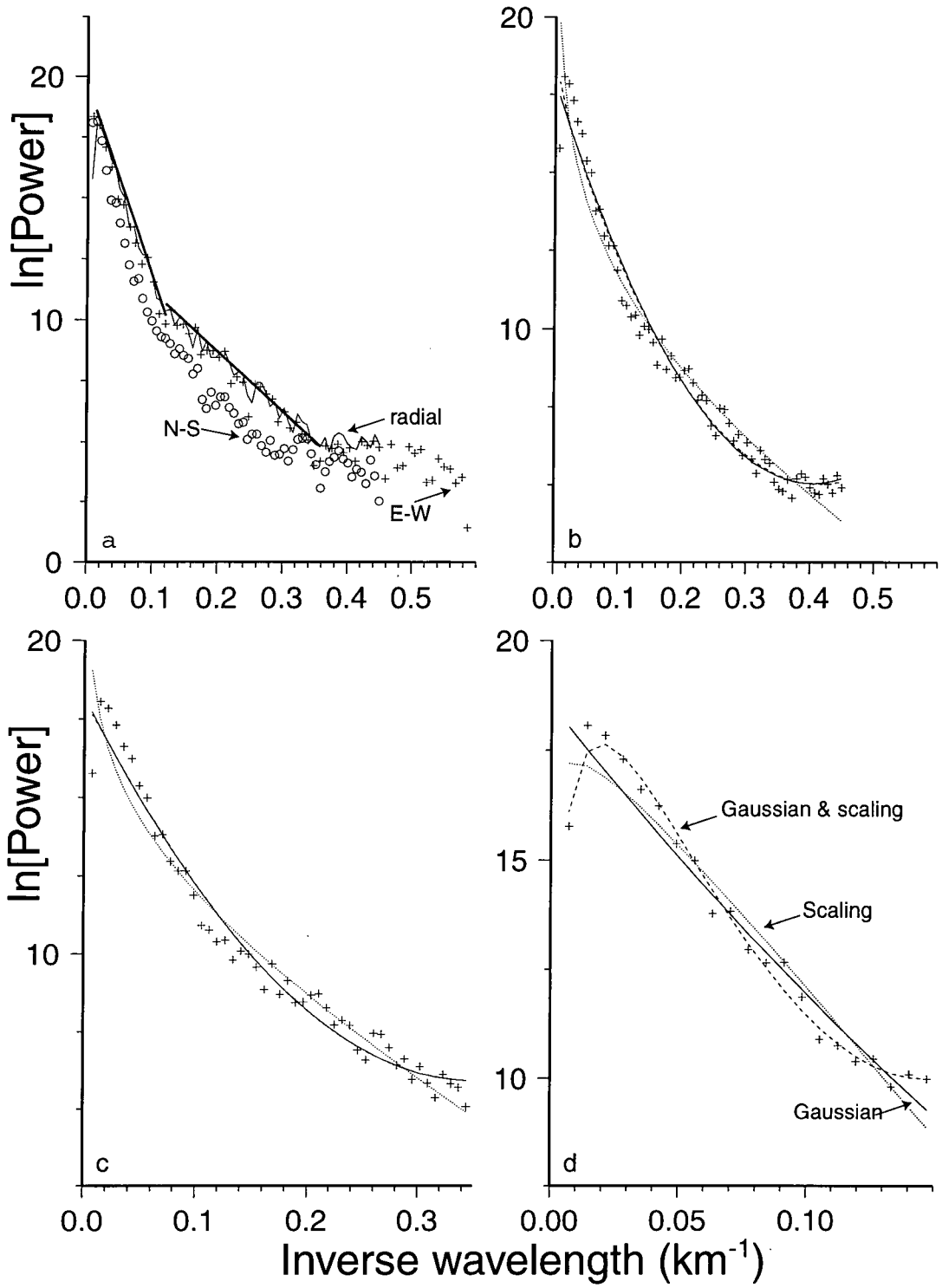

Figure 5.12 (a) Radially averaged (thin line), N-S (circles) and E-W (crosses) power spectra computed from the observed magnetic anomaly chart in region S3 (39.5°-40.5°N, 11°-12°W) in the OCT. Thick lines fitted to segments of the radially averaged power spectrum have slopes proportional to twice the depth of magnetic sources (Spector and Grant; 1970); these depths are 6.2 km and 2.0 km. (b), (c) and (d) show recalculted spectra from the inversion of the radially averaged power spectrum (crosses) in inverse wavenumber bands of (b) 0-0.6 km^{-1}, (c), 0-0.4 km^{-1} and (d) and 0-0.15 km^{-1} by the Gaussian method (solid line), scaling method (dotted line) and combined Gaussian and scaling method (dashed line). Optimum parameter triplets and quadruplets are shown in Table 5.5.

'crustal' band (models T5 and T8, respectively).

Prevention against the 'contamination' of spectra by signals from other types of geological source reinforces the philosophy that some preconceived notions are important when modelling power spectra. If instead, the region under analysis was chosen to be 11°W to 12.5°W, i.e. only 42 km wider, and with identical latitude variation (region S3B), a remarkable, but troublesome outcome results. This region was first analysed to try to account for the most westward part of the assumed OCT (directly adjacent to and east of R3; see Fig. 5.2)

band width (km^{-1})	$\ln C_3$	h (km)	σ_{hinv} (km)	σ_h^2	γ	$\sigma_{\gamma inv}$
0-0.6 (T1)	17.88	5.04	0.31	1.98	N/A	N/A
0-0.35 (T2)	18.20	5.56	0.47	2.52	N/A	N/A
0-0.15 (T3)	18.53	5.79	1.71	1.70	N/A	N/A
0-0.6 (T4)	11.52	0.87	0.18	N/A	2.68	0.33
0-0.35 (T5)	12.96	1.51	0.27	N/A	1.99	0.39
0-0.15 (T6)	19.78	5.88	1.11	N/A	-0.66	0.74
0-0.6 (T7)	17.02	4.53	0.80	1.77	0.41	0.58
0-0.35 (T8)	18.41	5.71	1.25	2.60	-0.09	0.72
0-0.15 (T9)	31.75	20.71	5.57	19.73	-4.44	1.59

Table 5.5. Optimum parameter triplets and quadruplets describing the best-fit power spectra from the inversion of the radially averaged power spectrum in three band widths in the ocean-continent transition zone (region S3). Parameter definitions as Table 5.4.

Computation of the radial and directional power spectra resulted in an almost identical match between the E-W spectrum and the radially averaged spectrum (Fig. 5.13a). In contrast, the N-S spectrum contains ~4 orders of magnitude (base *e*) less energy than its E-W and radial counterparts. Anomalies of significant amplitude therefore have a preferred lineation in a N-S direction. More specifically, because power is a measure of the square of anomaly amplitudes, it is deduced that E-W amplitude variations are ~7 times that of N-S amplitude variations (cf. continental crust). At first sight, these results quantitatively reinforcement the hypothesis that the OCT exhibits approximately N-S trending linear anomalies (Whitmarsh and Miles, 1995; see their Fig. 2b and Fig. 2.8 here).

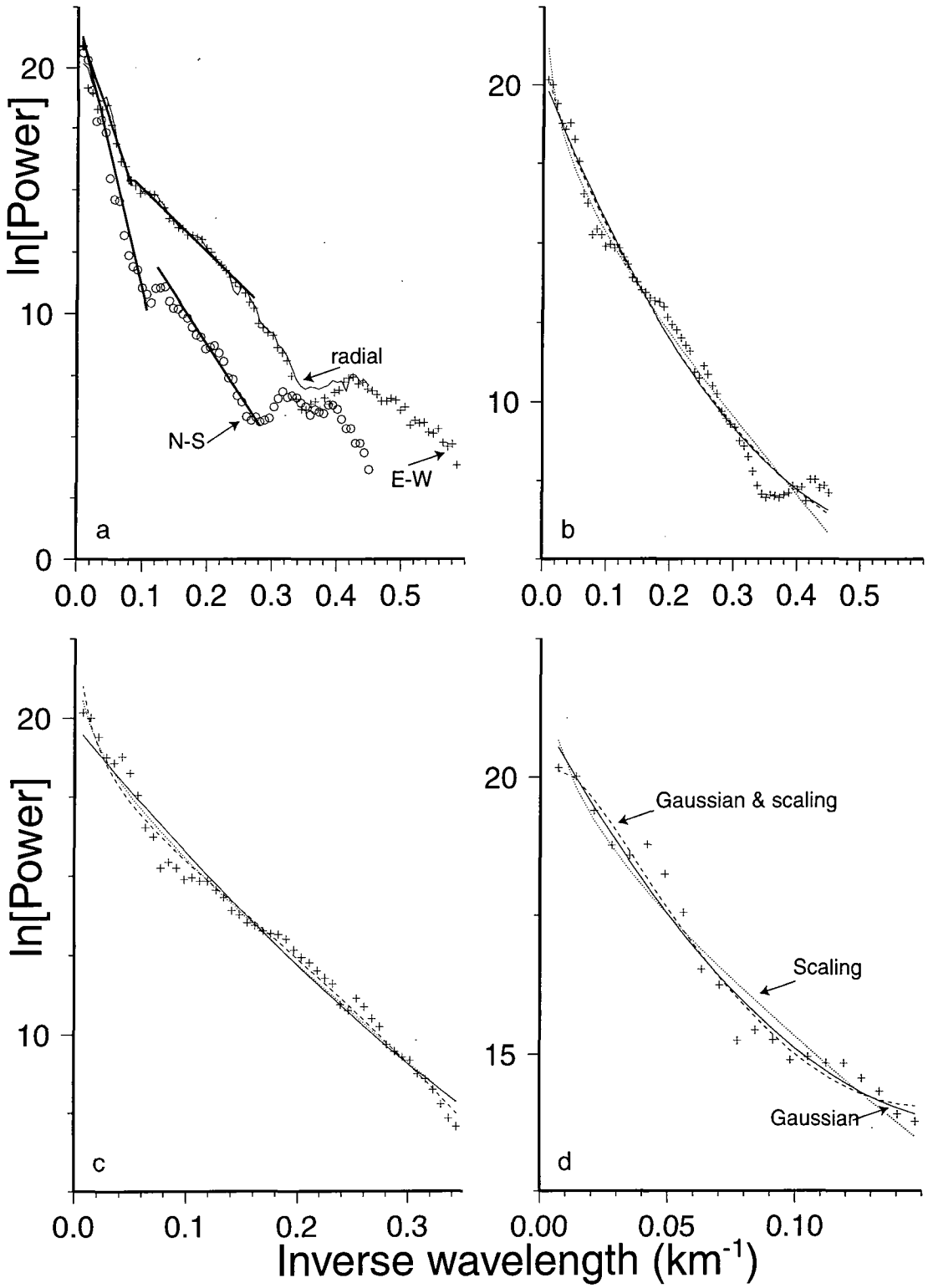

Figure 5.13 (a) Radially averaged (thin line), N-S (circles) and E-W (crosses) power spectra computed from the observed magnetic anomaly in region S3B (39.5°-40.5°N, 11°-12.5°W) in the OCT, including Tore seamount.Thick lines fitted to segments of the radially averaged or E-W power spectrum indicate sources are at 6.4 and 2.0 km depth whereas the same proceedure applied to the N-S power spectrum indicates depths of 8.6 and 3.2 km. The lower relative power in the N-S spectra and increased depth estimates suggests that anomalies show a preferred orientation in the N-S direction. (b), (c) and (d) as in Fig. 5.9 with optimum parameter triplets and quadruplets shown in Table 5.5.

Fitting straight line segments to the radially averaged spectrum in the crustal band (inverse wavelengths < 0.35 km^{-1}), in the style of Spector and Grant (1970) provides depths of 5.5 km and 2.5 km, the latter of which is impossible. Two distinct sources are defined by slopes either side of ~0.1 km^{-1} in the radial and E-W spectra and either side of ~0.125 km^{-1} in the N-S spectrum. However, proportionately more power in the lower wavenumber components of the N-S spectrum implies a greater depth of the source; in effect the method will overestimate source depths for directional spectral components deviating significantly from the normal to the trend of anomalies. This has particular significance for the analysis of spectra along profiles. Inversion of the radial spectrum, via the three methods of section 4.1, was also carried out; optimum parameter triplets and quadruplets are shown in Table 5.6.

band width (km^{-1})	$\ln C_3$	h (km)	σ_{hinv} (km)	σ_h^2	γ	$\sigma_{\gamma inv}$
0-0.45 (T10)	20.13	3.91	0.31	1.07	N/A	N/A
0-0.35 (T11)	19.76	3.38	0.45	0.59	N/A	N/A
0-0.15 (T12)	21.12	6.63	1.71	5.92	N/A	N/A
0-0.45 (T13)	16.62	1.63	0.18	N/A	1.51	0.33
0-0.35 (T14)	17.77	2.13	0.27	N/A	0.95	0.39
0-0.15 (T15)	18.02	2.49	1.11	N/A	0.92	0.74
0-0.45 (T16)	19.22	3.36	0.80	0.84	0.43	0.58
0-0.35 (T17)	16.01	0.77	1.25	-0.84	1.62	0.72
0-0.15 (T17)	24.01	9.92	5.57	9.88	-0.98	1.58

Table 5.6 Optimum parameter triplets and quadruplets describing the best-fit power spectra from the inversion of the radially averaged power spectrum in three bandwidths in the ocean-continent transition zone (region S3B). Parameter definitions as Table 5.4.

Basement depths in region S3B are only partially constrained by the basement chart of Figure 5.2. In approximately the northern half of the region (40°N to 40.5°N) basement depth is constrained and is on average 8 km below sea surface. In the southern half (39.5°N to 40°N) there is no control. It would therefore seem that all spectral methods produce gross depth underestimation. However, close examination of the bathymetric chart (Fig. 5.1a) reveals the presence of Tore seamount (39.5°N, 13°W) which in places is only 3 km below sea surface. Consequently, the crustal band of the power spectrum is likely to be broader; models T1, T2, T5 and T6 of Table 5.6 may represent good estimates of the optimum inversion parameters. The top of Tore Seamount is implied to be the magnetic source dominating the spectrum at all wavenumbers; the power spectrum is 2-3 [base e] orders of magnitude greater for all

wavenumbers in the crustal band, compared with the spectrum of the region S3. This translates as a 2.7-4.5 times magnetic anomaly amplitude increase, which is in fact the case (Fig. 5.1b). In addition, a 2-D scaling exponent (γ_{2D}) of 0.43 is highly anomalous for expected susceptibility distributions (see section 4.1); either the susceptibility distribution is anisotropic or does not follow a constant scaling law.

5.3.2.2 Euler analysis

3-D Euler deconvolution of the observed magnetic field anomaly in region S2 (Fig. 2.7) was implemented in exactly the same manner as above in the continental domain. Solution distributions are shown in Figure 5.14 whilst the results of a full statistical analysis are shown in Figure 5.15. Unlike the statistics derived from the deconvolution of the observed field over continental crust, the statistics here are incredibly uniform over all SI; modal estimates provide the only indication of a preferred SI due to the discontinuity between indices of 0.5 and 1.0 (Fig. 5.15). At higher indices modal depths flatten out to 11.5±1.5 km. Little skew and kurtosis is observed and a depth function based on the mean and median is given approximately by

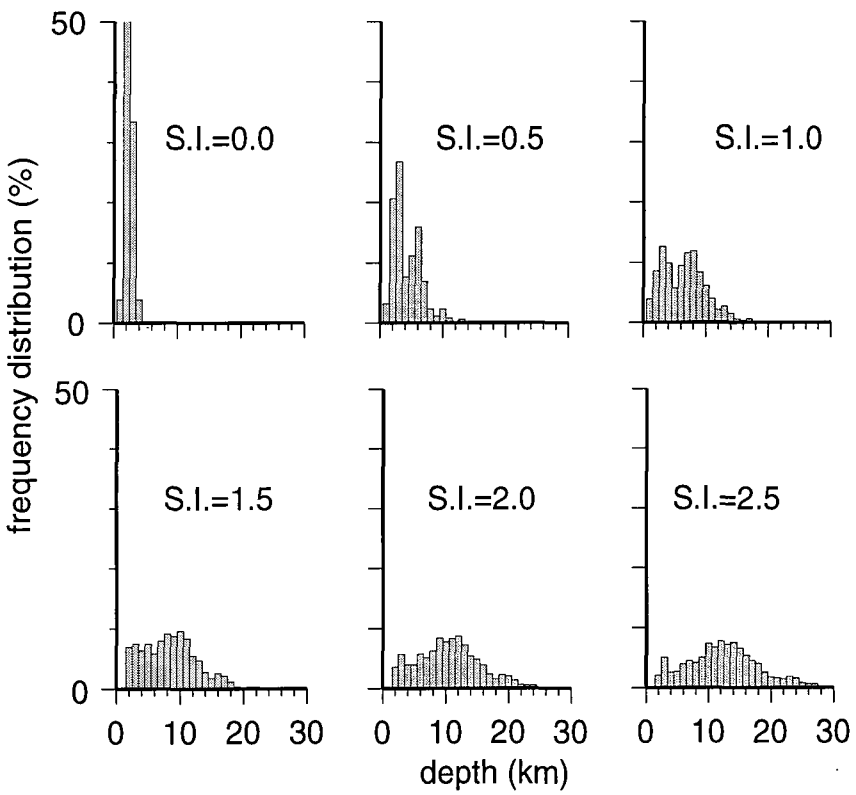

Figure 5.14 Distributions of Euler solutions for structural indices (SI) of 0.0-2.5 resulting from the deconvolution of the field over the ocean-continent transition in region S2 (40°-41°N, 13°-11°W).

$(4.2 \times SI) + 2.5$ km. Similar linear functions can be derived for maximum range and standard deviation. At first sight there is no indication of a preferred structural index, and no means of choosing a more probable source depth.

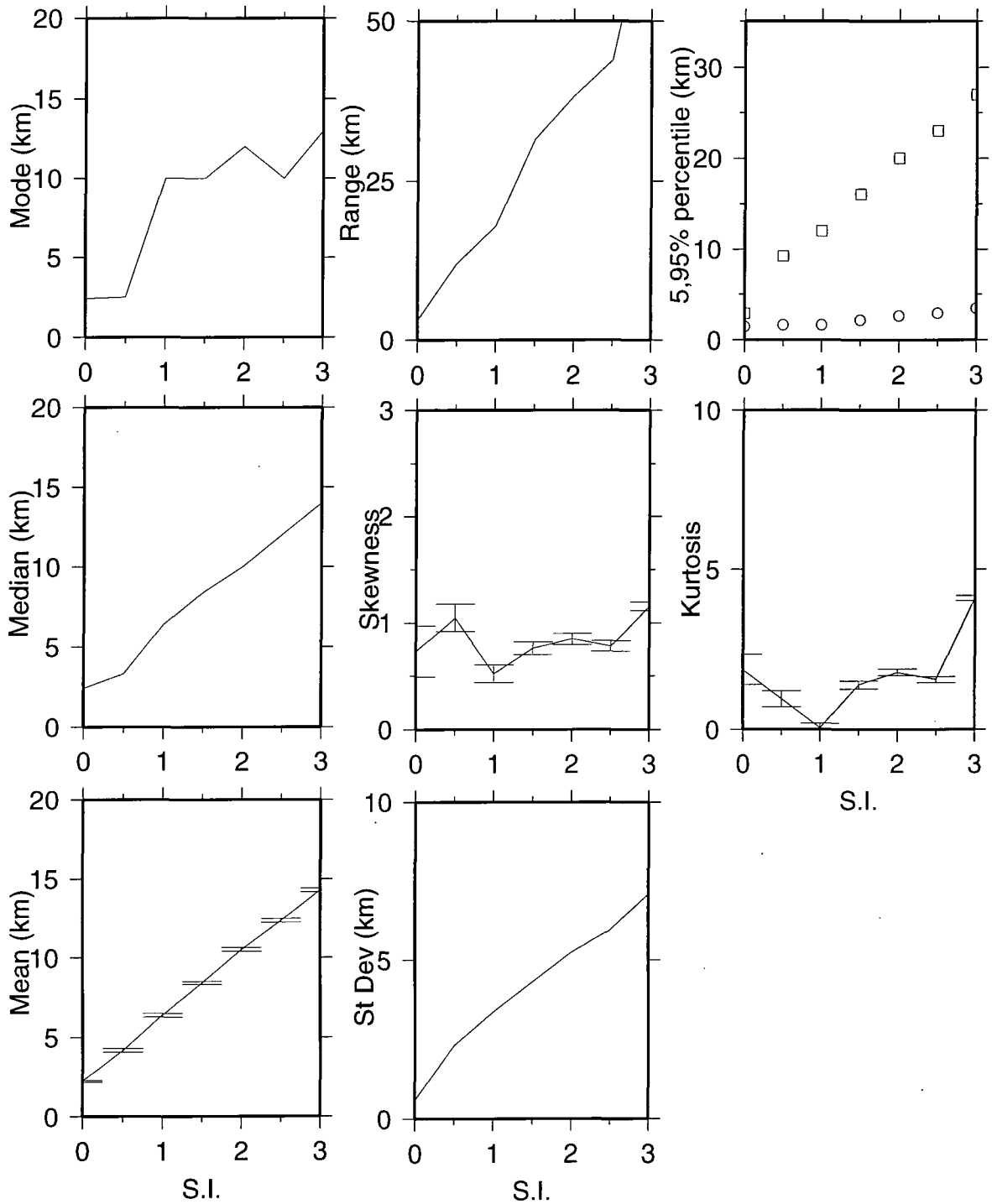

Figure 5.15 Results of a statistical analysis of source solutions derived from the 3-D Euler deconvolution of the observed magnetic field in region S2 (40°-41°N, 11°-13°W) within the OCT. Statistics are computed from all acceptable solutions (depth uncertainty < 1% of calculated depth) derived from the deconvolution using structural indices (S.I.) of 0.0-3.0 at discrete 0.5 steps. Error bars shown on mean, skewness and kurtosis plots. See text for discussion.

The four zones (A, B, C and D) defined by the character of basement topography and magnetic anomalies (after reduction to the pole) provide a means of zoning solutions based on their (x,y) position. Zoning is essentially a means of analyzing small groups of anomalies; the partitioning of analyses into section 5.3.1.2, section 5.4.1.2 and the present section is a coarse zoning.

Before presenting the results, it is worth noting that of all the solutions regarded as acceptable, based on having depth uncertainties less than 1% of their calculated depth, also exhibit small horizontal uncertainties that rarely exceed 0.5 km (Fig. 5.16). However, this measure is independent of the relocation of solutions due to non-linearity caused by the interference of adjacent sources (see section 4.2.6).

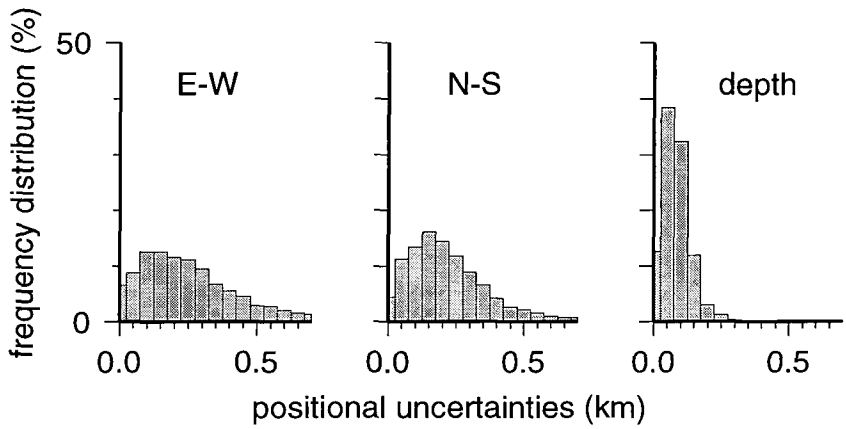

Figure 5.16 Distributions of positional uncertainties of Euler solutions of Fig. 5.15 in E-W and N-S directions and with depth. Uncertainties in depth are typically less than 0.25 km due to the acceptance level criterion. Horizontal uncertainties are typically less than 0.5 km.

After classification of Euler solutions into zones A, B, C and D, strong contrasts between the sets of depth distribution histograms of each of the four zones are apparent (Fig. 5.17):

Zone A. (Oceanic crust) Of all the four zones, the source depth distributions for all SI of zone A best approximate a normal distribution, especially when described by structural indices of 2.5 or 3.0. At index values of 1.0, 1.5 or 2.0 the distribution has a slight positive skewness and kurtosis that both reduce with increase in SI. Indices of 0.0 and 0.5 produce narrow distributions. Based on the assumption that zone A is composed entirely of oceanic crust, and the average depth to top basement is ~7 km (Fig. 5.2), the distribution of solutions in Figure 5.17a suggest a most probable structural index of 1.0 (because (a) the solution distribution for SI=1.0 is the least skewed, and (b) the average solution depth coincides with the top of acoustic basement). This

result and the existence of only one population of solutions supports the model that the main source of oceanic crustal anomalies originates within sill-, dyke-, or lavaflow-like bodies near to the top of the crust.

Zone B. The distribution of solutions in zone B are similar for all SI to those in zone A with one important exception; a second population of solutions is present ~5 km deeper than the first population for indices of 0.5 or more. Absolute depths are dependant upon the choice of SI; an index of 1.0, for example, places the average depth of shallower solutions at ~7 km, i.e., at the top of basement. The average depth of deeper solutions is at ~13 km. An SI=1.0 is chosen since lower SI values result in the shallow solutions which overlay the top of basement.

Zone C. This region of the ocean-continent transition zone is different from that of zone B in terms of solution depths, as well as basement topographic character and the qualitative nature of the observed magnetic field. No solutions for SI=0.0 were encountered in zone C and average solution depths were in general deeper than those encountered in zones B and C. For a SI=1.0 the most probable solution depth cluster lies at ~10 km, whilst an index of 1.5 indicates solutions at depths of ~13 km. At still higher indices solution depths cluster into two populations ~6 km apart; this may be representative of two overlapping solution populations which are not discernible at SI<2. If source geometry is assumed to be described by a combination of SI source depths may be present up to 6 km below the top of basement.

Zone D. With distributions vastly different from those of the three previous zones, zone D is characterized by a large bias towards shallow solutions (<4 km) even at high structural indices. Nevertheless, there is no other preferred solution depth; the solution distribution is broad and near rectangular for indices of 2.5 and 3.0. The interpretation here is that the main source of magnetic anomalies occurs in the range 1-3 km although other sources as deep as ~15 km may exist.

In summary, the nature of magnetic sources in the OCT have been constrained by spectral and Euler analyses and shown to be,

(1) lineated in a preferred N-S direction; resultant magnetic anomaly amplitude variations are ~7 times greater when observed E-W compared to when observed N-S (E-W fluctuations are greater than N-S fluctuations indicating N-S alignment of anomalies) [power spectral method];

(2) by the power spectral method, unresolved in depth because the power spectrum contains source scaling information at the expense of depth information (underestimated average source depths of ~5.6 km overlay top basement depths); a γ estimates of ~2 (models T5; Table 5.5) suggests magnetization variations occur in two Cartesian directions [power spectral method];

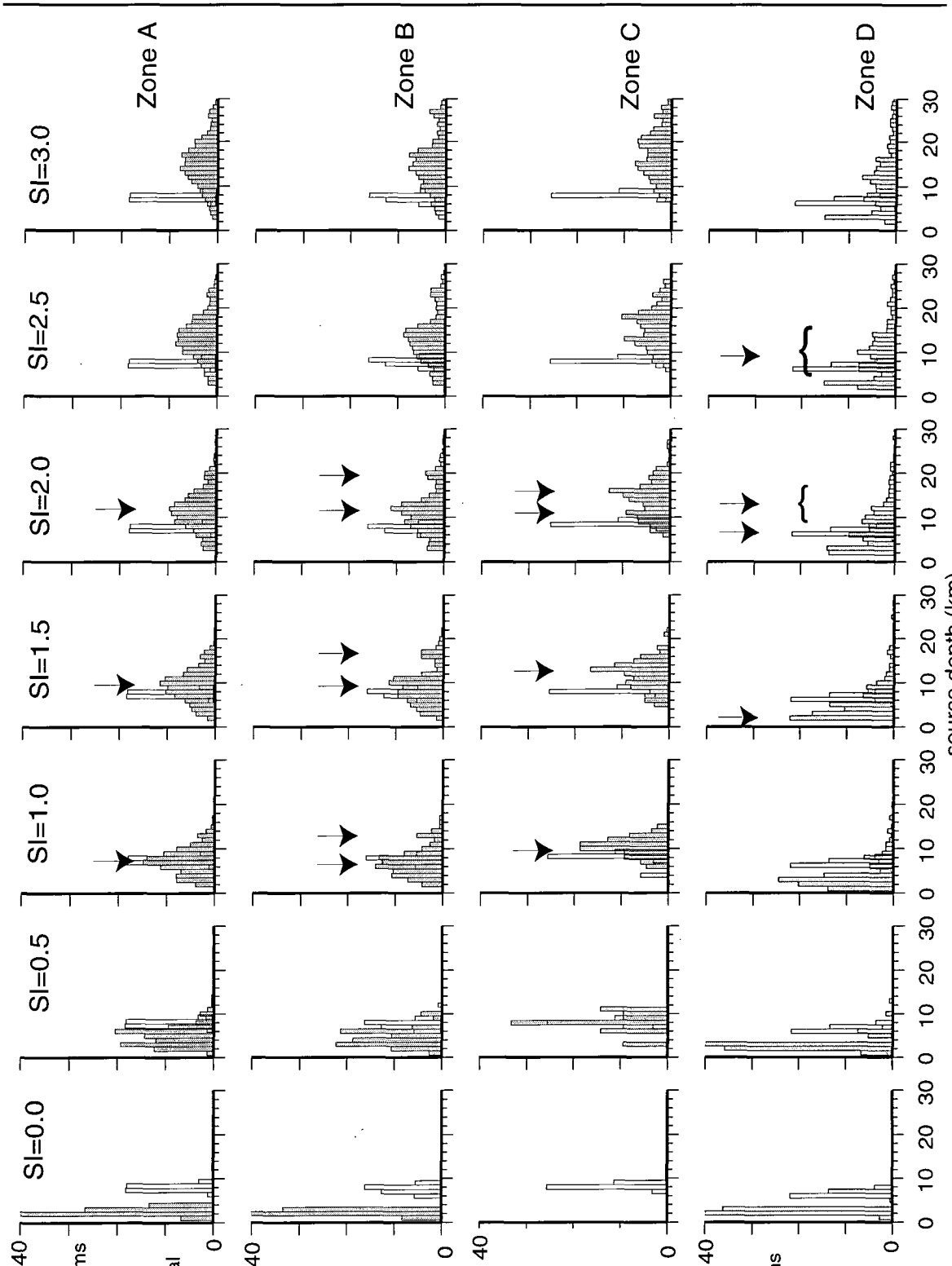

Figure 5.17 Matrix of Histograms of Euler solution distributions (shaded bars) and basement depth distributions (open bars; Note, ordinate tick mark interval is 25 %) in zones A-D (see text) as a function of SI. Frequency distributions are given as percentage of total number of solutions in the given zone and for the given SI. Arrows mark potential candidates for source clusters, whilst parentheses indicate a broad distribution in depth. Zone A is characterized by a symetrical distribution of source depths centred on 7 km for a SI=1.0. Zone B is clearly defined by two populations of sources ~5 km apart although absolute depths vary depending on SI. The character of zone C falls midway between zones A and B; a single source cluster at ~10 km depth splits into two populations with increasing SI. Solutions in zone D are heavily biased to shallow depths (<5 km) although the distribution has a large positive tail.

(3) different, in terms of depth, in zones B and C (see Fig. 5.2); beneath top basement in zone B (between peridotite ridges R3 and R4) magnetic sources are present at distinct depths of ~7 km (top basement) and ~13 km (~6 km beneath top basement), whereas in zone C, sources are present at ~10 km depth (~ 2 km below top basement) and represented by dyke-, sill- or lavaflow-like source geometries (SI=1.0). A deeper set of sources may be present in zone C at ~16 km (~8 km below top basement) which are represented by a vertical pipe geometry (SI=2.0). The shape of the solution distribution of zone A (oceanic crust) resembles that of zone B more so than that of zone C suggesting that solutions beneath the western part of the OCT are more akin to those of oceanic crust.

The significance of these results is discussed in Chapter 6.

5.3.3 Oceanic crust

Oceanic crust immediately adjacent to the ocean-continent transition was discussed in the previous section (zone A); from analysis of Euler solutions the depths of sources are different from those of the OCT (zones B and C) and continental crust (zone D). However, to better understand the nature of the oceanic crust immediately adjacent to the OCT a comparison with two adjacent regions of 'normal' slow-spreading oceanic crust was made. Firstly, region S4 (Fig. 2.7) whose crustal age is in the early anomaly 1-34 sequence, and secondly region S5 within the Cretaceous Magnetic Quiet Zone (crust formed in the Cretaceous Normal Polarity Chron, C34(N)) were used for spectral and Euler analyses.

5.3.3.1 Anomaly 1-34 sequence

An analysis of the radially averaged power spectrum yielded depth estimates of 8.3 km and 1.5 km by the Spector and Grant (1970) method (Fig. 5.18), and optimum parameter triplets and quadruplets from inversion of the spectrum as shown in Table 5.7.

The depth to oceanic crust ~75 Ma old is estimated (from simple isostatic calculations) to be within a likely range of ~5-7 km, depending on the density of overlying sediments and the degree of topographic variation. Therefore, although no model derived from the inversion of the power spectrum within a sensible bandwidth provides an adequate estimate of the source depth, models A2, A6 and A8 are the most likely candidates. A scaling exponent of near zero derived from model A8 suggests that oceanic crustal magnetization exhibits no scaling relationship between wavenumber components. This result is not surprising since magnetization models of

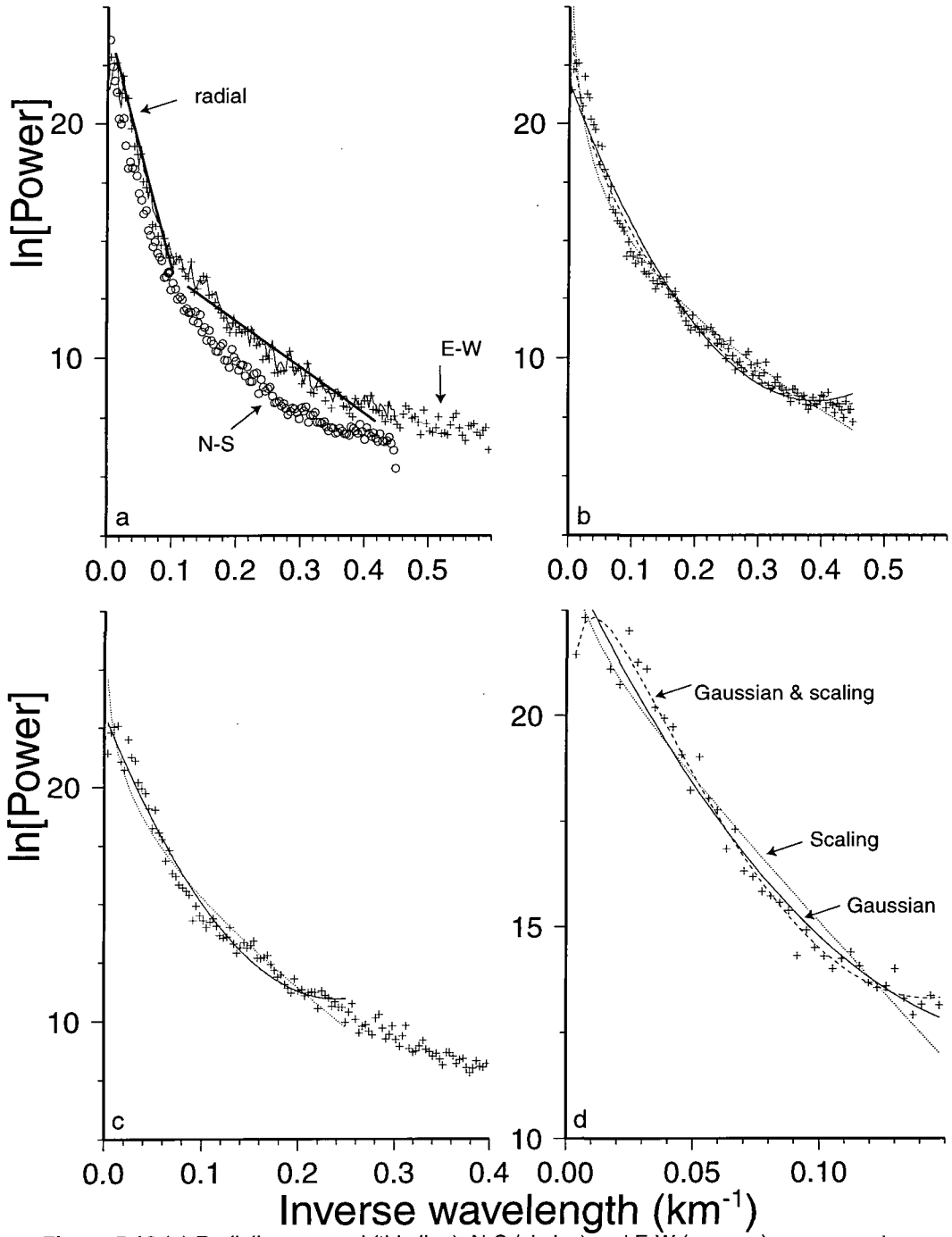

Figure 5.18 (a) Radially averaged (thin line), N-S (circles) and E-W (crosses) power spectra computed from the observed magnetic anomaly in region S4 (40°-42°N, 17°-19°W; within oceanic crust accreted during anomaly 1-34 sequence time). Thick lines fitted to segments of the radially averaged power spectrum have slopes proportional to twice the depth of magnetic sources (Spector and Grant; 1970) estimated to be 8.3 km and 1.5 km. (b), (c) and (d) show recalculated spectra from the inversion of the radially averaged power spectrum (crosses) in inverse wavenumber bands of (b) 0-0.45 km^{-1}, (c) 0-0.25 km^{-1} and (d) and 0-0.15 km^{-1} by the Gaussian method (solid line), scaling method (dotted line) and combined Gaussian and scaling method (dashed line). Optimum parameter triplets and quadruplets are shown in Table 5.7.

oceanic crust exhibits (a) no along axis (isochron parallel) variation in magnetization, (b) across axis (isochron normal) variation dependant upon spreading rate only, and (c) vertical variation

dependant upon the layer model of oceanic crust (e.g. Fig. 1.6), which can be approximated to a uniform block model (see section 3.3.3).

band width (km^{-1})	$\ln C_3$	h (km)	σ_{hinv} (km)	σ_h^2	γ	$\sigma_{\gamma inv}$
0-0.6 (A1)	21.75	5.53	0.22	2.25	N/A	N/A
0-0.25 (A2)	23.12	8.09	0.53	5.37	N/A	N/A
0-0.15 (A3)	23.69	9.71	1.18	8.34	N/A	N/A
0-0.6 (A4)	14.41	0.75	0.12	N/A	3.07	0.21
0-0.25 (A5)	16.85	1.98	0.30	N/A	2.05	0.30
0-0.15 (A6)	20.76	4.74	0.71	N/A	0.68	0.44
0-0.6 (A7)	18.57	3.57	0.51	1.41	1.47	0.35
0-0.25 (A8)	23.35	8.29	1.35	5.52	-0.08	0.54
0-0.15 (A9)	30.25	17.43	3.26	18.16	-2.09	0.82

Table 5.7 Optimum parameter triplets and quadruplets describing the best-fit power spectra from the inversion of the radially averaged power spectrum in three band widths over oceanic crust (region S4; accreted at beginning of anomaly 1-34 sequence). Parameter definitions as Table 5.4.

Alternatively, model A5 may describe the sources based on the reasoning of Maus and Dimri (1996); in this case, no depth information is supplied by the model, instead a scaling exponent of ~2 describes the source magnetization distribution which implies that scaling variations in magnetization occur in two directions; perhaps across axis and vertically down.

Depth distributions of Euler solutions are shown in Figure 5.19. Based on the computed depth to basement constraint of 5-7 km (see above), a structural index of 0.5 (which describes a source geometry as the edges of finite depth contacts) best describes the sources in this region; source depths are focussed at 5 to 7 km. The field is therefore a result of basement relief effects and/or layers of significant, but not infinite, thickness near to the top of basement (i.e. the extrusive layer).

5.3.3.2 Cretaceous Magnetic Quiet Zone

An analysis of the radially averaged power spectrum yielded depth estimates of 6.2 km and 2.5 km by the Spector and Grant (1970; Fig. 5.20) method, and optimum parameter triplets and quadruplets from inversion of the spectrum as shown in Table 5.8.

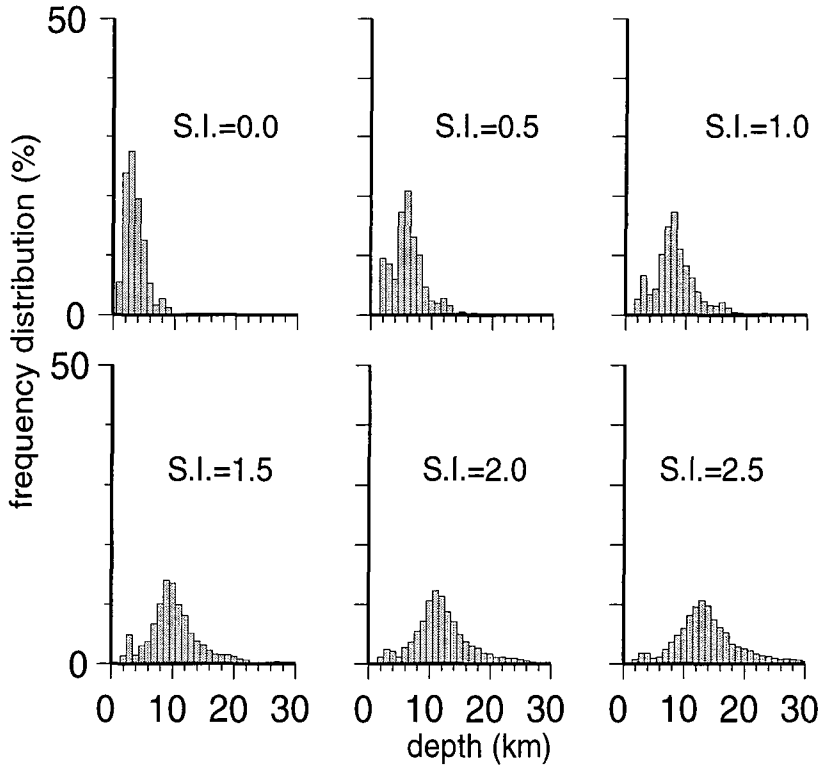

Figure 5.19 Distributions of Euler solutions for structural indices (S.I.) of 0.0-2.5 resulting from the deconvolution of the observed magnetic field over oceanic crust in region S4 (within the anomaly 1-34 sequence between 40°-42°N, 19°-17°W).

band width (km^{-1})	$\ln C_3$	h (km)	σ_{hinv} (km)	σ_h^2	γ	$\sigma_{\gamma inv}$
0-0.6 (Q1)	20.41	4.42	0.17	1.37	N/A	N/A
0-0.25 (Q2)	21.57	6.21	0.61	3.28	N/A	N/A
0-0.15 (Q3)	21.61	6.23	1.33	3.08	N/A	N/A
0-0.6 (Q4)	14.03	0.76	0.09	N/A	2.89	0.21
0-0.25 (Q5)	18.19	2.70	0.36	N/A	1.03	0.36
0-0.15 (Q6)	21.54	5.00	0.82	N/A	-0.18	0.52
0-0.6 (Q7)	18.58	3.43	0.40	1.04	1.00	0.35
0-0.25 (Q8)	24.14	8.41	1.61	4.95	-0.97	0.66
0-0.15 (Q9)	29.66	15.60	3.85	14.67	-2.61	1.01

Table 5.8 Optimum parameter triplets and quadruplets describing the best-fit power spectra from the inversion of the radially averaged power spectrum in three band widths over oceanic crust (region S5; accreted during Cretaceous Normal Polarity Chron). Parameter definitions as Table 5.4.

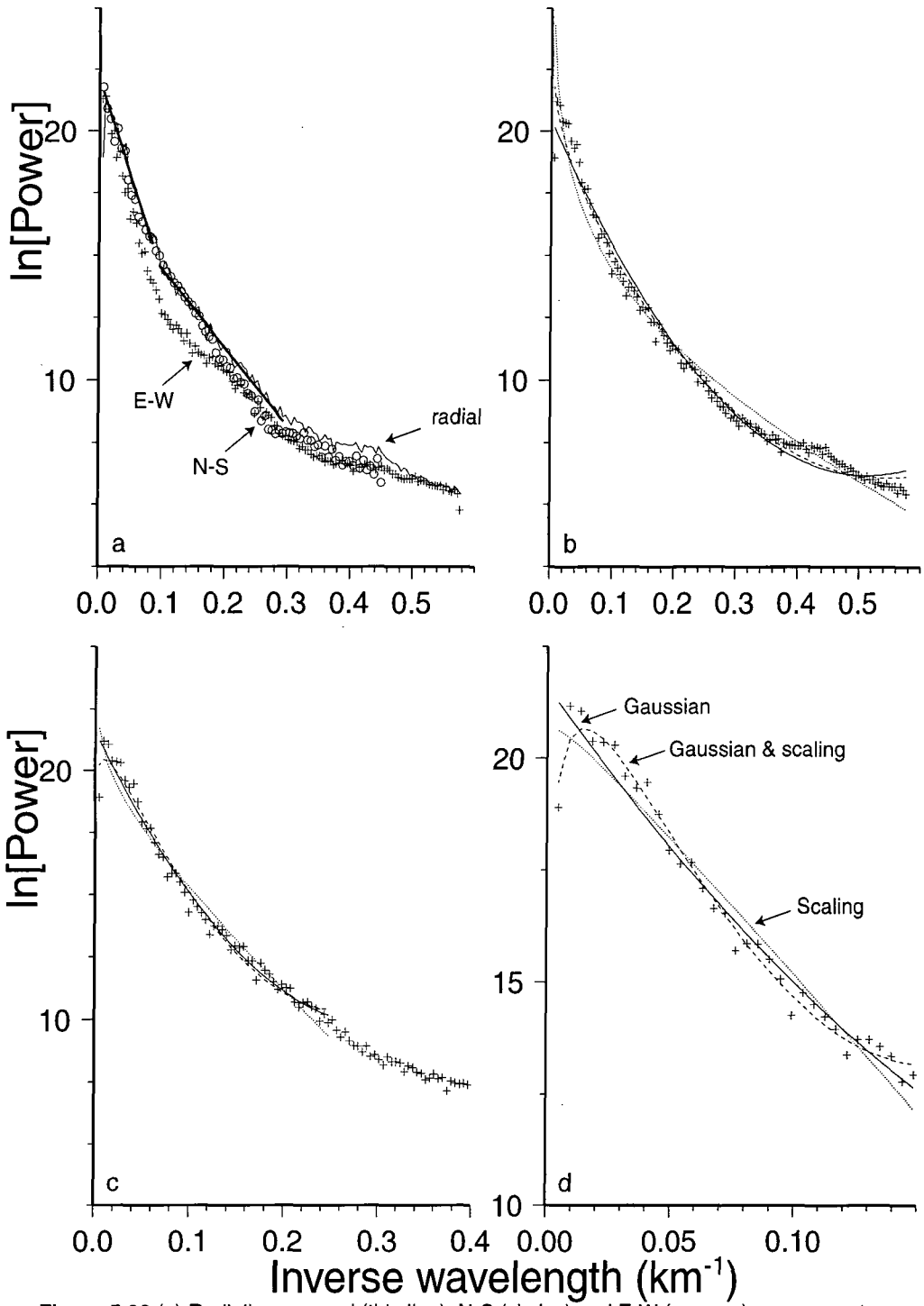

Figure 5.20 (a) Radially averaged (thin line), N-S (circles) and E-W (crosses) power spectra computed from the observed magnetic anomaly in region S5 (38°-39.5°N, 15°-17°W within oceanic crust accreted within the Cretaceous Normal Polarity Chron). Thick lines fitted to segments of the radially averaged power spectrum have slopes proportional to twice the depth of magnetic sources (Spector and Grant; 1970) estimated to be 6.2 km and 2.5 km. (b), (c) and (d) show recalculated spectra from the inversion of the radially averaged power spectrum (crosses) in inverse wavenumber bands of (b) 0-0.6 km^{-1}, (c) 0-0.4 km^{-1} and (d) and 0-0.15 km^{-1} by the Gaussian method (solid line), scaling method (dotted line) and combine Gaussian and scaling method (dashed line). Optimum parameter triplets and quadruplets are shown in Table 5.8.

In general the resultant depths for each model compare favourably with depths obtained from power spectral analysis in the anomaly 1-34 sequence. Models Q2 and Q3 may represent good source depth estimators; a calculated depth of 6.2 km with a topographic variation of ~±1.8 km is plausible for oceanic crust of this age with topographic variation similar to that observed west of Iberia (zone A; Fig. 5.2) and at the present day Mid-Atlantic Ridge (e.g. Fig. 2 of Searle et al., 1998).

Models Q2 and Q8 necessarily imply a scaling exponent of zero, whereas model Q5 has a near unity scaling exponent. Either value may be expected; by definition the Cretaceous Magnetic Quiet Zone, or Normal Polarity Chron, is not expected to display any significant isochron normal or isochron parallel magnetization variation, with the exception of variations in NRM due to geomagnetic field intensity variations. However, vertical variations in magnetization may be expected, in which case model Q5 represents the most plausible model of the scaling nature of the source (source depth is underestimated because of the trade-off with scaling information).

Euler solutions also compare reasonably well with those derived from the anomaly 1-34 sequence (Fig. 5.21). Source depths at ~6 km, i.e. top basement, and a structural index of 1.0 are preferred (based on the reasoning of the last section).

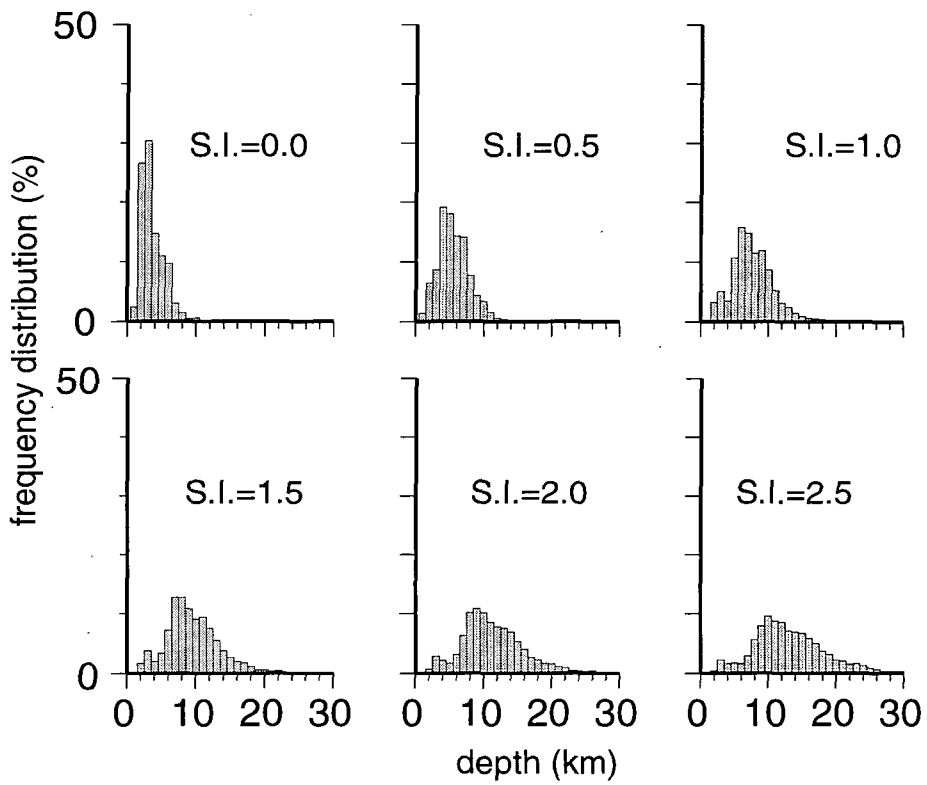

Figure 5.21 Distributions of Euler solutions for structural indices (S.I.) of 0.0-2.5 resulting from the deconvolution of the observed magnetic field in region S5 (oceanic crust accretwd within the Cretaceous Normal Polarity Chron between 38°-39.5°N, 17°-15°W).

5.4 Summary

An interpretation of the above analyses of basement depths and features, magnetic anomaly trends, and magnetic source depths, distributions and types, on a large scale (10^0-10^2 km), has revealed the following distinct characteristics across the West Iberia continental margin:

1) Continental crust east of ~11°W and in the region around and to the north of Vasco da Gama seamount (VDG) is characterized by (observed) magnetic anomalies that either possess no dominant trend or are sub-circular (1-D). However, after reduction to the pole N-S to NNW-SSE anomaly trends become apparent especially in the region near VDG seamount to the north of ODP Leg 149 and 173 Sites 901, 900, 1065, 1067, 1068 and 1069. These lineated anomalies parallel at least three basement topographic highs that may extend as far as 50 km south from VDG seamount beneath the southern Iberia Abyssal Plain. These lineated anomalies are most apparent after a reduction-to-the-pole of the observed magnetic field when a declination of 0° or -15° is employed.

Magnetic source depths are hard to define due to the probable scaling nature of the crustal susceptibility; scaling exponent values (γ) of 2-3 are consistent with the predicted value (of 3; see section 4.1.3). A slight underestimate in γ might suggest an anisotropy with less scaling variation in one Cartesian direction. Source depth distributions are broad essentially due to large variations (1-9 km) in basement topography in the vicinity of the continental slope. Nevertheless, some source depth variations may also be independent of bathymetry; the majority of source solutions occur near to the top of basement in the range ~3-7 km (bsl.) although a source depth window to depths of 15-20 km is possible with a likely cluster at ~12 km.

2) The region commonly referred to as the ocean-continent transition zone from ~11°W to 12.5°W south of 40°40'N can further be divided into two zones based on basement topographic character and the sources of magnetic anomalies. However, as a whole, observed magnetic anomalies show a slight preferred N-S lineation. A minimum bound on magnetic source depths of 5.5-6 km is governed by the actual depth to top basement and the scaling nature of the magnetization; a scaling exponent of near 2 suggests variations occur in one or half a Cartesian dimension less than in continental crust, i.e. anomalies are more lineated over the OCT than over continental crust.

In the western third of the OCT basement depth is typically <7.5 km with an average N-S trend in basement features although at its western side trends are slightly east of north and at its eastern side trends are west of north. The region is bounded in the west by peridotite ridge segments R3 and R4 and the region of overlap is deemed to be within the OCT domain. Observed

magnetic anomalies show no preferred lineations except in the region of overlap of the peridotite ridges where an approximate 010° trend is observed. Most other anomalies are sub-circular. After reduction-to-the-pole of the observed magnetic field, anomaly trends of NW-SE to N-S become apparent particularly at magnetization declinations of 0°, –15° and -30°; this suggests that if the magnetic sources posses a remanent magnetization it was acquired after the initiation of the rotation of Iberia (see section 2.2). In particular, the isolated sub-circular magnetic anomaly near ODP Leg 149 Sites 898 and 899 becomes reasonably well lineated in a NNW-SSE direction. Magnetic source depths within this sub-region fall into two populations; the dominant cluster at top basement depths (~7 km) and a second cluster at ~12 km depth. A structural index of 1.0 is preferred, thus sources are likely to be sill-, dyke-, or lavaflow-like in geometry.

The eastern and more southerly region of the transition zone is described by subdued basement relief at depths >~8 km. Observed magnetic anomalies are reasonably well lineated in a N-S direction and become more apparent after reduction-to-the-pole with magnetization declinations of 0° or -15°. This may suggest that sources possess a remanent magnetization which was acquired after the initiation of rotation of Iberia, or that sources possess induced magnetization. Source depths cluster at ~10 km i.e. within 0-2 km of basement surface, with a preferred structural index of 1.0. However, for structural indices of 2.0, typical of point pole sources, the population bifurcates; a more dominant population at ~15 km depth lies beneath a population at ~10 km depth. These sources may be explained by intrusive pipe-like magmatic bodies, especially within the lower set of sources, whereas sources near to the top of basement may represent serpentinization variations due to focussing of seawater hydrothermal activity along faults, for example.

3) Oceanic crust west of peridotite ridge segment R3 is defined by lineated anomalies with a dominant NNE-SSW trend. Moreover, anomalies are sharpened (i.e. they exhibit a more continuous linear character) when reduced-to-the-pole with a magnetization declination of 0°. This suggests that the source remanent magnetization was acquired after the cessation of the rotation of Iberia. Source depths are best described by a structural index of 1.0 when solutions plot near to the top of basement at ~7 km depth. Sources occurring at the top of basement in oceanic crust of the Cretaceous Magnetic Quiet Zone and the early anomaly 1-34 sequence are best described by indices of 1.0 and 0.5, respectively. Thus sources in the oceanic crust immediately adjacent to the OCT offshore West Iberia are possibly more akin to those of the CMQZ than sources in the anomaly 1-34 sequence.

Further discussion of the significance of these results and their geological implications is presented in Chapters 6 and 7.

Chapter Six

Geological structure of the crystalline basement in the Iberia Abyssal Plain

In this Chapter I consider the spatial distribution of magnetic sources in the southern Iberia Abyssal Plain by the analysis and modelling of magnetic anomalies at sea level and near-bottom. Together with the results of Chapter 5, the results presented here provide sufficient information to constrain the sources of magnetic anomalies in a geological context. The onset of seafloor spreading and the geological nature of the OCT is further constrained. Models of margin development and melt production, largely consistent with recent seismic and ODP results, are discussed.

6.1 Lateral variations in magnetization intensity and source layer thickness

Basement relief alone cannot explain the magnetic observations in the southern Iberia Abyssal Plain (section 5.2.3). Therefore it is implicit that at least one other physical property is dominant in shaping the observed magnetic field.

Continuous two-dimensional magnetization variations within a constant thickness source layer were determined objectively by the inversion of the observed magnetic anomaly chart in region S2 (40°-41°N, 13°-11°W; see Fig. 2.7). The basement depth chart of Figure 5.2 was used as the upper surface of the source layer in the 3-D method of Parker and Huestis (1974). Realistic layer thicknesses of 4 and 7 km were assumed in each inversion run (Fig. 6.1). A total of 20 terms in the summation series and 20 iterations were utilized in the Fourier procedure (see Chapter 3).

Short wavelength instability (< 5 km) was removed completely by application of a 2-D high-cut wavenumber domain filter, whilst wavelengths between 5 km and 10 km were cosine tapered (see $F_H(k)$ in equations 3.9 and 3.10). A minimum basement depth of ~5 km places a resolution limit on the scale of variations. All wavelengths in the band 10-100 km were passed whilst those in the band 100-200 km were cosine tapered to remove any residual regional effects (see $F_L(k)$ in equations 3.15). Hence, variations on scales of 5-200 km are sought. No preferred directional filtering was implemented in either $F_H(k)$ or $F_L(k)$ in order to avoid any

bias prior to the interpretation stage.

A severe disadvantage in removing lateral magnetization variations on scales less than 5 km is that the method cannot test if the basement in the southern Iberia Abyssal Plain is the product of seafloor spreading at rates less than ~10 mm/yr (see Fig. 3.9). At and below spreading rates of 10 mm/yr, almost all constant polarity intervals older than CM4(N) correspond to blocks that are less than 5 km wide. Even at spreading rates of 16 mm/yr many blocks are only marginally greater than 5 km wide. Rejection of higher wavenumbers, however, was unavoidable since it necessarily introduced false oscillations associated with the inverse Fourier method.

The resultant magnetization distributions exhibit a difference in character either side of an approximately NNE-SSW trending boundary which is coincident with peridotite ridge segment R3 and the western flank of zone B of Chapter 5 (Fig. 6.1). South of ~40°26'N this magnetization boundary shows continuity with no change in local trend, in contrast to the peridotite ridge which is offset east by ~20 km (where it continues south as segment R4). However, south of ~40°26'N the magnetization solutions immediately east of the boundary do parallel those to the west, although amplitudes are approximately half of those to the west of the boundary. West of the boundary, for an assumed layer thickness of 4 km, the region is characterized by layer magnetizations whose moduli are commonly >0.5 A/m and when contoured show a dominant trend in a NNE-SSW direction (Fig. 6.1a). Furthermore, amplitudes (of magnetization moduli) often exceed 1.5 A/m and gradients are commonly 0.00015 A/m^2. East of the boundary the region is characterized, on the whole, by a uniformly weakly magnetized layer (moduli < 0.5 A/m) with the exception of a number of small isolated highs whose moduli exceed 1.0 A/m (see also Discovery 215 Working Group, 1998).

East of peridotite ridge R3, four magnetization highs that are present in both solutions of Figure 6.1, occur in different settings, in terms of the zones A-D of Chapter 5 (Fig. 5.2), and each can be interpreted in a different way. Under the assumption of a 4 km thick source layer, magnetization amplitudes of ~1.5 A/m at and around 40°40'N, 12°12'W (H1; Fig. 6.1a) were also encountered in cores of serpentinized peridotite breccias from ODP Leg 149 Site 899 (Zhao, 1996). Thus, the magnetization magnitudes derived from the inversions can be 'calibrated' against those obtained from cores; a ~4 km thick source layer, at least in the region around Site 899, provides the means of satisfying the constraint.

At Site 1070 (Fig. 6.1) the same method of attempting to retrieve a layer thickness by 'calibrating' inversion and drilling results is more involved. Initial results (Whitmarsh et al., 1998) indicate that there is a large spread in the measured magnetizations within all basement

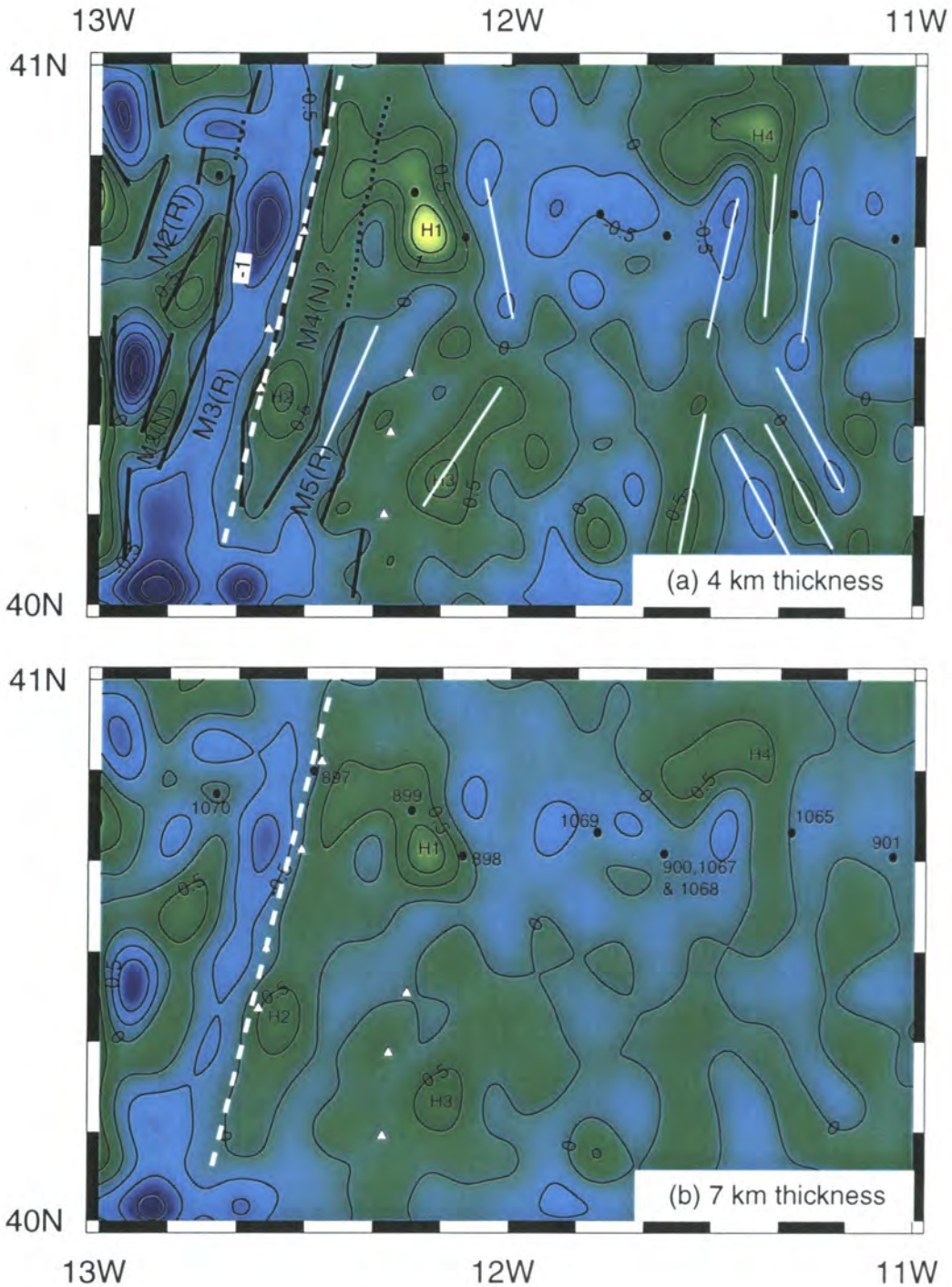

Figure 6.1 Magnetization solutions (0.5 A/m contour interval) from the 2-D inversion of the sea surface magnetic anomaly chart by the method of section 3.4.1. The upper surface of the magnetic layer is the top of acoustic basement (Fig. 5.2). Source magnetization direction; I=46°, D=0°. Constant layer thickness of (a) 4 km and (b) 7 km. Thick black lines mark the positions of sharp magnetization contrasts which can be modelled as seafloor spreading blocks M2(N)-M5(R). Black dots = ODP Sites; white triangles = peridotite ridge. Dashed white lines marks a boundary between regions of high (to the west) and low (to the east) magnetization, respectively. Solid white line mark linear trends in magnetization solutions. RMS residual between observed and inverse calculated anomalies = 15 nT.

cores (Table 6.1), and that it is possible for the gabbro veins and/or serpentinized peridotite to explain the magnetic field. Mean VRM inclinations in titanomagnetites from Unit 2B (serpentinized peridotites) are clustered around +46° which strongly suggests a Cretaceous origin for such rocks. However, in general all units possess an effective induced magnetization intensity greater than their respective remanent magnetization intensities. Therefore, based on the magnetizations in Table 6.1, and those computed beneath Site 1070, it is difficult to infer a more probable layer thickness (4 km or 7km). Published results of the spread in magnetization of the Site 1070 cores may provide further constraint on layer thickness.

Rock type	Remanent magnetization (A/m)	Induced magnetization (A/m)
Serpentinite breccia (Unit 1)	0.05-0.1	0.01-0.2
Gabbro veins (Unit 2A)	0.05-0.1	0.02-0.4
Serpentinized peridotite (Unit 2B)	0.005-0.05	0.02-0.5

Table 6.1 Range of magnetization intensities derived from basement cores at ODP Leg 173 Site 1070 (from Whitmarsh et al., 1998). Effective induced magnetization calculated at 40°N.

If the magnetic source layer is equivalent to a layer exhibiting 'crustal' velocities[1] a further constraint is provided by the modelling of wide-angle seismic data (Chian et al, in press.; Dean et al., submitted; Discovery 215 Working Group, 1998); a ~4-5 km thick source layer lies within the OCT and immediately west of the peridotite ridge, and a 6-7 km thick source layer lies ~20 km west of R3 (Fig. 6.2). These thicknesses agree closely with those required to produce realistic magnetizations in the inversion procedure that agree with modelling and drilling results. However, thicknesses are notably smaller than expected for normal slow spreading oceanic crust (7.1±0.8 km; White et al., 1992).

The magnetization high at 40°20'N, 12°33'W (H2) occurs in the region of overlapping peridotite ridges R3 and R4 (Fig. 6.1), and also where basement control is poor (Fig. 5.2). It may, therefore, be an artifact of the inversion which utilizes an overestimated basement depth (if basement were to be shallower the magnetization amplitude would be lower since anomalous magnetic field can be approximated by the product of depth to source and magnetization magnitude). A third magnetization high is present east of R4 at 40°11'N, 12°10'W (H3) and is coincident with a basement topographic high within zone C (see Fig. 5.2). The fourth high near to 40°50'N, 11°25'W (H4) is also located between basement control points. Layer thicknesses

[1] Velocities < 7.9 km/s are classed as 'crustal' velocities although the corresponding rocks are not necessarily crustal in nature.

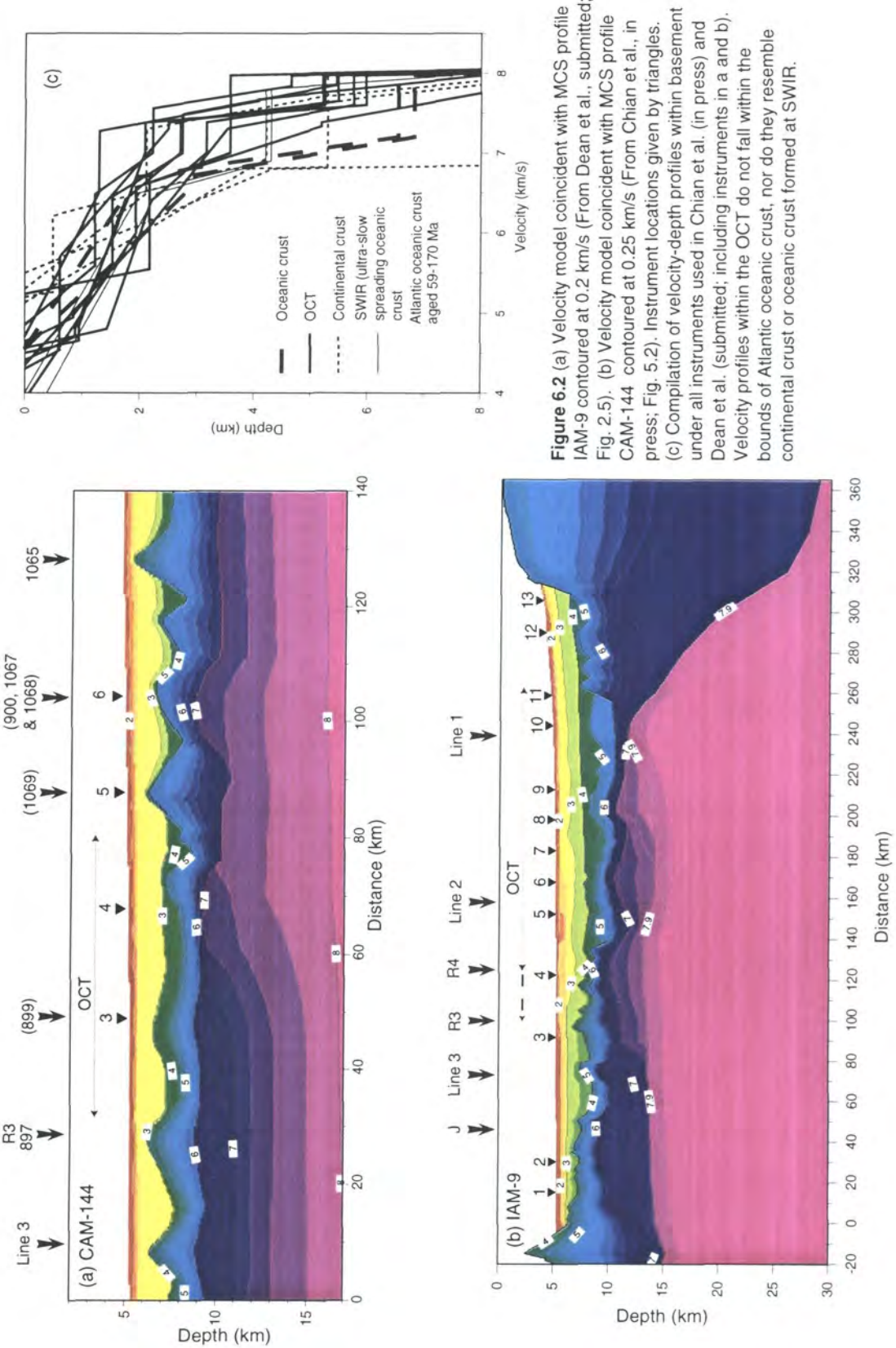

Figure 6.2 (a) Velocity model coincident with MCS profile IAM-9 contoured at 0.2 km/s (From Dean et al., submitted; Fig. 2.5). (b) Velocity model coincident with MCS profile CAM-144 contoured at 0.25 km/s (From Chian et al., in press; Fig. 5.2). Instrument locations given by triangles. (c) Compilation of velocity-depth profiles within basement under all instruments used in Chian et al. (in press) and Dean et al. (submitted; including instruments in a and b). Velocity profiles within the OCT do not fall within the bounds of Atlantic oceanic crust, nor do they resemble continental crust or oceanic crust formed at SWIR.

here may also be considerably greater than 4 km since continental crust is known to thicken to the north beneath Galicia Bank; again, magnetization amplitudes derived from the inversion may be overestimated. Thus, with the exception of H4, highs H1, H2 and H3 occur towards the western limit of the OCT, within 25 km of R3 (highs H1 and H2) and within ~15 km of R4 (high H3).

In general, although magnetization amplitudes fall into regions (east and west of R3), linear magnetization contrasts are present across the southern Iberia Abyssal Plain (Fig. 6.1a). In the west, over oceanic crust, between peridotite ridges R3 and R4, and in the western part of the OCT, the linear magnetization contrasts trend consistently east of north. In the central part of the OCT and in the vicinity of Site 1065, linear magnetization contrasts are relatively weak but also show a east of north to N-S trend. In the eastern part of the OCT linear magnetization contrasts trend consistently west of north.

Magnetization solutions derived from the inversion of total field measurements along near-bottom profiles SAR95, TOBI91 and SAR93 show a similar pattern of higher magnetization amplitudes towards the western side of the continental margin. Two sets of inversions, with different high-cut filter wavenumbers, show different features (Fig. 6.3). Firstly, with filter parameters identical to those applied to the inversion of the anomaly chart (Fig. 6.1), profile TOBI91 shows that west of 12°10'W (75 km on profile) magnetization solutions are characterized by peak to trough amplitudes of 3-3.5 A/m and wavelengths typically of 25 km. Gradients of 0.00014 A/m^2 compare favorably with those derived from the inversion of the sea surface magnetic anomalies with the same layer thickness (Fig. 6.1). East of 12°10'W solutions are characterized by peak to trough amplitudes of ~1 A/m or less, wavelengths of ~25 km, and gradients approximately one third of those to the west. Profile TOBI91 crosses 12°10'W ~30 km east of peridotite ridge segment R3.

Separately, profiles SAR93 and SAR95 are not long enough for a similar comparison to be made. However, together they represent a composite profile across the margin and it can be seen that either side of ~25 km distance on profile SAR95 (Fig. 6.3) the magnetization solutions can be defined by differences in character, exactly the same as those defining the two parts of the magnetization distribution of profile TOBI91. In addition, profile SAR95 exhibits a pair of magnetization peaks with peak-to-trough amplitudes of ~1.5 A/m between 70 and 120 km distance.

When shorter wavelength (2.5 km) magnetization variations are included in the model (Fig. 6.3b) a better fit between observed and forward calculated magnetic anomalies is achieved. On profile TOBI91 most of the additional high wavenumber energy is focussed into

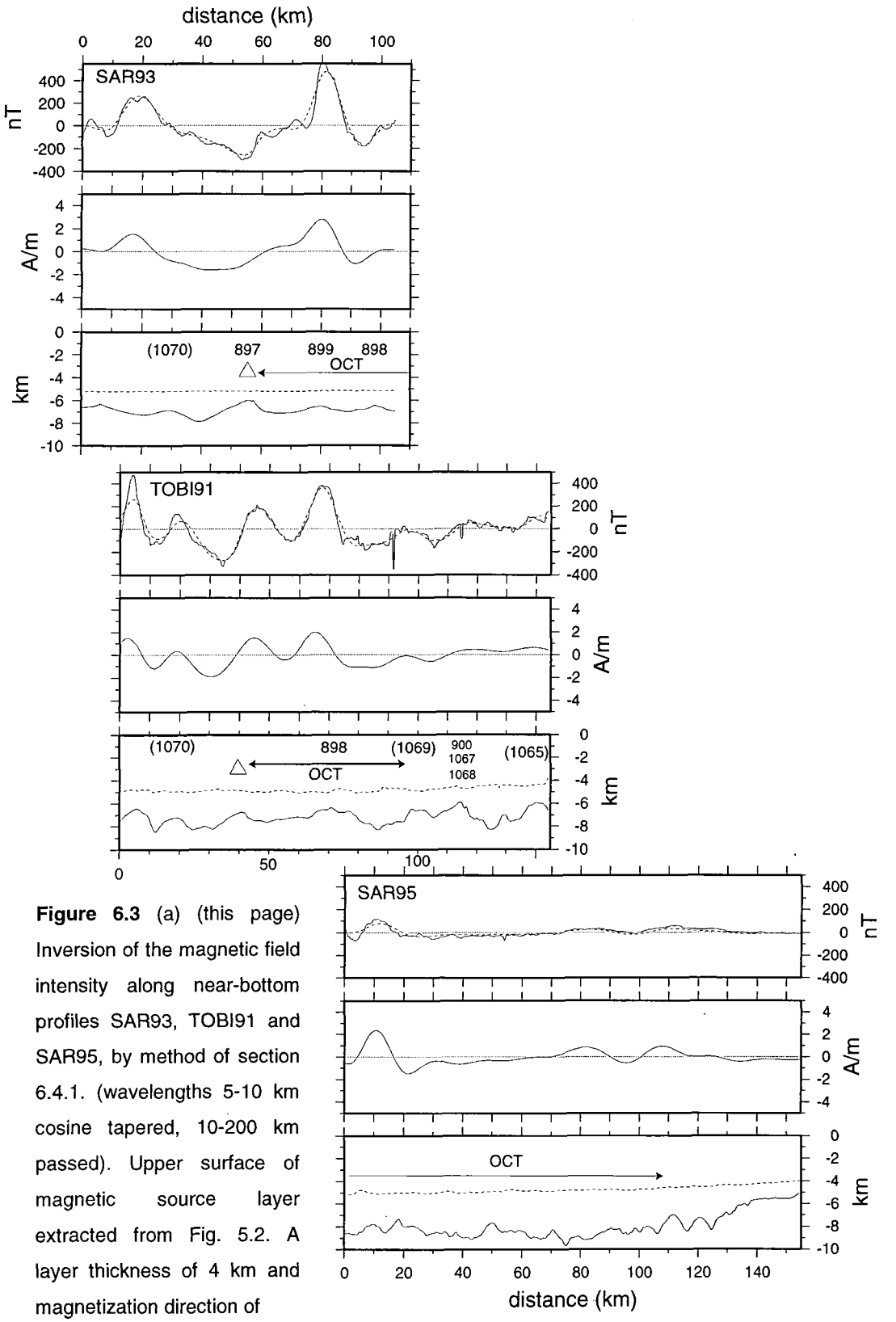

Figure 6.3 (a) (this page) Inversion of the magnetic field intensity along near-bottom profiles SAR93, TOBI91 and SAR95, by method of section 6.4.1. (wavelengths 5-10 km cosine tapered, 10-200 km passed). Upper surface of magnetic source layer extracted from Fig. 5.2. A layer thickness of 4 km and magnetization direction of Van der Voo (1990; see Fig. 6.1 caption) is assumed. Upper panels show observed (solid line) and recomputed magnetic anomalies (dashed line). Centre panels show magnetization solutions. Lower panels show top of acoustic basement (magnetic source layer; solid line), fish track (dashed line), peridotite ridge (triangles), ODP Sites over basement highs (Sites in parentheses are adjacent to tracks) and width of OCT. Profiles aligned along common longitude.

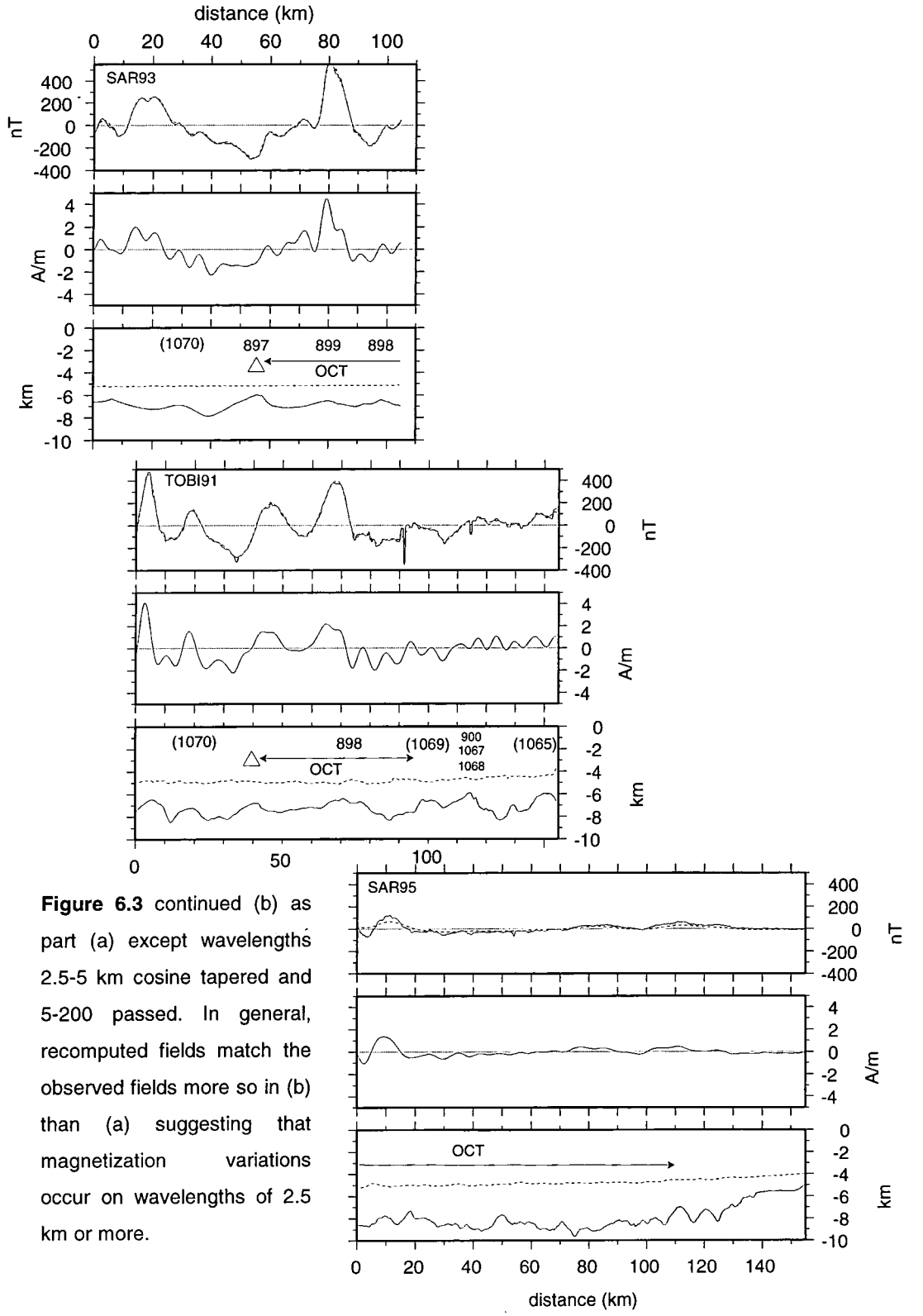

Figure 6.3 continued (b) as part (a) except wavelengths 2.5-5 km cosine tapered and 5-200 passed. In general, recomputed fields match the observed fields more so in (b) than (a) suggesting that magnetization variations occur on wavelengths of 2.5 km or more.

the solution east of 12°10'W (75 km on profile) thus changing its character more so than west of 12°10'W. On profile SAR93 additional high wavenumber energy is distributed throughout the solution whilst on profile SAR95 little change is apparent; this may suggest that variations

in magnetization structure beneath profile SAR95 occur on length scales of 5 km or more, whereas variations in magnetization structure beneath profiles TOBI91 and SAR93 occur on length scales ~2.5 km.

6.1.1 Basement formed by seafloor spreading

Based on the 2-D inversion of the anomalous sea surface magnetic field (Fig. 6.1), the zone west of R3 is defined by relatively linear, 010°-trending magnetization highs and lows of ~3 A/m amplitude (peak-to-trough), whereas to the east of R3, amplitudes are subdued, commonly <1 A/m (peak-to-trough), and with relatively little lineation. There also exist at least two local magnetization highs with characters akin to those west of R3, lying within 25 km east of R3. 1-D inversions of near-bottom magnetometer profiles indicate that a contrast in magnetization solutions occurs ~30 km east of R3, rather than at R3 itself. The magnetization high identified along SAR95 (at distances < 25 km along profile) is not observed the magnetization chart (Fig. 6.1; from the 2-D inversion of sea surface anomalies), although it lies along strike from high H3. Therefore, based on the inversion evidence, a change in the magnetic character of basement occurs at ~12°10'W, approximately coincident with the eastern limit of zone B (Fig. 5.2) rather than at the peridotite ridge R3. The region to the east possesses a weak magnetic signature (absolute magnetizations <0.5 A/m) except for a few isolated highs of <1 A/m. Discovery 215 Working Group (1998) used this as a means of determining the location of the first crust produced by seafloor spreading processes.

West of R3, the magnitude and lineated pattern of the magnetization solution (Fig. 6.1a) and the basement topographic patterns (Fig. 5.1) suggest that basement there is oceanic. At first sight and in contrast, magnetizations to the east of R3 are not indicative of basement with oceanic origins because of their lower amplitude and poorly developed linear nature. West of R3, estimates of reversal sequence block widths, as defined by approximate local zero crossings, match reasonably well with theoretical widths, thus indicating that the basement is most probably oceanic in origin (Fig. 6.1). Block M3(R) is well developed with almost constant width of ~14 km north of 40°15'N, and block M2(N) is moderately developed between ~40°15'N and 40°51'N with a width <7 km. Immediately west of M2(N) a region of reversed magnetization ~10 km wide is present; although too wide to be equated to block M1(R), the reasonably linear nature of its high gradient flanks (representing discrete changes in magnetization polarity) which are roughly parallel with the boundaries describing M3(R) and M2(N), suggest that this negative feature may represent M1(R) within the bounds governed by

the filter parameters in the inversion procedure. Table 6.2 shows that with the necessary high-cut filter (removing wavelengths <5 km), very few of the reversal blocks can be resolved by the inversion procedure, with the exception of M0(R), M1(N), M2(N), M3(R), M4(N) and M5(R) at the later end of the M-series.

Of all the high amplitude linear magnetization features in Figure 6.1, M3(R) is the most prominent, in terms of along strike continuity. Its near constant width of ~14 km can be explained by an infinite number of spreading rate and initiation time pairs. For example, if the estimated 14 km width represents the entire width of M3(R), then a spreading rate of ~7 mm/yr explains the observations (see Table 6.2). Alternatively, if seafloor spreading started exactly midway through CM3(R; Fig. 2.1) time then the observed 14 km width can be explained by a spreading rate of ~14 mm/yr. Spreading rates > 14 mm/yr with spreading commencing in the latter half of CM3(R), and spreading rates between 7 and 14 mm/yr with spreading commencing in the first half of CM3(R) would also explain the observed width.

In addition to the pre-CM3(R) seafloor spreading blocks, and contrary to the description given in section 6.1 and by Discovery 215 Working Group (1998), there is some evidence to suggest that M4(N) and M5(R) may also be present. A positive feature east of M3(R), which includes high H2, has along strike continuity from ~40°10'N to ~40°53'N, although the northern half is obscured, on its eastern flank, by high H1. Nevertheless, M4(N) has a width of ~11 km. Block M5(R), discernible from ~40°10'N to ~40°25'N, is even less continuous than M4(N), and exhibits a width of ~8.5 km. Such block widths for M4(N) and M5(R) imply spreading rates of 11.5 mm/yr and 16.5 mm/yr, respectively. Together with the estimate of 7 mm/yr, calculated from the width of M3(R) assuming continuous seafloor spreading, such frequent and large changes in spreading rate are not consistent with a steady-state model. However, the average spreading rate from M5(R) to M1(R) (inclusive) is 11.1 mm/yr.

On the sea surface magnetic profile, coincident with MCS profile IAM-9, magnetizations, derived from an inversion, were adjusted to account for a likely change in layer thickness based on the coincident velocity model of Dean et al. (submitted; Fig. 6.4a). Seafloor spreading can only be modelled west of R3 at a spreading rate of 12 mm/yr with only ~13 km width of block M3(R); within CM3(R) and CM2(N) time an increase in layer thickness derived from the velocity model can be adequately incorporated in the magnetic model. Such a block width is consistent with the widths derived from the 2-D inversion (Fig. 6.1). Magnetic bodies east of R3 cannot be modelled by seafloor spreading assuming a spreading rate of 12 mm/yr.

On profile TOBI91, with continuous seafloor spreading assumed, M4(N) is the oldest

block that can be modelled, with confidence, by inverse methods. However, with the peridotite ridge marking a gap in the reversal sequence (possibly emplaced post seafloor spreading?), M5(R) can also be modelled; this requires that between the beginning of CM5(R) (~128.25 Ma) and the end of CM3(R) (~125 Ma) seafloor spreading was constant at a rate of 8 mm/yr (Fig. 6.4b). After CM3(R) a rate of 10 mm/yr explains the observations.

Block	Width (km) @ 6 mm/yr	Width (km) @ 8 mm/yr	Width (km) @ 10 mm/yr	Width (km) @ 12 mm/yr	Observed width (km)
M0(R)	3.6	4.8	6.00	7.2	NO
M1(N)	16.14	21.52	26.9	32.28	NO
M1(R)	2.22	2.96	3.7	4.44	~10
M2(N)	4.08	5.44	6.8	8.16	~6.5
M3(R)	12.06	16.08	20.1	24.10	~14
M4(N)	5.7	7.6	9.5	11.40	~11
M5(R)	3.06	4.08	5.1	6.12	~8.5
M5(N)	0.84	1.12	1.4	1.68	NO
M6(R)	0.66	0.88	1.1	1.32	NO

Table 6.2 Theoretical widths (100 m accuracy) of seafloor spreading blocks at spreading rates of 6-12 mm/yr compared with observed widths derived from local near zero crossings of the inversely determined 2-D magnetization solution. NO=not observed.

6.1.2 Lateral variations in thickness of the source layer

Instead of assuming that the magnetic anomalies within the southern Iberia Abyssal Plain are caused by magnetization variations within a layer of constant thickness, it is not unreasonable to assume that they are in fact caused by thickness variations of a layer that possesses a constant magnetization direction and magnitude. In fact, both processes may contribute to the field, but as explained in Chapter 3 it is difficult, mathematically, to simultaneously determine variations in magnetization magnitude and layer thickness objectively using inverse methods. Therefore, I attempted to model layer thickness alone by the method described in Chapter 3. Unlike the inversions of section 6.1.1, which are typically used to retrieve the normal-reversed magnetization boundaries within oceanic crust, the inversions here require a source with constant magnetization direction. Thus it is somewhat meaningless to assume a remanent vector. Instead, a constant magnetization vector parallel to the present day geomagnetic vector was used in the inversion, i.e. the basement magnetization is assumed to be

induced. This assumption means that the method cannot test whether basement has an oceanic origin.

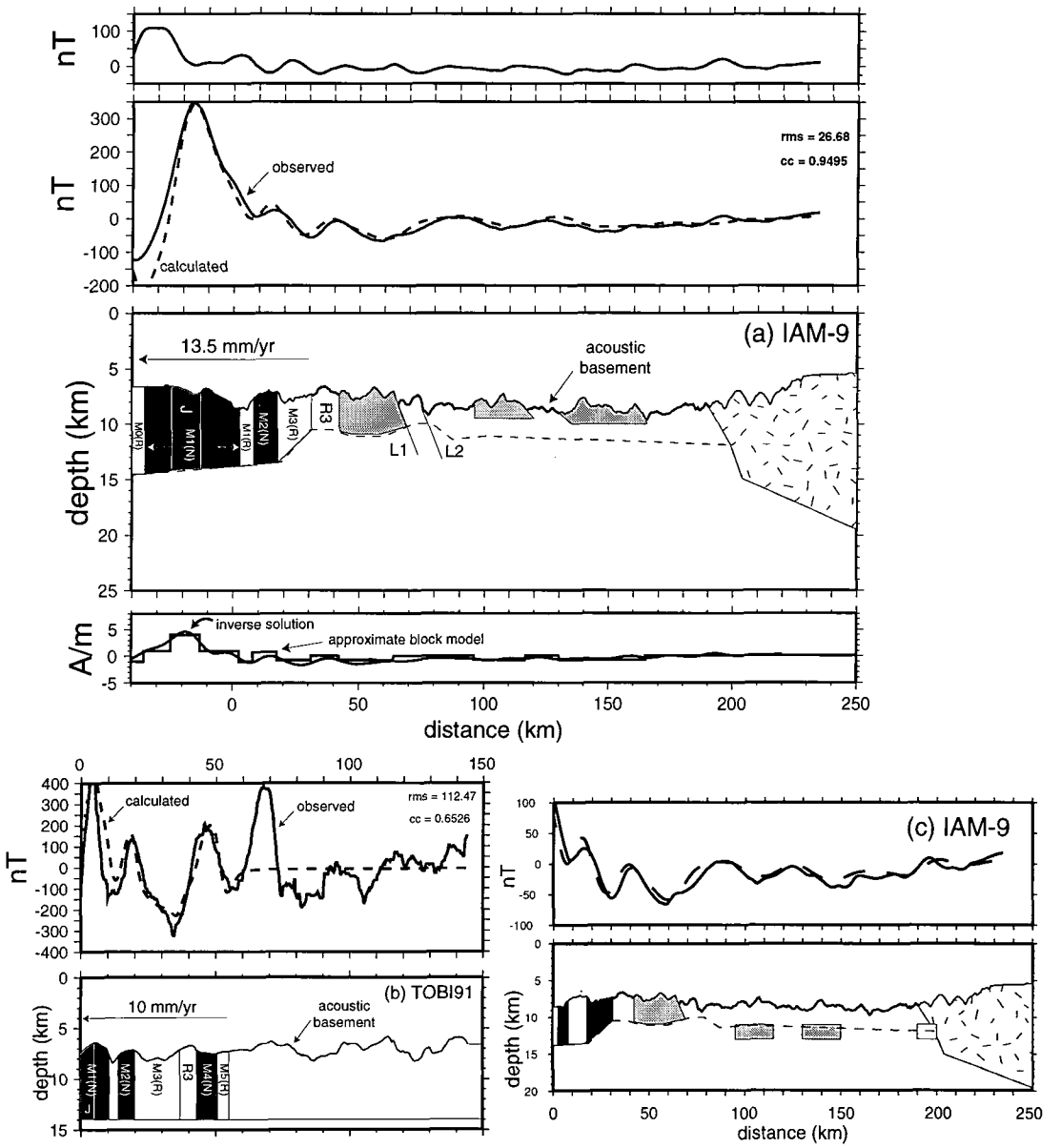

Figure 6.4 Magnetic models along profiles (a) and (c) IAM-9 and (b) TOBI91. (a) From bottom to top (1) inverse derived magnetization solution (7 km layer thickness and vector direction of Van der Voo, 1990) and best estimate of block magnetization structure; (2) magnetic model showing base of 'crustal' layer (dashed line; Fig. 6.2b), seafloor spreading blocks (±0.8 A/m), continental crust (0.1 A/m; stippled), undefined magnetic bodies (-0.8 A/m; grey); (3) observed and recomputed anomalies; (4) residual between anomalies in (3). (b) Seafloor spreading model (blocks ±0.8 A/m, except non-magnetic R3) and observed and recomputed anomaly. (c) Alternative model along IAM-9 showing that anomalies can be modelled by deeper sources in the OCT. Model parameters as in (a).

The upper surface of the magnetic source layer was extracted from the chart of Figure 5.2, and the coincident magnetic anomaly extracted from the chart of magnetic anomalies along four E-W profiles across the margin (Fig. 6.5). Inverse solutions were determined for a number of different initial layer thicknesses and magnetization magnitudes but convergence of the procedure was impossible to achieve in every case. Nevertheless, five models whose solutions generated after only 3 iterations are shown in Figure 6.5.

Models T1-T4 shows some interesting features; the source layer is (a) ~5 km or more thick from at 13°W (0 km) and steadily decreasing to 0 ~km thick at the peridotite ridge , (b) non-existent (~0 km thick) at the position of the peridotite ridge (~15 km wide), (c) up to 5 km thick in a region ~30 km east of the peridotite ridge. In model T5 the source layer is ~3-5 km thick east of 70 km, but negative west of 70 km. Although the models are not necessarily very good models in a quantitative sense, they provide a template for a possible geological scenario within the limits of the geophysical method, i.e. they are possibly the best models that can be achieved under the circumstances.

Variations in source layer thickness are better achieved through repeated inversions for magnetization. For each inversion, if a different source layer thickness is assumed, the solutions can be 'calibrated' against drilling results by matching the inversion-derived magnetization with the magnetization of basement cores; the most reasonable assumed source layer thickness creates the closest match in magnetization. This method is not only mathematically and computationally much easier to achieve but also allows one to test more likely working hypotheses; the assumption of a varying intensity magnetization can test the two hypotheses of ultra-slow seafloor spreading and unroofing and serpentinization of the mantle as means of margin development in the southern Iberia Abyssal Plain. The assumption of constant magnetization intensity and direction can necessarily only test a varying thickness continental crustal hypothesis for OCT make-up. However, based on drilling and other findings, this hypothesis is becoming increasingly more difficult to justify.

6.2 High resolution magnetic character from the analysis of near-bottom observations

Near-bottom observations can provide further constraints of the origin of the sources of magnetic anomalies in the southern Iberia Abyssal Plain. The following three sub-sections are therefore concerned with the analysis of the total field intensity and the three orthogonal components of the magnetic field.

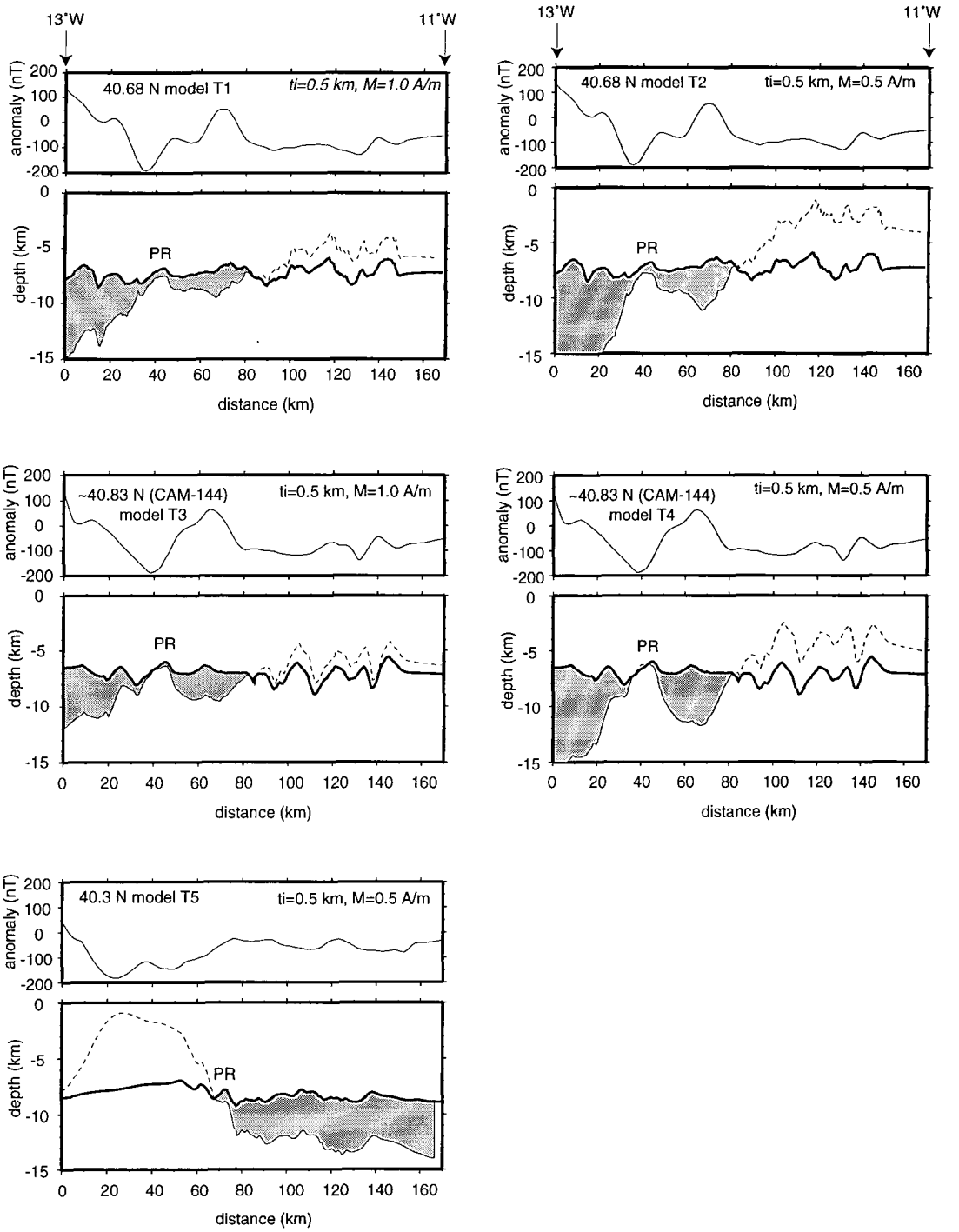

Fig. 6.5 The inversion of the magnetic field and basement relief extracted along three near E-W profiles (location labelled and see Figs. 2.5, 2.8 and 5.2). Initial thickness and constant magnetization given by ti and M, respectively. Positive layer thickness solutions are shaded grey, whilst negative layer thickness solutions are shown by the dashed line. Solutions shown are derived from only three iterations of equation 3.14; subsequent solutions resulted in geologically unreasonable solutions (high positive and negative values)

6.2.1 Euler analysis

The difference in source type either side of ~12°10'W, which has been determined from basement depth analysis (section 5.2.2) and magnetization solutions (section 6.1), is further supported by the 2-D Euler deconvolution solutions derived from near-bottom profiles SAR95, TOBI91 and SAR93 (Fig. 6.6).

Interpretation of the results, firstly by solution density (number of solutions per cross sectional area along track) suggests three different regions are sampled:

(1) A region of high solution density in which solution patterns are ∩-shaped and occur west of ~75 km on profile TOBI91, at the westernmost end of profile SAR95 (<15 km distance), and west of ~85 km on profile SAR93. Solutions pertaining to structural indices of 0.0 are typically characterized by ∩-shaped patterns. This can mean either (a) the structural index is underestimated (see Fig. 4.5 part b), or (b) the patterns are caused by interference due to close proximity of source bodies (non-linearity; see section 4.2.6 and Fig. 4.6). Some of the ∩-shaped patterns of solutions representing an index of 0.0 are mimicked by higher index solutions and therefore are regarded as being the result of the proximity of vertically sided bodies. Furthermore, each individual ∩-shaped pattern represents the occurrence of a magnetic boundary whose position is governed by the error associated with interference (see section 4.2.6 and Fig. 4.6); the positional error cannot be determined and therefore the magnetic boundary is assumed to occur at the position described by the apex of each ∩-shaped pattern.

(2) A second region of intermediate solution density occurs east of 75 km on profile TOBI91, east of 85 km on profile SAR93, and between 17 km and ~30 km on profile SAR95 (Fig. 6.6); ∩-shaped patterns of solutions are poorly developed which suggests that either neighbouring boundaries are sufficiently far apart such that little interference occurs, or that source body contrasts are weaker than those in zone (1).

(3) A region of very sparse solution density is present east of ~30 km on profile SAR95. Clusters of solutions at 78 km, 96 km and 112 km suggest only very weak magnetic contrasts exist at these positions.

Fitting theoretical reversal boundaries to solution apices shows that M4(N) on TOBI91 is the oldest seafloor spreading anomaly that can be modelled by this method. The peridotite ridge is also defined as a separate magnetic block on profiles SAR93 and TOBI91, consistent with the inverse models above. Moreover, the depths of Euler solutions west of R3 coincide almost exactly with the top of basement. In contrast, the boundaries marking the limits of the

peridotite ridge segment, block M4(N), and another body, B1(N), fall up to 2 km below the top of basement, providing they are defined as vertical boundary blocks (i.e. structural index of 0.0). If B1(N) is correctly identified as the same feature on all three profiles then it represents a significant margin parallel feature, which cannot be explained as a seafloor spreading block (see Fig. 3.10).

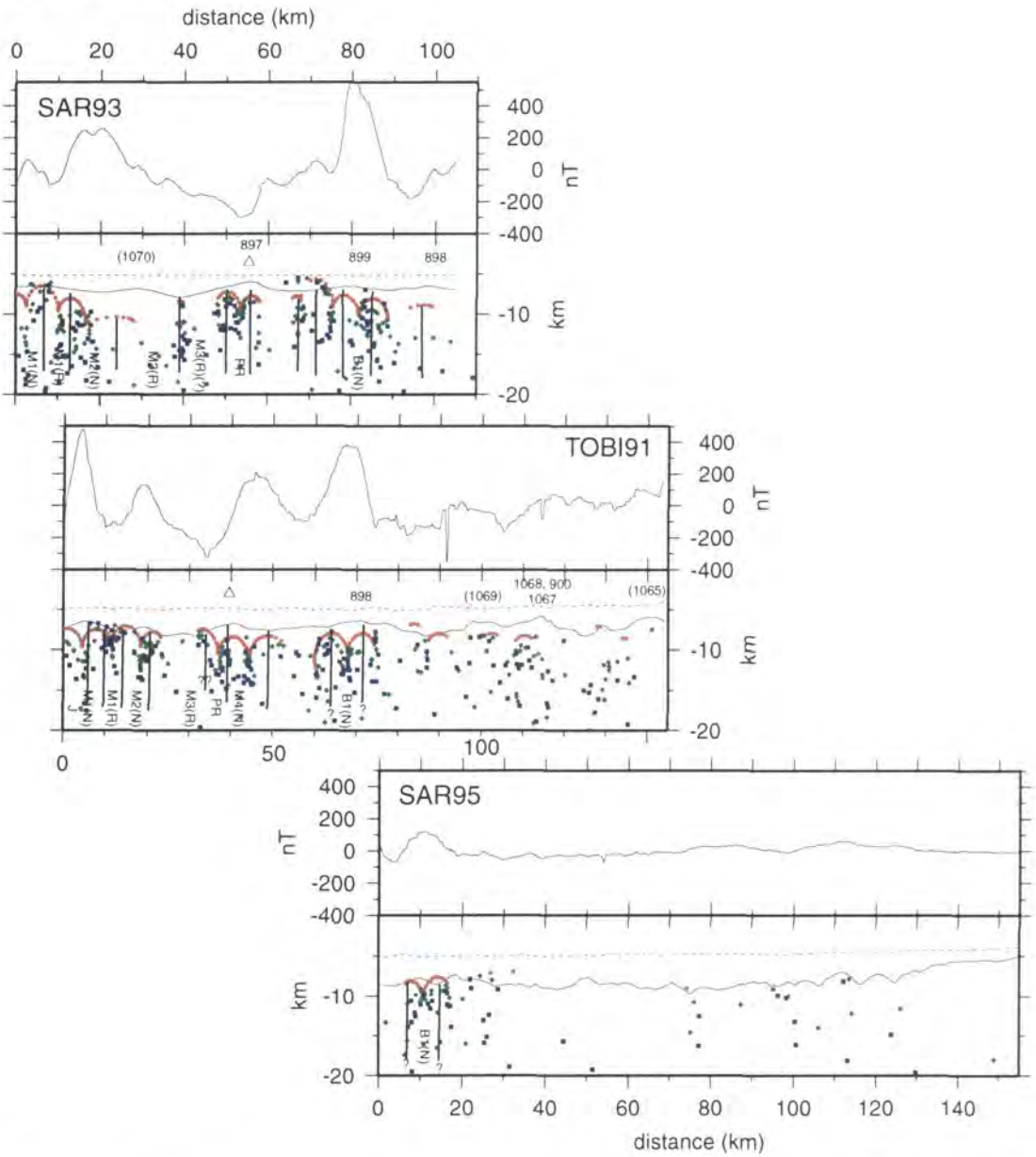

Figure 6.6 Euler deconvolution of magnetic anomalies (upper panels) along profiles SAR93, TOBI91 and SAR95 (aligned along common longitude). Window length = 2 km (see section 4.2). Solutions shown (lower panels) for structural indices of 0.0 (semi-infinite contact; red circles), 0.5 (step contact; *green diamonds*) and 1.0 (dyke-like contact; blue squares). ODP Sites, peridotite ridge, fish tracks and acoustic basement shown in lower panels (see Fig. 6.3 caption). Boundaries of magnetic blocks determined by positions of apices of solution clusters (SI=0.0); contacts of seafloor spreading blocks and other magnetic contacts (including B1(N)) labelled. See text for discussion.

6.2.2 The character of magnetic boundaries

The three orthogonal components of the magnetic field, in north, east and vertically downward directions, along near-bottom profiles TOBI91 and SAR95 were used to locate magnetic boundaries (significant magnetization contrasts), and to calculate the strike of each boundary. Although magnetic measurements were made in three orthogonal directions (fixed in the fish coordinate system) along profile SAR93, only the computed total field was recorded.

The intensity of spatial differential vectors (ISDV; see section 4.3.1) identified 22 and 11 magnetic boundaries along profiles TOBI91 and SAR95, respectively (Fig. 6.7). A threshold, or critical error level, of 50 nT/km, above which ISDV peaks are selected to determine the positions of magnetic boundaries, was chosen. Minima in ISDV are commonly ~50 nT/km and therefore such a level represents an ambient background level; ISDV maxima below 50 nT/km either mark the position of insignificant boundaries or are a result of noise. In addition, data within ~5 km of the ends of each profile were not used in the analysis because of the contribution of vehicle turning anomalies has a disproportionate effect on the componental field and its gradients (end of profile SAR95 are not included in Fig. 6.7).

Computation of magnetic boundary strikes was achieved via equations 4.19b and 4.20 using data in a window 2.8 km wide and centred on each ISDV maximum. The width of the window was limited by the minimum spacing of ISDV maxima; a constant window size was employed in the computation of each boundary strike to allow a fair comparison between strike estimates. A data spacing of 0.1 km resulted in 27 pairs of points in each inversion for boundary strike. Figure 6.8 shows the spatial distribution of magnetic boundaries whilst Table 6.3 lists explicitly the strikes, with their associated errors, at the location of each ISDV maximum.

It can be seen that the strikes of all magnetic boundaries are distributed about an approximate N-S trend although those within the northern region of the OCT (beneath profile TOBI91) generally possess a west of north trend, compared with a dominant east of north trend west of R3. Beneath profile SAR95, in the southern region of the OCT, magnetic boundaries strike east of north, although towards the eastern region of the OCT magnetic boundaries strike west of north and resemble those within the northern part of the OCT. In contrast, within continental crust beneath both profiles magnetic boundaries strike both east of north and west of north.

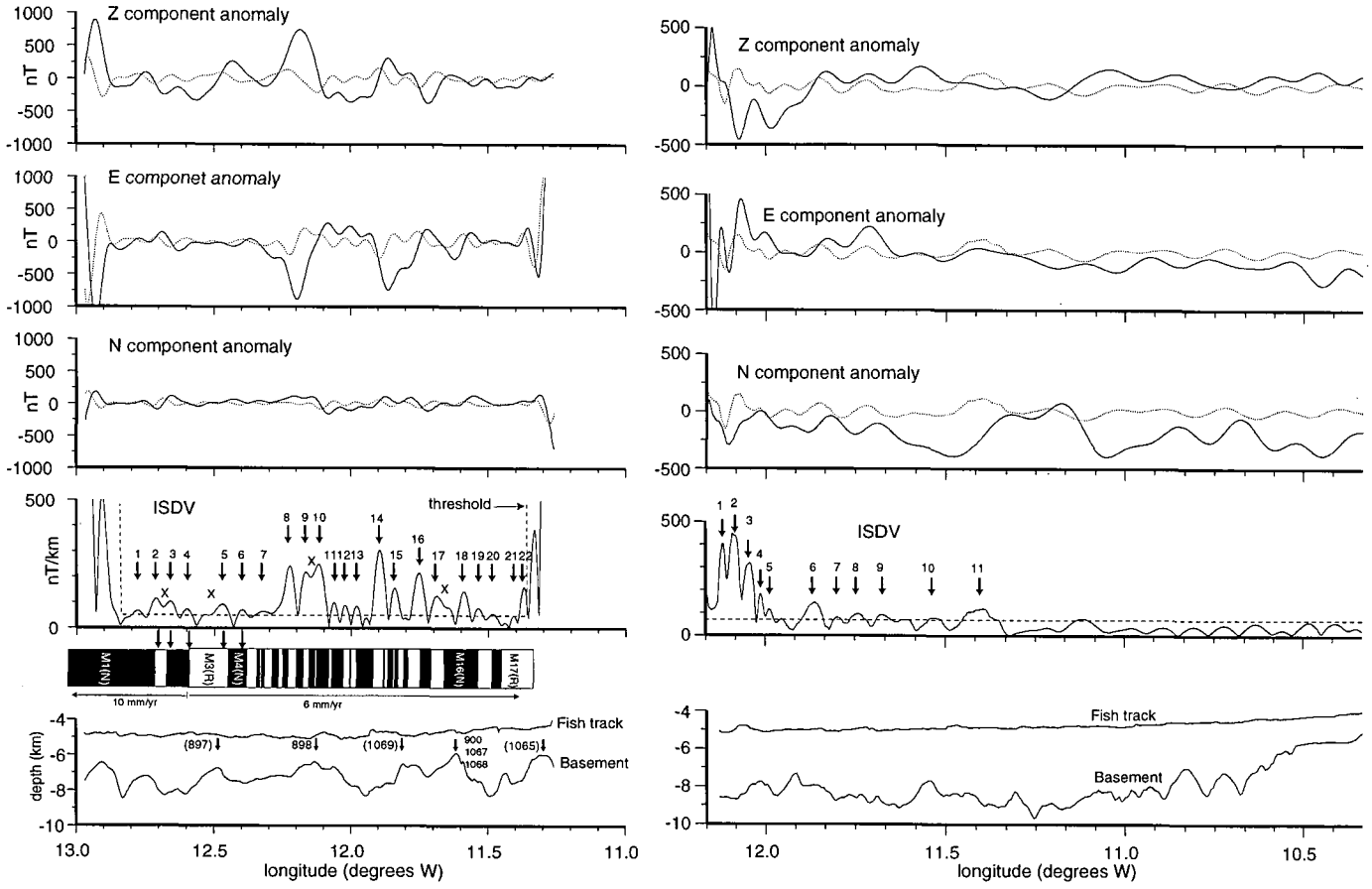

Figure 6.7 Vector anomaly (and gradient; dotted line) and ISDV profiles along TOBI91 (left) and SAR95 (right; note difference in ordinate scales). Position of magnetic boundaries indicated by maxima in ISDV (numbered arrows). On TOBI91, boundaries correlate reasonably well with theoretical magnetic contacts west of boundary number 6 (seafloor spreading model in which spreading rates of 10 mm/yr (west of 12°35'W) and 6 mm/yr (east of 12°35'W) are used in the computation of block widths). On SAR95 boundaries do not correlate with magnetic contacts derived from seafloor spreading models. X=distortions in ISDV.

Standard deviations of computed boundary strikes can also provide information other than the error in the strike estimate. Because each boundary was calculated using the same window size, relative standard deviations can be used to determine whether magnetic boundaries possess a three dimensional nature. As suggested by Seama et al. (1993), 3-D magnetic structures can be identified by relatively large standard deviations in the calculated strike because the boundary vector is non-constant within the window of data used to determine the actual strike. Therefore, although only qualitative, boundaries 8, 9, 10, 14, 15 and 16 on profile TOBI91, represent magnetic boundaries that are relatively more three-dimensional than the other calculated boundaries. Of these six boundaries, three lie in close proximity to the +100 nT magnetic high observed at the sea surface in close proximity to ODP Site 898 (Fig. 6.8); this single sea surface magnetic high is in fact observed as two highs on near-bottom profiles TOBI91 and SAR93 (see Fig. 6.3). The other three magnetic boundaries lie at the eastern side of the OCT beneath TOBI91. The remaining boundaries (with standard deviations $< 10°$) are considered to be relatively two-dimensional because of their small standard deviations. In general, magnetic boundaries agree well with the anomaly map, although near to Site 900 they appear to cross cut the sea surface magnetic contours at near right angles. However, once observed anomalies are reduced-to-the-pole, and therefore relocated over their respective source bodies, the strikes of these boundaries agree well with the trends of RTP anomalies (see Fig. 2.8).

On comparing the positions of ISDV maxima and a model of seafloor spreading (Fig. 6.7), boundaries 1-6 on profile TOBI91 match with the positions of reversal boundaries if spreading rates of 10 mm/yr and 6 mm/yr, west of peridotite ridge R3 (Site 897) and east of R3, respectively, are used. Other boundaries cannot be matched with theoretical reversal boundaries at any spreading rate.

6.2.3 Spectral character

The spectral character (Fig. 6.9) of each of the three near-bottom magnetic anomaly profiles reveals that the sources of magnetic anomalies are consistently at the top of basement within the vicinity of the ODP transect and MCS profile IAM-9. Also, a deep magnetic source is observed beneath profile SAR95 (coincident with IAM-9) at a depth of ~6.5 km below top basement. This source is not observed on profiles SAR93 and TOBI91. In addition, a deep source, at a depth of 25-26.5 km below the top of basement is observed on all profiles. This is interpreted to be a residual regional effect which was not removed by a first order regional fit.

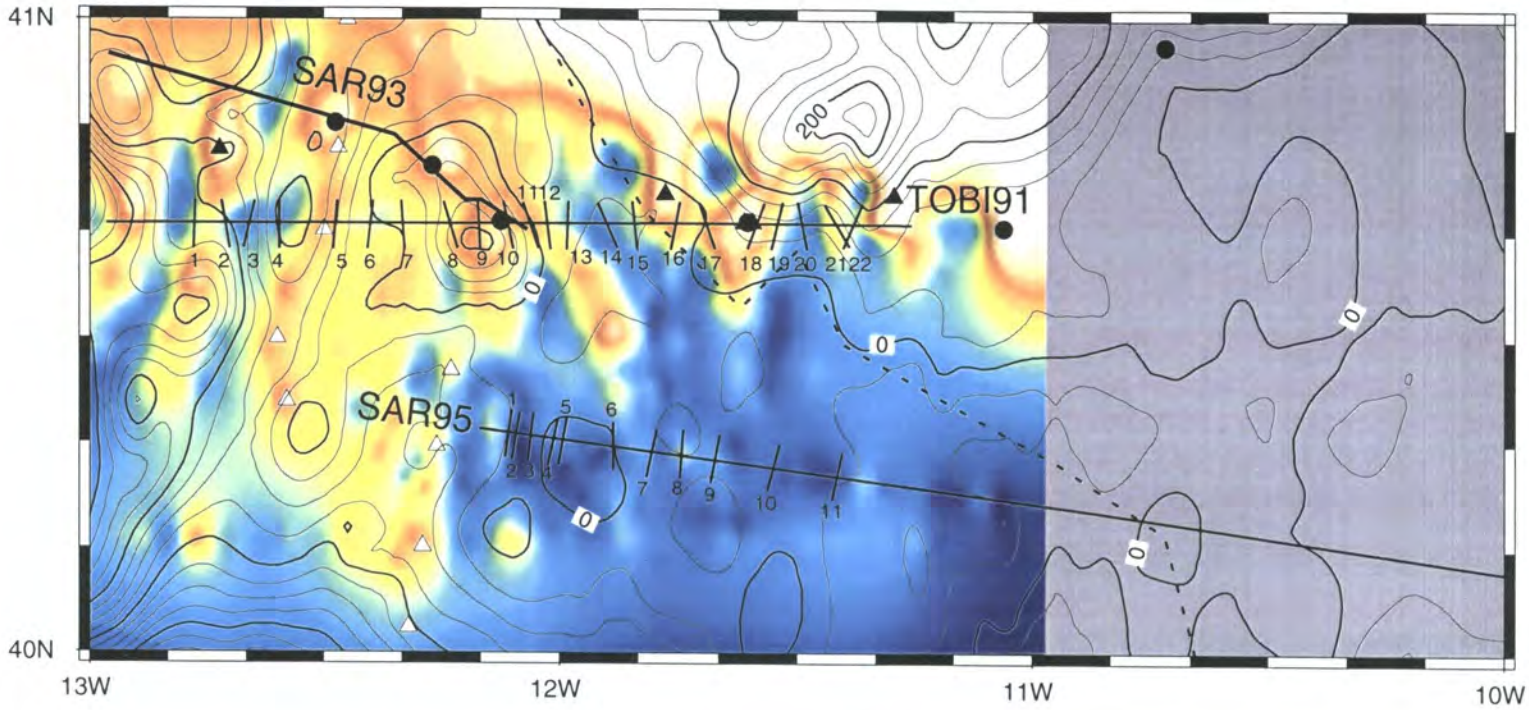

Figure 6.8 Depth to acoustic basement (colours; see Fig. 5.2) overlain by observed magnetic anomalies (contours 25 nT) and the locations and strikes of magnetic boundaries (identified in Fig. 6.7) along profiles TOBI91 and SAR95. Each boundary is numbered and its standard deviation is given in Table 6.3. West of ~12°15'W the strikes of magnetic boundaries show reasonable correlation with trends in basement relief and sea surface magnetic anomalies. East of ~12°15'W, most boundaries strike west of north beneath TOBI91 whilst boundaries generally strike east of north beneath SAR95. However, in the eastern region of the OCT and the western region of continental crust (regions TE and CW, respectively; Fig. 2.8) beneath SAR95 boundaries strike west of north. Magnetic boundaries augmented with asterisks are designated relatively three dimensional (see text). White triangles = peridotite ridge; black circles and triangles = ODP Sites.

Number	Strike	Standard deviation	Number	Strike	Standard deviation
TOBI91			TOBI91		
1	2.3	1.8	12	-6.8	3.5
2	-10.6	5.6	13	2.5	9.6
3	14.2	9.9	14	-24.4	15.1
4	0.4	3.3	15	-5.7	12.8
5	5.1	1.4	16	11.0	21.0
6	7.2	0.7	17	-19.4	5.4
7	-3.9	4.5	18	20.9	1.6
8	-17.3	14.8	19	14.2	2.5
9	-2.8	13.2	20	-11.2	3.1
10	-12.4	19.4	21	-31.4	1.8
11	-10.9	4.3	22	24.5	7.8
SAR95			SAR95		
1	8.1	5.0	7	12.5	5.5
2	9.7	7.3	8	4.1	7.9
3	6.8	8.9	9	11.0	1.1
4	12.3	4.7	10	15.4	6.7
5	10.5	9.1	11	12.2	8.2
6	-3.9	1.2			

Table 6.3 Magnetic boundary strikes, and standard deviations, of magnetic boundaries whose locations are determined from maxima in computed ISDV along near-bottom magnetometer profiles TOBI91 and SAR95 (Fig. 6.7).

The results suggest that the depth of magnetic sources are different beneath the two transects; in the south, beneath MCS profile IAM-9 (coincident with SAR95) there exists a deep magnetic source, ~6.5 km below top basement, in addition to the source near to the top of basement, whereas beneath, and in the vicinity of the ODP transect (approximately coincident with TOBI91 and SAR93), magnetic sources only exist near to the top of basement. However, comparison with the anomaly profiles and Euler solutions, the shallower source (near to top basement) is body B1(N) and the deeper source occurs within the bulk of the OCT beneath profile SAR95 and is described best by a structural index of 1.0. The significance of these sources are discussed in section 6.4.

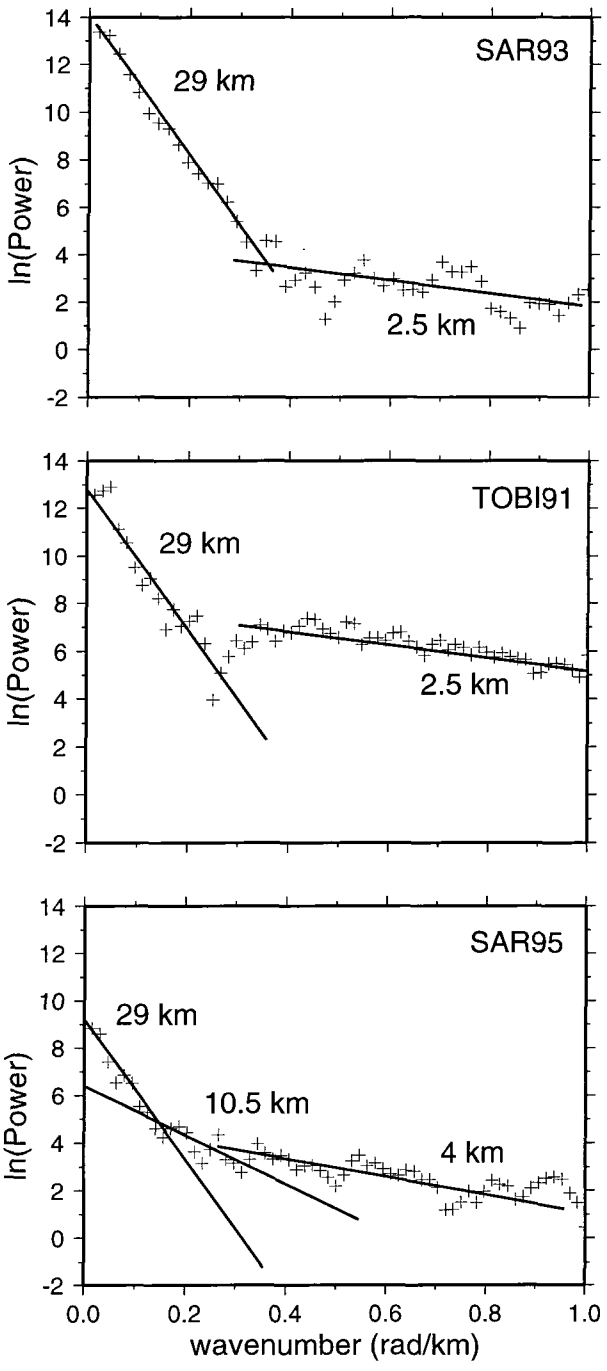

Figure 6.9 Logarithm of the power spectrum calculated from the total field anomaly along deep-tow magnetometer profiles SAR93 (top), TOBI91 (centre) and SAR95 (bottom). First order regional trends were removed from profiles before the computation of each spectrum. Each spectrum has been modelled using the Spector and Grant (1970) method of fitting straight lines to band limited segments. On profiles SAR 93 and TOBI91 identical and distinct source depths of 29 km and 2.5 km (below the observation level) are sucessfully modelled. Each fish was towed, on average, ~2.5 km above the top of basement. Therefore, source depths are shown to be consistently at the top of basement and ~26.5 km below basement in the vicinity of the ODP drilling transect. On profile SAR95, three sources are modelled sucessfully and found to be at the top of basement, and ~6.5 km and ~25 km beneath top basement. An average fish height of 4 km above basement was used. Th deepest source modelled is attributed to the residual regional field (unaccounted for by the removal of a first order trend).

6.3 The onset of steady-state seafloor spreading

Steady-state, or organized, seafloor spreading describes a geological process in which the accretion of a magmatic oceanic crust occurs continuously through geological time with the separation of two plates at a constant rate. Basement formed by such a process is recognized

geophysically primarily from (a) the identification of linear, seafloor spreading, magnetic anomalies, and (b) the vertical velocity structure of basement derived from seismic refraction modelling. Multichannel seismic reflection profiles can also provide additional, but less definitive, information.

Criterion (a) requires that magnetic anomalies be modelled by a series of normally and reversely magnetized blocks whose widths are determined from the duration of chrons and a given spreading rate. The application of criterion (b) is slightly more involved. The successful diagnosis is dependant upon crustal thickness, velocities, velocity gradients and spreading rate. If a velocity model fits within the velocity bounds of Atlantic oceanic crust (White et al., 1992; Fig. 6.2c) then it is considered to be 'normal' oceanic crust. However, at spreading rates of less than 10 mm/yr, mantle velocities (>7.9 km/s) are encountered at shallower levels with the reduction in seismic layer 3 thickness and overall crustal thickness (e.g. Muller et al., 1997). Both are still nevertheless the product of steady-state seafloor spreading.

Oceanic crust formed as a result of non-steady-state seafloor spreading processes, i.e. intermittent or varying melt production, is very difficult to define. If data do not satisfy both the magnetic and velocity criteria above then it may be difficult to justify an oceanic origin. However, if only one criterion is satisfied, or both are only partially satisfied (e.g. some, but not all, magnetic anomalies can be modelled, and parts of the velocity structure resemble parts of the oceanic crustal section) the subsurface may be considered to have some oceanic affinity, although not truly oceanic (as defined by the two criteria above). Although essentially a semantic enigma, here I define a geological process which, as will be shown in the following sub-sections, can explain the magnetic and seismic observations in the southern Iberia Abyssal Plain. The nature of the basement resulting from this geological process shows characteristics akin to those of oceanic crust and unroofed mantle. In a sense, the process is similar to one which occurs at ultra-slow and some slow oceanic spreading centres (e.g. Cannat, 1993), but I stress that the two are not necessarily synonymous.

6.3.1 Apparent location

The location of the onset of steady-state seafloor spreading in the Iberia Abyssal Plain has previously been estimated to be either immediately west of peridotite ridge segment R3 (Whitmarsh et al., 1990, 1996a; Whitmarsh and Miles, 1995; Fig. 2.3) or immediately east of R3 (Whitmarsh and Miles, 1995; Fig. 2.3). West of R3 seafloor spreading rates of 10 mm/yr and 14 mm/yr have been estimated from near-bottom profiles TOBI91 and SAR93,

respectively (Whitmarsh et al., 1996a); the difference in spreading rate can be explained by the SAR93 track obliquity with respect to the major axis of seafloor spreading related features. Spreading rate estimates of 9 and 10 mm/yr from modelling of sea surface anomalies were proposed by Whitmarsh and Miles (1995) for the Iberia Abyssal Plain and Tagus Abyssal Plain, respectively.

The inverse modelling and analyses presented earlier in this Chapter have yielded the following spreading rates, times and positions for the onset of steady state seafloor spreading; either (1) 10 mm/yr starting 124.7 Ma and at the position of the westward limit of M2(N; Fig. 6.1), or (2) 10 mm/yr starting 126.1 Ma, immediately west of R3 (Fig. 6.1). Under conditions of varying spreading rate, it is possible that seafloor spreading started ~10 km east of R4 128.2 Ma at 8 mm/yr, although Euler and magnetic boundary evidence suggest that 127.7 Ma at 8 mm/yr is a better estimate.

Because the inverse analyses implemented so far cannot resolve very short reversal sequence blocks (<5 km width) an alternative and common way of analyzing seafloor spreading magnetic anomalies over a region is to correlate peaks and troughs from track to track and compare them with theoretical anomalies generated from models of constant spreading rate, i.e., forward modelling. This method has provided the means of deriving some North Atlantic plate kinematic models (e.g. Masson and Miles, 1984) and has been used to determine the ages of onset of seafloor spreading, for example in the Labrador Sea (Srivastava and Roest, 1995). In the southern Iberia Abyssal Plain, gridded magnetic anomalies with good track control allow modelling with a higher degree of accuracy; rather than correlating track 'wiggles' of varying amplitude, the contoured chart, in which amplitude is represented by colour, can be used instead. This also eliminates problems associated with the extremely high amplitude of the J anomaly. Forward models, however, suffer from inherent non-uniqueness, and their interpretation generally suffers from a lack of objectivity.

Figure 6.10 shows that, west of R3, a spreading rate of 10 mm/yr rather than rates of 8 mm/yr and/or 6 mm/yr is more favourable; anomalies aM3(R), aM2(N) and aM1(R) are discernible and match well with the same theoretical anomalies, whilst aM1(N) and aM0(R) are obscured by the J anomaly. At and north of 40°30'N, in the vicinity of the ODP drilling transect (Whitmarsh et al., 1998) where the identification of R4 is uncertain (see section 5.2.2), anomalies east of the northward projection of R4 cannot be fitted by seafloor spreading models. In contrast, at and north of 40°30'N anomalies in the region between R3 and R4 can be satisfied by seafloor spreading models with spreading rates of 10 or 8 mm/yr.

South of 40°30'N, near to and in the vicinity of the IAM-9 transect, observed sea

surface anomalies can be explained by seafloor spreading at rates of 8 mm/yr as far east as ~12°30'W and as far west as the southern end of R3. In addition, anomalies in the region 12°30'W to 11°20'W can be explained by seafloor spreading at rates of 6 mm/yr. Most anomalies, and in particular the higher amplitude positive anomaly, aX(N), here assumed to be associated with the combined effects of M11A(N) and M12.1(N; Figs. 2.1 and 6.10), show little isochron parallel continuity but are instead sub-circular. The exceptions are a positive anomaly, aY(N), here assumed to be associated with the effects of M16(N), and a negative anomaly, aZ(R), here assumed to be associated with M17(R; i.e. aM16(N) and aM17(R), respectively) which exhibit linearity as far south as ~39°25'N where the effects of Estremadura Spur disrupt its continuity.

In the Tagus Abyssal Plain similar magnetic anomaly features to those in the southern Iberia Abyssal Plain are observed. West of ~12°W observed anomalies can be explained by seafloor spreading at a rate of 10 mm/yr, as previously determined by Pinheiro et al. (1992). Anomaly aM3(R) and anomaly aX(N) are linear and continuous features, whilst most other anomalies have little continuity in any direction. East of ~12°W, and as far east as 12°15'W, observed anomalies match well with theoretical anomalies derived from a seafloor spreading model at a rate of 6 mm/yr. Anomalies aY(N) and aZ(R) can be identified as linear features from 38°N to 37°N. Further support that these two anomalies (at 12°30'W and 12°15'W) are in fact aM16(N) and aM17(R), respectively, comes from their left lateral offset between the TAP and the IAP; the amount of offset (~40 km) is equal to the offset of the early M-series anomalies and the J anomaly which are identified with confidence.

If the anomalies are correctly identified the implications associated with these new magnetic anomaly identifications are very significant; they suggest a steadily increasing spreading rate from 6-10 mm/yr. The location of the onset of seafloor spreading south of ~40°30'N is displaced eastwards from previous estimates (Whitmarsh and Miles, 1995; Whitmarsh et al., 1996a). Hence, the distance between the first (i.e. most landward) seafloor spreading anomaly (aM17(R)) and the assumed most seaward continental crust, i.e. the ocean-continent transition zone, appears to be in the range 40-60 km in the region south of ~40°45'N, and in the range 20-30 km in the region north of 40°45'N adjacent to Galicia Bank. In contrast, seismic measurements have yielded OCT widths of 130 km (Pickup et al., 1996) and 170 km (Dean et al., submitted) along the IAM-9 profile (40°20'N), and at least 40 km along the ODP drilling transect (40°40'N; Chian et al., in press). In addition, if the newly calculated OCT width of ~40-60 km is also present in the Tagus Abyssal Plain an estimated position of the most seaward continental crust may be made (see Fig. 6.10).

The hypothesis that the peridotite ridge marks the landward limit of oceanic crust is not entirely supported by the work in this section. However, certainly within the southern Iberia Abyssal Plain, its position does represent the most landward location where relatively continuous, linear parallel magnetic anomalies occur. These anomalies can be explained by seafloor spreading models at rates of ca. 10 mm/yr; east of R3, anomalies are scarcely aligned in an isochron parallel direction but can be explained by 2-D seafloor spreading models at rates of less than 10 mm/yr. An eastward progression is accompanied by a decrease in spreading rate from 10 mm/yr to 8 mm/yr to 6 mm/yr. The peridotite ridge is therefore significant in that it may be present at the location where the spreading rate increases to 10 mm/yr, i.e. from ultra-slow to slow, rather than at the onset of seafloor spreading. In addition, this may provide a means of speculating about the position of a further peridotite ridge segment within the Tagus Abyssal Plain (Fig. 6.10).

6.3.2 Apparent timing

The timing of the initiation of seafloor spreading is one of the most important pieces of information that can be used to understand the development of the continental margin and the processes occurring between continental rifting and steady-state seafloor spreading. Models indicate that melt production is highly dependant on rift duration (see Chapter 1) and therefore a lower age bound provides a means of determining the time at which rifting processes subsided and gave way to seafloor spreading processes.

Based on the models of section 6.3.1, the presence of anomaly aZ(R), assumed to be aM17(R), in the southern Iberia Abyssal Plain suggests that seafloor spreading was active ~141 Ma. However, between aM17(R) and the approximate position of R3, spreading rate increases and the velocity structure does not resemble that of 'normal' Atlantic oceanic crust. Therefore, the basement cannot be assumed to be the product of a steady-state seafloor spreading process. Steady-state seafloor spreading can be assumed to commence at approximately the beginning of, or in the first half of, CM3(R; ~126.5 Ma), based on all the available modelling evidence to date (Whitmarsh et al., 1990, 1996; Whitmarsh and Miles, 1995; this study).

Not unlike anomalies aY(N) and aZ(R), some observed anomalies immediately predating CM3(R) can be explained by seafloor spreading blocks. However, most models require that the peridotite ridge segment R3 be non-magnetic, relative to its surroundings. Thus, the peridotite ridge may be a relatively non-magnetic body which was emplaced by later

horizontal extension or mechanical intrusion. Anomaly aX(N) can be successfully modelled as aM11A(N) and aM12.1(N) in the vicinity of IAM-9, and aM5(N) and aM5(R) can be successfully modelled on profile TOBI91. Seafloor spreading processes may therefore have been active at ~128 Ma and ~134 Ma in the northern and southern parts of the study region, respectively. Such timing for onset of seafloor spreading is compatible with the northward propagating rift model (Whitmarsh and Miles, 1995)

Based on forward models presented sections 6.2.1 and 6.2.2 (this section) only, the location of the onset of seafloor spreading may therefore be some 85 km further east than previously estimated in the Iberia Abyssal Plain and Tagus Abyssal Plain. However, as mentioned earlier, more than one change in spreading rate is not consistent with a steady-state seafloor spreading model. In addition, the velocity structures along IAM-9 and CAM-144 are incompatible with basement of oceanic origin (Fig. 6.2); only the top 3 km of basement, represented by the high velocity-gradient layer (Dean et al., submitted), fits within the velocity bounds of Atlantic oceanic crust (White et al., 1992). However, this may simply reflect the presence of fractures and voids in the upper layer. Dean et al. (submitted) do suggest, however, that a further 1.5 km of melt may be present within unaltered mantle peridotite to account for their high velocity, lower layer, although they favour a model of serpentinized mantle peridotite with no melt.

At first sight the seismic data of Dean et al. (submitted; Fig. 6.2b) and their subsequent review of expected melt volumes at the West Iberia margin, and the magnetic interpretation of this section do not agree. Moreover, estimated depths from Euler and spectral analyses suggest that magnetic sources within the southern region of the OCT are present at sub-basement depths of ~6 km. As indicated by Euler solutions along SAR95 (Fig. 6.6), magnetic sources which are present at the top of basement dominate the westernmost ~30 km of the OCT , whereas the deeper sources dominate the remainder of the OCT. Therefore, I suggest that the upper layer of Dean et al. (submitted) cannot be a major contributor to the magnetic field.

Because many geological processes that occur at ultra-slow spreading rates have been shown to be significantly different from those occurring at spreading rates >10 mm/yr (e.g. Bown and White 1994; Muller et al., 1997), the results presented so far do not rule out an oceanic origin for the basement in the OCT. If oceanic crust is assumed, the across-margin changes in spreading rate necessarily imply that non-steady-state seafloor spreading conditions prevailed and happened partly at ultra-slow spreading rates. Further discussion concerning the significance of these results is addressed in sections 6.4 and 6.5.

6.3.3 The J anomaly

The J anomaly obscures the latest M-series anomalies making their identification slightly problematic. However, J appears to be present at the position of aM1(R) at ~37°30'N, at the position of aM1(N) at ~38°N, and at the position of aM0(R) at ~40°30'N (Fig. 6.10). This suggests that although very nearly an isochron, the regional strike of J cross cuts the regional strike of the M-series anomalies and gets younger northwards such that regionally J trends ~10° west of the M-series anomalies. However, J is present in three en-echelon left lateral segments, each of which is locally parallel to the M-series lineations.

In addition to the northward younging of J, any model explaining its origin must also explain its anomalously high amplitude and its northward termination at ~41°N. Under the previous assumption of an isochron parallel J anomaly, Whitmarsh and Miles (1995) showed that its termination can be explained by the propagating rift model, where presumably the source of the J anomaly was similar to the source of the seafloor spreading lineations. However, this model does not explain the diachronous nature of J.

To explain the diachronous nature of J, I propose that the J anomaly is a feature derived from a point source. Figure 6.11 shows three possible scenarios in which a point source is stationary, migrating south, and migrating north as the rift system propagates northwards. Only a source whose northward propagation rate is greater than that of the rift propagation can explain the observation of the termination of J at ~41°N; the J source propagation rate of ~110 km/Ma (110 mm/yr) is approximately twice the rate of rift propagation under the assumption that seafloor spreading initiated ~133 Ma in the Tagus Abyssal Plain (Pinheiro et al., 1992) and ~127 Ma in the Iberia Abyssal Plain. It is also about 10 times the spreading rate. The migrating point source must however, cease to be active once it coincides with the tip of the propagating rift. One tentative explanation might be that the relatively 'cold' nature of the continental crust reduced, and in fact stopped, melt production by the J anomaly source.

The high amplitude of J can be modelled reasonably well by a crustal layer of anomalously high magnetization (e.g. 4 A/m; Fig. 6.4) and/or increased thickness, as suggested by Tucholke and Ludwig (1982). Even so, the J anomaly is as enigmatic as ever and it is not within the scope of this thesis to explain its origin, other than to further constrain its age and provide a speculative model for its possible formation.

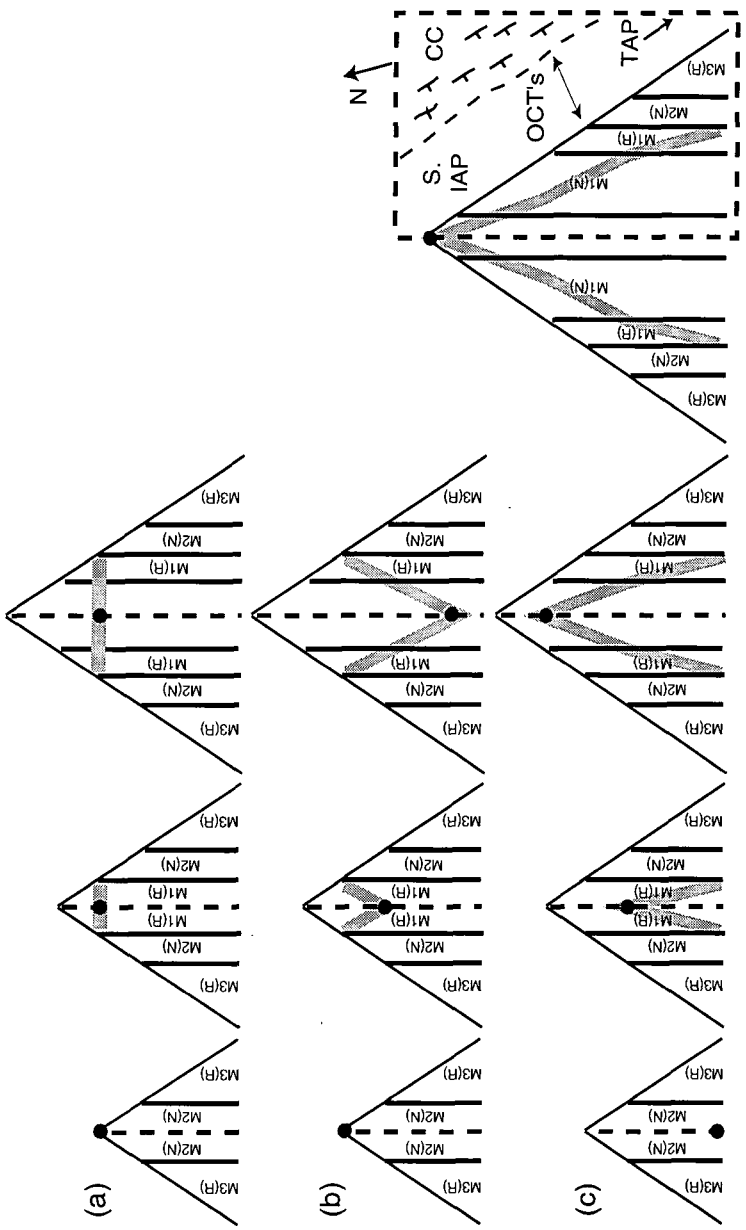

Figure 6.11 Schematic representations of the geometrical relationship observed between the M-series seafloor spreading magnetic anomalies, the J-anomaly and the continental margin offshore West Iberia. Each model is given within the context of a propogating rift scenario for margin development (Whitmarsh and Miles, 1995). Black circle marks the location of J-anomaly source; thick grey line marks the J-anomaly itself whilst the rift propogates northwards. Seafloor spreading blocks labelled, and mid-ocean ridge axis as dashed line. The J-anomaly source initiated at the start of CM1(R) in all models. (a) The J anomaly source as a stationary point source initiated at the continental margin; (b) Point source migrating southwards and initiated at the continental margin; (c) Point source migrating northwards at a rate greater than the rate of rift propogation, and starting at the ridge axis. Only model (c) explains the observed geometry offshore Iberia (see box; CC=continental crust; S. IAP=Southern Iberia Abyssal Plain; TAP=Tagus Abyssal Plain).

6.4. Geological nature of magnetic sources across the continental margin

Here I discuss the possible geological nature of the sources of magnetic anomalies across the West Iberia continental margin. In particular, I address the results in context with the results of seismic studies and drilling results. Models of margin development are discussed in section 6.5.

6.4.1 Thinned and extended continental crust

The region seaward of the continental slope, consisting of rotated fault bounded blocks observed on MCS profiles IAM-9, LG-14 (Pickup et al., 1996; Pickup, 1997), LG-12 (Beslier et al., 1993), CAM-146 and CAM-144 (Fig. 2.5) is interpreted to be thinned continental crust (Fig. 5.2). Pickup et al. (1996) also suggest that a strong reflector, M, on profile IAM-9 (Fig. 6.12), which rises from ~14 km to ~12 km depth (B/L.) over ~35 km probably represents the seaward shallowing of the Moho, which together with the concurrent seaward decrease in fault block size, is strongly indicative of a crust thinning from ~10 km to ~4 km. Furthermore, in the same region Pickup et al. (1996) identify top-to-the-west normal faults, for example D (Fig. 6.12), which continue almost as deep as the M reflector and are likened to reflectors H and L on LG-12 (Krawczyk et al., 1996) and the S-reflector off Galicia Bank (Winterer et al., 1988; Reston et al., 1995; Reston, 1996) all three of which are interpreted to be intra-continental detachment faults.

Seismic velocities obtained from wide-angle seismic experiments suggest that the eastern end of refraction line CAM-144 and the northern ends of refraction lines CAM-134 and CAM-136 (Chian et al., in press; see Fig. 2.5) are underlain by continental crust, thinned to only ~2 km. Dean et al. (submitted) show that their seismic velocity profiles at the eastern end of IAM-9 are consistent with the thinned continental crustal origin proposed by Pickup et al. (1996) on the coincident MCS profile (Figs. 6.2 and 6.12). Refraction Line 1 of Whitmarsh et al. (1990; Fig. 2.5), which intersects IAM-9 west of the proposed seaward extent of continental crust (see above), has also been interpreted to overlie thinned continental crust. However, a reinterpretation of the velocity model with the newer findings in mind suggests otherwise (see section 6.4.2); I interpret only the northern third of the profile as thinned continental crust. From the seismic data alone the location of the seaward extent of thinned continental crust is reasonably well constrained, at least along and between closely spaced seismic profiles.

Results from ODP Leg 149 and Leg 173 are largely consistent with the seismic

interpretation of the seaward extent of continental crust (Figs. 2.4 and 2.6). Continental crust had to be inferred at Sites 901, 1065 and 1069 since crystalline basement rocks were not cored; the overlying sedimentary rocks have features indicative of continental crust (Whitmarsh et al., 1998). Shallow water (few hundred meters) Upper Jurassic (Tithonian) sedimentary rocks in the deepest cores at Sites 1069 and 1065 indicate that the basement under both Sites is continental in origin (Sawyer et al., 1994; Whitmarsh et al., 1998). Moreover, assuming isostasy the Sites were necessarily underlain by only slightly thinned crust in the Tithonian. At Site 1069 a thin layer of shallow water limestone clasts is overlain by a clay which is very similar to that encountered at Sites 901 and 1065 (and therefore Tithonian (?) in age). The clay is overlain by a slumped nanofossil chalk (Upper Berriasian-lower Valanginian; ~137 Ma) whose assemblage indicates an outer shelf-slope depositional environment. However, the chalk may not be *in situ*. Nevertheless, Whitmarsh et al. (1998) suggest that the crust beneath Site 1069 is continental.

Results from Sites 900 and preliminary results from Sites 1067 and 1068, all of which lie within 1.4 km of each other on the same basement high (named Hobby High) and all of which penetrated crystalline acoustic basement, may suggest that basement here is also continental in origin. However, there is still much debate as to the origins of the cored rocks on 'Hobby High' and discussion of this subject is left until the next section.

The results of analyses presented in Chapter 5 successfully discriminated continental crust from basement to the west assumed to be part of the OCT. Source depths in continental crust derived from Euler deconvolution of the magnetic field between 9°W and 11°W (region S1; Fig. 2.7), and over the southern part of Vasco da Gama seamount, are broadly distributed in depth. In plan view the sources generally either possess no dominant trend or are point-like in nature. Their scaling nature is consistent with models of crustal susceptibility (values 2-3). Reduced-to-the-pole anomalies (Fig. 2.8) over the continental crust and are in fact only moderately lineated in a 350° direction, most of which occur at the westernmost edge of inferred continental crust with amplitudes of ~-125nT to 25nT. Anomalies over the continental shelf and over topographic highs, for example Galicia Bank (which includes Vasco da Gama seamount and Vigo seamount), Estremadura Spur and Tore seamount are generally sub-circular with positive amplitudes of typically 200 nT, very similar in character to those over the Iberian mainland (R.Macnab, pers. comm.).

The position at which anomaly trends change from ~350° to 010° (11°15'W; Whitmarsh and Miles, 1995) does not coincide exactly with the edge of the continental crust determined from seismic and drilling results; the easternmost region of the OCT (region TE;

Fig. 2.8), some 50 km wide at the position of IAM-9, possesses a magnetic character similar to that of the westernmost thinned continental crust (region CW; Fig. 2.8). Moreover, lineated anomalies in the OCT, in particular aZ(R), continues as far north as Site 1065, i.e. ~33 km north of, and ~50 km east of the suggested continental limit (Fig. 6.10). It is therefore unlikely that a distinct discontinuity in magnetic character occurs at the proposed edge of the continental crust. This may suggest that the sources of anomalies are in fact beneath the thinned continental crust and lie within the mantle; this agrees with source depths derived from Euler deconvolution (sections 5.3.1 and 5.3.2).

The origin of the lineated anomalies within the westernmost thinned continental crust (region CW) and easternmost OCT (region TE) are therefore likely to be related, possibly a result of the same phenomenon. Moreover, these anomalies are likely to be different in nature to those that exist over thicker continental crust (region CE; Fig. 2.8), including those over the Iberian mainland, because of their difference in amplitude and shape (R.Macnab, pers. comm.). The linear nature of the anomalies in region CW has previously been proposed to be the result of linear basement relief resulting from normal faulting within the context of a propagating rift model (Whitmarsh and Miles, 1995; see Chapter 2). However, because the anomalies within region CW also occur within region TE (the easternmost OCT), and are similar to those in the majority of the OCT, in amplitude and wavelength, but not trend, the sources of these anomalies may be more akin to those of the OCT (see next section).

To conclude, magnetic anomalies over the region inferred to be thinned continental crust (from drilling and seismics) have their sources beneath the base of, or deep within, thinned continental crust. I propose that sources of the same type exist within the eastern region of the OCT and therefore their origins are likely to be very similar.

6.4.2 The ocean-continent transition zone

RTP anomalies (Fig. 2.8) over the majority of the OCT trend at ~010°, parallel to the seafloor spreading anomalies yet oblique to those observed over thinned continental crust. Whitmarsh and Miles (1995) suggested that the sources of these anomalies were intrusive magmatic bodies, impregnated into continental crust under the same stress regime as that which accompanied oceanic crustal accretion. Since then however, the nature of the OCT has been proven to be unequivocally non-continental in nature, and in fact is probably unroofed and serpentinized upper mantle peridotite (Brun and Beslier, 1996; Beslier et al., 1996; Pickup et al., 1996; Discovery 215 Working Group, 1998; Chian et al., in press; Dean et al., submitted).

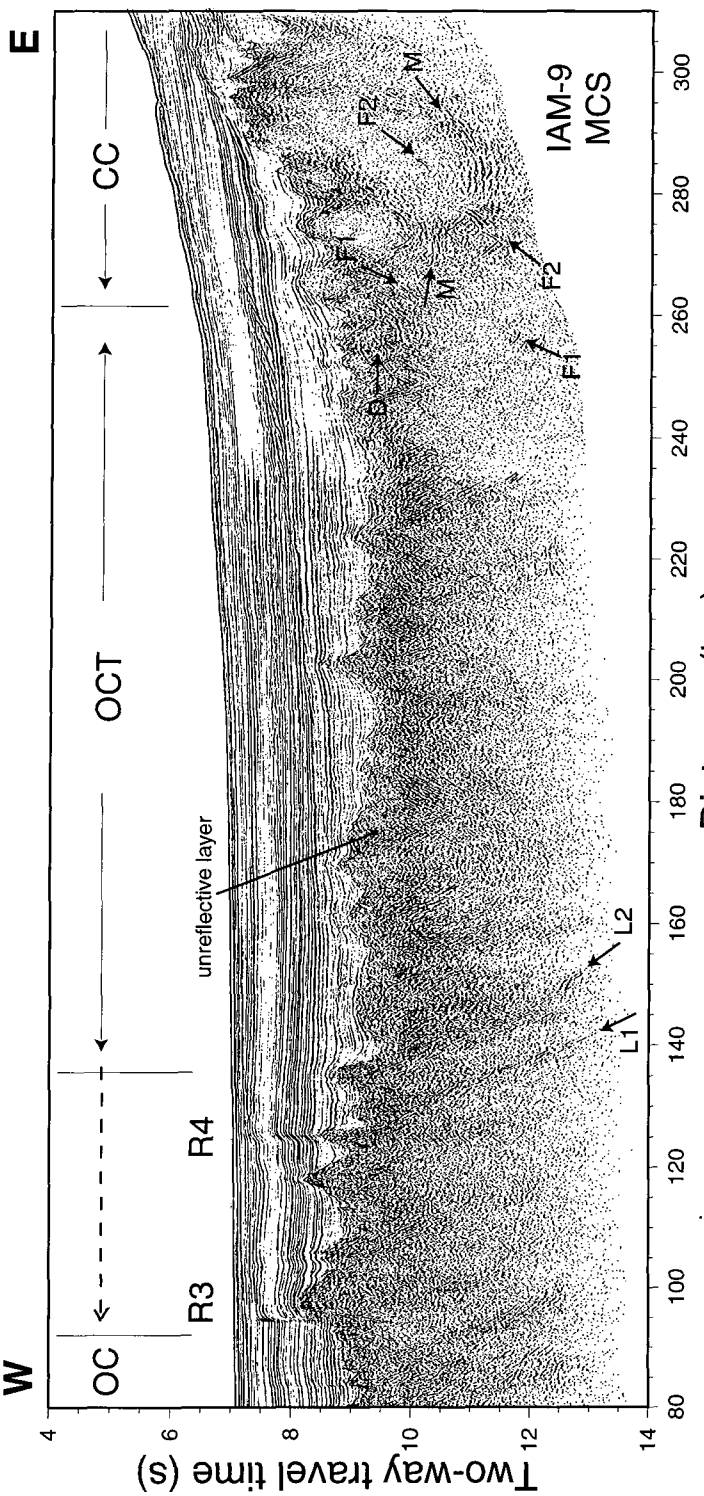

Figure 6.12 Multichannel seismic reflection profile IAM-9 (from Pickup et al., 1996) coincident with near-bottom magnetometer profile SAR95. The OCT is the region between continental crust (CC) and oceanic crust (OC) (although basement between peridotite ridge segments R3 and R4 exhibits a different relief and velocity structure; Fig. 6.2). Reflectors M and D are interpreted as the Moho and an intra-continental 'detachment fault', respectively, whilst reflectors L1 and L2 are interpreted as landward dipping faults which reach depths of at least 13 km (Pickup et al., 1996). Reflectors F1 and F2 are interpreted as faults which cut across the M reflector.

In section 6.3.1 I showed that some of the anomalies within the OCT can possibly be traced into and across the Tagus Abyssal Plain; these anomalies can be explained as seafloor spreading anomalies aM16(N) and aM17(R). Three-component magnetic profiles also show that the strikes of magnetic boundaries are in general consistent with those expected of seafloor spreading blocks (Fig. 6.7). Euler solution positions and local magnetization zero crossings, however, do not successfully retrieve the boundaries of reversal sequence blocks if seafloor spreading is assumed; in fact the results of Euler deconvolution support a model in which the depths of anomalies are up to ~5 km sub-top-basement, as does spectral analysis (see Chapter 5). But in addition, many other sea surface anomalies are only moderately lineated and cannot be explained by the reversal sequence.

In the next two sub-sections I suggest that the sources of the magnetic anomalies within the southern Iberia Abyssal Plain are (1) intrusive bodies at depths of up to ~5-6 km below the basement surface, and (2) serpentinization contrasts within upper mantle peridotite at the top of basement. Figure 6.13 shows, schematically, the possible mechanisms for generating the anomalies.

6.4.2.1 Magmatic intrusions

In the northern part of the southern Iberia Abyssal Plain, immediately south of Vasco da Gama seamount in the vicinity of ODP Sites 1065, 1067, 1068 and 900, the sources of linear reduced-to-the-pole anomalies in the upper mantle are continuous across the boundary between true sub-continental mantle, and mantle exposed within the OCT (Fig. 2.8). The most significant anomaly, possibly aZ(R), continues from a position ~8 km east of Site 1065 to ~39°30'N, an approximate distance of 115 km. Because the basement in the vicinity of Site 1065 is unequivocally thinned continental crust but further south it is unequivocally not continental crust, I propose that the source of this anomaly must originate within the upper mantle. It therefore cannot be a 'true' seafloor spreading anomaly source. In support of this argument is that in the vicinity of Sites 1069 and 900, Chian et al. (1998) found that continental crust was only ~2 km thick and thus very unlikely to produce any significant magnetic field.

The depths of linear magnetic sources within the OCT are derived from Euler deconvolution solutions (see Figs. 5.17 and 6.6). Taking the zonal nomenclature of Figure 5.2, those in zone C, the zone of subdued relief, are present at depths of ~11 km and ~13 km for structural indices of 1.0 and 1.5, respectively, and both at ~10 km and 16 km for a for

structural index of 2.0 (Fig. 5.17). If a combination of these realistic geometrical and geological models (dyke-, sill-like intrusions, intrusive cylinder; see section 4.2.3) exists, they all fall within ~7 km of the top of basement. Euler solutions in zone B, between peridotite ridges R3 and R4 where basement depths plateaus at ~7 km depth (see Fig. 5.2), show a bipolar distribution (Fig. 5.17) with solution foci ~5 km apart; for dyke- and sill-like geometries the upper set of solutions fall at top basement (~7 km depth). Solutions in zone A (oceanic crust) show a near-normal distribution clustering at the top of basement. The Euler solutions presented by Discovery 215 Working Group (1998) show such distributions along profile IAM-9, as does Figure 6.6, in part.

Comparing sensible estimates of scaling exponents, γ (derived from the modelling of power spectra; see Chapter 5) from the four regions (A, B, C and D) suggests that the anomaly sources within the OCT are more akin to those within oceanic crust created during a period within the anomaly 1-34 sequence (γ=1-2). Transition zone γ estimates are generally ≤ 2 whereas γ for continental crust is typically 2-3 and γ for CMQZ oceanic crust is $\cong 1$.

Based on all the evidence presented thus far, I propose that the sources of magnetic anomalies within the OCT are (a) syn-rift intrusions, and/or (b) intrusions associated with seafloor spreading. Further, because different magnetic analyses satisfy the conditions of both these scenarios, zones C, B and A represent a gradual progression from late-rift related magmatism (zone C; although, see section 6.5.3 for ages) to the organized oceanic 'block-model'-type section (zone A). The magmatic intrusions in parts of zone C and certainly those in zone B may be regarded as proto-oceanic-type bodies, because of their ability to satisfy seafloor spreading conditions, yet with poor continuity (e.g. Bonatti, 1985; see Chapter 7), and also show characteristics of those in zone C. The model presented here is consistent with geochemical models in which a temporal progression from early lithosphere-dominated magma sources to later asthenosphere-dominated sources is observed within rift zones (Wilson, 1989; Lavecchia and Stoppa, 1996; see section 1.1). This may be explained in terms of increasing degrees of partial melting and increasing rates of crustal extension and mantle upwelling (Bown and White, 1995).

In order to 'groundtruth' the magnetic interpretation, the preliminary interpretations of Sites 1067 and 1068, and the results of Site 900 are considered. These Sites represent the only locations in the southern Iberia Abyssal Plain where a significant proportion of mafic material was cored. However, as previously mentioned, the geological nature of the basement high over which Sites 1067, 1068 and 900 lie ('Hobby High') is not fully understood. A summary of the relevant evidence for the origin of 'Hobby High' is given below.

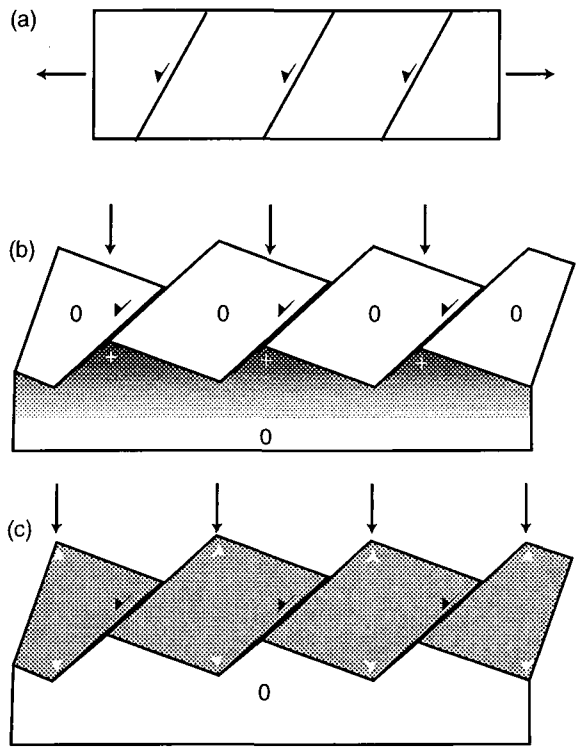

Figure 6.13 Schematic cross sections showing potential mechanisms by which linear magnetic anomalies are generated by serpentinized upper mantle and/or extended continental crust. 0's designate relatively non-magnetic parts of the model; +'s and shaded regions mark parts of the model which are relatively highly magnetic (normal or reversed). Arrows mark position of RTP anomaly maxima or minima. Anomalies are linear in a section-normal direction providing faults are lineated. (a) Crustal section prior to extension during 'domino' style faulting and rotation, ignoring problems associated with keels. (b) Relatively non-magnetic continental fault blocks are thinnest over most shallow, and therefore most serpentinized parts of upper mantle. Anomalies result from relative *distances* to sources. (c) Homogeneous continetal crust is extended above unserpentinized, and therefore relatively non-magnetic upper mantle. Anomalies result from relative *thicknesses* of source layers.

Evidence for a continental origin comes from, (1) Tilted fault blocks (with the same character as those observed within unequivocal continental crust; Beslier et al., 1993) are observed on profiles LG-12 and CAM-144 (Fig. 2.5) and form 'Hobby High' and the basement high located ~14 km west, respectively, over which Site 1069 lies only 5 km to the north and has been inferred to be continental crust (see section 6.4.1); (2) Two N-S ridges that extend south of Vasco da Gama seamount, which is unequivocally continental in origin (Capdevila and Mougenot, 1988), align with the two basement highs over which sites 900 and 1065 were drilled (Fig. 5.2). Because the Site 1065 high is probably continental in origin (see section

6.4.1), it is not unreasonable to suggest that the Site 900 high is also continental in origin. (3) Zircons from a vein of tonalite gneiss intruded into amphibolite at Site 1067 have recently been dated, by U-Pb methods, as Variscan in age (R.B. Whitmarsh, pers. comm.).

Evidence to suggest a non-continental origin comes from, (1) Gabbros cored at Site 900 have epsilon Nd values in the range +6 to +11 indicative of a MORB type source with subsequent seawater alteration (reflected in the Sr isotopic ratio; Seifert et al., 1997). Their major element compositions and low incompatible trace element content suggest they formed as cumulate gabbros and their REE patterns resemble those of cumulate gabbros from 26°N along the MAR (Seifert et al., 1997); (2) The gabbro has been dated, by Ar^{40}/Ar^{39} dating of feldspars, at ~136 Ma (Féraud et al., 1996), which together with petro-structural constraints (Cornen et al., 1996) has been used to infer a syn-rift origin. Alternatively, and more likely because the Ar^{40}/Ar^{39} date only corresponds to the closure time of feldspar (at approximately 280°C), this represents the time when the gabbro was exhumed above the 280°C isotherm, and therefore represents the minimum age of the gabbro. (3) The tonalite gneiss cored at site 1067, which could equally be named a plagiogranite (Streckeisen, 1976), together with the presence of epidosite (Site 1067), which probably lies stratigraphically above the cumulate gabbro at Site 900, suggest that the rocks here might be oceanic in origin. However, this is by no means conclusive and furthermore, no extrusive rocks were cored.

The conflicting drilling results presented above cannot be further resolved from the seismic refraction experiment of Chian et al. (in press; Fig. 2.5); Site 900 falls approximately midway between two OBS instruments, one of which (OBS 6) has been interpreted to overly thinned continental crust ~7 km to the north of the Site, the other (OBS 7) which indicates a basement origin of serpentinized upper mantle some 12 km south of the Site. Their velocity modelling cannot, therefore, discriminate against either of the two types of basement.

From the cores at ODP Sites 900, 1067 and 1068, there may be reasonable evidence to 'groundtruth' an accretionary/magmatic origin of the sources of magnetic anomalies within the OCT and beneath thinned continental crust. The quasi-oceanic origins of the mafic rocks on 'Hobby High', and a lack of extrusive rocks, provide potential evidence for the origins of the magnetic sources suggested (deep-seated intrusions). However, although the rock magnetization studies of the Site 900 gabbro remain unpublished, X. Zhao (pers. comm., 1994) has suggested that the average effective magnetizations of the gabbro are ~0.02 A/m. Although too low to explain near-bottom or surface magnetic anomalies of significant amplitude (~ 100 nT peak-to-trough), sufficient spread in the data might warrant the explanation of such rocks being the sources of magnetic anomalies. Similar MORB-like gabbros within layer 3 of oceanic

crust have been shown to be contributors to seafloor spreading magnetic anomalies; effective intensities of 0.5 A/m (Opdyke and Hekinian, 1967), 0.63 A/m (Irving et al., 1970) and ~1 A/m (Kent et al., 1978; Fig. 1.6) have been recorded. Dunlop and Prévot (1982), however assign magnetization intensities of ~1 A/m to isotropic gabbros yet assign only 0.2 A/m to cumulate gabbros.

Disregarding then apparent non-magnetic character of the Site 900 gabbro, gabbroic intrusions can provide the necessary magnetization contrast with unaltered peridotite to generate significant linear anomalies. Moreover, Harrison (1976) used spectral analysis to suggest that a deep source (oceanic layer 3?) contributes to seafloor spreading anomalies and therefore must retain a record of the field polarity. It is therefore possible that the gabbroic intrusions within the OCT can be modelled using the reversal sequence of Gradstein et al. (1994). There is therefore reasonable evidence to suggest that the modelling of seafloor spreading anomalies across the OCT is also consistent with the origin of sources suggested here.

6.4.2.2 Serpentinized peridotite

Intrusive magmatic bodies more likely account for the lack of correlation (or anti-correlation) between observed anomalies and those generated by basement topography, than sources which are assumed to be serpentinized peridotite (Fig. 6.13). If magnetic sources were serpentinized peridotite the existence of basement faults with lengths approximately equal to the lengths of anomalies would be a condition of the model. Continuous linear basement topographic variations, i.e. scarps, and sub-basement faults do not exist on scales equal to those of the anomalies (up to 100 km in length). However, shorter and sub-circular anomalies may possibly be caused by serpentinization variations along faults, and in general by homogenous seawater circulation throughout the uppermost exposed layer of peridotite (see section 6.4.2.2).

A logical argument, together with the results of studies at ODP Sites, suggests that some of the sources of magnetic anomalies in the southern Iberia Abyssal Plain might be strongly associated with the process of serpentinization of peridotite. Magnetite, the most common carrier of magnetism, is a common product of the reaction between olivine and/or pyroxene and water, under the required conditions for serpentinization to take place. Coleman (1971) has shown that magnetization intensities of serpentinization products are strongly related to the degree of serpentinization. Moreover, serpentinite density exhibits an inverse

relationship with the logarithm of magnetic susceptibility ($\rho \propto 1/\log K$) although the relationship is most reliable for serpentinized harzburgites and the susceptibility can vary by a factor of 10 at a given density. Because the density of a serpentinized peridotite is inversely proportional to the degree of serpentinization, it follows that the most magnetic serpentinized peridotites are those which have the lowest density, which are more likely to be at the highest basement levels.

Geophysical evidence strongly suggests that mantle rocks, unroofed during the formation of the West Iberian continental margin, were exposed at the seafloor, in a zone possibly 170 km wide, which underwent serpentinization by seawater circulation, everywhere, on a large scale (Beslier et al., 1996; Pickup et al., 1996; Pickup, 1997; Discovery 215 Working Group, 1998; Chian et al., in press; Dean et al., submitted). Moreover, Chian et al. (in press) and Dean et al. (submitted) have shown that the uppermost layer of basement has seismic velocities as low as ~4.5 km/s (Fig. 6.2c) which correlate with peridotite serpentinized up to 95% (Christensen, 1966, 1972). Such rocks were in fact cored at Sites 897, 899 (Sawyer et al., 1994) and 1068 (Whitmarsh et al., 1998), and these rocks were found to have average effective magnetizations of 0.74 A/m (at Site 897) and 1.47 A/m (at Site 899; Zhao et al., 1996). It is therefore plausible to suggest that a highly magnetic layer is present at, or close to, the basement surface throughout the OCT, and that this layer is responsible for the magnetic anomalies in the OCT of the southern Iberia Abyssal Plain.

Although my interpretation of the anomalies within the OCT does not exclude such a source for localized anomalies, there are arguments to suggest that this process is unlikely to contribute to the source of the majority of linear anomalies within the OCT:

(1) Uniform homogeneous/pervasive serpentinization of the upper basement, by vigorous seawater circulation to depths of ~2.5 km as suggested by Pickup (1997) and Pickup et al. (1996), would lead to a uniformly magnetized basement surface. With high magnetization intensities (> 1 A/m) as sampled at Site 899, such a layer would give rise to significant magnetic anomalies that would correlate well with basement relief. Synthetic basement relief, with wavelength and amplitude variations similar to those observed in the OCT (Fig. 5.2), produces anomalies with peak-to-trough amplitudes in excess of 50 nT (Fig. 3.11). However, no such correlation exists on any wavelength scale (Fig. 5.8).

(2) Localized serpentinization controlled by fluid flow preferentially along linear fault zones would create linear magnetic anomalies because a magnetization contrast between a highly magnetic fault zone and unaltered or uniformly altered (including point (1)) mantle would exist. However, inspection of very many closely spaced MCS lines suggests that individual faults can

rarely be traced laterally for more than 10 km. The linear anomalies within the OCT are continuous for many tens of kilometers and are unlikely to be related directly to specific faults or fault zones. Moreover, the characteristics and spatial relationship of some anomalies allows them to be traced in and across the Tagus Abyssal Plain (e.g. aMY(N) and aZ(R); Fig. 6.10).

(3) Source depths of up to ~5 km beneath the basement surface are unlikely to be associated with the most serpentinized, and therefore most magnetic, peridotites. Site 897 oxygen isotopes strongly suggest that serpentinization has occurred at temperatures < 200°C and by the downward throughput of seawater (Agrinier et al., 1996), implying that in general, the highest magnetization intensities will be found at the basement surface.

(4) If the serpentinization process was instead chaotic, i.e. random spatial distribution, and/or the assumption that the degree of serpentinization is related to magnetization intensity is incorrect, the pattern of magnetic anomalies would also be chaotic. Although some sub-circular anomalies do exists, this process cannot account for the presence of linear RTP-anomalies which are parallel to the seafloor spreading anomalies (Fig. 2.8).

In general, I do not support a model of serpentinized peridotite as the main source of deep-seated linear magnetic anomalies in the southern IAP. However, serpentinites may be the source of anomalies in two specific cases: (1) The anomalous magnetic high near to Sites 899 and 898 (which is in fact two magnetic highs; Whitmarsh et al., 1996; Fig. 6.14) is a likely candidate for a serpentinized peridotite origin because (a) high magnetization (1.47 A/m) of the Site 899 cores, (b) its relatively short continuity and anomalous trend at wavelengths >~30 km, but very high amplitude and point like on scales <~10 km. Indeed, the locations of the ODP Sites (899 and 898) were chosen in such a way to sample the potential source of the corresponding single sea surface anomaly, which is atypical of the sources within the OCT and is therefore not surprisingly unrepresentative of the OCT. (2) In addition to the usual sources of seafloor spreading magnetic anomalies (i.e., adjacent blocks of opposite polarity in the crust), serpentinites probably contribute significantly to the marine magnetic anomalies, as has been suggested by many studies (e.g., Kent et al., 1978; Dunlop and Prévot, 1982; Harrison, 1987; Nazarova, 1994; Dyment and Arkani-Hamed, 1995; and others); Site 1070 also provides direct evidence. There, magnetizations as high as 0.5 A/m were recorded through ~39 m of cored serpentinized peridotite whose VRM inclinations of 46° suggest they contribute strongly to the seafloor spreading anomalies (see Table 6.1). Although only based on the initial reports (Whitmarsh et al., 1998), the serpentinized peridotites at Site 1070 are not similar to those cored at Sites 897 and 1068. This may suggest that because the serpentinites are different in nature, origin and evolution, those within the OCT do not contribute to the magnetic field as

those beneath Site 1070 do.

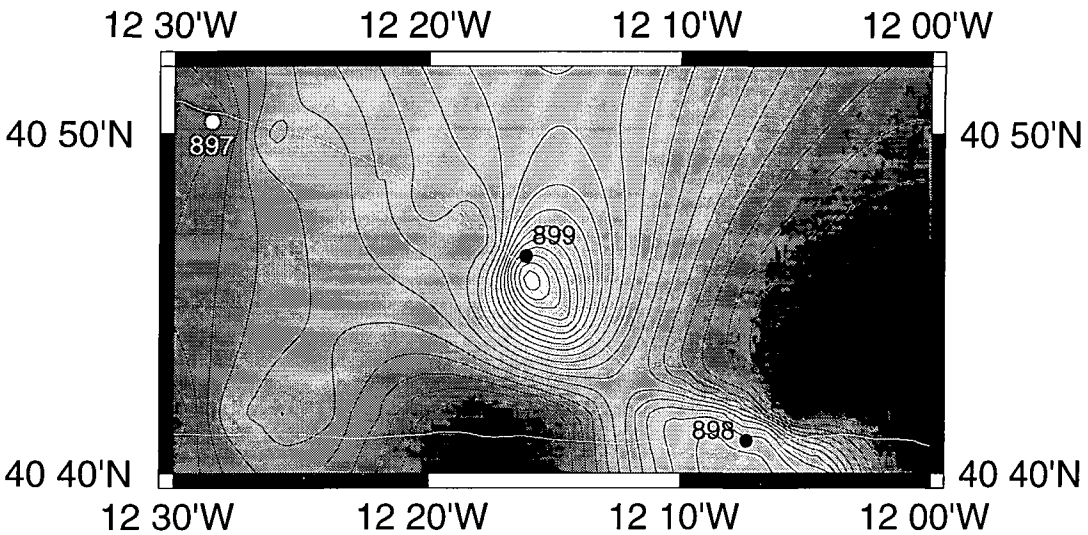

Figure 6.14 Magnetic anomalies from near-bottom profiles TOBI91 and SAR93 (tracks indicated by white lines) contoured at 50 nT in the vicinity of ODP Sites 897, 898 and 899. A d.c. shift was applied to the magnetic field along profile SAR93 in order to eliminate a mis-match in anomalies at the line crossing (east of Site 898). The single sea surface anomaly is represented as two individual anomalies at near-bottom altitudes. Their anomalously high amplitude and point like nature indicate that their sources might be atypical of those in the remainder of the OCT.

6.5 A composite model of upper mantle unroofing and magmatic accretion

I present a speculative model which is spatially and temporally consistent with evidence from other studies and forms a composite between the models of upper mantle unroofing (e.g. Brun and Beslier, 1996), serpentinization (e.g. Pickup et al., 1996; Discovery 215 Working Group, 1998; Dean et al., submitted) and rift-to-drift stage impregnation, intrusion and possibly extrusion of magmatic material into basement (Whitmarsh and Miles, 1995). The variation in source body depths and trends across the continental margin provides the basis for a model defined by spatial zones. Each zone has distinct characteristics that defines it from the others.

The plate tectonic significance of the model is discussed in Chapter 7, where parallels with the tectonic and magmatic processes that occur in the accretion of oceanic crust under at ultra-slow seafloor spreading rates are discussed. Similarly, the model also draws parallels

with the initiation of seafloor spreading observed at present in the Red Sea.

6.5.1 Margin-normal development

Although the actual sources of magnetic anomalies were not addressed quantitatively, Whitmarsh and Miles (1995) proposed the implementation of the propagating rift model of Martin (1984) to explain the organization and trends of the magnetic anomalies in the southern Iberia Abyssal Plain. Here this model is used to explain the new constraints from further magnetic analyses.

Continental rifting between West Iberia and Newfoundland occurred in three main phases, the first of which occurred in the Hettangian (~202 Ma; Gradstein et al., 1995) and the last, which eventually lead to breakup, occurred in the Lower Cretaceous (the exact times are discussed in section 6.5.3). The first two rifting phases, although not directly related to the eventual total lithospheric rupture and initiation of seafloor spreading, were probably instrumental in modifying the whole lithosphere for the final rifting stage, although for simplicity, their effects are not considered here. The discussion is primarily concerned with the final phase of rifting.

On the continental shelf and the mainland of Iberia (approximately east of 10°W), magnetic anomalies (R.Macnab, pers. comm.) and sources exhibit no significant and/or dominant trend. An estimate of the thickness of continental crust (defined by velocities and gradients) of ~25-30 km has been derived from a long wide-angle seismic experiment (Dean et al., submitted; Fig. 6.2)) along the coincident MCS profile IAM-9 in the southern Iberia Abyssal Plain, and it is therefore assumed that the crust here has undergone only slight amounts of thinning. Whitmarsh and Miles (1995) suggested that, based upon outcrops of Hercynian basement, any linear magnetic features, if they exist at all, will exhibit a variety of trends thus explaining the lack of any significant dominant trend and the abundance of sub-circular anomalies. Moreover, source characteristics suggest that magnetic sources are broadly distributed in depth, to perhaps 15 km depth (Fig. 5.17), and exhibit a scaling relationship typical of a nearly isotropic continental crustal susceptibility model.

In the region between ~10°W-11°15'W (in the vicinity of IAM-9) and between ~10°W-11°W (in the vicinity of the ODP drilling transect) magnetic anomalies show a dominant trend of ~350° (Fig. 2.8). This region is equivalent to the eastern zone of Whitmarsh and Miles (1995). In their model they suggest that the source of these anomalies arises from linear basement features within continental crust, which formed in response to tectonic stresses that

accompanied the northward propagation of the rift. However, such an explanation cannot explain (a) the computed depths of sources, and (b) how extremely persistent linear magnetic anomalies within the bulk of the OCT to the west, which is unequivocally non-continental crust, straddle the (well constrained; see section 6.4.1) seaward limit of continental crust with little change in character (amplitude or wavelength; Fig. 2.8). For the source of the anomalies to lie within the linear basement relief of continental crust, the sources would necessarily (a) be located at, or near to, top basement, (b) terminate, or be truncated, at the continental limit. Therefore, as explained in section 6.4.2.1, I infer that the sources of these anomalies are gabbroic type magmatic melt bodies that were intruded into the mantle under the stress conditions associated with the rifting stage of margin development. These intrusions are probably the first significant mantle melt derived products during the rifting process, since only small amounts of magmatism have been recorded on land in the Lusitanian Basin (Ribeiro et al., 1979; Martins, 1991). These intrusives have been shown to be transitional dolerites, gabbros and diorites and have been dated 130-144 Ma. The marine anomalies, however, do not parallel the trends of the mapped intrusive dykes (NNE-SSW and ESE-WNW), but nor do they parallel the seafloor spreading anomalies further west. Also the anomalies cannot be modelled as seafloor spreading anomalies (Fig. 6.10). The intrusive bodies are therefore very unlikely to be affiliated to any type of proto-oceanic process.

To explain the mismatch in the position of the seaward limit of thinned continental crust with the change in anomaly trends a dynamic model is required. Under the assumptions that the rheologies of continental crust and mantle are dominated by quartz and olivine, respectively, the lithospheric strength profile provides a simplified basis for understanding the behaviour of the lithosphere during the formation of the margin.

At the beginning of rifting, deformation of a four-layered brittle-ductile continental lithosphere is assumed to occur by bulk pure shear with localized simple shear occurring in the upper crust and upper mantle (e.g. Boillot et al., 1995; Brun and Beslier, 1996: Fig. 6.15). Continued extensional thinning of the crust and lithospheric mantle at extremely low rates (< 20 mm/yr; Pickup, 1997) results in the upward migration of the asthenosphere as well as the crust-mantle boundary until the entire continental crust and uppermost mantle are deforming entirely within the brittle regime (Bassi, 1995; Fig. 6.15). The extremely slow extension means that suppression of brittle deformation by rising hot asthenosphere does not occur due to heat loss by vertical and/or horizontal conductive cooling (e.g. Bown and White, 1995). However, as extension increases further, eventual decompression melting of the mantle occurs (Bown and White, 1995) and small amounts of melt rise upward due to their relative buoyancy. It is these

mantle-derived melt products that may form the 350° trending anomalies over the region of thinned continental crust (region CW) and in the easternmost OCT (region TE). Computed source depths do allow the intrusions to penetrate the thinned lower continental crust.

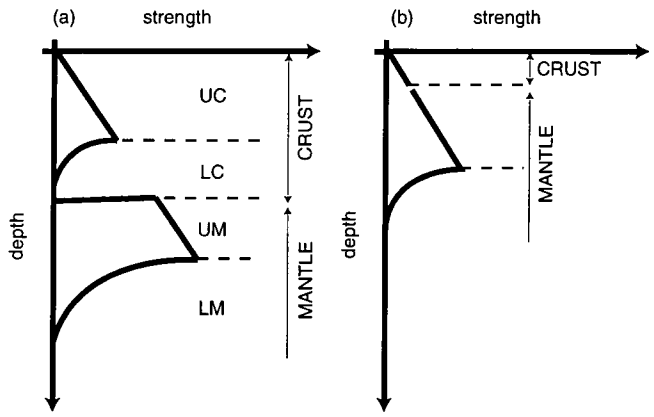

Figure 6.15 Schematic lithospheric strength profiles (not to scale) showing the strength envelope of a four-layered continental lithosphere at (a) the initiation of rifting and (b) at a subsequent time during rifting when continental crust has thinned to only a few kilometers. A prolonged period of rifting results in the exposure of upper mantle at the seafloor; prior to exhumation the entire continental crust and upper mantle deform entirely within the brittle regime. UC='brittle' upper crust; LC='ductile' lower crust; UM='brittle' upper mantle; LM='ductile' mantle.

During the period of crustal extension and mantle exhumation by brittle faulting (frictional sliding) the temporal and spatial activity of the faults, which for the purpose of this model are assumed to dip to the west and are assumed to be synthetic with the overall sense of motion, are likely to be the same as faults observed in other extensional terranes, i.e., fault motion youngs towards the centre of the rift, in this case westwards. This means that successive mantle rocks exposed in a westward direction across the margin become increasingly younger, in terms of the time at which they were exposed at the seafloor. This model may at first seem to be in disagreement with the interpretation of Pickup et al. (1996) who observe many landward dipping reflectors, especially at the western side of the OCT, along MCS line IAM-9 (Fig. 6.12). If the relative timing of these faults is such that they also become successively active in a westward direction, the model is still valid. However, since most tilted continental fault blocks show hanging-wall-to-the-west relative motion, and both the continental crust and upper mantle are deforming in the brittle regime, some faults may be

active through the crust-mantle boundary (e.g. on IAM-9 at 275 km, ~11 s twtt and at 245 km, 10 s twtt; Fig. 6.12).

During the exhumation and progressive faulting of the mantle, significant seawater penetration causes pervasive serpentinization (e.g. Gibson et al., 1996) of the uppermost layer of mantle. Pickup et al. (1996) suggest that the ~2.5 km unreflective layer observed on MCS profile IAM-9 may be a product of expansion and fracturing of mantle peridotite during vigorous convective serpentinization. Melt rising towards the surface from depth after serpentinization has occurred, is therefore halted beneath, or within the lowermost, serpentinite layer due its lack of relative buoyancy (e.g., Herzberg et al., 1983; Fig. 6.16), in much the same way that the denser melt products underplate the base of the continental crust at volcanic margins (White and McKenzie, 1989; Fig. 1.2a). Dean et al. (submitted) have shown that, by the reasoning of Hooft and Detrick (1993), a 1-2 km thickness of melt could theoretically exist at depths of ~3-4 km below the top of basement in their lower basement layer (7.3-7.9 km/s). They assume a basaltic melt density of 2.7 Mg/m^3, which is equivalent to seismic velocities of ~6 km/s (Carlson and Raskin, 1984). However, a melt density of ~3 Mg/m^3 equates to a seismic velocity of ~7 km/s, which would place the predicted melt within the interpreted magnetic source depth range and also be consistent with the seismic refraction model of Dean et al. (submitted; Fig. 6.2). Moreover, as pointed out by Dean et al. (submitted) although not favoured by them, their lowermost basement high velocity (7.3-7.9 km/s) layer can be explained by a thickness of ~1.5 km of melt added to fresh mantle peridotite, rather than the layer being composed of serpentinized peridotite. Homogeneous serpentinization of mantle to sub-basement depths of ~6 km is unlikely; Pickup et al. (1996) showed that only the uppermost 2.5 km of basement is likely to be pervasively serpentinized (their unreflective layer). Serpentinization to sub-basement depths of ~6 km is likely to be focussed along faults. An insufficient number of faults extend to such depths to warrant such homogeneous serpentinization. Moreover, since seismic velocity and degree of serpentinization are negatively linearly correlated (Christensen, 1966, 1972), a gradual increase in the degree of serpentinization would be reflected in a gradual decrease in seismic velocity. In fact, all the velocity profiles from the transition zone (Chian et al., in press; Dean et al., submitted; Fig. 6.2c) show a change in velocity gradient at ~3 km depth. Therefore, in my opinion, a model of intruded gabbroic material can better explain the seismic velocity and magnetic source depth observations, over a model of deeply, pervasively serpentinized mantle peridotite.

As the rift propagates northward, so does the locus of seafloor spreading activity. Therefore, further extension is coupled with a gradual shoaling of the melt zone, and an

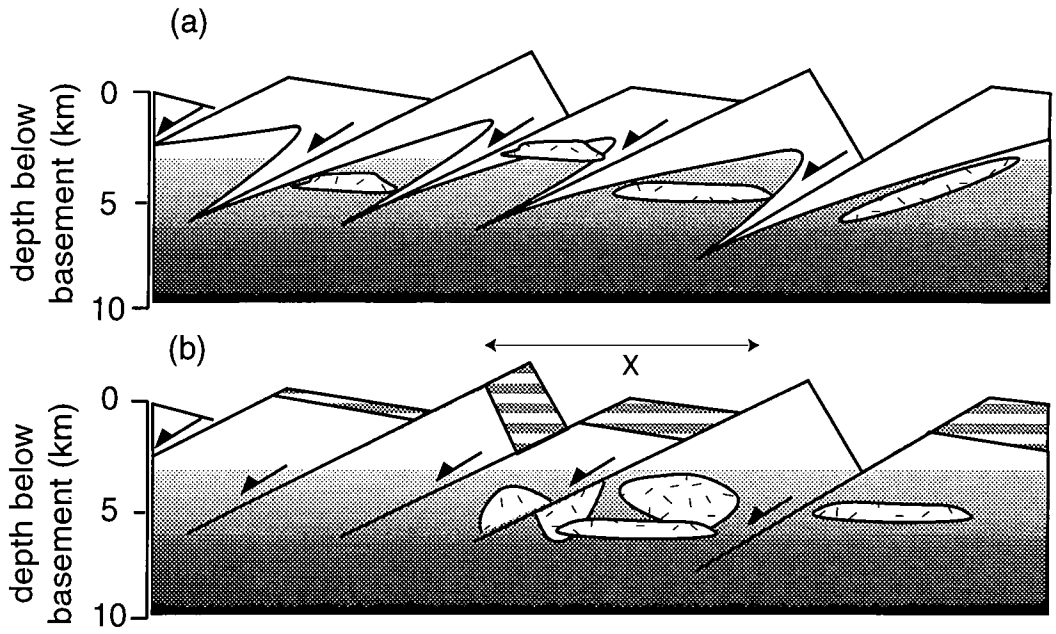

Figure 6.16 Illustrations showing two possible scenarios for the geological structure of the crystalline basement within the OCT in the southern Iberia Abyssal Plain. White = serpentinized mantle peridotite; dark grey = unaltered mantle peridotite; stripes = extrusive layer; dashed = gabbroic type intrusions. (a) Upper mantle is unroofed during prolonged tectonic extension and serpentinized by seawater circulation, pervasively in the uppermost 2.5 km, and locally along fault planes to depths of ~6 km (Pickup et al., 1996). Rising melt, generated by adiabatic decompression melting of the mantle, is halted and trapped below the uppermost highly serpentinized layer of lower density. (b) Thin and highly faulted igneous 'crust', similar to that forming at segment ends and/or at ultra-slow spreading centres (see text). In places, the extrusive and intrusive layers can be well developed (X; locally focussed melt) giving rise to significant magnetic signal resembling seafloor spreading anomalies.

increase in the focussing of melt, probably falling midway between rift related melting and mid-ocean ridge melting. These processes can explain the sudden change in trend of magnetic anomalies to ~010°; melt impregnation continues in the same manner, i.e., it rises and ponds beneath serpentinized mantle peridotite, but due to the increased melt focussing and approach of the spreading centre from the south, intrusions now become lineated under the 'drift' stage stress regime. A relatively 'continuous' but low supply of melt may result in a layer of intrusive material, here assumed to be gabbroic, which acquires a remanent magnetization in the same way that oceanic crust acquires its magnetization, i.e. adjacent normal and reversed bodies. A relatively continuous, but low supply, can also explain why the lower (7.3-7.9 km/s) velocity layer along IAM-9 (Dean et al., submitted) does not show localized lateral velocity contrasts pertaining to individual intrusive bodies; addition of melt to the mantle may take

place through interconnected pore space or fractures. Dean et al. (submitted) do suggest that melt bodies may exist within the unaltered peridotite layer but are in fact below the lateral resolution of their wide-angle seismic experiment. This condition is not necessary because bodies which are magnetically distinct, due to contrasting magnetization directions and/or intensities, are not necessarily, and more probably not likely, to be recognized as distinct seismic bodies. More importantly, a relatively continuous, but limited melt supply, can also explain why seafloor spreading anomalies can be modelled within the transition zone at increasing extension (half-) rates of 6 to 8, and eventually to 10 mm/yr within oceanic crust, from east to west. Such extension rates are remarkably similar to the <20 mm/yr full-rate (i.e., <10 mm/yr half-rate) proposed for the rifting rate by Pickup (1997). A significant component of the rifting rate might actually be accounted for by the intrusion of magmatic material.

With further increased extension in the mantle, younger mantle rocks become progressively exposed towards the west. Previous thinning by ductile deformation, possibly within a mantle shear zone (Brun and Beslier, 1996), has effectively brought deeper mantle rocks nearer to the axis of extension, nearer to the surface, to be later faulted (in such a scenario, brittle deformation events should overprint ductile deformation events). Because the computed spreading rate (6 and 8 mm/yr) required to match observed and calculated magnetic anomalies, is consistent with the rate of rift related extension, the minimum time at which mantle rocks were exposed can be inferred from the age of the polarity reversal. Together with this increase in extension, the products of decompression melting of the mantle become progressively more oceanic-like; seafloor spreading blocks M4(N), M5(R), M8 (Whitmarsh and Miles, 1995) are identified with greater confidence than blocks M11A(N), M12(N), M16(N) and M17(R). Moreover, solution depths at the very western end of the transition zone (in zone B) occur distinctly at both the top of basement and ~5 km beneath. It is therefore possible that in some instances melt reached the surface, i.e. an extrusive layer may form in addition to, or at the expense of the deeper-seated gabbroic bodies. Such a scenario satisfies the observed velocity structure. In addition, Pickup et al. (1996) tentatively suggest that landward dipping reflectors L1 and L2 (their Figs. 2 and 3), which represent the most significant fault-like reflectors on MCS profile IAM-9, could be faults that have provided a pathway for melt. They also suggest that the two steep-sided basement mounds that overlie the tops of L1 and L2 represent extrusive material.

An alternative suggestion (Pickup, 1997) is that L1 and L2, which penetrate to depths of at least 18.5 km, are controlled by the close proximity of the accretionary axis. The steep westward increase in isotherms, particularly the 600°C isotherm which represents the base of

the brittle regime (Lin and Parmentier, 1989), controls the mechanism by which faulting occurs. Fault displacements are therefore increased on landward dipping fault planes, since seaward dipping faults are truncated by the 600°C isotherm at much shallower depths (Fig. 6.17; Carbotte and MacDonald, 1990).

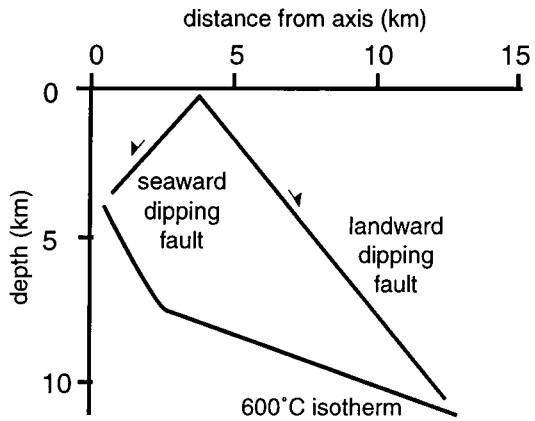

Figure 6.17 Diagram showing the likely depth extent of landward and seaward dipping faults near to the accretionary axis. Because the depth of brittle faults is governed by the depth to the 600°C isotherm, reflectors L1 and L2, which exist at the seaward end of the OCT beneath IAM-9, may be major faults which existed close to the accretionary axis (from Pickup, 1997 after Carbotte and MacDonald, 1990).

Because the location of L1 is approximately coincident with M5(R) (see Fig. 6.1 and 6.12) it can be assumed, by the reasoning given above, that it was active at that time. In fact, the time at which each landward dipping fault was active can be correlated with modelled reversal blocks. Although this assumes the fault was at the centre of the rift, present day fault growth at mid-ocean ridges (oceanic rifts) becomes inactive after a short time period. Searle et al. (1998) show that fault growth is complete within 15 km of the axis (1.2 Ma) of the Mid-Atlantic Ridge at 29°N, a distance comparable to that between L1 and a more positively identified oceanic reversal block, M4(N). Thus, increased magmatism and slow spreading oceanic type crustal tectonics dominate the western zone of the OCT.

Finally, oceanic crustal accretion becomes the dominant process immediately west of peridotite ridges R3; seafloor spreading magnetic anomalies can be modelled at spreading rates of ~10 mm/yr with normal and reverse magnetization blocks whose intensities can be modelled

by a full crustal section, i.e. layers 2 and 3. Source depths are focussed at or near the basement surface since the dominant magnetic body is the uppermost layer. The spatial model is shown in Fig. 6.18.

The model described above is consistent the sequence of events, derived from cores of serpentinized peridotites at ODP Sites 897 and 899, proposed by Beslier et al. (1996) and Cornen et al. (1990); (1) high temperature (~900°C) shear deformation; (2) limited partial melting; (3) syn-tectonic alkali melt impregnation at relatively low pressures (<1 GPa); (4) lower temperature (~780°C) and low pressure (< 1Gpa; lithospheric) deformation; (5) hydrothermal alteration (serpentinization) and low temperature deformation.

6.5.2 Margin-parallel development

The speculative model described above is based, although not exclusively, on observations in the southernmost region (in the vicinity of IAM-9) of the southern Iberia Abyssal Plain. However, as described by Discovery 215 Working Group (1998), variations in seismic structure, basement topography and magnetic character along the margin are as great as those across it. This necessarily implies that any model of the margin must account for three-dimensional changes in character. It also means that inferences made from the results of ODP drilling are not necessarily representative of the entire margin.

Significant margin-parallel changes concerned with the nature and formation of the OCT include (see Fig. 2.4):

(1) The seaward limit of thinned continental crust shows a gradual seaward progression towards the north of the southern Iberia Abyssal Plain. At ~40°N (in the vicinity of IAM-9), the continental crust extends westward to 10°45'W, whereas at ~41°N it extends as far west as ~12°W. This represents an approximate 105 km seaward shift in the limit of continental crust over the same N-S distance, i.e., the margin strike changes by ~45° over this distance.

(2) The segments of the peridotite ridge, R4 and R3, exhibit a left lateral step of ~30 km over 110 km N-S distance.

(3) From (1) and (2) above, the estimated width of the OCT varies from 160-170 km (Pickup et al., 1996; Dean et al., submitted) to 40 km (Chian et al., in press) south to north.

(4) In the southern and central parts of the OCT, excluding the most south-easterly region (region TE), reduced-to-the-pole magnetic anomalies have amplitudes 0 to -125 nT, trend at 010° and have significant lateral continuity (up to 120 km). In contrast, in the vicinity of Sites 898 and 899, one significant and anomalous magnetic anomaly, identified from sea surface

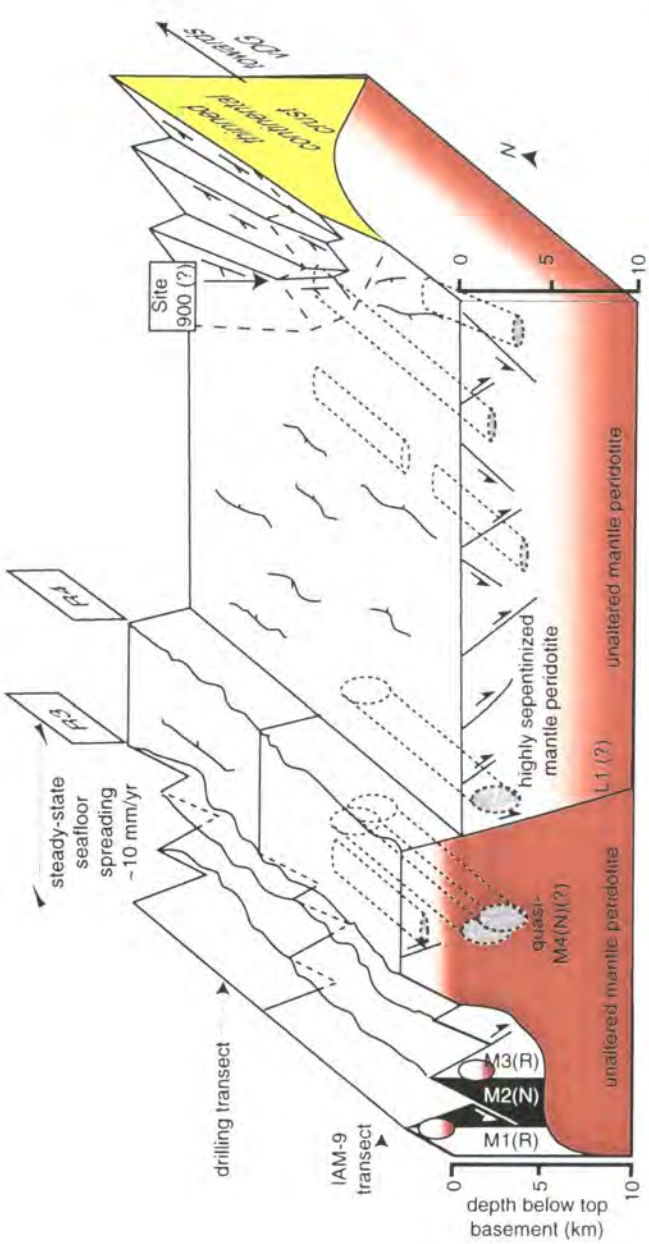

Figure 6.18 Schematic three-dimensional model of the proposed geological structure beneath the southern Iberia Abyssal Plain. During prolonged extension of the lithosphere during rifting, continental crust is totally thinned and mantle peridotite (red) is exposed at the seafloor. RTP magnetic anomalies over thinned continental crust (yellow) and the most landward region of the OCT (region TE) in the vicinity of MCS profile IAM-9 trend at ~350°. These anomalies are more linear in character and similar in amplitude to those further east (over continental crust), yet oblique, although of similar amplitude, to seafloor spreading anomalies and anomalies within the remainder of the OCT to the west (010°). The linear 350° trending anomalies result from the (syn-rift?) intrusion of dyke- and/or sill-like gabbroic bodies (grey) into exposed and sub-continental mantle under 'rift' related stress conditions. Serpentinization of exposed mantle (white) prevents intrusions rising above sub-basement depths of ~3 km. 010° trending anomalies over thinned continental crust are evidence of sub-continental intrusions which post-date the 'rift' stage stress conditions. Through time and spatially westwards, increased focussing of melt creates quasi- (punctiform?) and normal-oceanic crust (black and white), possibly aided by less serpentinization of mantle.

observations, trends at ~350°, locally parallel to the trend of the limit of continental crust. Even with near-bottom observations that reveal two separate anomalies, there still exists a trend which is not parallel to the dominant trend of anomalies within the OCT or oceanic crust. M3(R), and M4(N) (see Fig. 6.15) can be correlated between tracks which are over 15 km apart. In contrast, the magnetization high at Site 899 does not continue south with a trend that parallels the anomalies to the west or east. A negative magnetic anomaly to the north-east also exhibits a trend which is locally parallel to the trend of the limit of continental crust (Fig. 2.8). (5) South of ~40°20'N, reduced-to-the-pole magnetic anomalies in the easternmost 50 km of the OCT (region TE) exhibit trends of 350°, parallel to those over continental crust to the east.

To explain these observations, together with those normal to the margin, progressive stages in the rift-to-drift model are considered (Fig. 6.19). The model of the last section is assumed to apply through time as the rift propagated northwards. As the rift approached the region at ~40°20'N, because the local trend of anomalies in the OCT parallel those of the thinned continental crust and those in the southeastern OCT, I suggest that the transition from a 'rift' dominated stress regime to a 'drift' dominated stress regime was halted. This could have prevented the deep gabbroic bodies, with the same trend as seafloor spreading sources, from intruding the mantle. Because such bodies may contribute to the total extension in the southernmost part of the Iberia Abyssal Plain, this provides an explanation for the OCT width being somewhat less than the width of the OCT to the north. In fact, if the region between the continental edge and the first anomaly associated with the 'drift' stress field (aZ(R)=aM17(R); see Fig. 6.10) is estimated along the width of the margin it is approximately constant at ~40 km (Fig. 6.20). Not until 41°20'N, adjacent to Galicia Bank, does it reduce to ~20 km, as determined by the distance between the peridotite ridge and the region of high amplitude positive magnetic anomalies. The OCT has also been estimated to be ~25 km wide at 42°N (Sibuet, 1992). Moreover, application of the same procedure in the Tagus Abyssal Plain reveals that the distance only increases to ~50 km (Fig. 6.10) provided the anomaly identifications are correct.

An explanation for the lack of deep pre-'drift' stage deep gabbroic bodies is uncertain. It is possible that as a hypothetical 'pre-drift front', which propagates ahead of the region of seafloor spreading, encountered the relatively thick continental crustal fragment of Galicia Bank. Similarly, and more probably, margin-normal extension took place along a pre-existing basement structural boundary, which is seen downstrike in Iberia with the same trend (i.e. reactivation). Both suggestions would necessarily juxtapose relatively 'cold' thicker continental crust with the melt zone thus suppressing melt production by conductive cooling through the

relatively 'cold' continental crust.

6.5.3 Duration of continental rifting and predicted volume of melt

Melting models (e.g. Pedersen and Ro, 1992; Bown and White, 1995) necessarily require that (a) the onset of continental rifting and (b) the cessation of continental rifting (coincident with the onset of seafloor spreading) are discrete events in time which define a period when rift related geological processes dominated. In the model of Bown and White (1995), but also noted by Pedersen and Ro (1992), rift duration is one of four factors on which melt generation is most dependent; syn-rift basaltic melt is generated by decompression melting of anhydrous mantle lherzolite provided the rift duration is long enough to exclude significant heat loss by conductive cooling. Thus constraints on the exact duration of rifting are critical to the general understanding of margin evolution.

The onset of rifting in the southern Iberia Abyssal Plain has yet to be defined precisely; constraints from ODP Legs 149 and 173 drilling results can only place bounds on the earliest and latest possible ages for the onset of rifting. Lithostratigraphic and biostratigraphic analyses constrain pre-rift clays from Site 901 as early Tithonian in age (Sawyer et al., 1994), whilst $^{40}Ar/^{39}Ar$ dating of the Site 900 sheared metagabbro constrains a syn-rift age of 136.4 Ma (Féraud et al., 1996). In addition, the metamorphic conditions recorded by the gabbro suggest that such an age is consistent with the latest stages of rifting providing the gabbro is a product of syn-rift melting (Féraud et al., 1996; Cornen et al., 1996; but see section 6.4.2.1).

The precise onset of steady-state seafloor spreading is also difficult to define due to contrasting ages arising from a number of studies (Fig. 2.3 and this thesis). However, most magnetic models place the onset in the range mid-CM3(R) to CM8(R). Therefore, there are a number of possible rift durations, three of which, D1, D2 and D3, are described below (Fig. 6.21):

(1) The maximum possible rift duration, D1=~23 Ma, is based upon the assumptions that (a) rifting commenced in the Tithonian, as indicated by the pre- to syn-rift shallow marine sediments at Site 901 (Saywer et al., 1994), and (b) seafloor spreading commenced at the beginning of CM3(R). Under these assumptions it is implicit that (*i*) the intrusions in zones B and C, including those that produce anomalies aX(N), aY(N) and aZ(R), as well as aM4(N) and aM5(R), are considered syn-rift and therefore non-oceanic, and (*ii*) the slumped nanofossil chalk at Site 1069 is not *in situ*;

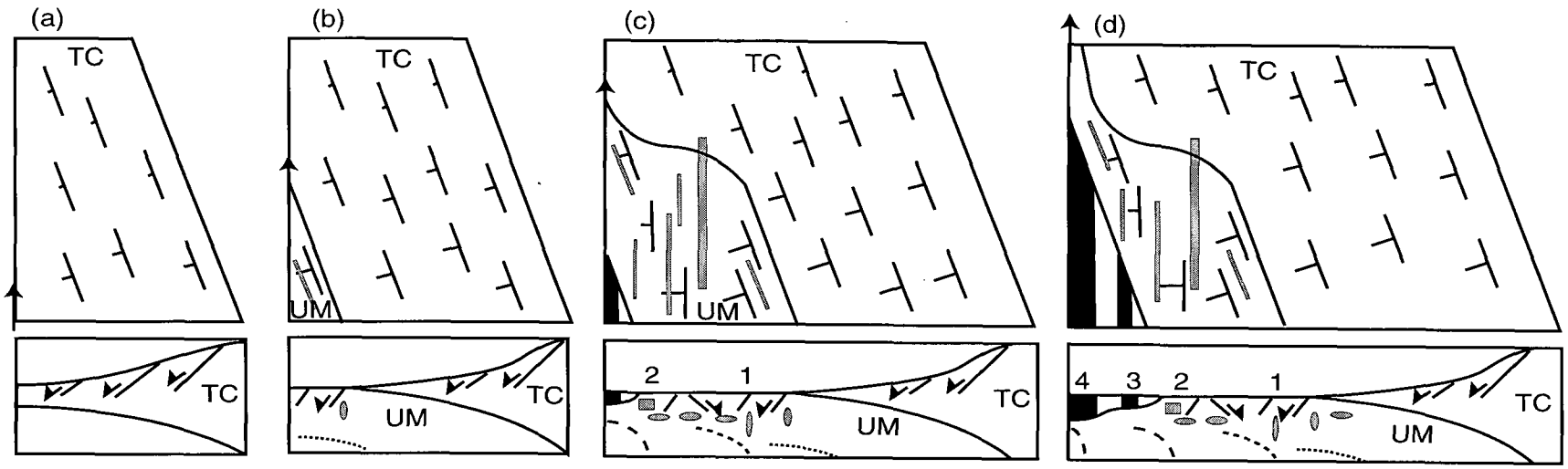

Figure 6.19 Cartoon sketch maps and sections across southern edges of maps (not to scale) showing the progressive rift-to-drift stages in the development of the West Iberia continental margin. The model is based upon the propagating rift model of Martin (1984) as used by Whitmarsh and Miles (1995). TC=thinned continental crust, UM=upper mantle. Fault tick sizes denote relative degrees of extension. Solid grey objects are syn-rift gabbroic type intrusions, black and white bars represent seafloor spreading type blocks within normal oceanic crust. Arrow indicates the northward propogation of the rift. Dashed lines mark successive locations and shape of the top of the melt zone. (a) Thinning of lithosphere by tectonic extension; strain is manifested in upper continental crustal fault blocks. (b) Prolonged lithospheric extension results in upper mantle exposure at the seafloor. Serpentinization of mantle may be aided by brittle deformation (or vice versa). Very small amounts of syn-rift melt intrude mantle and is halted by serpentinized layer (see text). Trends of magnetic anomalies, caused by intrusions and/or serpentinization are dominated by 'continental rift stress field'. (c) A combination of the melt zone becoming increasingly more focussed and shallow, together with the dominance of the 'oceanic rift stress field' as the rift propagates north, allows intrusions that produce magnetic anomalies oblique to those within thinned continental crust, which are more oceanic-like towards the west. Anomalies that straddle the westward continental limit must originate at depth as intrusions (see text). (d) Complete focussing of melt creates oceanic crust which thickens as cool continental lithosphere moves away from the melt zone.

(2) Rift duration, D2=~10 Ma, is based upon the assumptions that (a) rifting commenced 136.4 Ma, as indicated by the Site 900 gabbro (and its age) whose petro-structural evolution suggests it was emplaced at the final stages of rifting (Cornen et al., 1996), and (b) seafloor spreading commenced at the beginning of CM3(R). Under these assumptions it is implicit that anomalies aY(N) and aZ(R) are incorrectly identified as aM16(N) and aM17(R), and therefore the ages of their sources cannot be correlated with the reversal timescale;

(3) Rift duration, D3=~6.5 Ma, is based upon the assumptions that (a) as (a) in (1), above, and (b) seafloor spreading commenced at ~142 Ma, as indicated by the presence of anomaly aZ(R) which is interpreted to be seafloor spreading anomaly aM17(R). Under these assumptions it is implicit that (*i*) the intrusions in zones B and C, including the gabbro at Site 900 and those that produce anomalies aX(N), aY(N), aZ(R), aM4(N) and aM5(R), are considered oceanic, rather than syn-rift, in origin (i.e. aY(N)=a16(N) and aZ(R)=a17(R)), and (*ii*) the slumped nanofossil chalk at Site 1069 is not *in situ*.

Based on the three estimates of rift duration made here, Bown and White (1995) predict that, for a beta value of 11.5, (a) <1 km of melt is generated (D1=23 Ma), (b) ~ 2 km of melt is generated (D2=10 Ma), (c) ~3 km of melt is generated (D3=6.5 Ma; Fig.1.1). However, regardless of the duration of rifting chosen, the predicted melt thickness cannot be estimated at the margin in the southern Iberia Abyssal Plain because, (1) The model requires a constant, and finite, beta value, which is a measure of crustal extension; because mantle is exposed in the southern IAP a constant and finite beta cannot be calculated; (2) The model does not allow melt to freeze in the mantle. The composite model of mantle unroofing and magmatic accretion presented in section 6.5 necessarily implies that (a) $\beta \rightarrow \infty$ (because the crust is infinitely thinned), and (b) melt products are intruded into the mantle, and reside there. However, more importantly is the concept of a gradual progression from continental rifting to seafloor spreading processes; rather like 'an engine picking up steam' it is difficult to define the duration of rifting required by the model of Bown and White (1995).

6.6 Summary

An interpretation of sea surface and near-bottom magnetic anomalies west of Iberia, by forward and inverse modelling, spectral and Euler deconvolution analyses, and componental magnetometry, has revealed the following:

(1) Magnetic anomalies west of the peridotite ridge can be explained by a seafloor spreading

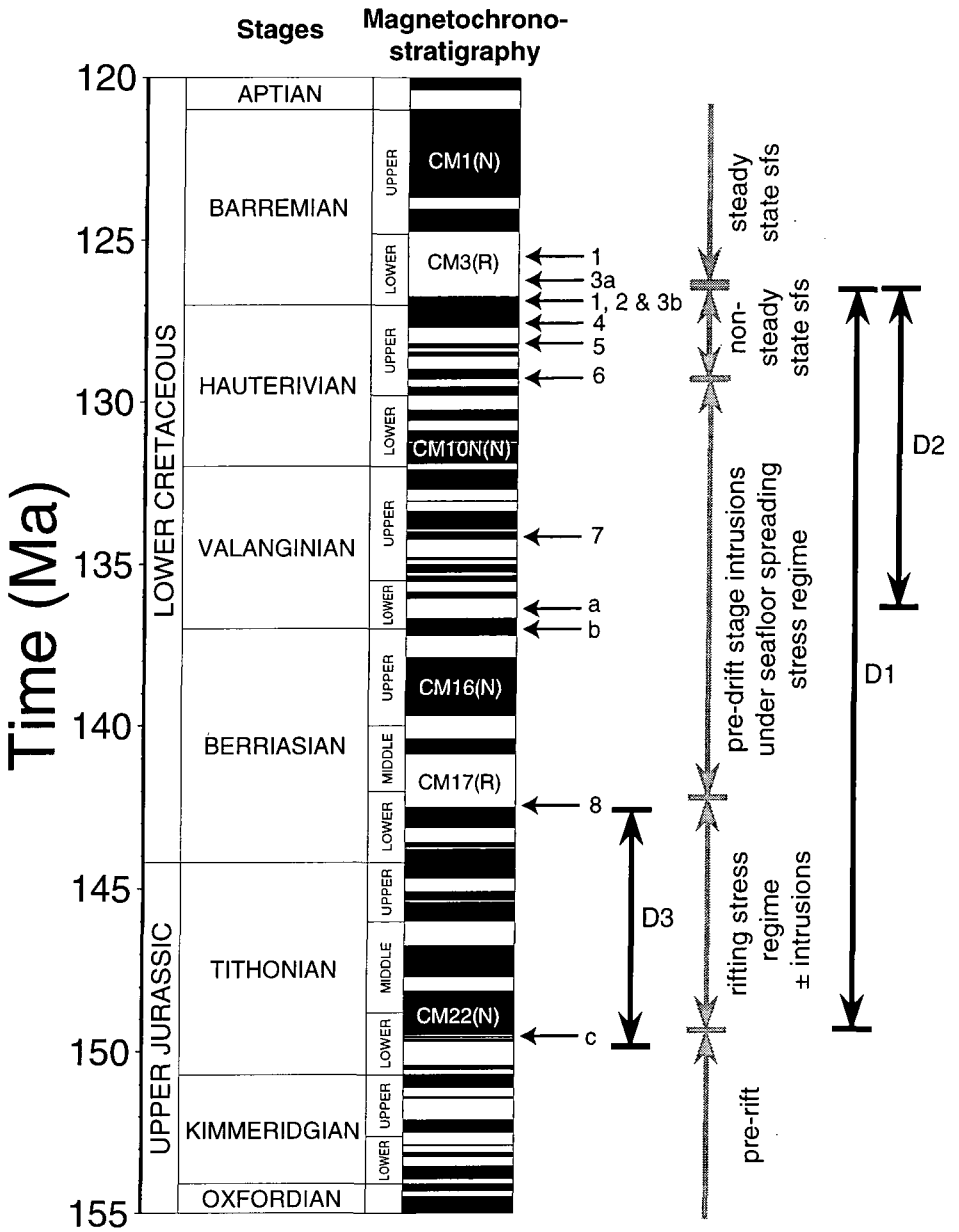

Figure 6.21 Possible durations of rifting (D1, D2 and D3) determined from magnetic anomaly identifications and ODP Legs 149 and 173 results (see text; modified from Dean et al., submitted, after Wilson et al., 1996). Rather than a discrete event, the transition from continental rifting to seafloor spreading may be a continually changing geological process comprising (1) extension and intrusion under 'rift' stress regime, (2) extension and increased intrusion under 'drift' stress regime, (3) unorganized (non-steady-state/punctiform) seafloor spreading, (4) organized seafloor spreading. See Table 6.4 for description of labels.

Onset of seafloor spreading	
1 Sea surface forward modelling	Whitmarsh et al. (1990)
2 Near-bottom forward modelling	Whitmarsh and Miles (1995), Whitmarsh et al. (1996)
3a Sea surface forward modelling and 1-D inversion	This study, spreading rate 10 mm/yr
3b Sea surface forward modelling and 1-D inversion	This study, spreading rate 8 mm/yr
4 Near-bottom and 2-D sea surface inversion	This study, variable spreading rate
5 2-D sea surface inversion	This study, variable spreading rate
6 Sea surface forward modelling	Whitmarsh and Miles (1995)
7 Identification of (combined) anomaly aM11A(N) and aM12.1(N)	This study, spreading rates of 8 and 10 mm/yr (east to west)
8 Identification of anomaly aM17(R)	This study, spreading rates of 6, 8 and 10 mm/yr (east to west)
Onset of rifting	
a Syn-rift 'crustal' gabbro (Site 900)	Feraud et al. (1996)
b Pre-rift nanofossil chalk (Site 1069)	Whitmarsh et al. (1998)
c Early Tithonian pre- (or early syn-) rift sedimentary rocks (Site 901 and possibly Sites 1065 and 1069)	Sawyer et al. (1994), Whitmarsh et al. (1998)

Table 6.4 Explanation of labels in Figure 6.21. Numbers mark the possible ages of the onset of seafloor spreading (end of rifting) whilst letters mark the possible ages of the onset of rifting.

model using a near constant spreading rate of ~10 mm/y. Magnetization solutions are consistent with expected magnetizations of up to approximately ±1.5 A/m for a typical layered oceanic crust (see Chapter 3). Magnetic models are consistent with seismic refraction models which suggest that oceanic crust immediately west of the peridotite ridge is only ~4 km thick.

(2) In a region including, and ~20 km east of, the peridotite ridge, magnetization patterns can be explained by seafloor spreading, although required spreading rates are, in general, non-constant and inconsistent with those required to model anomalies to the west of the peridotite ridge.

(3) Some magnetic layer thickness calculations suggest that oceanic crust thickens west of the peridotite ridge; although most computations failed due to theoretical problems (see section 3.4.3) some models reveal a thickening of 5.5-8 km over a distance of ~40 km. East of the peridotite ridge, in a region up to ~35 km wide, the magnetic layer is up to 5 km thick. The peridotite ridge represents an effectively non-magnetic region ~10 km wide.

(4) In a region immediately adjacent to, and ~30 km east of, the peridotite ridge, magnetic

sources, up to ~2 km below the top of acoustic basement, are represented by blocks with vertical sides, as determined by an Euler deconvolution structural index of 0.0.

(5) South of ~40°20'N, in the vicinity of MCS profile IAM-9, magnetic sources east of the region described in (4) are at depths of up to 5-6 km below the top of acoustic basement and are likely to be best described by structural indices of 1.0.

(6) Vertical magnetic boundaries, derived from vector magnetic field anomalies, are only observed west of 11°10'W, and their strikes are, on the whole, ~5° east of north. Magnetic boundaries are two-dimensional, with the exception of three boundaries near to, and immediately west of, ODP Site 898, and three to the south and southwest of Site 1069.

(7) At least two magnetic anomalies, which are continuous for ~250 km across the southern Iberia Abyssal Plain and Tagus Abyssal Plain, parallel the M-series seafloor spreading magnetic anomalies. Their lateral offset at ~39°20'N is consistent with a seafloor spreading origin for the sources of the anomalies; sea surface magnetic anomalies can be modelled by increasing (6-10 mm/yr) east-to-west spreading rates, although the depth of sources is inconsistent with a seafloor spreading model (which assumes that sources are at the top of basement).

(8) Magnetic anomalies, after reduction-to-the-pole, broadly fall into five categories, from east to west, based on their trends; (a) poorly lineated and sub-circular anomalies over continental crust, (b) lineated ~350° trending anomalies over the very westernmost thinned continental crust, (c) lineated ~350° trending anomalies over the easternmost ~50 km of the OCT, (d) lineated ~010° trending anomalies over the bulk of the OCT, and (e) lineated ~010° trending anomalies over oceanic crust.

(9) The J anomaly source, which can be modelled as a region of relatively high magnetization intensity (4 A/m), is very nearly an isochron but regionally cross cuts the trend of the M-series anomalies.

To explain the magnetic observations, presented in this Chapter and Chapter 5, I propose a composite model of upper mantle unroofing and the intrusion/impregnation of melt into the mantle, during margin development. The proposed geological character and the model of margin development are consistent with the results of recent seismic and drilling investigations. The OCT is characterized by the following:

(1) Gabbroic-type intrusions, at ~5 km depth in the OCT, which can be modelled using a seafloor spreading-type reversal sequence at spreading rates of 6 to 8 to 10 mm/yr, east to west. Because a model of seafloor spreading is inconsistent with seismic and drilling observations, I suggest that the gabbroic type intrusions resemble a hybrid between syn-rift

intrusions and oceanic accreted lower crust. A predicted thickness of melt of ~1-3 km, derived from models of rifting and melt generation, agrees with the thickness of melt suggested by seismic velocity models, in which melt is mixed with peridotite at sub-basement depths of ~3-7 km . This layer is the layer that explains the magnetic observations.

(2) Serpentinized mantle peridotite which is the cause of sub-circular magnetic sources at, and near to (within 1-2 km), the top of basement.

During extreme lithospheric thinning, which resulted in the exposure of the mantle, subsequent seawater serpentinization of peridotite created a low density layer which prevented melt rising to the surface. A near continuous, but low, supply created the lower layer of magnetic sources, which extends beneath thinned continental crust in the vicinity of ODP Sites 1065, 900, 1067 and 1068. Through time, and progressively westwards across the OCT, the geological conditions progressed from rift related conditions to seafloor spreading related conditions. Thus, reduced-to-the-pole magnetic anomalies, which trend 350° in the east and 010° in the west, reflect the change in dominant stress conditions as the North Atlantic Rift System propagated northwards.

Chapter Seven

Formation of the conjugate margin pair

The model presented in Chapter 6 is based on a magnetic study adjacent to only one margin within a conjugate pair. Therefore to further constrain the model of margin formation, in this chapter I present (a) a brief review of the literature concerned with the nature and formation of the conjugate Newfoundland margin, (b) the results of magnetic analyses adjacent to the Newfoundland margin, (c) a model for conjugate margin development, and (d) a comparison with other geological settings.

7.1 The Newfoundland margin

The conjugate margin to the West Iberian margin lies offshore Newfoundland in the northwest Atlantic, north of the Newfoundland Fracture Zone adjacent to the Grand Banks (Fig. 7.1). In the Newfoundland Basin, the margin south of ~45°N is approximately conjugate with the Tagus Abyssal Plain, the margin off the southern Flemish Cap is approximately conjugate with the margin off Galicia Bank, and the margin north of ~45°N and south of the Flemish Cap is approximately conjugate with the southern Iberia Abyssal Plain.

In a similar manner to the investigations offshore Iberia, many authors have attempted to infer or predict the location where, and the means by which, the transition from thinned continental crust to oceanic crust occurs (e.g. Keen and de Voogd, 1988; Tucholke et al., 1989; Srivastava et al., 1992). However, the relative sparsity of data, and in particular its broad distribution along the length of the margin has made detailed investigations similar to those in the southern Iberia Abyssal Plain difficult. In addition, from studies at the West Iberia margin it has been shown that margin parallel variations can be as great as those normal to the margin (Discovery 215 Working Group, 1998 and this thesis) and it is probable that similar, if not the same, variations occur along the length of the margin offshore Newfoundland. Therefore it is extremely important for the purpose of this study that axis-parallel reconstructions are well constrained in order to correctly identify the exact position of the margin conjugate with that in the southern Iberia Abyssal Plain.

A recent plate reconstruction (Srivastava and Verhoef, 1992; Fig. 2.2), at anomaly M0

time[1], predicts that the position of MCS profile LG-14 (up to 20 km south of, and roughly parallel with IAM-9) in the southern Iberia Abyssal Plain (Fig. 2.5) is roughly aligned with MCS profile LITHOPROBE 85-4 (Keen and de Voogd, 1988; Fig. 7.2) in the Newfoundland Basin. The constraining factor on such margin-parallel reconstruction is the termination of the J anomaly. Thus, on reconstruction the profiles IAM-9 and 85-4 represent an approximately continuous transect normal to both margins.

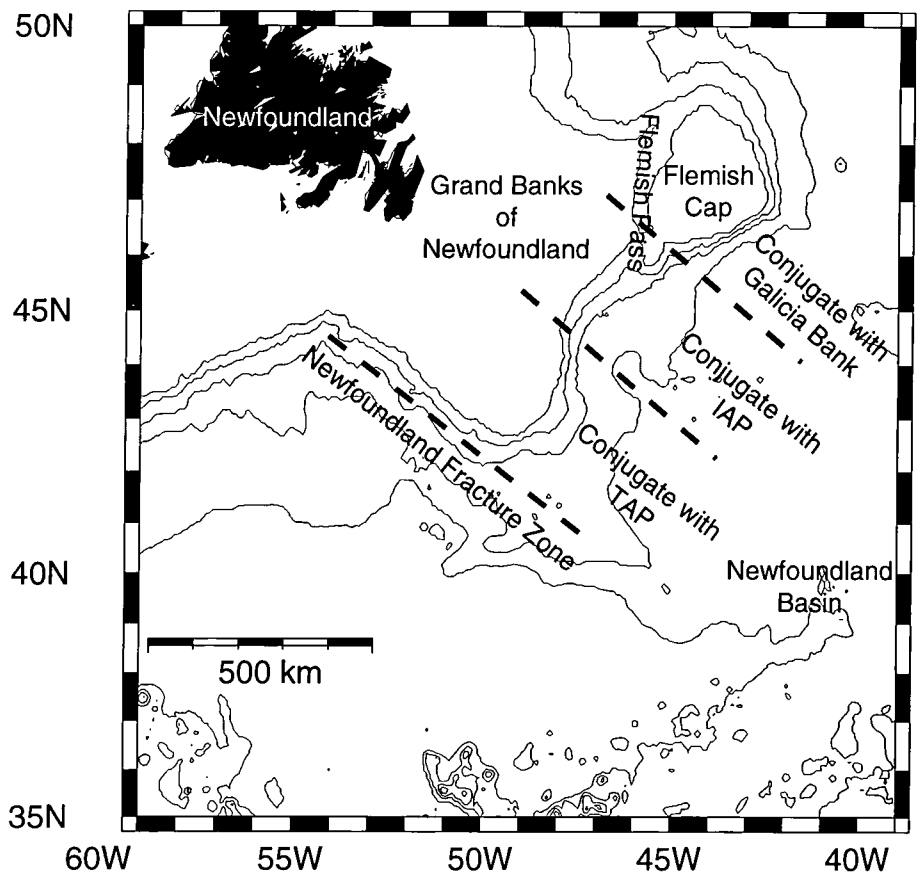

Figure 7.1 Bathymetric chart (contour interval 1000 m) of Newfoundland continental margin. Continental slope marks the approximate location of the seaward extent of continental crust. The margin can be divided into three regions which are approximately conjugate with Galicia Bank, the southern Iberia Abyssal Plain (IAP) and the Tagus Abyssal Plain (TAP) offshore West Iberia.

[1] Srivastava and Verhoef (1992) assume that the J anomaly formed at CM0 time.

In addition to MCS profile 85-4, six single channel seismic reflection profiles collected on cruise Farnella 80 (Parson et al., 1985) image basement in the region assumed to be directly conjugate with the southern Iberia Abyssal Plain (Fig. 7.2). To the north and east of profile FARN1, three short seismic refraction lines, HU-1, HU-2 and HU-6 (Todd and Reid, 1988) can be used to constrain the velocity structure of basement there. MCS profile LITHOPROBE 85-2 (Keen and de Voogd, 1988) and the coincident seismic refraction Line 7 of Reid (1994) image basement offshore Newfoundland that is conjugate with the Tore Seamount/Tagus Abyssal Plain offshore West Iberia.

7.1.1 Geological character of the OCT

To date, the position and extent of the OCT in the Newfoundland Basin has been poorly defined, not only due to the relative sparsity of data but also possibly due to the relative lack of recent investigations and subsequent understanding of the continent-ocean boundary as a gradational/transitional feature (OCT), rather than simply a discrete boundary (OCB). Keen and de Voogd (1988), Malod and Mauffret (1990) and Reid (1994) have suggested that the OCB is located near to the base of the continental slope (Fig. 7.2), whereas Pitman and Talwani (1972), Tucholke and Ludwig (1982), Srivastava et al., 1990, Sullivan (1983), Austin et al. (1989) and Tucholke et al. (1989) have suggested that the OCB is located immediately west of the J anomaly (Fig. 7.2). These two locations, ~100-130 km apart, mark the possible landward extent of oceanic crust; the two schools of thought arise due to the currently ambiguous nature of the region of basement between (OCT?).

Rotated fault blocks of continental crust overlain by sediments possibly syn-rift in origin are observed in the vicinity and landward of the continental slope on MCS profiles 85-4 and 85-2 (Keen and de Voogd, 1988; Fig 7.3a and b). On both profiles sub-horizontal events at ~11 seconds TWTT, equivalent to ~30 km depth, are observed beneath the continental shelf (The Grand Banks of Newfoundland) and are thought to represent Moho reflections at the base of unthinned or only slightly thinned continental crust. This is confirmed by the velocity model of Line 7 (Reid, 1994; Fig. 7c). Although Moho reflections cannot be confidently traced seaward beyond SP2250 and SP6000 on profiles 85-2 and 85-4 (Fig. 7.3a and b), respectively, and show little sign of shallowing, the velocity model of Line 7 indicates that the Moho shallows from ~28 km to ~15 km over a distance of only 40 km, and strongly resembles the model of Dean et al. (submitted) along IAM-9 (Fig. 6.2b). Therefore, Keen and de Voogd (1988) and Reid (1994) suggest that the seaward limit of continental crust marks the position of the OCB. However, an unambiguous oceanic crustal velocity structure is not observed until

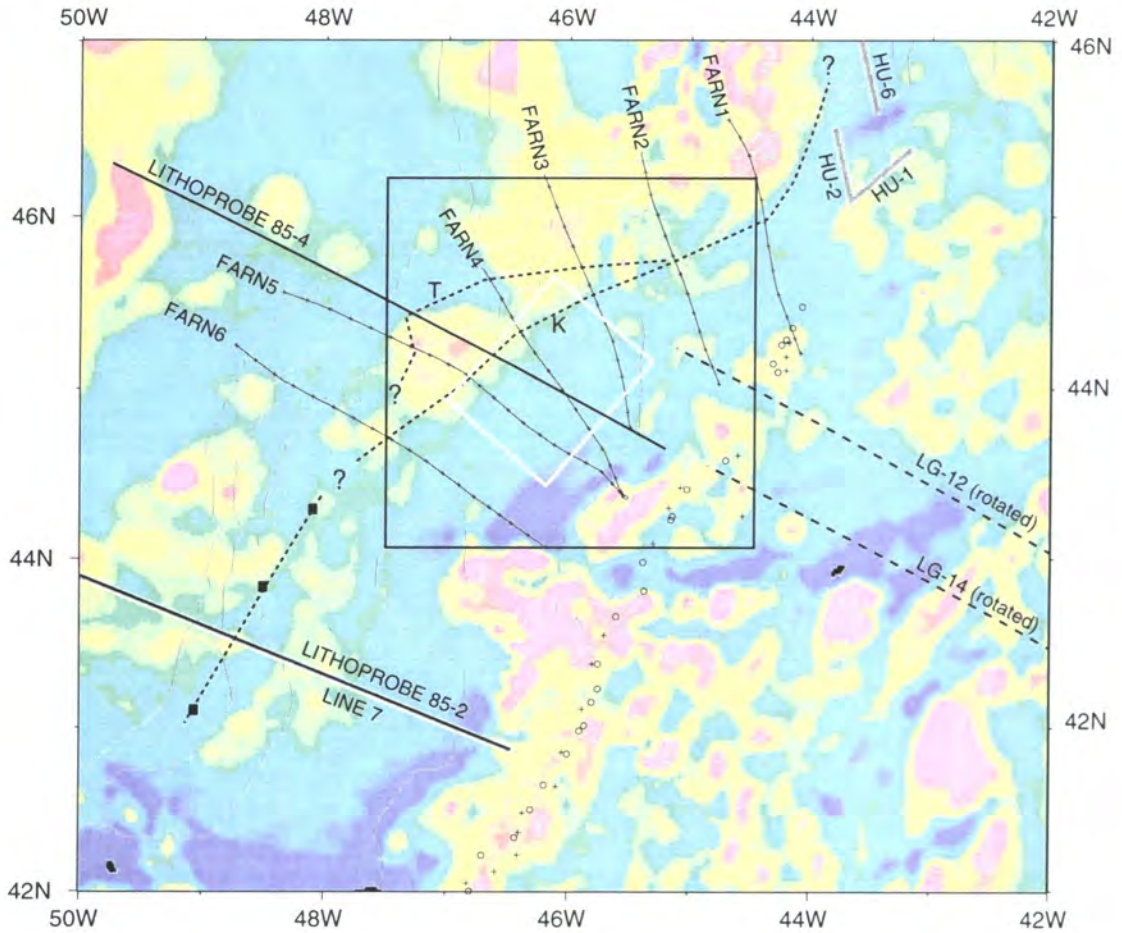

Figure 7.2 Magnetic anomalies (colours; palette as Fig. 2.7) at the Newfoundland continental margin, overlain by bathymetry (contours 1000 m). Single channel seismic reflection profiles FARN1-FARN6 are shown by thin lines with crosses at 1 hour intervals (equivalent to ~10 km). Multichannel seismic profiles 85-4 and 85-2 (Keen and de Voogd, 1988) shown by solid black lines. MCS profiles LG-12 and LG-14 (dashed), from the IAP have been rotated to the position at M0 time based on identification of M0 at the Newfoundland margin (crosses) and the West Iberia margin (circles; Srivastava et al., 1992). Thick grey lines mark position of seismic refraction lines (Todd and Reid, 1988; Reid, 1994). Fine dashed line labelled K is the OCB (seaward limit of continental crust) proposed by Keen and de Voogd (1988); dashed line labelled T is the limit suggested here (see text). Solid black squares mark position of landward dipping reflectors (Keen and de Voogd, 1988). White box marks the region for the magnetic study (in Figs. 7.8 and 7.9) which is approximately conjugate with the OCT in the southern Iberia Abyssal Plain. Black box shows area of Fig. 7.6.

a further 55 km seaward on Line 7 (Reid, 1994; Fig. 7.3c). In addition, Keen and de Voogd's (1988) interpretation of the rough or hummocky basement immediately seaward of their OCB on profiles 85-2 or 85-4 as oceanic is by no means conclusive.

Some 170-190 km east of the foot of the continental slope the presence of the J anomaly strongly constrains the basement there as oceanic, as previously determined by Tucholke and Ludwig (1982) and Rabinowitz et al. (1978). Todd and Reid (1989) and Srivastava et al. (1990) then noted that west of the J anomaly there were no high amplitude linear magnetic anomalies oriented parallel to the spreading axis and concluded that basement west of the J anomaly was unlikely to be oceanic in origin. However, the pattern of magnetic polarity reversals in the period at least 12 Ma prior to the formation of J (i.e. ~121-133 Ma; Fig. 2.1) will necessarily result in an absence of high amplitude anomalies (see Fig. 3.9) if the crust there is oceanic and formed at spreading rate < 16 mm/yr; as already discussed in the context of the West Iberia margin, if the basement landward of J was in fact similarly oceanic the magnetic anomalies would resemble a quiet zone (see Chapter 6). Moreover, a new and more recently compiled magnetic anomaly chart (Fig. 7.2; Macnab et al., 1997) indicates that some linear anomalies do exist landward of the J anomaly.

Additional constraint on the geological nature of the continental margin is provided by the character of the top basement reflector imaged on seismic reflection profiles FARN1-FARN6 (Fig. 7.4) and 85-4 (Fig. 7.5). Seaward of the proposed limit of continental crust on profile 85-4, basement relief is relatively low for ~110 km (140-250 km on profile; Fig 7.4). Although the exact position of the most seaward continental crust is ambiguous, this ~110 km wide region of relatively low relief may be comparable with the ~130 km wide OCT observed along the conjugate MCS profile IAM-9 (Pickup et al. 1996; Fig. 6.12) in the southern Iberia Abyssal Plain. Two single spread refraction lines, HU-1 and HU-2 (Todd and Reid, 1988; Fig. 7.2), which were shot over presumed oceanic crust, reveal that basement to the east of profile FARN1 consists of two layers defined by different velocity gradients. The high velocity gradient, upper basement layer, 2.0-2.5 km thick, is defined by velocities of 4.5-5.0 km/s, whilst the low velocity gradient, lower layer is defined by velocities of ~7.3 km/s. No mantle arrivals were recorded on either record section. The velocity model along refraction Line 7 (Reid, 1994; Fig. 7.3c) also defines a low velocity gradient layer with velocities of ~7.2-7.6 km/s below a high velocity gradient layer. The velocity structures from these three models are similar to some of those observed in the OCT of the southern Iberia Abyssal Plain (Fig. 6.2c).

Seaward of ~250 km on profile 85-4, basement relief of ~0.75 seconds twtt is comparable to basement in the vicinity of peridotite ridges R3 and R4 observed on IAM-9 (Fig. 6.12). Although the absolute relief on profile 85-4 is, in general, less than the absolute relief on

IAM-9, the relative relief across both margins allows a comparison to be made; on both profiles high relief of tilted continental fault blocks, relatively low relief of a region of ambiguous nature (OCT?), and the relatively high relief immediately seaward of the OCT are observed.

Margin-parallel changes in the character of acoustic basement are also observed offshore Newfoundland (Fig. 7.2). Beneath profile FARN1 the distance between the most seaward continental fault block (inferred from Figure 1 of Keen and de Voogd, 1988) and the J anomaly (definitive, but not necessarily the most landward, oceanic crust) is ~60 km, compared to ~130 km on profile FARN5 (Fig. 7.2). However, closer inspection of basement on profiles 85-4, FARN3, FARN4 and FARN5 may suggest that the seaward limit of continental crust is in fact further landward, based on the location of the foot of the continental slope and the basement relief, than predicted by Keen and de Voogd (1988; Figs. 7.2, 7.4 and 7.5). However, these identification are by no means conclusive. Nevertheless the distance between profiles FARN1 and FARN6 is ~200 km (parallel to the margin) and therefore such a change is comparable with that observed between ~41°N in the southern Iberia Abyssal Plain and ~38.5°N in the Tagus Abyssal Plain (Fig. 6.20). The character of basement relief of profile FARN1 also appears to be significantly different from that observed on profiles FARN2-FARN6 and 85-4. On FARN1 relief of ~1 sec twtt exists in the region between J and the proposed seaward limit of continental crust, whereas negligible relief is observed on the other profiles.

In addition to the nature of acoustic basement, folding in the post-rift sediments above a basement high at 295 km on profile 85-4 (Fig. 7.4) may suggest that the mechanical behaviour of basement rocks there is different to that of surrounding rocks and similar to that of the region between peridotite ridges in the southern Iberia Abyssal Plain (zone B of Fig. 5.2). Although the cause of the folding observed west of Iberia is the mid-Miocene compression associated with the Betic orogeny (Masson et al., 1994), and such a compressional phase is not associated with the Newfoundland margin, a possible origin for the focussing of folding here may be intra-plate compressional stresses (present off-axis at continental margins due to the ridge-push force) within a mechanically very weak zone. However, this is speculative.

The character of magnetic anomalies, the relief of acoustic basement and the velocity models over, and adjacent to, basement of ambiguous origin landward of the J anomaly show some similarities to the OCT in the southern Iberia Abyssal Plain. Therefore the character and the nature of their sources are discussed in the next section.

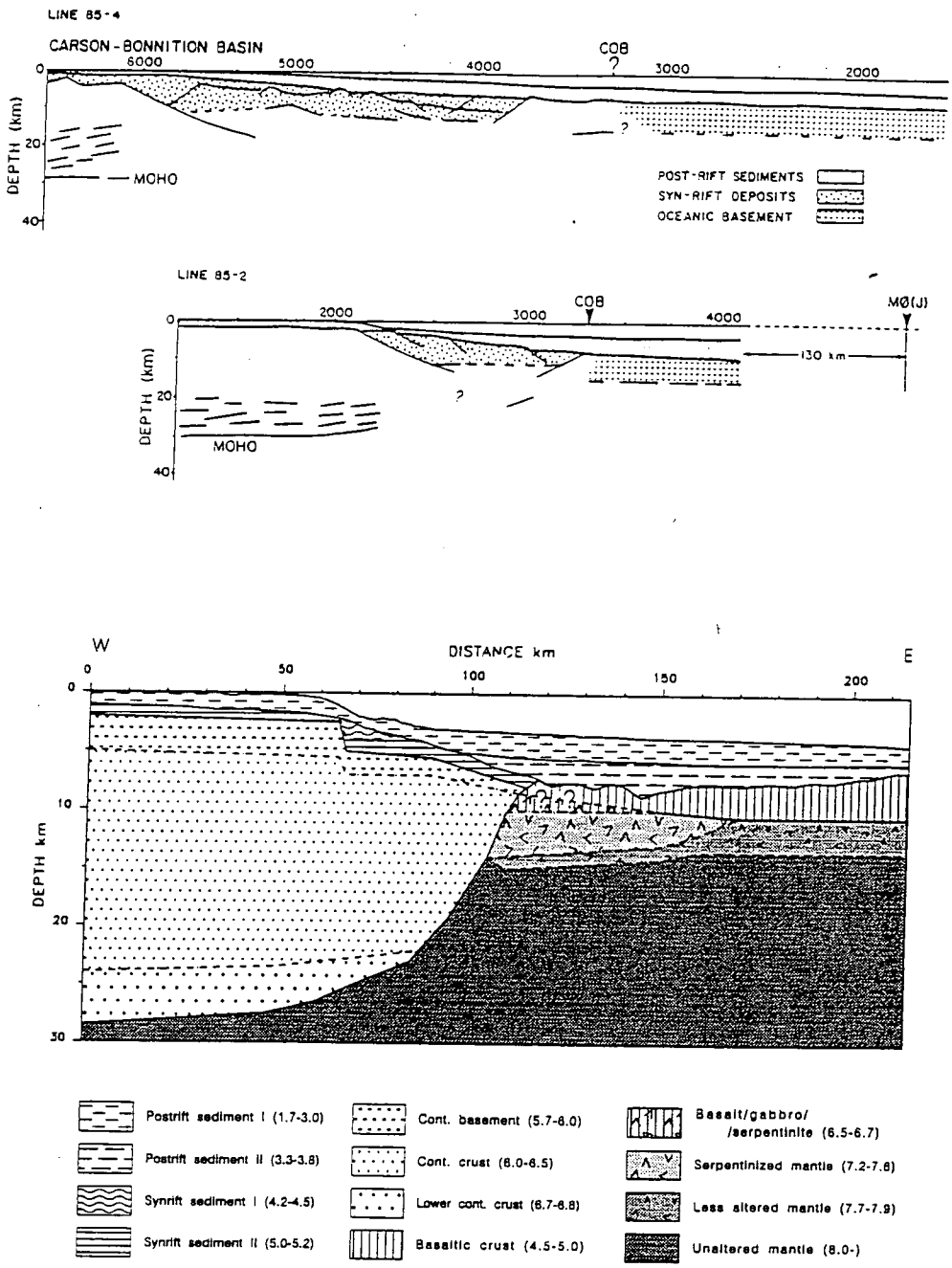

Fig. 7.3 Interpretive line drawings of MCS profiles (top) LITHOPROBE 85-4 and (middle) LITHOPROBE 85-2 (from Keen and de Voogd, 1988). (bottom) velocity model of Reid (1994) along Line 7, coincident with MCS profile 85-2.

7.1.2 Further constraints on the nature of the OCT from analysis of the magnetic field

The position of the most landward oceanic crust offshore Newfoundland, in the region conjugate with the southern Iberia Abyssal Plain and the Tagus Abyssal Plain, has not previously been thoroughly investigated by magnetic modelling; anomalies J and aM0(R) have been modelled and therefore oceanic crust has only been inferred to exist beneath and in the vicinity of these anomalies. At the conjugate margin in the southern Iberia Abyssal Plain, however, it has been shown that the onset of seafloor spreading definitely occurred in the period CM3(R)-CM5(R), and possibly earlier (see Fig. 6.21), i.e. at least ~5 Ma before J. In addition I propose that some magnetic anomalies observed in the southern Iberia Abyssal Plain can be explained by magmatic bodies intruded at depth into mantle peridotite during the rifting episode; some of these magnetic bodies can be modelled using the geomagnetic time scale with spreading rates gradually decreasing landward. Therefore, I have modelled magnetic anomalies at the Newfoundland margin to test (a) if the proposed timing of the onset of seafloor spreading is concurrent with that suggested at the West Iberia margin, and (b) if sources of magnetic anomalies within the OCT (defined by the outcome of (a) and the position of the most landward continental crust) agree with the model of margin development presented in Chapter 6.

7.1.2.1 Reduction-to-the-pole of magnetic anomalies offshore Newfoundland

Based on the reasoning of section 5.1, an analysis of magnetic anomalies by the reduction-to-the-pole method is used to attempt to constrain the nature of the magnetic sources offshore Newfoundland. A subset of the observed magnetic anomaly chart of Figure 7.2 was reduced-to-the-pole using four different sets of angular parameters; in each case I_G=65°, D_G=-20° (IAGA, 1995) and I_M=50° (Srivastava et al., 1988, 1990) were kept constant whilst four values for D_M were chosen to fully describe the angular RTP parameter (+20°, 0°, -20° and -40°). The reduced-to-the-pole anomalies are shown in Figure 7.6. It can be seen that, in general, magnetic anomalies become lineated if magnetization declinations of +20° and 0° are assumed more so than if declinations of –20° and -40° are assumed. The J anomaly, and a high amplitude positive anomaly ~20km to the west-northwest become lineated and trend 035° for any assumed declination, whilst most other anomalies to the north and northwest become lineated and trend 015°-035° when declinations of +20° and 0° are assumed. At greater westerly declinations linear anomalies within the region of ambiguous nature (OCT) are, in

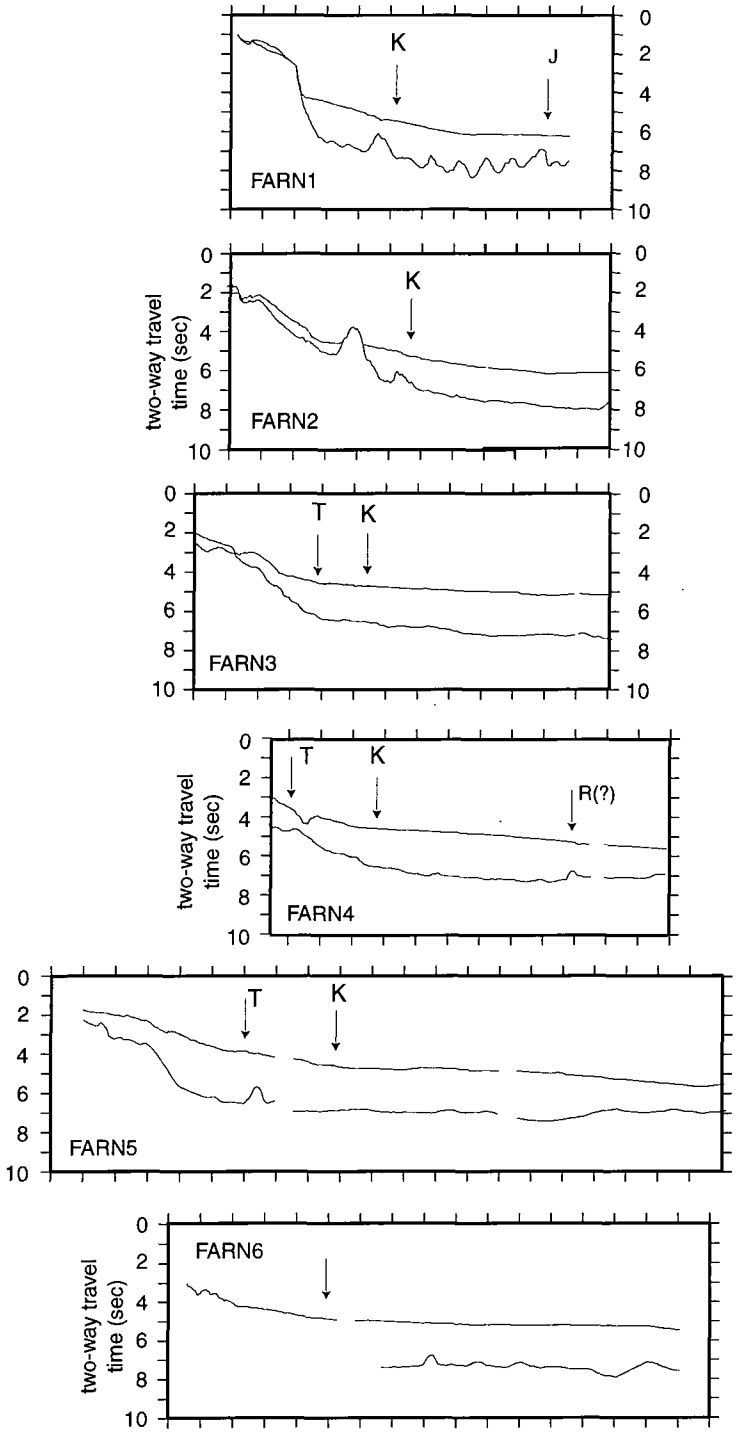

Figure 7.4 Line drawings of acoustic basement and seabed on single-channel seismic reflection profiles FARN1-FARN6 aligned parallel to the margin. Abscissa is tickmarked at 1 hour intervals, which is equivalent to ~10 km. Arrows labelled K mark the seaward extent of continental crust (from Keen and de Voogt, 1988); those labelled T mark alternative positions based on the character of the basement and the slope of the seabed. The arrow labelled R marks the position of a basement ridge downstrike of a basement ridge on MCS profile 85-4 (Fig. 7.5) which may be associated with the seaward extent of the OCT.

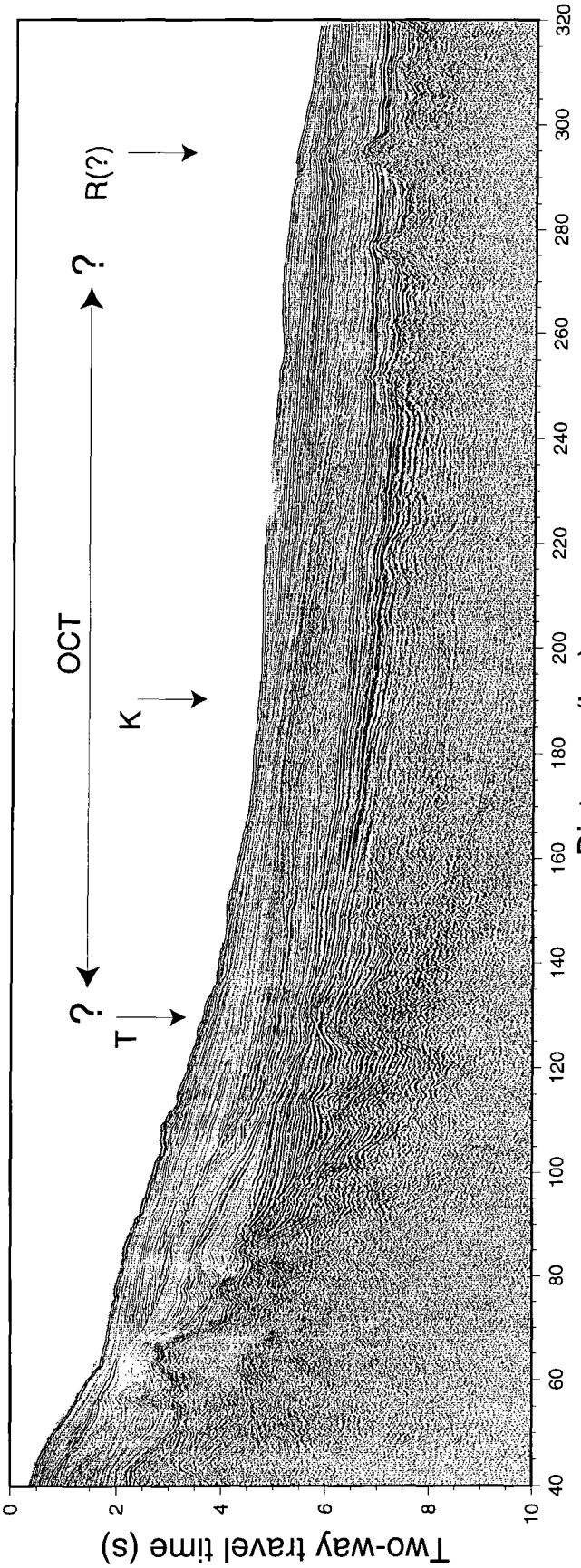

Figure 7.5 *Multichannel seismic reflection profile* LITHOPROBE 85-4 (from Keen and de Voogd, 1988). Arrow labelled K marks the proposed position of the OCB (Keen and de Voogd, 1988) whereas arrow labelled T marks the possible approximate position of the seaward limit of continental crust. Basement within the OCT possess little relief; the seaward limit of the OCT is defined approximately by the position of the oldest identifiable seafloor spreading anomaly (labelled aM5(R)). 25 km seaward of aM5(R) a basement ridge, which can be traced onto profile FARN4 (and possibly at the eastern end of FARN2 and FARN1(?; (Fig. 7.4), may be similar to the peridotite ridge identified off West Iberia.

general, not observed. Moreover, even assuming declinations of +20° or 0° linear anomalies within the OCT are by no means as apparent as those observed west of Iberia (cf. Figs. 2.8 and 5.1).

7.1.2.2 The onset of seafloor spreading

Forward modelling, by the method described in section 6.3.1 and shown in Figure 6.10, was carried out in order to compare synthetic seafloor spreading anomalies with the observed anomalies offshore Newfoundland (Fig. 7.7[2]). The top of the magnetic layer was assumed to be at a constant depth of 7 km; acoustic basement shows little relief (Figs. 7.4 and 7.5) and is almost consistently ~2 seconds twtt below the seabed (which is on average at ~5 seconds twtt below sea level). Although an accurate time-to-depth conversion cannot be applied (because of the absence of velocity information) equation 5.1 was used to compute the average depth of acoustic basement beneath the seismic profiles in Figures 5.4 and 5.5. Since basement relief in the southern Iberia Abyssal Plain is considerably greater than that observed offshore Newfoundland, and it was shown there that basement topography contributed an insignificant amount to the observed field (section 5.2.5), models with constant depths to their upper surfaces are sufficiently realistic.

In the region conjugate with the southern Iberia Abyssal plain, it can be seen that landward of, and within the vicinity of the J anomaly, seafloor spreading anomalies aM2(R), aM2(N), aM3(R), aM4(N) and aM5(R) can be identified and traced ~80-120 km parallel to the margin (Fig. 7.7). This distance is comparable to the distance over which the same anomalies can be traced across the southern Iberia Abyssal Plain (Fig. 6.10). The best fit between calculated and observed anomalies is derived from a model whose spreading rates are 10 mm/yr. Seafloor spreading anomalies older than aM5(R) cannot be identified north of ~44°30'N (in the region conjugate with the southern IAP). In contrast, south of ~44°30'N four anomalies, aW'(N), aX'(N), aY'(N) and aZ'(R), which are continuous for ~200 km parallel to the margin, can be modelled as seafloor spreading anomalies aM10N(N) and aM11(N) together, aM11A(N) and aM12.1(N) together, aM16(N) and a17(R), respectively (Fig. 7.7). Such modelling requires spreading rates of 10 mm/yr seaward of aM3(R) and 8 mm/yr landward of aM3(R), identical to spreading rates required to model seafloor spreading anomalies in the conjugate Tagus Abyssal Plain (Fig. 6.10).

[2] Figure 7.7 is included as a loose sheet at the back of this thesis.

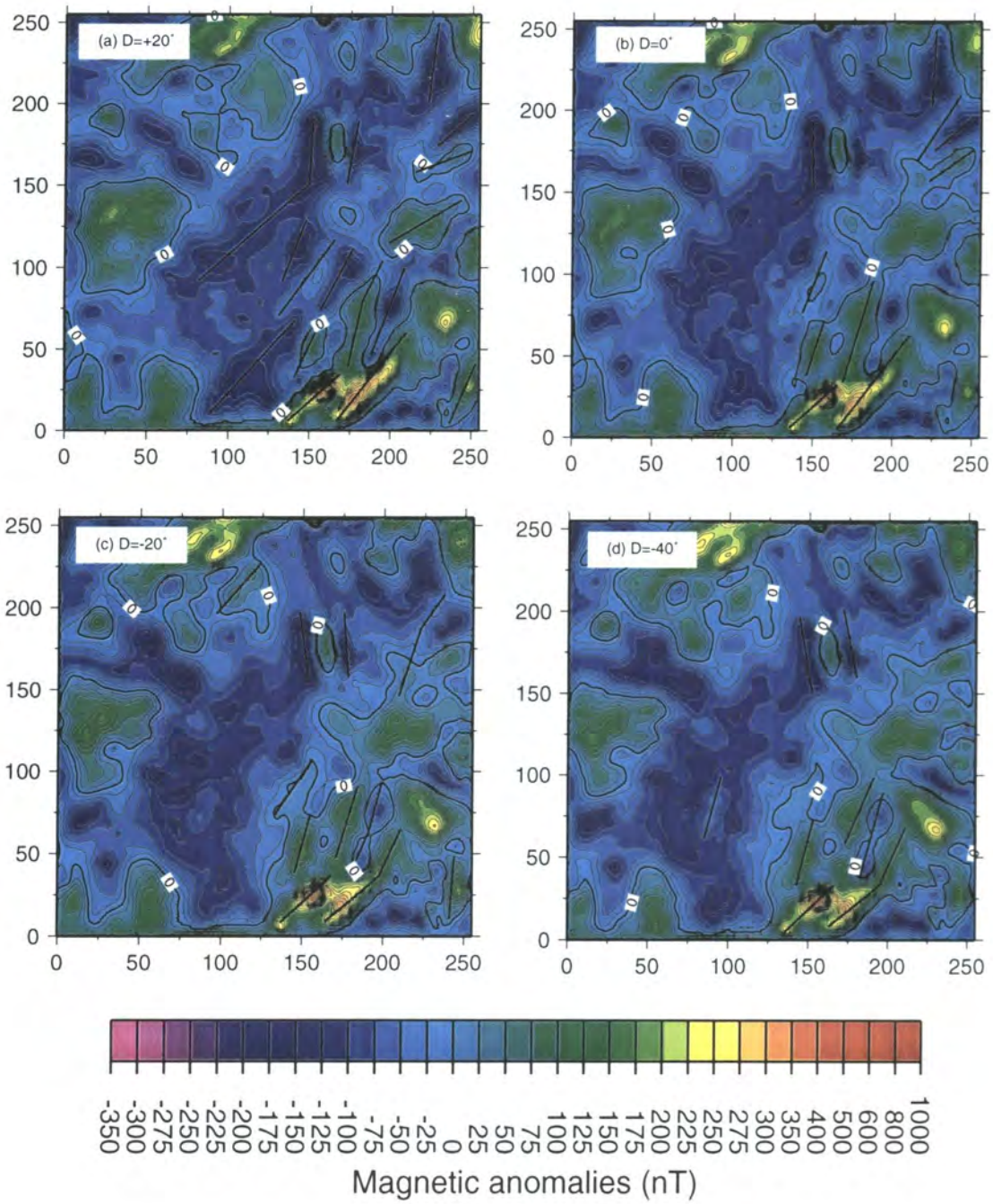

Figure 7.6 Magnetic anomalies (25 nT contour interval) at the Newfoundland continental margin (for location see Fig. 7.2) reduced-to-the-pole with four different phase filters defined by D_G=20°, I_G=65°, I_M=50° and (a) D_M=+20°, (b) D_M=0°, (c) D_M=-20°, (d) D_M=-40°. Anomaly chart converted to kilometers (sides aligned N-S and E-W). Black lines show trends of anomalies. Trends are most apparent when magnetization declinations of +20° and 0° are used; seafloor spreading anomalies trend 010°-035°, whilst no linear anomalies over observed in the OCT.

7.1.1.3 Source depth estimates

In the region assumed to be the OCT, approximately equal in area to the OCT off West Iberia (Fig. 7.2), the gridded sea-surface observed magnetic anomaly chart was (1) analysed by the power spectral method of Spector and Grant (1970; section 4.1) and (2) deconvolved by the Euler method (section 4.2), to estimate the depths to magnetic sources.

Figure 7.8 shows the logarithm of the power spectrum in the band 0-0.075 km^{-1}. This band width was chosen based on the analyses presented in Chapter 5; it was shown there that the best estimates of source depths were found in the lowest wavenumber band at inverse wavelengths <~0.1 km^{-1}. The spectrum reveals that the depths of magnetic sources are at 7.1 km below the sea surface, consistent with estimates of the depth to acoustic basement (section 7.1.2.1). Euler deconvolution of the magnetic field reveals that the depth of magnetic source solutions cluster in only one population for any given structural index (0.0-3.0; Fig. 7.9). Solutions pertaining to a structural index of either 1.0 or 1.5 represent the most likely type of magnetic source; skewness of solution distributions, which is a measure of the degree of under- or over-estimation of source depths (see section 4.2.7), is a minimum for SI=1.0, 1.5. Therefore, the most likely depth to magnetic sources can be estimated as 6-7 km or 7-9 km for structural indices of 1.0 and 1.5, respectively.

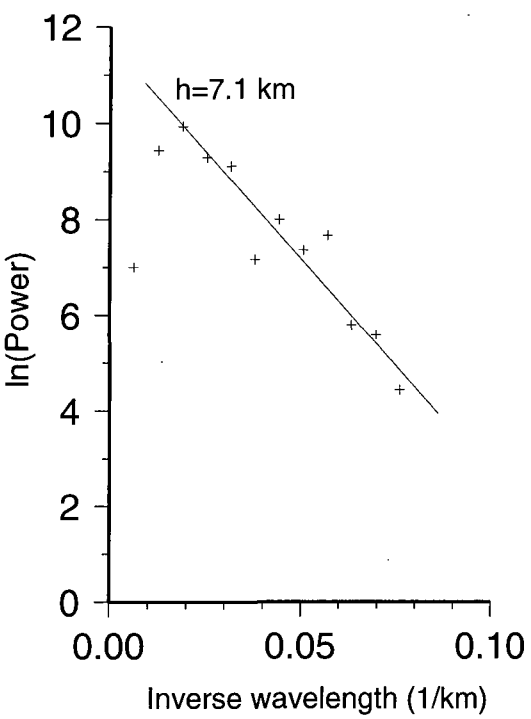

Figure 7.8 Logarithm of the power spectrum computed from magnetic anomalies in the OCT at the Newfoundland continental margin (region defined by the box of Fig. 7.2.) A straight line fitted to the observed power suggests that magnetic sources are present at a depth of 7.1 km bsl.

7.2 Contrasting and comparative features of the two conjugate margins

Based on the seismic reflection, seismic refraction and magnetic field evidence presented in Chapters 5, 6 and the present Chapter, the conjugate continental margins in the southern Iberia Abyssal Plain and offshore Newfoundland possess the following common characteristics:

(1) Magnetic anomalies, corresponding to oceanic crust as old as CM5(R), can be modelled with confidence assuming spreading rates of 10 and 8 mm/yr. The distance between the J anomaly and the oldest seafloor spreading magnetic anomaly is ~ 60 km.

(2) Both continental margins exhibit a region of relatively low basement relief between the most seaward continental crust and CM5(R); the origin of these regions is currently ambiguous and is assumed to be an ocean-continent transition zone (OCT).

(3) OCT widths are similar, but non-constant in a margin-parallel direction; in the southern Iberia Abyssal Plain current estimates suggest a width of ~40 km in the vicinity of profile LG-12 (coincident with the ODP transect) and ~130-170 km beneath and in the vicinity of profile IAM-9 (or LG-04). At the Newfoundland margin, OCT widths of ~30-60 km and 60-115 km have been estimated at the approximate conjugate positions to LG-12 and LG-04 (Fig. 7.2), respectively. Therefore, a similar pattern of northward narrowing of the OCT is observed at both margins.

(4) Seismic refraction experiments reveal two distinct layers, defined by seismic velocity and velocity gradients, within the OCT; an upper layer ~2 km thick with velocities 4.5-5 km/s and higher gradient, and a lower layer with velocities of ~7.3 km/s and lower gradient. The base of the lower layer is undefined; no mantle arrivals were recorded.

Contrasting features of the two margins are as follows:

(1) In the OCT of the southern IAP distinct linear magnetic anomalies, which parallel seafloor spreading anomalies younger than CM5(R), are observed on magnetic anomaly charts before and after reduction-to-the-pole. In the conjugate OCT no equivalent anomalies are observed before or after reduction-to-the-pole.

(2) Seafloor spreading anomalies as old as aM17(R) can be modelled in the southern Iberia Abyssal Plain; two significant anomalies (aY(N) and aZ(R) of Fig. 6.10) can be traced across the southern Iberia Abyssal Plain into the Tagus Abyssal Plain where their offset is consistent with the offset of J and younger seafloor spreading anomalies. Offshore Newfoundland, in the conjugate OCT to the southern Iberia Abyssal Plain, no equivalent anomalies are observed. However, south of ~44°N, in the region conjugate with the Tagus Abyssal Plain, four

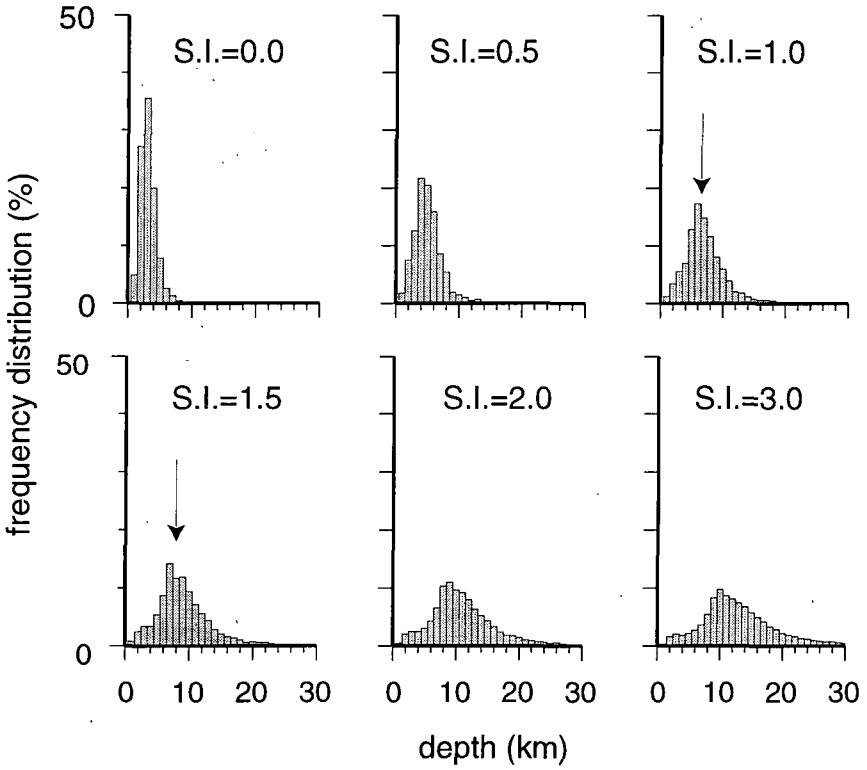

Figure 7.9 Distributions of Euler solutions for structural indices (S.I.) 0.0-2.5 from the deconvolution of magnetic anomalies in the OCT at the Newfoundland continental margin (region defined by the box of Fig. 7.2.). The least skewed distributions suggest that the most probable source geometries are defined by indices of 1.0 and 1.5 with an average source depth of ~7 km (arrows).

anomalies, aW'(N), aX'(N), aY'(N) and aZ'(R) can be modelled as seafloor spreading anomalies at spreading rates of 8 mm/yr.

(3) Two distinct populations of magnetic source depths are present beneath the southern Iberia Abyssal Plain; at, or very near to, the top of acoustic basement and up to ~6 km beneath. In contrast, magnetic sources in the conjugate OCT fall distinctly into one population which falls at, or very near to, the top of acoustic basement.

7.2.1 Implications for the model of margin formation

The proposed model for the geological nature of magnetic sources and development of the margin in the southern Iberia Abyssal Plain (sections 6.4.2 and 6.5) cannot be applied to the conjugate margin offshore Newfoundland for the following reasons:

(1) Significant linear (tens of kilometers long) magnetic anomalies are not observed within the

OCT at the Newfoundland margin; instead a 'magnetic quiet zone' exists in which magnetic anomalies are sub-circular, even after reduction-to-the-pole. In addition, anomalies cannot be modelled as seafloor spreading anomalies.

(2) Magnetic sources are present at, or very near to, the top of acoustic basement only.

Although the geological nature of crystalline basement within the OCT off Newfoundland is ambiguous, velocity structures derived from seismic refraction models to the north and south (Fig. 7.2) are consistent with a model of unroofed mantle peridotite. Therefore, based on the reasoning of sections 6.4.2.1 and 6.4.2.2, together with the evidence presented in this Chapter, I tentatively suggest that the sources of magnetic anomalies within the OCT off Newfoundland are much more likely to be serpentinized mantle peridotites than magmatic bodies. Although basement of continental origin is not ruled out, the very 'smooth' character of acoustic basement (Figs. 7.4 and 7.5) is extremely atypical of continental crust adjacent to rifted margins; unless obscured by large volumes of igneous material (usually at 'volcanic' margins), rotated continental fault blocks with significant relief are almost always observed (usually at 'non-volcanic' margins).

7.2.2 Tectonic versus accretionary processes during margin development

So far, the style of margin development has not been fully discussed. Therefore, in this section I address the possible styles of lithospheric extension which lead to conjugate margin formation west of Iberia and offshore Newfoundland.

Previous tectonic models of margin formation west of Iberia have generally been based on the identification of a deep subhorizontal reflector on MCS profiles. Off Galicia Bank, the S reflector (de Charpal et al., 1978), which is a group of locally undulating, but regionally flat, reflectors observed at 8-10 s TWTT east of peridotite ridge segment R2, is observed beneath tilted fault blocks of continental crust. It has been interpreted to be the brittle-ductile transition within the context of a pure shear extensional model (de Charpal et al., 1978) or a major lithospheric detachment in a simple shear or combined pure-simple shear model (Fig. 7.10; Winterer et al., 1988; Boillot et al., 1988a; Sibuet et al., 1992; Krawczyk and Reston, 1995; Reston et al., 1996). In the southern Iberia Abyssal Plain there is no evidence of a reflector which is as laterally persistent as S (>50 km), although Pickup (1997) has recognized reflectors, D, beneath thinned continental crust (persistent for only ~15 km). Although no extensive horizontal reflectors have been imaged beneath the OCT in the southern IAP, Krawczyk et al. (1996) suggest that reflectors H and L, observed along profile LG-12 (see Fig. 2.5), were part of an active detachment fault which was subsequently block faulted after

becoming inactive as it was raised to shallower crustal levels. In their model they predict a 'top-to-the-west' sense of motion along the detachment fault.

The sense of motion predicted by Krawczyk et al. (1996) necessarily implies that a master detachment surface must be present at the basement surface somewhere within thinned continental crust at the West Iberia margin. On their profile, and on all available MCS data in the southern IAP, a reflector resembling a master detachment is nowhere observed. Likewise on the Galicia margin, S does not clearly reach the basement surface. Therefore, there are some problems associated with interpreting S, or any other detachment surface, as a major low-angle fault on which a 'top-to-the-west' sense of motion occurred during continental breakup.

The S reflector has also been interpreted to represent a 'top-to-the-east' detachment surface based on the observation of a low angle reflector which is present at the basement surface at the conjugate southern Flemish Cap margin (Sibuet, 1992). This reflector is interpreted to be the western part of S separated from S at the Galicia margin after continental breakup. In his model, pure shear and simple shear are distributed asymmetrically across the two margins; the entire crustal section on the Flemish Cap margin deformed by simple shear, whilst the lower and upper crust of the Galicia margin deformed by pure shear and simple shear, respectively (Fig. 7.10). The detachment surface may merge with the brittle-ductile transition at depth below the Galicia margin.

A hypothesis of the formation of the West Iberia and Newfoundland margins by pure shear was first suggested by de Charpal et al. (1978). Although they suggested that S represented the brittle-ductile transition, more recently Reston et al. (1996) have shown, by analysis of the waveform and amplitude of S, that the reflector is indicative of a sharp change in acoustic impedance, such as that associated across a fault rather than through a transitional zone such as the brittle-ductile transition. In addition, Krawczyk and Reston (1995) note that parts of the S reflector were near to the surface (< 1 km depth) and therefore cannot represent the brittle ductile transition. Moreover, Boillot et al. (1988a, 1989) suggest that the S reflector is continuous with the eastern flank of the peridotite ridge, which outcrops at the seafloor, and therefore cannot represent the brittle-ductile transition.

The most recent model (which agrees with observations) of the formation of the West Iberia margin was proposed by Brun and Beslier (1996) in which they attempt to explain observations at the margins west of Galicia and in the southern IAP. They suggest that the whole lithosphere deforms by pure shear with local shear zones developing in the lower crust and mantle (Fig. 7.11); these shear zones coincide with weaker layers which are determined by the geotherm and mineralogy of crustal and mantle rocks. The ductile shear zones accommodate relative displacement between the brittle layers of the lithosphere; numerical

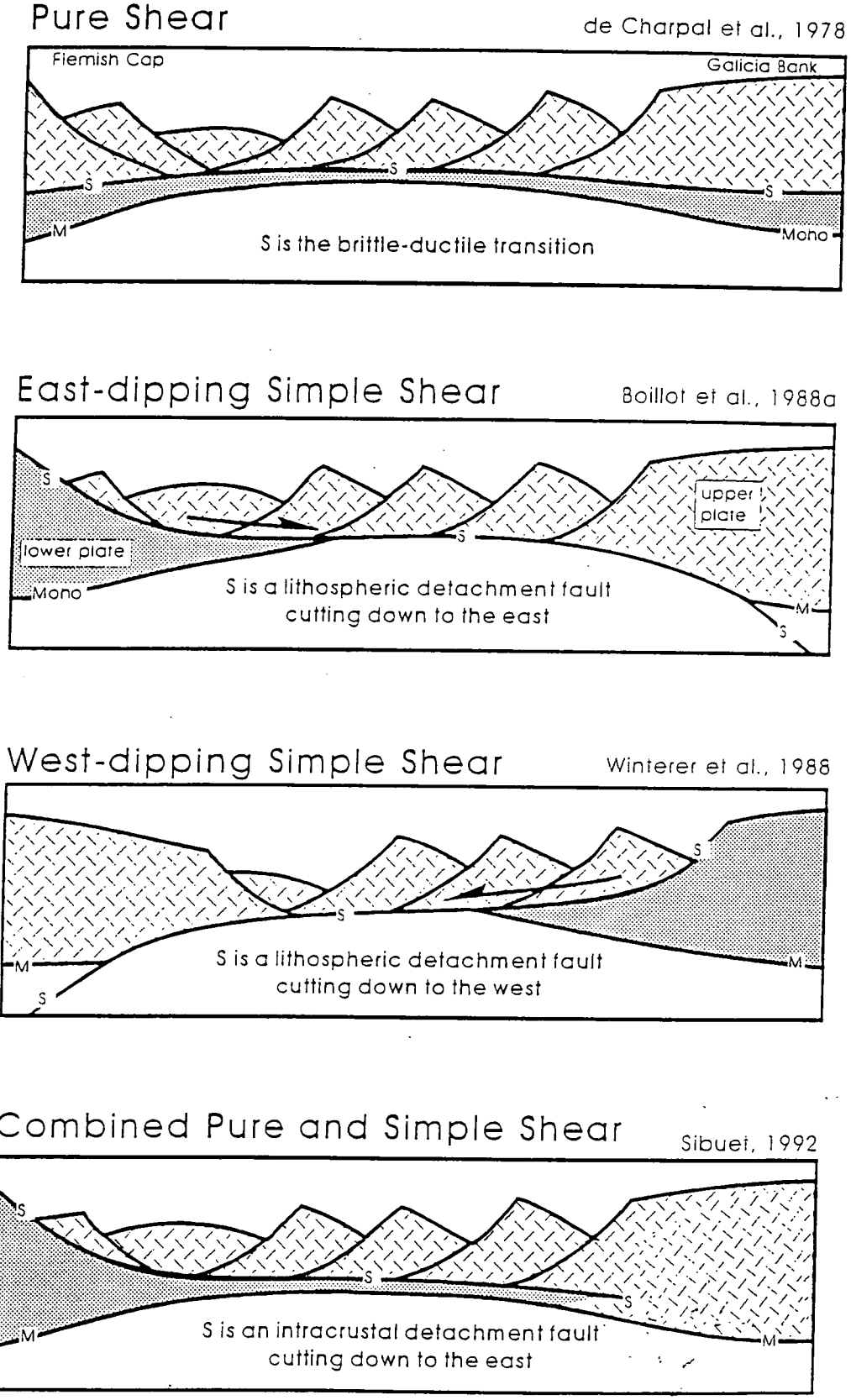

Figure 7.10 Four proposed models for the formation of the continental margin west of Galicia Bank. All models incorporate the S-reflector (from Reston et al., 1996).

models of lithospheric extension (Tett and Sawyer, 1996) also predicted similar shear zones. In cases of extreme extension and mantle exhumation their model predicts that the shear zones can be exposed at the surface; sheared gabbros sampled at Site 900 (Cornen et al., 1996) and off Galicia Bank (Gaulinaute II cruise; Boillot et al., 1995) and sheared peridotites sampled in cores at Sites 637, 897 and 899 agree with the model. Moreover, 'top-to-the-east' shear sense indicators are observed in peridotite from Site 637 (Boillot et al., 1988), consistent with a mantle shear zone origin.

The model of formation of the West Iberia margin in the southern IAP presented in Chapter 6 draws parallels with the pure shear models of Brun and Beslier (1996) and Pickup et al. (1996). However, the results from the conjugate Newfoundland margin allow a model of formation of the conjugate margin pair in which some parallels can be drawn with the simple shear models of margin formation of Krawczyk et al. (1996). This arises from the differences between the two margins as described in section 7.2 and because, in general, pure shear theoretically produces symmetric features whereas simple shear produces asymmetric features.

The asymmetry in suggested magnetic source body type (i.e. syn-rift/proto-oceanic magmatic intrusions at the West Iberia margin only), together with the difference in relief of acoustic basement and width of OCT at both margins, suggests that in general the conjugate margins are asymmetric and were possibly dominated by a simple shear tectonic mechanism. A simple shear model, for example that of Wernicke (1985) would necessarily produce an asymmetric distribution in melt products. Although Latin and White (1990) showed that very little melt is produced by lithospheric simple shear even for crustal β values of 50, their calculations show that considerably less melt would be produced beneath the lower plate than beneath the upper plate i.e. any melt products are generated almost exclusively beneath the upper plate. However, for large lateral offsets between crustal and mantle stretching (e.g. Lister et al., 1989) the calculations of Latin and White (1990), assuming a crustal β values of 50 and a potential temperature of 1280°C, predict that ~2 km of melt is generated beneath the axis of greatest mantle attenuation, whilst no melt is generated beneath the crustal rift. If the conjugate margins in the southern Iberia Abyssal Plain and offshore Newfoundland are assumed to be analogous to the upper and lower plates, respectively, in the model of Latin and White (1990), the suggested amount of melt in the lower layer of the OCT in the southern Iberia Abyssal Plain agrees with the ~2 km generated in the model. However, there is no evidence of detachment faulting in the southern Iberia Abyssal Plain.

The simple shear model may also account for the difference in relief of acoustic basement within the conjugate OCTs, whilst the asymmetric melt production may account for the differences in OCT width; as discussed in section 6.5.1, the intrusion of melt products

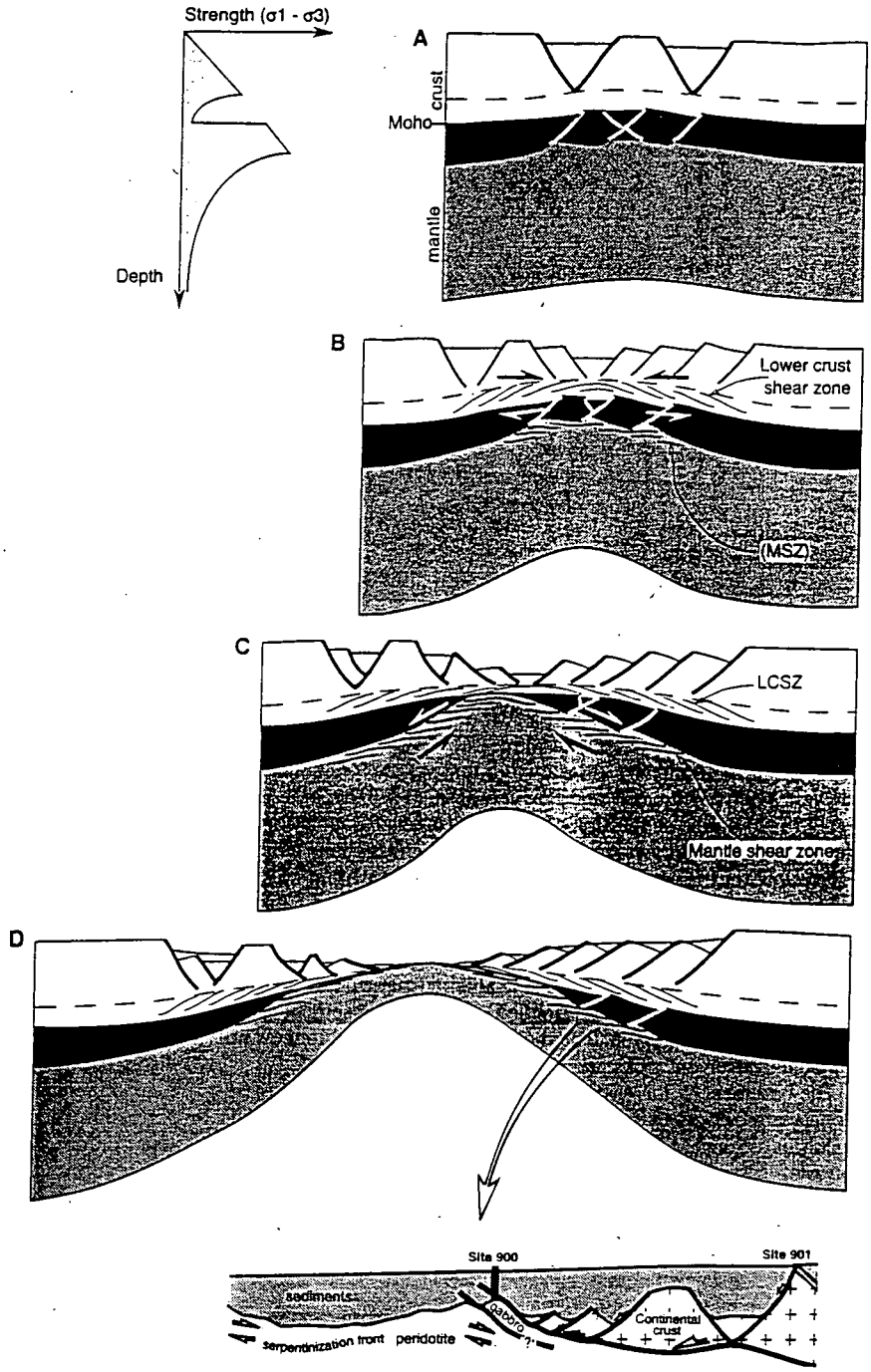

Figure 7.11 A model of progressive stretching, by pure shear, from the initiation of rifting to unroofing of mantle (A-D). A four layer brittle-ductile-brittle-ductile crust and mantle results in the formation of shear zones at the lower crust (LCSZ) and in the mantle (MSZ). The pure shear mechanism results in symmetrical features at both resultant margins (from Brun and Beslier, 1996).

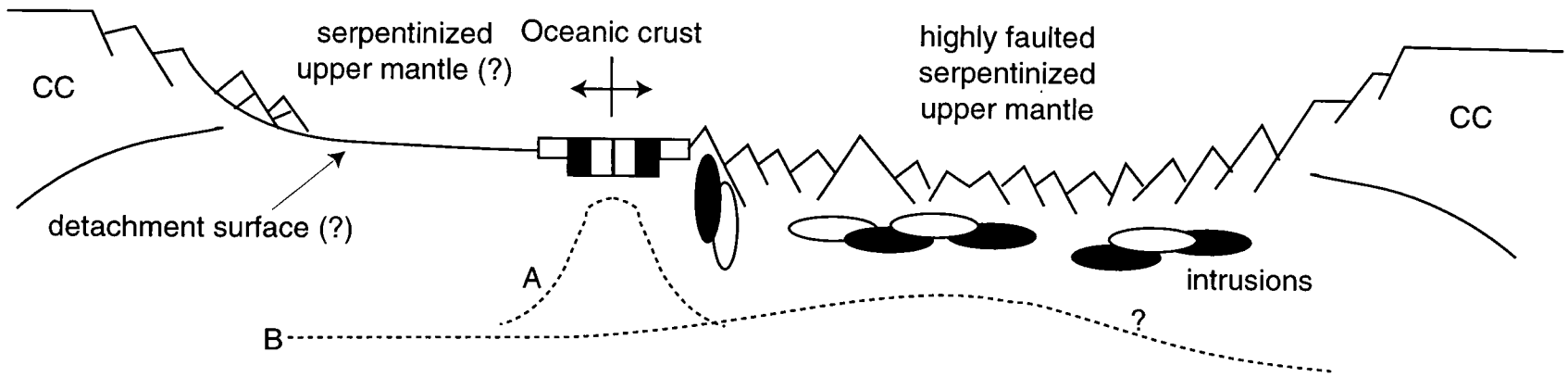

Figure 7.12 Schematic cross section through the continental margins in the southern Iberia Abyssal Plain and Newfoundland shortly after the onset of organized seafloor spreading (dashed line A marks top of melt zone). The asymmetric accretion of magmatic material may have been caused by asymmetric tectonism (i.e. simple shear). The melting model of Latin and White (1990) predicts that melt generation is much greater beneath the upper plate than the lower plate (dashed line B marks shape of top of melt zone prior to the initiation of seafloor spreading). Therefore, it is suggested that West Iberia represents the upper plate in a 'top-to-the-east' sense of simple shear model

might account for some of the observed extension. Figure 7.12 shows a schematic section through the two conjugate margins.

7.3 A comparison with other geological settings

The features observed at the conjugate continental margins of West Iberia and Newfoundland, and some of the processes that occur during the proposed model of formation are compared with three settings which exhibit similar features and/or phenomena. This allows the model to draw parallels with better understood geological processes and also link phenomena that are considered distinct or end-member processes within solid Earth geophysics.

7.3.1 Red Sea

From geological and geophysical observations in and around the Red Sea the processes that are occurring and that have occurred in the recent past are thought to be remarkably similar to those which occur when a continental rift propagates and is followed spatially and temporally by the formation of oceanic crust (Cochran, 1983). Although it is uncertain as to whether the opening of the Red Sea resulted from synchronous or propagating continental rifting (Omar and Steckler, 1995), the geophysical features observed do show the characteristics of discrete stages of rifting. From south to north, the Red Sea can be divided into three regions (Cochran, 1983; Cochran et al., 1992; Fig. 7.13). Firstly, the southernmost Red Sea between 15°-20°N is a region where active seafloor spreading has been taking place for 4-5 Ma; seafloor spreading anomalies are observed and a distinct spreading axis has formed and is active at present (Roeser, 1975). Seaward dipping reflectors are observed at the top of basement at the continental margins of the southern Red Sea (Bohannon and Eittreim, 1991) therefore suggesting that eventual continental break-up and initiation of seafloor spreading was probably plume driven. Such reflectors are typical of volcanic continental margins, for example at Hatton Bank (White et al., 1987; see Chapter 1), and are assumed to be basaltic lava flows. Flood basalts found in Ethiopia, Saudi Arabia and Yemen (Moseley, 1970; Mohr, 1983; Pallister, 1987) also indicate that large scale plume related volcanism accompanied rifting. Further, dykes and plutons are observed within the OCT of the Arabian margin in the southern Red Sea (Bohannon and Eittreim, 1991).

The second region within the Red Sea, commonly called the transitional region, lies north of the region of active seafloor spreading but south of ~24°N (Fig. 7.13), where late stage continental rifting processes dominate. These processes that are currently occurring in the

central region, from 20°-24°N, are assumed to be analogous to the processes that occur during the stage between continental rifting and the onset of seafloor spreading during the development of rifted continental margins. Moreover, because this central region is thought to be beyond the effects of the Afar hot-spot the processes may be typical of those occurring at so-called "non-volcanic" margins, or at most very weakly "volcanic" margins.

The transitional region shows an along axis progression from features of the northern continental region to those of the southern oceanic region. This is portrayed by the gradual north to south increase in the density of one-dimensional basement lows or deeps culminating in the formation of a continuous two-dimensional trough which describes the axial valley of the southern region (Bonatti, 1985). Moreover, the deeps become deeper, longer and wider southwards with those furthest south displaying morphotectonic features typical of slow spreading oceanic crustal rift zone. Modelling of magnetic anomalies across the Nereus deep (Bonatti, 1985) at ~23°N implies that seafloor spreading started >2 Ma in its central part although only ~1 Ma at its northern and southern flanks, suggesting that it may represent a small scale propagating oceanic rift. Indeed, Bonatti (1985) has suggested that seafloor spreading may well initiate at 'hot points' which are located in the deeps and serve as nuclei for the initiation of seafloor spreading.

The northernmost region of the Red Sea (Fig. 7.13) is thought to be underlain by highly thinned continental crust with magmatic bodies intruded to a greater (Bonatti and Seyler, 1987) or lesser (Cochran and Martinez, 1988; Martinez and Cochran, 1988; Bonatti, 1985; Gaulier et al., 1988) degree. The rift axis does not resemble the axis in the southern Red Sea, nor, in general, is it segmented into deeps like those observed in the central transitional region. However, the Conrad Deep and the Mabahiss Deep (Fig. 7.13) are associated with high amplitude linear magnetic anomalies whose causal bodies are suggested to be rift related magmatic intrusions (Cochran et al., 1986; Pautot et al., 1986). Basaltic rocks with transitional to alkaline affinities from Brothers Island (Taviani et al., 1984), which is adjacent to Conrad Deep, support a rift related origin of the magmatic intrusions rather than an oceanic origin, even though the magnetic anomalies have amplitudes and are lineated similar to those in the central and southern parts of the Red Sea where proto- and steady-state seafloor spreading processes are occurring, respectively. However, the magnetic anomalies in the northern Red Sea south of Brothers Island cannot be modelled by seafloor spreading. Regardless, Gaulier et al. (1988) have proposed, based on their velocity models, that the region south of Brothers Island is in fact oceanic crust; an upper layer (up to 4 km thick) with velocities 5.0-5.4 km/s and a lower layer (4-5 km thick) with a velocity of ~6.7 km/s which they interpret as fractured and altered basalt and gabbro, respectively.

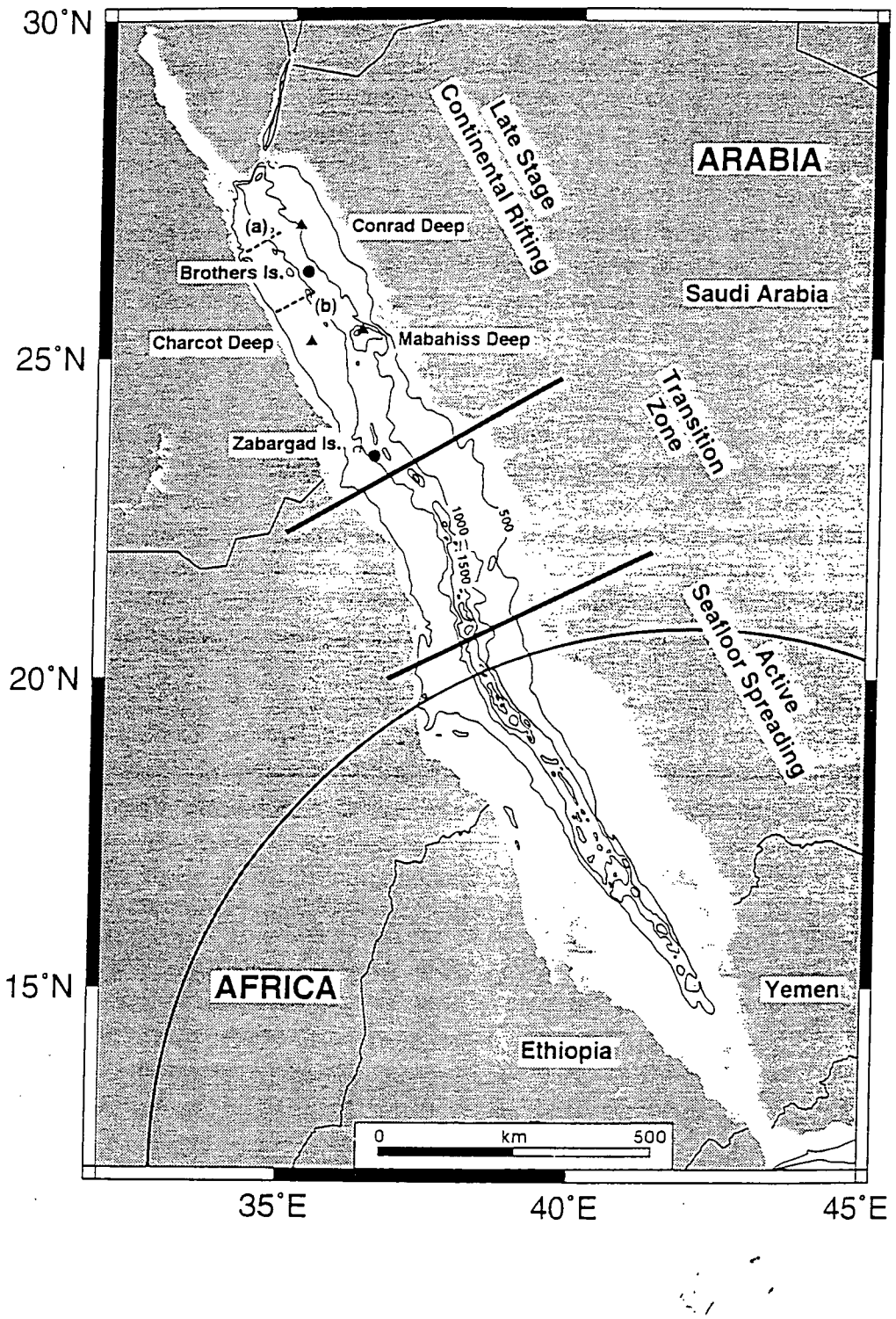

Figure 7.13 Bathymetric map (in meters) of the Red Sea showing its division into three sections which represent different stages of continental rifting (from Pickup, 1997, after Martinez and Cochran, 1988). Arc shows extent of Afar hotspot. Triangles are seafloor deeps and dots are islands.

At Zabargad Island (Fig. 7.13), near to the boundary between the central and northern regions, serpentinized mantle peridotites and metagabbros which are associated with silicic gneisses and intersected by basaltic dykes are exposed (Bonatti and Seyler, 1987). The silicic gneisses are believed to be lower continental crustal rocks which have been uplifted during rifting. Likewise mantle peridotites have been uplifted and exhumed and then presumably serpentinized by seawater. The intrusion of basaltic dykes is believed to have taken place during the uplift, i.e. syn-rift.

I propose that similar variations to those observed along axis at present in the Red Sea may also be preserved across the continental margin (axis normal) of West Iberia, but probably not across the conjugate Newfoundland margin. In this analogy, the southern Red Sea, where seafloor spreading is active along a continuous rift, represents the region seaward of the peridotite ridge where oceanic crust has been accreted by true seafloor spreading processes (basement west of and within zone A; see Chapter 5, Fig. 5.2). The central region of the Red Sea, which is described by 'deeps' of accreted crust believed to be associated with punctiform seafloor spreading (Bonatti, 1985) may represent the region immediately east of R3 and R4 in the southern Iberia Abyssal Plain (zone B; Fig. 5.2). East of the peridotite ridges, the igneous basement is made up of intrusive magmatic material which may be akin to the crust formed by punctiform seafloor spreading, i.e. immediately prior to 'organized' seafloor spreading. The basement beneath the northern region of the Red Sea, which is believed to be essentially continental crust intruded by transitional/alkaline basic syn-rift bodies, may be analogous to zone C in the southern IAP, with the exception that Red Sea basement is largely made up of (intruded) continental crust, in contrast to (intruded) upper mantle in the southern Iberia Abyssal Plain.

Although the Red Sea rift makes for a reasonable analogy to the southern Iberia Abyssal Plain and Newfoundland margins there is an important difference between the two rifts. Firstly, and most significantly, the 'country rock' for the intrusion of the gabbroic bodies across the southern Iberia Abyssal Plain is upper mantle peridotite, which has been tectonically unroofed and serpentinized. In contrast, in the northern Red Sea it is believed that the syn-rift magmatic bodies are intruded into continental crust, although the presence of serpentinized peridotites with associated dykes on Zabargad Island may suggest that they are present at or near to the top of basement in localized areas.

7.3.3 Ultraslow and slow spreading mid-ocean ridges

At ultraslow spreading ridges magma supply from the upwelling asthenosphere at the rift axis is limited, essentially due to the effects of conductive cooling (Reid and Jackson, 1981; Bown and White, 1994, 1995). At spreading rates of <~7.5 mm/yr the reduction in melt supply leads to a decrease in crustal thickness (Bown and White, 1994); at the Southwest Indian Ridge (SWIR), whose spreading rate is 6.5-7.5 mm/yr, Minshull and White (1996) observe, from seismic data, a crustal thickness of only 5 km. Likewise, at the extinct Labrador Sea spreading centre, where the spreading rate gradually diminished as the North Atlantic Rift moved location (see Chapter 2), a crustal thickness of 3-4 km is observed on seismic velocity models (Louden et al., 1996). At the Gakkel Ridge in the Arctic Ocean where the spreading rate is 3-6.5 mm/yr, Coakley and Cochran (1998) infer a crustal thickness of, at most, 4 km and suggest it may actually be vanishingly thin with large regions of uppermost basement consisting of exposed upper mantle peridotite.

The decrease in melt supply and the increased significance of mechanical extension at oceanic rifts whose plate separation is low (< 10 mm/yr) and at the inside corners of slow spreading ridge segments (e.g. MAR at 22°-24°N; Cannat et al., 1995) may be significant in the southern Iberia Abyssal Plain. If seafloor spreading models in the southern IAP (spreading rates of <10 mm/yr) are correct, or at least are correct within the context of the model presented in Chapter 6, the observed lack of melt derived products, in particular extrusives, in ODP Leg 149 and 173 cores may be explained by a similar mechanism to that which reduces melt at ultraslow spreading ridges. The dominance of tectonism and slow extension rates within the rift results in the reduction in melt. Furthermore, the exposure and relatively rapid serpentinization by seawater of upper mantle creates a impermeable lid to any upwardly rising melt products, thus preventing extrusion (see sections 6.4 and 6.5); the local absence of such a lid may result in the formation of a quasi-oceanic upper basement. However, it is extremely important to note that at the SWIR and the Gakkel Ridge the processes contributing to seafloor spreading are stable (i.e. steady-state) whereas processes responsible for the emplacement of intrusives within basement beneath the southern IAP were unstable. The transition from continental rift related conditions (intrusion under the 'rift' stress regime) to oceanic rift related conditions (intrusion under 'drift' stress regime) necessarily implies that the comparison with ultraslow spreading ridges conditions is not entirely valid. This may explain why the seismic velocity structure beneath the southern IAP does not match with that adjacent to the SWIR (Muller et al., 1997).

The along axis changes within slow spreading ridge segments may also provide an analogy for the observations in the OCTs of the southern Iberia Abyssal Plain and its conjugate in the Newfoundland Basin. At segment ends, it is now widely accepted that significantly different processes occur at the inside and outside corners. At inside corners, large low-angle slip surfaces have been observed (e.g. Cann et al., 1997); these have been interpreted to be low-angle detachment faults which result in asymmetric unroofing of lower crustal gabbros and upper mantle peridotites in a similar manner to the unroofing of metamorphic core complexes in the Basin and Range Province (e.g. Blackman et al., 1998). Serpentinization of peridotites may also significantly reduce the strength of these slip surfaces (Escartín et al., 1997) causing increased extension.

In contrast, the outside corners of slow spreading ridge segments have been shown to be made up of many steeper and closely spaced faults similar to the fault pattern observed at segment centres (Searle et al., 1998). More importantly, at segment ends the accretion of the magmatic crust has been shown to be highly asymmetric; spreading at inside corners can be primarily amagmatic and dominated by tectonism, whilst magma accretion is almost exclusively restricted to the outside corners (Sauter et al., 1997; Searle et al., 1998).

I tentatively suggest that the model for margin development presented above can be likened to the processes occurring at slow and ultraslow spreading ridge segment ends; the OCT in the southern Iberia Abyssal Plain, with a relatively rougher basement surface and a greater thickness of melt, is likened to the outside corner, whilst the conjugate OCT in the Newfoundland Basin, with a smooth basement surface and lack of melt, is likened to the inside corner. If this analogy of asymmetric accretion is valid, the sources of oldest seafloor spreading anomalies, which can be modelled in the Iberia Abyssal Plain (Fig. 6.10) at spreading rates of 6 mm/yr, actually represent the full width of accreted material at the ridge axis. Therefore, spreading rates of 12 mm/yr explain the magnetic observations (i.e. twice the spreading rate assumed under symmetric accretion) and therefore an approximately constant plate separation rate is observed across the width of the OCT. However, again I stress that the tectonic and magmatic processes contributing to seafloor spreading at present day mid-ocean ridges are stable (i.e. steady-state) whereas processes responsible for the generation of the OCTs in the southern IAP and offshore Newfoundland were unstable.

7.3.3 Southwest Greenland and Labrador conjugate margin pair

The margins of southwest Greenland and Labrador are remarkably similar to the West Iberia and Newfoundland margins in terms of their widths and geophysical properties. OCTs of

~170 km width have been inferred, from MCS data (Chalmers and Laursen, 1995), at both margins (Fig. 7.14). Landward of each OCT, tilted fault blocks indicative of thinned continental crust are present (Chian et al., 1995; Chalmers and Laursen, 1995). At the SW Greenland margin, seismic refraction models suggest that continental crust is thinned to ~3 km and is heavily intruded (Chian and Louden, 1994). Seaward of each OCT magnetic anomalies have been identified; the oldest anomaly, identified without question is a27(N) (Srivastava, 1978; Chalmers and Laursen, 1995). Beneath and seaward of a27(N) Moho reflections are observed (Keen et al., 1994) which are in excellent agreement with a crustal thickness of ~7 km from seismic refraction models (Chian et al., 1995).

The transitional basement between unequivocal continental crust and unequivocal oceanic crust on both margins has been studied by seismic refraction methods. At the Greenland margin two distinct velocity layers are observed; an upper 1-2 km thick layer with low velocity and high velocity gradients (4-5 km/s), and a lower 5 km thick layer with lower gradient and velocities of 6.4-7.7 km/s (Chian et al., 1995). A strong reflector is observed between the two layers as well as reflections interpreted to be faults, sill, dykes and larger igneous bodies within the lower layer (Chalmers and Laursen, 1995). A similar velocity structure is observed in the OCT at the Labrador margin (Chian et al., 1995).

Magnetic anomalies, which are observed in the OCT at both margins, are low in amplitude (<150 nT) and lineated approximately parallel to unequivocal seafloor spreading anomalies a27(N) and younger which are observed seaward of the OCTs (Srivastava, 1978; Roest and Srivastava, 1989a and b). Attempts to model these anomalies as seafloor spreading anomalies have been varied; Chalmers (1991) and Chalmers and Laursen (1995) could not produce a satisfactory model for a constant spreading rate, whilst Srivastava and Roest (1995) have modelled anomalies a33Y(N), and in some instances a33O(N), and younger, with variable spreading rates. At the SW Greenland margin spreading rates of 7.0, 6.5, 11.5, 15.6 and 11.5 mm/yr (from continent to ocean) are used to provide a fit between observed and calculated anomalies between a33O(N) and a24(N) within the OCT. At the Labrador margin, spreading rates of 5.8, 17.0, 10.3, 15.6 and 11.5 mm/yr (from continent to ocean) are required to model the same anomalies. Because such varied [up to ~3-fold increase in] spreading rates are necessary it is not usually considered satisfactory to accept the magnetic model as a plausible geological model; nowhere on Earth are such varied spreading rates observed within unequivocal oceanic crust. Indeed, Srivastava and Roest (1995) do note that these anomalies, because of their relatively lower amplitude and broader wavelength, may be caused by the injection of volcanic material into and through continental crust.

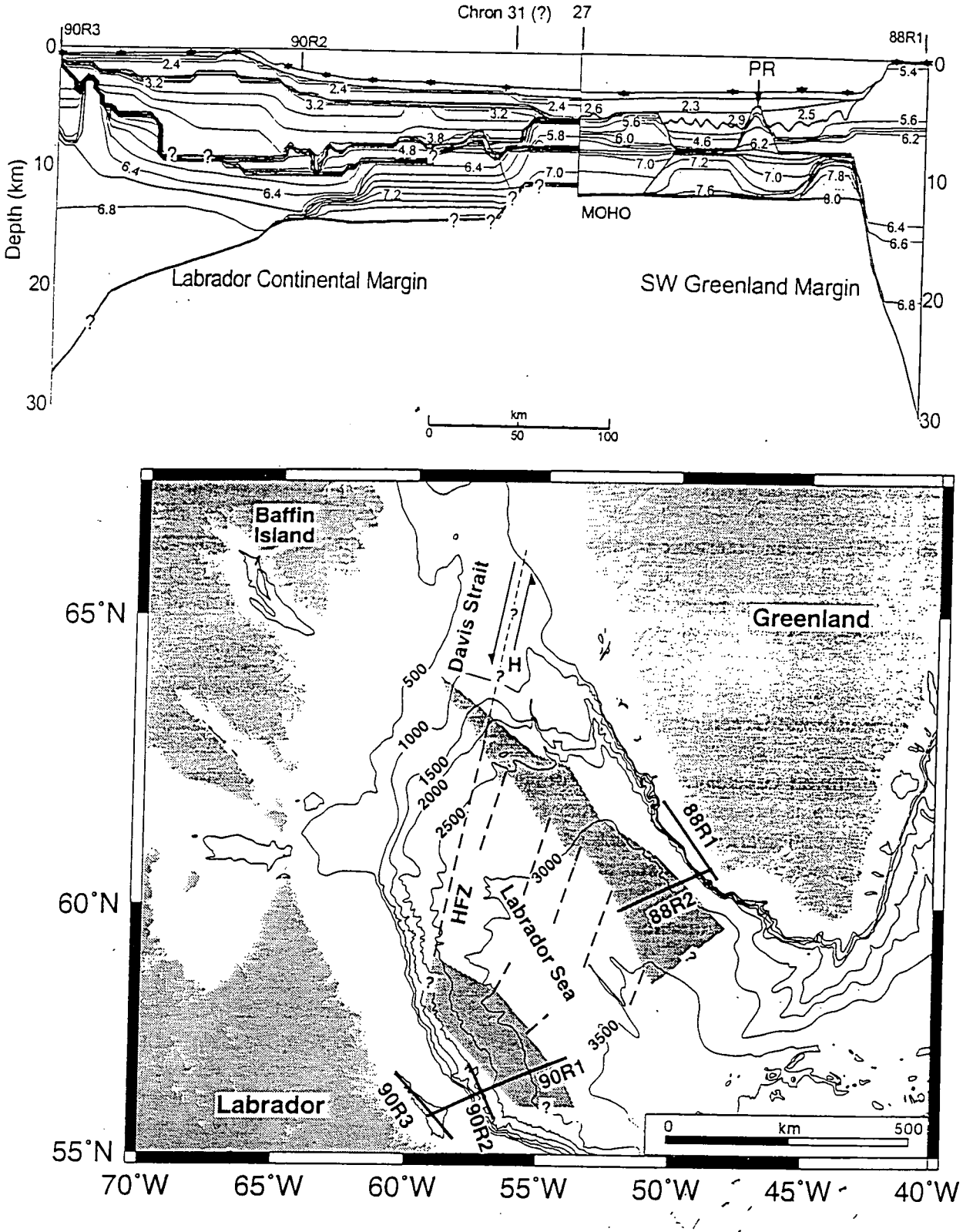

Figure 7.14 (top) Reconstruction at C27 time of crustal velocity contour profiles (in km/s) along seismic refraction lines 88R2 (Chian and Louden, 1994) and 90R1 (Chian et al., 1995) across the Labrador Sea. PR=possible peridotite ridge. (bottom) Bathymetric chart of the Labrador Sea (contoured at 500 m intervals) showing positions of seismic refraction lines 88R2 and 90R1. Shaded areas are regions of OCT. Dashed lines are fracture zones (HFZ=Hudson Fracture Zone) (figure and caption from Pickup, 1997).

Srivastava and Roest (1995) also suggest that there is a correlation between the modelled spreading rate and the degree of roughness of the basement surface. During [relatively] slow spreading the basement surface is rough, in contrast to during [relatively] fast spreading where the basement is smooth. Moreover, they suggest that the entire crust, if assumed to be oceanic, is only ~3 km thick, although, Louden et al. (1996) have suggested, from observations in the Central Labrador margin, that apparent thin layers of oceanic crust are actually faulted and rotated normal thickness layers of oceanic crust. In fact the thin igneous layer might actually be a result of limited melt supply (e.g. Bown and White, 1995) and increased tectonic thinning at slow spreading rates.

The magnetic character of the conjugate OCT pairs off West Iberia and Newfoundland compared with those off SW Greenland and Labrador show the following features common to both:

(1) Seismic velocity models suggest that a zone up to 170 km wide consisting of serpentinized mantle peridotite is present and makes up the OCT.

(2) Magnetic anomalies, some of which can be modelled by seafloor spreading at variable rates.

(3) Relatively smooth basement surface, as observed from MCS data.

I tentatively suggest that the anomalies within the OCT of the SW Greenland and Labrador margins may be caused by the processes which, as I interpret, have lead to the development of the margin within the southern Iberia Abyssal Plain. In both scenarios seafloor spreading anomalies can be modelled yet all other independent evidence suggests that the basement is composed essentially of serpentinized peridotite. It is the processes similar to those occurring at ultraslow spreading ridges and in the central and northern Red Sea that allow this dual character to exist.

7.5 Summary

A review of pre-existing geophysical data, and the interpretation of a new digital magnetic anomaly chart at the Newfoundland margin conjugate to the margin in the southern Iberia Abyssal Plain, have further constrained the possible model of conjugate margin formation presented in Chapter 6. Modelling of seafloor spreading anomalies has revealed that seafloor spreading commenced at CM5(R) time, consistent with the timing of initiation of organized seafloor spreading in the southern Iberia Abyssal Plain. Within the OCT, very few, if any, linear magnetic anomalies are observed on sea surface anomaly charts, before and after

reduction to the pole; instead anomalies are sub-circular. The mean depth to the sources of the sub-circular anomalies within the OCT was found to be at ~7 km depth, and more importantly, in a single distinct population whose skewness suggests structural indices of 1.0 or 1.5 best describe the geometry of sources.

Acoustic basement from six single-channel, and one multichannel, seismic reflection profiles was estimated to be at ~7 km depth. Moreover, the basement surface is extremely smooth on all but one seismic section. I suggest that, because of the almost constant depth to acoustic basement and the circular magnetic anomalies, whose sources are at the top of basement, the sources of magnetic anomalies are more likely to be bodies of serpentinized peridotite than magmatic intrusions. Velocity models located in the OCT to the north and south of the study region are consistent with basement consisting of serpentinized peridotite; in fact their velocity profiles strongly resemble some of those from the southern Iberia Abyssal Plain (Chian et al., in press; Dean et al., submitted).

Because of the contrasting sources of magnetic anomalies at the conjugate margins, I suggest that a significant asymmetry between the two margins exists, particularly when considering thicknesses of melt. Therefore, it is possible that margin formation was a result of simple shear; in comparison with the model of Wernicke (1985) a 'top-to-the-east' sense of shear can explain the observations. Calculations on theoretical melt thicknesses predict that ~2 km of melt is produced beneath the upper plate, whilst no melt is produced beneath the lower plate. Because these theoretical melt thickness agree with predicted thicknesses from the suggested model (derived from the results of this magnetic study with constraints from seismics), the margin in the southern Iberia Abyssal Plain is likened to the upper plate, whilst the Newfoundland margin is likened to the lower plate. Such an analogy can account for the differences in basement relief observed. However, the simple shear model predicts that significant displacement takes place along an intra-crustal or intra-lithospheric detachment fault, which is not observed on MCS profiles in the southern Iberia Abyssal Plain, or on profile 85-4 offshore Newfoundland.

The proposed model of margin development is compared with the Red Sea rift, slow and ultraslow present day spreading centres, and the conjugate rifted continental margins of southwest Greenland and Labrador. I tentatively suggest that the progressive south to north transition from normal oceanic crust, through unorganized and proto-oceanic crust, to thinned continental crust observed within the Red Sea rift, are also observed across the West Iberia margin in the southern Iberia Abyssal Plain from west to east. In contrast, at the conjugate Newfoundland margin, the absence of melt cannot be explained by the Red Sea analogy. Instead, the two conjugate margins draw similarities with the tectonic and magmatic processes

that occur at ultraslow and slow spreading centres. The extremely common occurrence of serpentinized peridotites and the vanishingly thin magmatic crust, which can result in the absence of seafloor spreading anomalies, are likened to the OCT in the southern Iberia Abyssal Plain. Moreover, at the ends of individual ridge segments, near to transform or non-transform discontinuities, the asymmetric accretion of magmatic crust and differences in tectonic styles are likened to the conjugate margins. In particular, the relatively smooth detachment-like slip surfaces and the absence of magmatism at tectonically dominated inside corners may be likened to the smooth, magma starved basement in the Newfoundland Basin. In contrast, the magmatically dominated, but frequently (relatively high angle) normal faulted basement at outside corners may be likened to the basement in the southern Iberia Abyssal Plain. The increased width of the IAP OCT may be accounted for by the asymmetric accretion of magmatic material, in this case; separation rates from seafloor spreading models therefore underestimate, by one half, the true separation rate.

Finally, geological and geophysical observations at the SW Greenland and Labrador continental margins reveal that the character of the OCTs there is very similar to the OCT in the southern Iberia Abyssal Plain. The velocity structures, and the need for varied seafloor spreading rates to model magnetic anomalies, suggests that the mode of formation of the margin pair may be similar to that proposed for the formation of the West Iberia and Newfoundland conjugate continental margin pair.

Chapter Eight

Summary and conclusions

The analysis of magnetic anomalies at the conjugate rifted continental margins at the southern Iberia Abyssal Plain and the Newfoundland Basin has revealed that the sources of magnetic anomalies are distinctly different at the two margins. The conjugate pair of, so-called, 'non-volcanic' rifted margins formed in Lower Cretaceous times when Iberia separated from Newfoundland as the North Atlantic rift system propagated northwards. Extension and thinning of continental crust was accompanied by unroofing and exposure of the upper mantle leading to the development of an ocean-continent transition zone (OCT) at each margin. In the southern Iberia Abyssal Plain, geological and geophysical research has constrained the origin of basement within the, up to 160 km wide, OCT as serpentinized mantle peridotite (e.g. Sawyer and Whitmarsh, 1994; Whitmarsh et al., 1996; Pickup et al., 1996; Discovery 215 Working Group, 1988; Whitmarsh et al., 1998; Chian et al., in press; Dean et al., submitted). In the conjugate OCT in the Newfoundland Basin basement is of ambiguous nature and origin. Thinned continental crust lies landward of, whilst oceanic crust lies seaward of, each OCT. This thesis therefore aims to constrain the width and geological nature of each OCT by analysing the nature of magnetic sources within crystalline basement at, and adjacent to, the OCTs at both margins, by analysis of magnetic anomalies.

Determining the character of magnetic sources was accomplished by the application of a number of interpretational techniques. These techniques fall broadly into two groups; direct and gradient methods and indirect methods. The application of direct methods relies upon fewer assumptions than the application of indirect methods, although the classification is somewhat subjective. The application of indirect forward and inverse modelling methods relies upon assumptions concerning the direction of magnetization and the position and geometry of magnetic sources. In contrast, in the application of direct methods these assumptions are not necessary. Both classes of method were tested on synthetic magnetic anomalies in order to assess and monitor their limits and resolving powers. Confidence in the application of these techniques to the magnetic anomalies at the continental margins of West Iberia and Newfoundland necessarily required the testing procedure.

Euler deconvolution and spectral analysis of magnetic anomaly charts were used to compute the depths to the sources of magnetic anomalies. The power spectrum, computed from the synthetic magnetic field over two ensembles of magnetic sources, was forward modelled by

the Spector and Grant (1970) method; source depths were underestimated. For realistic source layer thicknesses, the method was also found to be extremely insensitive to changes in thickness and therefore was unable to correctly determine the true layer thickness. In addition, recent criticism of the method, based on theoretical grounds, led me to apply other power spectral methods to the observed magnetic anomalies in order to determine source depth. Inversion of the power spectrum was accomplished by three different methods in which a more realistic description of the source was assumed. The Spector and Grant (1970) approach assumes that source depths are distributed, in a rectangular fashion, about a mean depth, and that no scaling relationship exists between length scales. In contrast the first inverse methods assume the more realistic Gaussian source depth probability distribution, the second inverse method assumes that a correlation exists between length scales, whilst the third inverse method is a combination of the two. Estimates of scaling exponents can be used to determine the geometrical distribution of magnetization.

Estimates of magnetic source depth were also made by application of Euler deconvolution. I showed that minimizing the operator size was sufficient to correctly depth-locate the sources of magnetic anomalies; reduction-to-the-pole was not necessary. However, the close proximity of magnetic sources and the indeterminate nature of magnetic source geometries did result in under- and over-estimation of source depths. Therefore, it was found that the most reliable means of interpreting source depth solutions was via a statistical approach. This also provided a practical solution to the problem of very many closely spaced Euler solutions. The most probable, and therefore the correct, source depth was determined from the averages in solution distributions. The degree of under- and over-estimation of solution depths was gauged through the skewness of distributions; the most probable source geometry, defined by a structural index, was assigned based on a minimum in the absolute value of distribution skewness. The average depth of sources was defined by the average depth for the chosen structural index. Multiple source depths were identified through the kurtosis parameter; large distribution tails are indicative of more than one set of sources. For two source depth populations the most probable depths were identified on solution histograms. The statistical interpretational methods were tested on synthetic anomalies are were found to be sufficiently accurate for further application to real anomalies.

Indirect magnetic methods have been used to model the observed anomalies at the continental margins in the southern Iberia Abyssal Plain and in the Newfoundland Basin, and also to assess the significance of such models. It was shown that two-dimensional magnetic models constructed either 7 km or 2 km below the observation level are a good approximation to 2.5-D bodies, providing half-strike lengths are > 20 km. Errors of less than 5% in anomaly

amplitude were found. Therefore, real sea surface and near-bottom magnetic observations, approximated by observations 7 km and 2 km above the source, respectively, can be modelled by 2-D bodies.

The sources of seafloor spreading anomalies can be modelled as normally and reversely magnetized vertically sided blocks with uniform magnetization. Magnetizations of 0.7-1.5 A/m are good representations of a realistically layered oceanic crust as determined from seismic, igneous and magnetization structures. Multiple juxtaposed blocks were used to compute the theoretical anomaly over oceanic crust accreted in the period CM0(R) to CM26(N) (120-155 Ma). Anomalies generated in the period CM0(R)-CM3(R) can be identified as distinct anomalies at spreading half-rates as low as 2 mm/yr. In contrast, anomalies generated in the period CM4(N)-CM16(N) cannot be identified as distinct anomalies at spreading half-rates less than 16 mm/yr when observed 7 km above the source layer. When anomalies are observed 2 km above the source layer most seafloor spreading anomalies can be identified if spreading rates > 8 mm/yr are used in the model construction. The inverse indirect method of solving the magnetization solution can, however theoretically retrieve anomalies formed between CM0(R)-CM16(N) at spreading rates of as low as 6 mm/yr. The amplitudes of seafloor spreading anomalies in the range CM4(R)-CM16(N), when computed 7 km above a source layer, compare with the amplitudes of anomalies observed at the sea surface generated by a realistic topography on the upper surface of a uniformly magnetized source layer. Therefore, theoretically a source layer topography should be used in magnetic models. Retrieval of a topography from the upper surface of a uniformly magnetized source layer cannot be accomplished by inverse methods; application is made difficult because of diverging solutions caused by the non-linear nature of the problem.

Application of the above techniques to magnetic anomalies observed west of Iberia, together with the interpretation of the top of acoustic basement, picked from over 1500 line km of multichannel seismic data, has revealed distinct types of magnetic sources over thinned continental crust, over the OCT and over oceanic crust. Over continental crust, observed magnetic anomalies become only moderately lineated, in a N-S and NNW-SSE direction, when reduced-to-the-pole using magnetization declinations of 0° and –15°. I interpret these declinations as indicative of an induced magnetization, although some contribution of NRM cannot be ruled out. Those anomalies which become moderately lineated at first sight appear to correlate well with linear N-S trending basement features that extend south from Vasco da Gama seamount beneath the southern Iberia Abyssal Plain. However, coherency tests reveal that there is no statistically significant correlation between basement topography and magnetic anomalies at any wavelength within this region. Because the results from ODP Legs 149 and

173 largely confirm the presence of continental rocks in this region, I infer that the sources of magnetic anomalies are not within the continental fault blocks, unlike previous speculations by Whitmarsh and Miles (1995). In addition, although numerical experiments showed that basement topography can produce significant magnetic anomalies, I found that no significant correlation between topography and magnetic anomaly existed at any wavelength anywhere in the southern Iberia Abyssal Plain. Although there exists one exception of a correlation at wavelengths of 17 km near 40°20'N, its lack of lateral continuity suggests that in general there the basement topography contributes an insignificant amount to the observed magnetic field in the southern Iberia Abyssal Plain.

Over the assumed region of continental crust source depths are hard to define by power spectral methods because of the probable scaling nature of crustal magnetization; scaling exponents of 2-3 are largely consistent with those predicted for the distribution of crustal susceptibility in continental areas. The trade off between scaling exponent and source depth estimates means that little depth information resides in the power spectrum. Source depths derived from an analysis of Euler solutions are broadly distributed, essentially due to large variations in depth to acoustic basement (1-9 km), and the large variation in depth to the base of continental crust. However, many solutions cluster at 3-7 km depth below sea level although it is possible that sources are present as deep as 15-20 km.

Over the OCT, magnetic anomalies become strongly lineated in two different directions after reduction-to-the-pole; over the majority of the OCT anomaly trends of 010° become apparent, whilst in the easternmost ~50 km of the OCT trends of 350° become apparent. Both sets of lineations are best achieved using a magnetization declination of 0°, although some of the same trends are apparent when declinations of -15° and -30° are used. I interpret these declinations as indicative of NRM acquisition after, and possibly during, the time period when Iberia was moving as an independent plate. Some of the 010° trending anomalies cross cut the seaward limit of continental crust as inferred from the interpretation of MCS records and ODP results. The depths of the sources of both sets of lineated anomalies fall into two populations; a population at, or near to, the top of acoustic basement, and a second population 5-6 km below the top of acoustic basement. Spectral analyses of the sea surface magnetic field could not determine source depths due to the probable scaling nature of the magnetization distribution; scaling exponents of ~2 suggest that the scaling nature of magnetization occurs in two Cartesian directions and is inconsistent with expected values of 3 if the region was underlain by continental crust.

Further constraint on the nature of the sources of these magnetic anomalies was provided by the results of Euler deconvolution and modelling of the power spectrum of three

near-bottom magnetometer profiles; the spatial distribution of solutions suggests that, in general, the shallower sources are present towards the western (immediately adjacent to the peridotite ridge) and northern (in the vicinity of the ODP drilling transect) regions of the OCT in the southern Iberia Abyssal Plain, whilst the sources at 5-6 km sub-basement depths are present in the widest part of the OCT in the vicinity of MCS profile IAM-9. In this region, preferred structural indices of 1.0 suggest the sources are dyke- or sill-like in geometrical terms. Towards the west of the OCT, Euler solutions for structural indices of 0.0, which define the edges of near vertically sided blocks, fall up to 2 km below the basement surface. At least one distinct magnetic body (B1(N)) can be traced between the three profiles, a distance of ~50 km.

Source depth estimates over oceanic crust cluster at ~7 km and are coincident with the top of acoustic basement. A structural index of 1.0 suggests that the sources may be lava-flow-like in geometry. Similar patterns of Euler solutions were observed when the magnetic field over two regions of unequivocal 'normal' oceanic crust, accreted in the early part of the anomaly 1-34 sequence and within the Cretaceous Normal Polarity Chron, was deconvolved. Euler solutions from near-bottom observations reveal that a structural index of 0.0 may better describe the solutions; seafloor spreading blocks M1(N), M1(R), M2(N), M3(R) and M4(N), derived from the inversion of the near-bottom magnetometer profiles, coincide with magnetic bodies whose sides are defined by the position of Euler solutions. Componental magnetometry also located some of these boundaries which were found to be essentially two-dimensional with ~N-S strikes.

The landward extent of oceanic crust was determined objectively by a 2-D inversion of the sea surface magnetic field and 1-D inversions of three near-bottom magnetometer profiles. Seafloor spreading blocks as young as CM5(R), defined by magnetizations of ±~1.0-1.5 A/m, are successfully identified west of peridotite ridge R3 and in a region ~10 km east of R3. The magnetization magnitudes of the oceanic blocks fall within the expected range for a realistically layered crust. An assumed crustal thickness of 4 km, which is ~3 km thinner than 'normal' Atlantic oceanic crust, is consistent with estimates derived from a wide-angle seismic experiment (Dean et al., submitted). Under a constant spreading rate assumption, only seafloor blocks younger than mid-CM3(R) can be modelled. A similar result was found when sea surface anomalies, extracted from the anomaly chart, were modelled in a less objective, forward sense. Therefore, steady-state (organized) seafloor spreading commenced ~126 Ma.

The forward modelling of sea surface magnetic anomalies across the OCT revealed that a seafloor spreading model could explain the observed anomalies, providing a variable spreading rate was assumed. Under the premise that the basement within the southern Iberia

Abyssal Plain is oceanic in origin, the pattern of magnetic reversals within the period prior to CM3(R) and the minimum depth to the magnetic source (governed by the depth to acoustic basement) necessarily results in a lack of significant seafloor spreading anomalies. However, I identified some linear anomalies which could be directly correlated with seafloor spreading anomalies generated by blocks whose widths produced a distinct anomaly. Anomalies a{M11A and M12.1}(N), aM16(N) and aM17(Y) were identified in both the southern Iberia Abyssal Plain and the Tagus Abyssal Plain; their margin parallel continuity for ~250 km, and left lateral offset consistent with anomalies aM3(R) and J, further support the hypothesis that these anomalies are similar to seafloor spreading anomalies. Moreover, anomaly a{M11A and M12.1}(N) was modelled by Pinheiro et al. (1992) in the Tagus Abyssal Plain and found to be very near to the onset of steady-state seafloor spreading. However, spreading rate increases of 6 to 8 to 10 mm/yr in the southern Iberia Abyssal Plain, and 6 to 10 mm/yr in the Tagus Abyssal Plain, were required to model these anomalies. In addition, from the direct interpretation methods described above, the sources of these anomalies are actually deeper than expected for oceanic crustal anomalies, and the velocity model of Dean et al. (submitted) does not resemble that of 'normal' oceanic crust. Therefore, it is difficult to justify a classical seafloor spreading origin for such anomalies.

To explain the results of the magnetic analyses and models presented above, in a context which is consistent with other geological and geophysical findings, I hypothesize that the origin of the magnetic anomalies within the southern Iberia Abyssal Plain originate from (1) intrusive magmatic bodies, which geophysically resemble a hybrid between syn-rift intrusions and oceanic accreted crust, and (2) serpentinized peridotite. Seismic velocity models, seismic reflection profiles and the results of ODP sampling provide strong constraints; serpentinized peridotite is thought to exist throughout the OCT (e.g. Sawyer and Whitmarsh, 1994; Pickup et al., 1996; Dean et al., submitted). I propose that relatively dense rising melt is impeded at the base of a layer of relatively less dense serpentinized peridotite, in much the same way that rising syn-rift melt is impeded and 'underplated' at the base of continental crust at 'volcanic' margins (White and McKenzie, 1989). The layer of pervasively serpentinized peridotite, determined from seismic velocity models (~2.5 km thick layer of velocity 4-5 km/s and low velocity gradient) and seismic reflection profiles (unreflective layer of Pickup et al., 1996), also acts as a source of magnetic anomalies at the basement surface. I suggest that the chaotic nature of magnetite production, and therefore secondary NRM growth, during pervasive serpentinization of peridotite results in the pattern of non-linear and sub-circular observed magnetic anomalies. For example, I propose that locally strong and point-like sources of serpentinized peridotite account for the high amplitude anomalies (~500 nT near-bottom)

observed in the vicinity of ODP Sites 899 and 898. This pattern of magnetization accounts for the lack of correlation between the observed magnetic field and basement relief, and the three-dimensional nature of magnetic boundaries derived from componental magnetometry.

The hypothesis of deeper-seated (up to ~6 km sub-basement depth) magmatic intrusions is consistent with seismic results. Dean et al. (submitted) showed that up to ~1.5 km (thickness) of melt could theoretically be added to unaltered mantle peridotite to explain the velocity structure of their 4.5 km thick lower layer (7.3-7.9 km/s). Because no distinct bodies are resolved on seismic refraction or seismic reflection records, I suggest that the intrusion of melt occurred homogeneously. Although the size of bodies may be below the seismic resolution, it is not a necessary condition; discrete magnetic bodies, which are described by their relative magnetization magnitudes and directions, are not necessarily discrete seismic bodies. Indeed, theoretical calculations of the volume of melt generated during rifting (Bown and White, 1995) predict that a melt thickness of ~1-2 km, based on estimates of rift duration, should exist at the West Iberia margin.

The spatial and temporal means by which melt is intruded is considered within the context of a propagating rift model (Whitmarsh and Miles, 1995). At some time during continental rifting, either immediately prior to or at the start of mantle exhumation, melt is intruded into exposed mantle, and perhaps even sub-continental lithospheric mantle under thin (< 10 km; Pickup et al., 1996; Chian et al, in press; Dean et al., submitted) continental crust. The alignment of intrusions is governed by the stress regime under which rifting occurs. The resulting magnetic anomalies over the westernmost thinned continental crust and the easternmost ~50 km of exhumed mantle in the vicinity of IAM-9, trend at ~350°. Increased extension, at slow rates (possibly 10 mm/yr half-rate; Pickup, 1997), results in tectonic exhumation of the mantle by the sequentially seaward activation of (brittle) normal faults, which overprint ductile deformation events from earlier uplift; these normal faults are observed on MCS profiles (e.g. Pickup et al., 1996). Such temporal faulting patterns are observed in other extensional terranes (e.g. Basin and Range). As the rift propagated northwards, the stress regime became dominated by that which accompanied oceanic crustal accretion, which was active to the south. Therefore, the continual, but limited supply of melt, and the progressive seaward activation of normal faults, resulted in a pattern of intrusions oriented parallel to the trend of [later] seafloor spreading anomalies. The resulting magnetic anomalies can therefore be modelled as 'seafloor spreading' anomalies.

The seaward shallowing of magnetic sources is attributed to the gradual increase from 'syn-rift' accretionary conditions to 'seafloor spreading' conditions. Modelled seafloor spreading blocks, M4(N) and M5(R) east of the peridotite ridge, previously assumed to be the

landward extent of accretionary crust, require that varied spreading rates of 11.5 mm/yr and 16.5 mm/yr be used. Together with spreading rates of ~10 mm/yr for oceanic crust west of the peridotite ridge, I interpret a non-steady-state-type accretion of oceanic crust, which immediately pre-dated the onset of normal seafloor spreading, and post-dated the intrusion of deeper-seated magma bodies. Furthermore, reflectors L1 and L2 identified on MCS profile IAM-9 immediately east of the peridotite ridge, are interpreted to be deeply penetrating landward dipping normal faults which are perhaps similar to those observed at mid-ocean ridges (Pickup et al., 1996).

I suggest that from the onset of continental rifting through the exhumation of the mantle and accretion of normal oceanic crust, conditions change gradually in response to the gradual approach of the northward propagating spreading centre. It is therefore very difficult to place a discrete age on the onset of seafloor spreading for the purpose of calculating volumes of syn-rift melt. However, the onset of 'organized' seafloor spreading may be assigned an age of CM3(R) (~126 Ma).

A similar, but far less detailed, magnetic study at the conjugate rifted continental margin in the Newfoundland Basin, revealed that the sources of magnetic anomalies there were distinctly different from those beneath the southern Iberia Abyssal Plain. Source depths within the OCT, which was found to be ~100 km wide, did not show a bipolar distribution. Instead the computed source depth of 7.1 km from spectral analysis, and the Euler solution distribution which clustered at ~7 km depth, were consistent with sources at the very top of acoustic basement. However, no linear anomalies were observed after reduction-to-the-pole for any sensible range of magnetization declinations used. Instead magnetic anomalies are sub-circular in plan view and cannot be modelled as seafloor spreading anomalies older than CM5(R). I therefore attribute the sources of the magnetic anomalies to serpentinized peridotite. Although continental crust cannot be ruled out based on the magnetic evidence alone, the character of acoustic basement is unlike that of thinned continental crust; the basement surface is extremely flat and uniform with the complete absence of tilted fault blocks. Moreover, seismic velocity models, to the north and south of the region, closely resemble those within the OCT in the southern Iberia Abyssal Plain, and therefore mantle rocks are interpreted to be present within the region of ambiguous character (the OCT).

Based on the results and interpretation of the magnetic study, I address the mechanism by which continental rifting and tectonic mantle exhumation took place. I draw similarities between the nature of basement in the OCT of the southern Iberia Abyssal Plain with basement generated at ultra-slow and slow-spreading mid-ocean ridges and in the transition zone of the central Red Sea. The presence of serpentinized peridotite and a reduced oceanic crustal

thickness at the Southwest Indian Ridge and Gakkel Ridge, and the presence of serpentinized peridotites and proto-oceanic type crust, generated by punctiform seafloor spreading, in the Central Red Sea, may be good analogues for the processes which resulted in the formation of the OCT in the southern Iberia Abyssal Plain. In contrast, however, I interpret the conjugate OCT in the Newfoundland Basin as essentially amagmatic. Together with the different character of acoustic basement, I tentatively suggest that there is a degree of asymmetry to the two conjugate margins which may be a result of a simple shear dominated tectonic regime. Models of melt generation under simple shear thinning of continental lithosphere predict that ~2 km thickness of magma is preferentially generated beneath the upper plate, compared to none below the lower plate. I therefore suggest that West Iberia represents the upper plate whilst Newfoundland represents the lower plate, as previously suggested for the style of rifting off Galicia Bank (e.g. Boillot et al., 1988; Sibuet, 1992). This model of conjugate margin formation also draws parallels with the asymmetric tectonic and magmatic processes which occur at the ends of slow spreading ridge segments. I compare the 'crust' at inside corners of ridge segments, typified by a lack of extrusives, and low angle faulting, with the OCT in the Newfoundland Basin, whereas the outside corners of ridge segments, typified by steeply dipping normal faults and relatively much more accretionary crust, to the OCT in the southern Iberia Abyssal Plain.

This thesis has provided vital insight into the development of a 'non-volcanic' rifted conjugate margin pair. The magnetic methods used here, although in some cases their application was shown to be problematic, have the potential to provide further insight into the development of other 'non-volcanic' rifted continental margins that posses similar geophysical features. I encourage a similar magnetic investigation at the non-volcanic margins of the North Atlantic, in particular the Tagus Abyssal Plain and its conjugate off Newfoundland, and the conjugate margins of southwest Greenland and Labrador.

I also particularly encourage the use of a statistical approach for the interpretation of Euler deconvolution solutions, when estimating source depths. Although near-bottom componental magnetometry provided vital and addition information, the analyses of sea surface magnetic anomalies can also provide information when developed to their full potential.

References

Anderson, D. L., Y. S. Zhang, and T. Tanimoto, 1992, Plume heads, continental lithosphere, flood basalts and tomography, *in* B. C. Storey, T. Alabaster, and R. J. Pankhurst, eds., Magmatism and the causes of continental break-up.: Geological Society Special Publications, London, United Kingdom, Geological Society of London, p. 99-124.

Arkani-Hamed, J., 1988, Differential reduction-to-the-pole of regional magnetic anomalies: Geophysics, v. 53, p. 1592-1600.

Atchuta Rao, D., H. V. Ram Babu, and P. Sanker Narayan, 1981, Interpretation of magnetic anomalies due to dikes: The complex gradient method: Geophysics, v. 46, p. 1572-1578.

Austin, J. A., B. E. Tucholke, and E. Uchupi, 1989, Upper Triassic-Lower Jurassic salt basin southeast of the Grand Banks: Earth and Planetary Science Letters, v. 92, p. 357-370.

Auzende, J. M., J. L. Olivet, A. Le Lann, X. Le Pichon, J. Monteiro, A. Nicolas, and A. Ribeiro, 1978, Sampling and observation of oceanic mantle and crust on Gorringe Bank: Nature, v. 273, p. 45-49.

Auzende, J. M., J. Charvet, A. Le Lann, X. Le Pichon, J. H. Monteiro, A. Nicolas, J. L. Olivet, and A. Ribeiro, 1979, Le Banc de Gorringe: résultats de la campagne CYAGOR (août 1977): Bull. Soc. géol. France, v. XXI, 5, p. 545-556.

Baker, B. H., P. A. Mohr, and L. A. J. Williams, 1972, Geology of the Eastern Rift System of Africa, Geological Society of America, Special Paper 136, 67 p.

Baker, B. H., 1987, Outline of the petrology of the Kenya Rift alkaline province, *in* J. G. Fitton, and B. G. J. Upton, eds., Alkaline igneous rocks.: Geological Society Special Publications, London, United Kingdom, Geological Society of London, p. 293-311.

Banda, E., and I A M Group, 1994, The deep structure of the Iberian Atlantic Margins investigated: the IAM Project: European Geophysical Society Newsletter, p. 4-5.

Banda, E., M. Torne, and Iberia Atlantic Margins Group, 1995, Iberian Atlantic Margins Group investigates deep structure of ocean margins: EOS, Transactions, American Geophysical Union, v. 76, p. 25-29.

Barberi, F., R. Santacroce, and J. Varet, 1982, Chemical aspects of rift magmatism, *in* G. Palmason, ed., Continental and oceanic rifts.: Geodynamics Series, Washington, DC, United States, American Geophysical Union, p. 223-258.

Basaltic_Volcanism_Study_Project, 1981, Basaltic volcanism on the terrestrial planets: New York, NY, United States, Pergamon Press, 1286 p.

Bassi, G., C. E. Keen, and P. Potter, 1993, Contrasting styles of rifting: models and examples from the eastern Canadian margin: Tectonics, v. 12, p. 639-655.

Bassi, G., 1995, Relative importance of strain rate and rheology for the mode of continental extension: Geophysical Journal International, v. 122, p. 195-210.

Belyaev, I. I., and A. M. Filin, 1995, Techniques for marine magnetic measurements, *in* A. M. Gorodnitsky, ed., Anomalous magnetic field of the world ocean., Boca Raton, FL, United States, CRC Press, p. 1-19.

Beske-Diehl, S. J., 1989, Comment on "Magnetization of the oceanic crust: thermoremanent or chemical remanent magnetization?" by C.A. Raymond & J.R. LaBrecque: Journal of Geophysical Research, v. 94, p. 3046-3048.

Beslier, M.-O., M. Ask, and G. Boillot, 1993, Ocean-continent boundary in the Iberia Abyssal Plain from multichannel seismic data: Tectonophysics, v. 218, p. 383-393.

Beslier, M.-O., G. Cornen, and J. Girardeau, 1996, Tectono-metamorphic evolution of peridotites from the ocean-continent transition of the Iberia Abyssal Plain margin, *in* R. B. Whitmarsh, D. S. Sawyer, A. Klaus, and D. G. Masson, eds., Proceedings of the Ocean Drilling Program, Scientific Results, College Station, TX, Ocean Drilling Program, p. 397-412.

Bhattacharyya, B. K., 1966, Continuous spectrum of the total magnetic field anaomaly due to a rectangular prismatic body: Geophysics, v. 31, p. 97-121.

Blackman, D. K., J. R. Cann, B. Janssen, and D. K. Smith, 1988, Origin of extensional core complexes: Evidence from th Mid-Atlantic Ridge at the Atlantis Fracture Zone: Journal of Geophysical Research, v. 103, p. 21315-21333.

Blakely, R. J., 1995, Potential theory in gravity & magnetic applications: Cambridge, United Kingdom, Cambridge University Press, 441 p.

Bohannon, R. G., and S. L. Eittreim, 1991, Tectonic development of passive continental margins of the southern and central Red Sea with a comparison to Wilkes Land, Antarctica: Tectonophysics, v. 198, p. 129-154.

Boillot, G., J. L. Auxietre, J. P. Dunand, P. A. Dupeuple, and A. Mauffret, 1979, The northwestern Iberian margin: a Cretaceous passive margin deformed during Eocene, *in* M. Talwani, W. Hay, and W. B. F. Ryan, eds., Deep Sea Drilling Results in the Atlantic Ocean: Maurice Ewing Series, Washington, D.C., AGU, p. 138-153.

Boillot, G., S. Grimaud, A. Mauffret, D. Mougenot, J. Kornprobst, J. Mergoil-Daniel, and G. Torrent, 1980, Ocean-continent boundary off the Iberian margin: a serpentinite diapir west of the Galicia Bank: Earth & Planetary Science Letters, v. 48, p. 23-34.

Boillot, G., E. L. Winterer, and Shipboard Scientific Party, 1987, Leg 103, Galicia margin: Proceedings of the Ocean Drilling Program, Initial Reports, v. 103, p. pp.663.

Boillot, G., E. L. Winterer, A. Meyer, and et al., 1988a, Leg 103: Proceedings of the Ocean Drilling Program, Scientific Results, v. 103, p. pp.858.

Boillot, G., M. C. Comas, J. Girardeau, J. Kornprobst, J.-P. Loreau, J. Malod, D. Mougenot, and M. Moullade, 1988b, Preliminary results of the Galinaute cruise: dives of the submersible Nautile on the western Galicia margin, Spain: Proceedings of the Ocean Drilling Program, Scientific Results, v. 103, p. 37-51.

Boillot, G., J. Girardeau, and J. Kornprobst, 1988c, Rifting of the Galicia margin: crustal

thinning and emplacement of mantle rocks on the seafloor: Proceedings of the Ocean Drilling Program, Scientific Results, v. 103, p. 741-756.

Boillot, G., J. Girardeau, and J. Kornprobst, 1989, Rifting of the West Galicia continental margin: a review: Bulletin Societe Geologique de France, v. 5, p. 393-400.

Boillot, G., 1990, Lusigal 90: Rapport de mission.

Boillot, G., P. Agrinier, M.-O. Beslier, G. Cornen, N. Froitzheim, V. Gardien, J. Girardeau, J.-I. Gil-Ibarguchi, J. Kornprobst, M. Moullade, U. Schaerer, and J.-R. Vanney, 1995, A lithospheric syn-rift shear zone at the ocean-continent transition: preliminary results of the GALINAUTE II cruise (Nautile dives on the Galicia Bank, Spain): Comptes Rendus Academie de Science de Paris, v. 321 Ser IIa, p. 1171-1178.

Bonatti, E., 1985, Punctiform initiation of sea-floor spreading in the Red Sea during transition from a continental to an oceanic rift: Nature, v. 316, p. 33-37.

Bonatti, E., and M. Seyler, 1987, Crustal underplating and evolution in the Red Sea rift: uplifted gabbro/gneiss crustal complexes on Zabargad and Brothers Islands: J. Geophys. Res., v. 92, p. 12803-12821.

Bott, M. H. P., 1995, Mechanics of rifting; Geodynamic modeling of continental rift systems, *in* K. H. Olsen, ed., Continental rifts; evolution, structure, tectonics., Amsterdam, Netherlands, Elsevier, p. 27-43.

Bown, J. W., and R. S. White, 1994, Variation with spreading rate of oceanic crustal thickness and geochemistry: Earth & Planetary Science Letters, v. 121, p. 435-449.

Bown, J. W., and R. S. White, 1995, The effect of finite extension rate on melt generation at continental rifts: Journal of Geophysical Research, v. 100, p. 18011-18030.

Brown, J. R., and J. A. Karson, 1989, Variations in axial processes on the Mid-Atlantic Ridge; the median valley of the MARK area: Marine Geophysical Researches, v. 10, p. 109-138.

Brun, J. P., and M.-O. Beslier, 1996, Mantle exhumation at passive margins: Earth and Planetary Science Letters, v. 142, p. 161-173.

Buck, W. R., 1986, Small-scale convection induced by passive rifting; the cause for uplift of rift shoulders: Earth and Planetary Science Letters, v. 77, p. 362-372.

Bullard, E. C., and R. G. Mason, 1961, The magnetic field astern of a ship: Deep-Sea Research, v. 8, p. 20-27.

Bullard, E. C., J. Everett, and A. G. Smith, 1965, The fit of the continents around the Atlantic: Philosophical Transactions of the Royal Society of London A, v. 258, p. 41-51.

Burke, K., 1977, Aulacogens and continental breakup: Annual Review of Earth and Planetary Sciences, v. 5, p. 371-396.

Cande, S. C., 1976, A palaeomagnetic pole from Late Cretaceous marine magnetic anomalies in the Pacific: Geophysical Journal of the Royal Astronomical Society, v. 44, p. 547-566.

Cande, S. C., and Y. Kristoffersen, 1977, Late Cretaceous magnetic anomalies in the North Atlantic: Earth and Planetary Science Letters, v. 35, p. 215-224.

Cande, S. C., 1978, Anomalous behaviour of the palaeomagnetic field inferred from the skewness of anomalies 33 and 34: Earth and Planetary Science Letters, v. 40.

Cann, J. R., D. K. Blackman, D. K. Smith, E. McAllister, B. Janssen, S. Mello, E. Avgreinos, A. R. Pascoe, and J. Escartin, 1997, Corrugated slip surfaces formed at ridge-transform intersections on the Mid-Atlantic Ridge: Nature, v. 385, p. 329-332.

Cannat, M., 1993, Emplacement of mantle rocks in the seafloor at mid-ocean ridges: Journal of Geophysical Research, v. 98, p. 4163-4172.

Cannat, M., C. Mevel, M. Maia, C. Deplus, C. Durand, P. Gente, P. Agrinier, A. Belarouchi, G. Dubuisson, E. Humler, and J. Reynolds, 1995, Thin crust, ultramafic exposures, and rugged faulting patterns at the Mid-Atlantic Ridge (22°-24°N): Geology, v. 23, p. 49-52.

Capdevila, R., and D. Mougenot, 1988, Pre-Mesozoic basement of the western Iberian continental margin and its place in the Variscan Belt, *in* G. Boillot, and E. L. Winterer, eds.: Proc. ODP, Sci. Results, College Station, TX, Ocean Drilling Program, p. 3-12.

Carbotte, S. M., and K. C. MacDonald, 1990, Causes of variation in fault-facing direction on the ocean floor: Geology, v. 18, p. 749-752.

Carlson, R. L., and G. S. Raskin, 1984, Density of the oceanic crust: Nature, v. 311, p. 555-558.

Celar, S. A. M., and K. Burke, 1978, Relative timing of rifting and volcanism on Earth and its tectonic implications: Geophysical Research Letters, v. 5, p. 419-421.

Chadwick, W. W., and R. W. Embley, 1998, Graben formations associated with recent dike intrusions and volcanic eruptions on the mid-ocean ridge: Journal of Geophysical Research, v. 103, p. 9807-9825.

Chalmers, J. A., 1991, New evidence on the structure of the Labrador Sea/Greenland continental margin: J. Geol. Soc. London, v. 148, p. 899-908.

Chalmers, J. A., and K. H. Laursen, 1995, Labrador Sea - the extent of continental and oceanic crust and the timing of the onset of seafloor spreading: Marine and Petroleum Geology, v. 12, p. 205-217.

Channell, J. E. T., E. Erba, M. Nakanishi, and K. Tamaki, 1995, Late Jurassic-Early Cretaceous time scales and oceanic magnetic anomaly block models, *in* W. A. Berggren, D. V. Kent, M. P. Aubry, and J. Hardenbol, eds., Geochronology time scales and global stratigraphic correlation, Society of Econ. Paleontol. Mineral., p. 95-128.

Chian, D., and K. E. Louden, 1994, The continent-ocean crustal transition across the southwest Greenland margin: Journal of Geophysical Research, v. 99, p. 809-818.

Chian, D., C. E. Keen, I. Reid, and K. E. Louden, 1995, Evolution of nonvolcanic rifted margins: New results from the conjugate margins of the Labrador Sea: Geology, v. 23, p. 589-592.

Chian, D., K. E. Louden, T. A. Minshull, and R. B. Whitmarsh, in press, Deep structure of the ocean-continent transition in the southern Iberia Abyssal Plain from seismic refraction profiles: I. The Ocean Drilling Program transect.: Journal of Geophysical Research.

Christensen, N. I., 1966, Elasticity of ultramafic rocks: Journal of Geophysical Research, v. 71, p. 5921-5931.

Christensen, N. I., 1972, The abundance of serpentinites in the oceanic crust: Journal of Geology, v. 80, p. 709-719.

Clarke, D. B., 1970, Tertiary basalts of Baffin bay; possible primary magma from the mantle: Contributions to Mineralogy and Petrology, v. 25, p. 203-224.

Coakley, B. J., and J. R. Cochran, 1998, Gravity evidence of very thin crust at the Gakkel Ridge (Arctic Ocean): Earth and Planetary Science Letters, v. 162, p. 81-95.

Cochran, J. R., 1983, A model for the development of the Red Sea: American Association of Petroleum Geology Bulletin, v. 67, p. 41-69.

Cochran, J. R., F. Martinez, M. S. Steckler, and M. A. Hobart, 1986, A new northern Red Sea deep. Origin and implications for continental rifting: Earth and Planetary Sciences Letters, v. 78, p. 18-32.

Cochran, J. R., and F. Martinez, 1988, Evidence from the northern Red Sea on the transition from continental to oceanic rifting: Tectonophysics, v. 153, p. 25-53.

Coggan, J. H., 1976, Magnetic and gravity anomalies of polyhedra: Geoexploration, v. 14, p. 93-105.

Coleman, R. G., 1971, Petrologic and geophysical nature of serpentinite: Geological Society of America Bulletin, v. 82, p. 897-917.

Connard, G., R. Couch, and M. Gemperle, 1983, Analysis of aeromagnetic measurements from the Cascade Range, Oregon: Geophysics, v. 48, p. 376-390.

Cornen, G., M.-O. Beslier, and J. Girardeau, 1996, Petrologic characteristics of the ultramafic rocks from the ocean/continent transition in the Iberia Abyssal Plain margin, *in* R. B. Whitmarsh, D. S. Sawyer, A. Klaus, and D. G. Masson, eds., Proceedings of the Ocean Drilling Program, Scientific Results, College Station, TX, Ocean Drilling Program, p. 377-396.

Cox, A., and G. B. Dalrymple, 1967, Statistical analysis of geomagnetic reversal data and the precision pf potassium-argon dating: Journal of Geophysical Research, v. 72, p. 2603-2641.

Cox, K. G., 1980, A model for flood basalt vulcanism: Journal of Petrology, v. 21, p. 629-650.

Cyagor Group, 1978, Le Banc de Gorringe (S-O du Portugal): un fragment de croute et manteau océanique reconnu par submersible: C.R. Acad. Sci. Paris, v. t. 285, sér. D, p. 1403-1406.

CYAGOR II Group, J. M. Auzende, G. Ceuleneer, G. Cornen, T. Juteau, Y. Lagabrielle, G.

Lensch, C. Mevel, A. Nicolas, H. Prichard, A. Ribeiro, E. Ruellan, and J. R. Vanney, 1984, Intraoceanic tectonism on the Gorringe Bank: observations by submersible, *in* I. G. Gass, S. J. Lippard, and A. W. Shelton, eds., Ophiolites and oceanic lithosphere, London, Geological Society of London, p. 113-120.

de Charpal, O., P. Guennoc, L. Montadert, and D. G. Roberts, 1978, Rifting, crustal attenuation and subsidence in the Bay of Biscay: Nature, v. 275, p. 706-711.

Dean, S. M., T. A. Minshull, R. B. Whitmarsh, and K. Louden, submitted, Deep structure of the ocean-continent transition in the southern Iberia Abyssal Plain from seismic refelaction profiles: II The IAM-9 transect at 40deg20'N: Journal of Geophysical Research.

Discovery_215_Working_Group, 1998, Deep structure in the vicinity of the ocean-continent transition zone under the southern Iberia Abyssal Plain: Geology, v. 26, p. 743-746.

Duncan, R. A., and M. A. Richards, 1991, Hotspots, mantle plumes, flood basalts, and true polar wander: Reviews of Geophysics, v. 29, p. 31-50.

Dunlop, D. J., and M. Prevot, 1982, Magnetic properties and opaque mineralogy of drilled submarine intrusive rocks: Geophysical Journal of the Royal Astronomical Society, v. 69, p. 763-802.

Dupeuple, P. A., J. P. Réhault, J. L. Auxiètre, J. P. Dunand, and L. Pastouret, 1976, Résultats de dragages et essai de stratigraphie des bancs de Galice et des montagnes de Porto et de Vigo (marge occidentale iberique): Marine Geology, v. 22, p. 37-49.

Dupeuple, P. A., G. Boillot, and D. Mougenot, 1987, Upper Jurassic - Lower Cretaceous limestones dredged from the West Galicia margin, *in* G. Boillot, and E. L. Winterer, eds.: Proc. ODP, Init. Repts, ODP, p. 99-105.

Dyment, J., S. C. Cande, and J. Arkani-Hamed, 1994, Skewness of marine magnetic anomalies created between 85 and 40 Ma in the Indian Ocean: Journal of Geophysical Research, v. 99.

Dyment, J., and J. Arkani-Hamed, 1995, Spreading-rate-dependent magnetization of the oceanic lithosphere inferred from the anomalous skewness of marine magnetic anomalies: Geophysical Journal International, v. 121, p. 789-804.

Edwards, R. A., R. B. Whitmarsh, and R. A. Scrutton, 1997, The crustal structure across the transform continental margin of Ghana, eastern Equatorial Atlantic: Journal of Geophysical Research, B, Solid Earth and Planets, v. 102, p. 747-772.

Emery, K. O., and E. Uchupi, 1984, The geology of the Atlantic Ocean: Springer-Verlag, 1050 p. .

Escartin , J., G. Hirth, and B. Evans, 1997, Effects of serpentinization on the lithospheric strength and the style of normal faulting at slow-spreading ridges: Earth and Planetary Science Letters, v. 151, p. 181-189.

Farrelly, B., 1997, What is wrong with Euler deconvolution?: EAGE 59th Conference and Technical Exhibition.

Féraud, G., D. York, C. Mével, G. Cornen, C. M. Hall, and J. M. Auzende, 1986, Additional

40Ar-39Ar dating of the basement and the alkaline volcanism of Gorringe Bank (Atlantic Ocean): Earth Planet. Sci. Lett., v. 79, p. 255-269.

Féraud, G., J. Girardeau, M.-O. Beslier, and G. Boillot, 1988, Datation 39Ar-40Ar de la mise en place des peridotites bordant la marge de la Galice (Espagne): Comptes Rendues Academie des Science de Paris, v. 307 Ser. II, p. 49-55.

Féraud, G., M.-O. Beslier, and G. Cornen, 1996, 40Ar/39Ar dating of gabbros from the ocean/continent transition of the western Iberia Margin: preliminary results, *in* R. B. Whitmarsh, D. S. Sawyer, A. Klaus, and D. G. Masson, eds., Proceedings of the Ocean Drilling Program, Scientific Results, College Station, TX, Ocean Drilling Program, p. 489-496.

Foucher, J. P., X. Le Pichon, and J. C. Sibuet, 1982, The ocean-continent transition in the uniform lithospheric stretching model: role of partial melting in the mantle: Phil. Trans. Roy. Soc. London, v. 305A, p. 27-40.

Frost, B. R., and P. N. Shive, 1986, Magnetic mineralogy of the lower continental crust: Journal of Geophysical research, v. 91, p. 6513-6521.

Furlong, K. P., and D. M. Fountain, 1986, Continental crustal underplating; thermal considerations and seismic-petrologic consequences: JGR. Journal of Geophysical Research. B, v. 91, p. 8285-8294.

Galdeano, A., M. G. Moreau, J. P. Pozzi, P. Y. Berthou, and J. A. Malod, 1989, New paleomagnetic results from Cretaceous sediments near Lisboa (Portugal) and implications for the rotation of Iberia: Earth and Planetary Science Letters, v. 92, p. 95-106.

Garcia-Abdeslem, J., and G. E. Ness, 1994, Inversion of the power spectrum from magnetic anomalies: Geophysics, v. 59, p. 391-401.

Gaulier, J. M., X. Le Pichon, N. Lyberis, F. Avedik, L. Geli, I. Moretti, A. Deschamps, and S. Hafez, 1988, Seismic study of the crust of the northern Red Sea and Gulf of Suez: Tectonophysics, v. 153, p. 55-88.

Gibson, I. L., M.-O. Beslier, G. Cornen, K. L. Milliken, and K. Seifert, 1996, Major- and trace-element seawater alteration profiles in serpentinite formed during the development of the Iberia Margin, Site 897, *in* R. B. Whitmarsh, D. S. Sawyer, A. Klaus, and D. G. Masson, eds., Proceedings of the Ocean Drilling Program, Scientific Results, College Station, TX, Ocean Drilling Program, p. 519-528.

Girardeau, J., G. Cornen, P. Agrinier, M. O. Beslier, G. Dubuisson, B. Le Gall, C. Monnier, L. Pinheiro, A. Ribeiro, and H. Whitechurch, in press, Resultats des plongees du Nautile sur le Banc de Gorringe: C.R. Acad. Sci. Ser. 2.

Goldberg, D., and B. Zinszner, 1988, Acoustic properties of altered peridotite at Site 637 from laboratory and sonic waveform data: Proceedings of the Ocean Drilling Program, Scientific Results, v. 103, p. 269-276.

Grachev, A. F., 1982, Geodynamics of the transitional zone from the Moma rift to the Gakkel Ridge, *in* J. S. Watkins, and C. L. Drake, eds., Studies in continental margin geology, Tulsa, American Association of Petroleum Geology Memoirs, p. 103-113.

Gradstein, F. M., F. P. Agterberg, J. G. Ogg, J. Hardenbol, P. Van Veen, J. Thierry, and Z. Huang, 1995, A Triassic, Jurassic and Cretaceous time scale, *in* W. A. Berggren, D. V. Kent, M. P. Aubry, and J. Hardenbol, eds., Geochronology time scales and global stratigraphic correlation, Society of Econ. Paleontol. Mineral., p. 95-128.

Gregotski, M. E., O. G. Jensen, and J. Arkani-Hamed, 1991, Fractal stochastic modelling of aeromagnetic data: Geophysics, v. 56, p. 1706-1715.

Groupe Galice, 1979, The continental margin of Galicia and Portugal, acoustic stratigraphy, dredge stratigraphy and structural evolution, *in* W. B. F. Ryan, and J.-C. Sibuet, eds.: Initial Reports of the Deep Sea Drilling Project, Washington, D.C., U.S. Government Printing Office, p. 633-662.

Gurnis, M., 1988, Large-scale mantle convection and the aggregation and dispersal of supercontinents: Nature (London), v. 332, p. 695-699.

Hahn, A., E. G. Kind, and D. C. Mishra, 1976, Depth estimation of magnetic sources by means of Fourier amplitude spectra: Geophysical Prospecting, v. 24, p. 287-308.

Harland, W. B., R. L. Armstrong, A. V. Cox, L. E. Craig, A. G. Smith, and D. G. Smith, 1990, A geologic time scale 1989, Cambridge University Press.

Harrison, C. G. A., 1976, Magnetization of the oceanic crust: Geophysical Journal of the Royal Astronomical Society, v. 47, p. 257-283.

Harrison, C. G. A., 1987, Marine magnetic anomalies - the origin of the stripes: Annual Review of Earth and Planetary Sciences, v. 15, p. 505-543.

Harry, D. L., and D. S. Sawyer, 1992, A dynamic model of extension in the Baltimore Canyon Trough region: Tectonics, v. 11, p. 420-436.

Herzberg, C. J., W. S. Fyfe, and M. J. Carr, 1983, Density constraints on the formation of the continental Moho and crust: Contributions to Mineralogy and Petrology, v. 84, p. 1-5.

Hess, H. H., 1962, History of ocean basins, Petrologic studies--A volume in honor of A. F. Buddington., p. 599-620.

Hinz, K., and H.-U. Schulter, 1978, The North Atlantic - results of geophysical investigations by the Federal Institute of Geoscience and Natural Resources on the North Atlantic continental margins: Erdol-Erdgas-Z., v. 04, p. 271-280.

Hoffman, H.-J., and T. J. Reston, 1992, Nature of the S reflector beneath the Galicia Banks rifted margin. Preliminary results from pre-stack depth migration.: Geology, v. 20, p. 1091-1094.

Holbrook, W. S., and P. B. Keleman, 1993, Large igneous province on the US Atlantic margin and implications for magmatism during continental breakup: Nature, v. 364, p. 433-436.

Hood, P., 1965, Gradient measurements in aeromagnetic surveying: Geophysics, v. 30, p. 891-902.

Hooft, E. E., and R. S. Detrick, 1993, The role of density in the accumulation of basaltic melts at mid-ocean ridges: Geophysical Research Letters, v. 20, p. 423-426.

Hopper, J. R., J. C. Mutter, R. L. Larson, C. Z. Mutter, P. Buhl, J. B. Diebold, J. Alsop, D. Falvey, P. Williamson, F. Brassil, and J. M. Lorenzo, 1992, Magmatism and rift margin evolution; evidence from Northwest Australia: Geology, v. 20, p. 853-857.

Horsefield, S. J., 1992, Crustal structure across the continent-ocean boundary: PhD thesis, Cambridge University.

Horsefield, S. J., R. B. Whitmarsh, R. S. White, and J. C. Sibuet, 1994, Crustal structure of the Goban Spur rifted continental margin, NE Atlantic: Geophysical Journal International, v. 119, p. 1-19.

Hussenoeder, S. A., M. A. Tivey, and H. Schouten, 1995, Direct inversion of potential fields from an uneven track with application to the Mid-Atlantic Ridge: Geophysical Research Letters, v. 22.

Hyndman, R. D., 1973, Evolution of the Labrador Sea: Canadian Journal of Earth Science, v. 10, p. 637-664.

Hyndman, R. D., 1975, Marginal basins of the Labrador Sea and the Davies Strait hot spot: Canadian Journal of Earth Science, v. 12, p. 1041-1048.

IAGA_Division_V_Working_Group_8, 1996, Revision of the Geomagnetic referenece field: EOS, Transactions, American Geophysical Union, v. 77.

Illies, J. H., 1981, Mechanism of graben formation, *in* J. H. Illies, ed., Mechanism of graben formation.: Tectonophysics, Amsterdam, Netherlands, Elsevier, p. 249-266.

Irving, E., and L. G. Parry, 1963, The magnetisation of some Permian rocks from NSW: Geophysical Journal of the Royal Astronomical Society, v. 7, p. 395-411.

Irving, E., W. A. Robertson, and F. Aumento, 1970, The Mid-Atlantic Ridge near 45N, VI. Remanent intensity, susceptibility and iron content of dredged samples: Canadian Journal of Earth Science, v. 7, p. 226-238.

Isezaki, N., 1986, A new shipboard three-component magnetometer: Geophysics, v. 51, p. 1992-1998.

Juarez, M. T., W. Lowrie, M. L. Osete, and G. Melendez, 1998, Evidence of widespread Cretaceous remagnetisation in the Iberian Range and its relation with rotation of Iberia: Earth and Planetary Science Letters, v. 160, p. 729-743.

Keen, C. E., and B. de Voogd, 1988, The continent-ocean boundary at the rifted margin off eastern Canada: new results from seismic reflection studies: Tectonics, v. 7, p. 107-124.

Keen, C. E., P. Potter, and S. P. Srivastava, 1994, Deep seismic reflection data across the conjugate margins of the Labrador Sea: Canadian Journal of Earth Sciences, v. 31, p. 192-205.

Kent, D. V., B. M. Honnorez, N. D. Opdyke, and P. J. Fox, 1978, Magnetic properties of dredged oceanic gabbros and the source of marine magnetic anomalies: Geophysical Journal of

the Royal Astronomical Society, v. 55, p. 513-537.

Klitgord, K. D., J. D. Huestis, J. D. Mudie, and R. L. Parker, 1975, An analysis of near-bottom magnetic anomalies: Seafloor spreading and the magnetized layer: Geophysical Journal of the Royal Astronomical Society, v. 43, p. 387-424.

Klitgord, K. D., and H. Schouten, 1986, Plate kinematics of the Central Atlantic, *in* P. R. Vogt, and B. E. Tucholke, eds., The western North Atlantic region: The Geology of North America, Geological Society of America, p. 351-378.

Klitgord, K. D., D. R. Hutchinson, and H. Schouten, 1988, Continental margin: structural and tectonic framework, The Atlantic continental margin, U.S.: The Geology of North America, The Geological Society of America, p. 19-55.

Korenaga, J., 1995, Comprehensive analysis of marine magnetic vector anomalies: Journal of Geophysical Research, v. 100, p. 365-378.

Krawczyk, C., and T. J. Reston, 1995, Detachment faulting and continental break-up: the S reflector offshore Galicia, *in* E. Banda, M. Torne, and M. Talwani, eds., Rifted ocean-continent boundaries: NATO ASI Series C: Mathematical and Physical Sciences, Kluwer, p. 231-246.

Krawczyk, C. M., T. J. Reston, M.-O. Beslier, and G. Boillot, 1996, Evidence for detachment tectonics on the Iberia Abyssal Plain rifted margin, *in* R. B. Whitmarsh, D. S. Sawyer, A. Klaus, and D. G. Masson, eds., Proceedings of the Ocean Drilling Program, Scientific Results, College Station, TX, Ocean Drilling Program, p. 603-616.

Kunaratnam, K., 1981, Simplified expressions for the magnetic anomalies due to vertical rectangular prisms: Geophysical Prospecting, v. 29, p. 883-890.

Larson, R. L., 1991, Geological consequences of superplumes: Geology (Boulder), v. 19, p. 963-966.

Latin, D., and N. White, 1990, Generating melt during lithospheric extension: pure shear vs. simple shear: Geology, v. 18, p. 327-330.

Lavecchia, G., and F. Stoppa, 1996, The tectonic significance of Italian magmatism; an alternative view to the popular interpretation: Terra Nova, v. 8, p. 435-446.

Leinen, M., D. K. Rea, and e. al., 1986, Site 504, *in* M. Leinen, D. K. Rea, and e. al., eds., Initial reports of the Deep Sea Drilling Project covering Leg 92 of the cruises of the drilling vessel Glomar Challenger, Papeete, Tahiti, to Balboa, Panama, February-April, 1983.: Initial Reports of the Deep Sea Drilling Project, College Station, Texas A & M University, Ocean Drilling Program, p. 187-214.

Leonardi, S., and H.-J. Kumpel, 1996, Scaling behaviour of vertical magnetic susceptibility and its fractal characterization: an example from the German Continental Deep Drilling Project (KTB): Geologische Rundschau, v. 85, p. 50-57.

Lesne, O., E. Calais, and J. Deverchere, 1998, Finite element modelling of crustal deformation in the Baikal rift zone; new insights into the active-passive rifting debate: Tectonophysics, v. 289, p. 327-340.

Lin, J., and E. M. Parmentier, 1989, Mechanisms of lithospheric extension at mid-ocean ridges: Geophysical Journal International, v. 96, p. 1-22.

Lister, G. S., and G. A. Davis, 1989, The origin of metamorphic core complexes and detachment faults formed during Tertiary continental extension in the Northern Colorado River region, U.S.A.: Journal of Structural Geology, v. 11, p. 65-94.

Louden, K., J. C. Sibuet, and J. P. Foucher, 1989, Heat flow anomalies across Goban Spur and Galicia Bank continental margins (NW Atlantic) (abstract): EOS, v. 70, p. 1328.

Louden, K. E., J. C. Osler, S. P. Srivastava, and C. E. Keen, 1996, Formation of oceanic crust at slow spreading rates: New constraints from an extinct spreading centre in the Labrador Sea: Geology, v. 24, p. 771-774.

Louden , K. E., 1997, Variations in heat flow across the ocean-continent transition in the Iberia Abyssal Plain: Earth and Planetary Sciences Letters, v. 151, p. 233-253.

Louvel, V., 1995, Les marge conjuguees de l'Atlantique Nord: Structure et modelisation de l'ouverture oceanicque: PhD thesis, Universite Lous Pasteur (Strasbourg I).

Louvel, V., J. Dyment, and J.-C. Sibuet, 1997, Thinning of the Goban Spur continental margin and formation of early oceanic crust: contsriants from forward modelling and inversion of marine magnetic anomalies: Geophysical Journal International, v. 128, p. 188-196.

Malod, J., and A. Mauffret, 1990, Iberian plate motions during the Mesozoic: Tectonophysics, v. 184, p. 261-278.

Mamet, B., M. C. Comas, and G. Boillot, 1991, Late Paleozoic basin on the West Galicia Atlantic margin: Geology, v. 19, p. 738-741.

Mandelbrot, B. B., 1967, How long is the coastline of Britain? Statistical self-similarity and fractional dimension: Science, v. 155, p. 636-638.

Mankinen, E. A., and G. B. Dalrymple, 1979, Revised geomagnetic polarity time for the interval 0-5 my BP: Journal of Geophysical Research, v. 84, p. 615-626.

Martin, A. K., 1984, Propagating rifts: crustal extension during continental rifting: Tectonics, v. 3, p. 611-617.

Martinez, F., and J. R. Cochran, 1988, Structure and tectonics of the northern Red Sea: catching a continental margin between rifting and drifting: Tectonophysics, v. 150, p. 1-32.

Masson, D. G., and P. R. Miles, 1984, Mesozoic seafloor spreading between Iberia, Europe and North America: Marine Geology, v. 56, p. 279-287.

Masson, D. G., J. A. Cartwright, L. M. Pinheiro, R. B. Whitmarsh, M.-O. Beslier, and H. Roeser, 1994, Compressional deformation at the ocean-continent transition in the NE Atlantic: Journal of the Geological Society of London, v. 151, p. 607-614.

Mauffret, A., and L. Montadert, 1987, Rift tectonics on the passive continental margin off Galicia (Spain): Mar. Petrol. Geol., v. 4, p. 49-70.

Mauffret, A., and L. Montadert, 1988, Seismic stratigraphy off Galicia: Proceedings of the Ocean Drilling Program, Scientific Results, v. 103, p. 13-30.

Maus, S., and V. P. Dimri, 1994, Scaling properties of potential fields due to scaling sources: Geophysical Research Letters, v. 21, p. 891-894.

Maus, S., and V. P. Dimri, 1996, Depth estimation from scaling power spectrum of potential fields?: Geophysical Journal International, v. 124, p. 113-120.

McKenzie, D., and J. G. Sclater, 1971, The Evolution of the Indian Ocean since the Late Cretaceous: The Geophysical Journal of the Royal Astronomical Society, v. 24, p. 437-528.

McKenzie, D., 1978, Some remarks on the development of sedimentary basins: Earth Planet. Sci. Letts., v. 40, p. 25-32.

McKenzie, D. P., and M. J. Bickle, 1988, The volume and composition of melt generated by extension of the lithosphere: Journal of Petrology, v. 29, p. 625-679.

McKenzie, D., and R. K. O'Nions, 1991, Partial melt distributions from inversion of rare earth element concentrations: Journal of Petrology, v. 32, p. 1021-1091.

Miles, P. R., J. Verhoef, and R. Macnab, 1994, Magnetic anomalies west of Iberia (abstract): EOS, Transactions, American Geophysical Union, v. 75, p. 131.

Miles, P. R., J. Verhoef, and R. Macnab, 1996, Compilation of magnetic anomaly chart west of Iberia, *in* R. B. Whitmarsh, D. S. Sawyer, A. Klaus, and D. G. Masson, eds., Proceedings of the Ocean Drilling Program, Scientific Results, College Station, TX, Ocean Drilling Program, p. 659-664.

Miller, S. P., K. C. MacDonald, and P. F. Lonsdale, 1985, Near bottom magnetic profile across the Red Sea: Marine Geophysical Researches, v. 7, p. 401-418.

Miller, J. S., K. R. Groves, and R. S. Whitmarsh, 1996, Sources of the Pleistocene Coso rhyolites; a Nd isotopic perspective, *in* Anonymous, ed., AGU 1996 fall meeting.: EOS, Transactions, American Geophysical Union, Washington, DC, United States, American Geophysical Union, p. 791.

Minshull, T. A., 1995, A geophysical study of the ocean-continent transition in the Iberia Abyssal Plain, R.R.S. Discovery Cruise 215 Report., Cambridge, Bullard Labs., Department of Earth Sciences, Cambridge University.

Minshull, T. A., and R. S. White, 1996, Thin crust on the flanks of theslow-spreading Southwest Indian Ridge: Geophysical Journal International, v. 125, p. 139-148.

Mohr, P. A., 1983, Ethiopian flood basalt province: Nature, v. 303, p. 577-584.

Montadert, L., O. de Charpal, D. Roberts, P. Guennoc, and J.-C. Sibuet, 1979, Northeast Atlantic passive continental margins: rifting and subsidence processes, *in* M. Talwani, W. Hay, and W. B. F. Ryan, eds., Deep drilling results in the Atlantic Ocean: Continental margins and paleoenvironment: Maurice Ewing Series, Washington, D.C., AGU, p. 154-186.

Morgan, J. V., P. J. Barton, and R. S. White, 1989, The Hatton Bank continental margin; III, Structure from wide-angle OBS and multichannel seismic refraction profiles: Geophysical Journal of the Royal Astronomical Society, v. 98, p. 367-384.

Moseley, F., 1970, The Aden Traps of Dhala, Musaymir and Radfan, South Yemen: Bulletin of Volcanology, v. 33, p. 889-909.

Muller, M. R., C. J. Robinson, T. A. Minshull, R. S. White, and M. J. Bickle, 1997, Thin crust beneath ocean drilling program borehole 735B at the Southwest Indian Ridge?: Earth and Plenetary Science Letters, v. 148, p. 93-107.

Mutter, J. C., W. R. Buck, and C. M. Zehnder, 1988, Convective partial melting 1. A model for the formation of thick basaltic sequences during the initiation of spreading: J. Geophys. Res., v. 93, p. 1031-1048.

Myhre, A. M., O. Eldholm, and E. Sundvor, 1984, The Jan Mayen Ridge: present status: Polar Research, v. 2, p. 47-59.

Naidu, P., 1968, Spectrum of potential fields due to randomly distributed sources: Geophysics, v. 33, p. 337-345.

Nazarova, K. A., 1994, Serpentinized peridotites as a possible source for oceanic magnetic anomalies: Marine Geophysical Researches, v. 16, p. 455-462.

Neumann, E. R., and I. B. Ramberg, 1978, Paleorifts; concluding remarks, *in* I. B. Ramberg, and E. R. Neumann, eds., Tectonics and geophysics of continental rifts; Volume two of the proceedings of the NATO Advanced Study Institute Paleorift Systems with emphasis on the Permian Oslo Rift.: NATO ASI Series. Series C: Mathematical and Physical Sciences, Dordrecht-Boston, International, D. Reidel Publishing Company, p. 409-424.

Ninkovich, Y. S., Y. Y. Rudakov, S. M. Mansurov, and L. G. Mansurova, 1966, Palaeomagnetic stratigraphy, rate of deposition and tephrachronology in north Pacific deep sea sediments: Earth and Planetary Science Letters, v. 1, p. 476-492.

ODP Leg 173 Shipboard Scientific Party, 1998, Drilling reveals transition from continental breakup to early magmatic crust: EOS, v. 79, p. 173,180-181.

Ogg, J. G., 1988, Early Cretaceous and Tithonian magnetostratigraphy of the Galicia margin (Ocean Drilling Program Leg 103), *in* G. Boillot, and E. L. Winterer, eds.: Proceedings of the Ocean Drilling Program, Scientific Results, College Station, TX, Ocean Drilling Program, p. 659-682.

Oldenburg, D. W., 1974, The inversion and interpretation of gravity anomalies: Geophysics, v. 39, p. 526-536.

Olsen, K. H., and P. Morgan, 1995, Introduction; Progress in understanding continental rifts, *in* K. H. Olsen, ed., Continental rifts; evolution, structure, tectonics.: Developments in Geotectonics, Amsterdam, Netherlands, Elsevier, p. 3-26.

Omar, G. I., and M. S. Steckler, 1995, Fission track evidence on the initial rifting of the Red Sea: two pulses, no propagation: Science, v. 270, p. 1341-1344.

Opdyke, N. D., and R. Hekinian, 1967, Magnetic properties of some igneous rocks from the Mid-Atlantic Ridge: Journal of Geophysical Research, v. 72, p. 2257-2260.

Pallister, J. S., 1987, Magmatic history of Red Sea rifting: Perspective from Saudi Arabian coastal plain: geological Society of America Bulletin, v. 98, p. 400-417.

Pariso, J. E., and H. P. Johnson, 1993, Do lower crustal rocks record reversals of the Earth magnetic field? Magnetic petrology of oceanic gabbros from ODP Hole 735B: Journal of Geophysical Research, v. 98, p. 16013-16032.

Pariso, J. E., and H. P. Johnson, 1993, Do layer 3 rocks make a significant contribution to marine magnetic anomalies? In situ magnetization of gabbros at Ocean Drilling Program Hole 735B: Journal of Geophysical Research, v. 98, p. 16033-16052.

Parker, R. L., 1972, The rapid calculation of potential anomalies: Geophysical Journal of the Royal Astronomical Society, v. 31, p. 447-455.

Parker, R. L., and S. P. Huestis, 1974, The invesion of magnetic anomalies in the presence of topography: Journal of Geophysical research, v. 79, p. 1587-1593.

Parson, L. M., D. G. Masson, C. D. Pelton, and A. C. Grant, 1985, Seismic stratigraphy and structure of the east Canadian Margin between 41 and 52 degrees N: Canad. J. Earth Sci., v. 22, p. 686-703.

Pedersen, T., and H. E. Ro, 1992, Finite duration extension and decompression melting: Earth and Planetary Science Letters, v. 113, p. 15-22.

Peters, L. J., 1949, The direct approach to magnetic interpretation and its practical application: Geophysics, v. 14, p. 290-320.

Pickup, S. L. B., R. B. Whitmarsh, C. M. R. Fowler, and T. J. Reston, 1996, Insight into the nature of the ocean-continent transition off West Iberia from a deep multichannel seismic reflection profile: Geology, v. 24, p. 1079-1082.

Pickup, S. L. B., 1997, Rifted margin development off West Iberia from deep seismic reflection profiles: PhD thesis, Royal Holloway University of London.

Pilkington, M., and W. E. S. Urquhart, 1990, Reduction of potential field data to a horizontal plane: Geophysics, v. 55.

Pilkington, M., and J. P. Todoeschuck, 1993, Fractal magnetization of continental crust: Geophysical Research Letters, v. 20, p. 627-630.

Pilkington, M., and J. P. Todoeschuck, 1995, Scaling nature of crustal susceptibilities: Geophysical Research Letters, v. 22, p. 779-782.

Pinheiro, L. M., R. B. Whitmarsh, and P. R. Miles, 1992, The ocean-continent boundary off the western continental margin of Iberia II. Crustal structure in the Tagus Abyssal Plain: Geophysical Journal International, v. 109, p. 106-124.

Pitman, W. C., and M. Talwani, 1972, Sea-floor spreading in the North Atlantic: Geological Society of America Bulletin, v. 83, p. 619-646.

Prichard, H. M., and J. R. Cann, 1982, Petrology and mineralogy of dredged gabbro from Gettysburg Bank, eastern Atlantic: Contrib. Mineral. Petrol., v. 79, p. 46-55.

Rabinowitz, P. D., S. C. Cande, and D. E. Hayes, 1978, Grand Banks and J-Anomaly Ridge: Science, v. 202, p. 71-73.

Ramberg, I. B., and P. Morgan, 1984, Physical characteristics and evolutionary trends of continental rifts, *in* N. A. Bogdanov, ed., Tesizy; 27-y mezhdunarodnyy geologicheskiy kongress-Abstracts; 27th international geological congress., International Geological Congress, p. 370.

Raymond, C. A., and J. L. LaBrecque, 1987, Magnetization of the oceanic crust: thermoremanent magnetization or chemical remanent magnetization?: Journal of Geophysical Research, v. 92, p. 8077-8088.

Reid, I., and H. R. Jackson, 1981, Oceanic spreading rate and crustal thickness: Marine Geophysical Researches, v. 5, p. 165-172.

Reid, A. B., J. M. Allsop, H. Granser, A. J. Millett, and I. W. Somerton, 1990, Magnetic interpretation in three dimesnions using Euler deconvolution: Geophysics, v. 55, p. 80-91.

Reid, I., 1994, Crustal structure of a nonvolcanic rifted margin east of Newfoundland: Journal of Geophysical Research, v. 99, p. 15161-15180.

Reston, T. J., C. M. Krawczyk, and H. J. Hoffmann, 1995, Detachment tectonics during Atlantic rifting: analysis and interpretation of the S reflection, the west Galicia margin, *in* R. A. Scrutton, ed., Special publication, Tectonics of the North Atlantic region, Geol. Soc. London.

Reston, T. J., C. M. Krawczyk, and D. Klaeschen, 1996, The S reflector west of Galicia (Spain). Evidence for detachment faulting during continental breakup from prestack depth migration: Journal of Geophysical Research, v. 101, p. 8075-8091.

Roberts, D. G., D. G. Masson, and P. R. Miles, 1981, Age and structure of the southern Rockall Trough: new evidence: Earth and Planetary Science Letters, v. 52, p. 115-128.

Roeser, H., 1975, A detailed magnetic survey of the southern Red Sea: Geologisches Jahrbuch Ser. D, v. 13, p. 131-153.

Roeser, H. A., H.-O. Bargeloh, G. Eilers, J. Fritsch, P. Keppler, P. Kewitsch, A. Klein, L. Pinheiro, and B. Schreckenberger, 1992, SONNE cruise SO-75: Geophysical investigations of the crustal structure of the North Atlantic off Portugal. Bundersanstalt fur Geowissenschaften und Rohstoffe.

Roest, W. R., and S. P. Srivastava, 1989, Seafloor spreading history 1 Labrador Sea. Magnetic anomalies along track, *in* J. S. Bell, ed., Labrador Sea: East Coast Basin Atlas Series, Dartmouth, Nova Scotia, Altlantic Geoscience Centre.

Roest, W. R., J. Arkani-Hamed, and J. Verhoef, 1992, The sea-floor spreading rate dependence of the anomalous skewness of marine magnetic anomalies: Geophysical Journal International, v. 109, p. 653-669.

Roest, W. R., J. Verhoef, and M. Pilkington, 1992, Magnetic interpretation using the 3-D analytic signal: Geophysics, v. 1, p. 116-125.

Rubin, A. M., and D. D. Pollard, 1988, Dike-induced faulting in rift zones of Iceland and Afar: Geology (Boulder), v. 16, p. 413-417.

Rubin, A. M., 1992, Dike-induced faulting and graben subsidence in volcanic rift zones: Journal of Geophysical Research, B, Solid Earth and Planets, v. 97, p. 1839-1858.

Sandwell, D. T., and W. H. F. Smith, 1997, Marine gravity anomaly from Geosat and ERS-1 satellite altimetry: Journal of Geophysical Research, v. 102, p. 803-827.

Sauter, D., V. Mendel, J.-C. Rommevaux, P. Patriat, and M. Munschy, 1997, Propagation of the Southwest Indian Ridge at the Rodrigues Triple Junction: Marine Geophysical Researches, v. 19, p. 553-567.

Sawyer, D. S., 1994, The case for slow-spreading oceanic crust landward of the peridotite ridge in the Iberia Abyssal Plain (abstract): EOS, Transactions, American Geophysical Union, v. 75, p. 616.

Sawyer, D. S., R. B. Whitmarsh, A. Klaus, and Shipboard Scientific Party, 1994, Leg 149 Initial Report: Proceedings of the Ocean Drilling Program, Initial Reports, v. 149: College Station, TX, Ocean Drilling Program, 719 p.

Schärer, U., J. Kornprobst, M.-O. Beslier, G. Boillot, and J. Girardeau, 1995, Gabbro and related rock emplacement beneath rifting continental crust: U-Pb geochronological and geochemical constraints for the Galicia passive margin (Spain): Earth & Planetary Science Letters, v. 130, p. 187-200.

Schouten, H., and K. McCamy, 1972, Filtering marine magnetic anomalies: Journal of Geophysical Research, v. 77, p. 7089-7099.

Seama, N., Y. Nogi, and N. Isezaki, 1993, A new method for precise determinantion of the position and strike of magnetic boundaries using vector data of the geomagnetic anomaly field: Geophysical Journal International, v. 113, p. 155-164.

Searle, R. C., P. A. Cowie, N. C. Mitchell, S. Allerton, C. J. MacLeod, J. Escartin, S. M. Russell, P. A. Slootweg, and T. Tanaka, 1998, Fault structure and detailed evolution of a slow spreading ridge segment; the Mid-Atlantic Ridge at 29°N: Earth and Planetary Science Letters, v. 154, p. 167-183.

Seifert, K., I. Gibson, D. Weiss, and D. Brunotte, 1996, Geochemistry of metamorphosed cumulate gabbros from Hole 900A, Iberia Abyssal Plain, *in* R. B. Whitmarsh, D. S. Sawyer, A. Klaus, and D. G. Masson, eds., Proceedings of the Ocean Drilling Program, Scientific Results, College Station, TX, Ocean Drilling Program, p. 471-488.

Seifert, K. E., C. Cheng-Wen, and D. A. Brunotte, 1997, Evidence from ODP Leg 149 mafic igneous rocks for oceanic crust in the Iberia Abyssal Plain ocean-continent transition zone: Journal of Geophysical Research, v. 102, p. 7915-7928.

Sengor, A. M. C., and K. Burke, 1978, Relative timing of rifting and volcanism on Earth and

its tectonic implications: Geophysical Research Letters, v. 5, p. 419-421.

Serri, G., R. Hébert, and R. Hekinian, 1988, Petrology of a plagioclase-bearing olivine websterite from the Gorringe Bank (northeastern Atlantic Ocean): Can. J. Earth Sci., v. 25, p. 557-569.

Shive, P. N., and D. M. Fountain, 1988, Magnetic mineralogy in an Archean crustal cross section: Implications for crustal magnetization: Journal of Geophysical Research, v. 93, p. 12177-12186.

Shuey, R. T., and A. S. Pasquale, 1973, End corrections in magnetic profile interpretation: Geophysics, v. 38, p. 507-512.

Sibuet, J. C., J.-P. Maze, P. Amortila, and X. Le Pichon, 1987, Physiography and structure of the western Iberian continental margin off Galicia from Seabeam and seismic data in, *in* G. Boillot, E. L. Winterer, and A. Meyer, eds.: Proceedings of the Ocean Drilling Program, Initial Report, College Station, TX, Ocean Drilling Program, p. 77-97.

Sibuet, J.-C., and B. J. Collette, 1991, Triple junctions of the Bay of Biscay and North Atlantic: new constraints on the kinematic evolution: Geology, v. 19, p. 522-525.

Sibuet, J.-C., 1992, New constraints on the formation of the non-volcanic continental Galicia-Flemish Cap conjugate margins: Journal of the Geological Society of London, v. 149, p. 829-840.

Sibuet, J.-C., and S. Srivastava, 1994, Rifting consequences of three plate separation: Geophysical Research Letters, v. 21, p. 521-524.

Sibuet, J.-C., V. Louvel, R. B. Whitmarsh, R. S. White, S. J. Horsefield, B. Sichler, P. Leon, and M. Recq, 1995, Constraints on rifting processes from refraction and deep-tow magnetic data: the example of the Galicia continental margin (West Iberia), *in* M. T. E. Banda, M. Talwani, ed., Rifted ocean-continent boundaries: NATO ASI Series C: Mathematical and Physical Sciences, Kluwer, p. 197-218.

Slack, H., V. M. Lynch, and L. Langan, 1967, The geomagnetic gradiometer: Geophysics, v. 32, p. 877-892.

Smellie, D. W., 1956, Elementary approximations in aeromagnetic interpretation: Geophysics, v. 21, p. 1021-1040.

Smith, R. A., 1959, Some formulae for local magnetic and gravity anomalies: Geophysical Prospecting, v. 7, p. 55-63.

Solomon, S. C., P. Y. Huang, and L. Meinke, 1988, The seismic moment budget of slowly spreading ridges: Nature (London), v. 334, p. 58-60.

Spector, A., and F. S. Grant, 1970, Statistical models for interpreting aeromagnetic data: Geophysics, v. 35, p. 293-302.

Spohn, T., and G. Schubert, 1982, Convective thinning of the lithosphere; a mechanism for the initiation of continental rifting: JGR. Journal of Geophysical Research. B, v. 87, p. 4669-4681.

Srivastava, S. P., 1978, Evolution of the Labrador Sea and its bearing on the evolution of the North Atlantic: Geophysical Journal of the Royal Astronomical Society, v. 52, p. 313-357.

Srivastava, S. P., and C. R. Tapscott, 1986, Plate kinematics of the North Atlantic, in The geology of North America, the western North Atlantic region ed. B.E.Tucholke, P.R. Vogt, Chapter 23 Geol. Soc. Amer. Decade of N. Amer. Geol. Ser., v. M, p. 379-404.

Srivastava, S. P., J. Verhoef, and R. Macnab, 1988, Results from a detailed aeromagnetic survey across the northeast Newfoundland margin, Part II. Early opening of the North Atlantic between the British Isles and Newfoundland: Mar. Petrol. Geol., v. 5, p. 324-337.

Srivastava, S. P., J. Verhoef, and R. Macnab, 1988, Results from a detailed aeromagnetic survey across the northeast Newfoundland margin, Part I. spreading anomalies and relationship between magnetic anomalies and the ocean-continent boundary: Mar. Petrol. Geol., v. 5, p. 306-323.

Srivastava, S. P., W. R. Roest, L. C. Kovacs, G. Oakey, S. Levesque, J. Verhoef, and R. Macnab, 1990, Motion of Iberia since the Late Jurassic: results from detailed aeromagnetic measurements in the Newfoundland Basin: Tectonophysics, v. 184, p. 229-260.

Srivastava, S. P., H. Schouten, W. R. Roest, K. Klitgord, L. C. Kovacs, J. Verhoef, and R. Macnab, 1990, Iberian plate kinematics: a jumping plate boundary between Eurasia and Africa: Nature, v. 344, p. 756-759.

Srivastava, S. P., and J. Verhoef, 1992, Evolution of Mesozoic sedimentary basins around the North Central Atlantic: a preliminary plate kinematic solution, *in* J. Parnell, ed., Basins on the Atlantic Seaboard: Petroleum Geology, Sedimentology and Basin Evolution, London, Geological Society of London, p. 397-420.

Srivastava, S. P., and W. R. Roest, 1995, Nature of thin crust across the southwest Greenland margin and its bearing on the location of the ocean-continent boundary, *in* M. T. E. Banda, M. Talwani, ed., Rifted ocean-continent boundaries: NATO ASI Series C: Mathematical and Physical Sciences, Kluwer, p. 95-120.

Srivastava, S. P., and C. E. Keen, 1995, A deep seismic reflection profile across the extinct mid-Labrador Sea spreading centre: Tectonics, v. 14, p. 372-389.

Streckeisen, A., 1976, To each plutonic rock its proper name: Earth-Science Reviews, v. 12, p. 1-33.

Sullivan, K. D., 1983, The Newfoundland Basin: ocean-continent boundary and Mesozoic sea-floor spreading history: Earth Planet. Sci. Letts., v. 62, p. 321-339.

Talwani, M., and J. R. Heirtzler, 1964, Computation of magnetic anomalies caused by two-dimensional structures of arbitrary shape, Computers in the mineral industries, part 1, Stanford University Publications, Geological Sciences, p. 464-480.

Talwani, M., and O. Eldholm, 1977, Evolution of the Norweigan-Greenland Sea: Bulletin of the Geological Society of America, v. 88, p. 969-999.

Talwani, M., J. Ewing, R. E. Sheridan, W. S. Holbrook, and L. Glover, 1995, The EDGE experiment and the U.S. East Coast magnetic anomaly, *in* E. Banda, M. Torne, and M.

Talwani, eds., Rifted ocean-continent boundaries: NATO ASI Series C: Mathematical and Physical Sciences, Kluwer, p. 155-181.

Taviana, M., E. Bonatti, P. Colantoni, and P. L. Rossi, 1984, Tectonically uplifted crustal blocks in the northern Red Sea: data from brothers Island: Memoirs of the Geological Society of Italy, v. 27, p. 47-50.

Tett, D. L., and D. S. Sawyer, 1996, Dynamic models of multiphase continental rifting and their implications for the Newfoundland and Iberia conjugate margins, *in* R. B. Whitmarsh, D. S. Sawyer, A. Klaus, and D. G. Masson, eds., Proceedings of the Ocean Drilling Program, Scientific Results, College Station, TX, Ocean Drilling Program, p. 635-648.

Thompson, D. T., 1982, EULDPH - A new technique for making computer-assisted depth estimates from magnetic data: Geophysics, v. 47, p. 31-37.

Tivey, M. A., and H. P. Johnson, 1987, The Central Anomaly Magnetic High; implications for ocean crust construction and evolution: Journal of Geophysical Research, v. 92, p. 12,685-12,694.

Todd, B. J., and I. Reid, 1989, The continent-ocean boundary south of Flemish Cap: constraints from seismic refraction and gravity: Canadian Journal of Earth Sciences, v. 26, p. 1392-1407.

Torne, M., J. Collier, M. Perry, and J. Gameira, 1993, Iberia Atlantic Margins, EEC Project - Contract #JOU2-CT92-O177, Marine data acquisition report.

Tucholke, B. E., and W. J. Ludwig, 1982, Structure and origin of the J-anomaly Ridge, western North Atlantic Ocean: Journal of Geophysical Research, v. 87, p. 9389-9407.

Tucholke, B. E., J. A. Austin, and E. Uchupi, 1989, Crustal structure and rift-drift evolution of the Newfoundland Basin, in Extensional tectonics and stratigraphy of the North Atlantic margins, ed. A.J. Tankard, H.R. Balkwill: AAPG Mem. 46, p. 247-263.

Turcotte, 1992, Fractals and chaos in geology and geophysics, Cambridge University Press.

Van den Berg, J., and H. Zijderveld, 1982, Palaeomagnetism in the Mediterranean, *in* H. Berckhemer, and K. Hsu, eds., Alpine-Mediterranean Geodynamics: Geodynamic Series, American Geophysical Union, p. 83-112.

Van der Voo, R., 1990, Phanerozoic palaeomagnetic poles from Europe and North America and comparisons with continental reconstructions: Reviews of Geophysics, v. 28, p. 167-206.

Verhoef, J., B. J. Collette, P. R. Miles, R. C. Searle, J.-C. Sibuet, and C. A. Williams, 1986, Magnetic anomalies in the northeast Atlantic ocean (35-50N): Marine Geophysical researches, v. 8, p. 1-25.

Vine, F. J., and D. H. Matthews, 1963, Magnetic anomalies over oceanic ridges: Nature (London), v. 199, p. 947-949.

Vogt, P. R., G. L. Johnson, and L. Kristjannson, 1980, Morphology and magnetic anomalies north of Iceland, *in* W. Jacoby, A. Bjornsson, and D. Moller, eds., ICELAND - Evolution, active tectonics and structure.

Vogt, P. R., 1991, Bermuda and Appalachian-Labrador rises; common non-hotspot processes?: Geology, v. 19, p. 41-44.

Wasilewski, P. J., H. H. Thomas, and M. A. Mayhew, 1979, The Moho as magnetic boundary: Geophysical Research Letters, v. 6, p. 541-544.

Wernicke, B. P., 1985, Uniform-sense normal simple shear of the continental lithosphere: Canadian Journal of Earth Sciences, v. 22, p. 108-125.

Wessel, P., and W. H. F. Smith, 1991, Free software helps map and display data: EOS, Transactions, American Geophysical Union, v. 72, p. 445-446.

White, R. S., G. K. Westbrook, S. R. Fowler, and et al., 1987, Hatton Bank (northwest U.K.) continental margin structure: Geophys. J. R. astr. Soc., v. 89, p. 265-271.

White, R. S., and D. P. McKenzie, 1989, Magmatism at rift zones: the generation of volcanic continental margins and flood basalts: J. Geophys. Res., v. 94, p. 7685-7730.

White, R. S., 1989, Initiation of the Iceland plume and opening of the North Atlantic, *in* A. J. Tankard, and H. R. Balkwill, eds., Extensional tectonics and stratigraphy of the North Atlantic margins.: AAPG Memoir, Tulsa, OK, United States, American Association of Petroleum Geologists, p. 149-154.

White, R. S., 1992, Magmatism during and after continental breakup, *in* B. C. Storey, T. Alabaster, and R. J. Pankhurst, eds., Magmatism and the causes of continental breakup: Geol. Soc. London Special Publication, Geological Society of London, p. 1-16.

White, R. S., D. McKenzie, and K. O'Nions, 1992, Oceanic crustal thickness from seismic measurements and rare earth element inversions: Journal of Geophysical Research, v. 97, p. 19683-19715.

Whitmarsh, R. B., P. R. Miles, and A. Mauffret, 1990, The ocean-continent boundary off the western continental margin of Iberia I. Crustal structure at 40deg30'N: Geophys. J. Int., v. 103, p. 509-531.

Whitmarsh, R. B., L. M. Pinheiro, P. R. Miles, M. Recq, and J.-C. Sibuet, 1993, Thin crust at the western Iberia ocean-continent transition and ophiolites: Tectonics, v. 12, p. 1230-1239.

Whitmarsh, R. B., and P. R. Miles, 1995, Models of the development of the west Iberia rifted continental margin at 40°30'N deduced from surface and deep-tow magnetic anomalies: Journal of Geophysical Research, v. 100, p. 3789-3806.

Whitmarsh, R. B., and D. S. Sawyer, 1996, The ocean/continent transition beneath the Iberia Abyssal Plain and continental-rifting to seafloor-spreading processes, *in* R. B. Whitmarsh, D. S. Sawyer, A. Klaus, and D. G. Masson, eds., Proceedings of the Ocean Drilling Program, Scientific Results, College Station, TX, Ocean Drilling Program, p. 713-736.

Whitmarsh, R. B., P. R. Miles, J.-C. Sibuet, and V. Louvel, 1996a, Geological and geophysical implications of deep-tow magnetometer observations near Sites 897, 898, 899, 900 and 901 on the west Iberia continental margin, *in* R. B. Whitmarsh, D. S. Sawyer, A. Klaus, and D. G. Masson, eds., Proceedings of the Ocean Drilling Program, Scientific Results,

College Station, TX, Ocean Drilling Program, p. 665-674.

Whitmarsh, R. B., R. S. White, S. J. Horsefield, J.-C. Sibuet, M. Recq, and V. Louvel, 1996b, The ocean-continent boundary off the western continental margin of Iberia: Crustal structure west of Galicia Bank: Journal of Geophysical Research, v. 101, p. 28291-28314.

Whitmarsh, R. B., D. S. Sawyer, A. Klaus, and D. G. Masson, 1996, Leg 149: Proceedings of the Ocean Drilling Program, Scientific Results, v. 149: College Station, TX, Ocean Drilling Program.

Whitmarsh, R. B., M.-O. Beslier, and P. J. Wallace, 1998, Leg 173, Initial Report: Proceedings of the Ocean Drilling Program, Initial Report, v. 173: College Station, TX, Ocean Drilling Program.

Wilson, M., 1989, Igneous Petrogenesis: A global tectonic approach: London, Chapman & Hall, 466 p.

Wilson, R. C. L., D. S. Sawyer, R. B. Whitmarsh, J. Zerong, and J. Carbonell, 1996, Seismic stratigraphy and tectonic history of the Iberia Abyssal Plain, *in* R. B. Whitmarsh, D. S. Sawyer, A. Klaus, and D. G. Masson, eds., Proceedings of the Ocean Drilling Program, Scientific Results, College Station, TX, Ocean Drilling Program, p. 617-634.

Winterer, E. L., J. Gee, and J. van Waasbergen, 1988, The source area for Lower Cretaceous clastic sedimants of the Galicia Bank margin: Geology and tectonic and erosional history, *in* G. Boillot, and E. L. Winterer, eds., Procceedings of the Ocean Drilling Program, Scientific Results, College Station, TX, p. 697-732.

Zehnder, C. M., J. C. Mutter, and P. Buhl, 1990, Deep seismic and geochemical constraints on the nature of rift-induced magmatism during breakup of the North Atlantic, *in* J. H. Leven, D. M. Finlayson, C. Wright, J. C. Dooley, and B. L. N. Kennett, eds., Seismic probing of continents and their margins.: Tectonophysics, Amsterdam, Netherlands, Elsevier, p. 545-565.

Zhao, X., 1996, Magnetic signatures of peridotite rocks from Sites 897 and 899 and their implications, *in* R. B. Whitmarsh, D. S. Sawyer, A. Klaus, and D. G. Masson, eds., Proceedings of the Ocean Drilling Program, Scientific Results, College Station, TX, Ocean Drilling Program, p. 431-448.

Zhou, S., and H. Thybo, 1998, Power spectra analysis of aeromagnetic data and KTB susceptibility logs, and their implication for fractal behavior of crustal magnetization: Pure and Applied Geophysics, v. 151, p. 147-159.

Appendix I

Pre-processing of near-bottom three-component magnetometer measurements

Three components of the magnetic field, measured using a system of three orthogonally-mounted fluxgate magnetometers, were recorded by IFREMER's Systèm Acoustique Remorqué (SAR) along near-bottom profile SAR95 (Fig. 6.8) during cruise RRS Discovery 215. The geometry of a near-bottom experiment is shown Figure 1.4. Because of their much closer proximity to the source, near-bottom magnetometer profiles are superior to sea surface profiles (see Fig. 1.5). However, deep-tow magnetic measurements suffer from two problems. Firstly, the exact location of the fish is unknown. Fish location has to be estimated using ship's heading and length of tow-cable out. Therefore random spatial noise is introduced (McKenzie and Sclater, 1971). Secondly, and more importantly, because the magnetic sensors and mounted on the fish, they record its induced and permanent magnetic fields, $\mathbf{H}_i$ and $\mathbf{H}_p$, respectively, in addition to the geophysical signal sought, $\mathbf{F}$. Thus, the observed vector field is given by (e.g. Bullard and Mason, 1961),

$$\mathbf{H}_{ob} = \mathbf{F} + \mathbf{H}_i + \mathbf{H}_p \qquad \text{(AI.1)}$$

The Earth's field is a weak field, therefore $\mathbf{H}_i$ is proportional to $\mathbf{F}$ when the sensors are located outboard of the platform. For short durations the permanent field, $\mathbf{H}_p$, is constant. The induced field, $\mathbf{H}_i$, is non-constant because measurements are made on a moving platform.

A method of determining $\mathbf{F}$, by the removal of $\mathbf{H}_i$ and $\mathbf{H}_p$ from $\mathbf{H}_{ob}$, was formulated by Isezaki (1986). Such a method requires that the sensors are towed in a loop, over a region of the Earth's surface where the magnetic field gradients are near-zero, i.e. in a region of no anomalous field. $\mathbf{F}$ is determined through an inverse procedure by optimizing $\mathbf{H}_p$, and the constants which describe the proportional relationship between $\mathbf{H}_i$ and $\mathbf{F}$. Measurements describing the motion of the platform, namely pitch, yaw and roll, allow these constants to be determined. In practice it is necessary to make many calibration loops to determine the constants well. Application of the method to the SAR data collected on cruise RRS Discovery 215 cannot be achieved because only one calibration loop was executed.

In contrast to the theoretical inverse approach of Isezaki (1986), I adopt an empirical procedure for removing the effects of the fish's magnetic fields. Magnetic observations from

the vehicle turning loop made at 750 m water depth, centred in a magnetically quiet region at 40°8'N, 10°4'W (Fig. 2.7), were used to test the variation in observed magnetic field with vehicle heading (Fig. AI.1). Once magnetic components were resolved into north, east and downward components, variations in the three orthogonal magnetic field components, due to the SAR itself, were found to be no greater than ~20 nT over all heading values (Fig. AI.2). For variations in the range 80-120° (i.e., ±20° about the mean towing direction), variations are negligible. In the same heading range total field variations are ~40 nT.

The magnetic effects associated with fish roll were ignored. The magnetic effect associated with vehicle pitch was assessed by observing magnetic variations as the fish was hauled up the continental slope. Only the total field anomaly proved to be significant (Fig. A1.3). Although a sinusoid over heading variations of 360°, for small variations the magnetic effect can be considered to be linearly related to pitch.

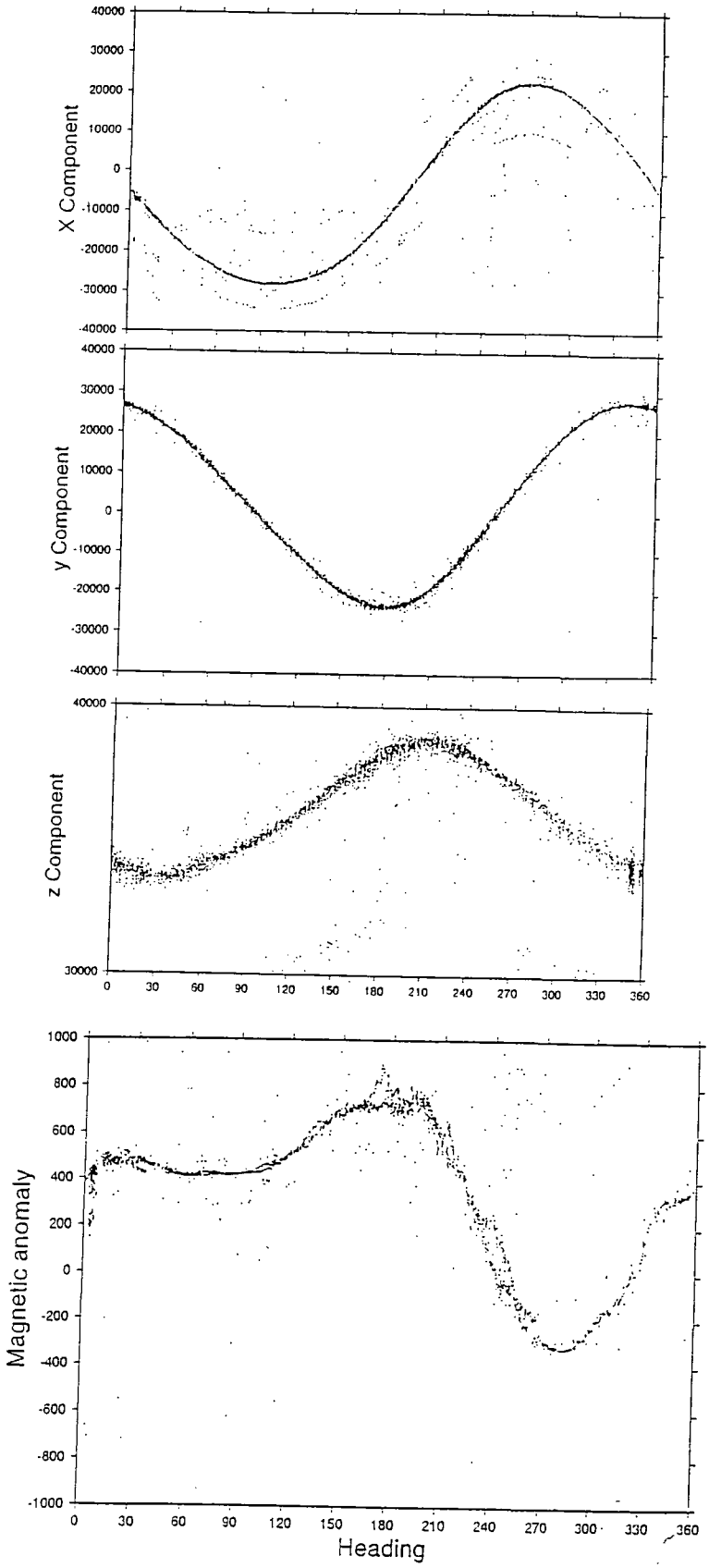

Fig. A1.1 Variation with heading of SAR measurement of X-, Y-, Z-components (fixed fish coordinate system) and total magnetic field (from top to bottom).

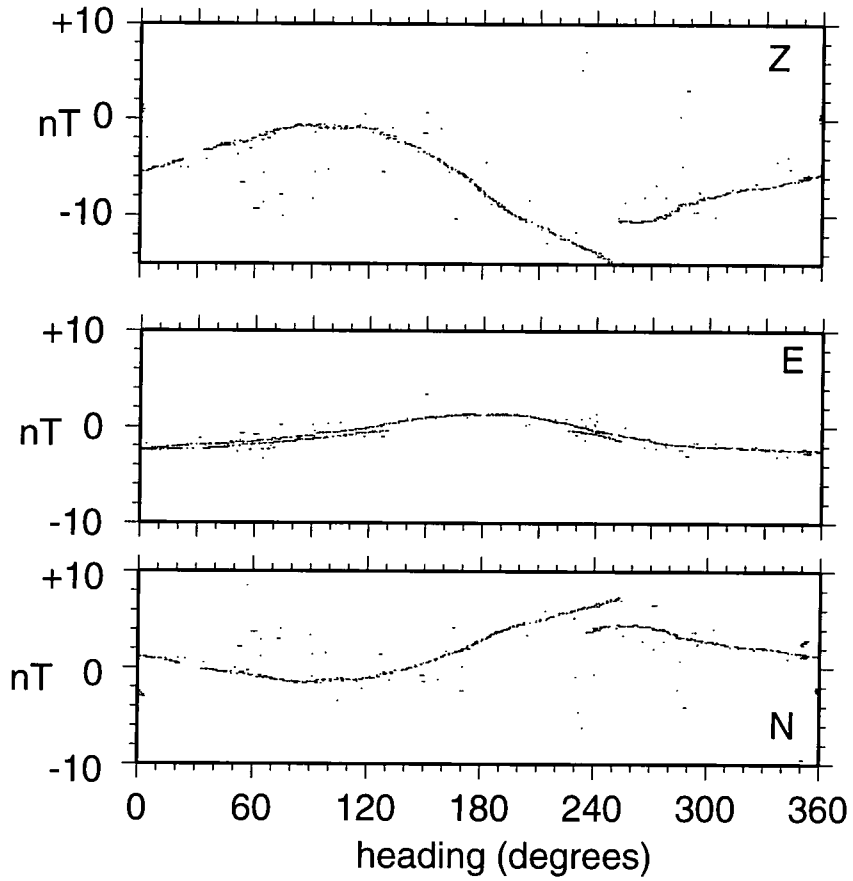

Fig. AI.2 Magnetic fields in down, east and north directions associated with the SAR vehicle as a function of heading. Offsets of up to 4 nT at ~270° are likely to be a result of instrument drift.

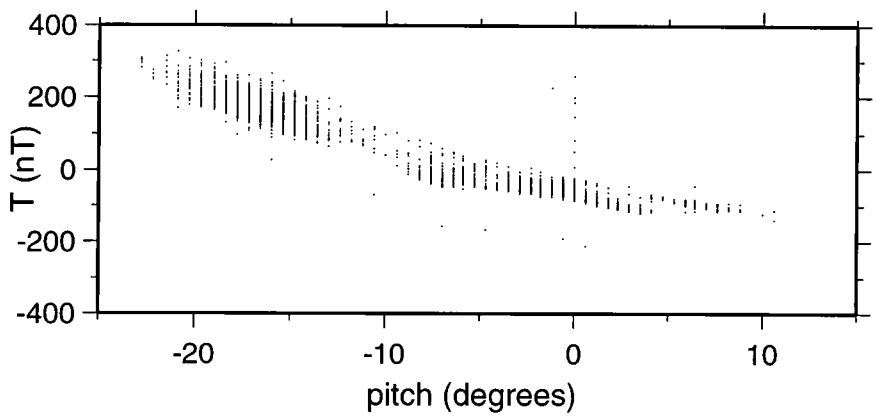

Fig. AI.3 Total field magnetic anomaly associated with pitching motion of SAR. For angles of ±5° anomaly produced is as large as ~100 nT.

Appendix II

Inversion of the power spectrum

The power spectrum as a function of wavenumber, $P(k)$, of a total magnetic field anomaly, can be related to a source (approximated by an ensemble of rectangular prisms) by the model given in equation (4.11),

$$\ln\left[P_{\text{mod}}(k)\right] = \ln C_3 - \gamma \ln k - 2hk + k^2\sigma_h^2 \qquad \text{(AII.1)}$$

where γ is the scaling exponent, h is the depth to the top of the source, σ_h^2 represents a measure of the spread in h, and C_3 is a constant related to the intensity of the magnetic source. The four unknown parameters, C_3, γ, h, σ_h^2 can be solved by the method of least-squares inversion for a given limited window in any given wavenumber range of the power spectrum. For a window of n samples, equation (AII.1) can be written explicitly as,

$$\begin{pmatrix} \ln P_1 \\ \ln P_2 \\ \ln P_3 \\ \vdots \\ \ln P_{n-1} \\ \ln P_n \end{pmatrix} = \begin{pmatrix} 1 & \ln k_1 & -2k_1 & k_1^2 \\ 1 & \ln k_2 & -2k_2 & k_2^2 \\ 1 & \ln k_3 & -2k_3 & k_3^2 \\ \vdots & \vdots & \vdots & \vdots \\ 1 & \ln k_{n-1} & -2k_{n-1} & k_{n-1}^2 \\ 1 & \ln k_n & -2k_n & k_n^2 \end{pmatrix} \cdot \begin{pmatrix} \ln C_3 \\ \gamma \\ h \\ \sigma_h^2 \end{pmatrix} \qquad \text{(AII.2)}$$

which is in the form,

$$\mathbf{y} = A\mathbf{x} \qquad \text{(AII.3)}$$

For $n > 4$, obtaining a solution of the over-determined case is a standard procedure whereby the error energy between the known observations, $\mathbf{y}$, and the forward calculated data, $\hat{\mathbf{y}} = A\hat{\mathbf{x}}$, is minimized in a least-squares sense. The solution is thus given by,

$$\hat{\mathbf{x}} = \left(A^T A\right)^{-1} A^T \mathbf{y} \qquad \text{(AII.4)}$$

Appendix III

Formulation of solutions to Euler's homogeneity relation

AIII.1 Estimation of the partial derivatives (directional gradients) of the total magnetic field in the wavenumber domain

Blakely (1995), amongst others, has shown that the first directional derivatives of a potential field are given by,

$$\Im\left[\frac{\partial T}{\partial x}\right] = ik_x \Im[T] F_H(k) \qquad \text{(AIII.1a)}$$

$$\Im\left[\frac{\partial T}{\partial y}\right] = ik_y \Im[T] F_H(k) \qquad \text{(AIII.1b)}$$

$$\Im\left[\frac{\partial T}{\partial z}\right] = |k| \Im[T] F_H(k) \qquad \text{(AIII.1c)}$$

where $F_H(k)$ is a high-cut wavenumber filter designed to remove high wavenumber instability associated with applying a FFT, and $\Im$ represents the Fourier transform operator.

AIII.2 3-D solution, structural index, $N > 0$

The rearrangement of equation 4.13a yields,

$$x_0 T_x + y_0 T_y + z_0 T_z + NB = xT_x + yT_y + zT_z + NT \qquad \text{(AIII.2)}$$

where T is the total field anomaly, B is the background field, N is the structural index, and subscript denotes partial first derivative of the field. For a single observation point equation AIII.2 can be written as,

$$\begin{pmatrix} T_x & T_y & T_z & N \end{pmatrix} \begin{pmatrix} x_0 \\ y_0 \\ z_0 \\ B \end{pmatrix} = xT_x + yT_y + zT_z + NT \qquad \text{(AIII.3)}$$

If, over a given area of a specified window of size n by n there exists a unique solution to $\begin{pmatrix} x_0 & y_0 & z_0 & B \end{pmatrix}$, then the $n^2 > 4$ equations can be written as,

$$\begin{pmatrix} T_{x1} & T_{y1} & T_{z1} & N \\ T_{x2} & T_{y2} & T_{z2} & N \\ \vdots & \vdots & \vdots & \vdots \\ T_{xn^2} & T_{yn^2} & T_{zn^2} & N \end{pmatrix} \begin{pmatrix} x_0 \\ y_0 \\ z_0 \\ B \end{pmatrix} = \begin{pmatrix} x_1T_{x1} + y_1T_{y1} + z_1T_{z1} + NT_1 \\ x_2T_{x2} + y_2T_{y2} + z_2T_{z2} + NT_2 \\ \vdots \\ x_{n^2}T_{xn^2} + y_{n^2}T_{yn^2} + z_{n^2}T_{zn^2} + NT_{n^2} \end{pmatrix} \qquad \text{(AIII.4)}$$

which are in the form $\mathbf{y} = A\mathbf{x}$. The standard least-squares solution, $\hat{\mathbf{x}}$, is given by equation AII.4.

AIII.3 3-D solution, structural index, $N = 0$

The rearrangement of equation 4.13b yields,

$$x_0T_x + y_0T_y + z_0T_z + A = xT_x + yT_y + zT_z \qquad \text{(AIII.5)}$$

which when extended in the same manner as above can be written explicitly as,

$$\begin{pmatrix} T_{x1} & T_{y1} & T_{z1} & 1 \\ T_{x2} & T_{y2} & T_{z2} & 1 \\ \vdots & \vdots & \vdots & \vdots \\ T_{xn^2} & T_{yn^2} & T_{zn^2} & 1 \end{pmatrix} \begin{pmatrix} x_0 \\ y_0 \\ z_0 \\ A \end{pmatrix} = \begin{pmatrix} x_1T_{x1} + y_1T_{y1} + z_1T_{z11} \\ x_2T_{x2} + y_2T_{y2} + z_2T_{z2} \\ \vdots \\ x_{n^2}T_{xn^2} + y_{n^2}T_{yn^2} + z_{n^2}T_{zn^2} \end{pmatrix} \qquad \text{(AIII.6)}$$

and solved in the same least-squares manner.

Subsidiary matter in support of candidate

Deep structure in the vicinity of the ocean-continent transition zone under the southern Iberia Abyssal Plain

Discovery 215 Working Group*

ABSTRACT

We present results from a seismic and magnetic study of acoustic basement beneath the southern Iberia Abyssal Plain. An ocean-continent transition zone (OCT), characterized by subdued basement relief and weak magnetization, lies seaward of thinned continental crust. Its western edge is a region with isochron-parallel ridges and generally higher basement magnetizations. The width of the OCT decreases to the north. The seaward change in basement morphology coincides with changes in seismic velocity structure, but in both regions, anomalously high velocities at shallow depths within acoustic basement suggest that the OCT consists largely of serpentinized peridotite. Our magnetic and seismic data support the hypothesis of exhumed upper mantle, more than that of ultraslow sea-floor spreading, for the origin of the OCT.

NTRODUCTION

At "nonvolcanic" rifted margins, where synrift neous activity is limited or absent prior to the set of sea-floor spreading, an ocean-continent nsition zone (OCT) up to 130 km wide is comonly found between the most seaward contintal fault blocks and the most landward seaor-spreading magnetic anomalies (e.g., Chian al., 1995; Pickup et al., 1996). The structure of is OCT provides important constraints on ermal and dynamic models of lithospheric tension and continental breakup. The southern eria Abyssal Plain, which has only a 1–3-kmck sedimentary cover, provides a good target a comprehensive study of the OCT, and cently has been the focus of extensive multiannel seismic reflection profiling (Beslier et al., 93), magnetic studies (Whitmarsh and Miles, 95; Whitmarsh et al., 1996a), and Ocean illing Program (ODP) drilling (ODP Leg 173 ipboard Scientific Party, 1998; Sawyer et al., 94; Whitmarsh et al., 1996b). The earlier dies led to three alternative hypotheses for the mposition of the OCT basement, corresponding three different breakup processes: 1) oceanic st formed by ultraslow (~5 mm/yr) sea-floor reading, 2) thinned and intruded continental st (both proposed in Whitmarsh and Sawyer, 96) or 3) upper mantle exhumed principally by mple shear (Boillot et al., 1989) or by pure shear un and Beslier, 1996; Pickup et al., 1996). re we present initial results of an extensive ltichannel reflection and wide-angle seismic survey of the OCT and new inversions of magnetic observations across it, which place further constraints on these hypotheses.

*T. A. Minshull and S. M. Dean (Bullard Laboratories, Department of Earth Sciences, University of Cambridge, Madingley Road, Cambridge CB3 0EZ, United Kingdom); R. B. Whitmarsh and S. M. Russell (Challenger Division, Southampton Oceanography Centre, Southampton SO14 3ZH, United Kingdom; also at Department of Geological Sciences, University of Durham, Durham DH1 3LE); K. E. Louden and D. Chian (Department of Oceanography, Dalhousie University, Halifax, Nova Scotia B3H 4J1, Canada). Authors for correspondence: Whitmarsh and Minshull.

DATA ACQUISITION

Wide-angle seismic data were acquired along a 340-km-long profile across the margin, coincident with the preexisting deep-reflection line IAM-9 (Pickup et al., 1996), and in a 60 by 60 km grid centered on the OCT (Fig. 1A). The source was a 12-gun, 104 L tuned airgun array towed at 20 m depth and fired every 40 or 50 s. During shooting of the grid, simultaneous reflection data were recorded with a 48-channel, 2.4 km hydrophone streamer. Wide-angle seismic data were recorded digitally on ocean bottom hydrophones (OBHs) and seismographs (OBSs) from Cambridge, Dalhousie, and Southampton. Few magnetic profiles extend normal to the margin across the entire area of Figure 1A, but the coverage of ship tracks is sufficiently dense for contouring at 25 nT (Miles et al., 1996).

BASEMENT RELIEF

The basement surface was picked from seismic reflection data as a boundary between parallel, flat-lying, and continuous reflectors above, and shorter events without a consistent dip below. Picks were reconciled at line crossings, converted to depth (by using bathymetry and a velocity function based on multichannel stacking velocities and traveltime modeling of sonobuoys), and contoured. Basement generally deepens southward (Fig. 1A). Two en echelon ridges (R3 and R4) have been proposed to consist of serpentinized peridotite (Beslier et al., 1993; Sawyer et al., 1994). Ridge R3 at 12°30′W extends over 60 km parallel to the sea-floor-spreading isochrons, as do a series of highly elongated highs and lows to the west of it with a spacing of ~20 km and relief of ~1–1.5 km, not unlike the present-day Mid-Atlantic Ridge. Ridge R4 at 12°15′W parallels R3 and dies out northward around 40°35′N. R4 and R3 overlap by over 20 km. To the east of R3 and R4, basement is characterized by highs that are more subcircular to elliptical in plan; in the north the relief is also 1–1.5 km, but southward it is much more subdued. The few elongated ridges and troughs are not isochron-parallel, and some ridges that trend approximately north may join the ridges of the Vasco da Gama seamount.

MAGNETIC MODELING

The 010°-trending magnetic anomalies west of peridotite ridge R3 have been attributed to Early Cretaceous sea-floor spreading (Whitmarsh and Miles, 1995; Whitmarsh et al., 1996a). The relatively low-amplitude, but nonzero, north-trending–anomalies that occur east of R3 and R4 suggest that even though the source bodies are likely aligned due north, subparallel to some basement trends and today's magnetic field, they too possess dominantly remanent magnetization with a –43° Cretaceous declination (Galdeano et al., 1989). We expect most of the contoured basement in Figure 1A to consist of normal oceanic crust, synrift melt products (including those representing early stages of sea-floor spreading), or serpentinized peridotite, and hence, to have a ratio of remanent to induced magnetization of >1 (Harrison, 1987). Only on the Vasco da Gama seamount itself (Capdevila and Mougenot, 1988) and farther east, e.g., at ODP Site 901, might continental crust, with a predominantly induced magnetization, be expected. We conducted a two-dimensional total field magnetic anomaly inversion (Parker and Huestis, 1974), assuming a remanent basement magnetization (Fig. 1B). The depth-to-basement contours and the contoured seamount bathymetry were merged to form the upper surface of the source layer. Immediately west of the weakly magnetic ridge R3, there is a region characterized by magnetizations mostly >0.5 A/m and by peak magnetizations >1.5 A/m. East of R3, the source

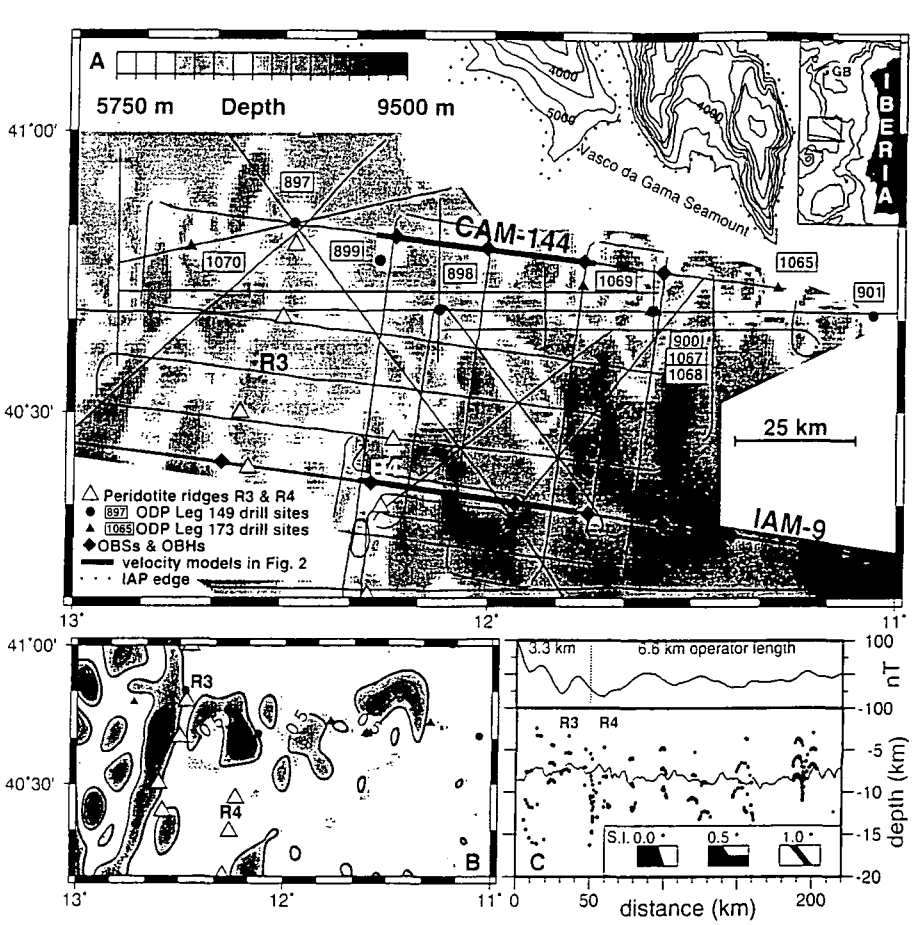

Figure 1. A: Depth to acoustic basement in Iberia Abyssal Plain (IAP) (contoured with help from L. Krawczyk and L. M. Pinheiro using data along tracks denoted by fine lines) and contoured bathymetry over Vasco da Gama seamount (J.-C. Sibuet, personal commun.). Ocean crust lies west of peridotite ridges R3 and R4 (triangles); ocean-continent transition zone (OCT) lies between these ridges and oceanward edge of continental crust. Bold lines locate Figures 2A (near Site 899) and 2C (including ridge R4) and inset locates Figure 1C; GB—Galicia Bank. B: Results from two-dimensional inversion of magnetic anomalies (contours of modulus of magnetization; contour interval = 0.5 A/m; remanent vector inclination = 58°, declination = –43°) assuming a 4-km-thick source layer, equivalent to layers with velocity < ~ 7.7 km/s (Fig. 2). Other plausible layer thicknesses yield similar results. C: Results (lower plot) of Euler deconvolution of a magnetic profile (upper plot) along IAM-9. In lower plot of C, top of basement is shown by black line and colored dots, and generic source shapes correspond to structural indices (SIs) of 0, 0.5, and 1.0.

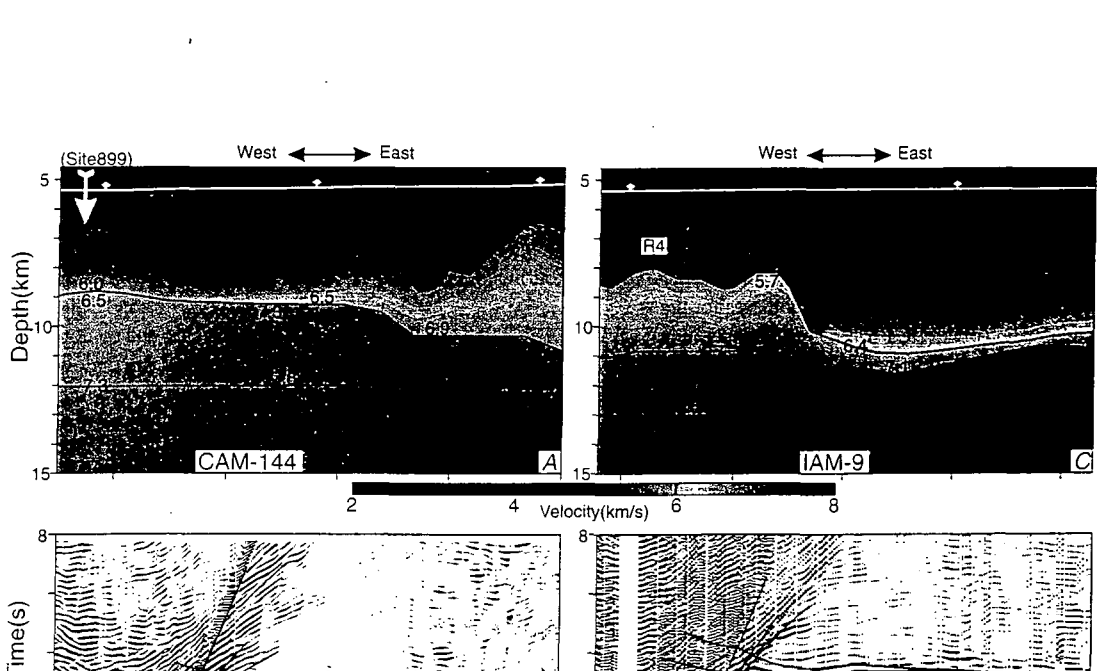

Figure 2. Wide angle seismic data (located in Fig. 1A) and corresponding P-wave velocity models from vicinity of OCT. Velocities are given in km/s. Data are bandpass filtered at 3–10 Hz, coherency filtered, and reduced at 7 km/s, and a gain proportional to range has been applied. Curves mark traveltimes of arrivals from raytracing through velocity models. Diamonds mark OBH and OBS positions. A: Model of part of line CAM-144. B: OBH 3 record on line CAM-144. C: Model of part of line IAM-9, with same distance scale as Figure 1C. D: OBS B vertical geophone record on line IAM-9.

ayer is uniformly weakly magnetized (<0.5 A/m) except for a few isolated highs, four of which exceed 1.0 A/m. The high at 40°40′N, 12°10′W coincides with a pair of basement highs that include ODP Site 899, which has already yielded 1.5 A/m cores of serpentinized peridotite breccias. The other highs lie in regions where basement control is poor or absent.

To constrain anomaly source depths, we applied the two-dimensional Euler deconvolution method (Thompson, 1982) to the magnetic anomalies along profile IAM-9. The method computes depths by assuming different generic source configurations or structural indices (SIs; Fig. 1C). Geologically realistic solutions were obtained for SIs of 0.5 or 1.0. An SI of 0.5 at the basement surface should correspond to a significant step in the basement surface or to a fault offsetting rocks of contrasting magnetization, but there is no correlation between such solutions and either basement relief or faults on IAM-9. Solutions with an SI of 1.0 seem more geologically plausible; they indicate sources close to the top-of-basement surface (20–40 km and >140 km distance) and deeper sources 1–3 km into the basement (40–140 km distance). An SI of 1.0 implies a dike- or sill-like body with a thickness much less than its height, e.g., a near-vertically sided body extending several hundred meters along the profile. Tentative explanations are that, within the serpentinized peridotite OCT (40–190 km distance), there are magnetization contrasts caused by original heterogeneities in the peridotite or even by intrusive mafic bodies, and at 190 km distance there are dikes coincident with the continent/OCT boundary.

SEISMIC DATA

The OBH and OBS record sections generally have very high signal-to-noise ratios (Fig. 2). At short ranges, a complex set of low-velocity arrivals appears from the sedimentary section and the uppermost acoustic basement; rarely is there a strong velocity contrast at the top of the basement. Within the OCT, where an absence of normal incidence Moho reflections was noted by Pickup et al. (1996), a clear wide-angle Moho reflection is never seen; instead, there appears to be a gradual increase to upper-mantle velocities that generates a weak triplication at 20–30 km offset. The clear, consistent crustal and upper-mantle arrivals allow well-constrained two-dimensional velocity models to be determined. Here, we present portions of these models for two lines, line CAM-144, close to the transect of ODP boreholes (Fig. 1A), and line IAM-9. Wide-angle seismic data were analyzed by using the traveltime modeling and inversion approach of Zelt and Smith (1992), constrained by the seabed and acoustic basement profiles. Traveltime uncertainties for basement arrivals were typically 50 ms, and models were run to about the same root-mean-square misfit.

Along line IAM-9, an abrupt lateral change in velocities is seen just east of the overlapping peridotite ridges R3 and R4, which here form a 30-km-wide zone of basement highs (Figs. 1A and 2C). East of this change, a ~3 km sedimentary section is underlain by a 2–3-km-thick layer in which velocities increase steeply from ~5 to ~7 km/s (Fig. 3). In the 2.5 km beneath this layer, velocities increase more gradually, from 7.3 to 7.6 km/s, and normal mantle velocities are reached about 4–5 km into acoustic basement. Close to ridge R4, where Pickup et al. (1996) interpreted a deep-penetrating, east-dipping normal fault from seismic reflection data, the upper-crustal velocity contours step steeply upward, and beneath the peridotite ridges velocities rise rapidly to ~7.3 km/s, only 3 km into acoustic basement. Normal mantle velocities are reached at 4–5 km depth.

At the eastern end of CAM-144 (Fig. 2A; 80–90 km), the velocity of acoustic basement is higher (5.1 km/s), and the velocity gradient in the underlying 2–3 km is lower than elsewhere in our models. This velocity structure, which is coincident with the presence of north-trending basement fault blocks (Fig. 1A), suggests the presence of thinned continental crust at shallow depths. In a narrow region to the west of the thinned continental blocks (60–75 km; Fig. 2A), there is a 1–2-km-thick high-velocity-gradient upper layer where velocities increase from 4.5 to 6.5 km/s. Beneath this layer, velocities increase gradually from 7.4 to 7.8–7.9 km/s at 6–8 km subbasement, and normal mantle velocities are not detected. This structure is similar to that of the OCT to the south along IAM-9 (Fig. 3) but has a much more limited horizontal extent. Beneath the basement high near ODP Site 899, low-velocity basement and a thin high-velocity-gradient upper layer remain, but velocities of 6.7–7.3 km/s in the underlying 3–4 km are lower than those to the east and more typical of oceanic layer 3 (White et al., 1992). However, normal mantle velocities are still not detected.

DISCUSSION

In our study area (Fig. 1), the OCT is characterized by low magnetizations and generally deeper and more subdued basement relief. West of this region lies a region of isochron-parallel basement ridges with greater magnetization west of peridotite ridge R3. The westward change in basement morphology also corresponds to changes in seismic velocity structure along CAM-144 (Site 899 high; Fig. 2A) and IAM-9 (75 km; Fig. 2C). Throughout the OCT and beneath the overlapping peridotite ridges along IAM-9, the velocity structure is not typical of either oceanic crust or thinned continental crust, since in neither case are such high velocities normally observed at such shallow depths. On both seismic lines in Figure 2, the velocities >7.3 km/s observed at 1–2 km into basement most likely represent upper mantle rocks, either <20% serpentinized (Christensen, 1972) and/or intruded by mafic rocks. The lack of Moho reflections is consistent with both these suggestions. Along line IAM-9, the upper high-velocity-gradient layer coincides roughly with the unreflective zone mapped by Pickup et al. (1996), which has also been interpreted as serpentinized upper mantle. The velocities in the central part (Fig. 2A; 60–75 km) of line CAM-144 are as much as 1 km/s higher than in the IAM-9 unreflective zone, but the same interpretation may apply. Possibly the mantle was less permeable and/or the thermal conditions were less favorable for serpentinization at this spot.

The absence of a magmatic crust in the OCT would be consistent with the melting model of Bown and White (1995). Given the thinnest continental crust we observe and an initial continental crustal thickness of ~32 km (Cordoba et al., 1987), then the crust has stretched by a factor $\beta \approx 8$. For a mantle potential temperature of 1300 °C, a rift duration of ~20 m.y. (Whitmarsh and Sawyer, 1996) and $\beta = 8$, only a few hundred meters of melt is expected because the lithosphere would be strongly affected by conductive cooling. The light rare-earth-element enrichment of the few basalt clasts recovered on Leg 149 (Seifert et al., 1997) indicates low degrees of melting, consistent with very limited evidence of magmatism in the OCT. The interpretation of the

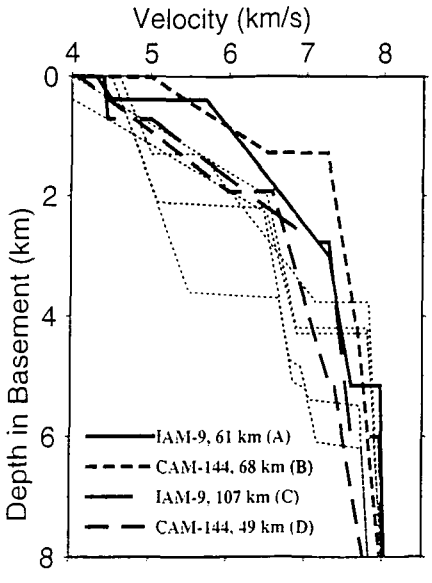

Figure 3. Representative velocity versus depth profiles with depth measured from top of acoustic basement. Patterned area indicates bounds for 59–170 Ma Atlantic oceanic crust (White et al., 1992). A: Peridotite ridge R4 on IAM-9. B: OCT on CAM-144. C: OCT on IAM-9. D: Site 899 basement high. Dotted lines show representative velocity structures for crust formed at Southwest Indian Ridge (Muller et al., 1997), extinct rift in Labrador Sea (Louden et al., 1996) and Aegir Rift (Grevemeyer et al., 1997).

OCT as oceanic crust produced by ultraslow sea-floor spreading is difficult to sustain with our velocity and magnetic results. First, the inferred intensities of magnetization are mostly too low, or the sources too deep, for oceanic crust, and the observed anomalies cannot be modeled simply by sea-floor spreading, unlike several other locations characterized by spreading rates of 3–8 mm/yr (Vogt et al., 1979; LeRoy, 1995; Muller et al., 1997). Second, crustal structures at unequivocal slow spreading ridges are different (Fig. 3). Whereas oceanic crust that formed at only 8 mm/yr along the Southwest Indian Ridge is only 3–4 km thick and may in places be underlain by partially serpentinized upper mantle, it differs from the OCT structures of Figure 2 in having a 2-km-thick oceanic layer 3 and a clear Moho (Muller et al., 1997). Oceanic crust formed at 3.5 mm/yr over the Labrador Sea extinct spreading center and at <6 mm/yr in the extinct Aegir Rift has lower upper crustal velocities and does not exhibit velocities of over 7.0 km/s within 3 km into basement (Louden et al., 1996; Grevemeyer et al., 1997). Furthermore, the very rare indications of mid-ocean ridge basalts in basement boreholes in the Iberia Abyssal Plain seem inconsistent with this hypothesis.

CONCLUSIONS

From our seismic and magnetic study of the southern Iberia Abyssal Plain, we draw the following conclusions.

1. The acoustic basement between thinned continental crust and a geophysically defined oceanic crust lying immediately west of the peridotite ridges may be characterized by its morphology, magnetization, and seismic velocity. The western boundary of the OCT is marked by one or more isochron-parallel basement ridges.

2. Variations in seismic structure and basement topography along the margin are as great as those across it. The OCT is broader in the south (IAM-9) than in the north (CAM-144 and ODP drilling transect).

3. The OCT has mostly relatively weak and/or deeper magnetization in contrast to the oceanic crust immediately west of the peridotite ridge(s). It probably has a predominantly remanent magnetization. The tops of the magnetic source bodies under IAM-9 lie mostly 1–3 km into basement.

4. Seismic velocities >7.3 km/s at 2–5 km into basement, which increase steadily with depth to normal mantle velocities, indicate that partially serpentinized upper mantle is widespread in the OCT. The depth and degree of serpentinization vary along strike, perhaps indicating variations in thermal structure and sediment cover immediately after continental breakup.

5. The seismic velocity structure in the upper 2 km beneath acoustic basement in the OCT is consistent with the suggestion that this too consists of serpentinized peridotite.

6. Our results support the hypothesis of exhumed serpentinized upper mantle, more than the hypothesis of ultraslow sea-floor spreading, for the origin of the OCT.

ACKNOWLEDGMENTS

Supported by the U.K. Natural Environment Research Council through grant GR3/9354 and studentships (to Dean and Russell), by National Science and Engineering Research Council of Canada grant CSP0149983, and by a Royal Society University Research Fellowship (to Minshull). We thank all who sailed with us on RRS *Discovery* cruise 215. Department of Earth Sciences, University of Cambridge, contribution no. 5220.

REFERENCES CITED

Beslier, M.-O., Ask, M., and Boillot, G., 1993, Ocean-continent boundary in the Iberia Abyssal Plain from multichannel seismic data: Tectonophysics, v. 218, p. 383–393.

Boillot, G., Féraud, G., Recq, M., and Girardeau, J., 1989, Undercrusting by serpentinite beneath rifted margins: Nature, v. 341, p. 523–525.

Bown, J. W., and White, R. S., 1995, The effect of finite extension rate on melt generation at continental rifts: Journal of Geophysical Research, v. 100, p. 18011–18030.

Brun, J. P., and Beslier, M.-O., 1996, Mantle exhumation at passive margins: Earth and Planetary Science Letters, v. 142, p. 161–173.

Capdevila, R., and Mougenot, D., 1988, Pre-Mesozoic basement of the western Iberian continental margin and its place in the Variscan belt, *in* Boillot, G., and Winterer, E. L., eds., Proceedings of the Ocean Drilling Program, Scientific results, Volume 103: College Station, TX, Ocean Drilling Program, p. 3–12.

Chian, D., Keen, C. E., Reid, I., and Louden, K. E., 1995, Evolution of nonvolcanic rifted margins: New results from the conjugate margins of the Labrador Sea: Geology, v. 23, p. 589–592.

Christensen, N. I., 1972, The abundance of serpentinites in the oceanic crust: Journal of Geology, v. 80, p. 709–719.

Cordoba, D., Banda, E., and Ansorge, J., 1987, The Hercynian crust in northwestern Spain: A seismic survey: Tectonophysics, v. 132, p. 321–333.

Galdeano, A., Moreau, M. G., Pozzi, J. P., Berthou, P. Y., and Malod, J. A., 1989, New paleomagnetic results from Cretaceous sediments near Lisboa (Portugal) and implications for the rotation of Iberia: Earth and Planetary Science Letters, v. 92, p. 95–106.

Grevemeyer, I., Weigel, W., Whitmarsh, R. B., Avedik, F., and Ali Deghani, G., 1997, The Aegir Rift: Crustal structure of an extinct spreading axis: Marine Geophysical Researches, v. 19, p. 1–23.

Harrison, C. G. A., 1987, Marine magnetic anomalies—The origin of the stripes: Annual Review of Earth and Planetary Sciences, v. 15, p. 505–543.

LeRoy, S., 1995, Structure et origine de la plaque caribe: Implications géodynamiques: Thèse de Doctorat, Université Pierre et Marie Curie, Paris.

Louden, K. E., Osler, J. C., Srivastava, S. P., and Keen, C. E., 1996, Formation of oceanic crust at slow spreading rates: New constraints from an extinct spreading center in the Labrador Sea: Geology, v. 24, p. 771–774.

Miles, P. R., Verhoef, J., and Macnab, R., 1996, Compilation of magnetic anomaly chart west of Iberia, Proceedings of the Ocean Drilling Program, Scientific results, Volume 149: College Station, Texas, Ocean Drilling Program, p. 659–664.

Muller, M. R., Robinson, C. J., Minshull, T. A., White, R. S., and Bickle, M. J., 1997, Thin crust beneath Ocean Drilling Program borehole 735B at the Southwest Indian Ridge?: Earth and Planetary Science Letters, v. 148, p. 93–107.

ODP Leg 173 Shipboard Scientific Party, 1998, Drilling reveals transition from continental breakup to early magmatic crust: Eos, v. 79, p. 173, 180–181.

Parker, R. L., and Huestis, S. P., 1974, The inversion of magnetic anomalies in the presence of topography: Journal of Geophysical Research, v. 79, p. 1587–1593.

Pickup, S. L. B., Whitmarsh, R. B., Fowler, C. M. R., and Reston, T. J., 1996, Insight into the nature of the ocean-continent transition off West Iberia from a deep multichannel seismic reflection profile: Geology, v. 24, p. 1079–1082.

Sawyer, D. S., Whitmarsh, R. B., Klaus, A., and Shipboard Scientific Party, 1994, Initial reports, Ocean Drilling Program, Leg 149: College Station, Texas, Ocean Drilling Program, 719 p.

Seifert, K. E., Cheng-Wen, C., and Brunotte, D. A., 1997, Evidence from ODP Leg 149 mafic igneous rocks for oceanic crust in the Iberia Abyssal Plain ocean-continent transition zone: Journal of Geophysical Research, v. 102, p. 7915–7928.

Thompson, D. T., 1982, EULDPH—A new technique for making computer-assisted depth estimates from magnetic data: Geophysics, v. 47, p. 31–37.

Vogt, P. R., Taylor, P. R., Kovacs, L. C., and Johnson, G. L., 1979, Detailed aeromagnetic investigations of the Arctic Basin: Journal of Geophysical Research, v. 84, p. 1071–1089.

White, R. S., McKenzie, D., and O'Nions, K., 1992, Oceanic crustal thickness from seismic measurements and rare earth element inversions: Journal of Geophysical Research, v. 97, p. 19683–19715.

Whitmarsh, R. B., and Miles, P. R., 1995, Models of the development of the west Iberia rifted continental margin at 40°30′N deduced from surface and deep-tow magnetic anomalies: Journal of Geophysical Research, v. 100, p. 3789–3806.

Whitmarsh, R. B., and Sawyer, D. S., 1996, The ocean/continent transition beneath the Iberia Abyssal Plain and continental-rifting to seafloor-spreading processes, Proceedings of the Ocean Drilling Program, Scientific results, Volume 149: College Station, Texas, Ocean Drilling Program, p. 713–736.

Whitmarsh, R. B., Miles, P. R., Sibuet, J.-C., and Louvel, V., 1996a, Geological and geophysical implications of deep-tow magnetometer observations near Sites 897, 898, 899, 900 and 901 on the west Iberia continental margin, Proceedings of the Ocean Drilling Program, Scientific results, Volume 149: College Station, Texas, Ocean Drilling Program, p. 665–674.

Whitmarsh, R. B., Sawyer, D. S., Klaus, A., and Shipboard Scientific Party, 1996b, Leg 149, Proceedings of the Ocean Drilling Program, Scientific results, Volume 149: College Station, Texas, Ocean Drilling Program, 785 p.

Zelt, C. A., and Smith, R. B., 1992, Seismic travel-time inversion for 2-D crustal velocity structure: Geophysical Journal International, v. 108, p. 16–34.

Manuscript received December 29, 1997
Revised manuscript received May 13, 1998
Manuscript accepted May 22, 1998

Reprinted from

EARTH AND PLANETARY SCIENCE LETTERS

Earth and Planetary Science Letters 154 (1998) 167–183

Fault structure and detailed evolution of a slow spreading ridge segment: the Mid-Atlantic Ridge at 29°N

R.C. Searle [a,*], P.A. Cowie [b], N.C. Mitchell [c,1], S. Allerton [b], C.J. MacLeod [c], J. Escartin [a,b], S.M. Russell [a], P.A. Slootweg [a], T. Tanaka [d]

[a] *Department of Geological Sciences, University of Durham, Durham DH1 3LE, UK*
[b] *Department of Geology and Geophysics, University of Edinburgh, West Mains Road, Edinburgh EH9 3JW, UK*
[c] *Department of Earth Sciences, University of Wales Cardiff, PO Box 914, Cardiff CF1 3YE, UK*
[d] *Department of Earth Sciences, Faculty Science Chiba University, 1-33 Yayoi-cho, Inage-ku, Chiba, Japan 263*

Received 28 January 1997; revised 11 September 1997; accepted 11 September 1997

ELSEVIER

ELSEVIER

Earth and Planetary Science Letters 154 (1998) 167–183

EPSL

Fault structure and detailed evolution of a slow spreading ridge segment: the Mid-Atlantic Ridge at 29°N

R.C. Searle [a,*], P.A. Cowie [b], N.C. Mitchell [c,1], S. Allerton [b], C.J. MacLeod [c], J. Escartin [a,b], S.M. Russell [a], P.A. Slootweg [a], T. Tanaka [d]

[a] *Department of Geological Sciences, University of Durham, Durham DH1 3LE, UK*
[b] *Department of Geology and Geophysics, University of Edinburgh, West Mains Road, Edinburgh EH9 3JW, UK*
[c] *Department of Earth Sciences, University of Wales Cardiff, PO Box 914, Cardiff CF1 3YE, UK*
[d] *Department of Earth Sciences, Faculty Science Chiba University, 1-33 Yayoi-cho, Inage-ku, Chiba, Japan 263*

Received 28 January 1997; revised 11 September 1997; accepted 11 September 1997

Abstract

We present preliminary results of a detailed near-bottom study of the morphology and tectonics of the 29°N "Broken Spur" segment on the slow spreading Mid-Atlantic Ridge, using principally the TOBI deep-towed instrument. The survey covered two-thirds of the segment length, including all of its southern non-transform boundary, and extended off-axis of 40 km (3.3 Ma) on either side. We obtained nearly complete near-bottom sidescan sonar coverage and deep-towed three-component magnetic observations along 2-km-spaced E–W tracks. Sidescan data reveal new details of fault structure and evolution. Faults grow by along-axis linkage. In the inside corner, they also link in the axis-normal direction by curving to meet the next outer (older) fault; this leads to wider-spaced faults compared to segment centre or outside corner. Outward facing faults exist but are rare. The non-transform offset is characterised by faults that are highly oblique, not parallel, to the spreading direction, and show cross-cutting relations with ridge-parallel faults to the north, suggesting along-axis migration of the offset. Almost all volcanic activity occurs within 5 km of the axis. Most fault growth is complete within 15 km of the axis (1.2 Ma), though large scarps continue to be degraded by mass-wasting beyond there. Crustal magnetisation is strongly three-dimensional. The current neovolcanic zone is slightly oblique to earlier reversal boundaries, and its magnetisation rises to a maximum of 30 A m^{-1} near its southern tip. The central magnetisation high tapers southwards and is asymmetric, with a sharp western but gradual eastern boundary. We infer a highly asymmetric accretion of layer 2 near the segment end. Older magnetic anomalies are kinked and sometimes missing. We interpret these observations as evidence of a rapid, 18 km southward migration of the segment boundary during the past 1.8 Ma, and present a series of reconstructions illustrating this tectonic history. © 1998 Elsevier Science B.V.

Keywords: Mid-Atlantic Ridge; median valley; sea-floor spreading; acoustical surveys; magnetic anomalies; faults

1. Introduction

We present preliminary results from a detailed, near-bottom geophysical study of a single, slow-spreading ridge segment to 3.3 Ma off-axis. Our data reveal details of the structure of normal faults and

* Corresponding author. Tel.: +44-191-374-2537; Fax: +44-191-374-2510; E-mail: r.c.searle@durham.ac.uk

[1] Now at Department of Earth Sciences, Parks Road, Oxford OX1 3PR, UK.

PII S0012-821X(97)00160-X

their growth by both axis-parallel and axis-normal linkage, suggest strongly asymmetric crustal accretion, and enable us to demonstrate rapid, recent along-axis migration of the non-transform offset.

Mid-ocean ridge spreading segments have been extensively studied over the past decade, and have come to be viewed in some sense as the basic units of lithospheric accretion [1–5]. Gravity, seismic and geochemical data suggest that melt is preferentially delivered to segment centres, where the crust is thickest [3,4,6–8]. The spreading axis is usually associated with an axial volcanic ridge a few kilometres wide within a broad median valley. Most segments end in short, non-transform offsets that do not appear to display strike–slip faults along the spreading direction [4,9]. Individual segments may lengthen or shorten and migrate along the ridge axis with time, but tend to persist for times ~ 10 Ma or more [10–13].

The young crust is pervasively cut by normal faults, but the kinematics and mechanics of faulting in this tectonic setting is poorly understood, and the amount of extensional strain represented by them is not well constrained. Near segment centres faulting is symmetric across-axis, with moderate throws of a few hundred metres and spacings of a few kilometres, forming a median valley of nested graben [14]. However, at segment ends it is suggested to be highly asymmetric: large offset (many hundreds of metres), widely spaced (~ 10 km) and possibly shal-

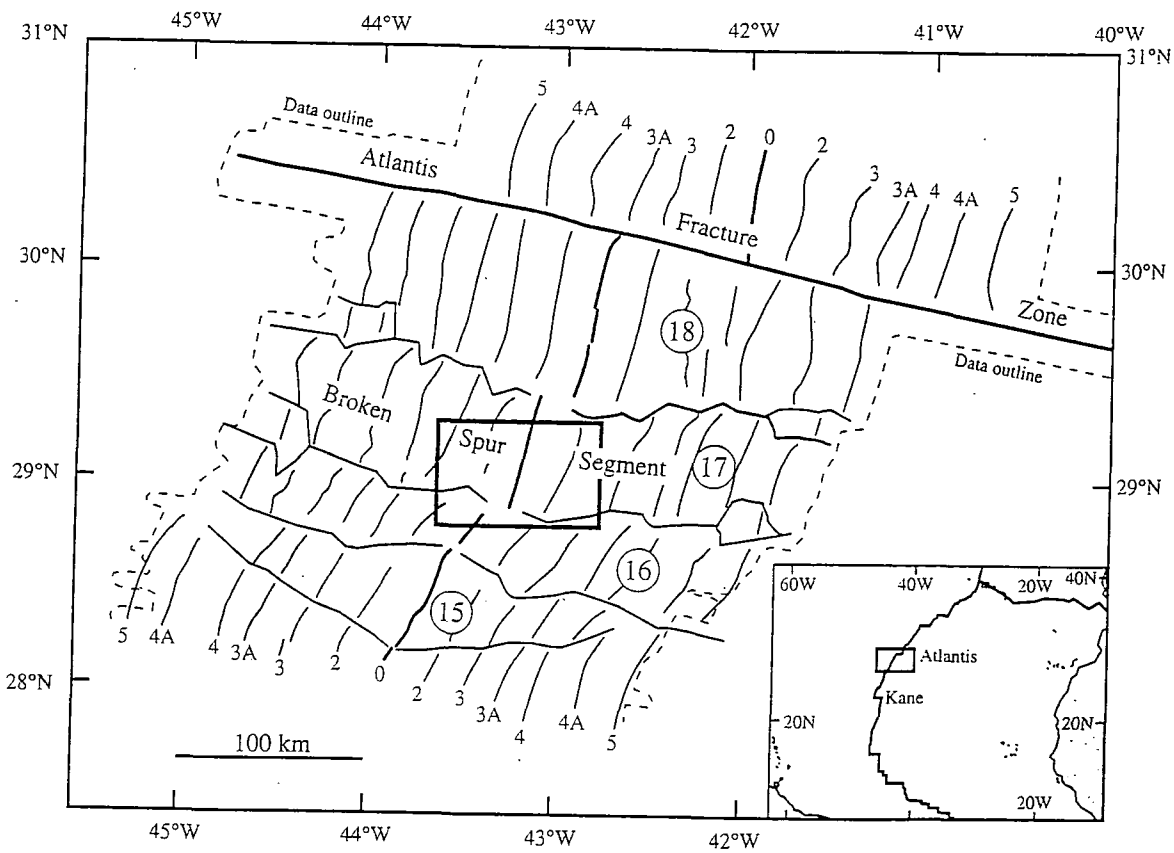

Fig. 1. *Inset*: location of study area between Atlantis and Kane transform faults on the Mid-Atlantic Ridge. *Main figure*: *heavy box* outlines area of present study. *Heavy lines* show current plate boundary and Atlantis fracture zone. *Lighter lines* give crustal isochrons (labelled by magnetic anomaly number) and bathymetric segment boundaries [10,11], with segment numbers [31] *circled*. *Dashed line* marks extent of regional gravity, magnetic and multibeam bathymetry coverage [10,11].

low-dipping normal faults occur on the inside corner, with smaller offset, probably closer spaced faults on the outside corner [5,14–19]. These variations may reflect fundamental along-axis variations in lithospheric structure and rheology [20,21].

The width of the zone of active faulting is uncertain. Several authors suggest that faults at the MAR are active only to distances of 8–12 km [22–24], but the crestal mountains increase in elevation to at least 20 km from the axis and appear to be fault controlled. The degree of outward facing faulting is also unclear. Some suggest that most faults face the spreading axis [25,26], but fast-spreading ridges show significant numbers of outward facing normal faults [27–29], and multibeam data at slow spreading ridges frequently show steep, linear, outward facing slopes (though with insufficient resolution to distinguish fault scarps from volcanic ridges).

There is thus considerable current interest in understanding the fine details of segment structure and evolution. Our objectives are to determine the nature and partitioning of the faulting and its along- and cross-segment variations including its temporal evolution, to map the tectonic strain within a single segment, and to relate these findings to the deeper lithospheric structure. Here we present our preliminary results.

2. The Broken Spur segment

The Broken Spur segment (named after its hydrothermal vent field [30]) is the second segment south of Atlantis transform (Fig. 1). It is number 17 in the nomenclature of Smith et al. [31] (which we adopt here), and number 2S of Pariso et al. [11]. We chose it for its relatively simple structure, clearly

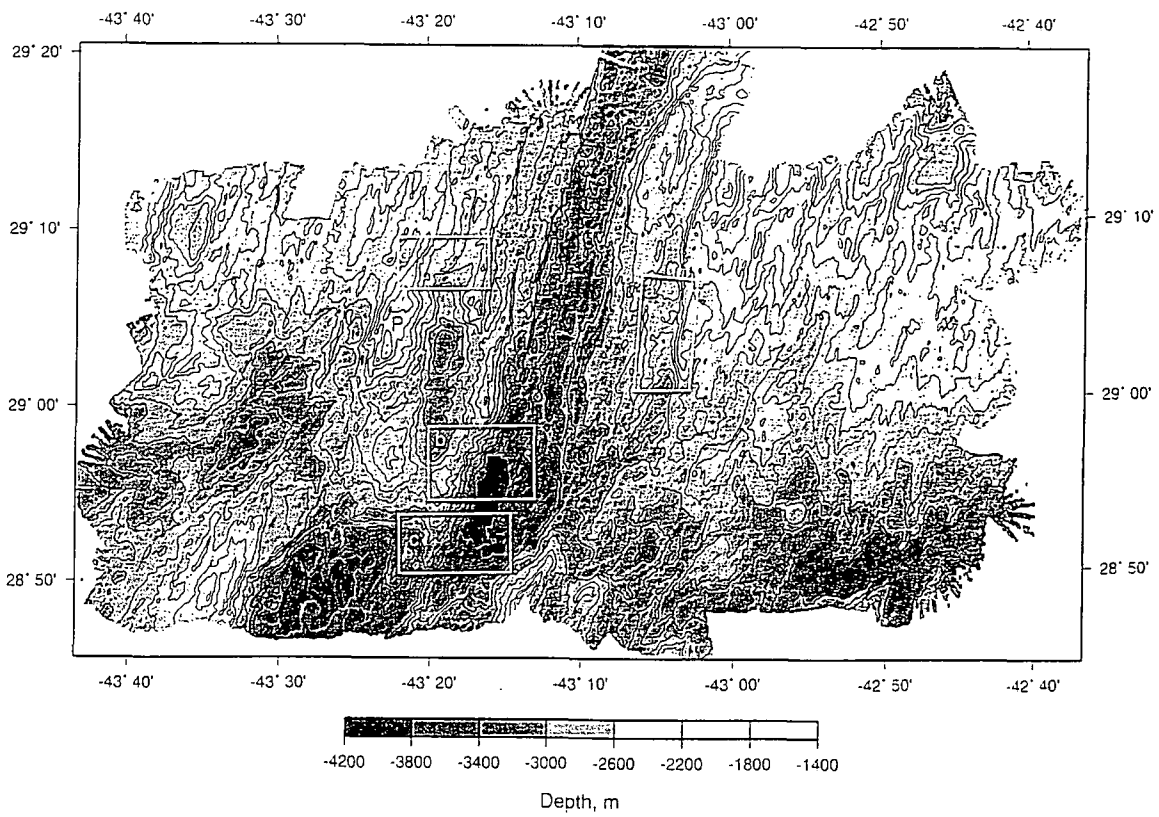

Fig. 2. *Shaded* relief bathymetry of study area from Simrad EM-12 multibeam data. Depths in metres, contour interval 200 m. Coverage is 100% from north of the centre of segment 17 through its southern non-transform offset to tip of segment 16. Positions of detailed sidescan images shown in Fig. 4 are indicated by *boxes*. *P* = Pink Mountain (see text).

defined offsets away from major transforms, good pre-existing multibeam bathymetry, gravity and magnetics coverage [10,11], and seismicity and seismic tomographic studies [32]. It is where Shaw originally identified differences in faulting style between segment centre and segment end [14,21].

The segment is 62 km long with a 5-km-wide median valley floor [4] (Fig. 2). It lies between the 28°51′ and 29°23′N non-transform discontinuities, which have dextral offsets of 11 km (0.8 Ma) and 15 km (1.2 Ma), respectively [19]. The scarps which bound the floor are 100–400 m high at the centre and outside corners, up to 1 km high at the inside corners, and strike between 010° and 040°. The rift mountains are also highest at the inside corners. The well-defined, 150–300-m-high axial volcanic ridge is displaced toward the west of the median valley floor; it strikes 010°, slightly anticlockwise from the median valley bounding faults, converging progressively onto the western fault toward the north [4,31].

The segment has existed for over 10 Ma, during which time it has propagated slowly south while its length fluctuated between 38 and 70 km [11] (Fig. 1). The spreading direction has remained fairly constant at 101° [10] since magnetic Anomaly 3A, ~6 Ma [33]. The plate divergence rate rose slowly from 22 km Ma^{-1} at Anomaly 3 (4.2 Ma) to the present 26 km Ma^{-1} [10]. Crustal thickness as inferred from gravity was a fairly uniform 6 km at 10 Ma, but has since increased steadily to 7.9 km at the segment centre and decreased to 5 km under the southern outside corner and 2.5 km under the southern inside corner [3,11].

Deep-towed sidescan sonar surveys [31] had previously covered the median valley floor and placed a few oblique swathes across the southern non-trans-

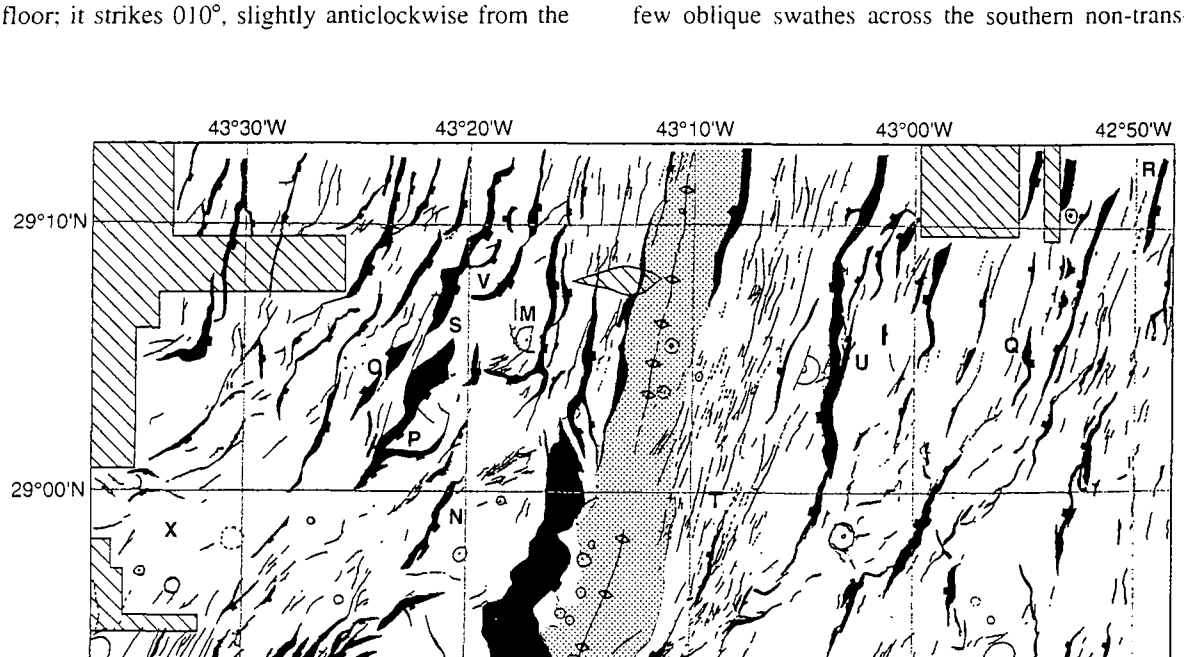

Fig. 3. Structural interpretation based on TOBI sidescan images and Simrad bathymetry. *Diagonal shading* shows data gaps. Widths of fault scarps measured on TOBI images are indicated by *line thickness*; *bar symbols* show fault facing direction. (In some cases, much of the mapped width comprises mass-wasting deposits.) *Stipple* indicates area of neovolcanic zone, and *line with anticline symbols* indicates axis of neovolcanic ridge. *Letters* denote features mentioned in text.

form offset and the segment centre. These suggested a landslide zone at the base of the southern inside corner high [31] and active faulting continuing to ~ 8 km (0.6 Ma) off axis at the centre [24,34].

3. New data

Our survey covered the southern two-thirds of Broken Spur segment. The principal tool was the deep-towed instrument TOBI [35], which carried a 6-km-swathe, 30-kHz sidescan sonar and three-component fluxgate magnetometer. We operated the ship's hull-mounted Simrad EM-12 multibeam echosounder throughout the cruise (Fig. 2).

TOBI was towed at 1 m s^{-1}, 300–500 m above the seafloor, along eighteen 70-km-long E–W lines, mostly 2.0 km apart, and two NNE–SSW lines. It was navigated using a combination of GPS-derived ship position, measured tow-cable length, and vehicle depth, guided by results from a dynamic cable simulation, and checked by comparison of its sidescan with the EM-12 bathymetry. N- and S-looking sidescan sonar mosaics with near continuous cover were produced manually at a scale of 1:50,000 and horizontal resolution of ~ 10 m, and were used to derive tectonic maps (Fig. 3). Digital sidescan mosaics were produced post-cruise (Fig. 4).

The ~ 2000-nT magnetic field of the TOBI vehicle was determined by towing in a circle over a region of low field gradient for a range of pitch and roll values. Measured field components were corrected using a modification of Isezaki's method [36].

4. Fault geometry

The combination of TOBI sidescan and EM-12 bathymetry allows us to identify fault scarps and discriminate between fault-controlled topography and volcanic constructions. Steep (up to at least 50°) fault scarps appear as bright acoustic reflectors that can be traced along the segment because of the degree of overlap between sidescan swaths (Fig. 3). Acoustic reflections come from both fresh rock face along the crest of each scarp and the apron of talus accumulated at its base. In some places fans of talus are actively accumulating on top of acoustically-attenuating (dark) pelagic sediments (*A*, Fig. 4a), while elsewhere less active fans are themselves draped by sediments (*B*, Fig. 4a). At 35–40 km from the axis (2.9–3.3 Ma), pelagic sediments obscure any volcanic morphology and all but the steep crestal faces of larger faults. Within ~ 15 km of the axis (0–1.2 Ma) sediment is thin enough to allow faults with displacements down to 20 m to be resolved.

Some more gently-dipping (~ 20°) planar surfaces are highly degraded and covered with mass-wasting debris (e.g., the main median valley wall scarp bounding the inside corner high between 28°53′N, 43°18′W and 29°01′N, 43°15′N; Fig. 4b). The along-strike continuity of these features, as well as the extent and asymmetric disposition of the talus deposits, suggests that they are large-scale fault-controlled structures. However, it is unclear whether a single gently-dipping major fault controls the scarp in all these features or whether several steeper faults are involved. In places our data show that considerable relief is produced by closely spaced normal faults with displacements of several hundreds of metres each. An example is "Pink Mountain" at 29°03′N, 43°23′W (*P*, Figs. 2 and 3) where a 1300-m-high horst is bounded by inward- and outward-facing faults in a complex three-dimensional geometry. Northwards (towards the segment centre) this horst dies out into a single inward-facing fault (*S*, Fig. 3).

The west side of Pink Mountain is a rare example of outward facing faults (*O*, Fig. 3). Other examples occur on the extreme eastern flank of the segment centre (*Q*, *R*, Fig. 3). TOBI images of many steep, linear, outward-facing bathymetric scarps lack typical fault-scarp textures such as Fig. 4a, instead displaying volcanic morphology or mass-wasting deposits that may or may not be fault-related.

The overall pattern of faulting is markedly asymmetric (Fig. 3). The western median valley wall comprises a well-developed system of linked normal faults. Towards the southern end of the segment displacement increases rapidly to ~ 1200 m on a single major fault structure which terminates abruptly at the non-transform offset. This scarp is heavily degraded and obscured by talus (Fig. 4b). In contrast, the eastern flank comprises many small, closely-spaced faults and broad zones of fissuring with a poorly delineated valley wall (*T*, Fig. 3).

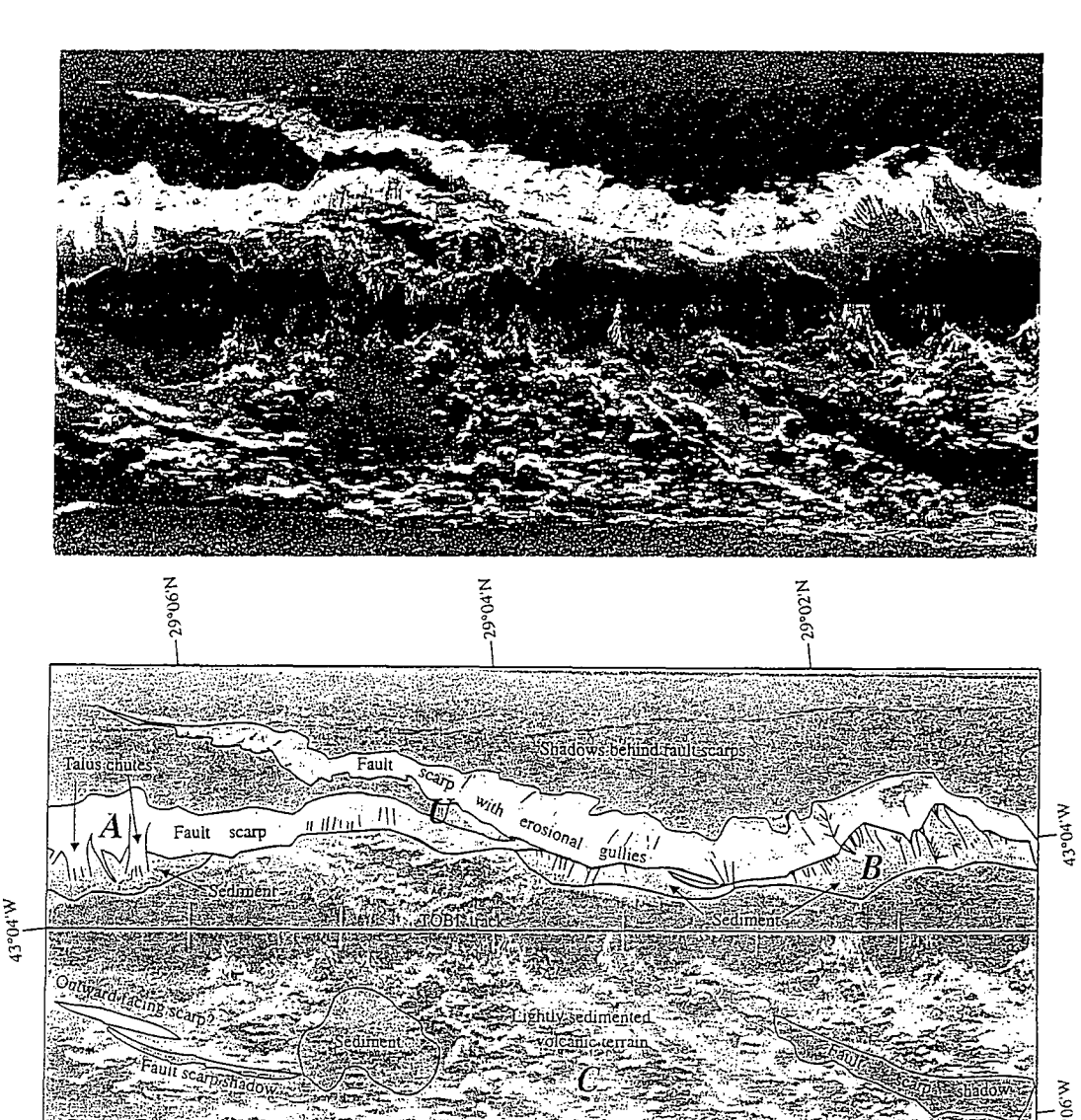

Fig. 4. Detailed TOBI sidescan sonar images with interpretative overlays illustrating key features of seafloor morphology discussed in text (see Fig. 2 for locations). Acoustic reflections are *white*. Interpretations based on combination of sidescan and bathymetry data.
(*a*) Ridge-parallel image from eastern flank showing relay-ramp (*U*) between linking inward-facing faults. Single sidescan swathe with vehicle track approximately N–S along centre. Note variation in scarp width which is proxy for normal displacement along fault trace. Scarp is heavily degraded, with recently active talus accumulations and gullies (acoustically reflective — *white*, e.g., *A*) and inactive fans covered by acoustically absorbing (*black*) sediments (e.g., *B*). Volcanic morphology is preserved in hanging wall of fault (*C*).

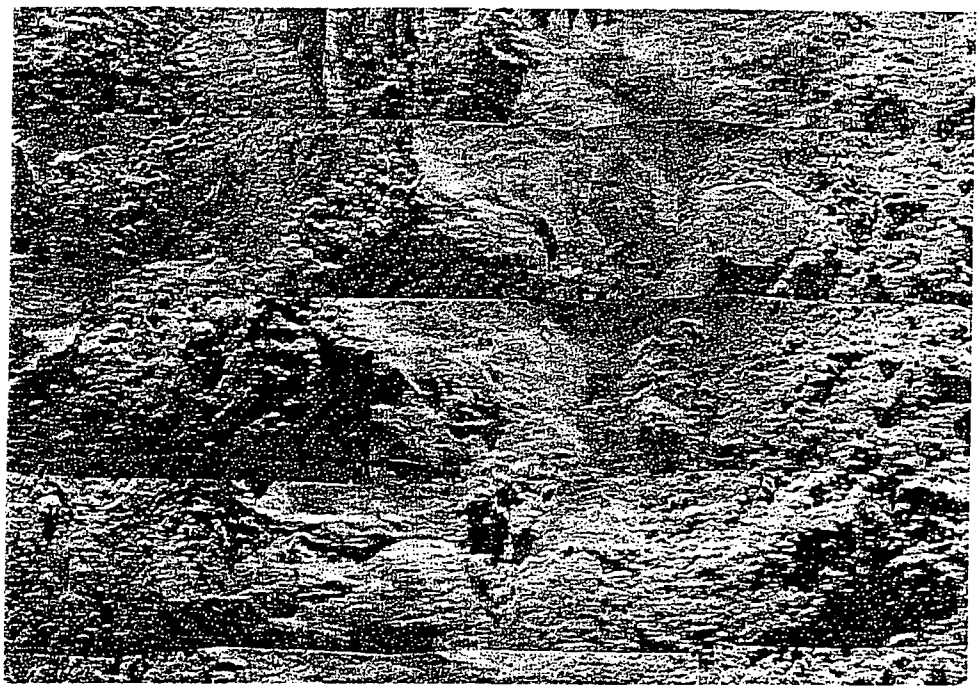

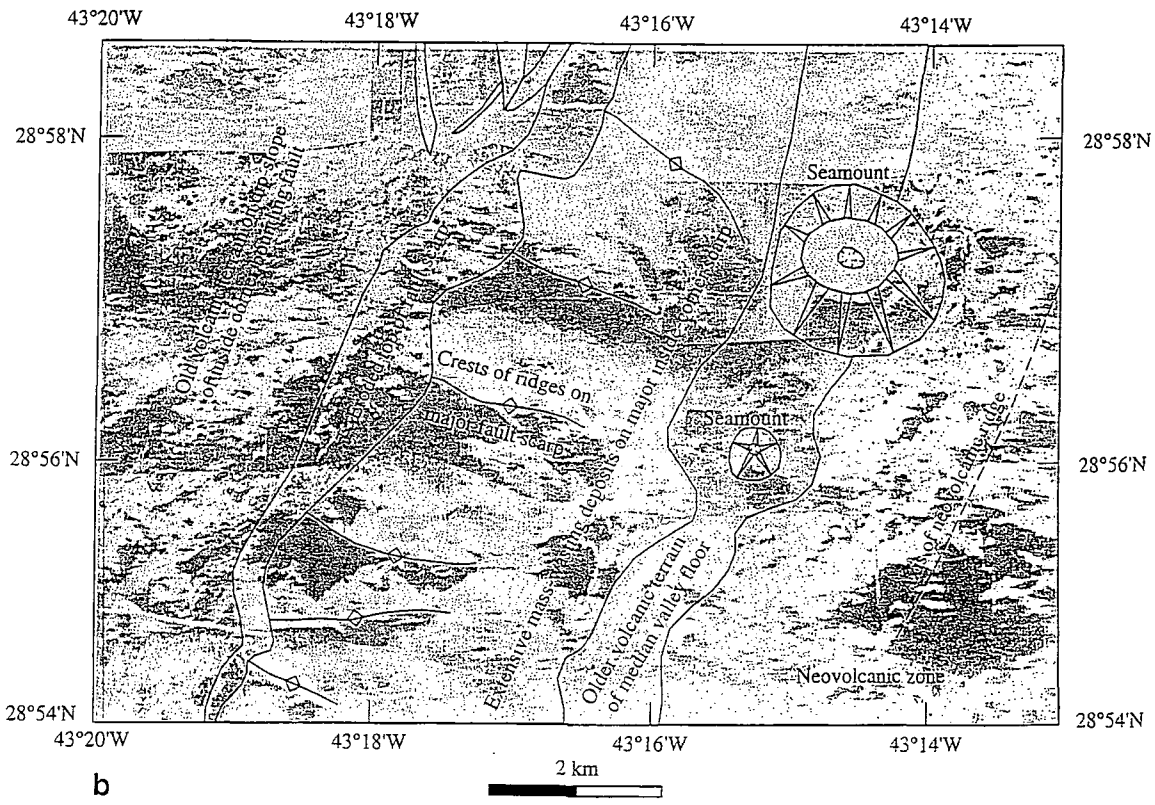
43°20'W
43°18'W
43°16'W
43°14'W
28°58'N
28°56'N
28°54'N
Seamount
Seamount
Crests of ridges on
major fault scarps
Older volcanic terrain
of median valley floor
Neovolcanic zone
2 km
b

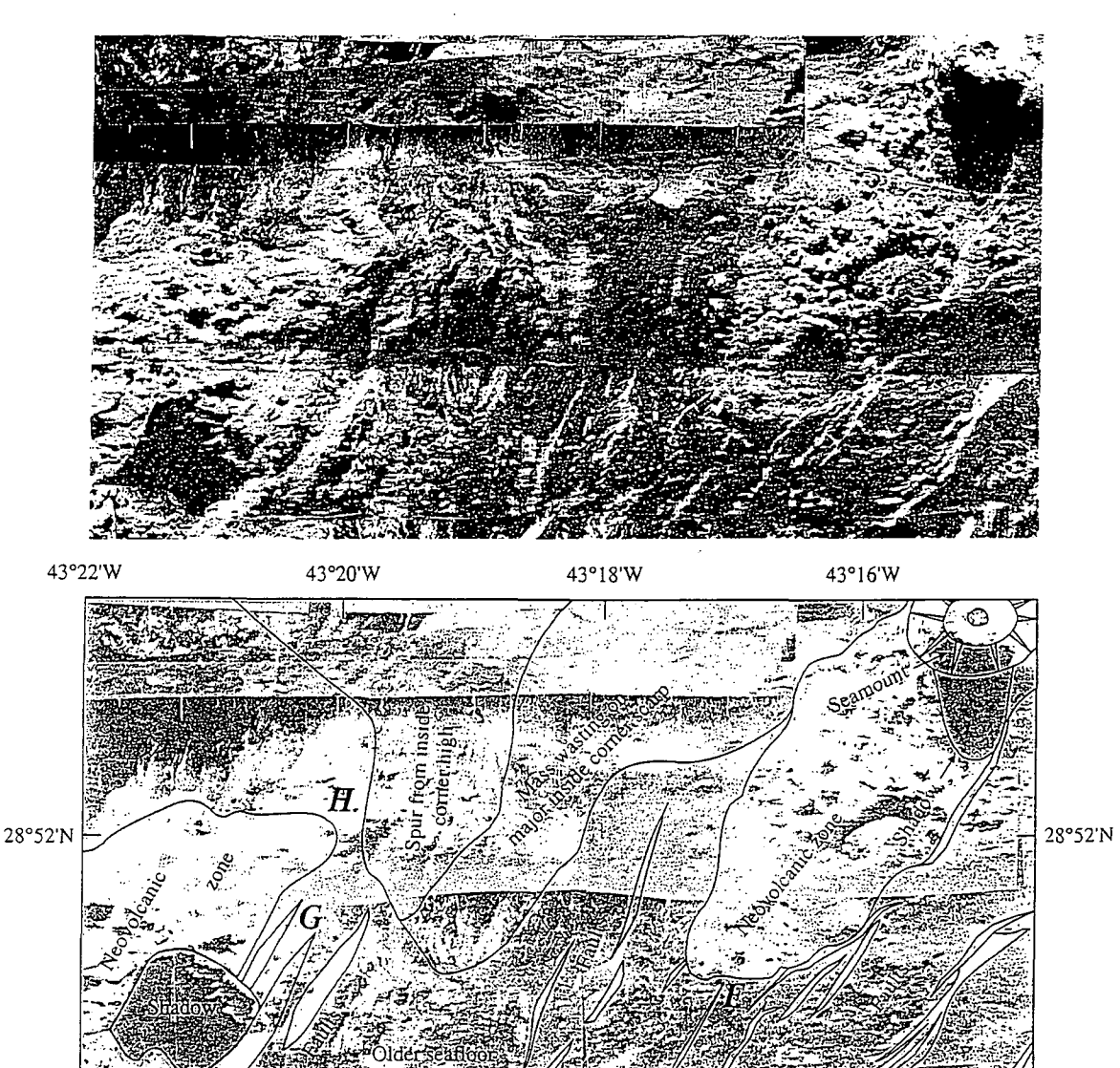

Fig. 4. (c) Detailed view of non-transform offset between segments 16 and 17. S-looking sidescan sonar mosaic except for small strip of N-looking images in top left and top centre. Southern tip of segment 17 neovolcanic zone (NVZ) is on right truncating W-facing normal faults of segment 16 (*F*). Northern tip of segment 16 NVZ is on left, with fresh volcanics ponded against large W-facing scarp (*G*) and in contact with wall of inside corner high (*H*). Note absence of E–W (transform) structures between NVZ tips.

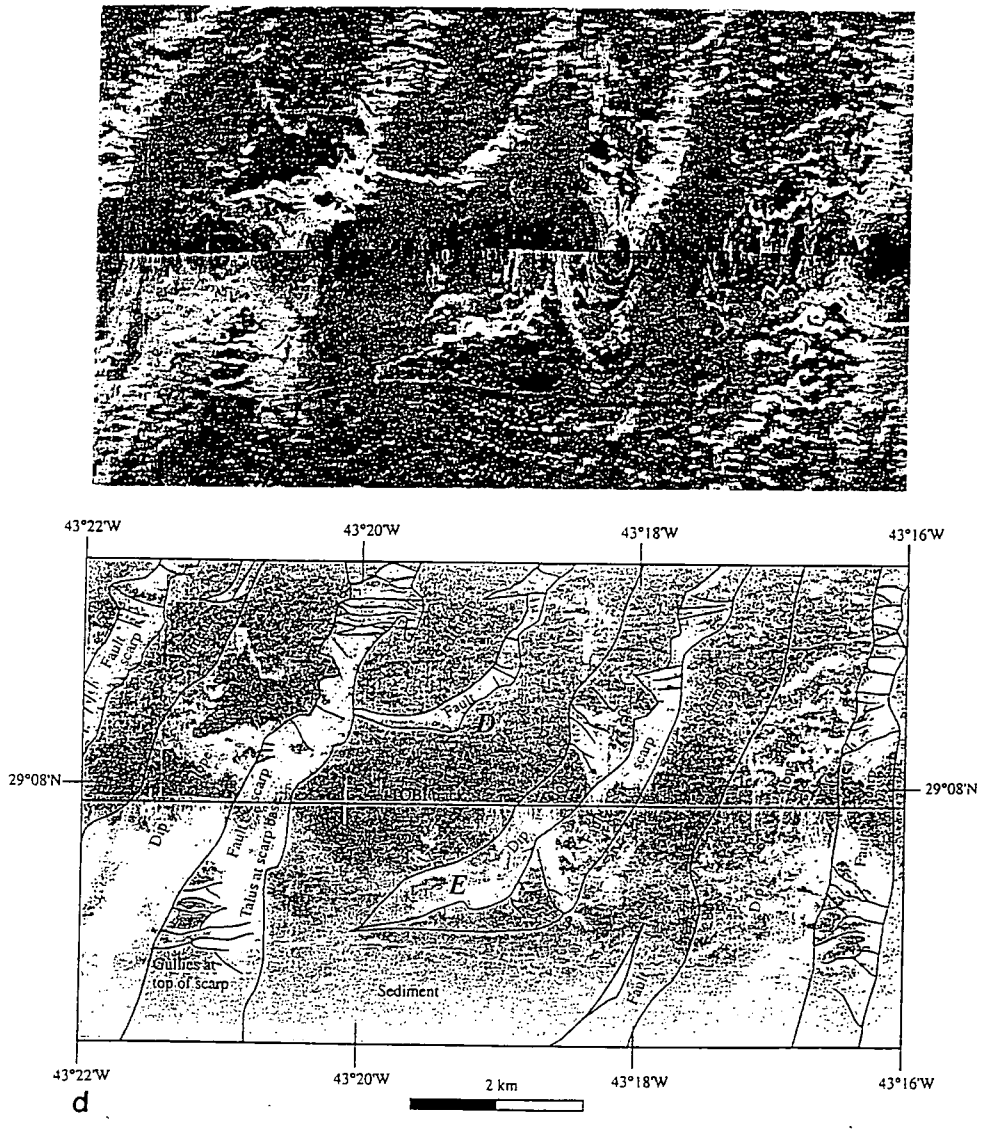

Fig 4. (d) Example of "hooked" fault terminations from western ridge flank (see text for discussion). Single swathe with vehicle track running E–W through centre. Five inward (east) facing normal faults are at top of image, with centre one (*D*) hooking west to join second from left. Insonification in northern half of image is to north, so face of this hooked fault is insonified along its whole length. Second fault from right hooks west in lower part of image, where insonification is to south, so face of hooked part is in shadow but dip slope is insonified (*E*).

Many faults cross-cut volcanic edifices within a few kilometres of the axial volcanic ridge (e.g., eastern edge of Fig. 4c; immediately west of *T*, Fig. 3). Faulting asymmetry is most marked near the segment end, although a small degree persists even at the segment centre. The sense of the asymmetry appears to reverse fairly abruptly near 29°09′N.

A simple picture of laterally continuous ridge-parallel, uniform normal faults clearly does not apply here (Fig. 3). Many faults, imaged continuously from tip to tip along the segment, show patterns of discontinuous structures of variable orientation and a wide range of scarp geometries. The discontinuous pattern is not due to burial by sediments or lava flows

because scarp heights, as shown by EM-12 bathymetry, vary systematically along the lengths of faults from a maximum near the centre to zero at the tips. This is what we expect if scarp heights are directly reflecting fault displacements: very similar displacement profiles have been obtained from continental normal faults (e.g., [37]). Some larger faults exhibit more complicated scarp height profiles and irregular curvilinear traces. In detail, breached relay ramps and abandoned splays are preserved in footwalls (e.g., *U*, Figs. 3 and 4a; [24]). This is evidence that along-strike linkage of coeval faults has been important in the evolution of brittle deformation at the axis, and is discussed below. Apart from continuing degradation of scarps by mass-wasting, there is little change beyond ~ 15 km (1.2 Ma) from the axis. Plots of cumulative heave show most faulting to be complete by 5–10 km off-axis at segment centre and outside corner, and by not more than ~ 15 km in the inside corner [38].

In contrast to simple ridge-parallel fault linkage, several faults on the western flank terminate abruptly in scarps trending almost orthogonal to the rift (e.g., *V*, Fig. 3; Fig. 4d). These are not a separate set of ridge-perpendicular faults but are "hooked" terminations of ridge-parallel inward-facing normal faults. The hook is always away from the axis in the direction of the segment-end offset, thus linking to faults further off-axis. The hooks occur only at the fault tip which terminates in the inside corner: outside corner tips are typically ridge-parallel. This pattern was confirmed by EM-12 data over the northern inside corner. Such linkage is clearly the mechanism that accommodates increased fault spacing towards the ends of segments [14].

There is a prominent set of faults which trend ~ 030° (20° clockwise of the ridge axis) in a 20–25-km-wide zone centred on the non-transform offset (*W–X* and *W–Y*, Fig. 3). In some places these faults cross-cut an earlier set of ridge-parallel faults (e.g., near *Z*, Fig. 3). This zone, and especially its northern boundary, defines a southward pointing "arrow" which we believe to be the trace of the non-transform offset as it migrated southwards during at least the last 1.8 Ma (see below). This is also consistent with the sharp contrast between fresh neovolcanic material at the southern tip of the segment and the old, heavily sedimented seafloor over which it extrudes (Fig. 4c). The zone of oblique faults is thus the slow-spreading equivalent of propagating rift pseudofaults [39,40], and is similar to the "discordant zones" that mark the traces of migrating overlapping spreading centres [41]. There are no spreading-parallel faults within the non-transform offset, and the 030° faults show substantial normal displacement (vertical offsets ≤ 900 m and dips ≤ 55° from EM-12 bathymetry). Thus any "transform" motion must occur by a combination of oblique slip and block rotation [42] and may involve more than one generation of superimposed faults.

5. Volcanic morphologies

The volcanic morphologies within the neovolcanic zone (NVZ) comprise hummocky mounds, hummocky ridges, and flat-topped, smooth, round volcanoes [8,14,17,18]. Fresh, acoustically bright, unsedimented volcanic morphologies are restricted to the inner median valley floor, with no evidence for active volcanism > 5 km away from the spreading axis. The NVZ axis, defined by the brightest volcanic morphologies and a narrow topographic ridge, lies asymmetrically to the western side of the valley. The eastern boundary of the NVZ is gradational south of 29°06′N, while to the north it is an inward-facing normal fault (Fig. 3). The western NVZ boundary is generally sharp, with either slump or debris flow material overlying neovolcanics, or fresh volcanics overlying faulted sediments.

The southern tip of the Broken Spur NVZ is at 28°51′N (Fig. 4c). Here, the NVZ is a well-defined, narrow ridge which makes a sharp contact with the sedimented median valley floor and truncates minor faults within the floor (*F*, Fig. 4c). Similar relationships occur at the northern tip of segment 16 (28°52′N, 43°21′N), where fresh volcanics truncate fault scarps and are in sharp contact with the sedimented slopes of the inside corner high (*G*, *H*, Fig. 4c).

Off axis, volcanic morphologies are dominated by an irregular terrain of sedimented hummocky volcanoes (e.g., *C*, western part of Fig. 4a). As sediment cover increases, this terrain outcrops preferentially at the crests and on the dip slopes of fault blocks. Sedimented flat-topped seamounts occur throughout

the area, but most commonly south of 29°N in the off-axis continuation of the non-transform offset (Fig. 3). Similar preponderances of seamounts around MAR segment ends occur near 22°N [43] and 24°N [8], perhaps because they suffer less tectonic dismemberment where faults are wider spaced. We identify two split volcanoes, at *M* and west of *U* (Fig. 3).

6. Magnetisation

6.1. Inversions

Magnetic and navigation data were merged, and were interpolated with EM-12 centrebeam bathymetry onto linear profiles at 100-m intervals. Since the vehicle altitude is much less than the bathymetric relief, upward continuation to a common datum [44] only produces stable solutions at or above sea level. Instead we directly inverted the observed field assuming that it approximates that which would be observed if the sources were on a horizontal plane and the vehicle were at its actual altitude above such a plane [45]. We assumed a 1-km-thick source layer. The resultant magnetisation, appropriately filtered, compares favourably with inverted sea-surface data [46] (Fig. 5), confirming that skewing errors [45] are insignificant.

6.2. Principal observations

The principal magnetisation features from the surface data are also seen in the deep-towed data, but the latter yield much sharper boundaries between normal and reversely-magnetised crust (e.g., the western boundary of Anomaly 1n on line *A* at 43°15′W is only 2.2 km wide).

The Brunhes anomaly (*B*, Fig. 5), 0–780 ka, is ~ 20 km wide and centred over the median valley floor at 29°10′N in the middle of Broken Spur segment. It apparently widens to ~ 35 km (e.g., *B*–*B*′, line *Q*) at the southern end of this segment, though it is again 20 km wide at the centre of segment 16 at 28°45′N [46].

Inferred magnetisation progressively decays away from the NVZ axis, probably due to low-temperature

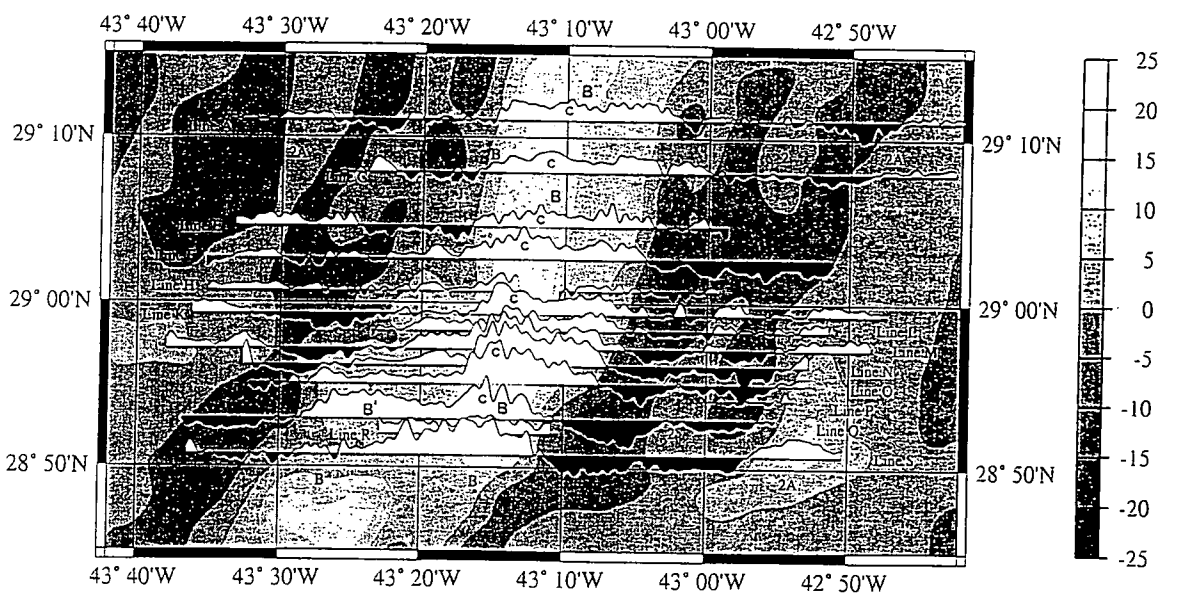

Fig. 5. Profiles of crustal magnetisation based on 2-D inversions [45] of TOBI total field, superimposed on contours of magnetisation inversion solution of Pariso [11] for sea-surface field (*scale bar*, A m^{-1}). TOBI inversion assumed constant 1-km-thickness source layer. Track lines at zero magnetisation, positive magnetisations white, maximum magnetisation (line *O*) ~ 30 A m^{-1}. Anomaly identifications [33] are: *B*, Brunhes (0–0.78 Ma); *J*, Jaramillo (0.98–1.04 Ma); 2 (1.79–2.01 Ma); 2*A* (2.61–3.60 Ma). *B*′ (line *Q*) indicates older part of Brunhes anomaly, and *C* indicates Central Anomaly Magnetic High (see text).

oxidation of basalt [47]. Particularly high apparent magnetisations occur at the southern end of the segment reaching 30 A m^{-1} on line, compared to 15 A m^{-1} on line *A* in the north. This appears to be a common expression of segmentation [46]. The central magnetisation high (*C*, Fig. 5) follows the NVZ, rather than the axis of the Brunhes normal zone which steps to the right leaving a large region of normally magnetised rock (*B'*) in the inside corner to the west of Broken Spur segment (number 17) and north of segment 16.

Within the central normal zone between 29°12′N and 28°57′N we identify a narrow band of low-amplitude normal magnetisation (e.g., at 43°07′W on line *C*, magnetisation is reduced from 25 to 5 A m^{-1}). This band follows the eastern valley wall fault. It may result from tectonic thinning, transfer of lower-magnetisation greenschist-facies rocks to the surface, or enhanced hydrothermal alteration perhaps marking the down-flow zone feeding the Broken Spur hydrothermal field. This last is the most plausible, because some faults in the band are relatively small and unlikely to have caused significant crustal thinning. A similar low-magnetisation zone follows the western valley wall fault between 29°12′N and 29°06′N (e.g., at 43°13′W on line *E*). It may continue south, but cannot be readily distinguished from the steep magnetisation gradient south of 29°00′N (see below).

The Broken Spur hydrothermal field is at 29°10′N, 43°10′N [30], between lines *A* and *C* and close to the central anomaly magnetisation high. Any magnetisation low associated with it (cf. [48]) is < 2 km in diameter.

South of 28°57′N, the central magnetisation high is asymmetric. From its maximum at the centre of the neovolcanic ridge, magnetisation decreases gradually eastwards over 20 km, but sharply to the west over only 4 km towards the large valley wall fault. This asymmetric pattern parallels that in the volcanic morphology, which shows a gradual increase in apparent age to the east but a sharp truncation to the west. If decreasing magnetisation reflects a gradual decay with time [49], this pattern may reflect asymmetric accretion with new crust preferentially accreted to the eastern flank. West of the western valley wall fault a low level of positive magnetisation (*B'*), which is absent farther north and on the east flank, extends nearly 20 km farther west (to about 43°28′W on lines *O* and *Q*). We discuss its origin below. A local magnetisation high on line *S* at 43°22′W may mark the northern tip of the segment 16 NVZ.

Reversals can be identified out to Anomaly 2An at ~ 30 km from the axis. On some lines a minor positive magnetisation within Anomaly 1r is interpreted as Anomaly 1r.1n (Jaramillo event). The spacing, width and amplitude of the older magnetisation anomalies are asymmetric, even near the segment centre, and the sense of asymmetry varies with time. For example, on lines *A* and *C* Anomaly 2n is large on the west flank but small on the east, while the opposite is true of the Jaramillo. On the western flank, Anomaly 2n appears to terminate at 29°02′N. The area to its south is dominated by normal magnetisation *B'* and Anomaly 2r cannot be identified. This area corresponds to the eastern end of a band of high, positive magnetisation along the off-axis nontransform offset trace and may reflect increased induced magnetisation in serpentinised lower crust or upper mantle [46].

7. Tectonic evolution

7.1. Evidence for migration

The interaction of tectonic and magmatic processes has important implications for the way that segments develop over time, particularly for the thermal and therefore rheological properties of the oceanic crust. At slow-spreading ridges it has been recognised that this interaction is a complex four-dimensional process, with mechanisms varying across-

Fig. 6. Cartoon of tectonic evolution of segmentation in study area during last 2 Ma based on integrated interpretation of faulting and magnetic reversal pattern. Fault scarps taken from Fig. 3, with regions of older seafloor progressively removed in three stages. At each stage, approximate positions of neovolcanic ridges are indicated by *diagonal hatching*. Segment numbers [31] shown in *bold*. See text for further explanation.

Intra-Brunhes (~0.3 Ma)

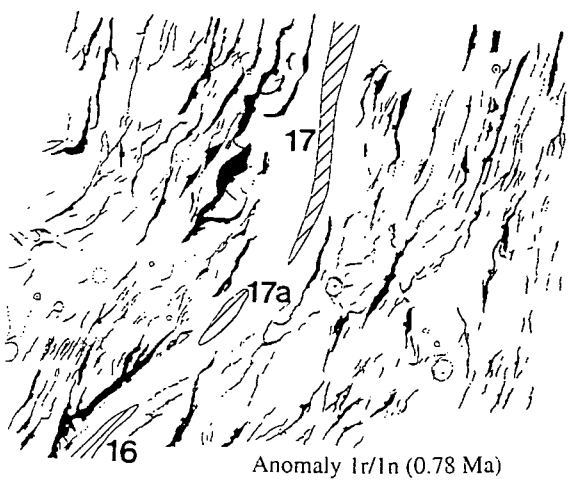

Anomaly 1r/1n (0.78 Ma)

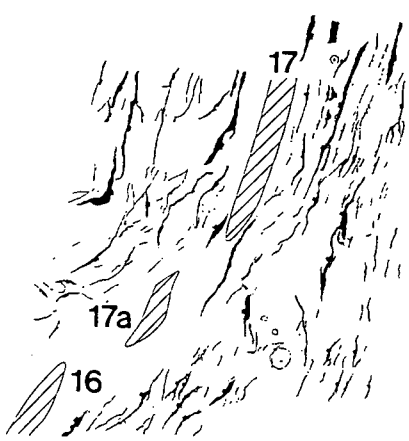

Anomaly 2n (1.8 Ma)

and along-axis as well as in time. This is evident in the present data set (Fig. 3), in particular the irregular development of faulting along the axis, the asymmetric geometry of the segment ends, and the accommodation of spreading in the non-transform offset by a zone of deformation rather than a long-lived transform fault.

The crust of the southern Broken Spur segment (number 17) did not form by simple, steady-state symmetric spreading, as demonstrated by the following key observations from the magnetisation reversal pattern (Fig. 5). First, in the inside corner west of segment 17 and north of segment 16 is a region of normally magnetised crust (*B'*) along-strike from reversely magnetised crust farther to the north. Second, Anomaly 2 is kinked or disrupted on the eastern flank at 28°55′N and on the western flank at 29°02′N, i.e. north of the current position of the segment 16/17 boundary. Third, the eastern side of the central normal zone of segment 17 narrows towards the end of the segment from about 20 km at 29°10′N to 10 km at 28°50′N.

Further evidence for tectonic evolution is provided by the pattern of faulting. In particular, the trace of the non-transform offset describes an oblique wake indicating continuous southward migration. Immediately to the north of the western trace is a series of topographic massifs, bounded by large fault scarps, which we interpret as the inside corner high and its fossil counterparts (*N* and *P*, Fig. 3). These lines of evidence are all consistent with progressive southward migration of the southern tip of segment 17, accompanied by discontinuous development and abandonment of inside corner highs.

We have used the fault patterns, bathymetry and magnetic data to reconstruct the segment evolution back to Anomaly 2 (1.8 Ma). We illustrate it by removing progressively older areas from Fig. 3 and closing the gap along the spreading direction (Fig. 6). We have not tried to restore fault heaves: at each stage, faults within and close to the NVZ have been deleted, but all others are left unchanged, except that for the 0.3 Ma case part of the large fault bounding the inside corner high has been removed for clarity. This is probably reasonably realistic for smaller faults, since our data and [24] suggest that most faults develop to their maximum extent close to the axis. It may be less accurate for the large segment-end faults which may develop over longer periods, but nevertheless the fault pattern provides a useful framework in which to view the evolution. At each step, we indicate the approximate positions of the NVZs as deduced from morphological and magnetic observations.

The reconstruction lets us review the evolving relative positions of the fault systems. It suggests that recently there was a small, short-lived segment (17a) between segments 16 and 17, which contracted as segment 17 propagated southwards.

7.2. Intra-Brunhes (0.3 Ma)

The area of the central magnetisation high has been removed (Fig. 6a). We assume that the narrow, high-amplitude normal magnetisation along the south of segment 17 is the result of post-0.3 Ma propagation during the latter part of chron 1n. The model predicts that the NVZ of segment 17 extended south to 28°55′N at this time and briefly overlapped segment 17a.

7.3. Anomaly 1n/1r (Brunhes/Matuyama) boundary (0.78 Ma)

At this time the NVZ of segment 17a was between 28°50′N and 28°56′N (Fig. 6b) and produced the normally magnetised crust currently lying north of segment 16 and west of segment 17 (*B'*, Fig. 5). The southern tip of segment 17 lay close to a large fault to the west of the axis (*N*, Fig. 3), which we believe bounded the previous inside corner high, now the massif immediately west of box *C* in Fig. 2. Relatively small, oblique faults occur on the eastern flank, similar to the pattern at the current non-transform offset.

7.4. Anomaly 2n (1.8 Ma)

The position is similar to that at the anomaly 1n/1r boundary, with a short, oblique segment 17a and short, oblique faults in the eastern non-transform offset traces (Fig. 6c). The southern inside corner high of segment 17 at this epoch is Pink Mountain (*P*, Figs. 2 and 3).

7.5. Implications of the reconstruction

Our reconstructions show that throughout the evolution of spreading in this system the relationship of the fault pattern to the segment geometry was similar to the present one. Large faults occurred at the inside corners of the non-transform offset and sets of oblique faults formed at the outside corner, while faults paralleled the axis at the segment centre. However, the large inside corner faults are more widely spaced than the others (earlier ones now being at *N* and *P*, Fig. 3), and formed at intervals of 0.8–0.9 Ma. The southern tip of segment 17 has propagated 18 km southward in the past 1.8 Ma at a rate of ~ 10 km Ma^{-1}, comparable to the half spreading rate (13 km Ma^{-1}).

7.6. Instability

Regional studies have demonstrated that the geometries of individual segments and discontinuities are relatively stable over periods ~ 15 Ma [13,46]. Our reconstruction illustrates significant instabilities on a much shorter time scale, giving rise to quite rapid, though possibly short-lived, fluctuations in segment length and geometry on timescales of ~ 1 Ma. Such variations may be responsible for the apparent breadth of segment discontinuities, which occupy zones up to ~ 30 km wide.

8. Conclusions

Our TOBI sonar images provide sufficient resolution to reveal mass-wasting and fault structures, but are extensive and continuous enough to show the overall faulting pattern. Deep-towed magnetisation inversions yield significantly increased resolution over inversion of sea-surface data. Our main conclusions are:

8.1. Faulting

(a) Fault geometry is highly three-dimensional. There is abundant evidence for fault growth by linkage along-axis.
(b) Towards inside-corners, faults curve sharply into the offset direction to form hooked terminations, often against older faults. This results in fewer but larger faults occurring on inside corners compared with outside corners and segment centres.
(c) Faulting is strongly asymmetric about the median valley towards the segment end, where the valley approximates a half graben, but more symmetric in the segment centre.
(d) Faulting produces most of the seafloor relief.
(e) Most faults cease to be active by 15 km off-axis.
(f) Most steep outward-facing slopes are not associated with large outward-facing faults, though there is some minor faulting along some of them.

8.2. Magnetisation

(a) High magnetisations, particularly at the south end of the segment, coincidence with the NVZ observed in the sidescan images.
(b) Low magnetisation over valley wall faults may reflect alteration due to fluid circulation.
(c) Most reversal boundaries are sharp.
(d) Anomaly size and decay rate are strongly asymmetric, especially in Anomaly 1n in the southern part of the segment. We propose that this reflects asymmetric accretion of layer 2A.

8.3. Tectonic evolution

(a) Fault patterns, magnetic reversal boundaries and gross morphology suggest that the segment boundary has migrated ~ 18 km southwards during the last 1.8 Ma.
(b) This propagation has transferred crust from the previous non-transform offset into the western crestal mountains.
(c) Reconstructions suggest that major faults bounding the inside corner high initiate at 0.8–0.9-Ma intervals.
(d) Our results suggest important links between segment propagation, fault growth, magmatic emplacement, and asymmetric spreading.

Acknowledgements

We acknowledge the invaluable assistance of the officers, crew, and scientific support party of RRS "Charles Darwin" cruise CD99. We are indebted to

the TOBI development team who worked long and hard to bring in the technical upgrades used, and especially Chris Flewellen and Ian Rouse who supported TOBI during the cruise. We are grateful for reviews from Suzanne Carbotte, Marty Kleinrock and an anonymous referee which helped us improve the paper substantially. This work was funded by the Natural Environment Research Council under its BRIDGE initiative. NCM was supported by NERC grant GR5/92/GS/5 and PC by a Royal Society Universities Research Fellowship. *[CL]*

References

[1] H. Schouten, K.D. Klitgord, J.A. Whitehead, Segmentation of mid-ocean ridges, Nature (London) 317 (1985) 225–229.

[2] K.C. Macdonald, P.J. Fox, L.J. Perram, M.F. Eisen, R.M. Haymon, S.P. Miller, S.M. Carbotte, M.-H. Cormier, A.N. Shor, A new view of the mid-ocean ridge from the behaviour of ridge-axis discontinuities, Nature (London) 335 (1988) 217–225.

[3] J. Lin, G.M. Purdy, H. Schouten, J.-C. Sempéré, C. Zervas, Evidence from gravity data for focussed magmatic accretion along the Mid-Atlantic Ridge, Nature (London) 344 (1990) 627–632.

[4] J.-C. Sempéré, J. Lin, H.S. Brown, H. Schouten, G.M. Purdy, Segmentation and morphotectonic variations along a slow spreading center: The Mid-Atlantic Ridge (24°00′N–30°40′N), Mar. Geophys. Res. 15 (3) (1993) 153–200.

[5] B.E. Tucholke, J. Lin, A geological model for the structure of ridge segments in slow spreading ocean crust, J. Geophys. Res. 99 (1994) 11937–11958.

[6] M. Tolstoy, A.J. Harding, J.A. Orcutt, Crustal thickness on the Mid-Atlantic Ridge — Bull's-eye gravity-anomalies and focused accretion, Science 262 (5134) (1993) 726–729.

[7] R.S. Detrick, H.D. Needham, V. Renard, Gravity anomalies and crustal thickness variations along the Mid-Atlantic Ridge between 33°N and 40°N, J. Geophys. Res. 100 (B3) (1995) 3767–3787.

[8] K. Lawson, R.C. Searle, J.A. Pearce, P. Browning, P. Kempton, Detailed volcanic geology of the MARNOK area, Mid-Atlantic Ridge north of Kane transform, in: C.J. MacLeod, P.A. Tyler, C.L. Walker (Eds.), Tectonic, Magmatic, Hydrothermal and Biological Segmentation of Mid-Ocean Ridges, Geol. Soc. London, Spec. Publ. 118 (1996) 61–102.

[9] N.R. Grindlay, P.J. Fox, K.C. Macdonald, Second-order ridge axis discontinuities in the South Atlantic: Morphology, structure and evolution, Mar. Geophys. Res. 13 (1991) 21–49.

[10] H. Sloan, P. Patriat, Kinematics of the North American–African plate boundary between 28 and 29°N during the last 10 Ma: evolution of the axial geometry spreading rate and direction, Earth Planet. Sci. Lett. 113 (1992) 323–341.

[11] J.E. Pariso, J.-C. Sempéré, C. Rommevaux, Temporal and spatial variations in crustal accretion along the Mid-Atlantic Ridge (29°–31°30′N) over the last 10 m.y.: Implications from a three-dimensional gravity study, J. Geophys. Res. 100 (B9) (1995) 17787–17794.

[12] J.-C. Sempéré, P. Blondel, A. Briais, T. Fujiwara, L. Geli, N. Isezaki, J.E. Pariso, L. Parson, P. Patriat, C. Rommevaux, The Mid-Atlantic Ridge between 29°N and 31°30′N in the last 10 Ma, Earth Planet. Sci. Lett. 130 (1–4) (1995) 45–55.

[13] B. Tucholke, J. Lin, M. Kleinrock, M. Tivey, T. Reed, J. Goff, G. Jaroslow, Segmentation and crustal structure of the western Mid-Atlantic Ridge flank, 25°25′–27°10′N and 0–29 m.y., J. Geophys. Res. 102 (B5) (1997) 10203–10223.

[14] P. Shaw, Ridge segmentation, faulting and crustal thickness in the Atlantic Ocean, Nature (London) 358 (1992) 492–493.

[15] J.A. Karson, G. Thompson, S.E. Humphris, J.M. Edmond, W.B. Bryan, J.R. Brown, A.T. Winters, R.A. Pockalny, J.R. Casey, C.A.C.G. Klinkhammer, M.R. Palmer, R.J. Kinzler, M.M. Sulanowska, Along-axis variations in seafloor spreading in the MARK area, Nature (London) 328 (1987) 681–685.

[16] J.C. Mutter, J.A. Karson, Structural processes at slow-spreading ridges, Science 257 (1992) 627–634.

[17] S. Allerton, B.J. Murton, R.C. Searle, M. Jones, Extensional faulting and segmentation of the Mid-Atlantic Ridge north of the Kane fracture zone (24°00′N to 24°40′N), Mar. Geophys. Res. 17 (1995) 37–61.

[18] S. Allerton, R.C. Searle, B.J. Murton, Bathymetric segmentation and faulting on the Mid-Atlantic Ridge, 24°00′N to 24°40′N, in: C.J. MacLeod, P.A. Tyler, C.L. Walker (Eds.), Tectonic, Magmatic, Hydrothermal and Biological Segmentation of Mid-Ocean Ridges, Geol. Soc. London, Spec. Publ. 118 (1996) 49–60.

[19] J. Escartin, J. Lin, Ridge offsets, normal faulting, and gravity anomalies of slow spreading ridges, J. Geophys. Res. 100 (B4) (1995) 6163–6177.

[20] G.A. Neumann, D.W. Forsyth, The paradox of the axial profile: Isostatic compensation along the axis of the Mid-Atlantic Ridge?, J. Geophys. Res. 98 (B10) (1993) 17891–17910.

[21] P.R. Shaw, J. Lin, Causes and consequences of variations in faulting style at the Mid-Atlantic Ridge, J. Geophys. Res. 98 (B12) (1993) 21839–21851.

[22] K.C. Macdonald, B.P. Luyendyk, Deep-tow studies of the structure of the Mid-Atlantic ridge crest near 37°N (FAMOUS), Bull. Geol. Soc. Am. 88 (1977) 621–636.

[23] L.S. Kong, R.S. Detrick, P.J. Fox, L.A. Mayer, W.B.F. Ryan, The morphology and tectonics of the MARK area from Sea Beam and Sea MARC I observations (Mid-Atlantic Ridge 23°N), Mar. Geophys. Res. 10 (1988/1989) 59–90.

[24] E. McAllister, J. Cann, Initiation and evolution of boundary wall faults along the Mid-Atlantic Ridge, 25–29°N, in: C.J. MacLeod, P.A. Tyler, C.L. Walker (Eds.), Tectonic, Magmatic, Hydrothermal and Biological Segmentation of Mid-Ocean Ridges, Geol. Soc. London, Spec. Publ. 118 (1996) 29–48.

[25] R.C. Searle, A.S. Laughton, Sonar studies of the Mid-Atlantic Ridge crest near Kurchatov Fracture Zone, J. Geophys. Res. 82 (1977) 5313–5328.

[26] A.S. Laughton, R.C. Searle, Tectonic processes on slow spreading ridges, in: M. Talwani, C.G. Harrison, D.E. Hayes (Eds.), Deep Drilling Results in the Atlantic Ocean: Ocean Crust, vol. 2, Am. Geophys. Union, Washington, DC, 1979, pp. 15–32.

[27] P. Lonsdale, Structural geomorphology of a fast-spreading rise crest: The East Pacific Rise near 3°25′S, Mar. Geophys. Res. 3 (1977) 251–293.

[28] R.C. Searle, GLORIA survey of the East Pacific Rise near 3.5°S: tectonic and volcanic characteristics of a fast-spreading mid-ocean rise, Tectonophysics 101 (1984) 319–344.

[29] S.M. Carbotte, K.C. Macdonald, Comparison of seafloor tectonic fabric at intermediate, fast, and super fast spreading ridges: Influence of spreading rate, plate motions, and ridge segmentation on fault patterns, J. Geophys. Res. 99 (B7) (1994) 13609–13631.

[30] B.J. Murton, G. Klinkhammer, K. Becker, A. Briais, D. Edge, N. Hayward, N. Millard, I. Mitchell, I. Rouse, M. Rudnicki, K. Sayanagi, H. Sloan, L. Parson, Direct evidence for the distribution and occurrence of hydrothermal activity between 27°N–30°N on the Mid-Atlantic Ridge, Earth Planet. Sci. Lett. 125 (1–4) (1994) 119–128.

[31] D.K. Smith, J.R. Cann, M.E. Dougherty, J. Lin, S. Spencer, C. MacLeod, J. Keeton, E. McAllister, B. Borroks, R. Pascoe, W. Robertson, Mid-Atlantic Ridge volcanism from deep-towed side-scan sonar images, 25°–29°N, J. Volcanol. Geotherm. Res. 67 (4) (1995) 233–262.

[32] C.J. Wolfe, G.M. Purdy, D.R. Toomey, S.C. Solomon, Microearthquake characteristics and crustal velocity structure at 29°N on the Mid-Atlantic Ridge: The architecture of a slow-spreading segment, J. Geophys. Res. 100 (B12) (1995) 24449–24472.

[33] S.P. Huestis, G.D. Acton, On the construction of geomagnetic timescales from non-prejudicial treatment of magnetic anomaly data from multiple ridges, Geophys. J. Int. 129 (1) (1997) 176–182.

[34] E. McAllister, Tectonic processes on the Mid-Atlantic Ridge, Ph.D. Thesis, University of Leeds, Leeds, 1995.

[35] Q.J. Huggett, N.W. Millard, Towed Ocean Bottom Instrument TOBI: A new deep-towed platform for side-scan sonar and other geophysical surveys, 24th Annu. Ocean Technol. Conf., Houston, TX, 1992, pp. 349–354.

[36] N. Isezaki, A new shipboard three-component magnetometer, Geophysics 51 (10) (1986) 1992–1998.

[37] N.H. Dawers, M.H. Anders, Displacement-length scaling and fault linkage, J. Struct. Geol. 17 (5) (1995) 607.

[38] J. Escartin, R.C. Searle, N.C. Mitchell, P.A. Cowie, S. Allerton, C. MacLeod, Strain partitioning at a slow-spreading segment, Ann. Géophys. 15 (Suppl. 1) (1997) C162.

[39] R.N. Hey, F.K. Duennebier, W.J. Morgan, Propagating rifts on mid-ocean ridges, J. Geophys. Res. 85 (1980) 2647–2658.

[40] M.C. Kleinrock, B.E. Tucholke, J. Lin, Geometry and structure of inside corners and pseudofaults at a slow-spreading ridge, Trans. Am. Geophys. Union 77 (46, Suppl.) (1996) F723.

[41] S. Carbotte, K. Macdonald, East Pacific Rise 8°–10°30′N: Evolution of ridge segments and discontinuities from SeaMARC II and three-dimensional magnetic studies, J. Geophys. Res. 97 (B5) (1992) 6959–6982.

[42] S. Allerton, Distortions, rotations and crustal thinning at ridge-transform intersections, Nature (London) 340 (1989) 626–628.

[43] P. Gente, R.A. Pockalny, C. Durand, C. Deplus, M. Maia, G. Ceuleneer, C. Mével, M. Cannat, C. Laverne, Characteristics and evolution of the segmentation of the Mid-Atlantic Ridge between 20°N and 24°N during the last 10 million years, Earth Planet. Sci. Lett. 129 (1–4) (1995) 55–71.

[44] F. Guspi, Frequency-domain reduction of potential field measurements to a horizontal plane, Geoexploration 24 (1987) 87–98.

[45] S. Hussenoeder, M.A. Tivey, H. Schouten, Direct inversion of potential field data from an irregular observation surface with application to the Mid-Atlantic Ridge, Geophys. Res. Lett. 22 (23) (1995) 3131–3134.

[46] J.E. Pariso, C. Rommevaux, J.-C. Sempéré, Three-dimensional inversion of marine magnetic anomalies: implications for crustal accretion along the Mid-Atlantic Ridge (28°–31°30′N), Mar. Geophys. Res. 18 (1) (1996) 85–101.

[47] E. Irving, W.A. Robertson, F. Aumento, The Mid-Atlantic Ridge near 45°N. VI: Remanent intensity, susceptibility and iron content of dredge sample, Can. J. Earth Sci. 7 (1970) 226–238.

[48] M.A. Tivey, P.A. Rona, H. Schouten, Reduced crustal magnetization beneath the active sulfide mound, TAG hydrothermal field, Mid-Atlantic Ridge at 26°N, Earth Planet. Sci. Lett. 115 (1993) 101–115.

[49] H.P. Johnson, R. Merrill, Low temperature oxidation of a titanomagnetite and the implications for paleomagnetism, J. Geophys. Res. 78 (1973) 4938–4949.